



Provided by the author(s) and University of Galway in accordance with publisher policies. Please cite the published version when available.

Title	Investigation of various ligand design approaches and synthesis of diverse heterocyclic bioactive compounds
Author(s)	Negi, Arvind
Publication Date	2019-09-27
Publisher	NUI Galway
Item record	http://hdl.handle.net/10379/15468

Downloaded 2024-04-19T19:20:02Z

Some rights reserved. For more information, please see the item record link above.



*Investigation of Various Ligand Design approaches &
Synthesis of Diverse Heterocyclic Bioactive Compounds*

By
Arvind Negi



A Thesis presented to
The National University of Ireland
For the degree of
Doctor of Philosophy.

Based on the research carried out in the
School of Chemistry,
National University of Ireland,
Galway.

Under the supervision and direction of
Prof. Paul V. Murphy
National University of Ireland,
Galway.

Declaration

Declaration

This thesis has not been submitted before, in whole or in part, to this or any other university for any degree, and is, except where otherwise stated, the original work of the author.

Arvind Negi

Abstract

Structure-based design and ligand-based design are one of the most common approaches used to develop new inhibitors against druggable protein targets in various human disorders. Mcl-1 is a protein belongs to Bcl-2 family which has a prime role in apoptosis and therefore its targeting improvises its mitogenic effect in a number of serious complications such as neurodegenerative disorders and cancers. However, various heterocyclic cores were used to developed Mcl-1 inhibitors in last few decades (mainly, *polyphenols, thiazoles, thiazolo[3,2-a]pyrimidinone, indoles, acenaphthylene-phenalenes, pyrroles, isoquinoline-quinolines, anthraquinone-quinazolines, naphthols, salicylic-anthranilic acids, benzylpiperazines, pyrazolo[1,5-a]pyridines, isoindolines, imidazolidine-2,4-dione, non-peptidomimetic macrocycles*), and is compiled in *objective 2.1* of chapter 2 of this thesis. Also, various naturally-derived compounds (such as *gymnochrome-F, oxy-polyhalogenated diphenyl ethers, anacardic acids, endiandric acids, marinopyrroles cryptosphaerolide, meiogynins*) were also discovered in the past and had shown low micromolar activity against Mcl-1. However, lack of their biophysical studies leads to *objective 2.2* of chapter 2 where the concept of multiple-receptor conformation and multiple-ligand conformation was used initially to evaluate the employed methodology, used for finding the precise and accurate docking structures of these naturally derived Mcl-1 inhibitors. Finally, the resulted dock scores of respective naturally derived Mcl-1 inhibitors were compared with their Mcl-1 binding affinities. The previous ligand design information clearly indicates simple structures such as diphenyl propenone structures could be beneficial in tight binding to P₂-P₃ or P₃-P₄ pocket of Mcl-1 protein. Based on parent structure binding, further exploration of these structures were performed to enhance the scope of the structure-activity relationship (such as synthesis of pyrazolines, pyrazoles, *O*-phenyl alkyl bromides, *N*-substituted pyrazoles, 5-amino-4-cyano-diphenyl pyridines, symmetrical and asymmetrical triphenyl pyridines, imidazoles and indoles). However, a novel synthetic method was also developed to improve the yield and scope of triphenyl pyridines.

Chapter 3 involves the designing and synthesis of non-peptidomimetic secondary protein structures as alpha-helix or as beta-sheets where *Objective 3.1* contains synthesis of Bis-triphenyl pyridine core and Triphenyl pyridine-pyrazole core as BH3 alpha helix. This is the first time that a Bis-triphenyl core and triphenyl pyridine pyrazole core is reported. However, the second objective (*objective 3.2*) provides a computational study of macrocycle-embedded carbohydrates for serotonin isoforms and ions channels (Negi *et al.*, *Eur J Med*

Chem, 2019, 176, 292-309). The highlights of this study were the construction of the homology models of NK2, 5HT1A, 5HT2A Site-2 of the sodium channel and retro screening of *in-house* compounds.

In chapter 4, special focus was given on the biophysical studies of somatostatin isoforms and fucosidase enzyme (Zhou *et al.*, 2019, *Biorg Chem*, 2019, 84, 418-433). Initially, homology models of somatostatin isoforms (Negi *et al.*, *Eur J Med Chem*, 2019, 163, 148-159) and fucosidase enzymes were constructed and later, successfully found in agreement with Ramachandran plot, Errat plot and ProSA. Also, various ligand metrics based on lipophilicity were also used. Also, the computational studies were correlated with the IC₅₀/Ki data.

Acknowledgment

First and foremost, I would like to thank my wife, “*Nitisha Bhandari*” who has been there for me when I needed the most. Also, I would like to thank my family members: *Bhagat Singh Negi, Chaya Negi, Amresh Negi, Anita Negi, Karnika Kandari* and *Arhaan*.

I am also thankful and grateful to *Prof. Paul V. Murphy* for supervising my research throughout the Ph.D. journey. Without his kind support and time-to-time suggestions, a dream of accomplishing Ph.D. in Organic Medicinal Chemistry would not come true. Also, special thanks for his support for IRC scholarship 2014 and CoS fellowship for Ph.D. 2014.

I would like to thank the following contributors to the research:

Dr. Eva Szegezdi for supervision in screening compounds using MTT assay and putting her valuable advice in the development of Mcl-1 acceptor-donor bead assay, and *Mr. Sukhraj Dhammi* for his assistance in all biology experiments.

Special Thanks to *Dr. Claudia* for helping me out in problem-solving classes, *Dr Styliana Mirallai, Dr Laura, Dr Rekha Chaddha, Dr Vikramjeet Sarkar* and *Dr Sirinivas Jagula*, for their valuable advices and being kind as a friend during my stay in Galway, and other lab members which are very essential to mention and helped me at some stage of PhD: *Syl Byrne, Eoin Hever, Kerin Fox, Adele gabba, Jack Bennett, Fiach Meany, Lisa Doyle, Sweeny Sinclair, Nipun Mahajan, Daria Firsova*.

Special thanks to *Mrs Marian Vignoles* for helping in during experiments in Mass spectrometry and First-Year demonstrations, *Dr Roisin Doohan* for setting up and acquiring the spectra on 500 and 600 MHz NMR.

Also, I give my loveliest thanks to all my friends at NUIG.

Table of Content

CHAPTER 1	6
<i>Introduction</i>	6
CHAPTER 2	14
Objective 2.1 Literature review of various heterocyclic scaffold as Mcl-1 inhibitor development.	15
2.1.1 <i>Cancer and Apoptosis</i>	15
3.1.2 <i>Role of Bcl-2 family proteins in apoptosis</i>	16
3.1.3 <i>Mcl-1 as a Cancer Target</i>	17
3.1.4 <i>Structural insights into the Mcl-1 protein</i>	18
3.1.5 <i>Mcl-1 protein inhibitors</i>	19
<i>Polyphenols and derivatives</i>	19
<i>Thiazole derivatives</i>	22
<i>Thiazolo[3,2-a]pyrimidinone</i>	23
<i>Indole derivatives</i>	24
(a) <i>Fesik indole compounds</i>	24
(b) <i>AbbVie compounds</i>	28
(c) <i>Liu & Zhou compounds</i>	29
(d) <i>Fang group's work</i>	30
(e) <i>Zhang's group work</i>	31
(f) <i>Covalent Mcl-1 inhibitor</i>	31
<i>Acenaphthylene & phenalene derivatives</i>	32
<i>Pyrrole derivatives</i>	34
<i>Isoquinoline & Quinoline derivatives</i>	37
<i>Anthraquinone and quinazolone derivatives</i>	40
<i>Naphthol derivatives</i>	41
<i>Salicylic and anthranilic acid</i>	42
<i>Benzylpiperazine derivatives</i>	43
<i>Pyrazolo[1,5-a]pyridine</i>	44
<i>Isoindolines</i>	44
<i>Imidazolidine-2,4-dione</i>	45
<i>Oligomers</i>	45
<i>Non-peptidomimetic Macrocycles</i>	46
<i>Miscellaneous heterocyclic inhibitors</i>	47
<i>Inhibitors based on natural products</i>	50
2.1.6 <i>Conclusion</i>	52
Objective 2.2. Recognition of binding mode of the diverse natural-derived Mcl-1 inhibitor	53
2.2.1 <i>Introduction: Structural specificity of naturally occurring Mcl-1 inhibitors</i>	53
2.2.2 <i>Result and Discussion</i>	55
2.2.2.1 <i>Rationalization of molecular modeling protocols</i>	55
2.2.2.2 <i>Evaluating the precision and accuracy of docking methods</i>	58
2.2.2.3 <i>Docking of naturally occurring Mcl-1 inhibitors</i>	60
<i>Gymnochrome-F & oxy-polyhalogenated diphenyl ethers</i>	61
<i>Anacardic acid derivatives</i>	62
<i>Endiandric Acid Analogous</i>	66

<i>Marinopyrrole analogues (maritoclax & its cyclic analogue)</i>	68
MIMI (Mcl-1 Inhibitor Molecule 1)	71
<i>Cryptosphaerolide</i>	71
<i>Meiogynin derived Mcl-1 inhibitors</i>	72
2.2.3 <i>Conclusion & Future Perspective</i>	75
Objective 2.3 Synthesis of heterocyclic chemotypes as Mcl-1 inhibitors	76
2.3.1 <i>Rationale design</i>	76
2.3.2 <i>Synthesis of desired heterocyclic compounds</i>	76
<i>Synthesis of chalcones</i>	76
<i>Synthesis of Pyrazolines & Pyrazoles</i>	82
<i>Synthesis of O-Phenyl alkyl Bromides & N-substituted pyrazoles</i>	84
<i>Synthesis of diphenyl pyridines</i>	87
<i>Triphenyl Pyridines: previous reports</i>	91
<i>Triphenyl Pyridines: Reported Mechanisms for triphenyl pyridine formation</i>	92
<i>Triphenyl Pyridines: Synthesis</i>	95
<i>Development of synthetic method for formation of non-symmetric triphenyl pyridines</i>	98
(a) <i>Copper (II) triflate catalyzed triphenyl pyridine synthesis</i>	98
(b) <i>Changes to the copper triflate catalyzed method</i>	99
(c) <i>Optimisation of order of addition of reactants to improve the synthesis of non-symmetrical triphenyl pyridines</i>	99
(d) <i>Ammonification of reaction</i>	100
(e) <i>Investigating of new catalyst for synthesis of non-symmetrical triphenyl pyridines</i>	100
<i>Synthesis of Imidazoles</i>	107
<i>Quantitative NMR (qNMR) to determine the purity of imidazole dicarboxylic acid</i>	109
<i>Synthesis of indole derivatives</i>	111
<i>Unexpected formation of benzylated indole</i>	112
2.3.3 <i>Cytotoxicity of synthesized heterocycles</i>	116
2.3.4 <i>Conclusion & Future perspective</i>	118

CHAPTER 3 119

Objective 3.1 Ligand-based design and synthesis of non-peptidomimetic BH3 alpha helix based heterocyclic chemotypes	120
3.1.1 <i>Introduction</i>	120
3.1.2 <i>Result and Discussion</i>	121
3.1.2.1 <i>Ligand design and synthesis</i>	121
3.1.2.2 <i>Cytotoxicity evaluation of the BH3 α-helix mimetics</i>	135
3.1.3 <i>Conclusions & future perspective</i>	137
Objective 3.2 Rational design of multi-targeting macrocyclic ligands based on embedded carbohydrates (MECs) as protein (peptide)-protein interaction inhibitors	138
3.2.1 <i>Introduction</i>	138
3.2.2 <i>Results and Discussion</i>	139
3.2.2.1 <i>Ligand design strategy</i>	139
3.2.2.2 <i>Molecular modelling, biological evaluation and validation of the ligand design strategy</i>	143
<i>Homology modelling</i>	143
<i>Inverse docking</i>	146
<i>Docking of control inhibitors</i>	148
3.2.3 <i>Conclusion</i>	154

CHAPTER 4 **155**

Objective 4.1 To develop a proper understanding of ligand design for somatostatin receptors	156
4.1.1 Introduction	156
4.1.2 Results and Discussion	158
Compounds designed to target SSTRs	158
Binding affinities, molecular modeling and structure-activity relationship	159
4.1.3 Conclusions and Future Perspective	172
Objective 4.2 To rationalize the targeting of L-fucose analogs with fucosidases of various origin	174
4.2.1 Introduction	174
4.2.2 Results and Discussion	176
4.2.2.1 Inhibition of fucosidases and structure-activity relationship	176
4.2.2.2 Molecular modeling	177
4.2.2.3 Cytotoxicity against BT-474, MCF-7 and DU-145 cell lines using the MTT assay	197
4.2.2.4 Inhibition of proliferation of human head and neck carcinoma cell lines	198
4.2.3 Conclusions	198

CHAPTER 5 **199** **Experimental Section**

Experimental section for Objective 2.2	199
Ligand structures and minimizations	199
Selection of Protein structure	199
Preparation of Protein Structure and	199
Triangle matcher-based docking using MOE	199
Genetic algorithm-based grid docking using AutoDock	200
GRIP docking by VlifeDock	200
Post docking analysis	200
Experimental section for Objective 2.3	200
General Experimental conditions	200
General procedure for synthesis of non-hydroxylated-chalcone	201
General procedure for synthesis of hydroxylated-chalcone	201
(E)-1,3-Bis(3,4-dimethoxyphenyl)prop-2-en-1-one (2.3.10)	201
(E)-1-(4-chlorophenyl)-3-(3,4-dimethoxyphenyl)-prop-2-en-1-one (2.3.11)	202
(E)-1-(4-chlorophenyl)-3-(4-methoxyphenyl)-prop-2-en-1-one (2.3.12)	202
(E)-1-(4-Chlorophenyl)-3-(3-methoxyphenyl)-2-propen-1-one (2.3.13)	202
(E)-3-(3,4-dimethoxyphenyl)-1-(4-methoxy-3-nitrophenyl)-prop-2-en-1-one (2.3.14)	203
(E)-1-(3-Hydroxyphenyl)-3-(3,4,5-trimethoxyphenyl)prop-2-en-1-one (2.3.15)	203
(E)-1-(3-hydroxyphenyl)-3-phenylprop-2-en-1-one (2.3.16)	204
(E)-1-(3-methoxyphenyl)-3-(4-methoxyphenyl)prop-2-en-1-one (2.3.17)	204
(E)-1,3-bis(4-methoxyphenyl)prop-2-en-1-one (2.3.18)	204
(E)-chalcone (2.3.1)	205
(E)-3-(4-nitrophenyl)-1-phenylprop-2-en-1-one (2.3.20)	205
(E)-3-(4-chlorophenyl)-1-phenylprop-2-en-1-one (2.3.19)	205
(E)-1-(3,4-dimethoxyphenyl)-3-(3-nitrophenyl)-prop-2-en-1-one (2.3.22)	206
(E)-3-(3,5-dimethoxyphenyl)-1-(3-hydroxyphenyl)prop-2-en-1-one (2.3.21)	206
Synthesis of Pyrazolines and Pyrazoles	207
Pyrazolines from chalcones	207
Pyrazoles from Pyrazolines	207
Direct method for pyrazole formation from chalcones	207
3,5-Bis(3,4-dimethoxyphenyl)-4,5-dihydro-1H-pyrazole (2.3.29)	207

5-(4-Nitrophenyl)-3-phenyl-4,5-dihydro-1H-pyrazole (2.3.30)	208
5-(4-Chlorophenyl)-3-phenyl-4,5-dihydro-1H-pyrazole (2.3.31)	208
5-(4-Chlorophenyl)-3-phenyl-1H-pyrazole (2.3.32)	209
3,5-Diphenyl-1H-pyrazole (2.3.2)	209
Synthesis of bromoalkoxybenzenes	209
(4-Bromobutoxy)-benzene (2.3.37)	210
5-(4-Bromobutoxy)-2-chloro-1,3-dimethylbenzene (2.3.38)	210
1-(4-Bromobutoxy)-4-methoxybenzene (2.3.39)	210
1-(4-Bromobutoxy)naphthalene (2.3.40)	211
2-(4-Bromobutoxy)naphthalene (2.3.41)	211
Synthesis of N-substituted pyrazoles	211
1-(4-Methoxybenzyl)-3,5-diphenyl-1H-pyrazole (2.3.42)	212
1-Benzyl-3,5-diphenyl-1H-pyrazole (2.3.43)	212
1-(2-Phenoxyethyl)-3,5-diphenyl-1H-pyrazole (2.3.44)	213
1-(3-Phenoxypropyl)-3,5-diphenyl-1H-pyrazole (2.3.45)	213
1-(4-Phenoxybutyl)-3,5-diphenyl-1H-pyrazole (2.3.46)	214
General procedure for synthesis of diphenyl pyridines	215
2-Amino-4,6-diphenylnicotinonitrile (2.3.56)	215
2-Amino-6-(4-chlorophenyl)-4-phenylnicotinonitrile (2.3.57)	216
Synthesis of triphenyl pyridines by conventional route	216
General procedure for synthesis of triphenyl pyridine using methyl ketone pyridinium salt	216
Evaluation of previously reported methods for symmetrical triphenyl pyridines	217
(a) Iodine catalyzed triphenyl pyridine synthesis	217
(b) Triflic acid assisted synthesis of triphenyl pyridine synthesis	217
(c) Copper triflate catalyzed Triphenyl pyridine synthesis	217
(d) Ferrous bromide catalysed Triphenyl pyridine synthesis	217
Development of synthetic method for formation of Non-symmetrical Triphenyl pyridine	218
(1) Copper triflate catalyzed non-symmetrical Triphenyl pyridine synthesis	218
2,4,6-Triphenylpyridine (2.3.4)	218
4-(4-Chlorophenyl)-2-(3-methoxyphenyl)-6-phenylpyridine (2.3.75)	219
2-(4-Methoxyphenyl)-4,6-diphenylpyridine (2.3.76)	220
3-(4,6-Diphenylpyridin-2-yl)phenol (2.3.77)	220
4-(4,6-Diphenylpyridin-2-yl)phenol (2.3.78)	221
2-(3,4-Dimethoxyphenyl)-4,6-diphenylpyridine (2.3.79)	222
2-(3-Nitrophenyl)-4,6-diphenylpyridine (2.3.80)	223
2,6-Bis(3-nitrophenyl)-4-phenylpyridine (2.3.84)	223
4-(3-Nitrophenyl)-2-(4-nitrophenyl)-6-phenylpyridine (2.3.85)	224
2-(3,4-Dimethoxyphenyl)-4-(4-nitrophenyl)-6-phenylpyridine (2.3.86)	225
4-(4-Chlorophenyl)-2-(4-nitrophenyl)-6-phenylpyridine (2.3.87)	225
4-(4-Chlorophenyl)-2-(3,4-dimethoxyphenyl)-6-phenylpyridine (2.3.88)	226
4-(4-Chlorophenyl)-2-(3-nitrophenyl)-6-phenylpyridine (2.3.89)	226
4-(4-(4-Chlorophenyl)-6-phenylpyridin-2-yl)phenol (2.3.90)	227
4-(4-(4-Nitrophenyl)-6-phenylpyridin-2-yl)phenol (2.3.91)	228
3-(4-(4-Nitrophenyl)-6-phenylpyridin-2-yl)phenol (2.3.92)	228
3-(4-(4-Chlorophenyl)-6-phenylpyridin-2-yl)phenol (2.3.93)	229
4-(4-Chlorophenyl)-2,6-diphenylpyridine (2.3.94)	230
4-(4-Nitrophenyl)-2,6-diphenylpyridine (2.3.95)	230
2-(3-Methoxyphenyl)-4-(4-nitrophenyl)-6-phenylpyridine (2.3.96)	231
4-(4-Chlorophenyl)-2-(4-methoxyphenyl)-6-phenylpyridine (2.3.97)	231
2-(4-Methoxyphenyl)-4-(4-nitrophenyl)-6-phenylpyridine (2.3.98)	232
Synthesis of imidazole	232
5-Amino-1-benzyl-1H-imidazole-4-carbonitrile (2.3.101)	232

<i>1-Benzyl-5-(benzylamino)-1H-imidazole-4-carbonitrile (2.3.102)</i>	233
<i>General procedure for synthesis of N-benzyl-1H-imidazole-4,5-dicarbonitrile</i>	234
<i>General procedure for N-benzyl-imidazole-4,5-dicarboxylic acid</i>	234
<i>Quantification of NMR (qNMR)</i>	234
<i>1-Benzyl-1H-imidazole-4,5-dicarboxylic acid (2.3.107)</i>	235
<i>1-(4-Methoxybenzyl)-1H-imidazole-4,5-dicarbonitrile (2.3.106)</i>	235
<i>1-(4-Methoxybenzyl)-1H-imidazole-4,5-dicarboxylic acid (2.3.108)</i>	235
<i>Synthesis of indole derivatives</i>	236
<i>Ethyl 1-(4-phenoxybutyl)-1H-indole-2-carboxylate (2.3.111)</i>	236
<i>General procedure for 3-Methoxybenzyl-1H-indoles</i>	237
<i>3-(4-methoxybenzyl)-1H-indole (2.3.114a)</i>	237
<i>5-Chloro-3-(4-methoxybenzyl)-1H-indole (2.3.115)</i>	238
<i>Ethyl 1-(4-methoxybenzyl)-1H-indole-2-carboxylate (2.3.116)</i>	238
<i>1-(4-Methoxybenzyl)-1H-indole-2-carboxylic acid (2.3.117)</i>	239
<i>Cytotoxicity evaluation of synthesized compounds</i>	239
<i>Cell culture</i>	239
<i>Cell counting and cell number determination</i>	240
<i>MTT cell proliferation assay</i>	240
<i>MTT assay protocol</i>	241
<i>Experimental Section of Objective 3.1</i>	241
<i>Preparation of bis-chalcones</i>	241
<i>Impurity and TLC profiles from reactions described herein</i>	241
<i>(2E, 2'E)-1,1'-(1,4-Phenylene)-bis(3-(3,4-dimethoxyphenyl)-prop-2-en-1-one) (3.1.3)</i>	241
<i>(2E,2'E)-1,1'-(1,3-phenylene)-bis(3-(3,4-dimethoxyphenyl)-prop-2-en-1-one) (3.1.5)</i>	242
<i>(2E,2'E)-1,1'-(1,4-Phenylene)-bis(3-(3,4,5-trimethoxyphenyl)-prop-2-en-1-one) (3.1.7)</i>	243
<i>(2E,2'E)-1,1'-(1,3-Phenylene)-bis(3-(3,4,5-trimethoxyphenyl)-prop-2-en-1-one) (3.1.8)</i>	244
<i>Preparation of bis triphenyl pyridine 3.1.9</i>	245
<i>Bis-Triphenyl Pyridine [1,4-bis(4-(3,4-dimethoxyphenyl)-6-phenylpyridin-2-yl)-benzene] (3.1.9)</i>	245
<i>General method for preparation of acetylated chalcones</i>	246
<i>(E)-1-(4-Acetylphenyl)-3-(3,4-dimethoxyphenyl)prop-2-en-1-one (3.1.10)</i>	246
<i>(E)-1-(3-acetylphenyl)-3-(3,4-dimethoxyphenyl)-prop-2-en-1-one (3.1.11)</i>	247
<i>(E)-1-(4-acetylphenyl)-3-(3,4,5-trimethoxyphenyl)-prop-2-en-1-one (3.1.11)</i>	247
<i>(E)-1-(3-acetylphenyl)-3-(3,4,5-trimethoxyphenyl)prop-2-en-1-one (3.1.13)</i>	248
<i>Preparation of acetylated triphenyl pyridines</i>	249
<i>1-(4-(6-(4-bromophenyl)-4-(3,4-dimethoxyphenyl)-pyridin-2-yl)-phenyl)-ethan-1-one (3.1.14)</i>	249
<i>1-(4-(4-(3,4-dimethoxyphenyl)-6-phenylpyridin-2-yl)phenyl)ethan-1-one (3.1.15)</i>	250
<i>Preparation of Pyrazole-pyridine conjugate</i>	251
<i>[3-(4-(4-(3,4-dimethoxyphenyl)-6-phenylpyridin-2-yl)phenyl)-1-(4-methoxyphenyl)-1H-pyrazole-4-carbaldehyde] (3.1.17)</i>	251
<i>Cytotoxicity evaluation of synthesized heterocyclic compounds as BH3 mimetics</i>	252
Experimental section of Objective 4.1	253
<i>Homology Modelling & refinement</i>	253
<i>Molecular Docking</i>	253
Experimental section of Objective 4.2	254
<i>Molecular modelling</i>	254
REFERENCES	255

Chapter 1

Introduction

What are the Targets?

The term, “target” represents a broad range of biological entities of the body where a drug can bind and is connected with the physiological state of any disease condition [1]. Targets mainly include receptors, such as G-protein coupled receptors (like somatostatin receptors, serotonin receptors, and cannabinoid receptors), Ion channels (like sodium channels, potassium channels), Enzyme-linked receptors (like kinase receptors), nuclear receptors (like estrogen and steroid receptors); accessory proteins or down signalling proteins and enzymes (fucosidase and other metabolic enzymes). However, it has been estimated that not even 25% of all known proteins are have had their 3D structure determined up to now [2], which limits the use of most conventional drug designing approaches such as structure-based drug design and fragment-based design and, therefore in such cases only ligand-based design approaches are applicable. However, recent development and incorporation of new physical/biophysical parameters in computational chemistry improve the overall accuracy of these tools in the construction of a hypothetical model of an unknown structure of protein, which also called as homology modeling.

What is Homology modeling

Homology modeling is a very useful computational tool, where a three-dimensional atomic model of an unknown structure protein (more commonly called as, “target protein”) is constructed from its primary amino acid sequence by using a template (which is usually a homologous protein of known structure). However, the concept of homology modeling mainly relies on the basis that the primary sequence of at least one or two proteins of known three-dimensional structures is likely to resemble with the query sequence. However, it has been noticed that if a template protein doesn’t match with more than 25% identity with the target sequence then it could be assumed to have a very different protein structure then the target protein. Moreover, 35% is the minimum limit of identity required for a template protein for building a reliable homology model [3].

There are five steps involved in homology modeling [4, 5].

a) Selection of template

The target protein sequence is either retrieved from Uniprot or NCBI website. Later, a Blast search on target sequence on a protein structure database provides a number of protein

structures as a possible candidate in a role of template for constructing a homology model, based on their pairwise sequence alignment score with the target sequence.

b) Geometry assignment of amino acids of the target sequence

The geometry specification for amino acid residues of the target sequence is initially copied from similar regions of a template. If target sequence and template sequence share similar regions of conserved domains, then all coordinates of amino acid residues of target sequence directly copied, otherwise, backbone coordinates only copied (as amino acids share same backbones, except their side chains). While, if a proline residue of the target sequence is aligned to a non-proline amino acid residue of selected template and the ϕ dihedral angle at that position is positive, then no coordinates are copied, and position would be considered as an *indel* (explained below).

c) Editing of missing gaps in the sequence

After an initial geometry assignment for building a homology model from a template, there would be few residues usually left with no assigned backbone coordinates. These residues are usually either found in loops or outgaps or in deletions regions. In the latter case, it is unlikely that copied geometry in deletion regions would be correctly assigned therefore indels are usually used, which are modeled fragments from high-resolution chains retrieved from the protein data bank.

d) Selection of appropriate loop modeling and side-chain packing

After indels collections, a set of independent models for loops are created in a random fashion. For each loop, an energy function is used to analyze the list of possible candidates and then later selected based on ranking. After loop modeling, side chains are then modeled, which usually retrieved from an extensive rotamer library generated by systemic clustering of conformations and selected by a Unary Quadratic Optimisation and further optimized packing is performed. Later, missing hydrogens are added to complete the valency of atoms of the model and thereafter model undergoes a series of minimizations to resolve any steric clashes between the atoms of amino acid residues.

e) Selection of model and refinement

There are several parameters which provide information related to the quality of structure in order to select a final model, as enlisted below.

- (i) RMSD of each intermediate model to the average positions of all the intermediate models
- (ii) Electrostatic Solvation energy: this uses a generalized born/volume integral (GB/VI) methodology to score the models [6]
- (iii) Residue packing quality function, which utilizes previous knowledge in which similar amino acid residues typically find themselves. Each residue is characterized based on solvent accessibility and its involvement in H-bond contacts and the ratio of polar vs non-polar contact atoms in its microenvironment.
- (iv) An estimation of the *effective atomic contact energy* which determines effective energy difference if residue-solvent contacts replaced with residue-residue contacts and are then compared with observed contact frequencies in a database of high resolved protein structures

Evaluation of Homology model

The constructed homology model is then evaluated against a set of parameters, which are listed below, to assess the quality of the structure.

- (a) Ramachandran Plot: The Ramachandran plot is one of the most important tools to evaluate the stereochemical quality of all the amino acids in a constructed homology model. It displays the ψ and ϕ backbone conformational angles (torsional angles) for each residue of homology model, which can be represented as, ϕ is the N (i-1), C (i), C α (i), N (i) torsion angle while ψ is the C (i), C α (i), N (i), C (i+1) torsion angle [7]. The plot is divided into 4 main regions: most favored regions, additional favored regions, generously favored regions and disallowed regions (*as shown in later of the thesis in case of somatostatin receptors, fucosidase enzyme, serotonin isoforms, NK2 and site-2 of sodium channel*). In a Ramachandran plot, the main core (containing alpha and beta sheets) or allowed regions are the areas in the plot show the preferred regions for residues in a protein. If the homology model is reliable, most ψ/ϕ angle pairs would be in the favored regions of the plot and only a few would be in disallowed regions. This also helps in highlighting amino acids or regions of the homology model of unusual geometry. For running a Ramachandran plot, the easiest option is to use a web tool called “PROCHECK” which evaluates covalent geometry, planarity, dihedral angles (Ramachandran plot), chirality, non-bonded interactions, main-chain hydrogen bonds, disulfide bonds and stereochemical parameters

of homology model [8]. Those amino acids which were not in agreement with the consistent stereochemistry based on Ramachandran plot (called as “outliers”) are further energy minimized.

- (b) The ERRAT program analyses the statistics of non-bonded interactions between different atom types, to give the plot of the value of the error function versus position of a 9-residue sliding window (*as shown in later in the thesis of somatostatin receptors, fucosidase, serotonin isoforms, NK2 and site-2 of sodium channel*) [9]. By comparing with highly refined structures, the error values have been calibrated to give confidence limits [9]. In the plot, two lines are present on error axis to indicate the confidence with which the residues that exceed error value can be rejected. The overall quality factor is expressed as a percentage of protein for which the calculated error value falls below the 95% rejection limit.
- (c) ProSA examines a PDB file and generates a score based on the quality of the local structure surrounding each residue, based on the typical ranges of dihedral angles and side-chain contacts observed in real proteins [10]. This program generates a plot which gives a measure of structure error at each residue in the protein. It also calculates an overall score for structural quality (*as shown in later of the thesis in case of somatostatin receptors, fucosidase enzyme, serotonin isoforms, NK2 and site-2 of sodium channel*). The overall measure of quality is given at the top of the plot, and each bar in the histogram is shaded according to the significance of the local structural error (*as shown in later chapter objectives*).
- (d) In verify 3D, the accuracy of the 3D model is ascertained by comparing it with its own sequence using a 3D profile calculated using atomic coordinates of its structure. 3D profiles of correct protein structure have high S scores in contrast with poor structures with low S scores. The S score/3D-1D profile score is the sum over all residue positions of a 3D-1D score for amino acid sequence of the protein (*as shown in later of the thesis in case of fucosidase enzyme of different origins*) [11].

Molecular Docking

Molecular docking is one of most extensively used computational tools nowadays to predict an orientation of one molecule with respect to another molecule to form a stable complex, which could be either “small molecule vs macromolecule” or “macromolecule vs macromolecule” (e.g.

protein-DNA, protein-protein). The biological relevance of docking could be seen from interacting partners as their complementary binding conformation with each other is of prime importance which alters any biochemical state of the cell. Such as, insulin and IGF-1 are two different endogenous peptide structures which bind to insulin receptor within a close range of affinities irrelevant of their structural differences providing sufficient evidence that both peptides somehow attained similar conformational during their binding, also presenting a prime example of the induced fit theory of protein/enzyme kinetics. However, binding of these peptides to insulin receptor brings a different overall cellular change as one (insulin peptide) does increase the cellular uptake of glucose in skeletal muscle while IGF-1 binding brings mitogenic alterations like cellular division and differentiation. In recent time, molecular docking is extensively used in structure-based drug design approach as it helps in suggesting a putative binding conformation against a particular binding site of a target of interest which could further rationalize the concept of drug design in various medicinal chemistry projects. However, docking is broadly utilized two approaches: Shape matching method and simulated docking.

Shape matching method

This approach has been called with various names, depending on the concept/method used for docking: *Shape matching method* or *geometric matching* or *shape complementary method*. Generally, under this approach, a certain number of biophysical features are considered (or taken into account), based on the complementary structure of both target and ligand. These features include the solvent-accessible surface area of target vs ligand molecular surface area; complimentary geometric shape of target and ligand; hydrophobic/hydrophilic features of pockets in target with respect to hydrophobic/hydrophilic functional groups in ligand structures. However, this approach of docking is typically fast and ligand is with flexible feature can be additively added during docking but still lacks the elementary information required to study or accurately measure the dynamic changes in ligand-protein conformation. These approaches could be usually in ligand virtual screening, pharmacophore-based approaches, and peptide-protein docking.

Simulated Docking

The limitation of the shape matching method is overcome by using molecular dynamics assisted docking where docking of a ligand is simulated. In this approach a ligand is left in space, to interact with the active site of the target. The dynamic nature of ligand conformation is accounted for based on energy change with respect to change in amino acid backbone of binding site during its adoption

of any specific binding conformation. Each of these conformations induces a total energetic cost of the system and therefore can be precisely calculated. These approaches mainly involve grid-based docking and induced fit docking.

Issues with molecular docking

Often, it is assumed that a low binding computational score proportionally associated with the binding affinity of molecules. However, docking can be divided into two parts: finding a correct positioning of a ligand-binding conformation in context of a particular binding site (i.e. binding pose or binding conformation) and its successful identification or attained highest rank by using a scoring function (scoring). However, these two points are still of huge concern and need to be addressed every time whenever docking is incorporated in any research projects {Erickson, 2004 #441}. Although, the deficiency of docking in reproducing the results is mainly based on some of the enlisted key factors like (i) inadequate incorporation of factors over the ligand-protein interacting space, electrostatics, electronic polarization, aqueous desolvation and ionic effects, (ii) lack of knowledge about factors accounting for entropy changes during ligand binding to the target (iii) insufficient ligand conformer sampling (iv) inadequate sampling and weighting of protons (such as in case of tautomers, rotamers) and charges states of ligand and target (v) assumption of rigidity in target state (vi) lack in scoring functions to rank properly the final ligand binding conformations to the target [12].

Protein-protein interactions

Protein-protein interactions (PPIs) are highly specific physical contacts between two or more different proteins, which ultimately leads to altering of a biochemical event in a cell. These interactions are highly governed by electrostatic forces between amino acids of both protein partners, also called “hot spots”. Although, most of the human proteins have multi-partner proteins and, therefore serves as number of possible key combination in regulation/transduction of any signal to a function for maintaining a normal homeostasis (like cellular translation and transcription, multi-molecular assembly of protein subunits, regulation of immune response), but also found in malfunctioning and diseases (say e.g. Creutzfeldt–Jakob, Alzheimer's diseases) [13]. Although, in 1980’s when the resolution of protein structure improved it was seen that mainly that these surfaces are flat and larger than the comparative small-molecule druggability space. *More details on protein-protein interactions have been provided in objective 4.1 and objective 4.2 of chapter 4.*

Ligand designing

There are a number of physicochemical factors involved, which affects the bioavailability of drug, however in this chapter only Lipinski's rule of five and lipophilicity are discussed.

The Lipinski's rule of five was reported in 1997 [14], which were concerned with the drug-like character of small molecules and involves molecular and structural parameters like molecular size, shape, lipophilicity, hydrogen bonding and polarity. This rule of five was derived from a database of clinical candidates reaching either in Phase II clinical trials or which reached a consequent phase. This rule is useful to evaluate the oral route tolerance of relevantly small and moderately lipophilic molecules [14, 15]. However, a good agreement of a compound with Lipinski's rule of five does not guarantee that a compound is pharmacologically active. In order to get in the agreement with this rule, an orally active drug or new chemical entity (NCE) should have no more than one violation of the following criteria:

- No more than 5 hydrogen bond donors (the total number of nitrogen-hydrogen and oxygen-hydrogen bonds: OH + NH count), this parameter is quite useful where the active site contains basic amino acid residues.
- No more than 10 hydrogen bond acceptors (all nitrogen or oxygen atoms) this parameter is quite useful where the active site contains acidic amino acid residues.
- A molecular mass less than 500 daltons (Da): lower molecular mass is an indicator of likely transport across the membrane.
- Lipophilicity: this is a structure-dependent parameter calculated in terms of octanol-water partition coefficient [16] ($\log P$) and $\log P$ should not be greater than 5.

The parameter which mostly influences bioavailability is lipophilicity, and altering lipophilicity is extensively exploited by drug discovery researchers in various forms of ligand metrics. It also depends on the solubility of the molecule or NCE.

Lipophilicity and ligand metrics

Lipophilicity has been extensively exploited and correlated with various characteristics of drugs, such as their solubility and permeability across the membranes [17-19]; their metabolism and pharmacokinetics [20]; their potency [21], selectivity, and promiscuity [22]; and also altering the pharmacodynamic and toxicological profile [23]. A trend has been observed that high lipophilicity (> 5) leads to rapid metabolic turnover [24], low solubility, and poor absorption [14] of drug-like compounds. Molecules with too high lipophilicity had increased chances of *in-vitro* target

promiscuity [19, 21, 22, 25-28] and *in-vivo* cellular toxicity [23, 29, 30], along with poor solubility and metabolic clearance. On other hand, molecules with too low lipophilicity exhibited poor ADMET properties. However, average lipophilicity value of drugs has slightly changed since 1983 for oral drugs (2.6) and a trend was found that lipophilicity increases as drug candidates progress through Phase I, II, and III. However, Lipinski stated that a log P value (lipophilicity range) less than 5 is a key for a NCE to reach Phase II clinical trials [14], but Gleeson specifically stated that a NCE (of mol. Wt less than 400) with log P < 4 has better chance of success and having optimised ADMET parameters [20].

Also, lipophilicity has been merged into other parameters. Ligand efficiency is one of them and, defined as the binding free energy for a ligand divided by its molecular size [31]. Ligand efficiency (LE) has become a significant tool in drug discovery as because of the incorporation of larger or bulkier hydrophobic ligands needed in certain types of drug discovery projects with NCEs. These include CNS drug discovery projects, where drug needs to cross the blood-brain barrier, antiprotozoal drug discovery, where the drug has to cross increasingly lipophilic membranes of parasites and; protein-protein interactions, where the interfaces are flat, featureless and requires hydrophobic bulky groups in ligand structures for binding. In recent time, LE gained significant level of usability in fragment-based design approaches, where it assesses the relative binding efficiencies of the fragments [32]. The fragment-based design utilizes the concept, that there is additivity from the different functional groups in a drug candidate structure, therefore now LE is in common practice to optimize different regions in a lead structure [32].

Leeson and Springthorpe introduced another lipophilicity derivatized parameter, lipophilic ligand efficiency (LLE or LiPE) which links the potency and lipophilicity in an order to estimate drug-likeness. LLE is the difference between log P (or log D) and the negative logarithm of a potency measure (pK_d, pK_i). LLE also considered being optimal if found between 5 and 7 [23]. There are various examples of LE and LLE in optimization of drug-like compounds, such as identification of novel α -acyloxy carboxamides as caspase-3/7 activators [33]; indanone derivatives as MAO B/H3R dual-targeting ligands for treatment of Parkinson's disease [34], inhibitors for dopamine (D3) and histamine (H4) receptor [35]; 2-hydroxynicotinamide derivatives as Mcl-1 inhibitors [36]; discovery of drug-like inhibitors of 15-lipoxygenase-1 [37]; N-substituted piperidin-4-yl-methanamine as CXCR4 chemokine receptor antagonists [38]; Non-imidazoles as ligands for histamine H3 receptor [39].

Chapter 2

This chapter includes various studies related to the heterocyclic chemotypes as Mcl-1 inhibitors

Therefore, based on studies the sections were divided into three objectives:

Objective 2.1. Literature review of various heterocyclic scaffolds in Mcl-1 inhibitor development.

Objective 2.2. Study of the binding mode of the diverse classes of naturally derived Mcl-1 inhibitor

Objective 2.3. Investigation of various heterocyclic scaffolds in Mcl-1 inhibitor development.

Objective 2.1 Literature review of various heterocyclic scaffold as Mcl-1 inhibitor development.

The first section of this chapter is a review where I compiled structure-activity data for all the heterocycles investigated as inhibitors of Mcl-1, and compare them in terms of, “how heterocyclic core or scaffolds can be used and derivatized to alter Mcl-1 activity. As the aim of this chapter is to develop new inhibitors for target Mcl-1 dependent apoptosis in cancer, and therefore I commence this section providing an overview of cancer and apoptosis.

2.1.1 Cancer and Apoptosis

Any cancer is a serious and complex cellular disorder that leads to abnormal cell growth and proliferation. Hanahan and Weinberg described it by its 8 different hallmarks, as briefly summarized in **Figure 1**: (a) sustaining proliferative signaling, (b) inducing angiogenesis, (c) evading immune destruction, (d) activating invasion and metastasis, (e) evading growth suppressors, (f) enabling replicate immortality, (g) reprogramming of energy metabolism, (h) resisting cell death (i.e. apoptosis). Among all these 8 hallmarks, metastasis and apoptosis are considered as most threatening and therefore their targeting with new inhibitors sustainably improves the longevity and standard of living for a cancer patient.

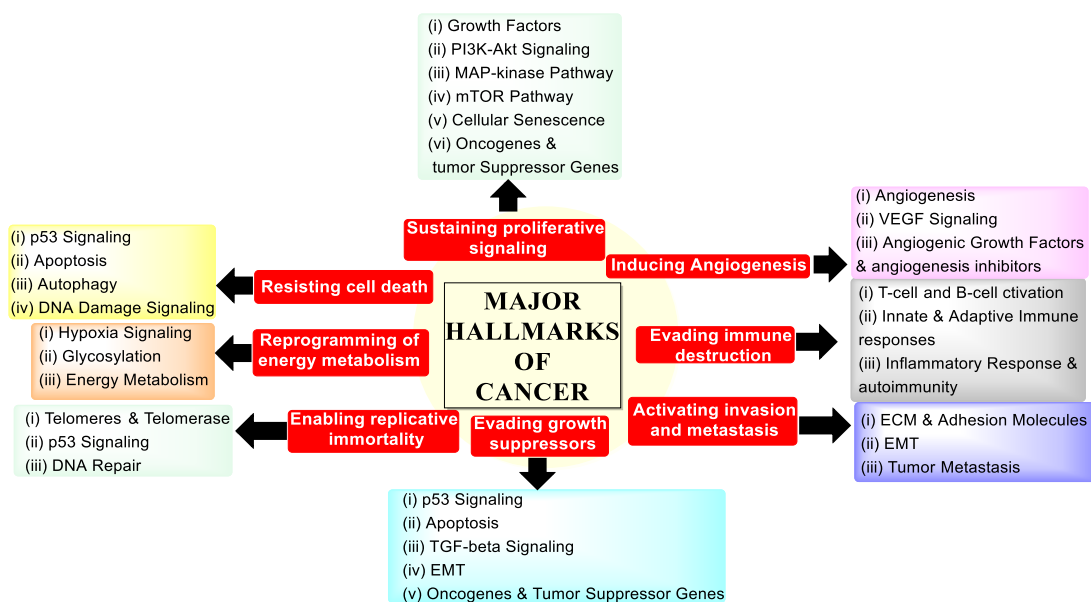


Figure 1 Eight major hallmarks of cancer

Apoptosis is a necessary key function for normal cellular physiology. Its evasion in cancer is often found as a key attribute in precipitating the resistance against various anticancer chemotherapy [40]. Broadly, there are two pathways to induce apoptosis in a cell: extrinsic pathway and intrinsic pathway. In most cases, the extrinsic apoptosis pathway is activated by ligands of tumor necrosis

factor receptors (TNFR) superfamily or Fas and DR4/DR5 receptors [41]. While, the intrinsic pathway is regulated by Bcl-2 family proteins [42].

3.1.2 Role of Bcl-2 family proteins in apoptosis

The intrinsic apoptosis pathway is initiated by exogenous and endogenous stimuli, such as DNA damage, ischemia, oxidative stress, chemotherapy or radiotherapy. The interplay between the B-cell lymphoma 2 (Bcl-2) family proteins hold a key in the activation of the intrinsic pathway. The proteins of the Bcl-2 family are divided into 2 main subgroups based on their structural homology: (a) pro-apoptotic, which are single Bcl-2 homology 3 domain proteins (also known as, “BH3-only proteins”), such as Bid, Bim, Bad, Puma, Bmf, and Noxa; and (b) multiple BH domain containing proteins, which are further divided into two subcategories, one which includes pro-apoptotic proteins such as Bcl-2 associated X protein (Bax), Bcl-2 homologous antagonist/killer (Bak) and Bcl-2 family apoptosis regulator (Bok), while the other one includes anti-apoptotic proteins (such as Bcl-2, Bcl-xL, and Mcl-1).

When stimulated by an apoptotic signal, BH3-only proteins activate the apoptotic effector proteins Bax and Bak by two ways, either by binding directly to Bax and Bak or by binding to free state anti-apoptotic proteins (such as Bcl-2, Bcl-xL, Mcl-1) to set free Bax and Bak. Further, oligomerization of Bax and Bak forms a pore on the mitochondrial membrane (also, called as “mitochondrial outer membrane permeabilization (MOMP)), through which cytochrome-c goes into the cytosol, leads to the formation of apoptosome and activation of the caspase cascade and finally results in apoptosis [43]. On the other hand, the antiapoptotic proteins tend to block the formation of oligomerization of Bax and Bak, which arrests cell death. Therefore, their relative ratios inside the mitochondria have a high significance in deciding the fate of cell either to die or to live, as shown in **Figure 2**.

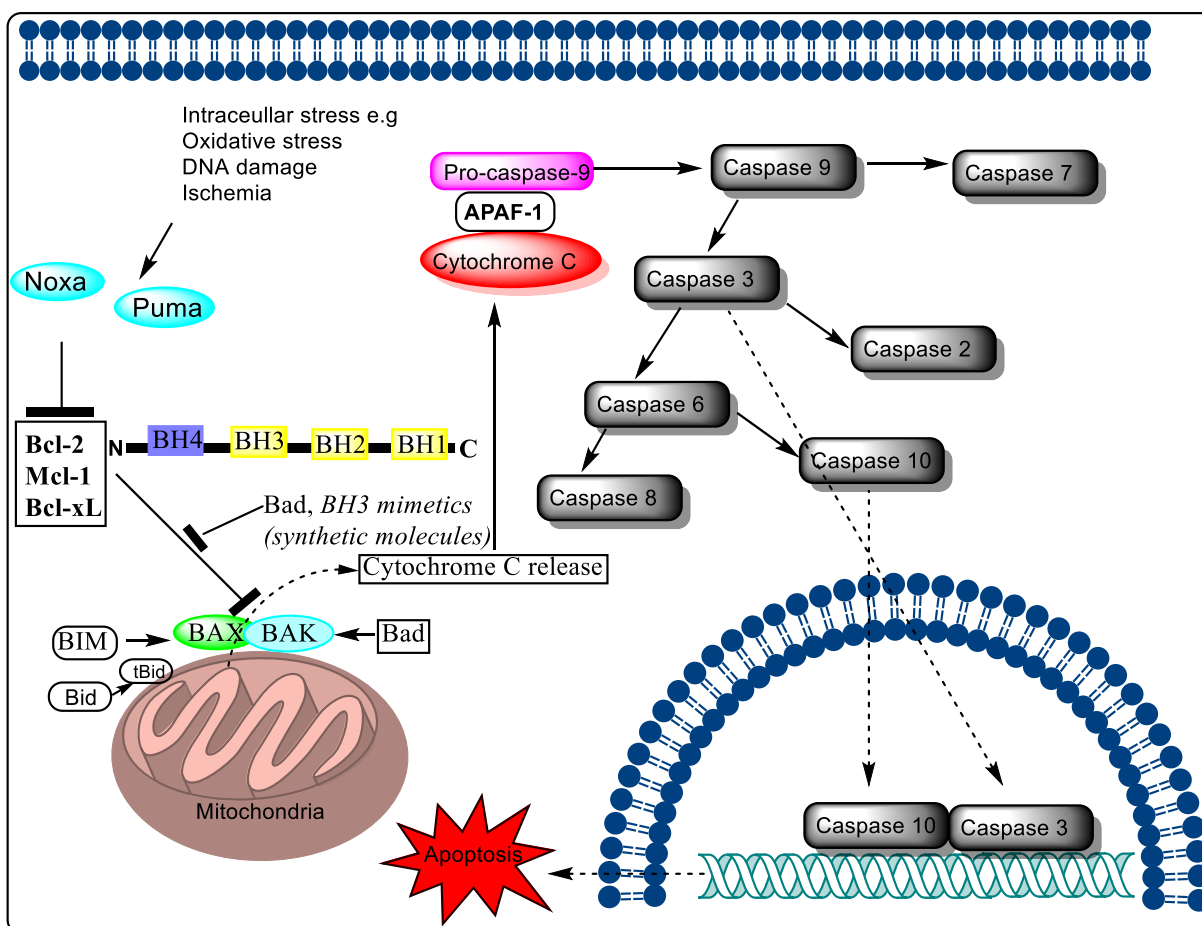


Figure 2 Intrinsic pathway of apoptosis: The pro-apoptotic molecules cause permeabilization of the outer mitochondrial membrane, leading to efflux of cytochrome c, which binds the adaptor Apaf-1 and the initiator caspase-9 in the cytosol to form the apoptosome complex. This stimulates caspase-9, which in turn activates the effector caspases. The anti-apoptotic proteins Bcl-2 and Bcl-xL inhibit cytochrome c release, whereas Bax, Bak, and Bid, all pro-apoptotic proteins, promote its release from mitochondria. Cytochrome c and deoxyadenosine triphosphate (dATP) bind to APAF-1 to form a multimeric complex that recruits and activates pro-caspase-9, that in turn activates the caspase cascade, resulting in cell apoptosis. During this process, caspase-2, caspase-8, caspase-9, and caspase-10 are involved in the initiation of apoptosis. Caspase-3, caspase-6, and caspase-7 are involved in apoptosis. Caspase-3 and caspase-7 regulate the inhibition of DNA repair and start DNA degradation which also further contribute in inducing cellular apoptosis. Synthetic molecules that block Bcl-2/Mcl-1/Bcl-xL interaction with BH3 helix of Bid, Bim, Bad, Puma, Bmf, and Noxa, which leads to increase the intracellular level of BAX/BAK and resulted in their oligomerization to form a pore, through which cytochrome-c release into the cytosol and activates the intrinsic pathway of apoptosis in tumour cells.

3.1.3 Mcl-1 as a Cancer Target

In cancer, the relative activity ratio is inclined more towards the antiapoptotic than apoptotic proteins, therefore, most of the antiapoptotic proteins serve as attractive targets in various cancers [44]. Various strategies were implemented to identify inhibitors of these in the last few decades, but only few molecules (small molecule inhibitor, SMI) have been a success clinically: **(R-(-)-Gossypol (AT-101)** [45], **GX15-070 (Obatoclox)** [46], **ABT-737**, **ABT-263** [46, 47]), **ABT-199**. A few compounds are also in preclinical development (see **Figure 3**). As an important member of

the Bcl-2 family, the anti-apoptotic nature of Mcl-1 is one of the most frequently observed in various cancers and in cases of resistance towards anticancer therapies. Also, its overexpression has been reported in human breast [48], non-small cell lung [49], melanoma [50, 51], leukemia [52], ovarian [53] and liver cancers [54, 55]. Even its high expression drives the resistance against **ABT-199** and its analogues therefore limits their utility in other types of cancers [42]. Also, Mcl-1 is responsible for resistance in various other conventional chemotherapies, like cisplatin-resistant ovarian carcinoma cells [51, 56], lapatinib resistance in HCT116 cells (human colon cancer cell line) [57], resistance to prednisone in MLL-rearranged infant acute lymphoblastic leukemia [58]. However, studies show that its downregulation or reducing its stability, improves either, the sensitivity or efficacy of other drugs in solid tumors and blood cancers [52, 59, 60], such as, it improves the chemosensitivity to gemcitabine in pancreatic carcinoma [61] and triggers apoptosis in case of taxol and vincristine based chemotherapies [62]. Therefore, number of research groups have been working to develop Mcl-1 inhibitors in recent years.

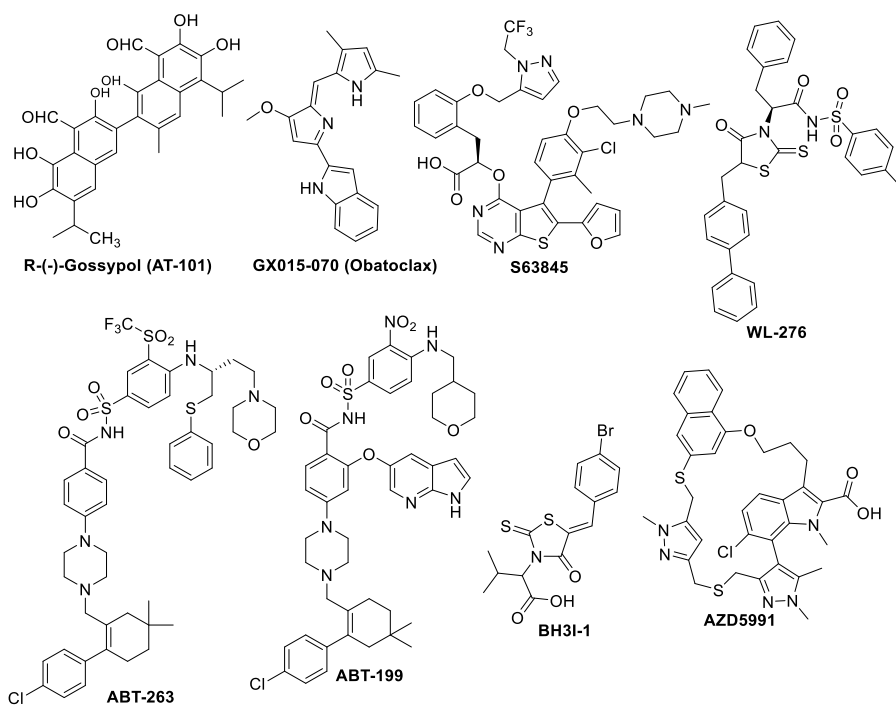


Figure 3 Representation of small molecule inhibitors of anti-apoptotic Bcl-2 family.

3.1.4 Structural insights into the Mcl-1 protein

Structurally, the Mcl-1 gene forms two products through alternative splicing where one is a larger form (Mcl-1 protein) whereas another form is smaller (called as Mcl-1s or Mcl-2 and works as an apoptotic protein). The larger form (i.e. Mcl-1) protein has three BH domains, while the other anti-

apoptotic proteins contain four BH domains. However, while Mcl-1 lacks one BH domain less than other members, it still is the largest member among these proteins, contains 350 amino acid residues [63]. In addition, it is also different from other anti-apoptotic proteins in its N-terminus. It has two weak (lower case) and two strong (upper case) PEST (proline/glutamic acid/serine/threonine) regions on the basis of pest score which is -45 to +50 (weak pest has -5 to 0 while strong PEST has score >0) [64]. The PEST regions may be responsible for Mcl-1's short half-life (<1-4 hr) in that they are recognized for the rapid degradation of proteins [65]. Furthermore, Mcl-1's N-terminal region contains regulatory motifs that account for the expression of Mcl-1 protein to respond to intra/ extracellular stimuli [63]. Also, it has a transmembrane (TM) domain in C-terminal region which helps Mcl-1 mainly locate at the mitochondrial outer membrane [55] (as shown in **Figure 3**). Also, it contains 4 pockets (P₁, P₂, P₃, P₄) which could occupy 4 hydrophobic side chains (H1, H2, H3, H4) of α -helix of a BH3 peptide of pro-apoptotic member. Therefore, BH-3 helix is an α -helix which was used to develop small molecule-based ligands against Mcl-1.

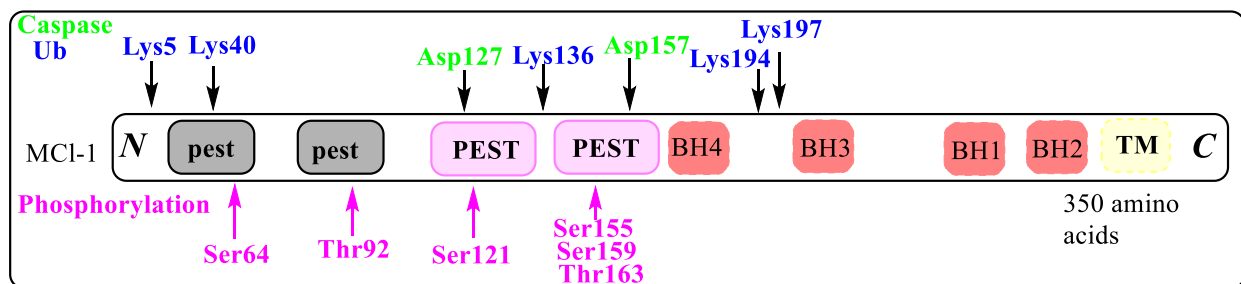


Figure 3 Sequence structure representation of Mcl-1 protein. The PEST regions [66], are more enriched in proline (P), glutamate (E), serine (S) and threonine (T) residues, which are characteristic features of rapidly degraded proteins [67], contains two caspase cleavage sites (shown in Green color), ubiquitination sites (shown in blue) and phosphorylation sites (magenta). Differential phosphorylation at these specific sites results in different outcomes [68]

3.1.5 Mcl-1 protein inhibitors

Polyphenols and derivatives

In 2002, Wang's group at the University of Michigan showed **R-(-)-gossypol (AT-101)** is a Bcl-2 family inhibitor. **AT-101** was also found to inhibit all anti-apoptotic of Bcl-2 family except Bfl-1 [69]. Although, when the Wang group tried to derivatized the (-)-gossypol (K_i value from fluorescence polarization assay (FPA) method: Bcl-xL: $0.32 \pm 0.02 \mu\text{M}$; Bcl-2: $0.48 \pm 0.04 \mu\text{M}$; Mcl-1: $0.18 \pm 0.01 \mu\text{M}$) into a more preferential selective synthetic molecule (**TW-127**, K_i value (FPA method): Bcl-xL: $0.29 \pm 0.06 \mu\text{M}$; Bcl-2: $1.11 \pm 0.4 \mu\text{M}$; Mcl-1: $0.26 \pm 0.01 \mu\text{M}$), they achieved a dual inhibitor (Bcl-xL/Mcl-1) [70], as shown in **Figure 5**. Further, derivatization leads

to apogossypol (**ApoG2**), which showed ~ 20 fold more selectivity for Bcl-2/Mcl-1 as compared to Bcl-xL [71]. Later based on the **AT-101** structure, the Pellecchia group (at Burnham Institute for Medical Research) utilized structure-based design to improve the affinity against the Bcl-2 family members (**2.1.1** & **2.1.2**) [72]. They also tried to resolve the optical isomers and found (*R*, -, *R*) stereoisomer for **3.1.2** (**BI-97C1**) was most active [73]. Later derivatization of the **ApoG2** structure led to formation of pan-Bcl-2 inhibitors (**BI97D6**) [74], which were further optically purified to the (-) stereoisomer (-)-**BI97D6** [75], as shown in **Figure 6**. While, the naturally occurring (-)-epigallocatechin gallate (**EGCG**) showed a similar activity profile to **AT-101**, with inhibitory activity in the submicromolar range for Bcl-2 ($K_i = 490$ nM) and Bcl-xL ($K_i = 335$ nM) [76] while Reed & coworker, later found it as highly active to most of Bcl-2 family members [69], as shown in **Figure 6**.

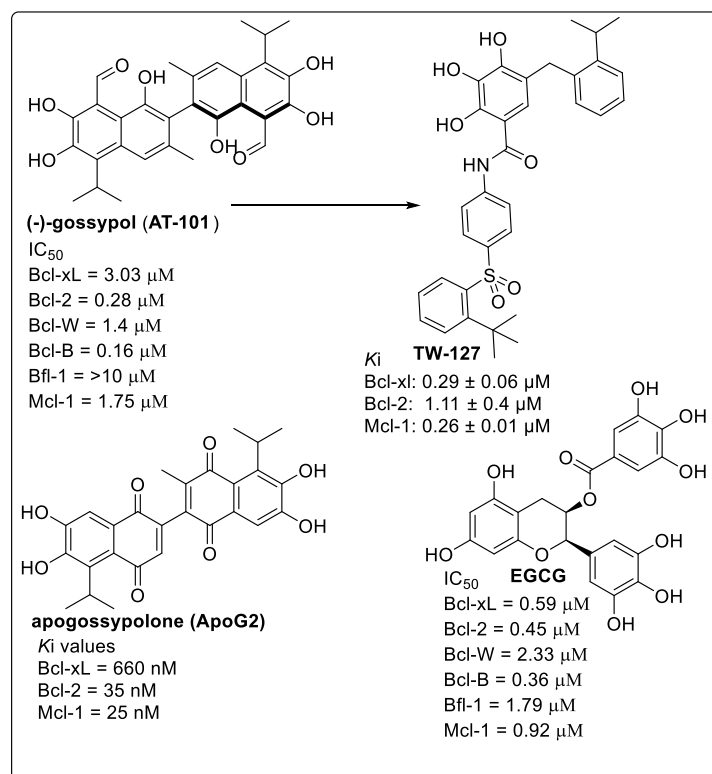


Figure 5 Showing various **AT-101** derivatives and **EGCG** and their IC_{50} values

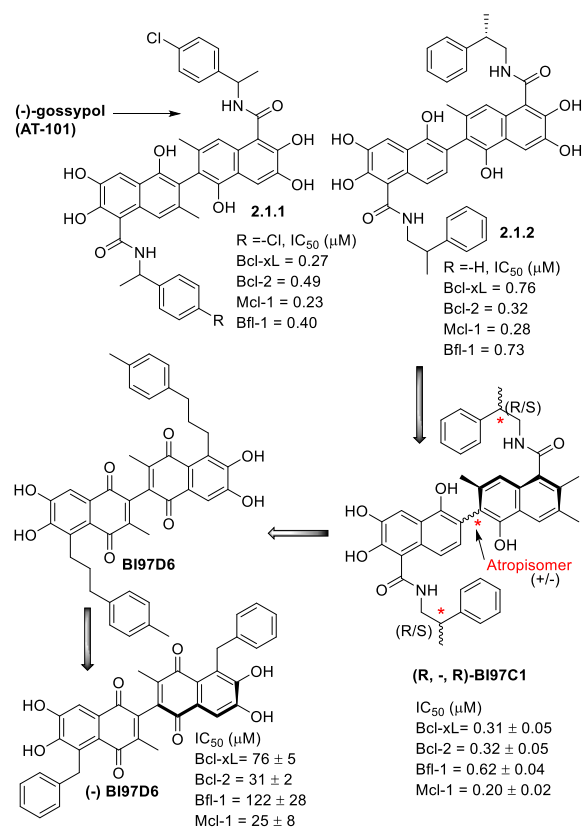


Figure 6 Various derivatives of **AT101** and **ApoG2** and their affinities.

In 2012, the Walensky group at the Dana-Faber Cancer Institute (Harvard Medical School, Boston) identified a selective small inhibitor of antiapoptotic Mcl-1 by screening stapled peptides. They initiated this work with a high-throughput screening (HTS) based on fluorescence polarization assay (FPA) on 71,296 compounds and attained **MIM1** (IC_{50} of 4.7μ M as Mcl-1 inhibitor), which on further testing showed no activity for Bcl-xL/Bid complex ($IC_{50} > 50 \mu$ M). It was also seen that MIM1 induced apoptosis by blocking the Mcl-1-mediated suppression of Bax. The MIM1 structure contains a thiazolyl core substituted with methyl, cyclohexylimino, and benzenetriol groups, as shown in **Figure 7** [77]. Structure activity relationship (SAR) studies showed the significance of positioning of the methyl and cyclic groups at the thiazolyl core and all three -OH positioning on benzenetriol moiety important for Mcl-1 activity. **MIM1** occupied that part of the BH3-binding site engaged by residues ETLRRV (amino acid 211–216) of Mcl-1 SAHB_D. While, the cyclohexyl ring made complementary hydrophobic contacts with the region residues L213 and V216, the thiazolyl core and its methyl substituent were predicted to pointed directly into a deep crevice. Interestingly, the benzene-1,2,3-triol (or pyrogallol) moiety engaged in hydrophilic contacts with Asp256 and Arg263.

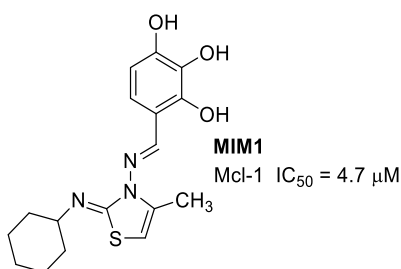


Figure 7 Chemical structure and binding affinity of MIM1.

Thiazole derivatives

Similar to indoles, thiazoles were also highly exploited for Mcl-1. In 2004, **Yc137** was reported as a potent Bcl-2 inhibitor [78]. Further testing showed that it was active against Bcl-2, Bcl-W, Bcl-B and Mcl-1 ($\sim 5 \mu M$) while for Bcl-xL and Bfl-1, it was not active ($> 20 \mu M$) [69], as shown in **Figure 8**.

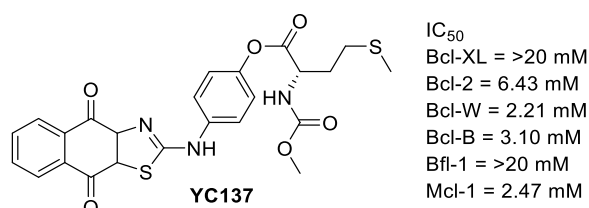


Figure 8 Molecular structure and affinity data of **Yc137**.

From previous studies [79], it was already known that **BH3I-1** and **Sanguinarine** binding are in close proximity in Bcl-xL binding site, therefore Chai's group at National University of Singapore utilized the structural features of BH3I-1 and sanguinarine in a hybrid molecule [80], as shown in **Figure 8.A**.

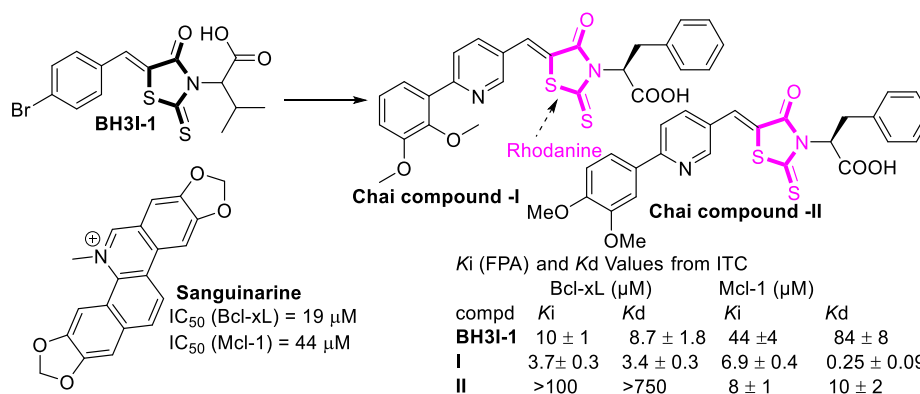


Figure 8.A Development of Chai's compounds.

Encouraged from **WL-276**, Fang's group (at the School of Pharmacy, Shandong University, China) implemented the structure-based design to form the 2-thioxo-4-thiazolidinone heterocyclic

core derivatives, which were found to be pan-Bcl-2 inhibitors (**2.1.3a-d**) [81], as shown in **Figure 9**. While the Fletcher group (School of Pharmacy, University of Maryland) revealed similar inhibitors based on a related heterocycle, as the thiazolidine-2,4-dione, where they found a moderate inhibitor (**2.1.4a**) which was later optimized to give the potent Mcl-1 inhibitor (**2.1.4b**) [82], as shown in **Figure 9**.

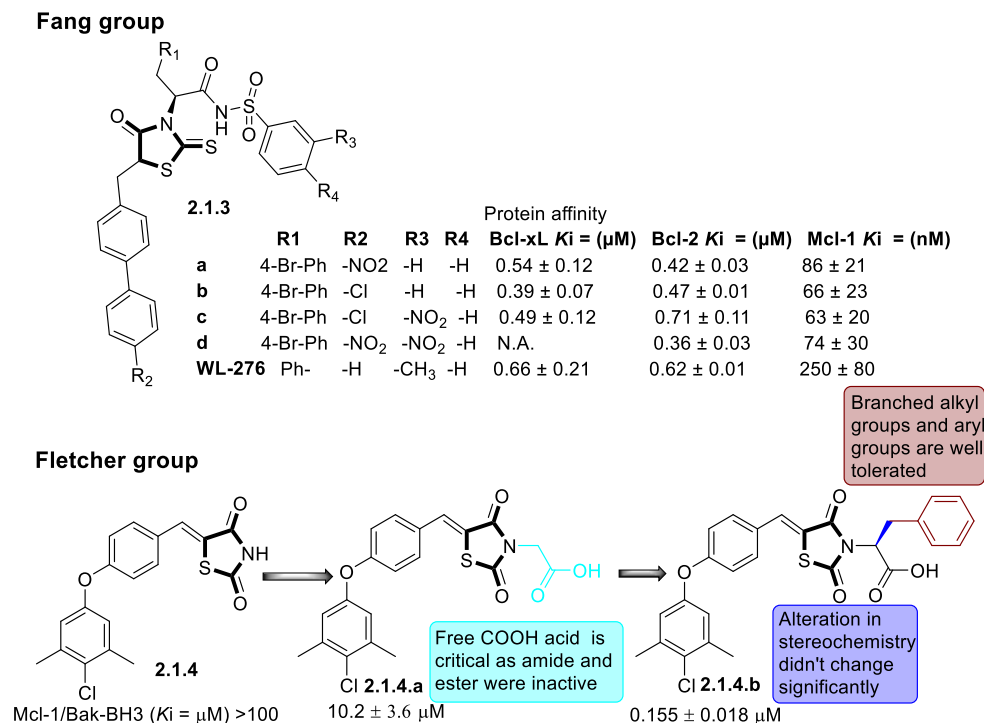


Figure 9 Showing the derivative of 2-thioxo-4-thiazolidinone (from Fang's group) and thiazolidine-2,4-dione

Thiazolo[3,2-a]pyrimidinone

In 2010, Feng *et al* discovered a thiazolo[3,2-a]pyrimidinone molecule (**2.1.5**) from a virtual database screening as a pan-Bcl-2 inhibitor [83], as shown in **Figure 10**. Although they tried derivatization of the A and B-rings of **2.1.5** which only diminished the Mcl-1 activity.

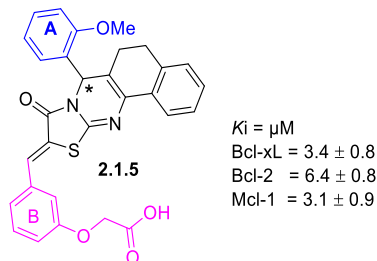


Figure 10 Thiazolo[3,2-a]pyrimidinone (**2.1.5**) as pan Bcl-2 inhibitor

Later, in 2011, the Wang & Yu group performed the FPA (fluorescence polarization assay) based screen on 95 *in-house* compounds, where they found a compound active against Bcl-2, Bcl-xl and Mcl-1 in low micromolar concentrations (**2.1.6**). This compound which also shares similar

structural features with a phosphatase inhibitor (**CDC25B**)[84], as shown in **Figure 11**. By molecular modeling based studies, they observed that the phenyl amide region has π - π -interactions with Tyr195, whereas N-benzyl substitution was found necessary as it utilizes a subpocket of the binding site [85]. In their next study (2015), they resolved the stereochemistry of the most active compounds by separating the R and S-isomers and this led to the identification of a more potent compound [86], see in **Figure 11**.

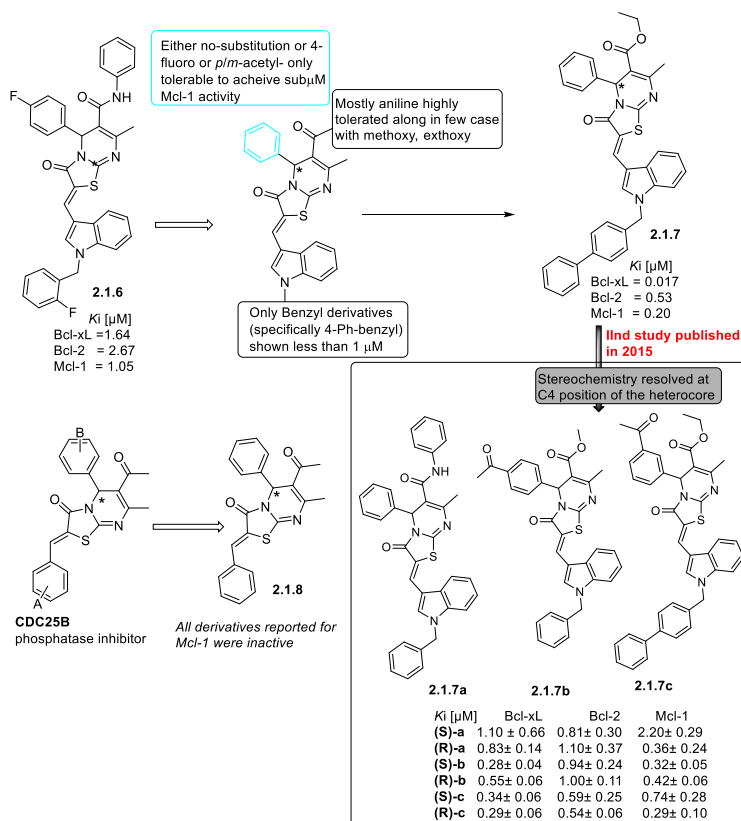


Figure 11 The structure activity relationship (SAR) of thiazolo[3,2-*a*]pyrimidinone derivatives by Wang's group at Shanghai Institute of Organic Chemistry, Shanghai (China).

Indole derivatives

Mcl-1 inhibitors based on indole have been explored more than any other heterocyclic system. Most of the contribution was from Fesik's group at Vanderbilt University (USA).

(a) Fesik indole compounds

In 2013, Fesik's group from Vanderbilt University utilized fragment-based methods and structure-based design to discover a series of potent and selective Mcl-1 inhibitors. Sequential optimization of the molecule in three different regions was performed: (a) fragment 1 (main heterocyclic core), where they selected indole over benzofuran, benzothiophene; (b) fragment-2, where they used various substituted and unsubstituted aryl groups; (c) linker region, where they used carbon

backbone of 1, 2 or 3 carbon atoms. After a number of subsequent optimization steps, they finally achieved a potent 2-indole carboxylic acid derivative (**2.1.10a**) (**Figure 12**), with a 16-fold selectivity for Mcl-1 over Bcl-2 and 270-fold over Bcl-xL. The interactions show that the 2-COOH functionality of indole ring has a H-bond acceptor interaction with Arg263 of the NWGR domain of Mcl-1. While, the presence of aromatic ring in fragment-2 seems essential for a π - π interaction with Ph270 (pdb id: 4HW2 & 4HW3) [87]. In another study, they transformed the indole ring into a tricyclic indole where they form a 6 membered cyclic linkage between N₁/C₇ of indole 2-carboxylic acid ring (**2.1.11**) as shown in **Figure 12**. The tricyclic indole-2-carboxylic acid (**2.1.11**) itself showed better affinity for Mcl-1 protein ($K_i = 38 \mu\text{M}$) when compared to the indole-2-carboxylic acid **2.1.9** ($K_i >1000 \mu\text{M}$) [88].

Also, the derivatives of tricyclic indole (**2.1.12-15**) showed a high level of Mcl-1 preferential selectivity over Bcl-xL (**2.1.14** showed a 1750-fold selectivity while **2.1.15** showed ~ 2000-fold selectivity, see in **Figure 12**) [88].

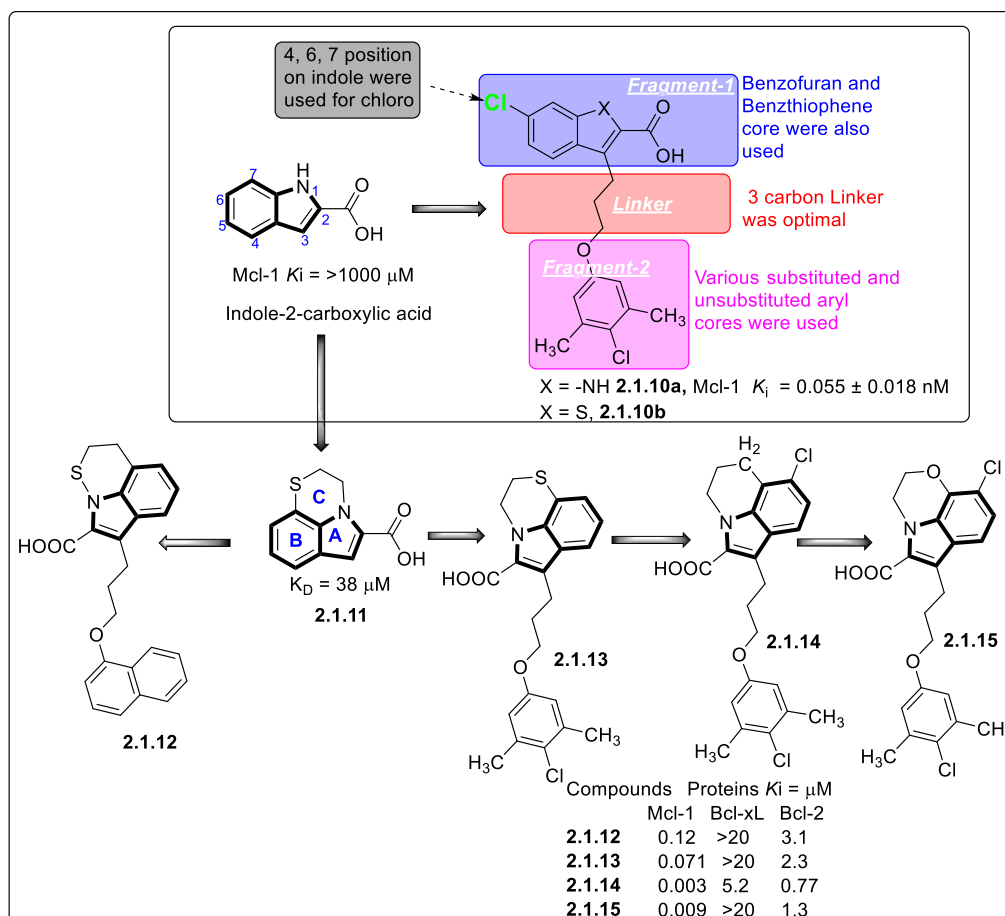


Figure 12 Chemical structures and binding affinities of indole and tricyclic indole derivatives.

In order to guide the design of analogues that could bind to the P3 and P4 pocket of Mcl-1, they performed a fragment-based screening of 13,824 molecules while saturating the P₂ pocket of Mcl-1 with compound **2.1.10a**. Later, they utilized acylsulfonamide (compound **2.1.16** & **2.1.17**) linkage so that it would provide them a synthetic handle for fragment linking and, also, at the same time retain the acidic group to interact with Arg263. Further, screening of various cyclic fragments with a carbon backbone linkage to sulfonamide of **2.1.18**, yielded compounds (compound **2.1.19-26**) which showed submicromolar activity against Mcl-1. The crystal structure of **2.1.18a** with Mcl-1 (PDB id: [5FDO](#)), shows that the substituted phenyl group pointed towards the P4 pocket and sulfonamide linker retains a H-bond acceptor interaction with Arg263 of Mcl-1. In order to improve further binding affinity, they derivatized the indole ring at the C-7 position. Various heterocycles, such as pyridine & pyrazole derivatives, were tried and **2.1.27** was attained as one of the most potent analogs at this step of the optimization. Further, they replaced the sulfonamide linker attached phenyl ring (as seen in **2.1.27**) with a furan carboxylic acid group and, performed a co-crystallization of **2.1.28** with Mcl-1 (PDB id: [5FDR](#)). The 3D co-crystal structure showed that the newly incorporated dimethyl pyrazole group adopted a nearly orthogonal binding conformation to the indole core, and 6-Cl is in the P₂ pocket of Mcl-1. While the free carboxylic acid of furan positioned in the groove within H-bonding distance to the amide NH of Asn260 explaining the sudden improvement in Mcl-1 affinity. Interestingly, the NH of the pyrazole points up from the binding pocket and therefore explained why methylation did not improve any Mcl-1 affinity. However, this kind of binding could be more useful if an additional group could be substituted to the NH of pyrazole to improve its drug-like characteristics or to transform the molecule into a probe for biochemical assays without affecting the affinity for Mcl-1 [89].

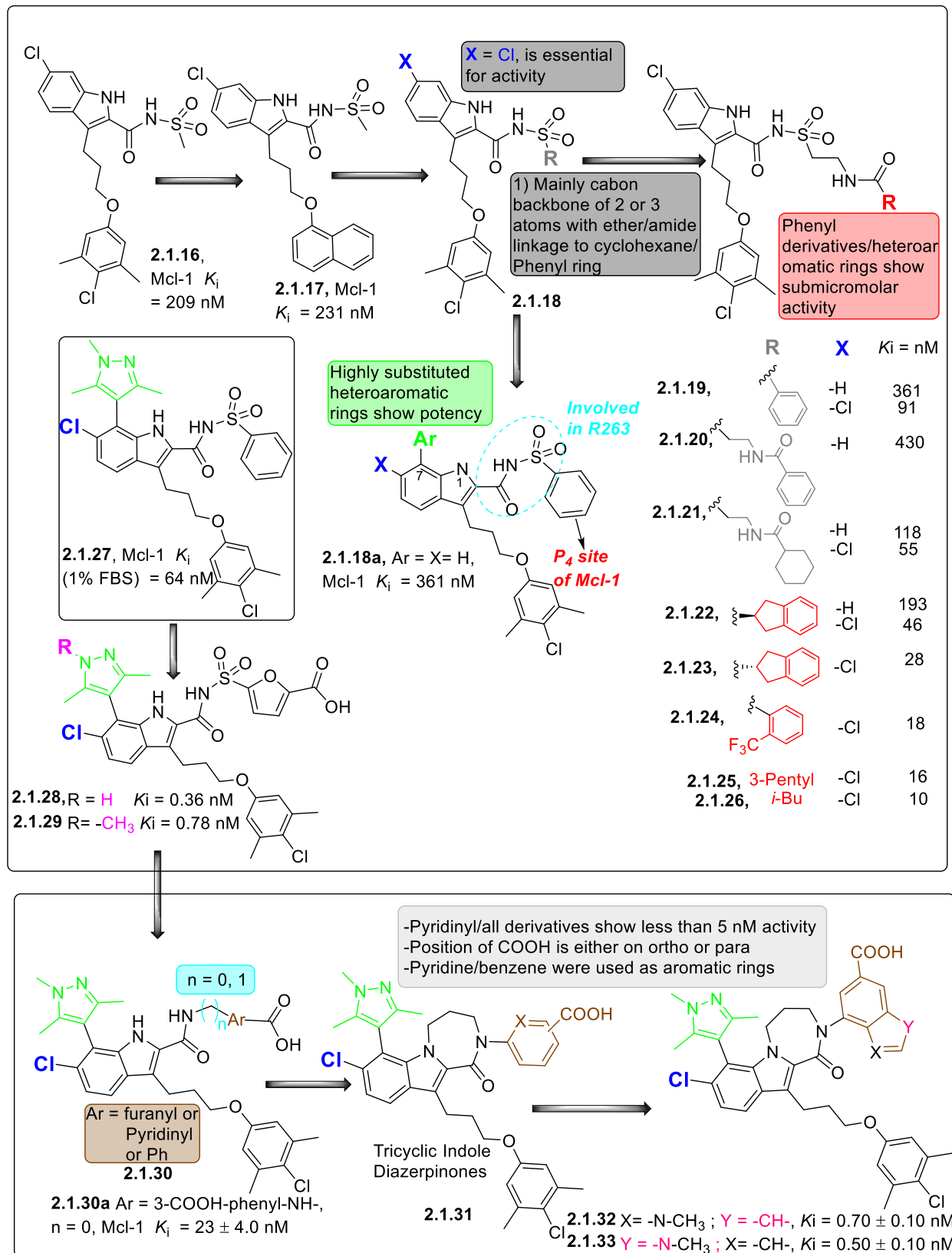


Figure 13 Utilization of indole heterocycle into improve Mcl-1 selective inhibitor.

In order to make **2.1.28** more drug-like while retaining its high on-target potency, its acidic sulfonamide linker was replaced with a neutral amide linker as shown in **Figure 13**. However, in this way, it lost the charge–charge interaction of its sulfonamide with Arg263, but attempts were made to improvise the terminal carboxylic acid of furan by using varying length of linker in order to compensate. Various pyridine/phenyl/furan derivatives were used as shown in **Figure 13 (2.1.30)**, where they co-crystallized **2.1.30a** with Mcl-1 (PDB id: [5IEZ](#)). The binding of **2.1.30a** showed that the indole amide substructure is nearly coplanar and both two -NH- (indole and amide linker) could adopt a geometry to form a cyclic structure, which ultimately leads to the formation of a new scaffold (**2.1.31**). The compounds **2.1.32** and **2.1.33** were found most potent and selective [90]. Further *in-vitro* investigation on **2.1.33** exhibited reduced cell activity in the presence of serum. Unlike many other acidic lipophilic compounds that bind to drug site 1 or 2, they found that **2.1.33** predominantly binds to drug site-3 of Mcl-1, which is unusual but the X-ray structure of **2.1.33** bound to site-3 provides a basis to design drugs with hopefully reduced albumin binding [91].

(b)AbbVie compounds

Through high throughput screening (HTS) AbbVie Inc. have reported an indole carboxylic acid derivative compound **2.1.34** similar to the Fesik compound **2.1.10**. Initially, they formed **2.1.35** as generalized structure, which (**2.1.35**) on co-crystallization with Mcl-1, disclosed 2-COOH acid interaction with Arg263 and naphthyl functionality going deep into the cavity (packed tightly by hydrophobic side chains of Leu235, Leu246, Met250, Tyr270, and Ile294). Later, SAR (structure activity relationship) studies showed indole N-substitution with 2 carbon tethered morpholinyl group along with various *O*-tolyl substitution at C6 position on **2.1.35**, improved Mcl-1 affinity even less than 10 nM. Afterward, the co-crystal structure showed that the 7'-*O*-tolylmethyl group was oriented toward the P3 and P4 pockets of the BH3 binding groove. Further derivatization, replaces the *O*-tolyl with pyrazole (as in case of **2.1.36**, improved the activity to the picomolar range) and extended bicyclic sulphonamide group that ultimately lead to formation of **A-1210477** [92]. Further, cellular-based assays showed **A-1210477** was effective against multiple cancer cell lines such as multiple myeloma and small cell lung cancer and is presently used as a clinical agent in various cell-based assays [93].

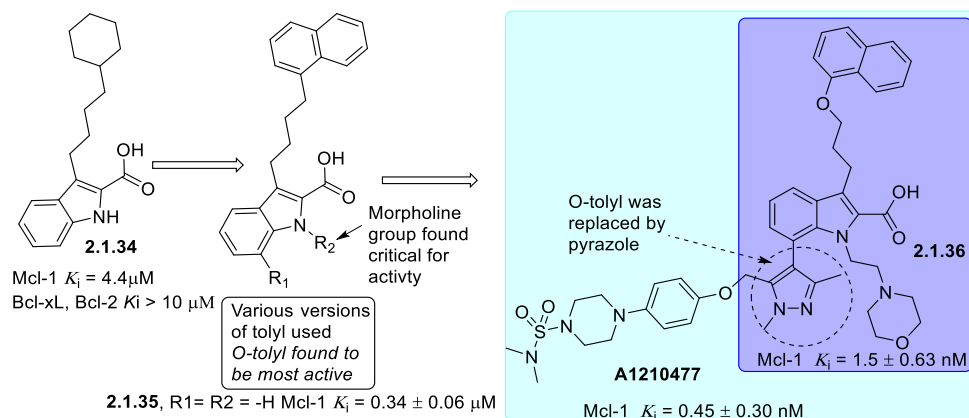


Figure 14 The substructure is in blue color while **A-1210477** has the full structure.

(c) *Liu & Zhou compounds*

Liu & Zhou co-workers (Shenyang Pharmaceutical University, Shenyang, China) performed a fluorescence polarization assay (FPA: Bid-BH3 peptide labeled fluorescein) on a small *in-house* compound library, where they discovered **LSL-A6** as a hit ($K_i = 7.78 \pm 1.21 \mu\text{M}$). Optimization by using various functionalities on molecule, such as: (a) substituted phenol derivative, (b) positioning of O-tethered carbon backbone between substituted phenol derivative/indole core and (c) positioning of 2-COOH-benzyl substituent. These optimizations led to a series of submicromolar Mcl-1 active compounds (**2.1.37-43**), where **2.1.37** (K_i value of $0.11 \mu\text{M}$) was the most potent and 7-fold selective over Bcl-2, as shown in **Figure 15**. Further, docking showed that these compounds bind to the pocket (P_2) and interact with Arg263 [94]

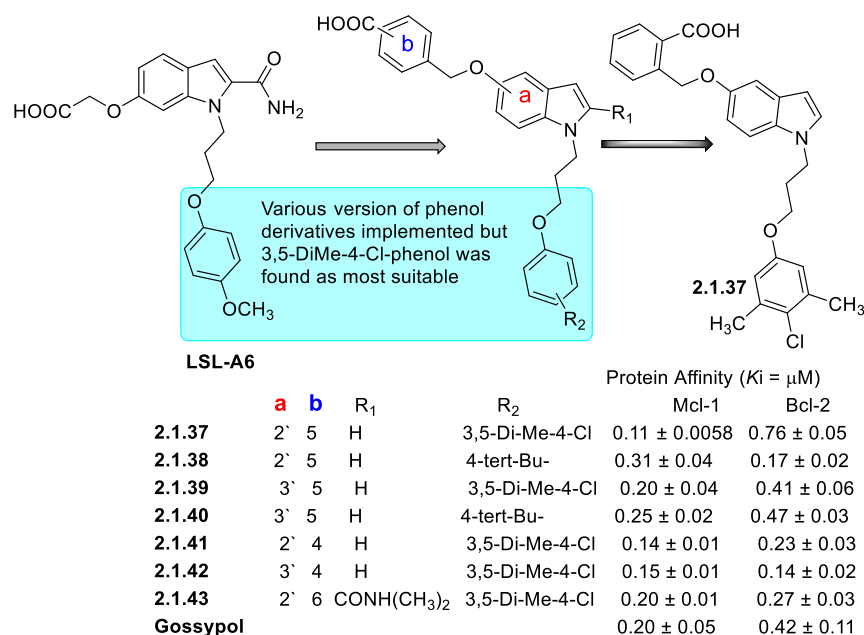


Figure 15 Liu & Zhou N-substituted indole derivatives.

(d) Fang group's work

Fang's group (School of Pharmacy, Shandong University, China) used structure-based design to form an inhibitor which contains three parts (a) indole ring as main heterocyclic core scaffold (b) aryl sulphonamide (c) substituted biphenyl functionality. They achieved a compound (**2.1.45**) with IC_{50} 72 nM against Mcl-1 and also found 10-folds selective over Bcl-xL, as shown in **Figure 16**. However, cell line testing against (MDA-MB-231 (breast cancer cell), PC-3 (prostatic cancer cell), K562 (chronic myelogenous leukemia cells)) shows moderate inhibitory activity when compared to **R-(-)-Gossypol**, as shown in **Figure 16** [95]

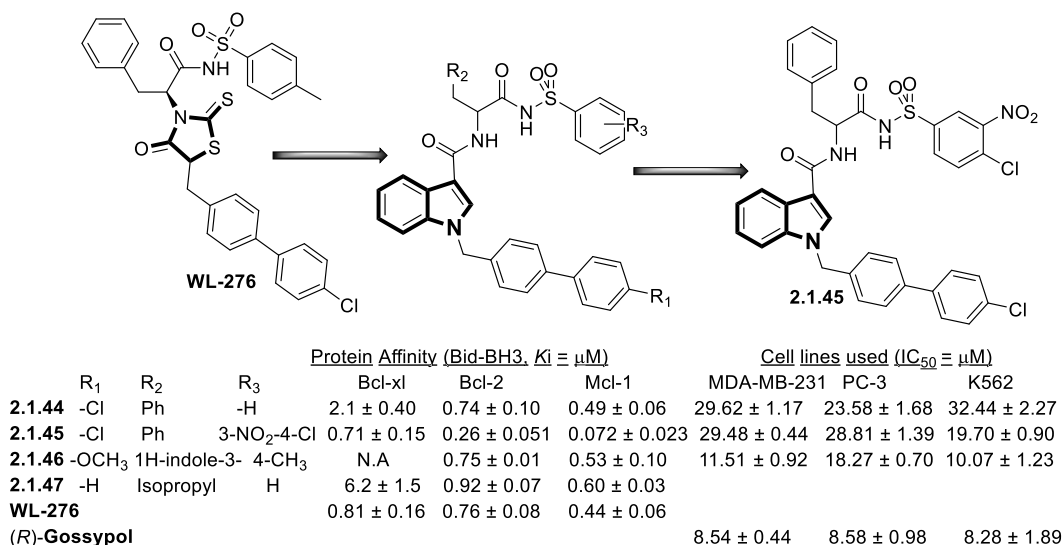
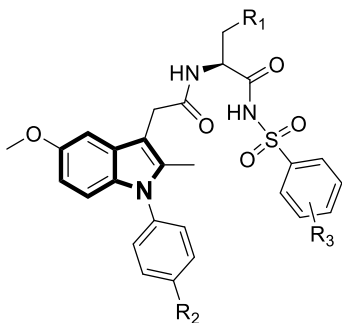


Figure 16 Fang's group disclosed indole-3-carboxylic acid-based skeleton of Bcl-2/Mcl-1 dual inhibitors. Included are toxicity data against various cancer cell lines.

Fang's group improvised their above-mentioned synthetic chemistry to explore their scaffold further for Mcl-1 inhibitor development, where they increased the carbon linkage between sulfonamide functionality and indole core as shown in **Figure 17** where they identified compounds as dual Bcl-2/Mcl-1 inhibitors (**2.1.48-50**). These compounds showed a better activity profile when compared to **WL-276** [96], especially compound **2.1.50** in cell line testing.



	R_1	R_2	R_3	Protein Affinity ($K_i = \mu\text{M}$)		Cell lines used ($\text{IC}_{50} = \mu\text{M}$)			
				Bcl-xl	Bcl-2	Mcl-1	MDA-MB-231	PC-3	K562
2.1.48	-Ph	-Ph	H	NA	0.35 ± 0.03	0.96 ± 0.01	33.55 ± 5.01	17.49 ± 4.22	18.75 ± 2.88
2.1.49	-Ph	-Ph	4-OMe	NA	0.47 ± 0.03	0.88 ± 0.06	38.62 ± 2.81	23.48 ± 1.34	27.53 ± 1.94
2.1.50	-Ph	-Ph	3-NO ₂ -4-Cl	NA	0.58 ± 0.06	0.48 ± 0.02	42.06 ± 3.26	13.90 ± 0.24	13.02 ± 1.52
WL-276				1.2 ± 0.10	0.94 ± 0.14	0.47 ± 0.03	45.89 ± 1.34	30.13 ± 4.52	43.97 ± 1.31

Figure 17 Fang's group improvised their previous core of indole-3-carboxylic acid-based skeleton into a 1-phenyl-1H-indole against Bcl-2/Mcl-1

(e) Zhang's group work

However, the Zhang group (at School of Chemistry, Dalian University of Technology, Dalian China) implemented the fragment-based design to synthesize 1-substituted-indole-2-carboxylic acids (**2.1.51**) as Mcl-1-selective inhibitors where their most potent compound (**2.1.52**) showed ~8 fold preferential selectivity over Bcl-2 protein, as shown in **Figure 18**. Further, they tested these compounds against 4 cell lines: Mcl-1 dependent NCI-H235 ($\text{IC}_{50} = 2.2 \mu\text{M}$), Bcl-2 dependent HL-60 ($\text{IC}_{50} = 63.3 \mu\text{M}$), both Mcl-1 and Bcl-2 dependent H22 ($\text{IC}_{50} = 9.2 \mu\text{M}$) and MCF-7 ($\text{IC}_{50} = 19.2 \mu\text{M}$) [97].

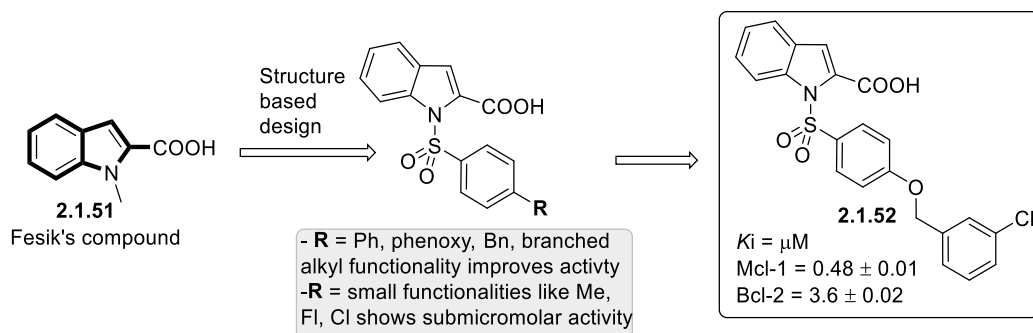


Figure 18 Zhang group disclosed 1-substituted-indole-2-carboxylic acids as selective Mcl-1 inhibitors

(f) Covalent Mcl-1 inhibitor

AstraZeneca discovered a covalently binding Mcl-1 inhibitor which they achieved by incorporating boronic acid onto the molecules and found its proposed bonding interaction with amino group of Lys234 supported by site mutagenesis (K234A). Further, they performed time-resolved fluorescence resonance energy transfer (TR-FRET) binding assay and caspase-3/7 activation assay in MOLP- 8 cells, which showed compound **2.1.53** as the most potent one, while

the methylated version (**2.1.56**) of **2.1.53** showed a 6 fold increase in cellular potency as shown in **Figure 19** [98]. While **2.1.57** was used to compare the effect of incorporation of boronic acid in these compounds (**2.1.53-56**).

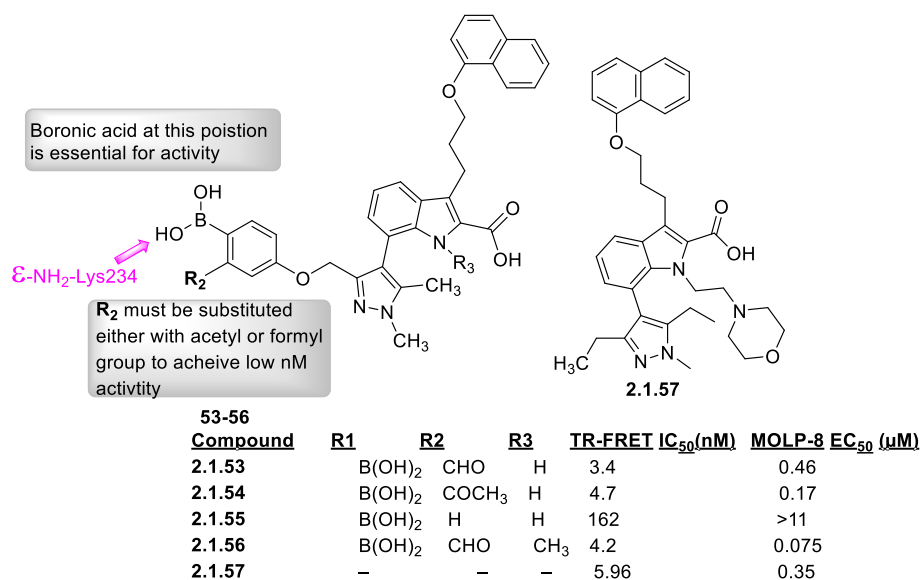


Figure 19 IC₅₀ and EC₅₀ values for covalent Mcl-1 inhibitors.

Acenaphthylene & phenalene derivatives

In 2009, Zhang's group at Dalian University of Technology, reported a small molecule **S1 (2.1.58)** (3-thiomorpholin-8-oxo-8H-acenaphtho[1,2-*b*]pyrrole-9-carbonitrile) as pan inhibitors with preferential selectivity (~6 fold) for Mcl-1 over Bcl-2 protein [99]. Later SAR studies showed that **2.1.58** binds in the BH3 groove of Mcl-1 and Bcl-2, with the thiomorpholine extended into the P₂ binding pocket of Mcl-1 and Bcl-2 [100]. Also, they noted that Mcl-1 binding pocket is shorter and wider in comparison to Bcl-2 binding pocket. Based on these difference, they further probed the difference between the P₂ pocket of Mcl-1 and Bcl-2 [101] by replacing thiomorpholine with phenol derivatives, where they found more potent Mcl-1 activity (**2.1.59**) with ~7 fold improvement over Bcl-2.

Further in their 2nd study, they tried fragment-based design where they used fragment-1 (cynoacetamide, **2.1.60**) and fragment-2 (**2.1.61**, 2, 2-[2-oxo-2H-acenaphthylen-1-ylidene]-malononitrile) for further derivatization and found the compounds from fragment 1 (**2.1.60**) were much more potent (**2.1.60a-d**) [102]. In their third study, they derivatized the fragment-2 (**2.1.61**) into a series of hydroxy pyridine core-compounds (**2.1.62**), as shown in **Figure 20**. This hydroxy-pyridine core was substituted with various thiophenol substituents (such as methyl, bromo, amino and t-amyl) but only *p*-isopropyl thiophenol derivative was able to show less than 1 μM activity.

The isopropyl derivative (**2.1.62**) was further derivatized at 2-position where -OH group was replaced with amide derivatives and attained **2.1.63** as the most potent compound [36]. In their another study they derivatized **2.1.58** structure at cyano and thiomorpholine functionality position and identified **2.1.64**, which showed activity (IC_{50}) at 10 nM for Mcl-1 and 2-fold less potent against Bcl-2 [103].

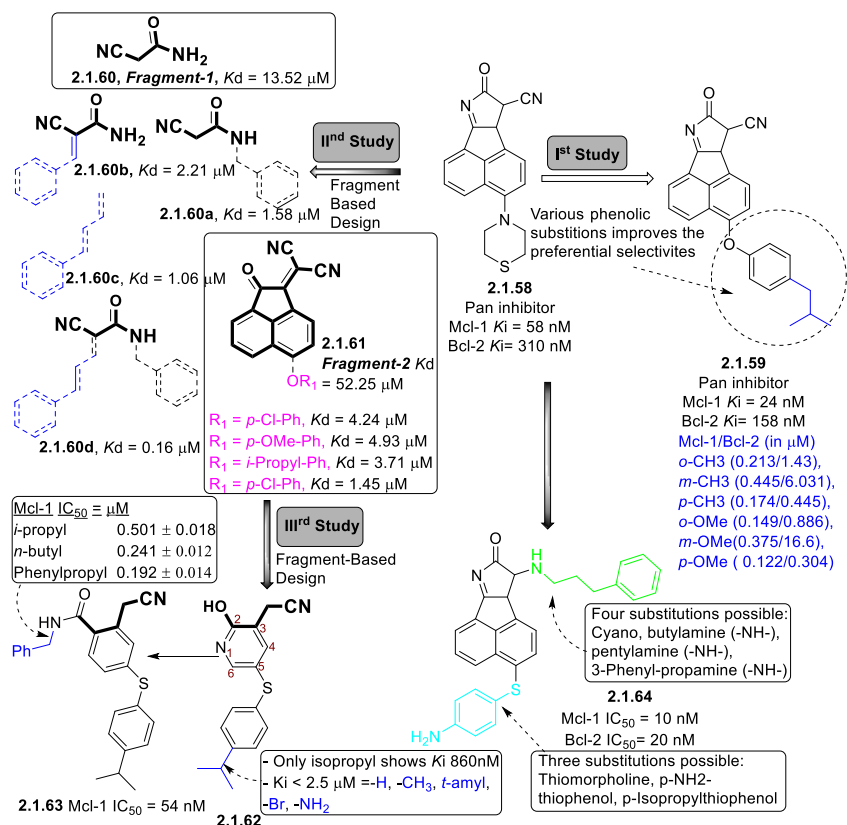


Figure 20 Chemical structures and binding affinities of acenaphthylene derivatives.

In order to study phenalene heterocyclic core candidature as Mcl-1 inhibitor, Zhang's group published a report where they utilized the concept of the "binding of proapoptotic proteins also differentiate the fate of the anti-apoptotic proteins: Noxa^{BH3} binding biases the QRN motif toward a helical conformation, leading to an enhance ubiquitination of Mcl-1, while Bim^{BH3} binding biases the QRN motif toward a nonhelical conformation, which does not lead to ubiquitination". They improved the molecular structure (**2.1.65**) as it plays a role in binding to QRN motif (a Glu-Arg-Asp peptide) and reported **2.1.66**, as a dual function molecule by targeting the Bcl-2 homology 3 domain (BH3) and facilitating Mcl-1 ubiquitination by forming hydrogen bond with His224 to drive a helical QRN conformation [104], as shown in **Figure 21**.

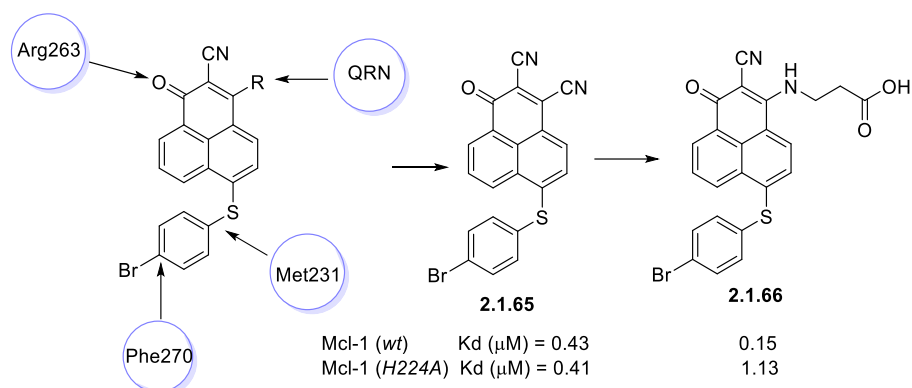


Figure 21 Chemical structures and binding affinities of phenalene derivatives.

Pyrrole derivatives

(a) Marinopyrrole analogs (maritoclax, it's cyclic and disulphide linker analog)

Marinopyrrole A (**maritoclax**) was isolated from a marine *Streptomyces* and found active against methicillin-resistant *Staphylococcus aureus* (MRSA) [105]. Structurally, it contains 2 pyrrole rings. Later, Doi *et al* reported its preferential selective Mcl-1 activity compared to other family members of Bcl-2 family, and provided NMR based docking on the *m*Mcl-1, where: (a) one pyrrole moiety of maritoclax pointing its chlorine atom toward the deep cleft of Mcl-1, (b) phenol group (OH) to the same pyrrole moiety has H-bond with Gly308 (c) phenol group of another pyrrole group has H-bond with Thr247 of Mcl-1, (d) carbonyl group shows H-bond with Asn204 [106]. Further, Li and Qin group worked on its derivatization where initially they tried sulfide spacers (**2.1.67**, **2.1.68**, **2.1.69**) and found submicromolar activity against both Mcl-1 and Bcl-xL, as shown in **Figure 22**. However, in another study, they derivatized the molecule by incorporating cyclic constraints which was principally based on a concept, “to restrict the conformations of flexible ligand and improves mostly the preferential selectivity for a given physiological target by minimizing the entropic loss associated with the ligand adopting a preferred conformation for binding” [107]. Therefore, they achieved slight improvement in preferential selectivity to Mcl-1 over Bcl-xL (compound **2.1.70** and **2.1.71**) [108].

Later in 2015, they tried to incorporate various functional groups on both sides of these structures. They incorporated various polar as well as non-polar substituents at the para-position in both the pyrrole rings and found better hydrophobicity tolerance than hydrophilicity (**2.1.74**, **2.1.75** vs **2.1.72**, **2.1.73**) as dual Mcl-1/Bcl-xL inhibitors, as shown in **Figure 22**. However, further extension by a triazole ring at the *para*-position of both phenyl rings on pyrrole and -NH- substitution of the triazole ring, clarified a key role of lipophilicity (trends **2.1.76**→**2.1.81**) in attaining the potency

towards Mcl-1. Although, these molecules showed high potency against Mcl-1 as well as for Bcl-xl (as shown in **Figure 22**), but failed to lower Mcl-1 expression and Caspase-3 activation at low micromolar concentration in further biological testing [92].

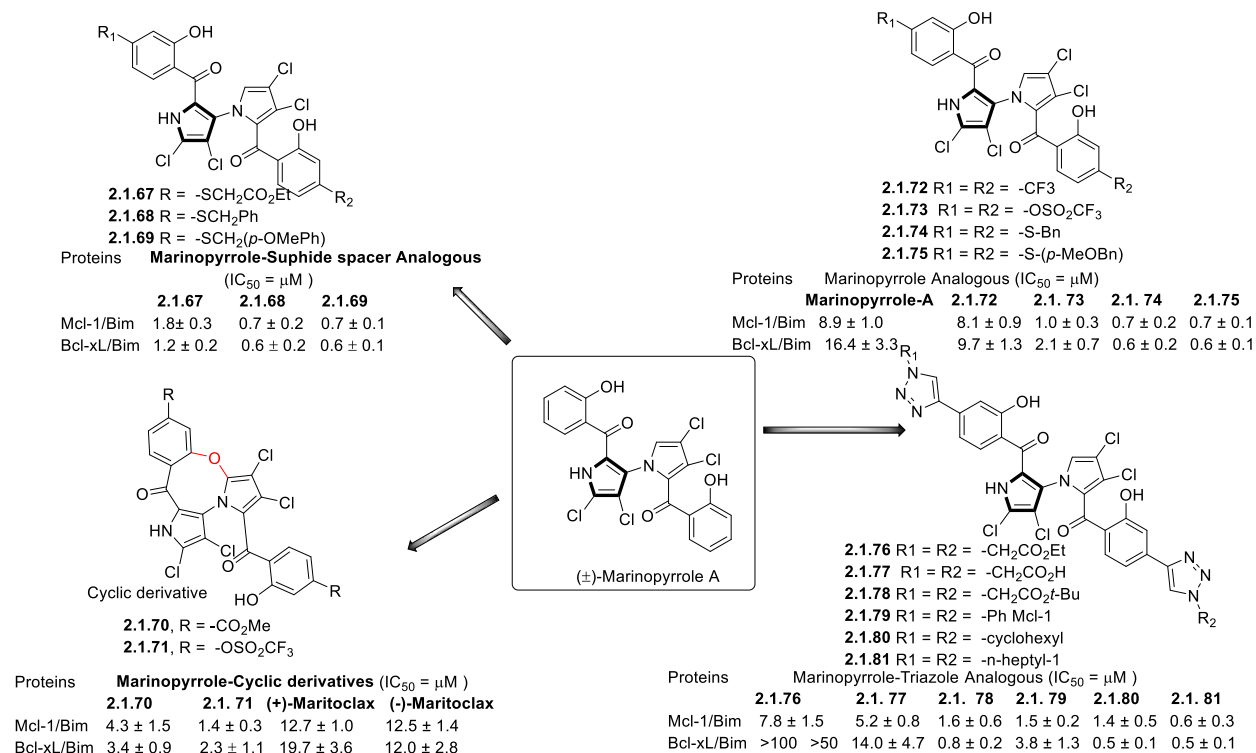
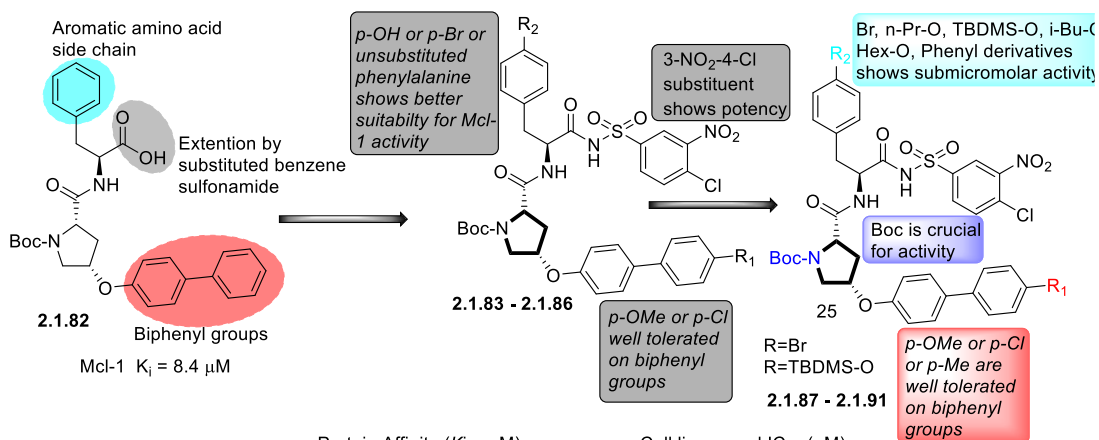


Figure 22 Chemical structures and binding affinities of pyrrole derivatives **Marinopyrrole A**

(b) Fang group's pyrrole derivatives

In 2015, Fang's group (at School of Pharmacy, Shandong University) reported a tetrahydropyrrole (pyrrolidine) derivative (**2.1.82**) by virtual screening (**Figure 23**) as a moderate Mcl-1 inhibitor ($K_i = 8.4 \mu M$) with reasonable aqueous solubility. Later, by optimization they identified **2.1.83** as the most potent Mcl-1 inhibitor and its binding mode predicted as similar like α -helix of BH3-only protein (Bim) by molecular modeling, such as (a) acyl-sulfonyl group formed two hydrogen bonds with Arg263 and one hydrogen bond with Asn260, (b) carbonyl of the pyrrolidine ring interacted with Thr266 through one hydrogen bond. While compound **2.1.84**, was found better Mcl-1 preferential selective inhibitor than **2.1.83**, with 8.2-fold against Bcl-2 protein, and 15.5-fold against Bcl-xL protein. In further cell line testing, MDA-MB-231 (breast cancer cell), PC-3 (prostatic cancer cell) and K562 (chronic myelogenous leukemia cell), were chosen to evaluate the antiproliferative activities of active compounds **2.1.83**, **2.1.84**, **2.1.85** and **2.1.86** by MTT assay [109]. As the interface between pro-apoptotic proteins and Mcl-1 is large and flexible therefore

Fang group further extended the aromatic amino acid region in their 2nd study in 2017, as shown in **Figure 23**. They substituted that region with various non-classical amino acids obtained from etherification and arylation on the aryl ring of L-4-Br phenylalanine and additionally evaluated the necessity of Boc protecting group on the pyrrolidine scaffold for activity as shown in **Figure 23**. The most potent compound **2.1.87** ($K_i = 0.077 \mu\text{M}$) was ~10-fold more potent than **2.1.83** and over 2-fold potent than **R- (-)-Gossypol** ($K_i = 0.18 \mu\text{M}$) (Figure 13). Further molecular modelling predicted that: (a) a biphenyl group of compound (**2.1.87**) could mimic the α -helix of Bim protein, (b) an acyl-sulfonyl group could form three hydrogen bonds with Arg263 and Trp261 (c) a Boc protecting group on pyrrolidine ring formed one hydrogen bond with Thr266, which also explains why Boc presence on the structure is essential for binding affinities for Mcl-1 protein. Later cell-based assays showed compound **2.1.87** had moderate activity against MDA-MB-231 and K562 cells when compared to **R- (-)-Gossypol** while being equipotent with an IC_{50} of 10.2 and 7.54 μM in cytotoxicity assays with PC-3 cell line, respectively [110].



R ₁	R ₂	Protein Affinity ($K_i = \mu\text{M}$)			Cell lines used IC_{50} (μM)		
		Bcl-xl	Bcl-2	Mcl-1	MDA-MB-231	PC-3	K562
2.1.83	Ph 4-Br	2.2 ± 0.06	0.93 ± 0.06	0.53 ± 0.09	13.6 ± 0.61	10.7 ± 1.1	23.0 ± 1.9
2.1.84	4-CH ₃ - H-	8.7 ± 2.5	4.6 ± 0.15	0.56 ± 0.18	5.4 ± 1.7	13.5 ± 0.42	22.4 ± 1.8
2.1.85	4-CH ₃ - 4-Br-	1.2 ± 0.36	0.55 ± 0.05	0.63 ± 0.20	14.9 ± 2.4	13.8 ± 0.55	22.1 ± 1.5
2.1.86	4-Cl- 4-Br-	2.1 ± 0.17	0.83 ± 0.04	0.58 ± 0.07	15.8 ± 1.9	11.2 ± 0.65	21.9 ± 0.60
Gossypol		0.77 ± 0.40	0.56 ± 0.06	0.39 ± 0.04	9.42 ± 0.43	5.78 ± 0.36	5.91 ± 0.77

R ₁	R ₂	Protein Affinity ($K_i = \mu\text{M}$)			Cell lines used IC_{50} (μM)		
		Bcl-xl	Bcl-2	Mcl-1	MDA-MB-231	PC-3	K562
2.1.87^a	-H TBDMS-O	1.3 ± 0.65	0.93 ± 0.07	0.077 ± 0.0042	23.4 ± 0.80	10.2 ± 2.4	17.3 ± 1.2
2.1.88	-Cl Ph-(CH ₂) ₂ -O	N.A	0.67 ± 0.08	0.26 ± 0.02	25.2 ± 1.3	13.2 ± 1.3	17.8 ± 2.1
2.1.89	-Cl Bn-O	N.A	0.51 ± 0.031	0.22 ± 0.017	20.6 ± 2.8	9.06 ± 0.46	17.0 ± 2.1
2.1.90	-H 4-Br-Bn-O	N.A	0.68 ± 0.04	0.32 ± 0.03	21.3 ± 2.5	10.6 ± 1.4	16.4 ± 2.5
2.1.91	-CH ₃ 4-NO ₂ -Bn-O	N.A	0.75 ± 0.09	0.30 ± 0.09	16.9 ± 0.54	8.45 ± 1.8	16.6 ± 2.4
Gossypol		1.4 ± 0.54	0.45 ± 0.03	0.18 ± 0.01	9.23 ± 1.2	7.54 ± 0.28	5.60 ± 0.29

^aThere was a binding affinity data mistake in EJMC 146 (2018)471-482 as when compared to original manuscript (Bioorg. Med. Chem. 25 (2017)138-152).

Figure 23 Chemical structures and binding affinities of pyrrole derivatives.

Isoquinoline & Quinoline derivatives

In 2008, Prakesch *et al* generated a tetrahydroaminoquinoline-based library in order to find a small molecule modulator for protein-protein interactions. Through, *in-silico* and ^{15}N NMR studies, they filtered the molecules which showed their ability to bind to Bcl-xL and Mcl-1. The NMR study led to the identification of the tetrahydroaminoquinoline-based scaffold (**2.1.92**) as a weak inhibitor to both the proteins ($K_d = 200 \mu\text{M}$ for Bcl-xL and $K_d = 300 \mu\text{M}$ for Mcl-1). Later, fragment-based design was implemented to afford the compound (MIPRALDEN, **2.1.93**) as their most potent inhibitor of Mcl-1 and Bcl-xL ($K_d = 25$ and $70 \mu\text{M}$) [111], as shown in **Figure 24**.

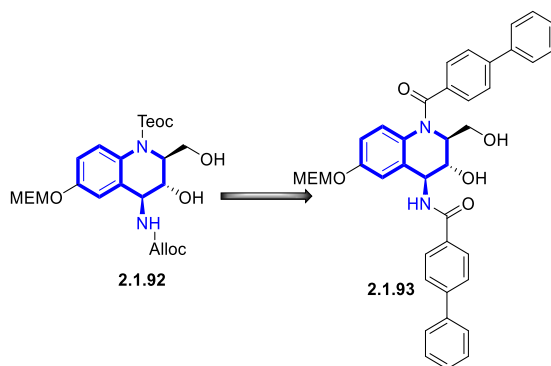


Figure 24 Discovery of tetrahydroaminoquinoline as Mcl-1 inhibitor

The first report on polyquinoline derivatives was published by the Moreau group (from Clermont University, France) [112], where they found that poly-heterocyclic systems adopt similar conformations to the BH3 helix of Bak. Also, they used a symmetric tri-quinoline core, where C5 of every quinoline core was substituted with a branched alkyl functionality (**2.1.94**). Later when they chemically modified this scaffold to compounds (such as **2.1.95** & **2.1.96**) and tested them against a wide variety of Bcl-xL-apoptotic PPI, they found **2.1.94** comparatively superior to the derivatives. Therefore, it was further evaluated against antiapoptotic-Bax PPI [113], as shown in **Figure 25**. In their another study, they derivatize the core through C2 and C5 substitution into an asymmetric polyquinoline core. Surprisingly, their most promising compounds had an isopropyl substituent at C5 position of one quinoline ring along with C2 substitution of both quinolines either O/N-tethered heterocycles or alkyl groups (**2.1.97**, **2.1.98**, **2.1.99**, **2.1.100**, **2.1.101**) [114], as shown in **Figure 25**. However, **2.1.97** was found as the most potent Mcl-1 inhibitor but was also non-selective in nature [114].

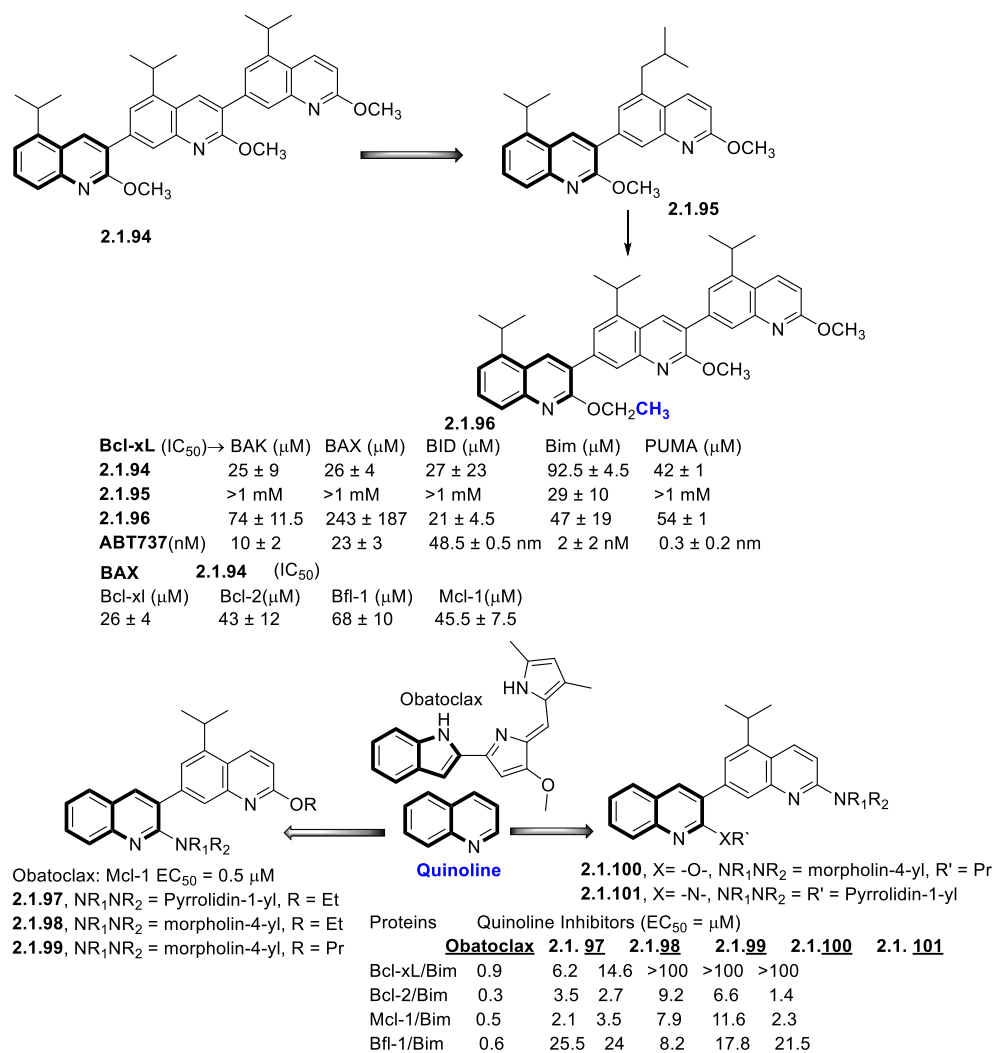


Figure 25 Mcl-1 inhibitors based on polyquinolines.

In 2013, Richard *et al* performed a high throughput screening on 315,000 compounds (NIH Molecular Libraries Small Molecule Repository, MLSMR). There, they found 2141 compounds showing greater than 40% inhibition of Mcl-1 and filtered off the compounds based on the showing considerable Bcl-xL binding, which reduced the number of hits to 1720 compounds. Further, the categorization of compounds with Mcl-1 activity and deficient of Bcl-xL activity, reduced the number further to 179. Among them, only 52 compounds demonstrated IC₅₀ \leq 10 μ M against Mcl-1, while only 24 of these found showed reduced Bcl-xL inhibitory activity (IC₅₀ \geq 10 μ M against Bcl-xL) [115]. Through these studies, the 7-hydroxyquinoline (**2.1.102**) was identified, and various substituents were investigated in the phenyl region of **2.1.102**. Based on SAR studies, the quinoline nitrogen atom and the 8-hydroxyl group were found essential for Mcl-1 activity. *Ortho*- and *meta*-substituted compounds were found to be weaker Mcl-1 inhibitors (**2.1.104** & **2.1.105**),

whereas bis-substituted analog (**2.1.106**) was also found to be a moderate inhibitor. However, the *para*-substituted methoxy derivative (**2.1.107**) and compounds with five-membered heterocycles (furan **2.1.108**) showed high potency. The presence of an electron-withdrawing group (such as -F) at the *para*-position (**2.1.100**), expected to enhance metabolic stability [116, 117] and found ~5-fold more potent inhibitor than the precursor molecule (**2.1.109**), as shown in **Figure 26**. Further, they modified the scaffold to give **2.1.110** as a potent selective Mcl-1 inhibitor. Modeling of the R-isomer of **2.1.110** shows a H-bond between Asn260 and hydroxyquinoline group. The N-ethylpiperazine group fits into one of the four hydrophobic pockets typically occupied by side chains of BH3-only peptides [115].

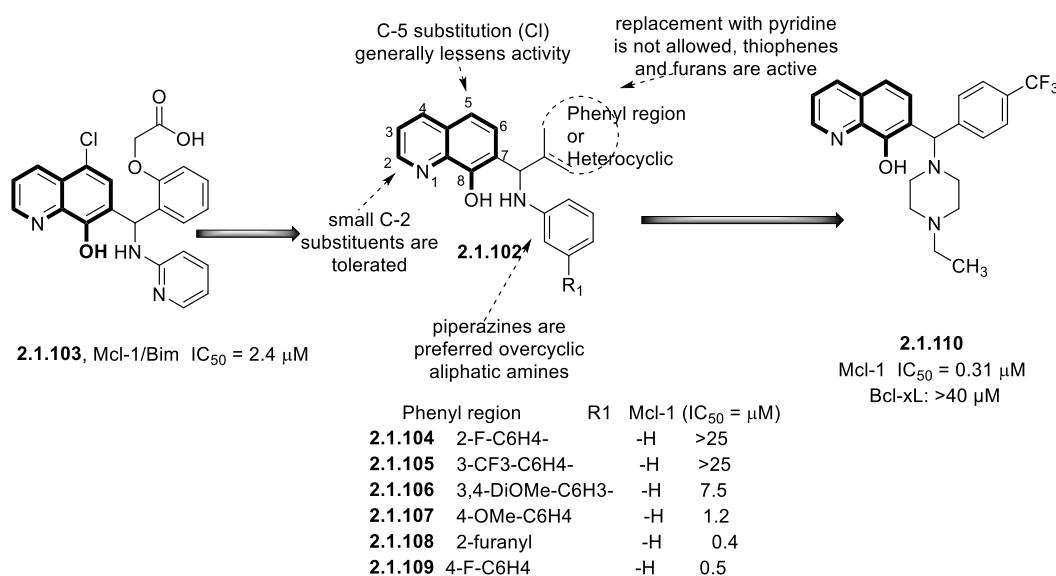


Figure 26 Hydroxyquinoline as Mcl-1 inhibitors.

In 2016, Fletcher's group disclosed a series of 3-carboxy-substituted 1,2,3,4- tetrahydroquinolines as Mcl-1 inhibitors. They used the structure-based design (SBD), where they considered two molecules (**2.1.111** from AbbVie Inc and **2.1.10.b** from Fesik group) and attained a series of compounds (e.g. \pm **2.1.112**) including a potent inhibitor of Mcl-1 (\pm **2.1.113**) [118], as shown in **Figure 27**.

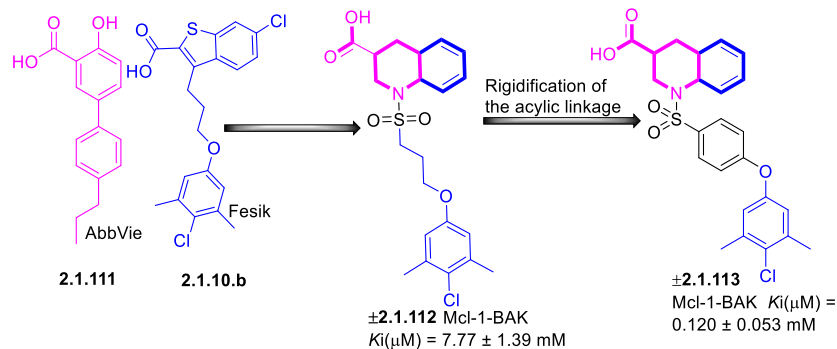


Figure 27 SBD of tetrahydroquinoline carboxylic acids as Mcl-1 inhibitors.

Anthraquinone and quinazolone derivatives

In 2012, the Zhang group at Dalian University of Technology utilized structure-based design which was based on the concept that, “two faces of the Bim BH3 α -helix are utilized in binding with Mcl-1 and Bcl-2” [7]. However, interestingly the other known inhibitors such as ABT-737 and nonpeptide α -helix mimics, terphenyl scaffolds, only act on one face of the α -helix of Bim-BH3, and therefore cannot mimic the opposite side of another α -helix face, which is conserved in all BH3 domains [119, 120]. Therefore, Zhang *et al* introduced anthraquinone based inhibitors (**2.1.114**) which can mimic two-faces of the Bim BH3 α -helix, where one side/face of core was substituted with hydroxyl groups (at C1, C2, and C3) while on other side either C6 or C7 position was substituted (with either bromo, isopropyl or thiophenols), as shown in **Figure 28**. They found better Mcl-1 activities when substitutions were performed on both faces/sides than one face/side of the anthraquinones, and **2.1.115** was their most potent Mcl-1 inhibitor [121]. Based on their anthraquinone study [121], they developed into a quinazolones, where they found **2.1.116** as a dual inhibitor of Bcl-2/ Mcl-1 proteins, with K_i values of 179 nM and 123 nM, respectively, holding typical BH3 like two-faced binding characteristic [122].

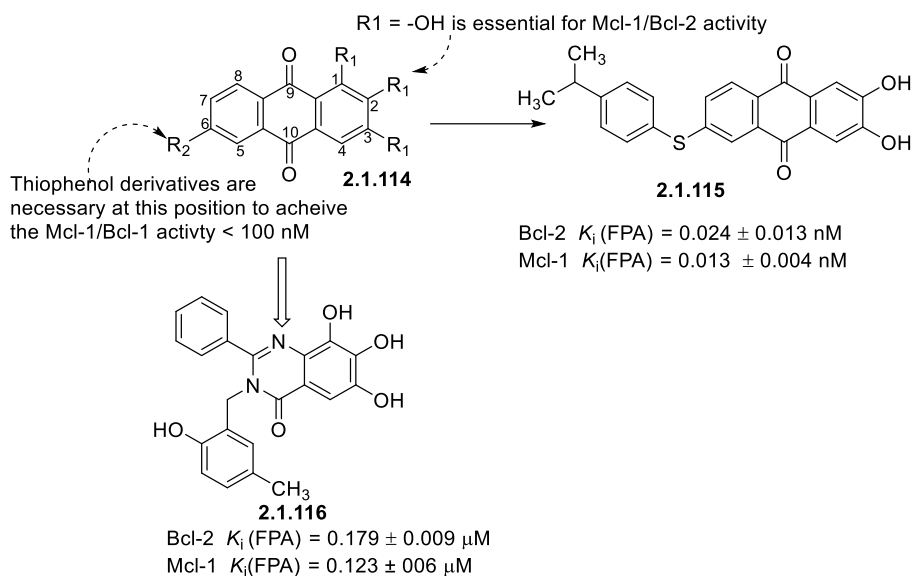


Figure 28 Anthraquinone and quinazolinone derivatives as Mcl-1 inhibitors

Naphthol derivatives

In 2014, Nicolovska-Coleska *et al* performed a high throughput screening on a library of 53000 SMIs to attain a **UMI-59** as a validated hit. Later they synthesize **UMI-77** and **UMI-101** as analogous and tested them against Bcl-2 family proteins as shown in **Figure 29**. By NMR-based docking, they confirmed that bioactive **UMI-77** is utilizing the h2 and h3 pockets similar to the BH3 helix (which utilize its four hydrophobic residues H1, H2, H3, H4) and mimic 2 conserved hydrophobic residues from mNoxa Leu78 and Ile81 respectively. They also observed that *p*-Br-phenyl group occupies the h2 pocket and interacts through hydrophobic interactions with Met231, Met250, Val253, Leu267, and Phe270, which is further supported by 2D-NMR data. Whereas, **UMI-101** was found inactive [123].

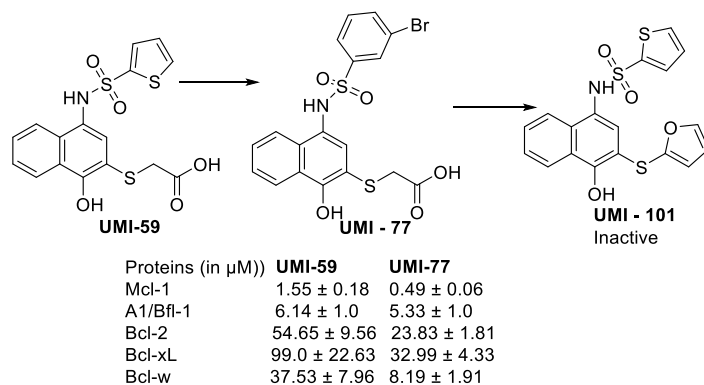


Figure 29 Structures (**UMI-59**, **UMI-77** & **UMI-101**) displaying naphthol as basic heterocyclic core

In 2016, Fletcher's group, used similar structure-based design, as uses for tetrahydroquinolines [118] to design naphthol derivatives. They utilized an innovative approach called, "site-

identification by ligand competitive saturation (SILCS)” to quantitatively predict the relative affinities of ligands bindings to Mcl-1 and Bcl-xl, and could be useful for differentiating the binding behaviors of compounds to Mcl-1/Bcl-xL in further designing of Mcl-1 selective inhibitor. The initial SAR study showed that mono-N-substitution of the sulfonamide improved Mcl-1 activity (**2.1.116a-h**) and further substitution of sulfonamide helps in optimization of potent Mcl-1 inhibitor (as N, N-, **2.1.117**) [124], as shown in **Figure 30**.

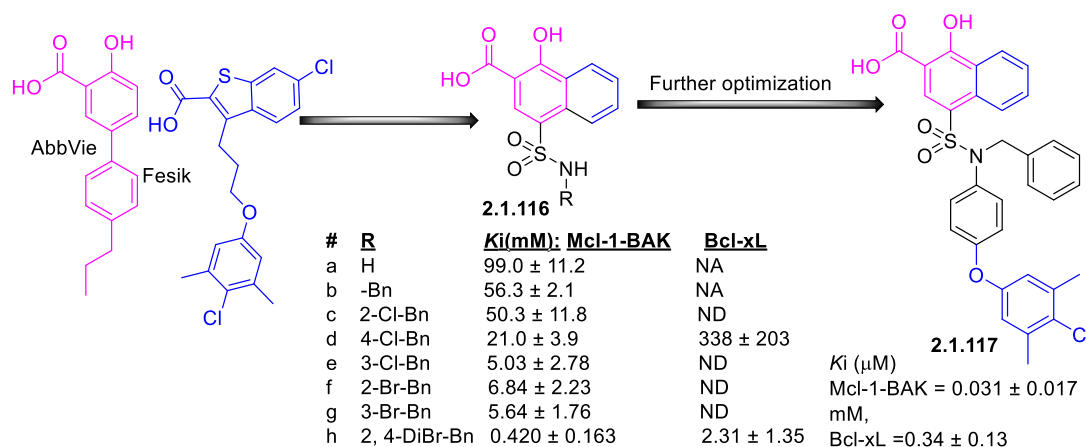


Figure 30 Structure-based design assisted the optimization of the naphthol heterocyclic containing structures.

Salicylic and anthranilic acid

AbbVie pharmaceuticals implemented a fragment-based design, where they identified fragment (**2.1.118**) as the most potent one, and this was derivatized in order to improve the potency for Mcl-1 as shown in **Figure 31**. Later, a co-crystal structure with **2.1.120** (PDB ID: 4OQ5), disclosed the mode of binding of this series of compounds: the COOH group in these ligands interacted with Arg 263, as for the amphipathic peptides from the pro-apoptotic proteins Bim and Noxa [125], while the naphthyl group occupies the leucine ‘hot spot’ in the Mcl-1 groove. The sulfonamide orient the bi-aryl ether along this groove [126].

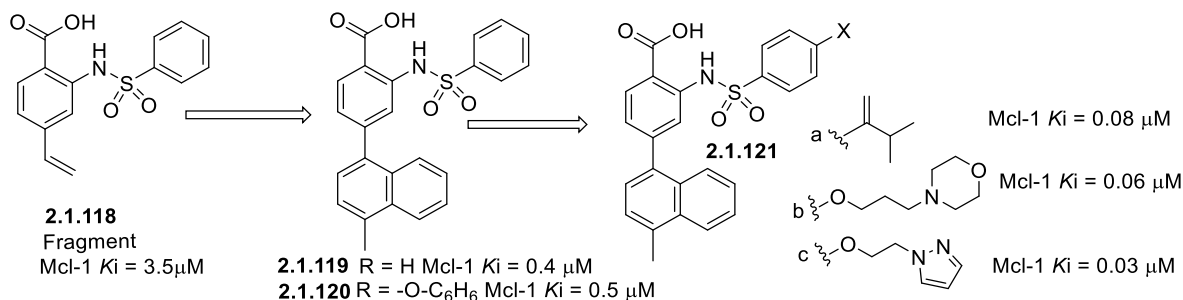


Figure 31 Anthranilic acid-based heterocycle as Mcl-1 inhibitor.

In 2016, the Fletcher group reported 2,6-di-substituted nicotines, by simplifying the α-helix mimetic (**JY-1-106**), as disrupt one of the Mcl-1-BH3 PPI. They reported that the BH3 α-helix

mimetic **JY-1-106** is a dual Bcl-xL/Mcl-1 inhibitor [127]. They began with **JY-106** and simplified it to identify a compound which was a very weak Mcl-1 inhibitor (**2.1.122**), but further derivatization led to a more improved Mcl-1 inhibitor (**2.1.123**), as shown in **Figure 32** [128].

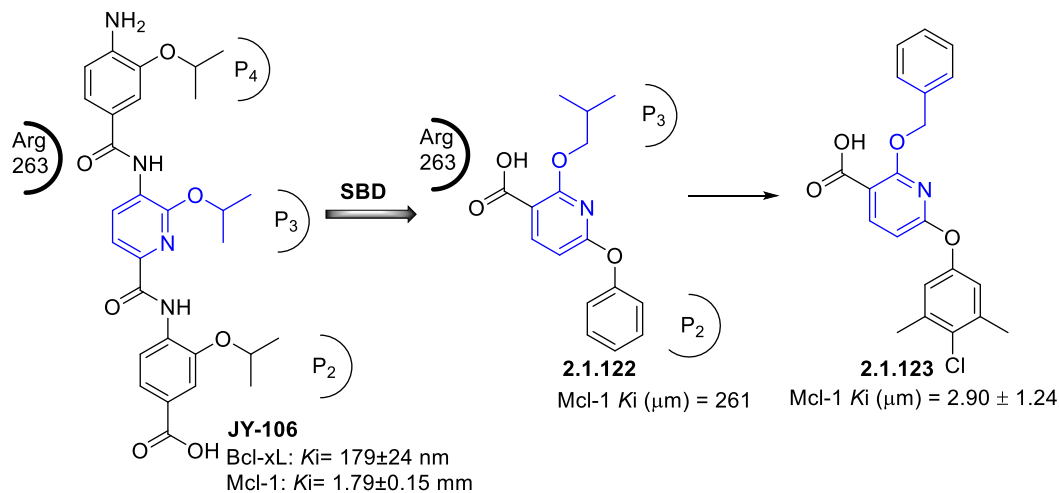


Figure 32 Salicylic acid derivative as Mcl-1 inhibitor.

Benzylpiperazine derivatives

In 2013, Ding *et al* evaluated four series of benzylpiperazine derivatives as inhibitors of Mcl-1. In order to achieve high preferential selectivity, they compared the binding site of the BH3 domain of Bcl-xL and Mcl-1. They divided these sites in both proteins into three subsites: (i) P-site (hydrophobic site: hydrophobic, mainly consisting of Leu108, Val126 and Phe97 residues in the case of Bcl-xL, and Met231, Leu235, Val249 residues in the case of Mcl-1), (ii) Q-site (a hybridized site, which mainly consists of Arg100, Asn136 and Tyr195 residues in the case of Bcl-xL, and His224, Asn260, Phe319 residues in the case of Mcl-1); (iii) L-site (region between the P-site and the Q-site: where a linker fragment is to be placed in order to connect the chemical fragments fitting to the P-site and Q-site) [129]. They applied a fragment-based design, where they found various fragments for every site. Ultimately, they synthesized four series (**A**→**D**) of benzylpiperazine derivatives (81 compounds). The most potent compounds were from A (**2.1.124**, $K_i = 0.18$ μ M) and D-series (**2.1.125**, $K_i = 0.32$ μ M), while compounds from B and C series showed less than 50% inhibition against these proteins at 50 μ M concentration, as shown in **Figure 33**.

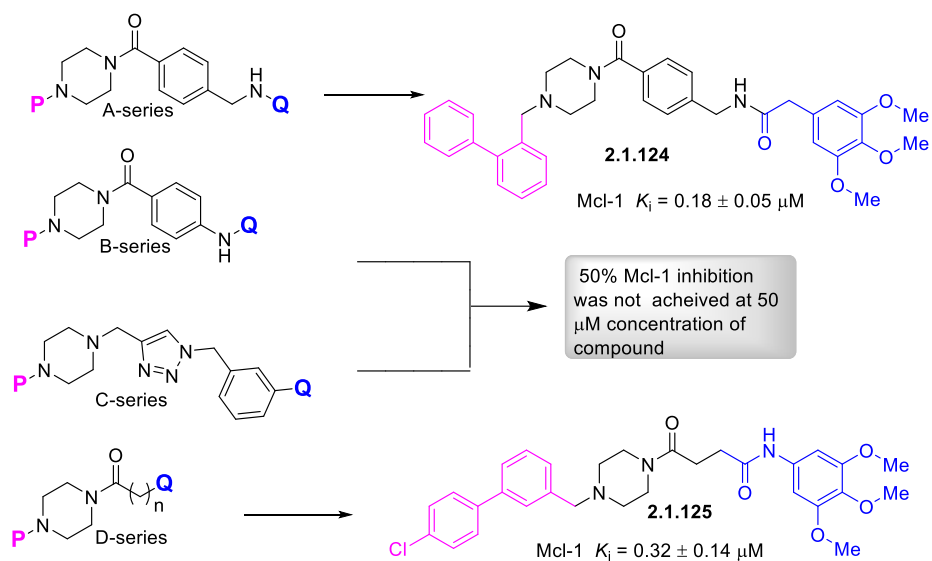


Figure 33 showing 4 different series (A-D) of benzylpiperazine as Mcl-1 inhibitors.

Pyrazolo[1,5-a]pyridine

Takeda Pharmaceuticals disclosed molecules, which were Bcl-xL/Mcl-1 dual inhibitors. They used a structure-based hybridization strategy where they fused two different scaffolds. Among the series, one is selective for Bcl-xl (**2.1.127**) while another one was Mcl-1 selective (**2.1.126**) and they attained a much more potent inhibitor (**2.1.128**), which was a dual inhibitor than the corresponding parent molecule [130], as shown in **Figure 34**.

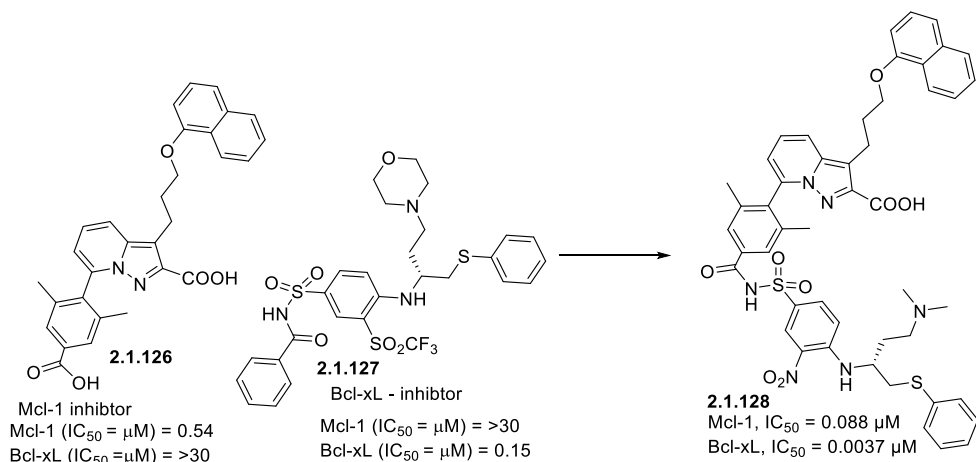


Figure 34 Pyrazolo[1,5-a]pyridine as Mcl-2 inhibitors.

Isoindolines

Zhang's group (at Dalian University of Technology China) used their previously identified scaffold (S1 (**2.1.58**)) and developed submicromolar active isoindolines [131], as shown in **Figure 35**.

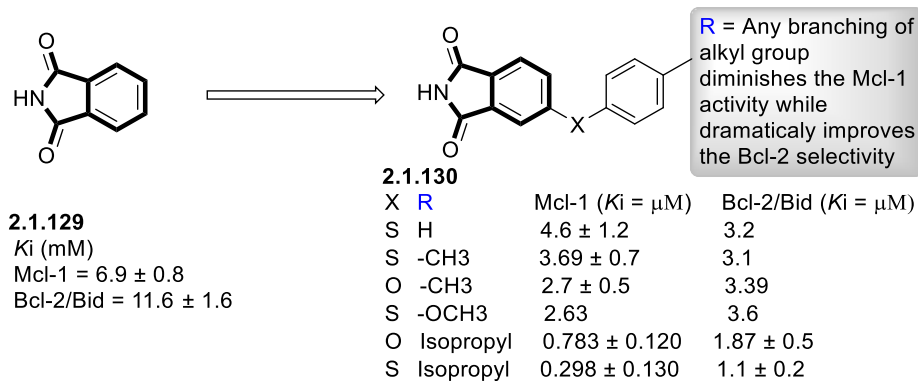


Figure 35 Isoindolines as Mcl-1 inhibitors.

Imidazolidine-2,4-dione

Fang's group used SBD where they replace the 2-thioxo-4-thiazolidinone core (as already shown in the previous section of a series of compounds **2.1.3a-d**) by imidazolidine-2,4-dione. The moderate activity of Mcl-1 was attained with compound **2.1.131d** [132] as shown in **Figure 36**

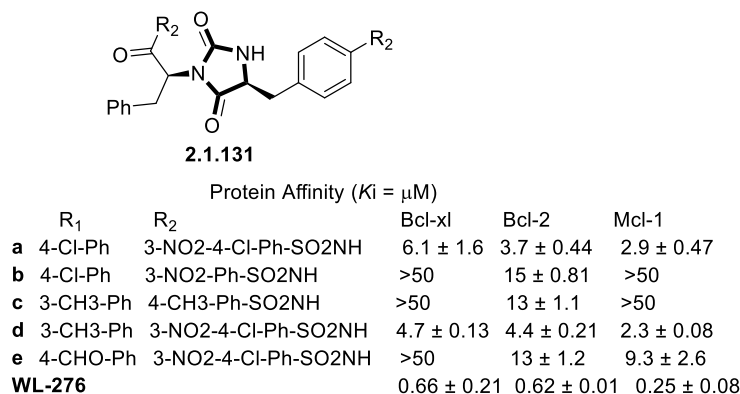


Figure 36 Imidazolidine-2,4-dione core as Mcl-1 inhibitor

Oligomers

BH3M6

In 2002 Hamilton's group developed a potent Bcl-xL antagonist based on α-helix mimicry [133]. Later, they developed a pan Bcl-2 antagonist, whose activity is associated with cytochrome c release from mitochondria, caspase-3 activation, and PARP cleavage. They also found that it induces Bax-dependent, but not Bak-dependent apoptosis [134], as shown in **Figure 37**.

Pyridoclax

A similar strategy based on α-helix mimicry was adopted by Gloaguen et al in 2015 [135], where they designed and synthesized oligopyridines to target the Mcl-1 hydrophobic pocket. They identified a compound (MR29072 or pyridoclax). Also, it had been seen that **pyridoclax**, when administered as a single agent, induces apoptosis in various cell lines (IGROV1, OAW42-R,

SLOV3, A549 and MSTO-211 H) and ABT-737-chemoresistant ovarian cancer cells (IGROV1-R10 and SKOV3) at 25 μM , as shown in **Figure 37** [136].

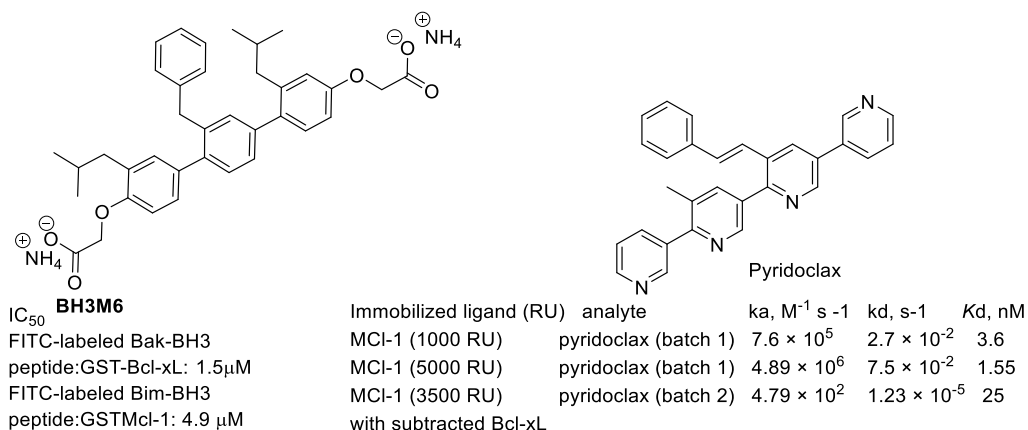


Figure 37 Terphenyl and quaterpyridines as Mcl-1 inhibitors.

Non-peptidomimetic Macrocycles

AstraZeneca discovered a library of tripeptide DNA-linked compounds from affinity-mediated screen of DNA-encoded libraries, that bound to Mcl-1 and found an inhibitor with a $K_i = 1.49 \mu\text{M}$ (**2.1.132**). The compound contains a tripeptide based dihydrobenzazepine heterocyclic basic core. On the contrary, most Mcl-1 inhibitors possess a free COOH group on their structures to interact with Arg263, but this inhibitor has a terminal primary amine. Also, SAR studies showed that any halogen atom removal diminishes the Mcl-1 activity, with most influence was found from *para*-halogen. Also, for Mcl-1 activity, *R, S, S* stereochemistry is preferred. However the macrocyclization improved the potency of the molecule (**2.1.133**) [91], as shown in **Figure 38**.

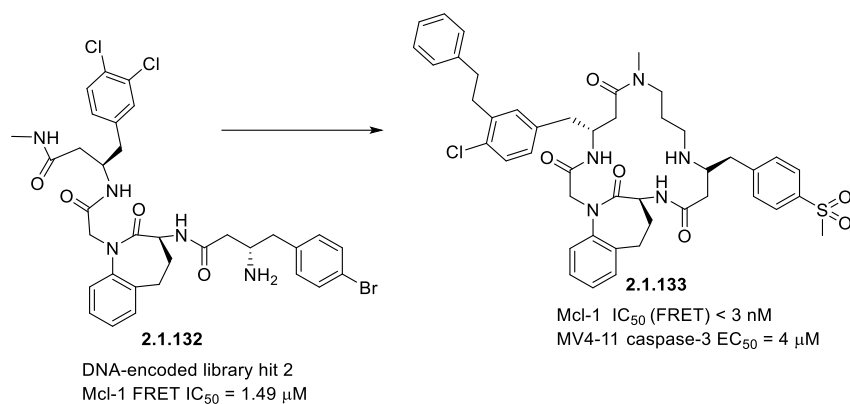


Figure 38 Molecular structures of tripeptide DNA-linked compound as Mcl-1 inhibitor.

AstraZeneca discovered a rationally designed macrocyclic molecule (**AZD5991**) with high selectivity and affinity for Mcl-1. Their studies demonstrate, that **AZD5991** inhibits to Mcl-1-Bak interactions which lead Bak-dependent apoptosis in myeloma and acute myeloid leukemia. SAR

studies showed that incorporation of two substituents (6-Cl & 1-N-Me) limits the rotation around the biaryl bond, which resulted in formation of atropisomers [137]. Also, N₁-methylation pushed the -COOH group orthogonal to the indole, improving H-bond acceptor interaction with Arg263 of Mcl-1, while 6-Cl is 3.2 Å from the peptide backbone of Ala227 (shows possibility of halogen-carbonyl bond) [138]. They found ¹H-NMR chemical shift for H₃-pyrazole (Ra)-AZD5991 was unexpectedly upfield (δ 4.75 ppm vs 2-D predicted shift δ 5.83 ppm), which indicate the strong anisotropic shielding and led to suspect the adoption of rigid conformation of macrocyclic structure in solution. Further extensive NMR based investigation studies showed that (Ra)-7 adopted a free ligand conformation quite like the bound conformation observed in the Mcl-1 co-crystal structure (PDB id: 6FS0) [139], as shown in **Figure 39**.

A direct binding screen of 100,000 sp³-rich molecules using DSF (differential scanning fluorimetry), which ultimately leads to the identification of single diastereomer of a macrolactam core that specifically binds to Mcl-1 at 4.5 μ M [140], as shown in **Figure 39**.

Antimycin A is a secondary metabolite produced by *Streptomyces* bacteria and also known for its antibiotic property, but Reed and co-workers shows its non-selective Bcl-2 antiapoptotic protein inhibition at low μ M concentration except (Bfl-1 >10 μ M), as shown in **Figure 39**.

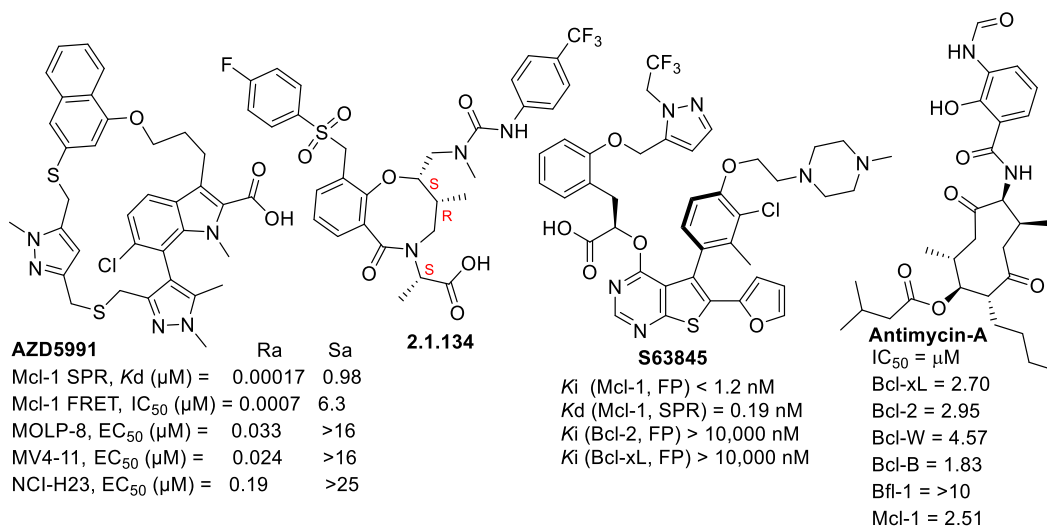


Figure 39 Non-peptidomimetic macrocyclic cores as Mcl-1 inhibitors

Miscellaneous heterocyclic inhibitors

In 2016, Walensky's group reported a small-molecule covalent Mcl-1 inhibitor (**2.1.135**), which interacts at an allosteric site (with Cys286) from the BH3-binding groove. Later studies showed that it impairs the binding capacity of Mcl-1/BAX *in-vitro* and in mouse cells [141]. In order to find new scaffold for Bcl-2 family protein inhibitor development, Yang *et al*, performed a virtual

screening on 56,000 compounds they selected 3-different types scaffolds (**2.1.136**, **2.1.137**, **2.1.138**) [142], as shown in **Figure 40**.

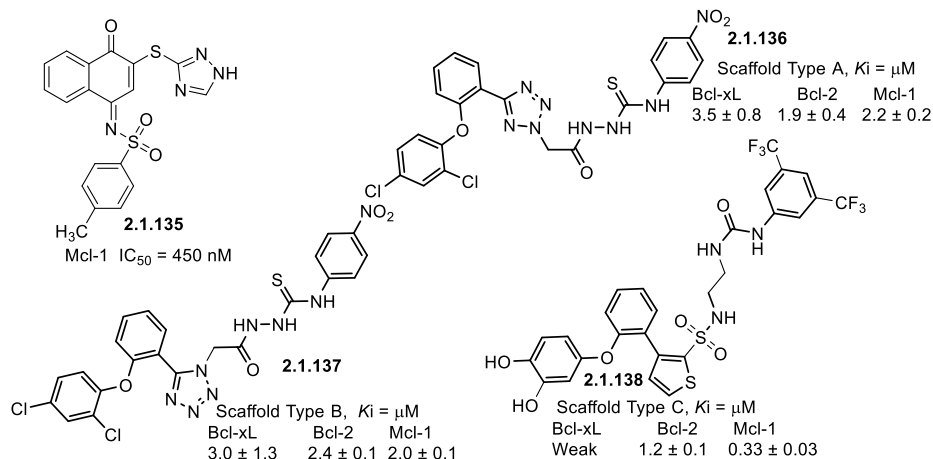


Figure 40 Heterocyclic Mcl-1 inhibitor based on various heterocyclic cores.

The Fletcher's group disclosed Kröhnke pyridines (**2.1.140a-b** & **2.1.141**), as low-micromolar inhibitors of Mcl-1 wherein the 2,4,6-substituted compounds were predicted to mimic the i, i + 2 and i + 7 side chains of the BH3 α-helix [143], as shown in **Figure 41**.

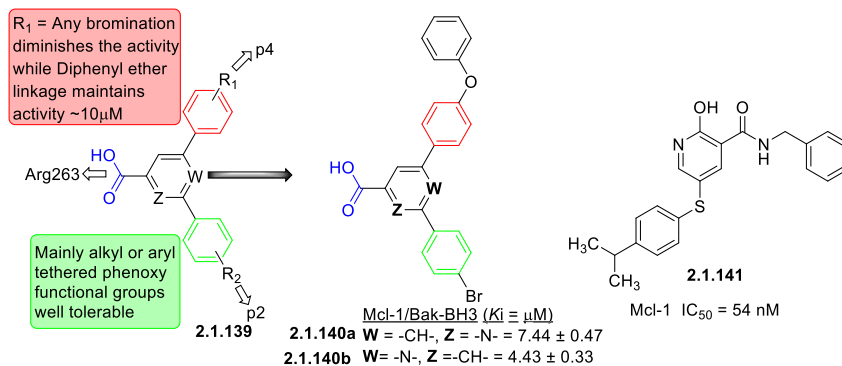


Figure 41 Kröhnke pyridines as Mcl-1 inhibitors

Based on previous work by Fang's group (Shandong University), they improvised the amino acid core with L-tyrosine (**2.1.142**), where further modification leads to the formation of **2.1.143** and **2.1.144** [144]

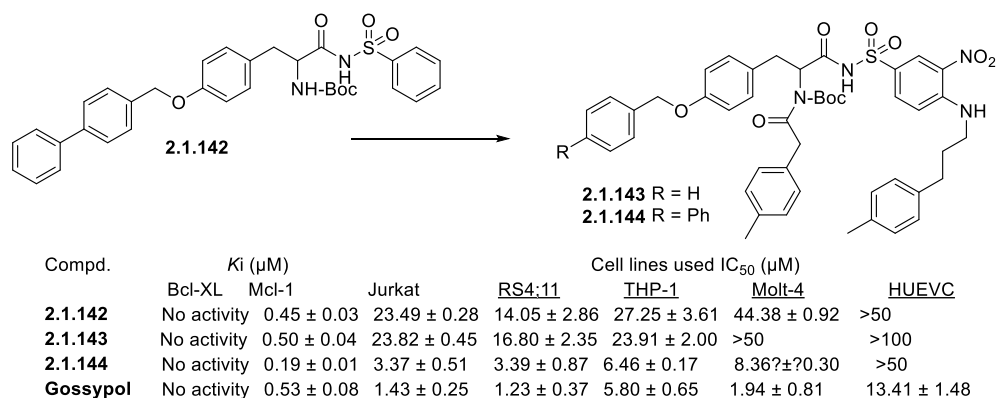


Figure 42 Fang's group improvised the heptacyclic core as Mcl-1 inhibitor

Triazines

The Nikolovska-Coleska group at Michigan University performed a HTS on 102,255 compounds using two different labeled BH3 peptides derived from the Noxa and Bid pro-apoptotic proteins and identified the difuryl-triazine (**2.1.145**) as an Mcl-1 inhibitor [145]. The compound was further studied as part of a structure-activity relationship by substituting various in the place of furan rings and the benzamide. However, they attained **2.1.146** as their most potent compound, as shown in

Figure 43.

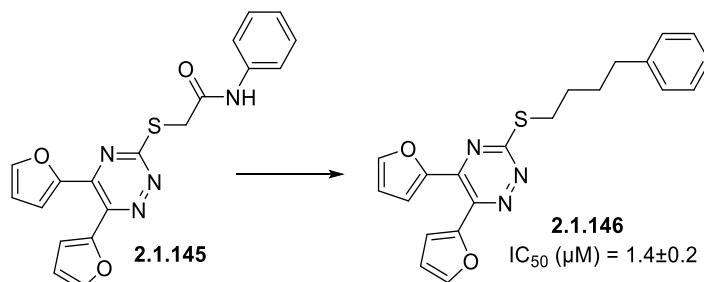


Figure 43 Triazine heterocyclic core used as Mcl-1 inhibitor.

Zhu & Zhou (School of Pharmacy, Second Military Medical University, Shanghai, China) identified a broad-spectrum inhibitor of Bcl-2 family proteins. They developed two different molecules (**2.1.147** & **2.1.148**) [146]. In their subsequent study they improved the selectivity for the P₁ pockets in the anti-apoptotic Bcl-2 proteins and identified an Mcl-1 selective compound (**2.1.149**). **2.1.149** was ~ 70-fold more potent for Mcl-1 than Bcl-2 and nearly 330-fold more potent for Mcl-1 than Bcl-xL [147], as shown in **Figure 44**.

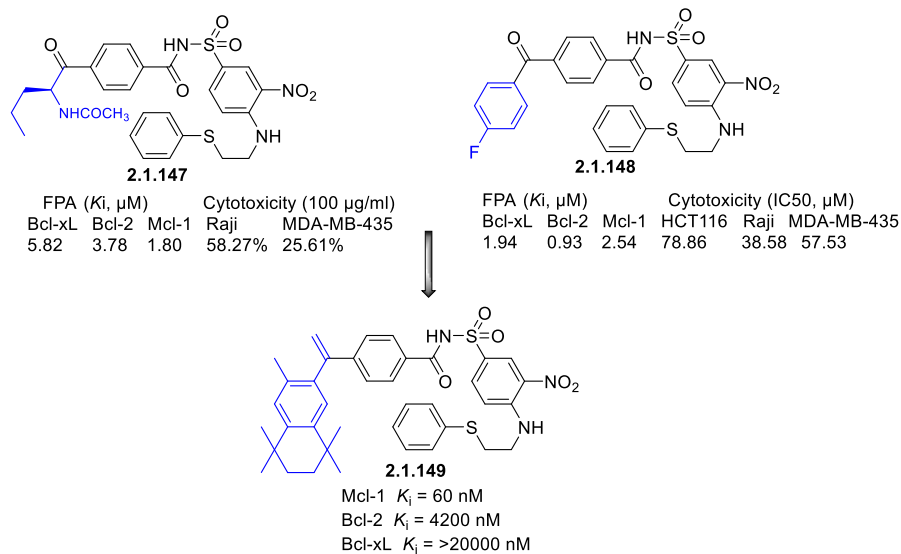


Figure 44 Zhu & Zhou co-worker utilized SBD to form Mcl-1 selective compounds

Inhibitors based on natural products

Meiogynins are the most studied class of natural products inspired Mcl-1 inhibitors. While **Meiogynin A** was not found cytotoxic, however its derivatized stereoisomer showed cytotoxicity and induced apoptosis as a dual inhibitor of Bcl-xL and Mcl-1 proteins (as seen in **2.1.150**, **2.1.151** & **2.1.152**) [148]. Further derivatization, by incorporating aromatic side chain in the structure did not change its dual inhibition of Bcl-xL and Mcl-1 but improved its affinity towards both targets as could be seen for compounds **2.1.153** and **2.1.154** [149, 150]. Further derivatization showed the ambiguous nature of the inhibition of Bcl-2 proteins where most of the derivatives were dual inhibitors of Bcl-2 and Mcl-1 (**2.1.155** to **2.1.157**) [151], as shown in **Figure 45**.

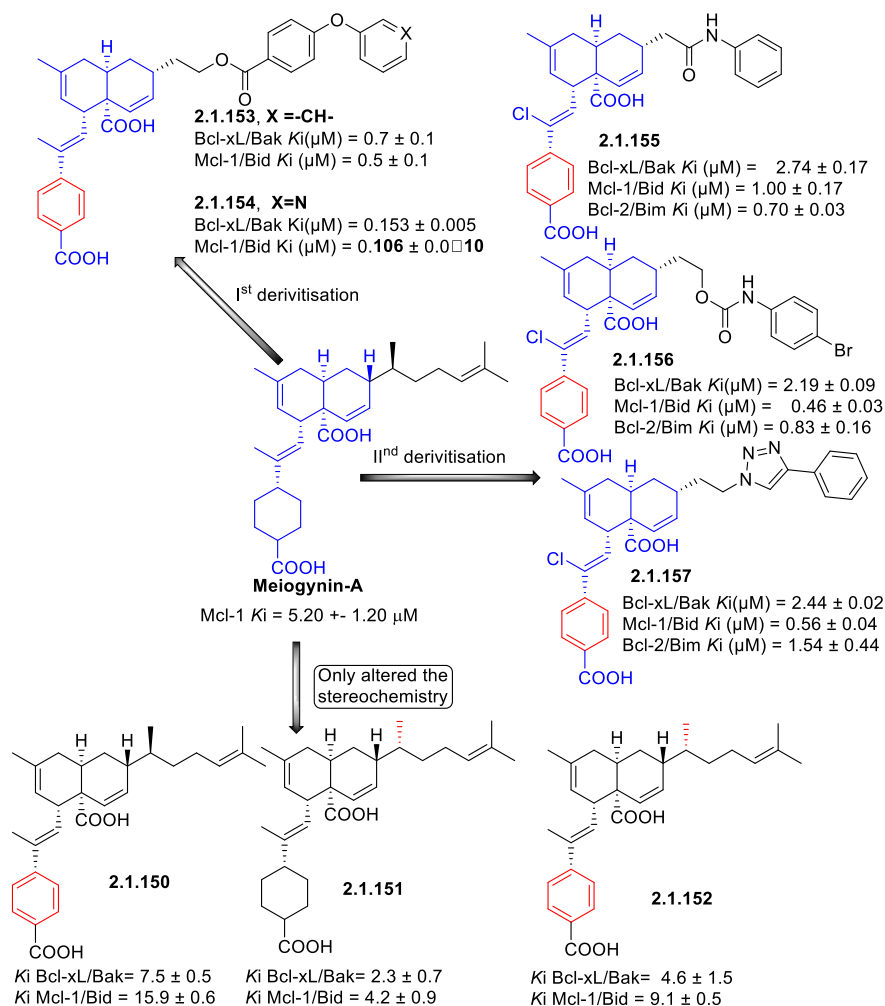


Figure 45 Meiogynins and its derivatives as Mcl-1 inhibitors

There has been various other natural product based Mcl-1 inhibitors, and these are shown in **Figure 46** and are discussed in the next part of this chapter.

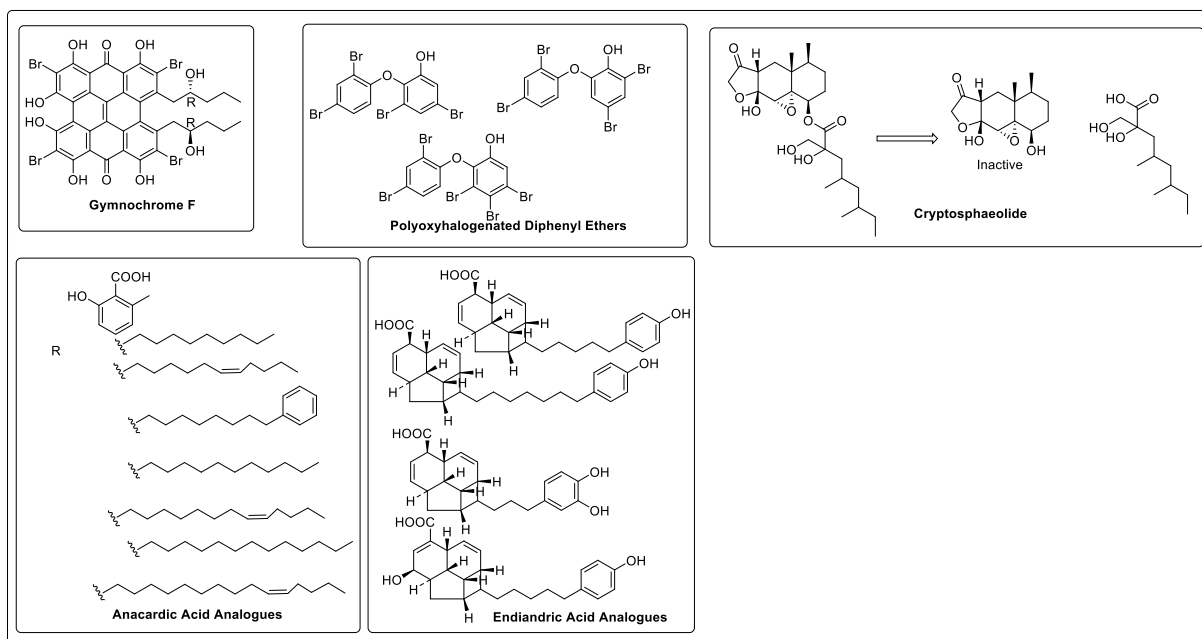


Figure 46 Mcl-1 inhibitors based on natural products

2.1.6 Conclusion

There were various heterocyclic compounds evaluated against Mcl-1 protein, but as the protein shares similar active site structural features with other members of the Bcl-2 family, therefore it poses a challenge to attain any preferentially selectively against the protein. However, the majority of these reported heterocyclic compounds did show a selective targeting of Mcl-1 and bound to the same region as that of the BH3 helix of the apoptotic proteins in order to achieve this. Mainly these heterocycles contain rigid hydrophobic rings (like indole, tricyclic indole core, anthraquinone, isoquinoline) as the main basic scaffold with a carboxylic acid, or similar bioisostere, to interact with Arg263 of NWGR domain. Also, commonly they also have a hydrophobic group (such as 3,5-diMe-4-Cl-phenyl) that can insert into the P₂ pocket of Mcl-1. In few cases, an additional group can be extended from the basic core to directed towards the P₄ pocket by using a suitable length linker to enhance the binding affinity for Mcl-1, as seen in Fesik and AbbVie pharmaceutical designed Mcl-1 inhibitors.

Objective 2.2. Recognition of binding mode of the diverse natural-derived Mcl-1 inhibitor

2.2.1 Introduction: *Structural specificity of naturally occurring Mcl-1 inhibitors*

Several reports have established a link between Mcl-1 up-regulation with the development of resistance to various anticancer chemotherapies [59, 152-155], as described in previous **objective 2.1**. Also, its amplification is found as one of the most common genetic aberrations observed in human blood cancers and even, its RNA-mediated knockdown and gene silencing showed substantial inhibition of cancer cell growth and restored the sensitivity of chemo-resistant cells [52, 59, 60]. Functionally, Mcl-1 is endogenously inhibited by its proapoptotic partner proteins, which utilize their BH3-helix domain for binding to Mcl-1. The BH3-helix is an α -helix which was used in ligand-based design to develop inhibitors of Mcl-1, as shown in **Figure 47**. The key interactions between Mcl-1/BH3-helix of proapoptotic proteins provide significant information that has been used by various researchers to generate BH3-helix mimetics. Researchers developed various BH3-helix based chemotypes, such as oligopeptides, stapled α -helices, α - β -peptide foldamers, reverse BH3 (rBH3) peptide and small molecules (as mentioned in *objective 2.1*) as Mcl-1 inhibitors but none of them have attained clinical application so far. Mcl-1 is an antiapoptotic protein, belonging to a large family of proteins, sharing structural homology in its binding site with other members of its family, especially with other antiapoptotic proteins, such as Bcl-2 and Bcl-xL. Therefore, structure-based Mcl-1 inhibitor design faces several challenges in attaining preferential selectivity. It is well known that Mcl-1 has the NWGR domain (asparagine-tryptophan-glycine-arginine), which has an active role in binding of BH3 helix of pro-apoptotic proteins. However, in recent years, seven new natural compound classes were reported as low micromolar Mcl-1 selective inhibitors as shown in **Table 5**. As there were no studies performed regarding their binding behavior with Mcl-1 therefore under this objective, I included studies on the computed binding modes of these seven new classes of natural compounds as shown in **Figure 48**, along with the validation of implemented computational methods with available experimental affinity data.

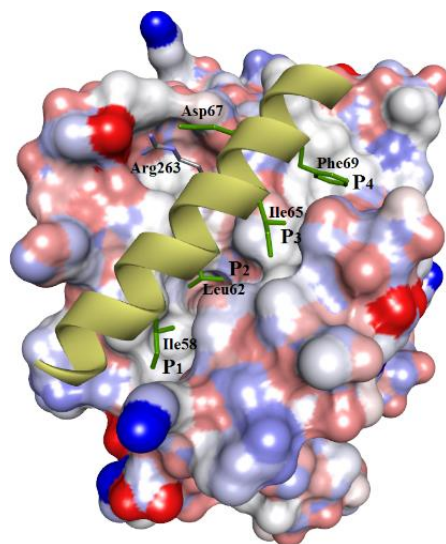


Figure 47 The co-crystal structure of Mcl-1 protein with α -helix peptides sheds insight into the binding cavity, showing 4 pockets (P₁, P₂, P₃, P₄) in the active site, where each hydrophobic amino acid side chain of BH3 helix (H1, H2, H3, H4) utilizes these pockets.

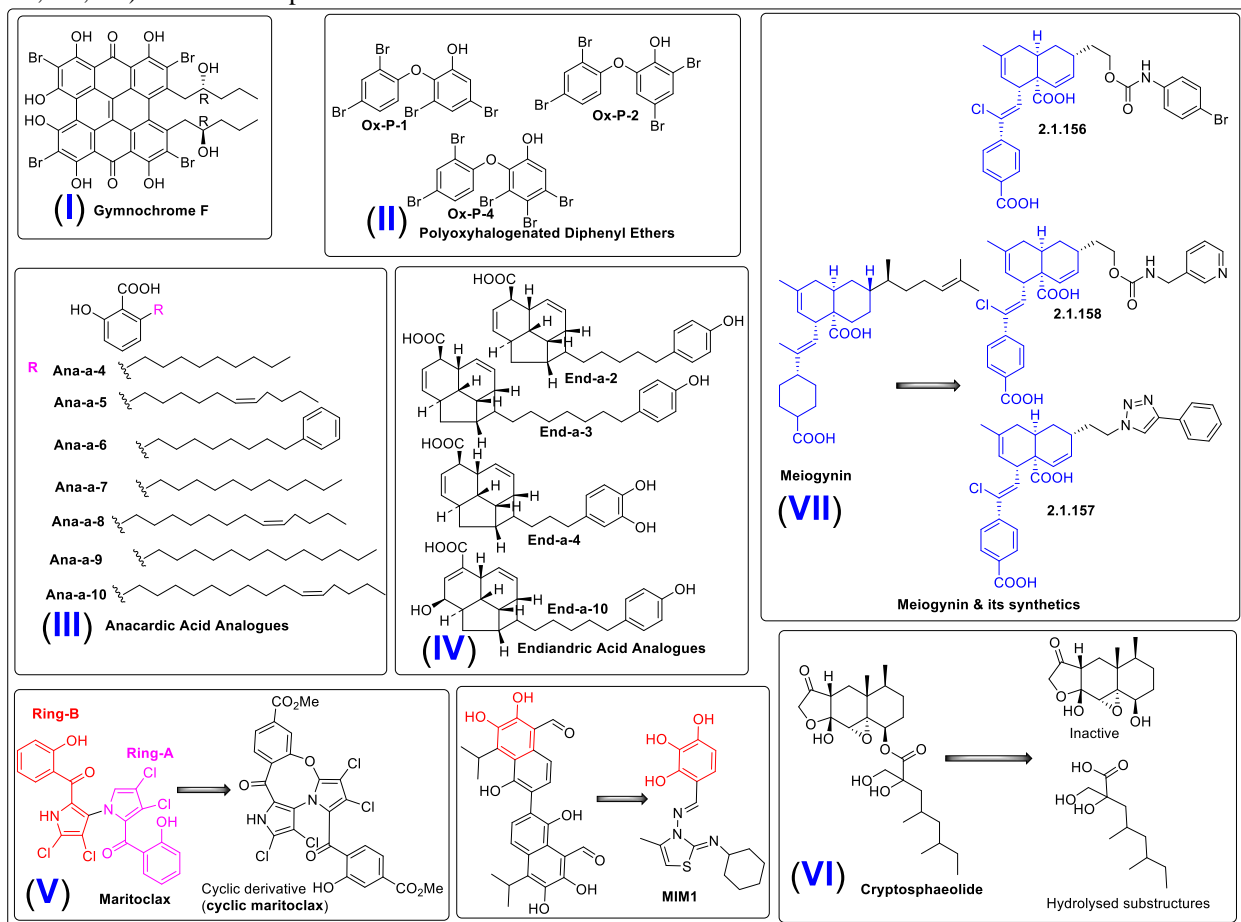


Figure 48 (adopted from Figure 46) Structure of the natural product Mcl-1 Inhibitors: (I) **Gymnochrome-F**, a phenanthroperylenequinone containing core compound isolated from a deep water Crinoid, *Halopus rangii* [156]; (II) **Oxy-polyhalogenated diphenyl ethers** from a sponge *Dysidea (Lamellodysidea) herbacea* [157]; (III) Anacardic Acids from *Knema hookeriana* [158]; (IV) **Endiandric Acid Analogues** from *Beilschmiedia ferruginea* [159]; (V) **Maritoclax** and its synthetic analogue: maritoclax structure can be divided into ring-A (magenta) and ring-B (red) for

easy presentation; Mcl-1 inhibitor molecule 1 (**MIM1**), a high throughput screening compound, shares similar structural features like Gossypol. (VI) **Cryptosphaerolide** from a marine-derived ascomycete related to the genus *Cryptosphaeria* [160]; (VII) **Meiogynin** and its synthetic derivatives. Mcl-1 inhibitor molecule 1 (**MIM1**), a high throughput screening compound and not a natural product, shares similar architectural features with naturally occurring Gossypol.

2.2.2 Result and Discussion

2.2.2.1 Rationalization of molecular modeling protocols

Initially, I investigated the protein structure of the *hMcl-1* protein available from the protein data bank (www.rcsb.org/). It is evident that in a few instances, that the protein crystal structures could contain some structural anomalies (e.g., missing atom coordinates, stereochemical/geometry issues in amino acids), therefore the selection of *hMcl-1* crystal structures was focused on finding crystal structures of Mcl-1 protein with a low number of anomalies, so that further computational studies can be performed more accurately to identify the binding conformation of naturally derived Mcl-1 inhibitors. Nineteen X-ray crystal structures for *hMcl-1* protein were retrieved from the Protein Data Bank. Although these crystal structures belong to the same species (*Homo sapiens*), their crystal structure quality was different from one another. Therefore, I compared all these structures together, in order to select the highest quality *hMcl-1* protein structure for the computational study, as shown in **Table 1**. I found Mcl-1 crystal structures that contained co-crystallized peptides as shown in **Table 1** (*table cells colored in grey*), and these showed typical interactions with amino acids of the cavity (including pockets: P₁, P₂, P₃, and P₄). I did not proceed further with these structures as (a) they lacked molecular diversity in their structure (as most of them were BH3 helix peptide analogs) and therefore had interaction with similar amino acids of P₁-P₄ of Mcl-1; (b) Also, peptide backbone are prone to hydrolysis and devoid of ability to cross cell bilipid transmembrane, limits their futuristic usability as oral drugs; (c) On the other hand, small molecule inhibitors have been based on diverse scaffolds and diverse binding modes and therefore, provide guidelines to exploit the other regions of the active site of *hMcl-1* protein in comparison to peptides and therefore could be useful in attaining better selectivity comparatively among other members of Bcl-2 Family. Therefore, I focused on analysis of co-crystal structures based on small molecule inhibitors (SMI) with *hMcl-1* protein, rather than choosing the *hMcl-1*-peptide co-crystal structures, for the molecular modeling studies. The main initial objective was to choose one structure to commence docking experiments.

Table 1: Analysis of available co-crystal structures where *hMcl-1* is bound to a small heterocyclic molecule. X-ray structures and structural parameters (R-Value vs R-Observed, Clash score, etc) are summarized.

<i>PDB</i>	<i>Res.</i>	<i>Co-crystallise ligand</i>	<i>R-Val. (obs.)</i>	<i>R-Fr.</i>	<i>Clash Score</i>	<i>Ramachandran Outliers</i>	<i>Side chain outliers</i>	<i>RSRZ outliers (%)</i>	<i>RMS D</i>	<i>Reference</i>
4WMR	1.70	SMI	0.171	0.206	1	0	0	4.0	0.73	[161]
4ZBF	2.20	SMI	0.184	0.233	6	0.2	4.5	2.0	0.75	[88]
4ZBI	2.50	SMI	0.183	0.242	7	0.6	8	1.7	0.96	[88]
4OQ5	2.86	SMI	0.200	0.235	9	2.1	11.3	8.1	0.81	[126]
4OQ6	1.81	SMI	0.203	0.205	11	0	7.3	1.4	1.02	[126]
3WIX	1.90	SMI	0.246	0.291	4	0	3.3	3.2	0.69	[130]
3WIY	2.15	SMI	0.214	0.283	3	0.7	4.0	2.5	0.79	[130]
4HW2	2.80	SMI	0.217	0.251	32	1.7	17.6	1.8	1.12	[87]
4HW3	2.40	SMI	0.216	0.269	13	1	11.4	3.2	0.97	[87]
4HW4	1.53	Pept.	0.140	0.182	2	0	0	2.1	NA	[87]
3TWU	1.80	Pept.	0.184	0.223	2	0	0	2.3	NA	[162]
3PK1	2.49	Pept.	0.213	0.245	3	0.9	8.1	0.9	NA	[163]
3MK8	2.32	Pept.	0.233	0.275	9	0.7	0	1.9	NA	[164]
3KZ0	2.35	Pept.	0.224	0.270	10	0	0	9.9	NA	[165]
3KJ0	1.70	Pept.*	0.187	0.223	8	0	0.6	4.4	NA	[165]
3KJ1	1.95	Pept.*	0.188	0.213	3	1.2	0.7	9.4	NA	[166]
3KJ2	2.35	Pept.*	0.210	0.233	2	0	1.3	6.7	NA	[166]
3IO9	2.40	Pept.*	0.211	0.269	7	0.6	4.9	4.1	NA	[167]
2PQK	2.00	Pept.	0.196	0.234	6	0	1.4	7	NA	[167]

PDB: id code that is in protein data bank; *Res.*: Resolution of protein crystal; *R-Val*: measure the quality of the atomic model obtained from the crystallographic data, whereas a perfect fit would have a value of 0 and, typical values are about 0.20; *R-free*: This is a less-biased biophysical parameter evaluated for crystal structure. To calculate R-free, 10% experimental observations were removed from the data set and then refinement is performed using 90% and lastly R-free calculated how well the model predicts that 10%, that was not used in refinement. Typically, R-free found slightly higher than *R-value* and with a value of close to 0.26; *Clash Score*: This score shows the number of pair of atoms in protein structure clashing sterically with each other and expressed such clashes per 1000 atoms; *Ramachandran Outliers*: This is stereochemical geometry evaluation of amino acid residues of protein structures where the combination of their ϕ and ψ torsion angles are assessed; *Side chain Outliers*: In general, sidechains of residues in protein usually adopted number of combinations of preferred torsion angle values (rotamers), which are usually evaluated from a set of torsion angles and the ones whose values found outside from these values, called as side chain outliers. The score is calculated as the percentage of unusual sidechain conformation residues with respect to the total number of amino acid residues; *RSRZ outliers*: an amino acid residue is said to be an RSRZ outlier if its RSRZ value is more than two. The RSRZ outlier score represents the percentage of the total number of RSRZ outliers in comparison to the total amino acid residues assessed [168]; RMSD: root mean square deviation, was attained from self-docking; SMI: small-molecule inhibitor; Pept: peptide structure.

The study involved using various crystal structures of *Mcl-1* with small molecule inhibitors (SMIs) bound and, therefore, I implemented the *multiple receptor conformation* approach (MRC) [169], which generates an ensemble of conformations of *hMcl-1* from these crystal structures (as seen in **Figure 49.a**). The MRC approach involved the superimposition of the backbone of all *Mcl-1* structures over each other and then calculating their RMSD values, to estimate the differences between these crystal structures. The *Mcl-1* conformation was found to be reasonably conserved in all these structures based on RMSD between 0.61 to 1.79 Å, especially when considering the total number of amino acids in the backbone of these protein crystals (~ 157 amino acids). This MRC methodology helps in calculating the structural differences among these crystal structures in

the form of RMSD values (in Å), which can be useful in estimating the possible error in docking pose conformations when performed on these crystals, individually. These deviations/differences might originate from the crystal quality and biophysical techniques adopted during the characterization of these *hMcl-1* crystals, as shown in **Figure 49.a**. This methodology resulted in the identification of a pdb (3WIX), which showed lowest RMSD values and found closest to the average structure of all those in **Table 2**, and which was then later chosen for molecular modeling. Next, I employed a multiple ligand conformation (MLC) approach, which was achieved by cross-docking of all the individual co-crystallized ligands to the 3WIX pdb. This kind of cross-docking of co-crystal ligands from other pdbs to a particular pdb (3WIX) helps in comparing the relative deviation of conformations of docked poses from their original co-crystal binding poses in their pdbs, where lower deviations ($\geq 1\text{Å}$ in terms of RMSD) further supports the extent of usefulness of the selected pdb. Through this MLC approach, I observed the details of computed ligand binding to *hMcl-1*. In that way, it helped in allocating the active and passive amino acids of the cavity (mapped as shown in **Figure 49 (b)**) which are either directly involved or help indirectly in the binding of ligand to adopt a conformation (docked conformations of all co-crystallise ligand binding to the 3WIX shown in **Figure 49 (c)**).

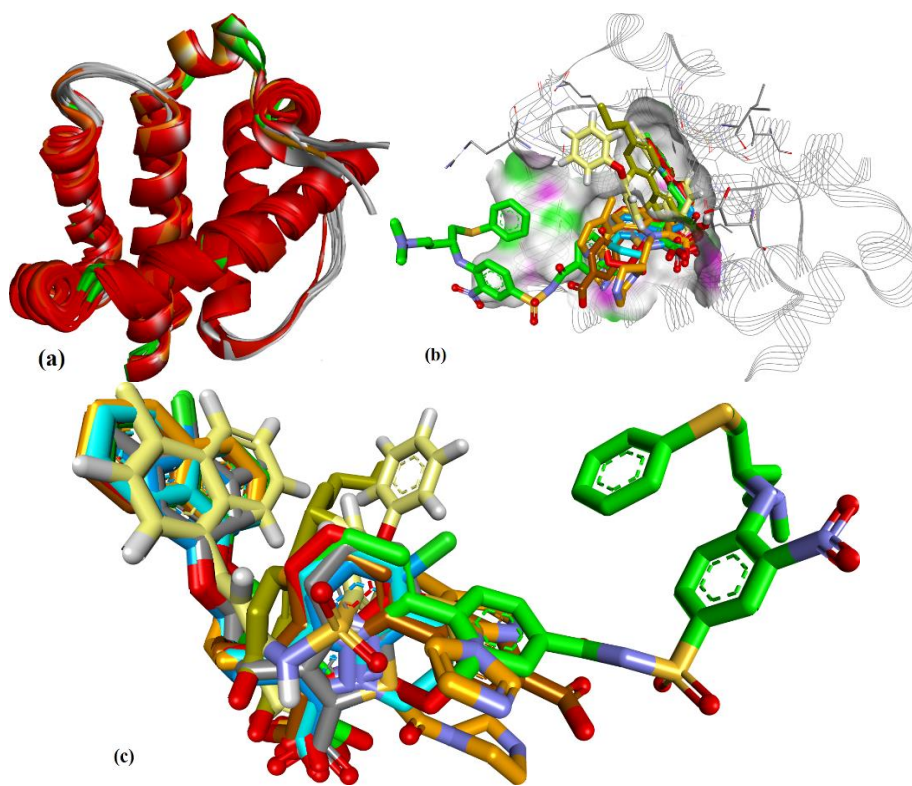


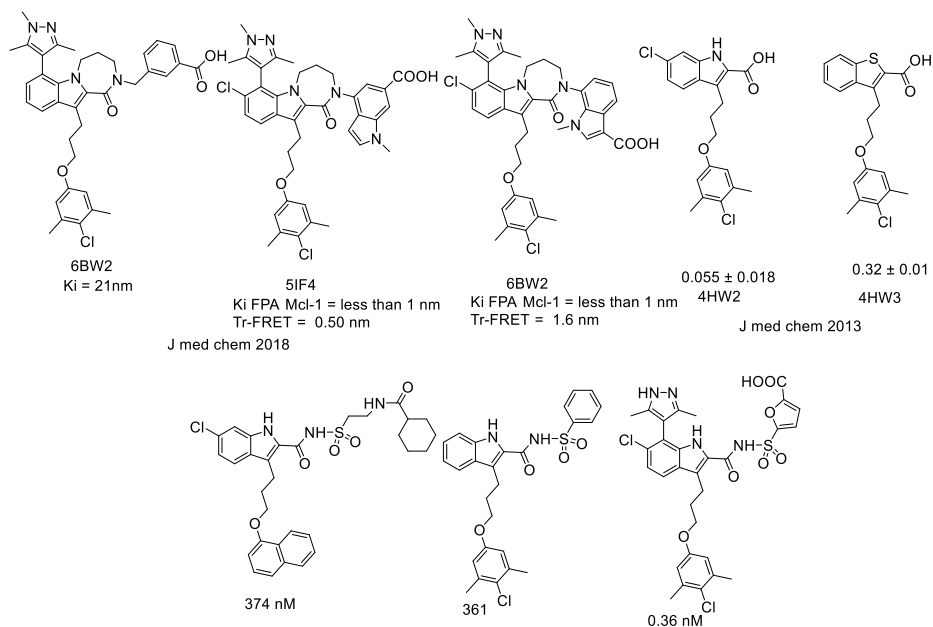
Figure 49 (a) Superposition of crystal structures of Mcl-1; (b) H-donor/acceptor integrated cavity in Mcl-1 identified by the MLC approach; (c) Various docked binding orientations of ligands in the co-crystal structures

Table 2: MRC approach: Estimation of RMSD values (Å) of superpose individual PDBs over each other

Proteins	4WMR	4ZBF	4ZBI	4OQ5	4OQ6	3WIX	3WIY	4HW2	4HW3
Ligands									
4WMR	0.73	1.12	1.23	2.34	1.45	0.83	0.93	0.88	1.02
4ZBF	1.05	0.75	1.02	1.02	1.02	0.92	1.02	1.02	1.02
4ZBI	1.01	1.02	0.96	1.02	1.02	0.89	1.02	1.02	1.02
4OQ5	1.89	1.02	1.02	0.81	1.02	0.79	1.02	1.02	1.02
4OQ6	1.97	1.02	1.02	1.02	1.02	0.95	1.02	1.02	1.02
3WIX	1.09	0.98	0.78	1.05	1.02	0.69	1.01	0.79	0.88
3WIY	1.33	1.12	1.96	1.38	1.02	0.74	0.79	1.02	1.02
4HW2	1.87	1.02	1.02	1.02	1.02	0.98	1.02	0.76	1.02
4HW3	1.71	1.02	1.02	1.02	1.02	0.82	1.02	1.02	0.83

Higher the RMSD value more will the deviation of PDB with each other

2.2.2.2 Evaluating the precision and accuracy of docking methods

**Figure 50** Fesik group's ligands which had been co-crystallized with Mcl-1.

In order to evaluate the precision and accuracy of the docking methods, I compared the docking scores of a set of Mcl-1 inhibitors with their corresponding K_i values as shown in **Figure 50** [170]. The reason for choosing these Mcl-1 inhibitors was: firstly, they were characterized by the same group ([Fesik](#)) and therefore the binding assay method conditions were uniform for all compounds. Secondly, they all have been co-crystallised with Mcl-1 and the crystal structures determined, which also provided their original native bound conformation for comparisons with docking. I employed three docking methods in order to see how they varied in their results, as shown in **Table 3**. The results from all the three docking methods showed an identical pattern, where MOE [171] was found with the lowest RMSD values for its docked poses followed by AutoDock [172] and

then VLifeDock [173] when compared with native bound ligand conformation in *hMcl-1*, as shown in **Table 3**. This may be expected as MOE docking utilized the knowledge of active binding site directly from the co-crystal ligand binding site of pdb, while Autodock accessed the binding site for docking through a grid box formation around a defined ligand binding site.

Table 3. Comparison of docking scoring with *hMcl-1* inhibitor K_i values (Fesik's group): This methodology involves docking of co-crystal ligands to their own pdb files and then calculating the RMSD with respect to their crystal pose.

pdbs	K_i value (nM)	MOE		AutoDock		VLifeDock		Reference s
		<i>Score</i>	<i>RMSD</i>	<i>Score</i>	<i>RMSD</i>	<i>Score</i>	<i>RMSD</i>	
5FDO	361	-7.29	1.81	-8.30	1.94	-7.02	3.49	[89]
5FDR	0.94	-8.59	2.82	-7.22	3.07	-7.48	3.14	[89]
6BW2	21.0	-10.52	1.86	-9.94	2.30	-9.11	2.33	[90]
6BW8	< 1.00	-10.34	0.54	-9.84	1.36	-9.17	1.45	[90]
5IF4	< 1.00	-10.76	1.24	-10.14	1.36	-10.87	1.51	[174]
4HW2	55 ± 18	-8.41	0.39	-7.99	0.67	-8.02	0.71	[87]
4HW3	320 ± 10	-6.46	0.19	-6.47	0.63	-6.10	0.65	[87]

Reproducibility of docking results is always a concern in drug design, which is defined as how precisely a particular docked conformation can be repeatedly observed in docking results. However, as reproducibility is an independent term and relates to the close prediction of docking predicted pose to that found in the co-crystal structure (i.e. accuracy of docking method). Therefore in order to assess the reproducibility or accuracy of the adopted docking methods, iterative self-docking was performed using the 3WIX pdb [175] where the co-crystal ligand of pdb (3WIX) was self-docked five times into its own binding site and each time it was compared with the orientations of its own conformation in the co-crystal structure by measuring the RMSD. In this way, I compared and evaluated the adopted docking methods. As in most methods, the docking was usually initiated by calculating docking score of docked conformation of a flexible ligand which is in most cases commenced from a random conformation of the ligand, and therefore it severely affects the precision of reproducibility of particular docking method (precision is defined as repetition of the same pose) [176]. The measurement of reproducibility (*NRMSE*) was achieved using a mathematical expression, which determines the percentage of the closest RMSD of docked conformation of co-crystallise ligand of 3WIX attained during iterative self-docking (*closest RMSD attained*) with a factor (termed here as, "RMSE" which is a difference between the most deviated RMSD value and least deviated RMSD value of docked pose from original co-crystallise conformation), as shown in the footnote of **Table 4** and in **Figure 51**. As can be seen from **Table 4**, MOE (triangle matcher method) docking has shown 86% reproducibility (*NRMSE*)

compared to AutoDock (genetic algorithm, 56%) and VLifeDock (GRIP method-based docking: 36%).

I also observed comparatively fast, accurate bound conformation prediction from VLifeDock when compared with AutoDock. However, AutoDock was more precise in predicting and reproducing docking poses [177] but less accurate in reproducing the co-crystal pose.

Table 4: Reproducibility of computational docking poses

Docking Phase Trials	RMSD [£] (Å)		
	MOE	Autodock	VLifeDock
I	0.690	1.007	0.902
II	0.681	0.989	0.884
III	0.682	0.996	0.879
IV	0.681	0.996	0.857
V	0.681	0.994	0.871
<i>RMSE</i> ($\Delta = \text{Å}$)	0.008 [§]	0.018 [§]	0.025 [§]
<i>NRMSE</i> [£]	86.12 %	55.94%	36.08%

Note: § Lower value for RMSE indicate more precision £ Less value indicate more accuracy; RMSE : root-mean-square deviation error = RMSD (maximum value) – RMSD (Minimum value) & Higher value indicates more reproducibility; Reproducibility was measure in terms of normalized root-mean-square deviation or error (NRMSD or NRMSE: This is fraction number which measures the degree of reproducibility) [178-180]

$$\text{NRMSE} = (\text{Closest RMSD attained} / \text{RMSE}) \times 100$$

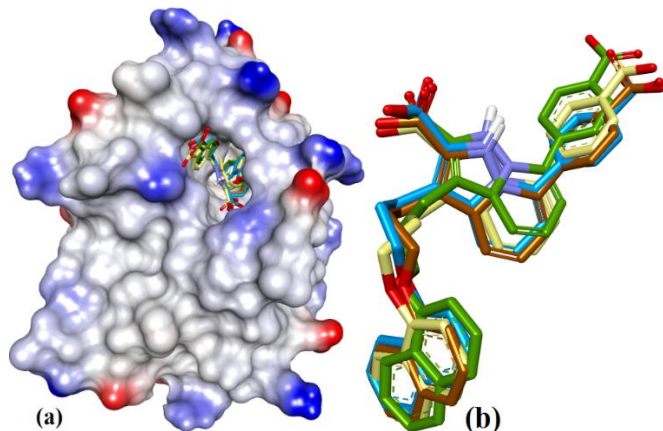


Figure 51 Implementation of differential docking (differential docking represents the docking performed by more than 2 methods) along with similar-pose ensemble clustering [181] provided support to use these docking methods for further molecular modeling. (a) The left-hand side (LHS) figure shows the ionized solvent-exposed surface mapping of Mcl-1 where ligands were fitted to the binding site. (b) The right-hand side (RHS) shows the similar-pose ensemble clustering [12, 182]. Here the co-crystal bound conformation of the ligand (in blue), MOE based docking conformation (in brown), AutoDock based docking (in green) and GRIP-based docking (in yellow) were overlapped.

2.2.2.3 Docking of naturally occurring Mcl-1 inhibitors

After evaluating the docking methods, I performed screening of seven classes of naturally occurring Mcl-1 inhibitors which showed low micromolar inhibitory activity against Mcl-1.

Gymnochrome-F & oxy-polyhalogenated diphenyl ethers

In the case of **Gymnochrome-F**, I employed docking using MOE, AutoDock, and VlifeDock to determine the docking pose. Later, similar-pose ensemble clustering confirmed the attained docking poses from these three different methods within $\text{RMSD} \leq 2 \text{ \AA}$. This low RMSD value attained from these methods could reasonably be possible because of high rigidity possessed by the fused heteroaromatic rings in the ligand structure, which limits the number of binding conformations of **Gymnochrome F**.

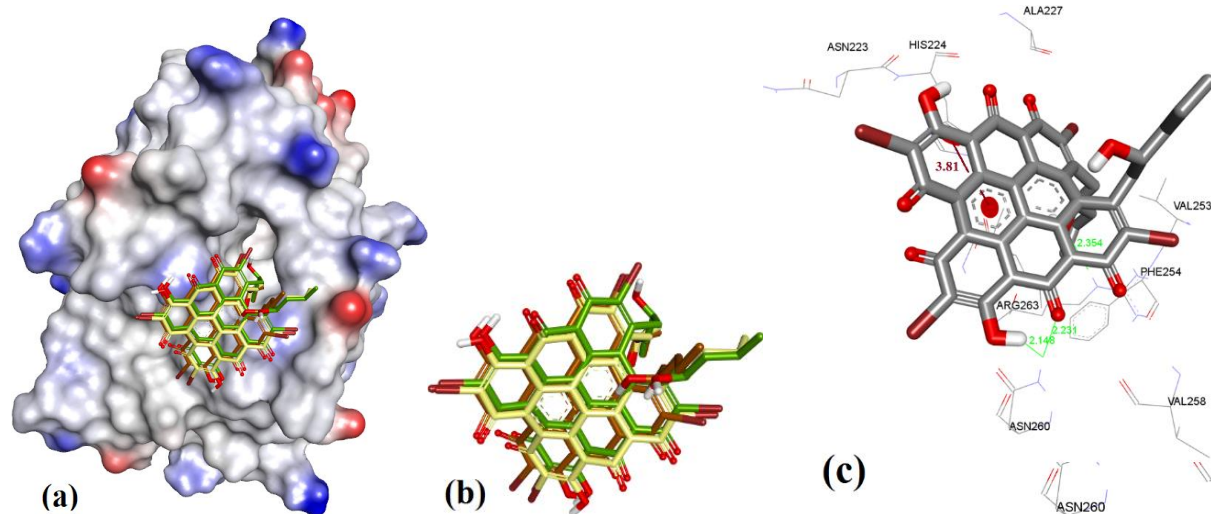


Figure 52 (a) The ionized solvent-exposed surface mapping of *hMcl-1* along with the docked poses of **Gymnochrome-F** from MOE (in brown), AutoDock (in Green), VlifeDock (in yellow) show their fitting to the cavity within 1.08 \AA RMSD. (b) Similar-pose ensemble clustering of all three poses attained from three different docking methods. (c) Interactive mode of **Gymnochrome-F** with *hMcl-1*.

The docking of **Gymnochrome-F** also shows its interaction with His224 (π - π interaction, 3.81 \AA) and H-bond donor/acceptor interaction with Asn260 (2.14 \AA & 2.23 \AA), as shown in **Figure 52**. In case of the diphenyl ether derivatives (sponge-derived oxy-polyhalogenated diphenyl ethers), I observed various bound conformations with similar docking energies (with the difference $\leq 0.2 \text{ kcal/mol}$). However, the similar docking energies and binding conformations are in contradiction with respect to their *Mcl-1* binding affinity data (Ox-p-1 (2.4 \mu M), Ox-p-2 (8.9 \mu M) & Ox-p-4 (7.3 \mu M), for 2D ChemDraw structures see figure 48). This is due to their smaller structure enabling them to adopt a wide number of potential bound conformations and orientations over a comparatively larger active site of *hMcl-1*, as shown in **Figure 53**.

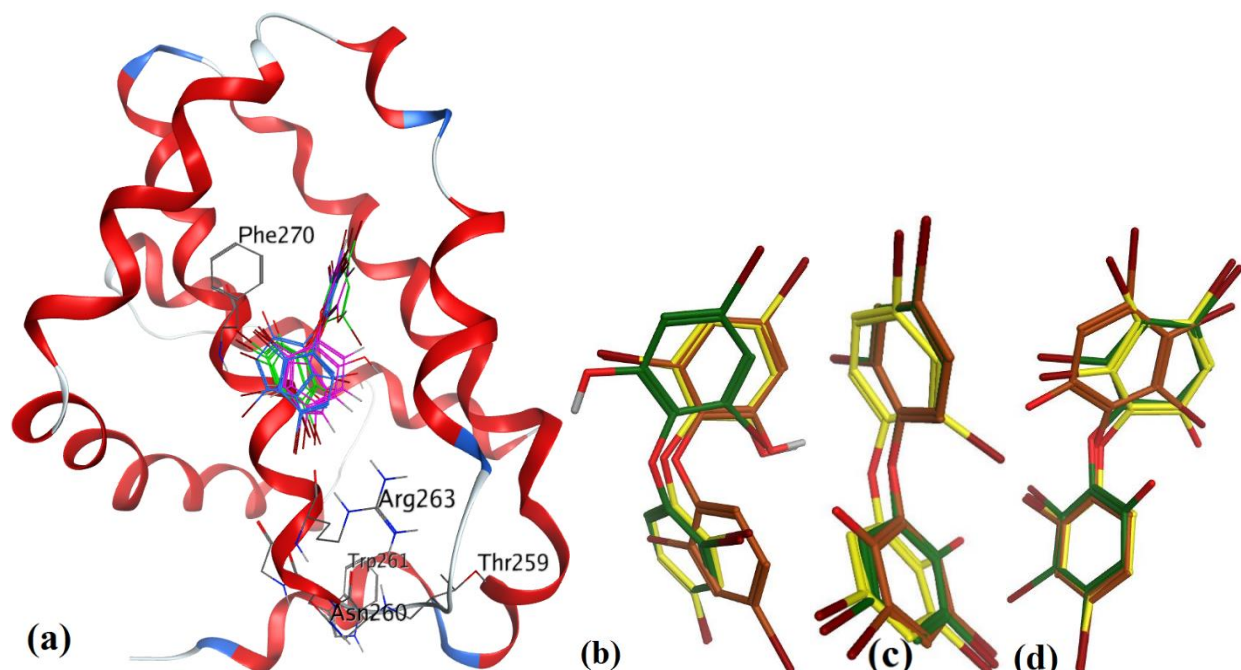


Figure 53 (a) Interactive mode of diphenyl derivatives: **Ox-p-1** (magenta), **Ox-p-2** (Green) & **Ox-p-4** (Blue); (b) docked poses of **Ox-p-1** from MOE (in brown), AutoDock (in Green), VlifeDock (in yellow); (c) docked poses of **Ox-p-2** from MOE (in brown), AutoDock (in Green), VlifeDock (in yellow); (d) docked poses of **Ox-p-4** from MOE (in brown), AutoDock (in Green), VlifeDock (in yellow)

Anacardic acid derivatives

In case of anacardic acids, **Ana-a-4** showed significantly close binding poses from all the three docking methods (1.17 Å RMSD). The docking showed a close interaction of polar phenolic head and carboxylic acid with Arg263 (2.36 & 2.21 Å) and intramolecular interaction (1.81 Å), as shown in **Figure 54**.

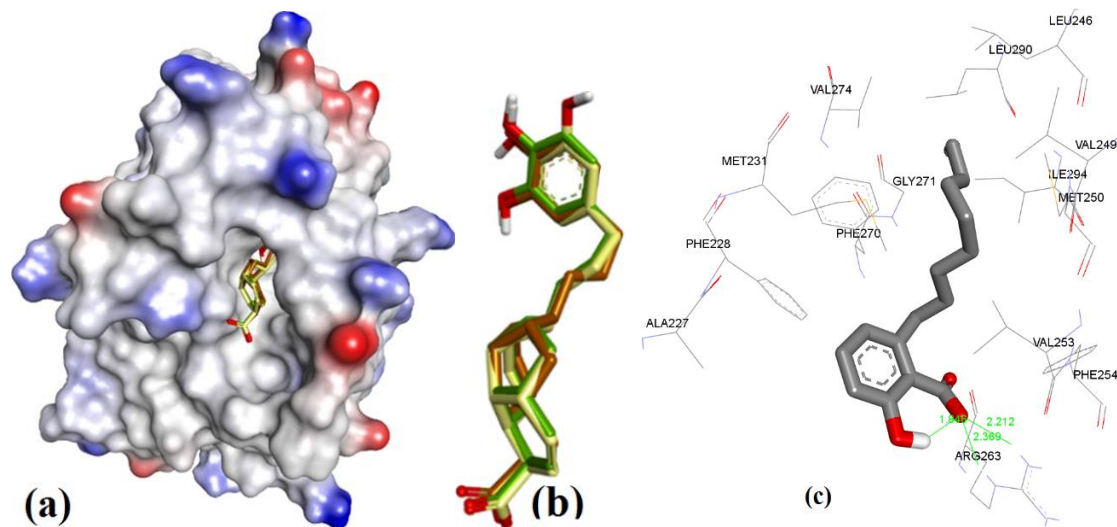


Figure 54 (a) The ionized solvent-exposed surface mapping of Mcl-1 along with the docked poses of **Ana-a-4** from MOE (in brown), AutoDock (in Green), VlifeDock (in yellow) show their fitting to the cavity. (b) similar-pose ensemble clustering of all three poses attained from three different docking methods. (c) Interactive mode of **Ana-a-4** with Mcl-1.

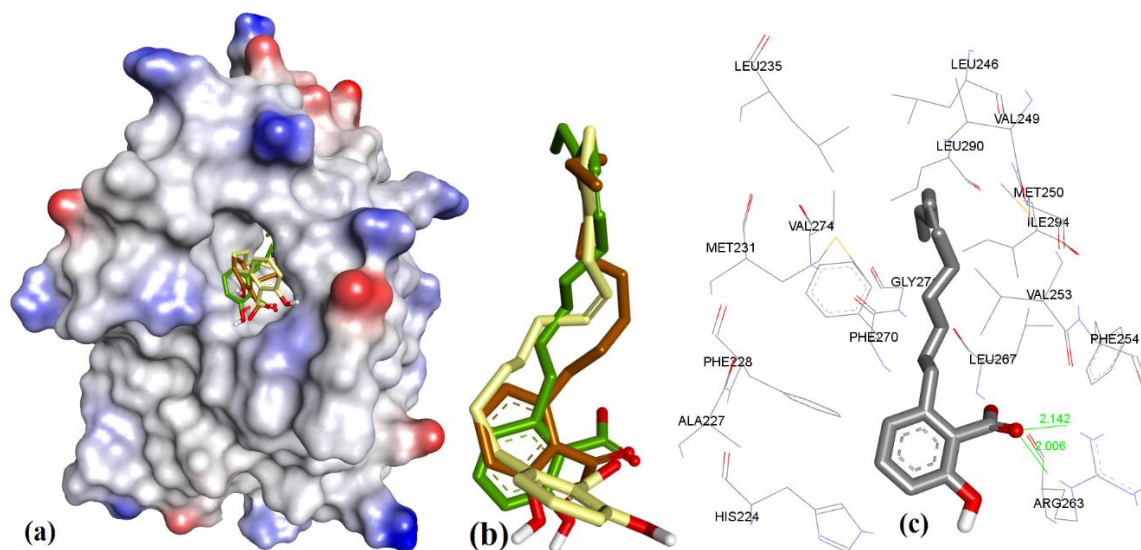


Figure 55 (a) The ionized solvent-exposed surface mapping of Mcl-1 along with the docked poses of **Ana-a-4** from MOE (in brown), AutoDock (in Green), VlifeDock (in yellow) show their fitting to the cavity. (b) Similar-pose ensemble clustering of all three poses attained from three different docking methods. (c) Interactive mode of **Ana-a-5**.

The extra length in the hydrocarbon chain of **Ana-a-5** compared to **Ana-a-4** hydrocarbon chain, projected the salicylic acid substructure of **Ana-a-5** more towards the NWGR domain, where it interacted with Arg263 as a H-bond acceptor (2.0 & 2.14 Å), which also supports its improved Mcl-1 affinity ($IC_{50} = 5.8 \mu M$) than **Ana-a-4** ($IC_{50} = 17.7 \mu M$), as shown in **Figure 55**.

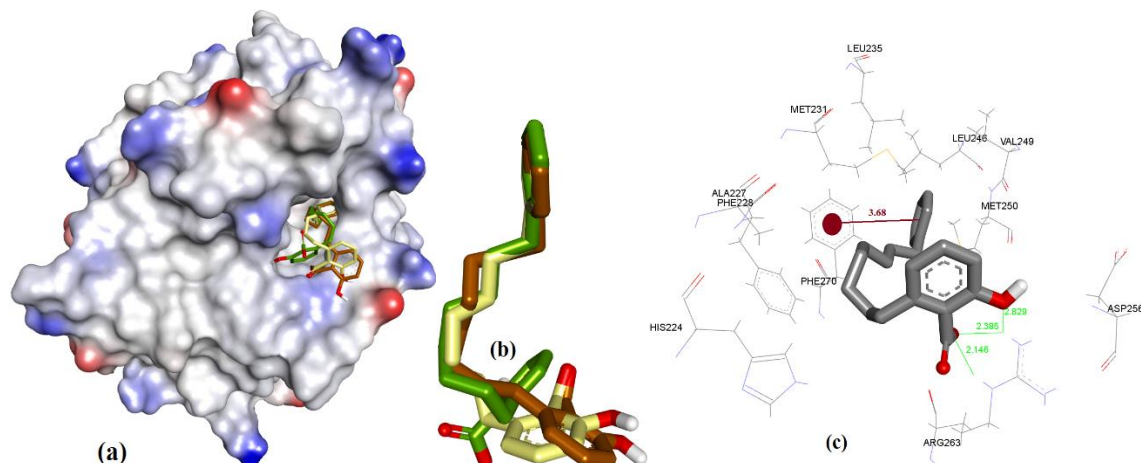
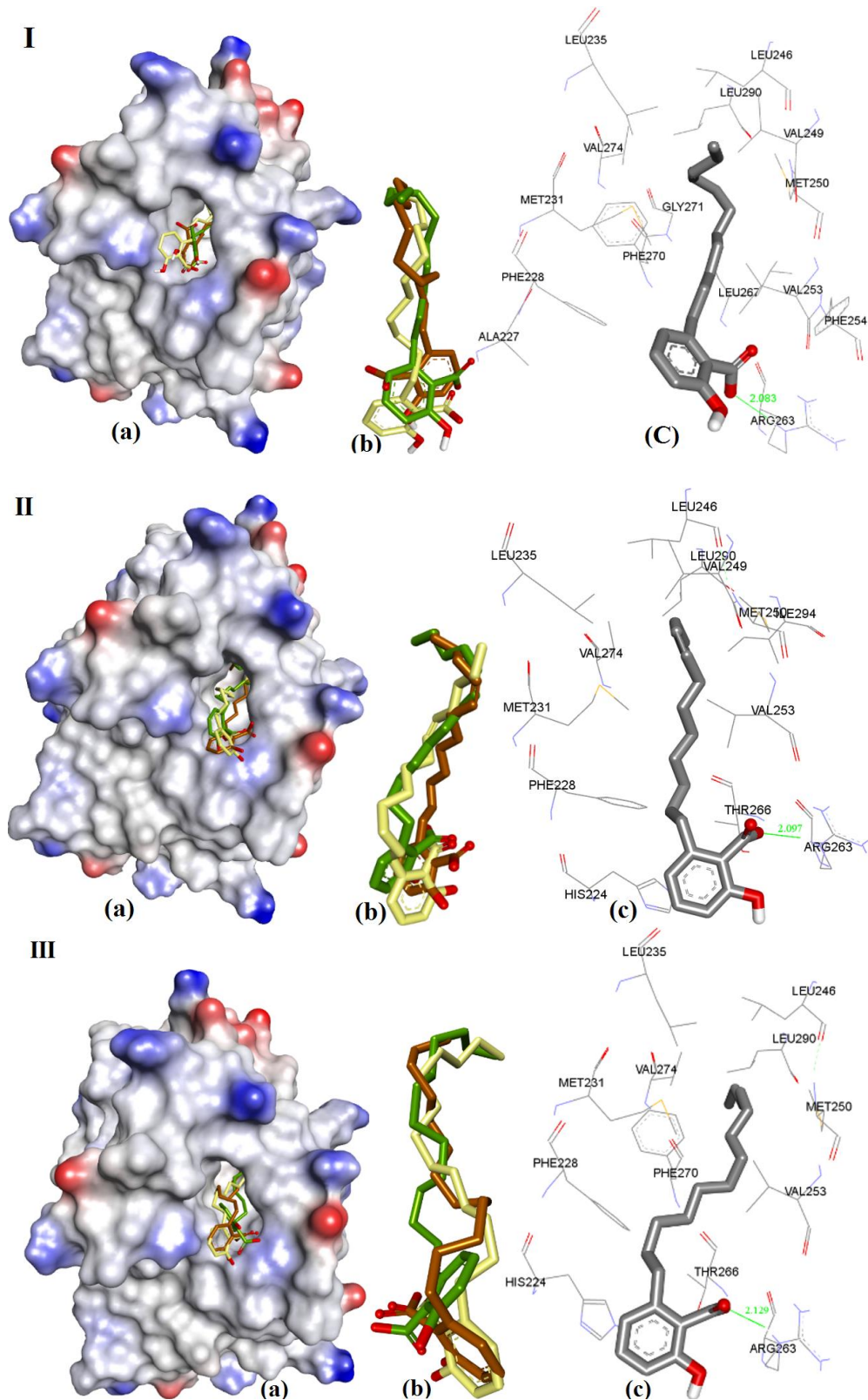


Figure 56 (a) The ionized solvent-exposed surface mapping of Mcl-1 along with the docked poses of **Ana-a-6** from MOE (in brown), AutoDock (in Green), VlifeDock (in yellow) show their fitting to the cavity. (b) Similar-pose ensemble clustering of all three poses attained from three different docking methods. (c) Interactive mode of **Ana-a-6**.

In comparison to **Ana-a-4/5**, shortening of a hydrocarbon chain and incorporation of phenyl ring, as in **Ana-a-6**, further improved the affinity for *h*Mcl-1 (0.6 μM) which could be understood with its additional π - π interaction with Phe270 which was missing in previously mentioned Anacardic acids, as shown in **Figure 56**. Clustering ensemble of docking conformations was found within

RMSD of 1.67 Å and showed π - π interaction with Phe270 (3.68 Å) along with Arg263 (2.14, 2.38 & 2.82 Å).



IV

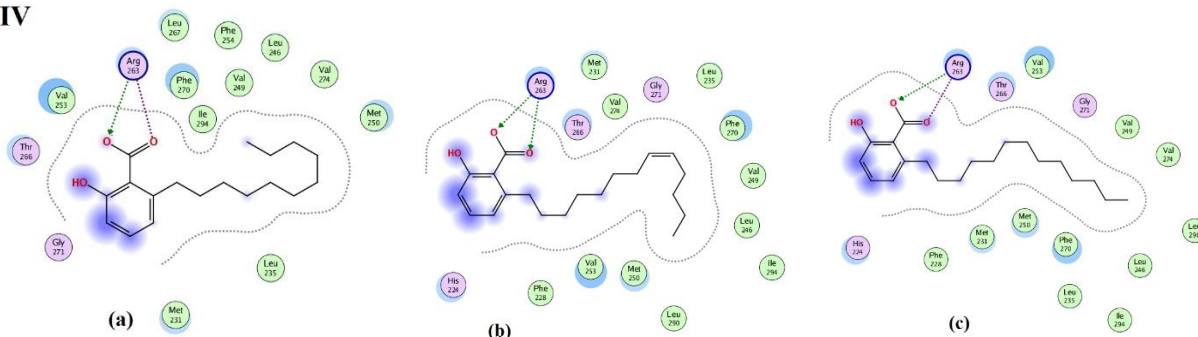


Figure 57 Representation of modelling for (I) **Ana-a-7**; (II) **Ana-a-8**; & (III) **Ana-a-9**: (a) The ionised solvent-exposed surface mapping of Mcl-1 along with the docked poses from MOE (in brown), AutoDock (in Green), VlifeDock (in yellow) show their fitting to the cavity. (b) Similar-pose ensemble clustering of all three poses attained from three different docking methods. (c) Interactive mode of **Ana-a-7/8/9**. (IV) 2D interaction of **Ana-a-7** (LHS), **Ana-a-8** (Middle) & **Ana-a-9** (RHS)

The docking of **Ana-a-7**, **Ana-a-8** and **Ana-a-9** showed almost identical docking interactions with Arg263, as shown in **Figure 57**, which is supported by their similar docking energies (-8.34, -8.47 and -8.22 kcal/mol respectively). These anacardic acids binding mode and binding energies are similar, which pointed out that the hydrocarbon chain length of (11-13 carbons) play a less significant role in influencing binding of these molecules to Mcl-1

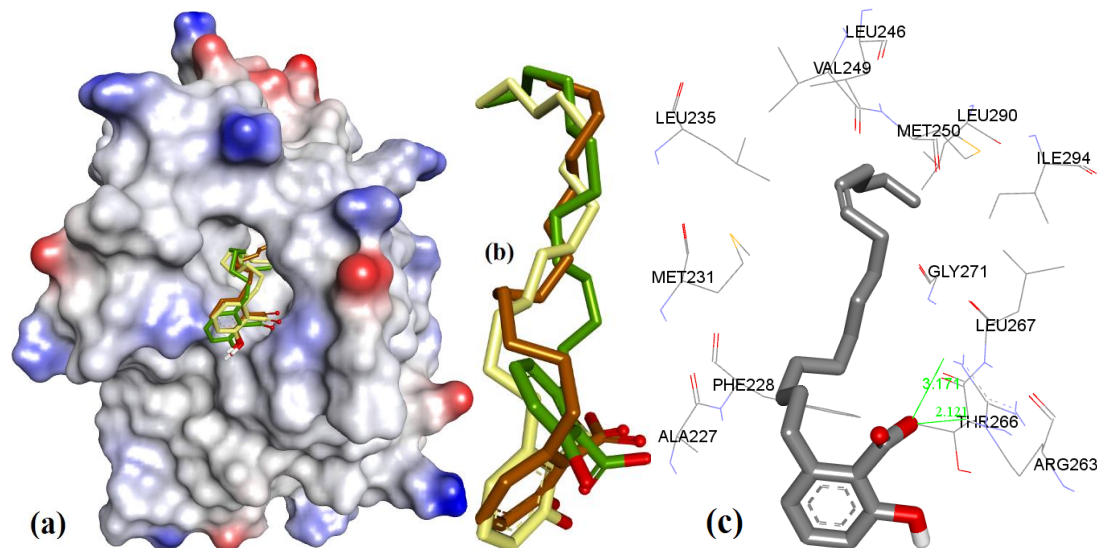


Figure 58 (a) The ionized solvent-exposed surface mapping of Mcl-1 along with the docked poses of **Ana-a-10** from MOE (in brown), AutoDock (in Green), VlifeDock (in yellow) show their fitting to the cavity. (b) Similar-pose ensemble clustering of all three poses attained from three different docking methods. (c) Interactive mode of **Ana-a-10**.

In case of **Ana-a-10** ($IC_{50} = 1.2 \mu M$) when compared to **Ana-a-8** ($IC_{50} = 0.2 \mu M$) and **Ana-a-9** ($IC_{50} = 0.2 \mu M$), has longer unsaturated hydrocarbon chain length, led to reduced affinity which is most likely to be due to its limited flexibility and steric effect (as shown in **Figure 58**)

Endiandric Acid Analogous

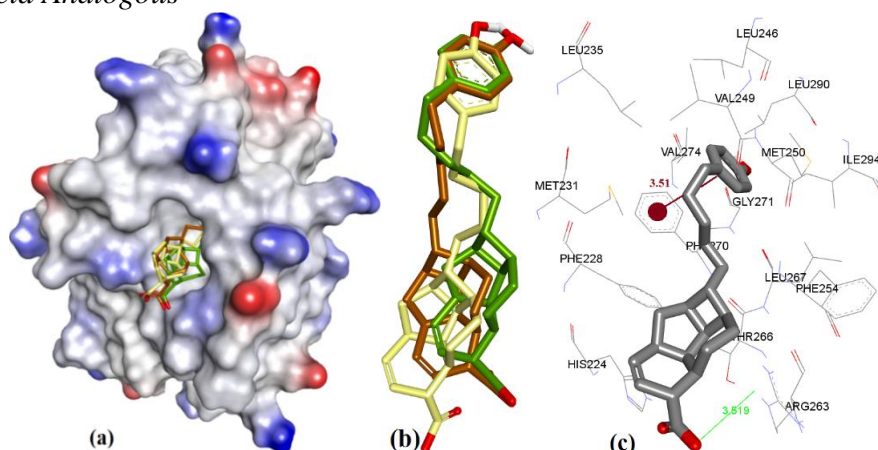


Figure 59 (a) The ionized solvent-exposed surface mapping of Mcl-1 along with the docked poses of **End-a-2** from MOE (in brown), AutoDock (in Green), VlifeDock (in yellow) show their fitting to the cavity. (b) Similar-pose ensemble clustering of all three poses attained from three different docking methods. (c) Interactive mode of **End-a-2**.

The docking showed **Enda-a-2** and **Ana-a-6** share similar binding modes, where their molecular structures have two different terminals/ends contain rings, which utilizes two different regions of Mcl-1 active site. However structurally (see **Figure 48**), **Enda-a-2** has only a COOH group while **Ana-a-6** has both a phenol and COOH groups in the same ring, where these polar functional groups interact with Arg263 of Mcl-1. Also, these rings in both molecules have structurally diverse from each other, where **Ana-a-6** has salicylic acid and **Enda-a-2** possess a highly constrained fused ring system. This constrained fused ring in **Enda-a-2** might prevent its adoption of the optimal binding conformation for interaction with Arg263, and therefore could possibly be reasoning of observing of a weak H-bond interaction with Arg263 (3.51 Å) when compared to the **Ana-a-6** docking pose (has three H-bond acceptor interaction with Arg263: 2.14, 2.38 & 2.82 Å, see **Figure 56**). Also, docking of **Enda-a-2** showed a π - π interaction with Phe270 (3.51 Å) of, as shown in **Figure 59**. Similar interactions were also seen with **Enda-a-3** ($K_i = 13 \mu\text{M}$), where it displayed an improved geometry for H-bonding as evaluated by its closer proximity to Arg263 (3.02 Å) and π - π interaction with Phe270 (3.50 Å) as shown in **Figure 60**. The latter leads to marginal improvement in *in-vitro* Mcl-1 affinity and docked binding energy, as in **Table 5**.

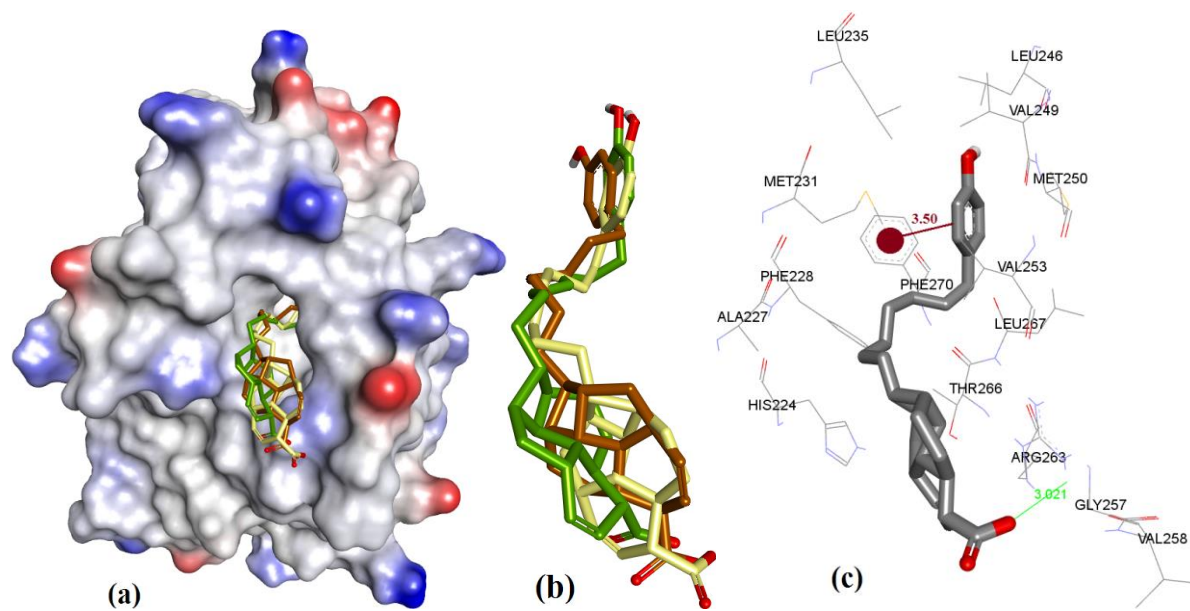


Figure 60 (a) The ionized solvent-exposed surface mapping of Mcl-1 along with the docked poses of **End-a-3** from MOE (in brown), AutoDock (in Green), VlifeDock (in yellow) show their fitting to the cavity. (b) Similar-pose ensemble clustering of all three poses attained from three different docking methods. (c) Interactive mode of **End-a-3**.

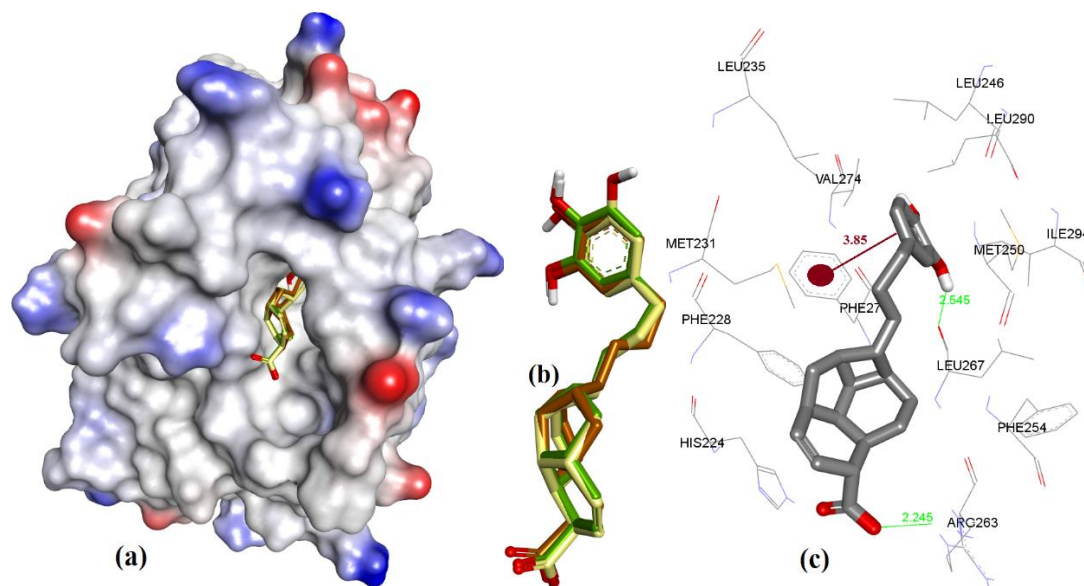


Figure 61 (a) The ionized solvent-exposed surface mapping of Mcl-1 along with the docked poses of **End a-4** from MOE (in brown), AutoDock (in Green), VlifeDock (in yellow) show their fitting to the cavity. (b) Similar-pose ensemble clustering of all three poses attained from three different docking methods. (c) Interactive mode of **End a-4**.

Comparatively shorter analogue of endiandric acid class (**Enda-A-4**) have an additional phenolic polar head and therefore shows an additional new H-bond donor interaction with peptide backbone of Leu267 and also has close proximity with Phe270 (π - π interaction, 3.85 Å) when compared to longer analogues (**Enda-A-2** and **Enda-A-3**), as shown in **Figure 61**; therefore explains why **Enda-A-4** achieved better *in-vitro* Mcl-1 affinity than later two, as shown in **Table 5**.

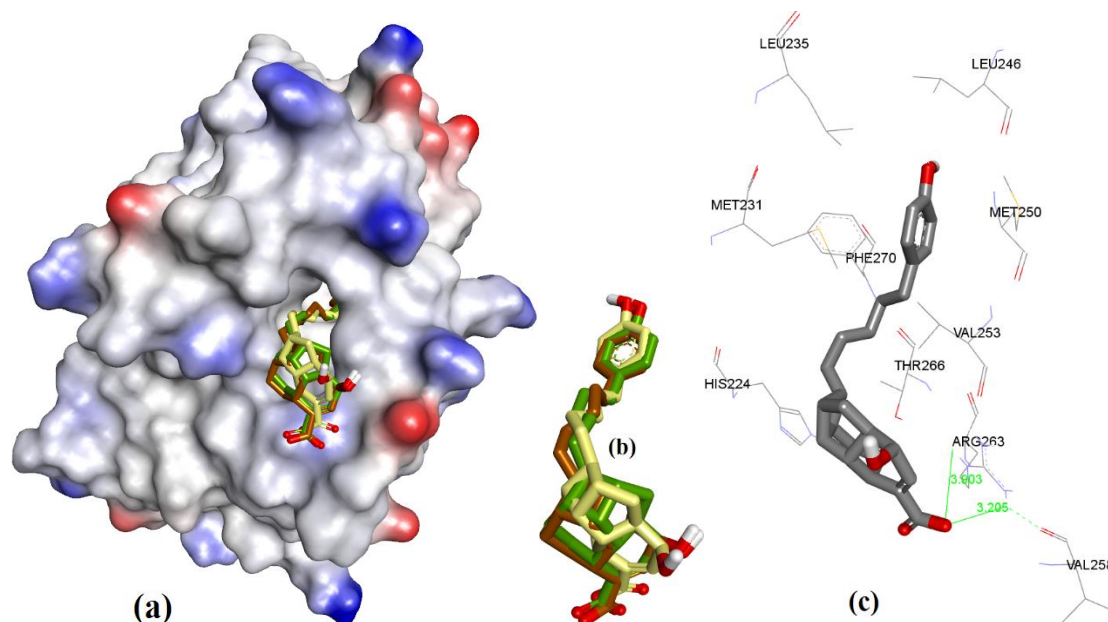


Figure 62 (a) The ionized solvent-exposed surface mapping of Mcl-1 along with the docked poses of **End-a-10** from MOE (in brown), AutoDock (in Green), VlifeDock (in yellow) show their fitting to the cavity. (b) Similar-pose ensemble clustering of all three poses attained from three different docking methods. (c) Interactive mode of **End-a-10**.

Enda-A-10 has a different stereochemistry in its fused cyclic ring substructure with respect to the other analogues of this series, which leads to its COOH functionality being more inclined towards Arg263 (3.29 & 3.90 Å) as compared to a similar analog (like **Enda-A-2**), as shown in **Figure 62**, which might be the reason of its improved binding affinity (5.2 μM) over **Enda-a-2** (14.3 μM).

Marinopyrrole analogues (maritoclax & its cyclic analogue)

Doi *et al* disclosed NMR spectroscopic data that supported outcome of the docking of marinopyrrole-A (**maritoclax**) with *mMcl-1* and its interaction: (a) the chloro group in one of the pyrrole ring of **maritoclax** was facing inwards towards the active site of *Mcl-1*, (b) phenol group of the same pyrrole ring has a H-bond with Gly308, (c) while phenol group of another pyrrole group has a H-bond with Thr247, and (d) the carbonyl group has H-bond with Asn204. On the basis of NMR data provided by Doi *et al*, the corresponding amino acids of *hMcl-1* with respect to *mMcl-1* amino acids were enlisted see **Table 4** [106]. This comparison led to some of the key differences in their active sites: (a) point mutation of G222-D241 and (b) V262-I281, and (c) slightly more hydrophobic character of cavity of *mMcl-1* than *hMcl-1* (16 out of 25 reported amino acids are hydrophobic) see **Table 4**.

Table 4. Comparison between *mMcl* and *hMcl-1* active sites: The enlisted amino acids of *mMcl-1* were showing chemical shift perturbation (^1H - ^{15}N HSQC spectrum) during the addition of **Maritoclax**. The amino acids in black color in table were only able to be detected through ^1H - ^{15}N HSQC spectrum of ^{15}N -labeled *Mcl-1*. However, the amino

acids shown in green were undetected due to large intensity change. The unbolded and bolded amino acids in black colour in table were shown at least 0.05 and 0.08 ppm chemical shift (δ) respectively [183].

<i>Corresponding amino acids</i>					
<i>mMcl-1</i>	<i>hMcl-1</i>	<i>mMcl-1</i>	<i>hMcl-1</i>	<i>mMcl-1</i>	<i>hMcl-1</i>
G150	-	N241	N260	R229	R248
I163	I182	G243	G262	F235	F254
T172	T191	I245	I264	D237	D256
G184	G203	S250	S269	R244	R263
G200	G219	F251	F270	V246	V265
Q202	Q221	V255	V274		
R203	R222	V262	I281		
N204	N223	V278	V297		
R214	R233	L279	L298		
L216	L235	F300	F319		
N220	N239	Q306			
G222	D241	G307			
S228	S247				

The **maritoclax** binding to *hMcl-1*, predicted by docking, was found similar to the bound conformation as reported in *mMcl-1* but the binding conformation was found slightly different than the reported with *mMcl-1*. For a better understanding, *mMcl-1* (PDB i.d. 2JM6) structure was superimposed over the *hMcl-1* and an RMSD value of 6.91 Å was determined for this. This high deviation in terms of RMSD value, clearly provided the reasoning behind the differences observed in binding conformations among these proteins with **maritoclax**. Structurally, **maritoclax** is a dimer which contain two pyrroles: ring-A and ring-B (as shown in **Figure 48**). The docking studies of **maritoclax** with *hMcl-1* showed that the phenyl group of ring-A displays a π - π interaction and its phenolic OH makes a H-bond donor interaction with Thr266, as shown in **Figure 63**. Whereas the ring B show π -CH hydrophobic interaction and carbonyl (C=O) showed two H-bond acceptor interaction with NH- functional group of guanidine moiety of Arg263. It has been observed that the **maritoclax** is structurally fitting in close proximity of some of amino acids Asp256, Met 231, Phe254, Leu 267, His224, Phe228 of the cavity, which were also reported by Doi *et al* [106].

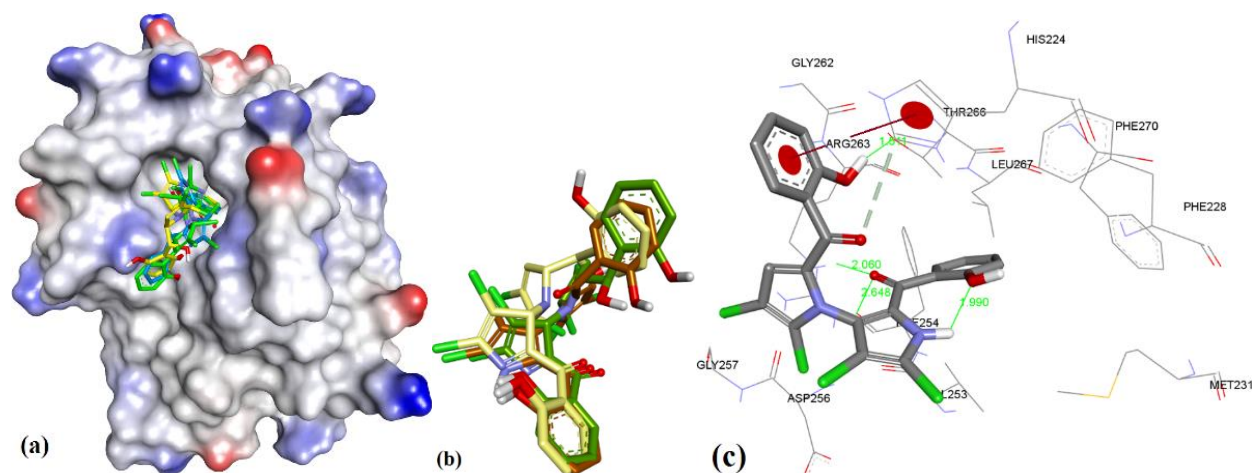


Figure 63 (a) The ionized solvent-exposed surface mapping of Mcl-1 along with the docked poses of **marinopyrrole** from MOE (in blue), AutoDock (in Green), VlifeDock (in yellow) show their fitting to the cavity. (b) Similar-pose ensemble clustering of all three poses attained from three different docking methods MOE (in brown), AutoDock (in Green), VlifeDock (in yellow). (c) Interactive mode of **marinopyrrole**.

Later, Cheng *et al.* synthetically modified the **maritoclax** into cyclic derivatives, which were also evaluated for their physicochemical properties. These evaluations resulted an optimized structure (**cyclic maritoclax**) with improved drug-like properties and more potent Mcl-1 IC₅₀ value (4.3 μ M) compared to the parent maritoclax (8.9 μ M) [108]. This strategy of cyclization of **maritoclax** into **cyclic maritoclax**, is commonly used technique in drug design and the explanation often used is that the cyclization preorganises the conformations of a flexible ligand to improve the preferential selectivity for a given physiological target by minimizing the entropic loss associated with the ligand adopting a preferred conformation for binding [107]. However, docking from all the three methods failed to show any significant differences in binding energies between *maritoclax* and its cyclic derivative, which indicates that the docking algorithm used for calculating the binding energies might be underutilized the physicochemical parameters.

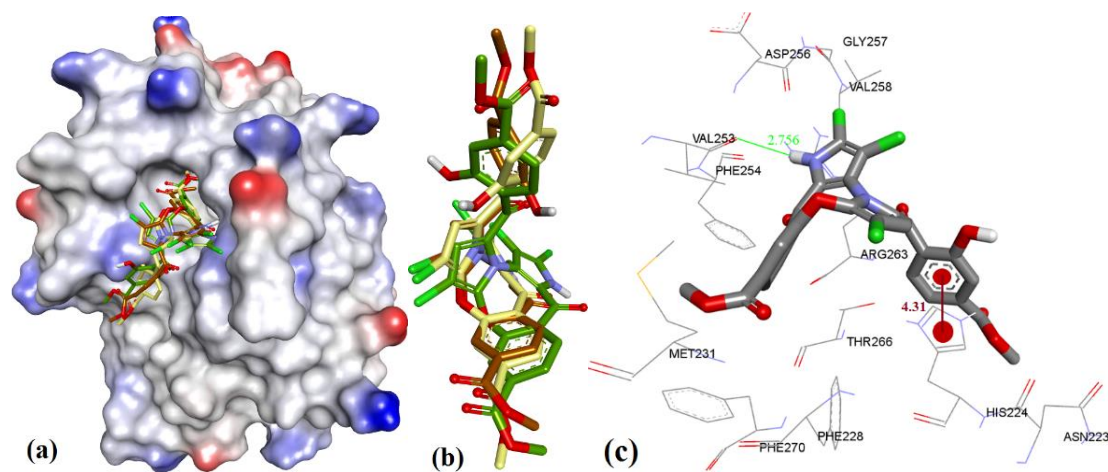


Figure 64 (a) The ionised solvent exposed surface mapping of Mcl-1 along with the docked poses of **cyclic marinopyrrole** from MOE (in brown), AutoDock (in Green), VlifeDock (in yellow) show their fitting to the cavity.

(b) Similar-pose ensemble clustering of all three poses attained from three different docking methods. (c) Interactive mode of **cyclic marinopyrrole**.

MIMI (Mcl-1 Inhibitor Molecule 1)

Similar to **maritoclax**, NMR-assisted docking was performed to identify the binding pose of **MIMI** by Cohen *et al* (see in **Figure 65**) [77]. The ensemble clustering of docked poses from MOE, AutoDock and VlifeDock had RMSD values of 1.07 Å, 1.61 Å and 2.02 Å respectively (see in **Figure 65**). The attained docking pose in my study was compared with previous reported binding of **MIMI**. In previous report, it had been reported that the **MIMI** had a cyclohexyl group hydrophobic interaction with Val216 and Leu213 [77], which was not seen in my case as both residues were away from cyclohexyl functionality (> 5.5 Å), which is too long even for a weak hydrophobic interaction. However, other interactions were found similar with the previous study: (a) imidazole ring of His224 with a CH- π interaction (4.19 Å) with the methylated thiazole, (b) *H*-bond donor interaction (2.49 Å) with *ortho*-substituted -OH of pyrogallol functionality. On the other hand, the guanidine moiety of the side chain of Arg263 and alcoholic side chain (-OH) of Thr266 showed a *H*-bond acceptor interaction (2.47 and 2.06 Å) with *para*-substituted and *ortho*-substituted -OH of pyrogallol functionality. I also observed that the Asp256 is in close vicinity with Arg263 (2.63 Å), and could be better suited to hold pyrogallol group *via* H-bonding [77].

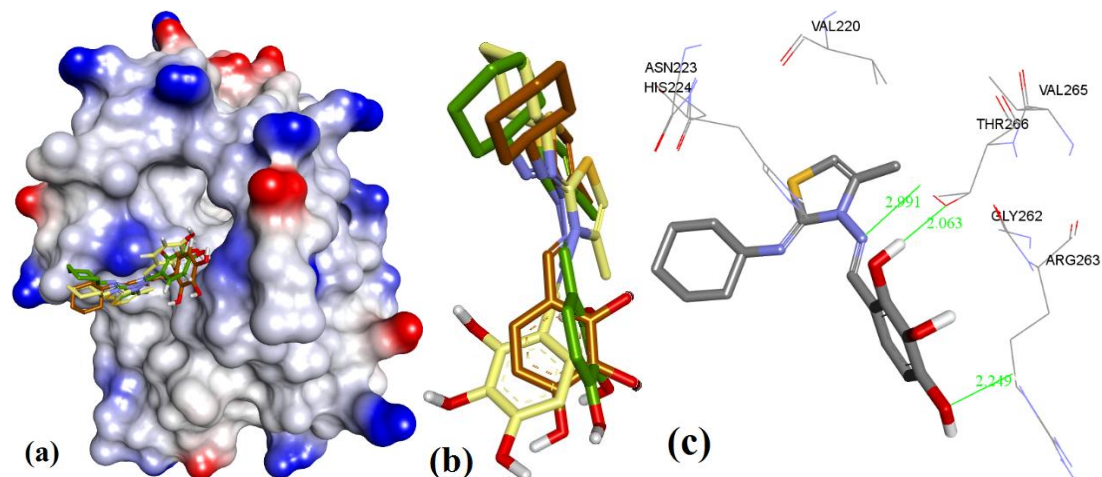


Figure 65 (a) The surface mapping (displayed style used: solvent, mapping: ionizability); (b) Alignments of docked MIMI of MOE (Blue), Autodock (green) Autodock Vina (yellow); (c) MIMI interaction with Mcl-1. (a) The ionised solvent exposed surface mapping of Mcl-1 along with the docked poses of **MIMI** from MOE (in brown), AutoDock (in Green), VlifeDock (in yellow) show their fitting to the cavity. (b) Similar-pose ensemble clustering of all three poses attained from three different docking methods. (c) Interactive mode of **MIMI**.

Cryptosphaerolide

Cryptosphaerolide (TR-FRET, $K_i = 11.4$ μ M) contains 2 substructures: cyclic and acyclic. The absolute stereochemistry was reported for cyclic substructure but not for the acyclic substructure.

Therefore, I accounted all the possible conformers for **cryptosphaerolide**. As three stereochemical centers geometry were not assigned therefore I docked all the 8 possible stereoisomers. These stereoisomers were later ranked based on their docking scores. As shown in **Figure 66**, the **cryptosphaerolide** docking showed that the cyclic substructure of all eight stereoisomers (coded in different color in figure) does not fit into the cavity and is projected out from the binding cavity, that is why Fenical co-workers [160] did not observe any Mcl-1 inhibition activity for the cyclic substructure of **cryptosphaerolide**.

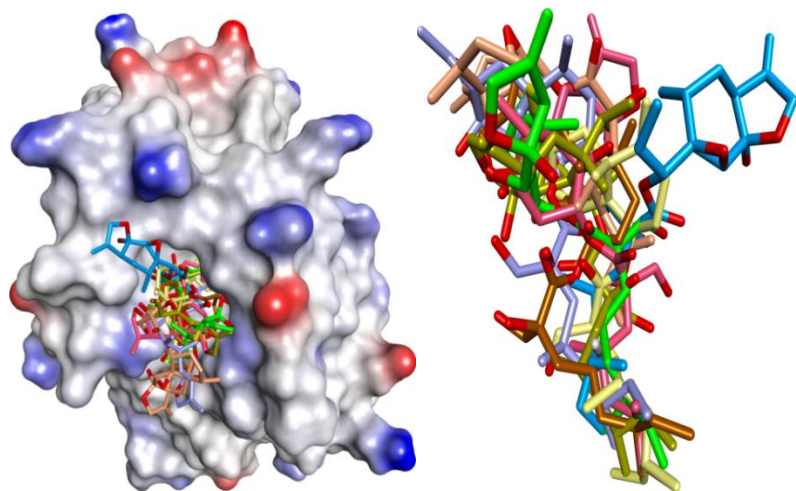


Figure 66 There were three chiral centers of unknown stereochemistry in **Cryptosphaerolide** structure (see **Figure 48**), therefore 8 isomers were docked. The cyclic substructures of all 8 conformers were not involved in binding (as seen in interactive mode in the figure (a: right hand side) and binding conformation of all 8 conformers (b: On left hand side) in the figure with *hMcl-1*.

Meiogynin derived Mcl-1 inhibitors

Meiogynin-A derived compounds have shown a wide range of activity against antiapoptotic proteins of the Bcl-2 family [148-151]. Docking predicted similar binding interactions for meiogynins except in case of their parent molecule **meiogynin A** ($K_i = 5.2 \mu\text{M}$), which showed H-acceptor interactions with the imidazole side chain of His224. Meiogynin derivatives showed π - π interactions with Phe270. Previous studies of **Meiogynin A**, which showed proximal binding with Arg100 and Tyr195, were also observed in my docking experiments (meiogynin A was found within 5 Å of these residues). However, my docking generated distinctive poses compared to those previously disclosed [150, 184] for meiogynins as shown in **Figure 67, 68, 69** and **70**.

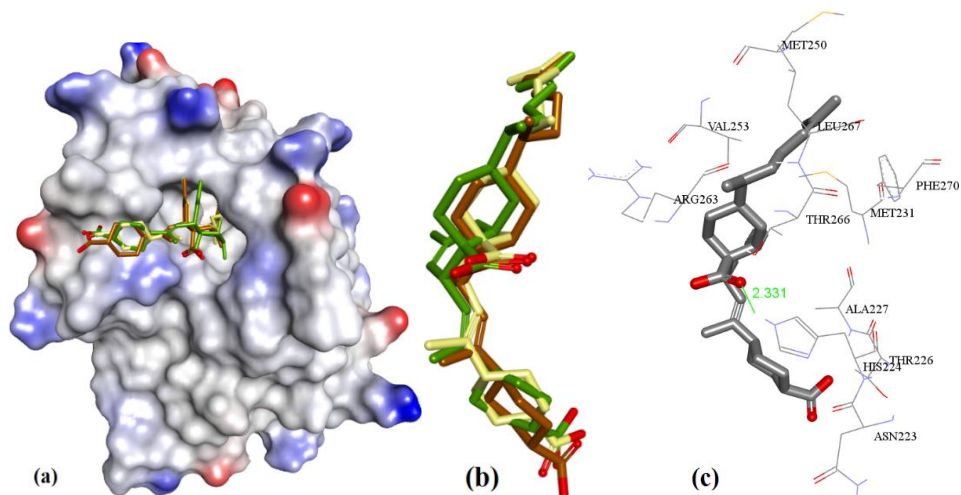


Figure 67 (a) The ionised solvent exposed surface mapping of Mcl-1 along with the docked poses of **Meiogynin-A** from MOE (in brown), AutoDock (in Green), VlifeDock (in yellow) show their fitting to the cavity. (b) Similar-pose ensemble clustering of all three poses attained from three different docking methods. (c) Interactive mode of **Meiogynin-A** .

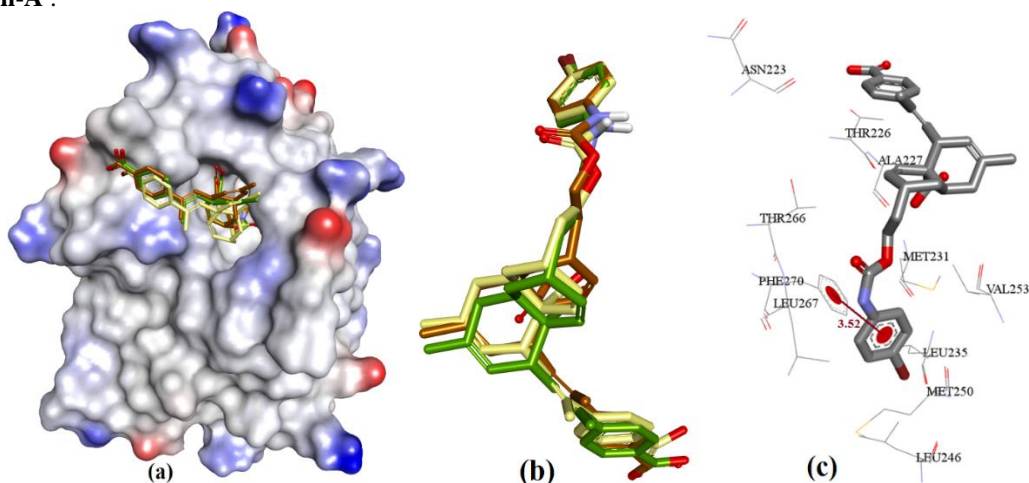


Figure 68 (a) The ionised solvent exposed surface mapping of Mcl-1 along with the docked poses of **2.1.156** from MOE (in brown), AutoDock (in Green), VlifeDock (in yellow) show their fitting to the cavity. (b) Similar-pose ensemble clustering of all three poses attained from three different docking methods. (c) Interactive mode of **2.1.156**.

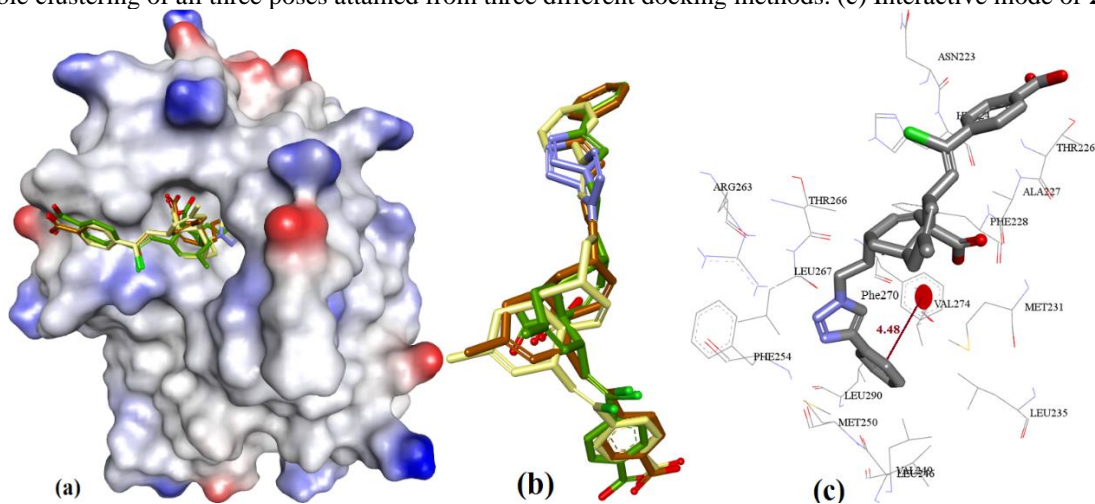


Figure 69 (a) The ionised solvent exposed surface mapping of Mcl-1 along with the docked poses of **2.1.157** from MOE (in brown), AutoDock (in Green), VlifeDock (in yellow) show their fitting to the cavity. (b) Similar-pose ensemble clustering of all three poses attained from three different docking methods. (c) Interactive mode of **2.1.157**.

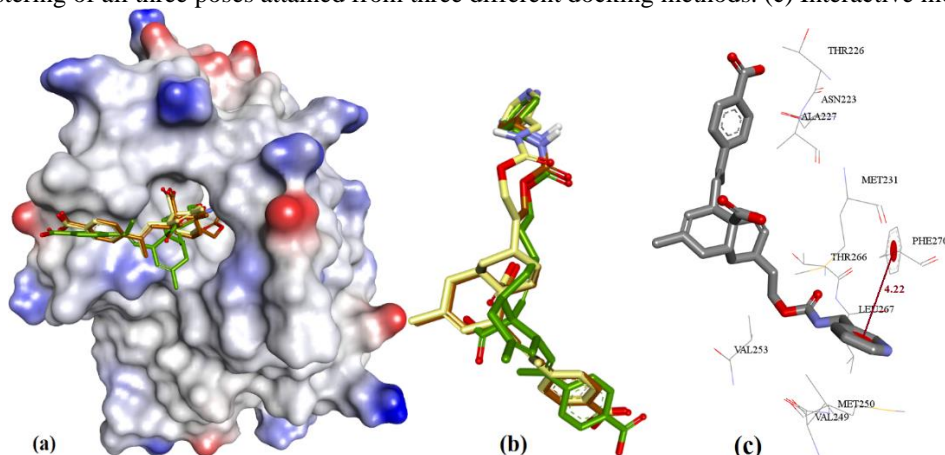


Figure 70 (a) The ionised solvent exposed surface mapping of Mcl-1 along with the docked poses of **2.1.158** from MOE (in brown), AutoDock (in Green), VlifeDock (in yellow) show their fitting to the cavity. (b) Similar-pose ensemble clustering of all three poses attained from three different docking methods. (c) Interactive mode of **2.1.158**.

Table 5. Comparison of the structures Ki's with their respective cumulative docking energies of a particular mcl-1 inhibitor.

#	Compound	<i>Mcl-1</i> Ki/ IC ₅₀ = μM	Bcl-2 ^a / Bcl-xL ^b Ki/ IC ₅₀ = μM	Ref.	Triangle Matcher (KJ/mol)	AutoDock (KJ/mol)	GRIP docking (KJ/mol)	RMSD (Å)
1	Gymnochrome F	3.3 ^d	NR	[156]	-7.36	-7.71	-6.17	1.08
2	Ox-p-1	2.4 ± 0.1	NR	[157]	-8.33	-8.29	-8.76	0.81
3	Ox-p-2	8.9	NR	[157]	-8.42	-8.22	-8.67	0.72
4	Ox-p-4	7.3	NR	[157]	-8.27	-8.16	-8.64	1.04
5	Ana-a-4	17.7 ± 3.1 ^d	> 23 ^{b, d}	[158]	-7.14	-6.82	-7.17	1.22
6	Ana-a-5	5.8 ± 0.3 ^d	3.2. ± 0.1 ^{b, d}	[158]	-7.83	-7.14	-7.67	2.09
7	Ana-a-6	3.7 ± 2.0 ^d	16.3 ± 0.5 ^{b, d}	[158]	-7.98	-7.61	-8.13	1.58
8	Ana-a-7	0.7 ± 0.1 ^d	1.2 ± 0.1 ^{b, d}	[158]	-8.34	-7.42	-8.91	2.18
9	Ana-a-8	0.2 ± 0.1 ^d	0.3 ± 0.1 ^{b, d}	[158]	-8.47	-8.22	-9.09	1.97
10	Ana-a-9	0.2 ± 0.1 ^d	0.2 ± 0.1 ^{b, d}	[158]	-8.22	-7.53	-8.76	2.05
11	Ana-a-10	1.2 ± 0.9 ^d	5.7 ± 0.6 ^{b, d}	[158]	-8.00	-7.68	-8.27	2.31
12	End-a-2 ^a	14 ± 3.3 ^e	19.2 ± 1.6 ^{b, e}	[159]	-7.15	-6.71	-7.19	1.86
13	End-a-3	13 ± 5.0 ^e	12.6 ± 0.2 ^{b, e}	[159]	-7.42	-6.32	-7.53	1.59
14	End-a-4	5.2 ± 0.2 ^e	> 100 ^{b, e}	[159]	-8.02	-7.60	-8.11	0.88
15	End-a-10	5.9 ± 0.5 ^e	19.4 ± 3.0 ^{b, e}	[159]	-7.89	-7.14	-8.02	1.03
17	Maritoclax	8.9 ± 1.0 ^d	16.4 ± 3.3 ^{b, d}	[108]	-7.51	-6.67	-7.92	1.23
18	Cyclic maritoclax form	4.3 ± 1.5 ^d	3.4 ± 0.9 ^{b, d}	[108]	-7.06	-6.39	-7.84	1.70
19	MIM1	4.72 ^d	NR	[77]	-8.77	-7.88	-8.90	2.13
20	Cryptosphaerolide (R, R, R)	NA ^c	NR	[160]	-6.88	-5.29	-6.16	2.64
21	Cryptosphaerolide (R, R, S)	NA ^c	NR	[160]	-7.17	-6.02	-6.31	2.37
22	Cryptosphaerolide (R, S, S)	NA ^c	NR	[160]	-7.04	-5.89	-6.20	3.14
23	Cryptosphaerolide (S, S, S)	NA ^c	NR	[160]	-7.22	-6.17	-6.47	1.76
24	Cryptosphaerolide (S, R, R)	NA ^c	NR	[160]	-6.53	-5.56	-5.90	2.22
25	Cryptosphaerolide (S, S, R)	NA ^c	NR	[160]	-6.70	-5.82	-6.13	2.90
26	Cryptosphaerolide (R, S, R)	NA ^c	NR	[160]	-7.34	-6.31	-6.41	2.46

27	Cryptosphaerolide (S, R, S)	NA ^c	NR	[160]	-7.12	-6.12	-6.28	1.94
29	Meiogynin-A	5.2 ± 1.2 ^e	1.46 ± 0.12 ^{a,e} / 8.30 ± 1.20 ^{b,e}	[151]	-6.66	-6.42	-6.24	1.48
30	Meiogynin 2.1.156	0.46 ± 0.06 ^e	0.83 ± 0.16 ^{a,e} / 2.19 ± 0.09 ^{b,e}	[151]	-7.22	-7.14	-6.94	1.14
31	Meiogynin 2.1.157	5.92 ± 0.47 ^e	> 23 ^{a,e} / 8.48 ± 0.40 ^{b,e}	[151]	-7.33	-7.25	-7.22	1.85
32	Meiogynin 2.1.158	0.56 ± 0.04 ^e	1.54 ± 0.44 ^{a,e} / 2.44 ± 0.02 ^{b,e}	[151]	-6.97	-6.89	-6.77	1.57

^a Bcl-2 protein inhibition; ^b Bcl-xL protein inhibition; NA^c uncharacterised cryptosphaerolide was found to have a Ki of 11.4 μM so all the isomers were listed here; ^d IC₅₀ values; ^e Ki values; NR not reported.

2.2.3 Conclusion & Future Perspective

In recent years, many efforts have been made in the development of Mcl-1 inhibitors. However, the development of the synthetic inhibitors have fallen short to attain any significant preferential Mcl-1 binding selectivity and therapeutic efficacy, which leads to adverse effects like drug-drug interactions (e.g. eicosanoid metabolism [185]) and drug-tissue toxicity (such as increases the progression of neurodegeneration of neurons in neurodegenerative disorders). On the other hand, various naturally-derived compounds have been isolated and shown low micromolar selectivity for Mcl-1 (**Figure 48**). It is quite evident, that naturally-derived compounds can be used to explore ligand-based drug design. My studies in this section mainly focuses on those natural Mcl-1 inhibitors showing their potential for their future exploration in natural product-based Mcl-1 inhibitor design. Seven natural product classes were studied and evaluated by various docking methods and biophysical parameters. The docking poses of individual molecules from various docking methods and associated docking scores were compared with the published Mcl-1 affinity data (*in-vitro* IC₅₀) in order to validate or evaluate the reliability of the adopted computational docking methodologies. The methodology used in this section of thesis could be useful for natural product chemists or drug designers, who are interested in exploring natural products in medicinal chemistry. Various interactions like hydrogen bonding, electrostatic force, Van der Waal's forces, etc. are commonly seen in binding of these natural products. This provides the much sought-after rationale and opportunity to design pharmacophores by congregating various steric and electronic features required for the interaction with Mcl-1, which would eventually be able to a trigger biological response effectively.

Objective 2.3 Synthesis of heterocyclic chemotypes as Mcl-1 inhibitors

2.3.1 Rationale design

From *objective 2.1*, which is a review of the literature of heterocyclic inhibitors of Mcl-1 protein, shows that most of the inhibitors utilize groups that bind into P₂-P₃ or P₃-P₄ pockets of the target. This is referred to as cavity-based design (see **Figure 71** for more information about cavity-based design). Here, I employed a similar strategy and tried to target adjacent pairs of pockets in Mcl-1 (P₂ and P₃), as shown in **Figure 71**. Diphenyl (or diaryl) derivatives (**2.3.2-2.3.5** as shown in blue in **Figure 71**) were selected for synthesis, as it was observed that both of their hydrophobic phenyl rings (non-substituted or substituted) could go inside these cavity pockets for possible interactions.

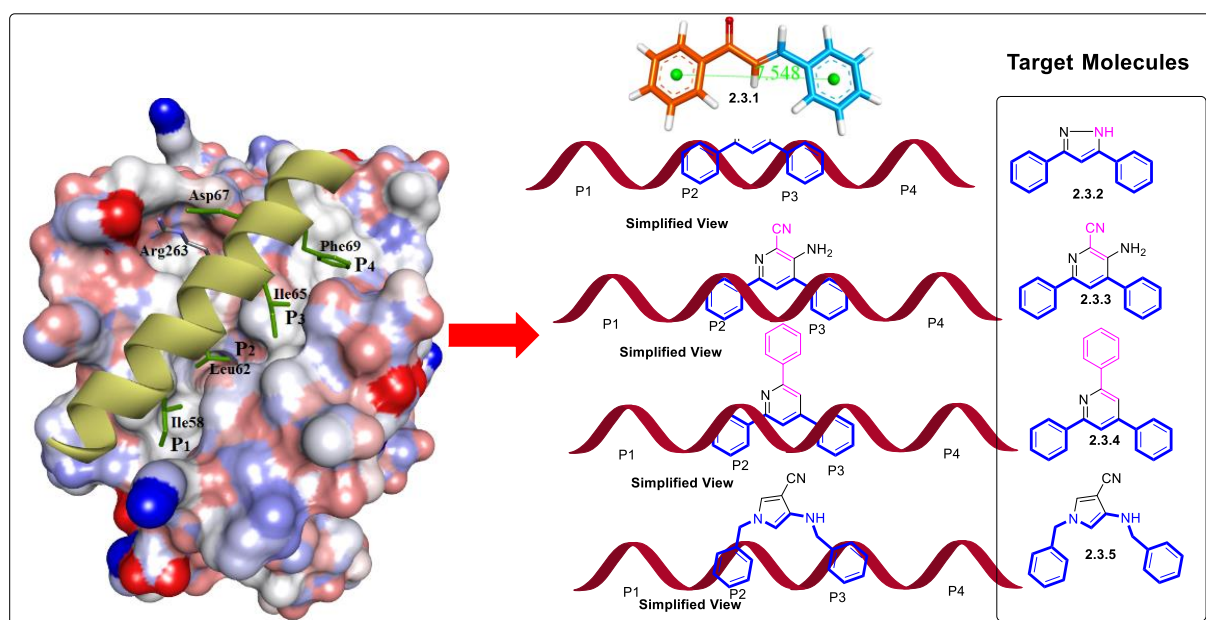


Figure 71 Prototype of cavity-based design: active site of Mcl-1 protein has 4 pockets (named as P₁-P₄). These pockets are used by the hydrophobic side chain of amino acids of BH3 helix proteins during their interaction with Mcl-1 protein. As the length of BH3 helix is too big to replicate by any small-molecule therefore, researchers often tried to target adjacent pockets (in most cases either P₂/P₃ or P₃/P₄ of Mcl-1 protein). On the other side, simple molecules like diphenyl propanone as represented in the structures of sponge halogenated compounds were found low micromolar Mcl-1 activity, which could be further evident with their two phenyls as left and right, where they could go to either P₂-P₃ or P₃-P₄ pockets and can be only confirmed by X-ray co-crystal structure.

2.3.2 Synthesis of desired heterocyclic compounds

Synthesis of chalcones

Trans-1,3-diphenyl propenones are commonly known as chalcones. These are α , β -unsaturated carbonyl containing compounds, where one part of the molecule is derived from an aromatic aldehyde and other part from an aromatic ketone. The reaction of these synthons are known as crossed-aldol condensation reactions (i.e. Claisen Schmidt condensation), where an aromatic

ketone gets enolized under either basic or acidic conditions into an enolate/enol form, which later undergoes nucleophilic attack on aromatic aldehyde followed by elimination of water molecule to form the chalcone as a product, as shown in **Figure 72**. In this study, chalcones were prepared by 2 methods (method A & B). Method-A was based on the base promoted aldol reaction while method-B (as shown in **Figure 73** and synthesized compounds in blue colour) utilized acid promoted aldol reaction for formation of hydroxy-substituted chalcones.

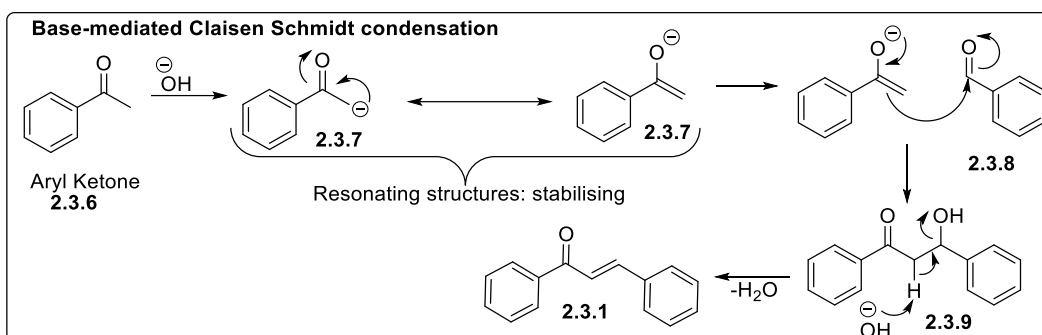
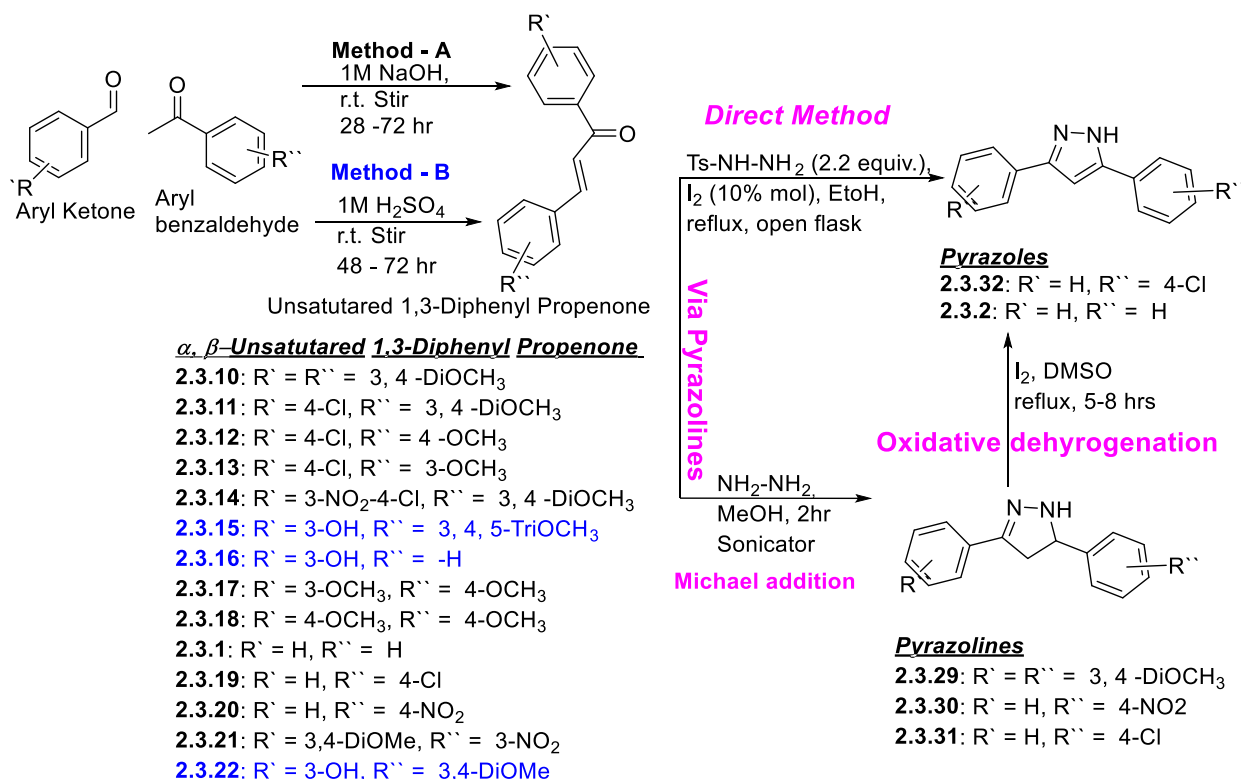


Figure 72 Mechanism of Claisen Schmidt condensation



Scheme 1 This scheme shows the scope of chalcone synthesis (14 analogues: 2.3.1, 2.3.10-2.3.22); those in blue were prepared under acidic conditions (Method B). Subsequently, these chalcones were used for synthesis of pyrazolines and pyrazoles. Pyrazoline synthesis was achieved through Michael addition reaction using hydrazine, which later undergo oxidative dehydrogenation (oxidative aromatisation) to form pyrazoles. Pyrazole synthesis was also possible more directly as was reported by Zhang et al in 2016 [186].

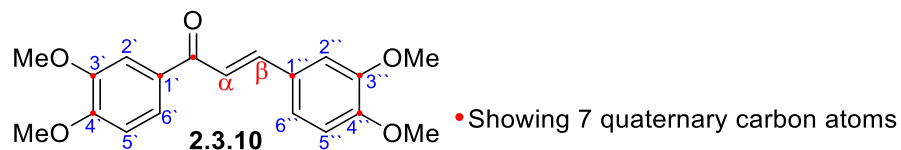


Figure 73 Numbering of representative compound of 1,3-diphenyl propenone derivative

In order, to characterize the compounds of non-hydroxy chalcone series, 1-D and 2-D NMR of one of the compounds (**2.3.10**) is shown in **Figure 73**. I started characterizing the compound with detailed ^{13}C NMR spectroscopic assignments rather than ^1H NMR as it gave a better understanding of aromatic region in synthesized compound. Study of the ^{13}C NMR and C-APT spectra as shown in **Figure 74**, provided evidence for the presence of 7 quaternary carbons in **2.3.10** (marked in red dots in **Figure 73**). Therefore, signals at 189.69, 153.13, 151.28, 149.25, 149.24, 131.57 and 128.07 (highlighted in the **Figure 74**), where four signals were so downfield (region from 149 to 153 ppm) indicate that these signals belong to the four methoxy in these two phenyl rings of **2.3.10**, as shown in **Figure 74**. While, signal at 188.69 ppm clearly belongs to carbonyl functionality and signals (at 131.57 & 128.07 ppm) shows that these are either C-1' & C-1'' or vice-versa of the respective phenyl rings. The downfield signal at 144.15 ppm shows that it is β -carbon of enone functionality as shown in **Figure 74**.

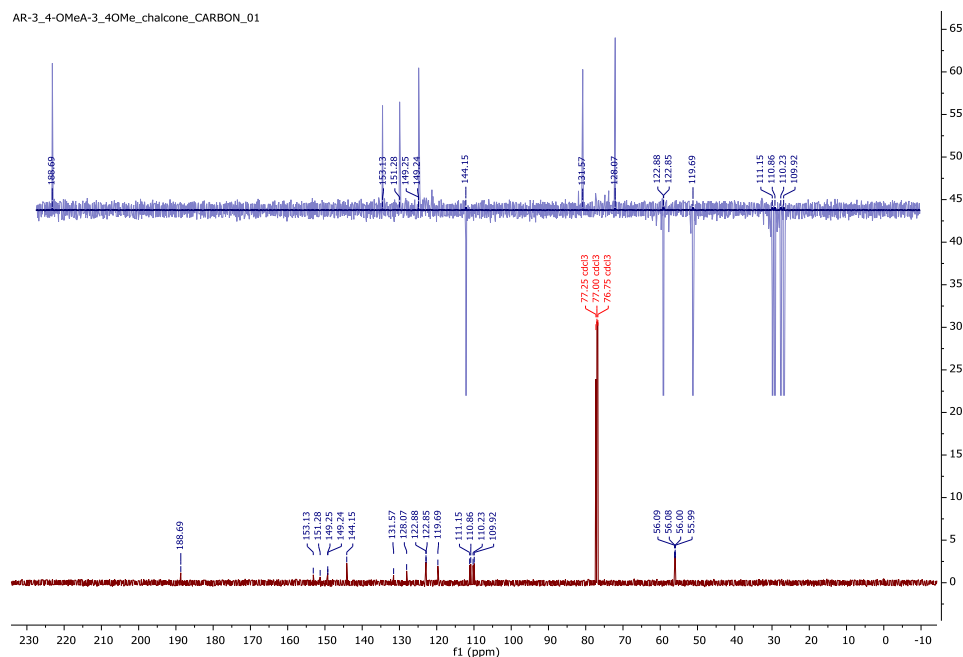


Figure 74 ^{13}C NMR (brown colour, bottom) and of C-APT/ ^{13}C NMR (blue colour, top) spectra of chalcone compound (**2.3.10**).

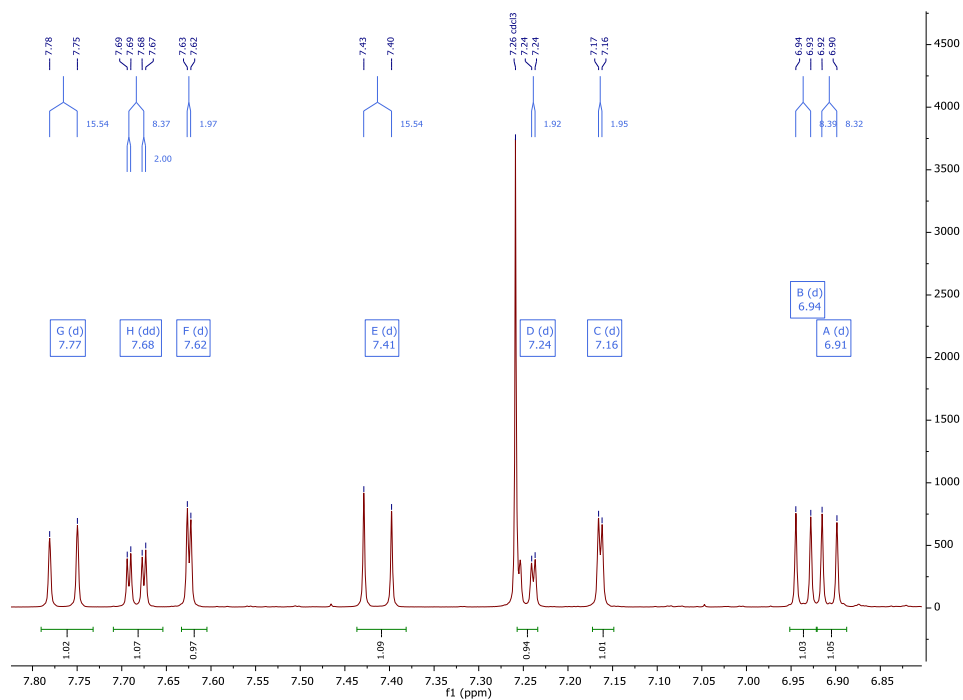


Figure 75 ^1H NMR of representative chalcone compound (**2.3.10**).

Table 6 gCOSY coupling and HSQC correlation studies of compound (**2.3.10**).

HSQC		gCOSY	
^{13}C	^1H (ppm)	7.77	7.42
109.96	6.94	7.69	6.94
110.24	7.17	7.24	6.91
110.90	7.63		
111.19	6.91		
119.71	7.39		
119.69	7.43		
122.88	7.24		
122.85	7.69		
144.08	7.75		
144.15	7.78		

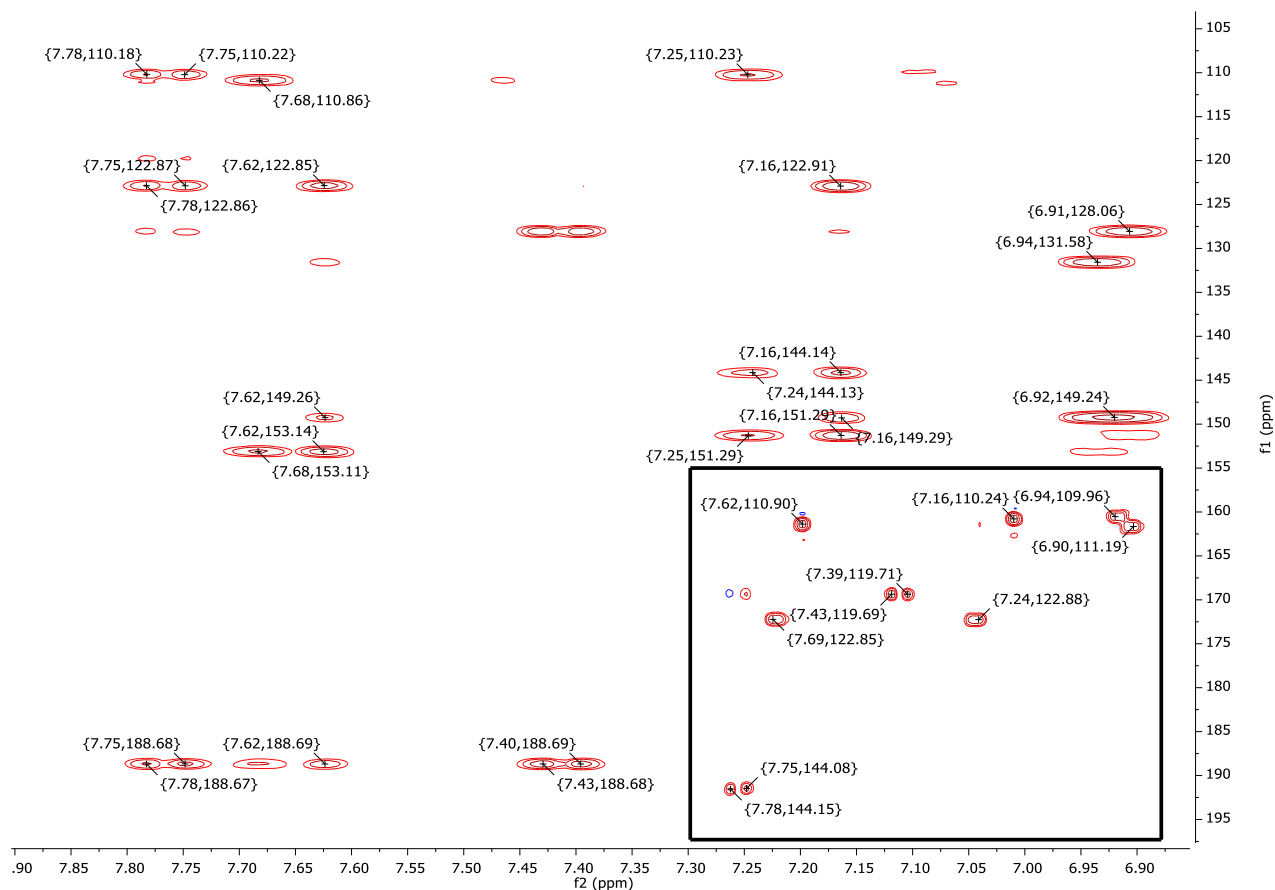


Figure 76 HMBC & HSQC (enclosed in black framed box) correlation of (2.3.10).

From HMBC in **Figure 76**, the carbon signal at δ 144.15 ppm (i.e. β -carbon of enone functionality) was correlated with protons at δ 7.17 and 7.24 ppm. HMBC showed further correlation between the proton at δ 7.17 ppm with δ 149.25 and 151.28 ppm carbon signals while proton at δ 7.24 ppm showed correlations with signals at δ 151.28 ppm and δ 110.28 ppm. Based on these the following assignment was made: the signal at δ 7.17 ppm is at H-1 $''$ while δ 7.24 ppm at H-6 $''$. Also, gCOSY showed further coupling of proton at δ 7.24 ppm with δ 6.91 ppm therefore δ 6.91 is at C-5 $''$. However, HMBC correlations between the signal at 188.69 ppm carbon (i.e. carbonyl signal) with the protons at δ 7.77, 7.62 and 7.42 ppm and, also gCOSY showed correlations between protons at δ 7.77 and 7.42, with high J-value (15.5 Hz) as shown in **Table 6**, showing that these protons belongs to the unsaturated propenone functionality in its E-configuration as shown in **Figure 75**. The proton at δ 7.62 ppm also further correlates with carbons at δ 149.24 and 153.13 ppm, which shows its position at H-2 $''$. While, proton at δ 7.69 ppm correlates with carbons at δ 153.13 and 110.86 ppm shows that it is H-6 $''$, as shown in **Figure 77**. The protons at δ 6.94 ppm

and 6.91 ppm are correlated with δ 131.57 and 128.07 ppm respectively, which shows that δ 131.07 is C-1' and 128.07 is C-1''.

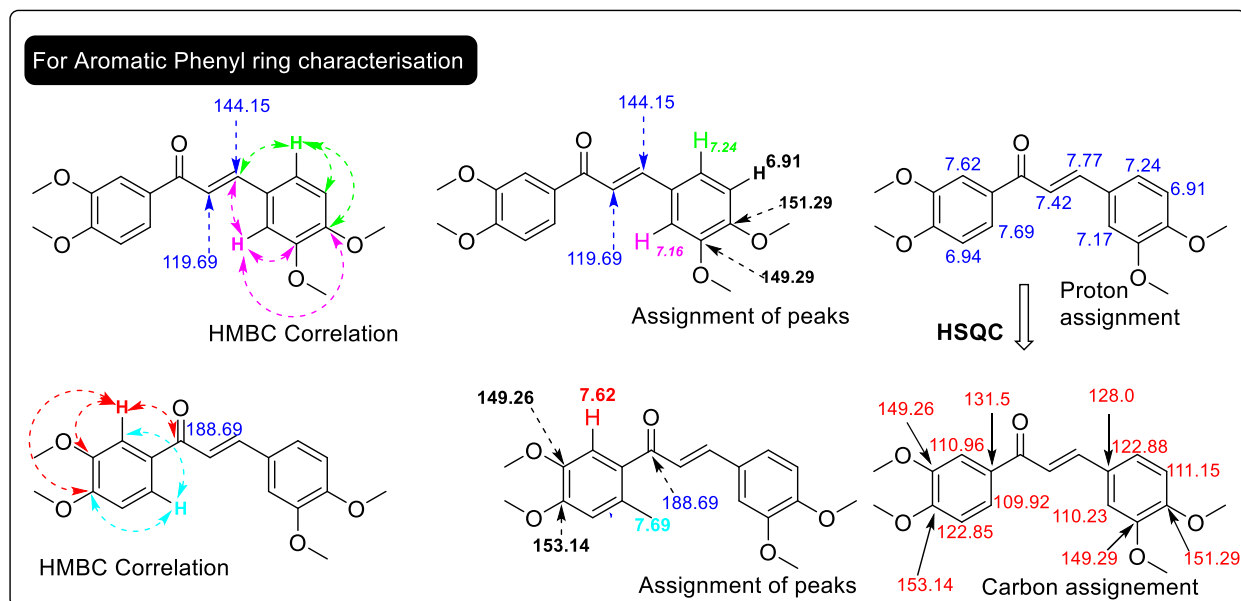


Figure 77 Signal characterisation of **2.3.10**, where individual colors were provided to particular protons and arrows. During the synthesis of **2.3.10**, I also found the formation of a more polar compound (based on TLC analysis), which was later characterized as 3,4-dimethoxy benzoic acid (**2.3.34**). This product was formed from a Cannizzaro reaction, which competes with the Claisen Schmidt aldol condensation during the formation of diphenyl propenone [187].

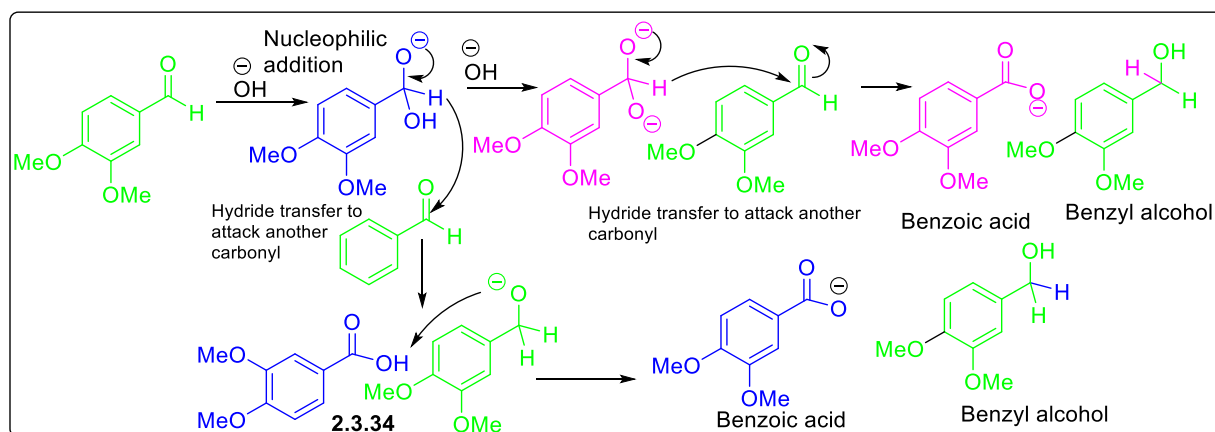


Figure 78 Mechanism of formation of 3,4-dimethoxy benzoic acid by competitive Cannizzaro reaction

Similar NMR (1D/2D-NMR ($^{13}\text{C}/\text{C}$ -APT) based characterisation was also performed for the hydroxylated chalcones (e.g. for **2.3.15**), as shown in **Figure 79**

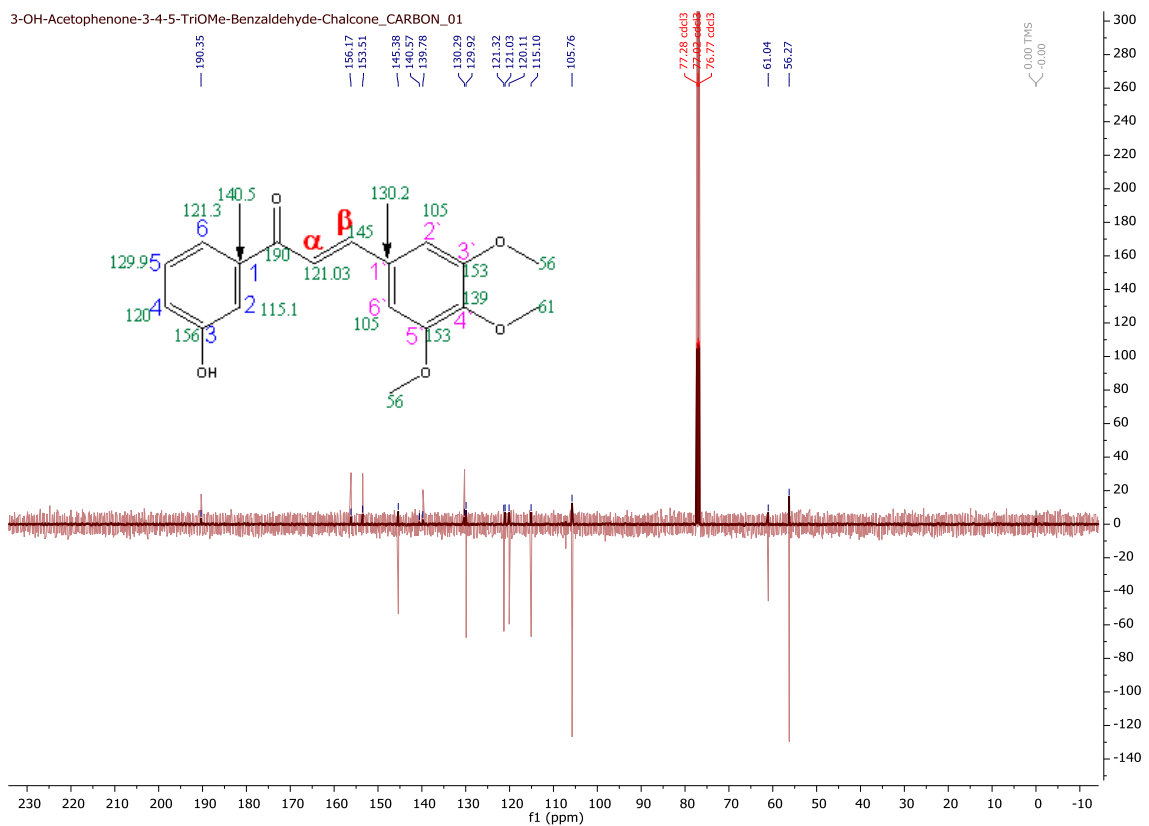
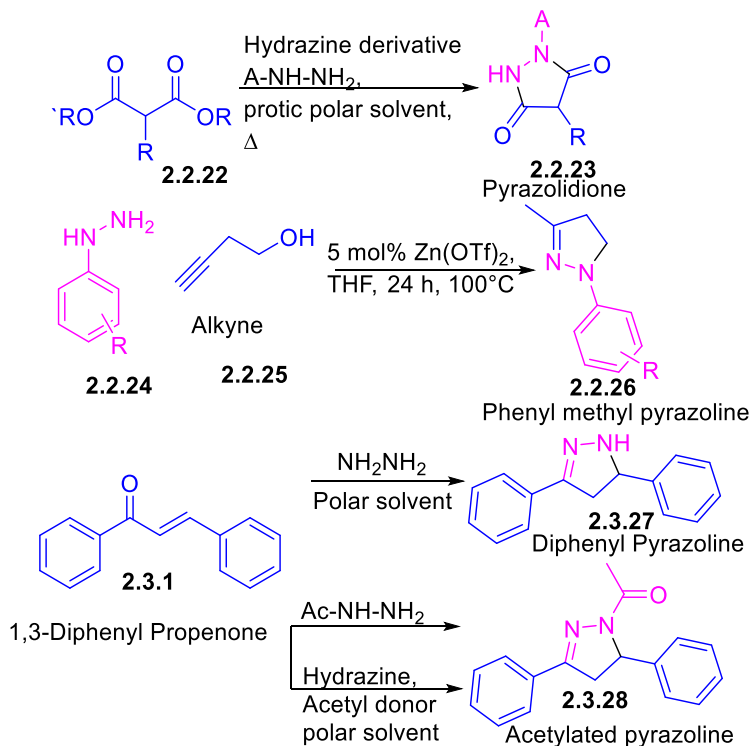


Figure 79 Superpose of $^{13}\text{C}/\text{C}$ -APT of **2.3.15**, which leads to assignments of ^{13}C signals of hydroxy chalcones

Synthesis of Pyrazolines & Pyrazoles

Pyrazolines are reduced forms of pyrazoles and can be synthesized in various ways. A commonly used route involves the reaction of hydrazine derivatives with active methylene diesters or 1,3-propenone derivatives as shown in **Scheme 1B** [188, 189]. The formation of pyrazolines, involves Michael addition of propenones followed by cyclization and there are a few reports that show that catalyst can be useful in improving the kinetics of these reactions, such as zinc triflate [190], TBD (1,5,7-triazabicyclo[4.4.0]dec-5-ene) [191], as shown in **Scheme 1B**. In my study, I used hydrazine in MeOH with previously the acquired chalcones to achieve the pyrazolines as shown in **Scheme 1**, which readily precipitated upon cooling, giving orange/yellow coloured solids.



Scheme 1B Some of the known procedures involved for the formation of pyrazolines

There are various synthetic routes available for synthesis of pyrazoles: (a) condensation of hydrazine derivatives with 1,3-dicarbonyl derivatives or their synthetic equivalents [192-194]; (b) condensation of α,β -unsaturated carbonyl compounds with hydrazines followed by oxidative dehydrogenation [195, 196]; (c) [3 + 2] cycloadditions of 1,3-dipoles to dipolarophiles like alkenes and alkynes [197] (d) nucleophilic attack of hydrazines to flavones, chromones or isoxazoles [198, 199]. However, these methods can be severely limited by their drawbacks. Condensation and dipolar cycloaddition methods usually lead to the formation of two regioisomers, whereas nucleophilic addition methods involve multistep sequences before attaining pyrazoles and reactions involving diazo substrates, which can be hazardous to health and potentially explosive. However, I utilised oxidative dehydrogenation of pyrazoline by using iodine in DMSO, along with a direct method reported by Zhang *et al* [186] where the chalcone can be converted to pyrazoles, as shown in **Scheme 1**.

In order to characterize the pyrazoles, 1D/2D-NMR was used on a synthesized compounds (**2.3.32** used as an example for characterization), as shown in **Figure 81**, the coupling of H⁻2 and H⁻3 (in magenta) and H⁻2 to H⁻3 and H⁻3 to H⁻4 (in blue) was found and ¹³C NMR values were found in agreement with a previous report [200].

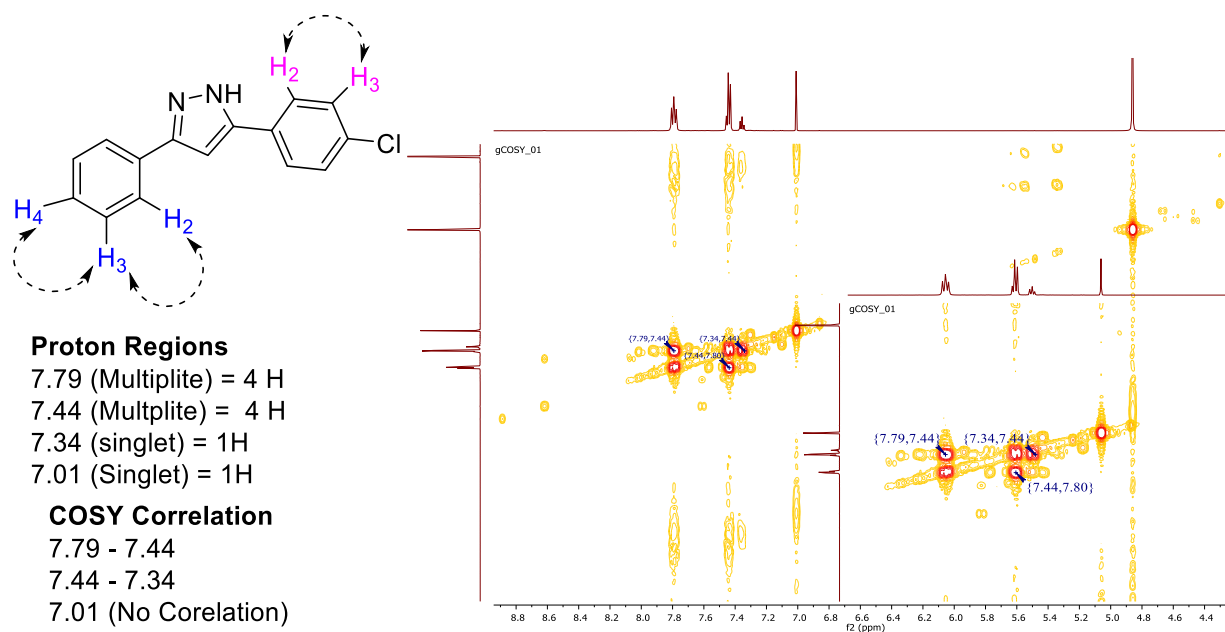
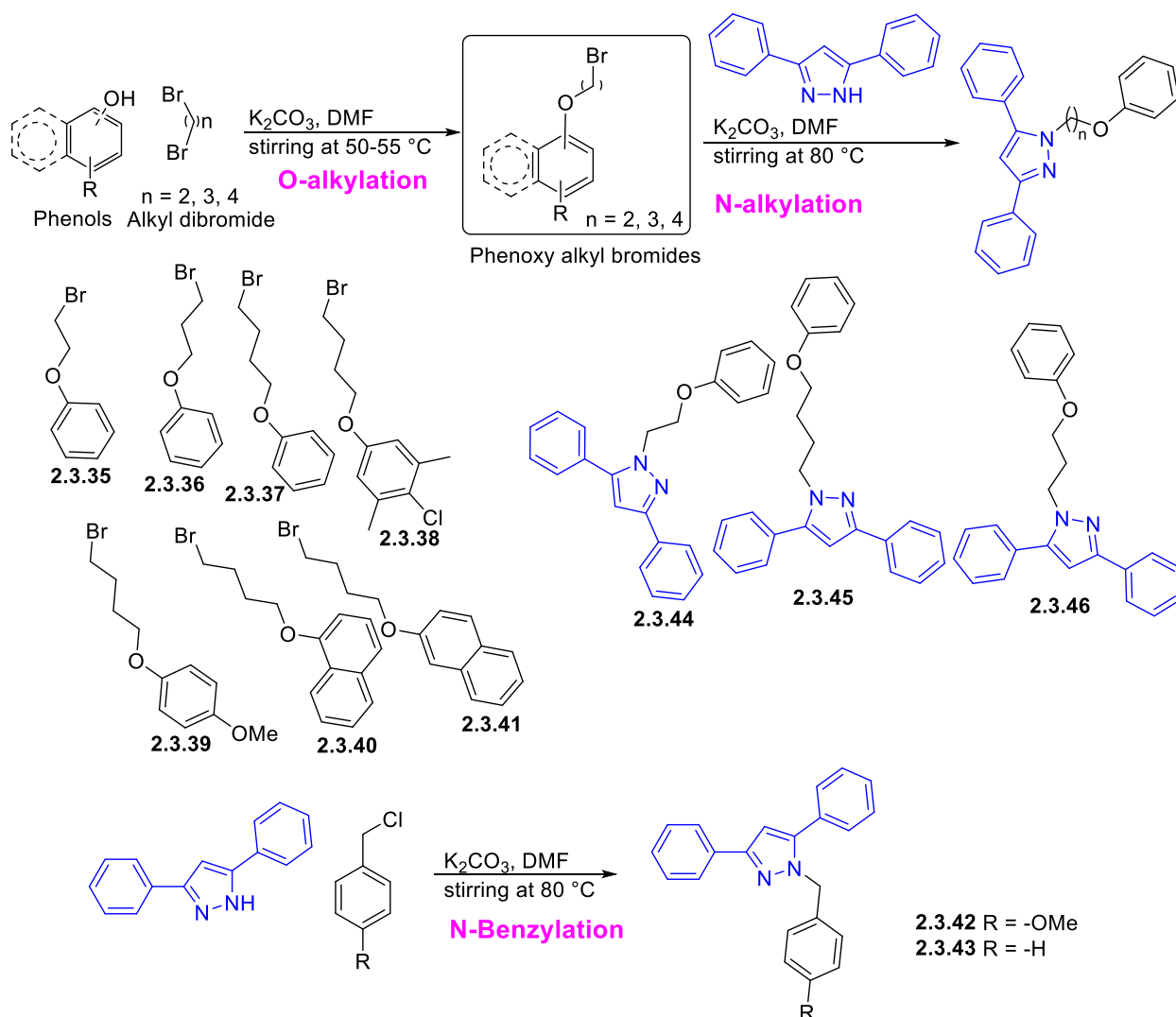


Figure 81 ^1H NMR/gCOSY NMR of **2.3.32**

Synthesis of O-Phenyl alkyl Bromides & N-substituted pyrazoles

As from *objective 2.2*, it was seen that some natural compounds have two phenyl rings which are separated with an alkyl tethered chain, and these show reasonably potent Mcl-1 activity (especially anacardic acid and endiandric acid derivatives). Taking inspiration from the structures of these nature class, and in interest in establishing a structure-activity relationship, N-substitution on these pyrazoles (especially **2.3.33**) was investigated. In order to replicate similar di-phenyl system found in the natural compounds, then O-alkylation of phenols with dibromoalkanes was performed. Later, these phenoxyalkyl bromides (alkyl chain linker contains 2 to 4 carbon length backbone) were used in N1-alkylation of pyrazoles. Benzylation was also carried out, as shown in **Scheme 2**



Scheme 2 Synthesis of O-alkylation of phenols and N-substituted pyrazoles

Similarly, one representative compound of these pyrazole derivatives (**2.3.44**) was characterized using 1D/2D-NMR studies. The $^1\text{H-NMR}$ of **2.3.44** contains 10 regions of aromatic protons, which were overlapped therefore gCOSY spectra was used (as coupling of proton partners were shown in magenta color in **Figure 81**), showed that coupling of the protons at 7.84 (region contains 2 protons) with 7.41 ppm region of protons (contains 2 protons) and further, protons at 7.41 ppm coupled with 7.32 protons (7.32 has only 1 protons) indicates that these two couplings particular belong to particular phenyl ring. While coupling of 6.92 ppm (which contains 2 protons) with 7.23 (2 protons) and 6.81 (1 protons) shows that they belong to phenoxy ring with upfield 6.92 ppm for *meta*-protons while 7.23 is for *ortho*-position and 6.81 (*para*-position) as shown in **Figure 82**. However, HSQC (in **Figure 83**) data drew further correlation of these protons to their

corresponding carbons (shown in Figure) in the molecule, compiled data shown in **Figure 82** & **Table 7**.

The quaternary carbons were assigned based on HMBC, where correlations shown in red arrows (as shown in **Figure 82**): The protons at δ 7.84 ppm correlated with carbon on δ 151.24 ppm shows that it is C-2 of 3-phenyl ring. While, protons at 7.57 ppm correlated with 146.10 (pyrazole-C-5) and δ 6.82 protons correlated with 158.30 (-OPh-C-1), as shown in **Figure 82**.

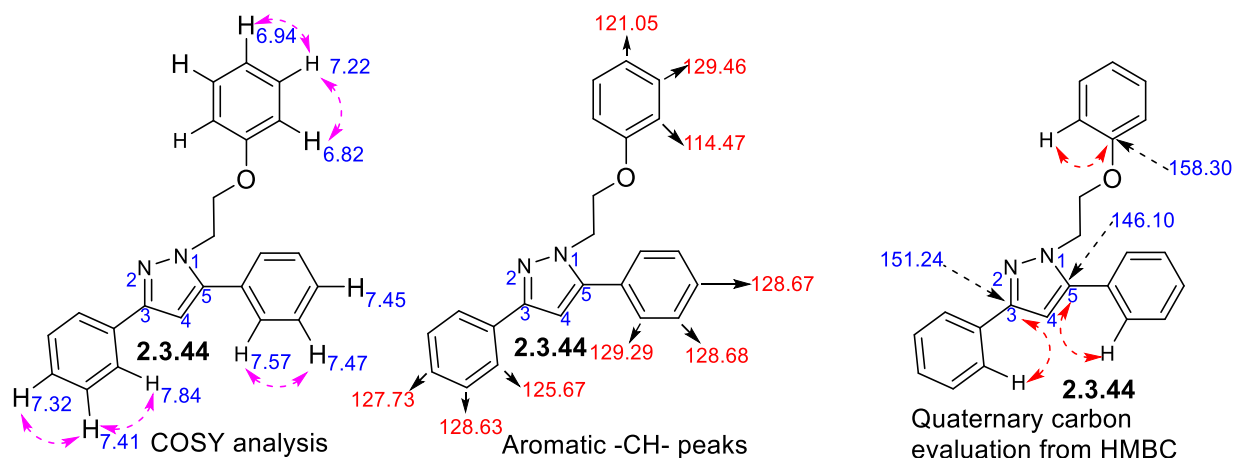


Figure 82 Featuring gCOSY, HMBC based quaternary carbon analysis and aromatic (-CH-) carbons of **2.3.44**

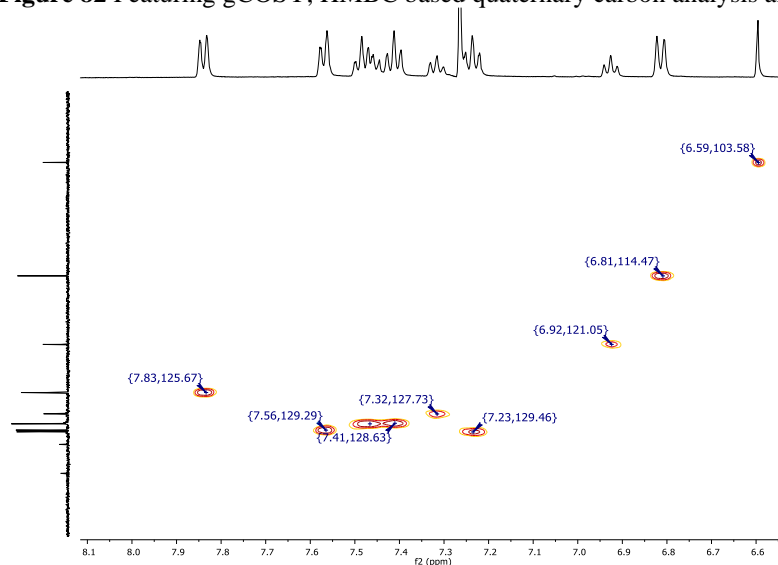


Figure 83 Assigned HMBC for **2.3.44**

Table 7 Compiled data retrieved from proton NMR, HSQC and gCOSY of **2.3.44**

Proton NMR		HSQC	gCOSY	
Regions (ppm)	No. of ^1H	^{13}C	7.84	7.41-7.43
4.45	2	48.70	7.56	7.47
4.53	2	66.64	7.43	7.32
6.60	1	103.5	7.22	6.82
6.81	2	114.4	7.22	6.94

6.93	1	121.05		
7.23	2	129.46		
7.32	1	127.73		
7.41	2	128.63		
7.46 – 7.44	1			
7.50 – 7.47	2	128.68 (7.47)		
7.59 – 7.54	2	129.29 (7.56)		
7.81	2	125.67		

Synthesis of diphenyl pyridines

Various conditions were reported for synthesizing diphenyl pyridines (summarized in **Figure 84**), however only few of these diphenyl pyridines have been studied to date for their medicinal activity; these activities are summarized in **Figure 85**.

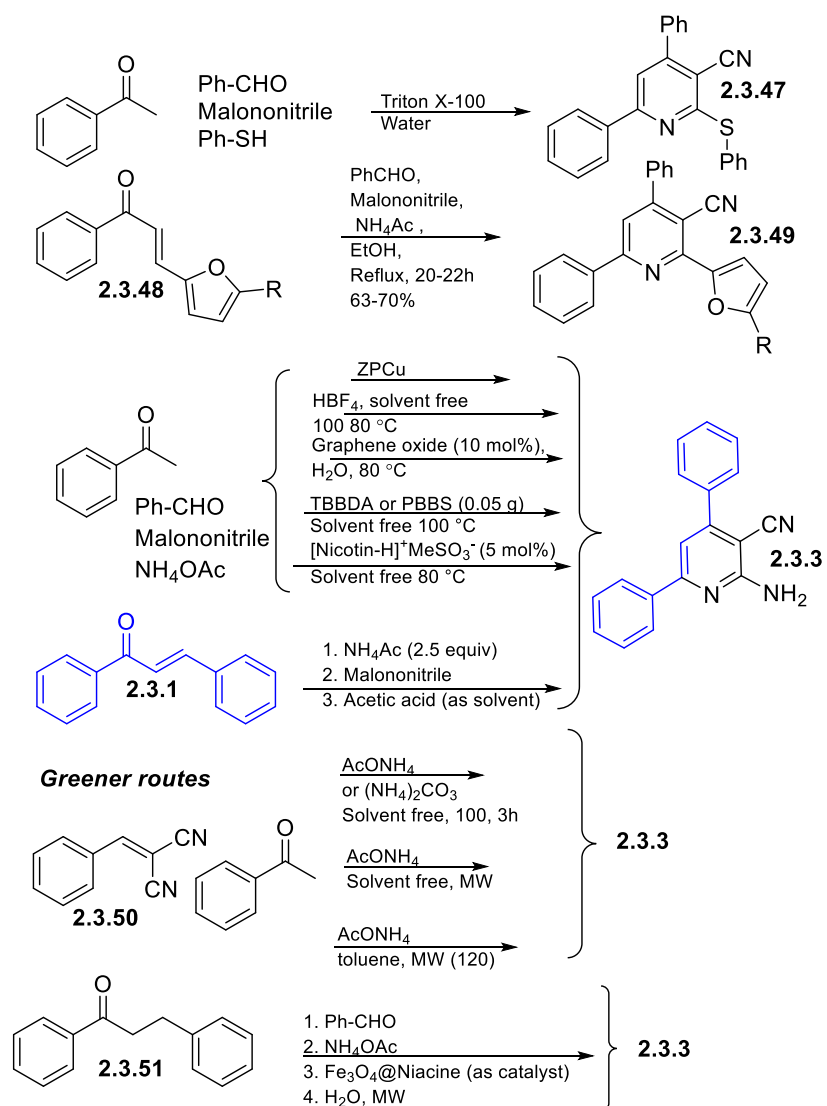


Figure 84 Various Available methods for preparing the diphenyl pyridines (4,6-diaryl-2-(arylthio)nicotinonitriles).

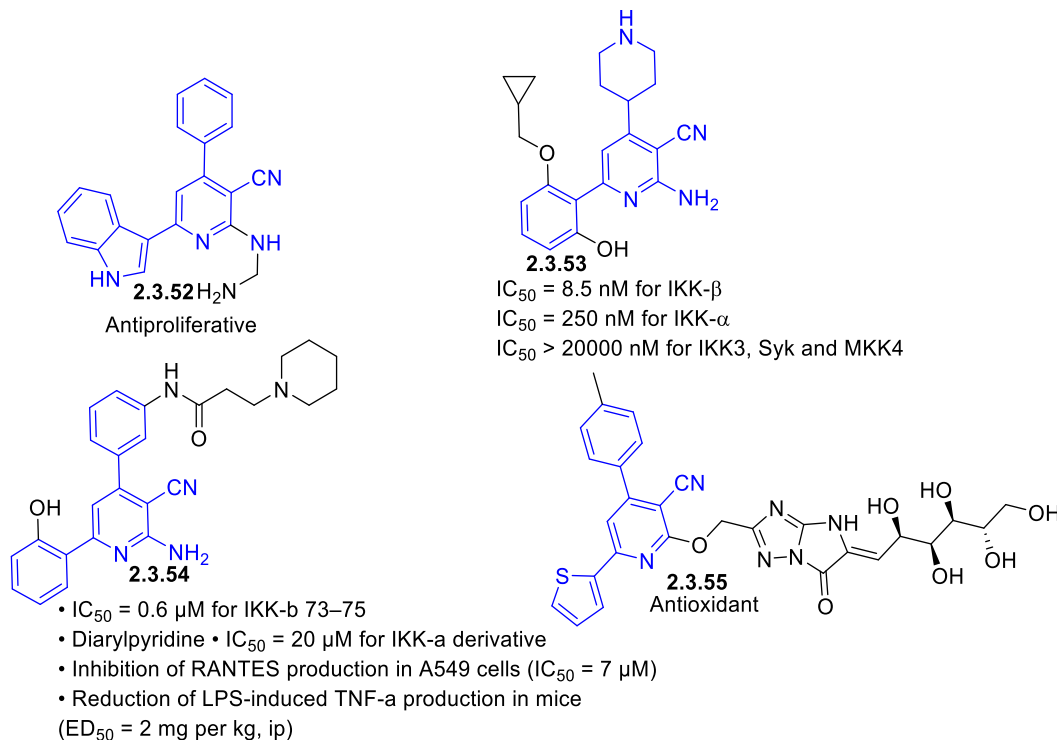
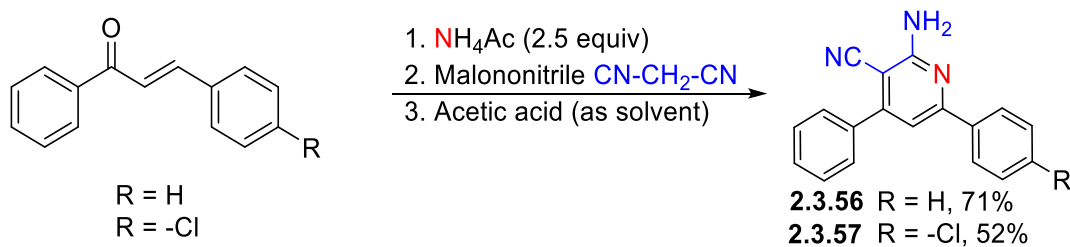


Figure 85 Medicinal attributes of selected pyridines: antioxidant [201], orally active anti-inflammatory IKK- β inhibitors [202], anti-proliferative [203]

In my study, I utilized ammonium acetate along with malononitrile in AcOH as solvent to synthesize the diphenyl pyridines, as shown in **scheme 3**



Scheme 3 Synthesis of 2-amino-3-cyano-diphenyl-pyridines

The mechanism of formation of diphenyl pyridines show that the reaction started with the addition of malononitrile to the chalcone, which later tautomerizes back into keto form. This keto group is attacked by *in-situ* produced ammonia, to form imine, which then rearranges into an enamine. The amino group of the enamine attacks an electron deficient methylene carbon to form dihydropyridine which latter undergo aromatic dehydrogenation to aromatise the ring into pyridine. The driving factor for the final step was the dehydrogenation to generate the aromatic ring (aromaticity) **Figure 86** [204].

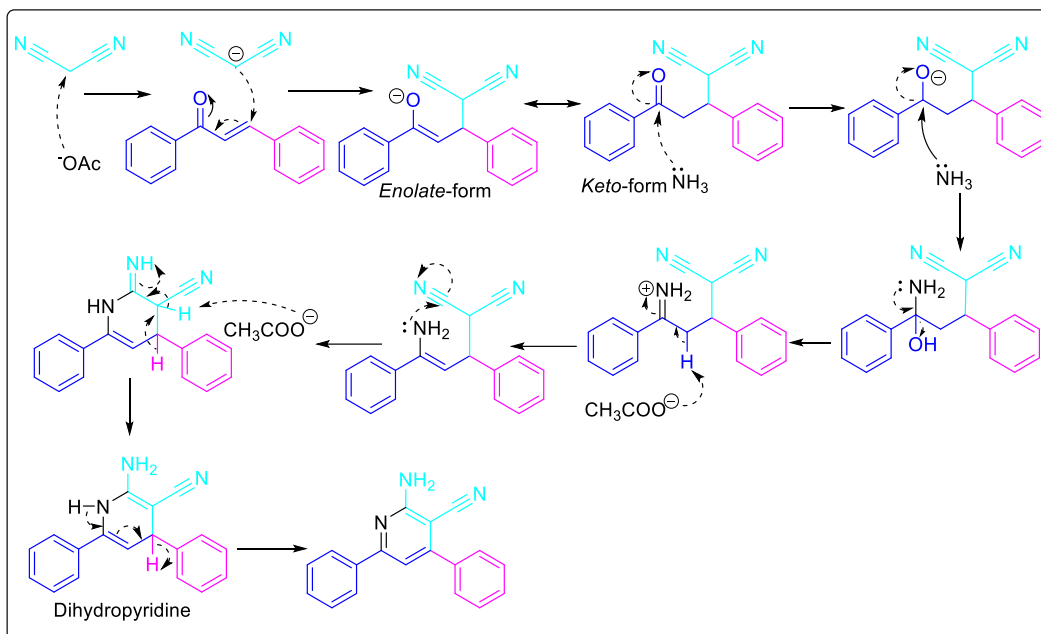


Figure 86 Mechanism of diphenyl pyridine formation (**2.3.56**)

The characterisation of the compound (**2.3.56**) was performed through 1D/2D NMR (as shown in **Figure 87** & **Figure 88**) and compiled into **Table 8**

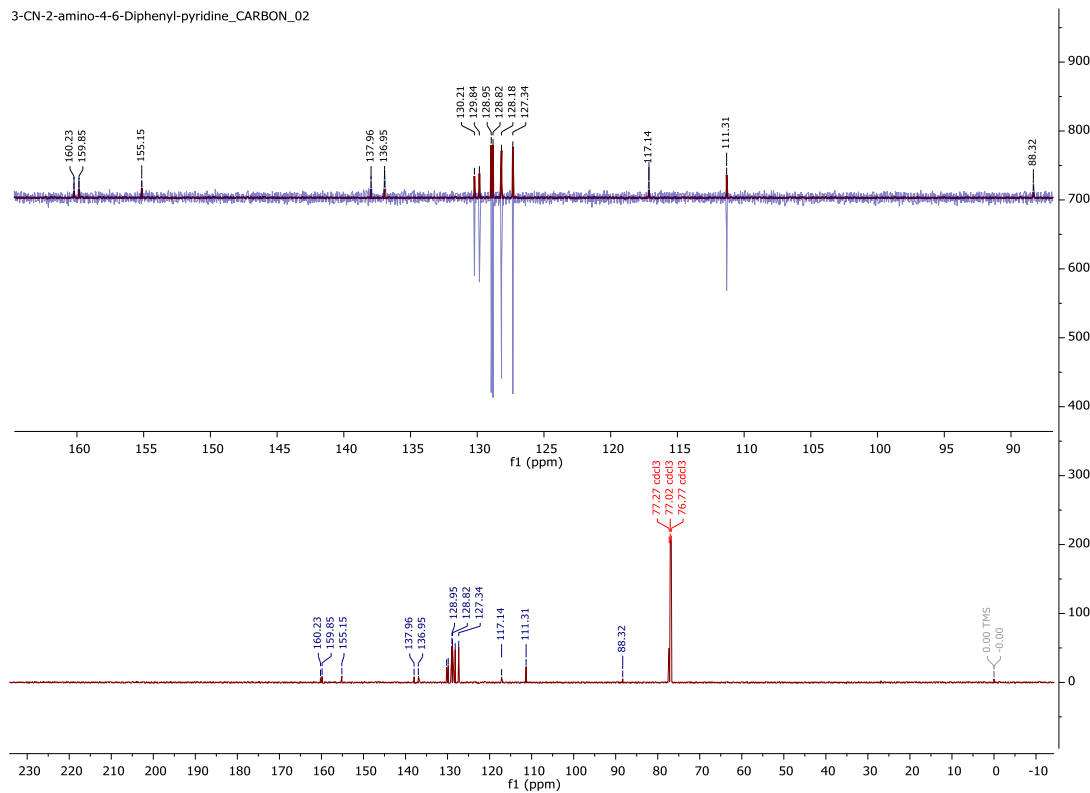


Figure 87 ^{13}C NMR (brown colour) and superpose of C-APT/ ^{13}C NMR of representative of diphenyl pyridine (**2.3.56**)

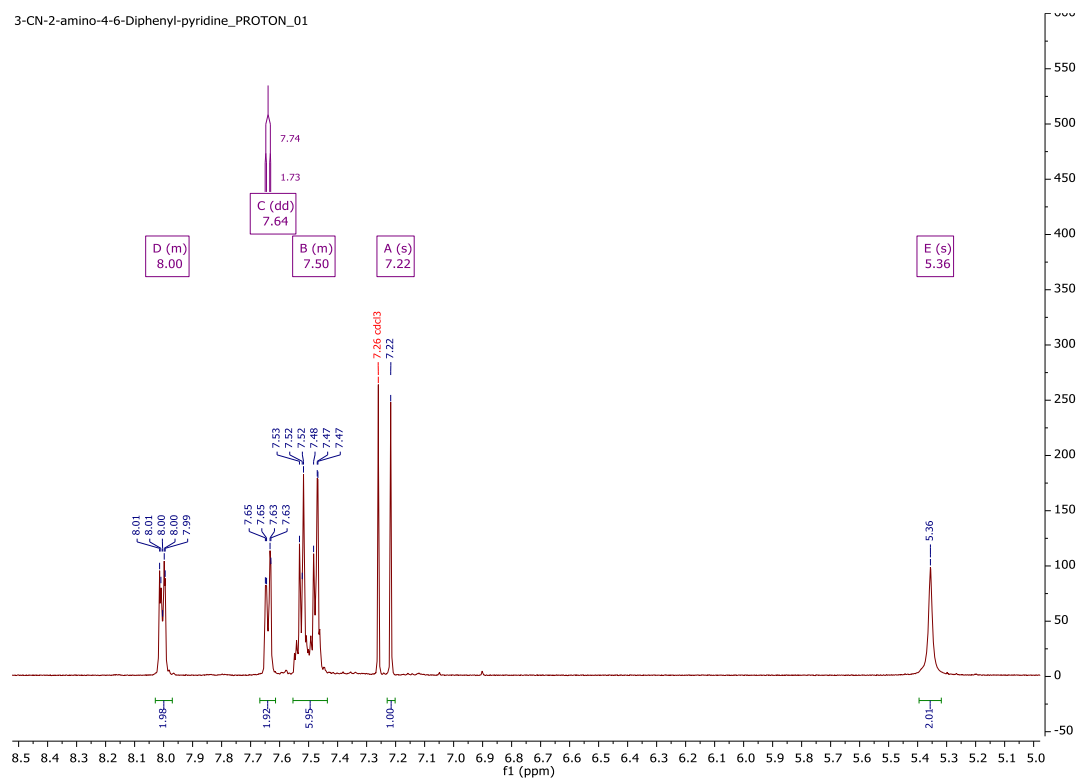
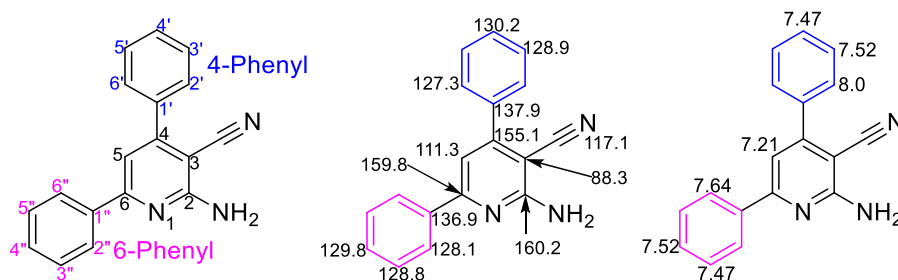


Figure 88 $^1\text{H-NMR}$ of 2-amino-3-cyano-diphenyl pyridine (**2.3.56**)

Table 8 Assignment of signals of 2-amino-3-cyano-diphenyl pyridine (**2.3.56**)



HSQC correlation		from C-APT/ ^{13}C	Conclusion	gCOSY Correlation		Inferences
^1H	^{13}C					
8.00	127.3	2 x -CH-	either <i>ortho</i> or <i>meta</i>	8.00	7.47	(a) As no further gCOSY correlation has been seen for signals at 8.00 ppm & 7.64 ppm, therefore protons should at <i>ortho</i> position (b) Also, carbon signals at 127.3 and 128.1 also at <i>ortho</i> position in either 4-phenyl or 6-phenyl ring
7.64	128.1	2 x -CH-	either <i>ortho</i> or <i>meta</i>	7.64	7.52	
7.52	128.9	2 x -CH-	either <i>ortho</i> or <i>meta</i>	It is evident that 2 x -CH- (7.52 ppm & 7.47) are at <i>meta</i> -position while signals (at 7.52 & 7.47) are at Para-position in 4-Phenyl and 6-Phenyl rings		
7.52	129.86	1 x -CH-	<i>Para</i>			
7.47	130.15	1 x -CH-	<i>Para</i>			
7.47	128.8	2 x -CH-	either <i>Ortho</i> or <i>meta</i>			
7.21	111.3	1 x -CH-	H-5 of Pyridine			

Triphenyl Pyridines: previous reports

The trisubstituted pyridine core is very versatile heterocyclic scaffolds, which has been found in compounds showing promising biological activity against number of targets, as summarized in

Figure 89.

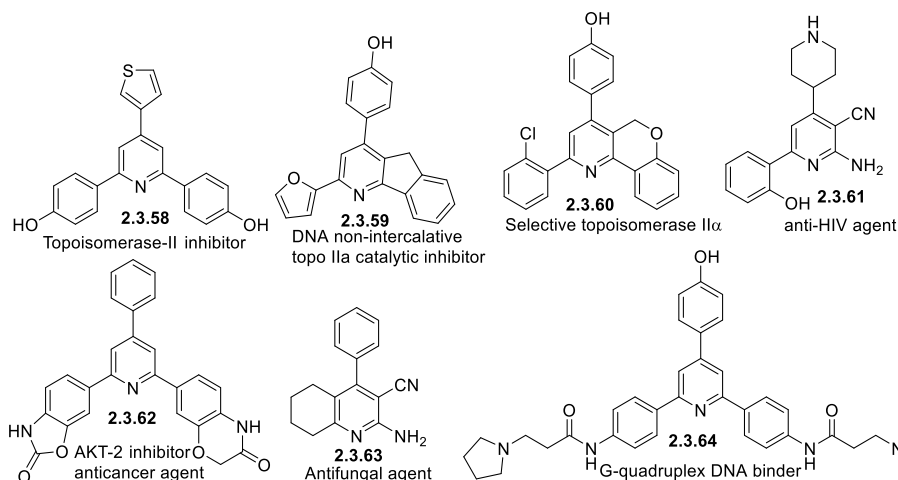


Figure 89 Topoisomerase II inhibitor [205, 206], DNA non-intercalative selective topoisomerase II α [207], Topo IIa catalytic inhibitor [208] G-quadruplex DNA binder [209-211].

There are various methods available for the formation of triphenyl heterocycles. Even researchers have also devised greener routes based on catalysts, such as using pentafluorophenylammonium triflate (PFPA) [212], mesoporous nanocrystalline MgAl₂O₄ [213], nano-Fe₃O₄-supported, hydrogensulfate ionic liquid [214], PTSA [215], cerium (IV) carboxymethylcellulose (CMC-Ce (IV) [216], L-proline functionalized magnetic nanoparticles [217], activated fuller's earth (10 wt%) [218], chitosan based vanadium oxo (ChVO) [219], as few of them listed in **Figure 90**.

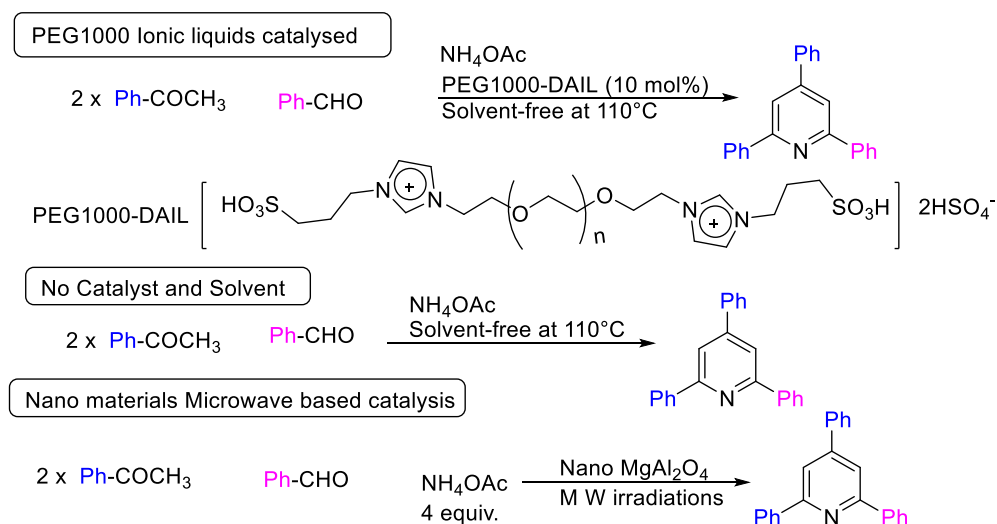


Figure 90 Some of key greener route for formation of triphenyl pyridine: (a) using catalytic amount of PEG1000-based dicationic acidic ionic liquid under solvent-free conditions [220]; (b) Without catalyst and solvent [221]; (c) MgAl₂O₄ nanocrystals and microwave-assisted synthesis of 2,4,6-triarylpyridines [222].

Triphenyl Pyridines: Reported Mechanisms for triphenyl pyridine formation

The conventional mechanism was postulated by Kröhnke [223, 224], where he reported a condensation of α -pyridinium methyl ketone salts (**2.3.68**) with α, β -unsaturated carbonyl compound (**2.3.1**) via a Michael reaction in presence of ammonium acetate (NH_4OAc) to give 2,4,6-trisubstituted pyridines in high yields under mild reaction conditions [39] as shown in **Figure 91**, which provide more functionalization over most exploited pyridine synthesis reaction (Hantzsch pyridine synthesis) [41].

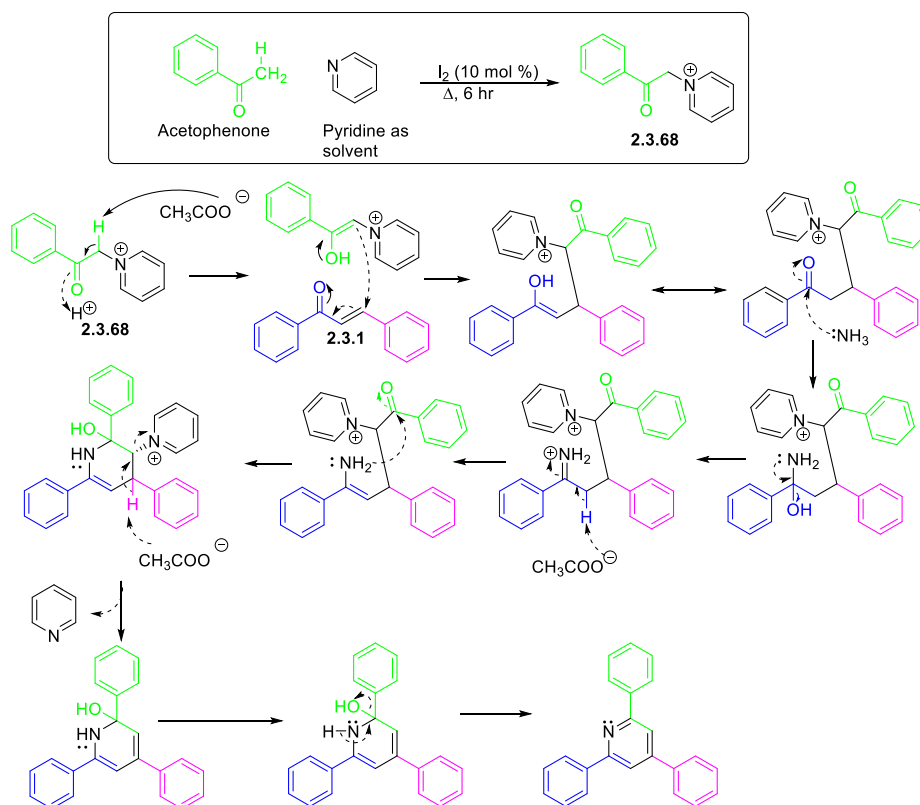


Figure 91 Conventional route: Kröhnke reported mechanism for triphenyl pyridine formation.

As the route utilizes pyridine as solvent, and its reaction with the α haloacetophenone can give acetophenone-pyridine salt and, as pyridine has a high boiling point then remnants of pyridine residues in the residues from these reactions. Therefore, various new methods were devised by researchers in order to avoid the use of α -pyridinium methyl ketone salts and therefore new routes for formation of triphenyl pyridines emerged, such as (a) one-pot synthesis of 2,4,6-triarylpyridines from β -nitrostyrenes, substituted salicylic aldehydes and NH_4OAc as shown in **Figure 92** [225]; (b) $\text{Bi}(\text{OTf})_3$ -catalysed solvent-free synthesis of 2,4,6-triaryl pyridines as shown in **Figure 93** [226]; (c) chitosan supported vanadium oxo in the synthesis of 2,4,6-triarylpyridines via anomeric based oxidation as **Figure 94** [227].

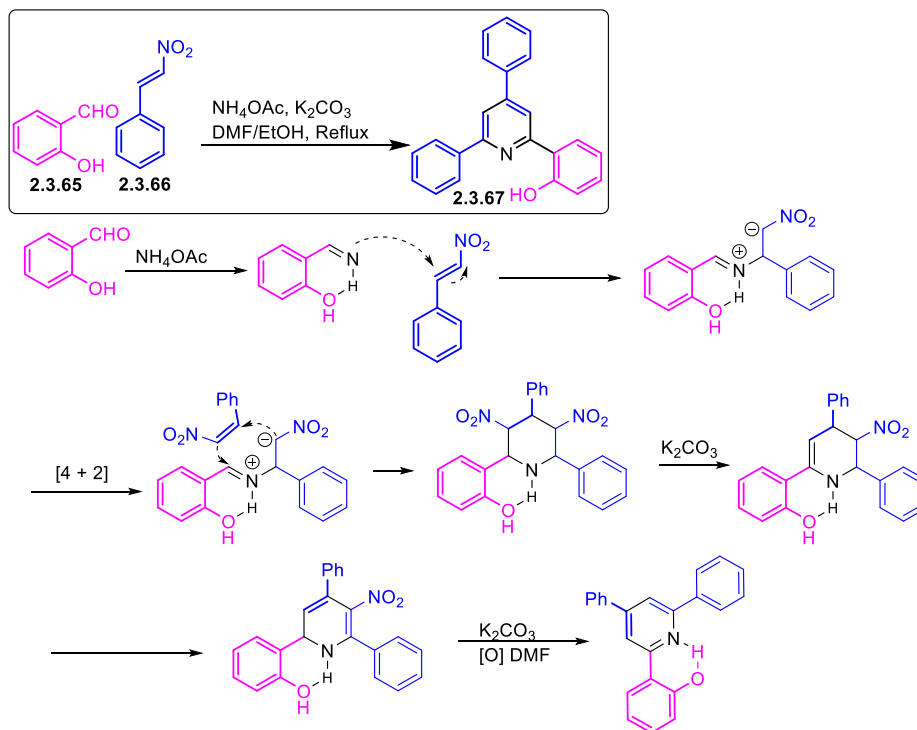


Figure 92 Mechanism of triphenyl pyridine formation from salicylaldehyde and β -nitrostyrene through intermolecular [4 + 2] cyclization [225].

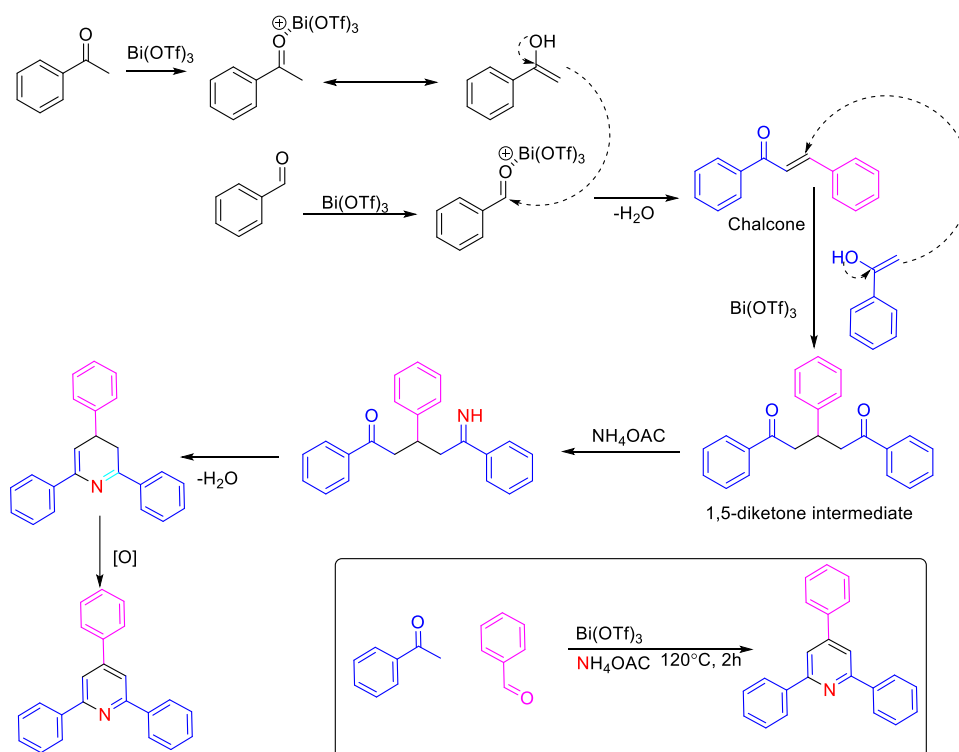


Figure 93 Shinde *et al* in 2012 reported a solvent free method where they utilized Bismuth triflate catalysis to form 2,4,6-triaryl pyridines [226].

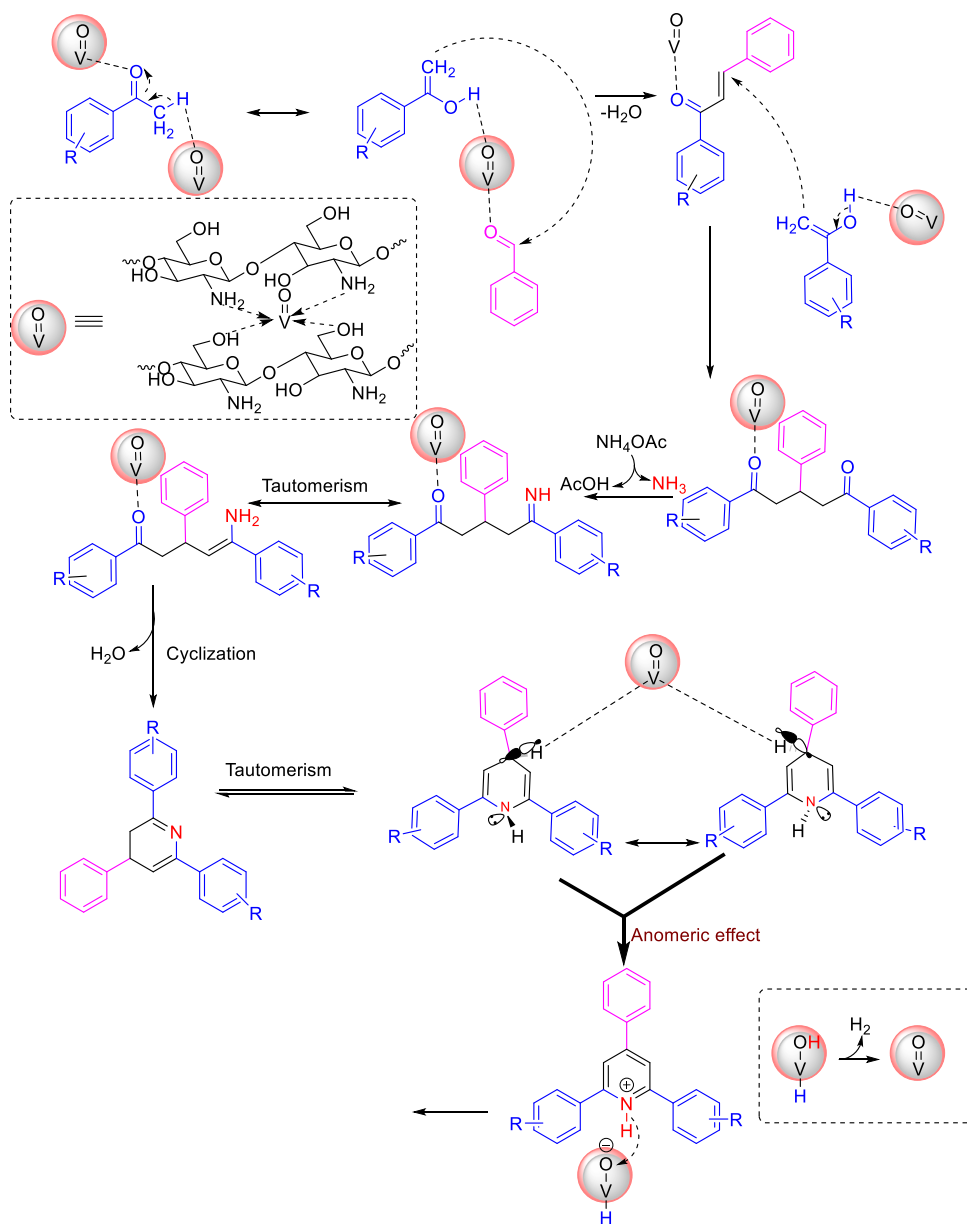
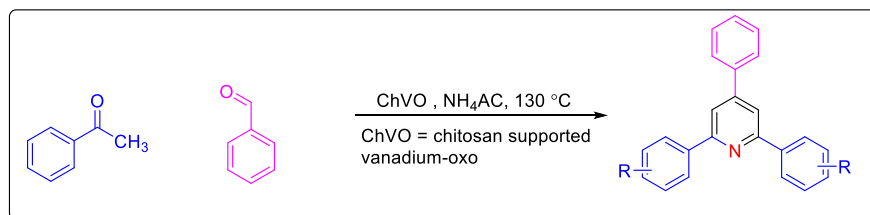
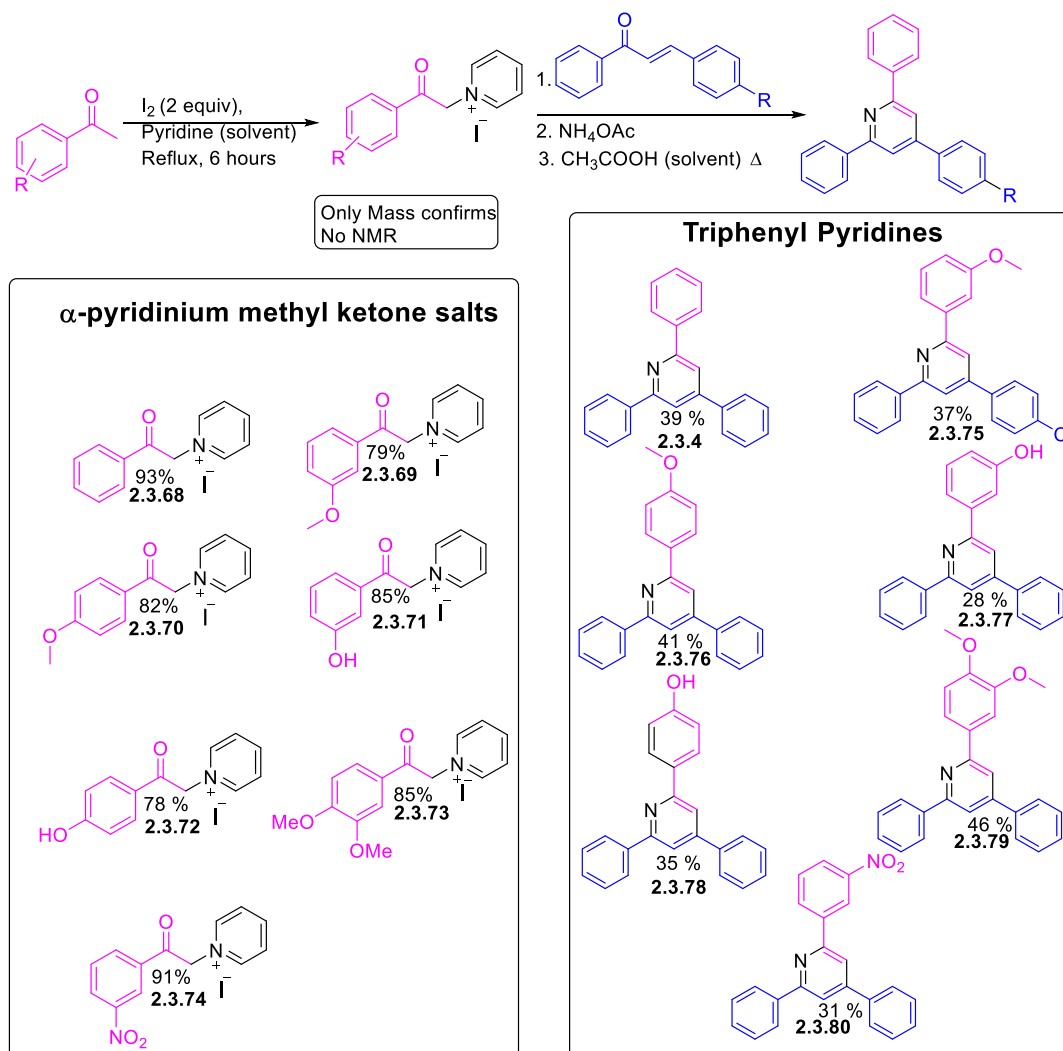


Figure 94 Mechanism of chitosan-based vanadium oxo (ChVO) catalyst formation of triphenyl pyridine [219, 228, 229].

Triphenyl Pyridines: Synthesis

Initially I used the conventional Kröhnke route for formation of triphenyl pyridines, which involve the formation of various α -pyridinium methyl ketone salts via the α -iodoacetophenone, as shown in **Scheme 4**. Later these salts were reacted with chalcones (α , β -unsaturated carbonyl compounds), whereas the overall highest yield after subsequent reactions, i.e Claisen Schmidt condensation (for formation of chalcones) followed by Kröhnke triphenyl pyridine synthesis was only 46%.



Scheme 4 Synthesis of α -pyridinium methyl ketone salts and triphenyl pyridine derivatives through conventional route

Interestingly in two cases where reaction of trans-chalcone (**2.3.1**) with 3-nitro (**2.3.74**) and 3-hydroxy (**2.3.71**) pyridinium methyl ketone salts were preformed, desired triphenyl pyridines (**2.3.77** & **2.3.80**) along with 13 % and 22 % of unsubstituted triphenyl pyridine (**2.3.4**) respectively was also found, which indicated the progression of intramolecular or self-condensation Kröhnke

pyridine synthesis along with intermolecular Kröhnke pyridine synthesis. There is only one report published on intramolecular Kröhnke pyridine synthesis by Adib *et al*, where they proposed a mechanism on how intramolecular Kröhnke pyridine progresses in the same reaction vessel [230] as shown in **Figure 95**.

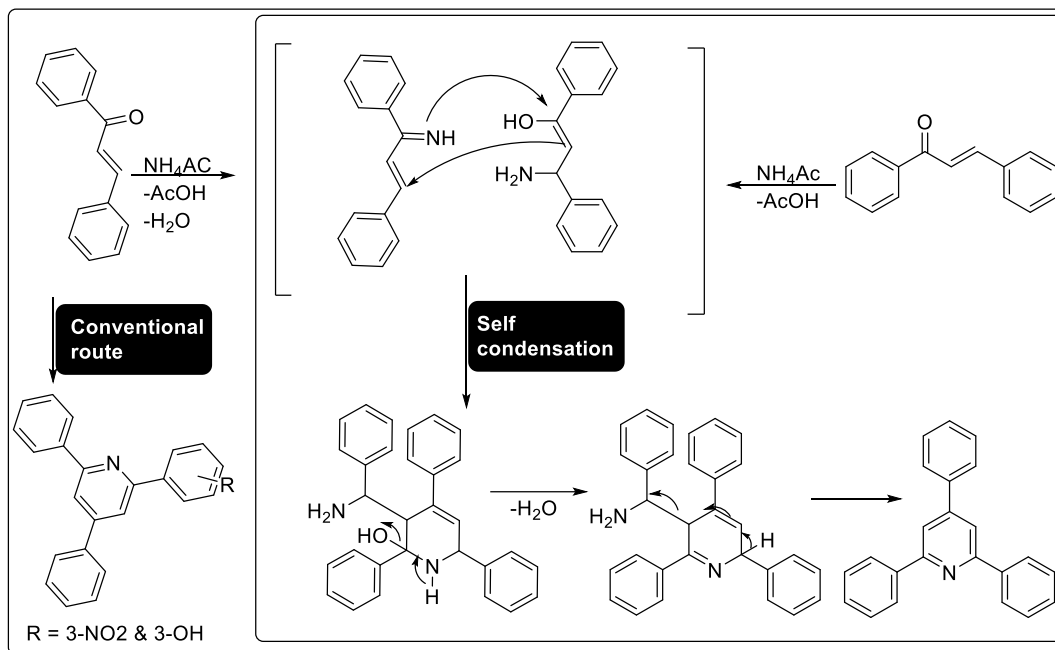
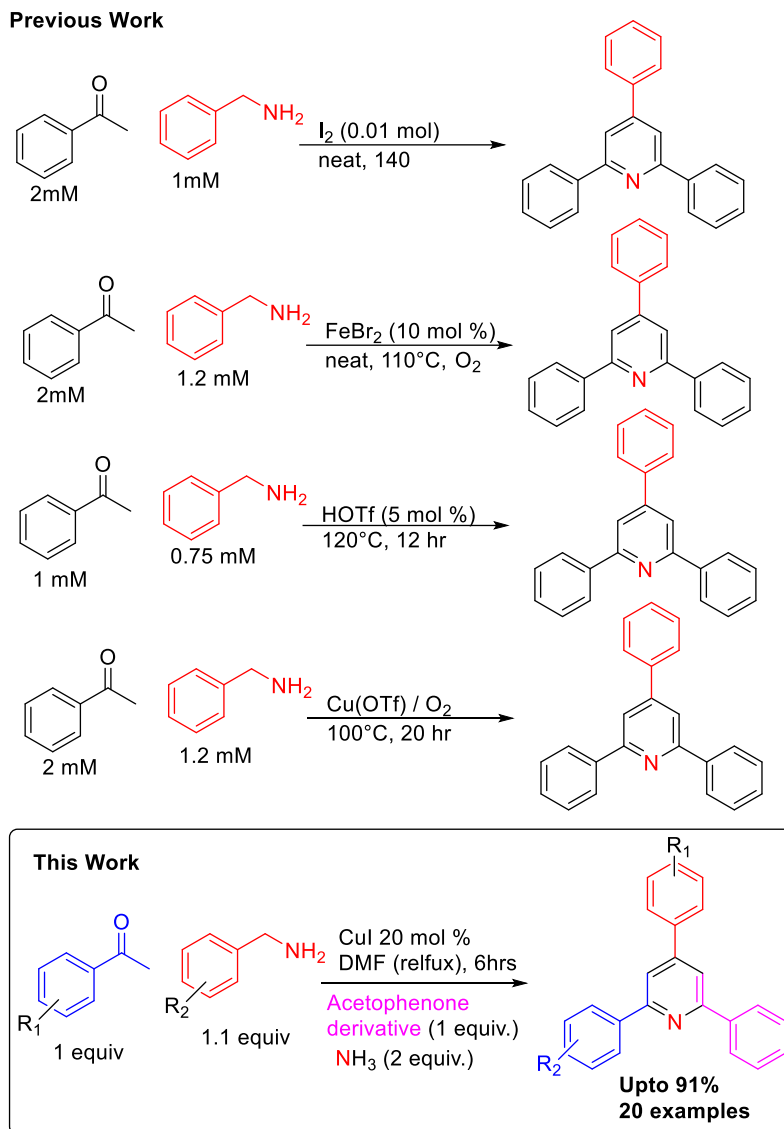


Figure 95 Mechanism of intermolecular (conventional route, as shown in **Figure 91**) and intramolecular Kröhnke pyridine synthesis.

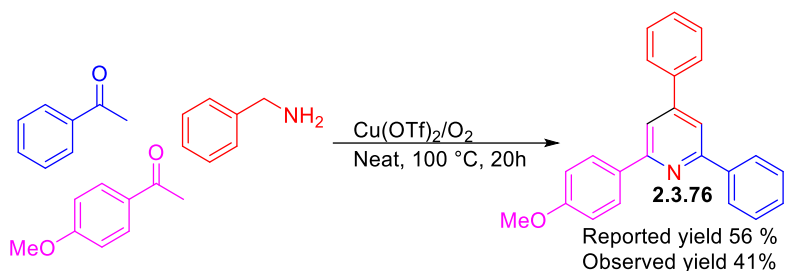
After study of the Kröhnke pyridine synthesis, shortcomings were identified: (a) in most cases, the overall yields were $\sim \leq 50\%$; (b) The method is not very green as excess of pyridine and its derivatives were used; (c) observation of the undesired side reaction (i.e self-condensation) as well as difficulty in isolation as these triphenyl pyridines which share similar R_f values according to TLC analysis with various gradient solvent systems. In order to address these issues, researchers have already reported solvent-free multi-component one pot methods where they used acetophenone derivatives (2 equiv.) along with 1 equiv. of benzylamine, as shown in **Scheme 5** [231-234]. These methods utilize the one pot concept and, therefore, the overall yield was higher than from the Kröhnke pyridine synthesis. However, as these reported methods involve use of 2 equiv. of acetophenone with 1 equiv. of benzylamine, which leads to the formation of symmetrical triphenyl pyridine core and therefore limits these methods usability triphenyl pyridines when substitution is needed on one of the phenyl rings. Also, during reactions, I found isolated yields were lower than reported in the earlier papers, even after column chromatography, see **Table 9.A**. Therefore, investigation of a new method was carried out, in order to achieve improved isolated

yields and provide a higher degree of functionalisation of the phenyl rings in these triphenyl pyridines.



Scheme 5 One pot triphenyl pyridines from benzylamine and acetophenone derivatives : (a) Gopalaiah *et al* [231] solvent-free iron catalyzed (10 mol% FeBr_3) (b) Xu *et al* solvent free iodine catalyzed (1.0 mol %)[232]; (c) Zhang *et al* HOTf-catalyzed [233], (d) Hunag *et al* air oxidised/copper triflate catalysed (0.1 mM) [234].

Among, all these reported methods only Huang *et al* successfully showed synthesis of four non-symmetric triphenyl pyridine compounds in moderate yields, as method shown in **Scheme 6**. Therefore, I initially replicate similar conditions, i.e. the solvent-free reaction between 4-methoxy acetophenone, acetophenone and benzylamine in presence of copper triflate under O_2 -atmosphere, as shown in **Scheme 6**. Although in their case, they reported 56% yield, whereas I achieved 41 % isolated yield.



Scheme 6 Multicomponent one pot reaction between two different acetophenone derivative with benzylamine.

They proposed two paths for the mechanism, shown in **Figure 96**. Path-A involves Cu (II)-mediated single-electron oxidation [235] of benzylamine and aminolysis formed imine (**2.3.82**) [236] (96 %, isolated in their report) which undergo a reversible hydrolysis to produce benzaldehyde and benzylamine. Path-B runs subsequently and promoted by Lewis acidic Cu (II), the condensation [237] of ketone, benzylamine, and benzaldehyde yielded an intermediate 1,4-dihydropyridine (**2.3.83**). Finally, this intermediate undergo oxidative hydrolysis (Cu/O₂ catalytic system) to produce triphenyl pyridine (**2.3.4**) and benzaldehyde. The released benzaldehyde would participate in the next pyridine formation (**Figure 93**, Path-B). Also, they assumed that it could be either imine (**2.3.82**) replacing benzaldehyde or ammonia replacing benzylamine could serve as corresponding component in the condensation process.

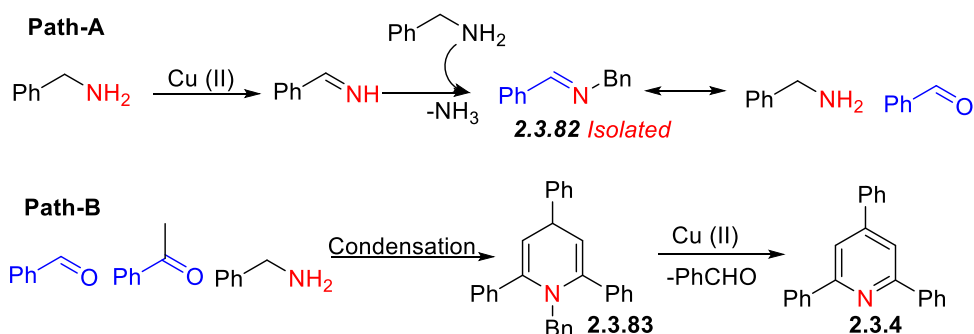
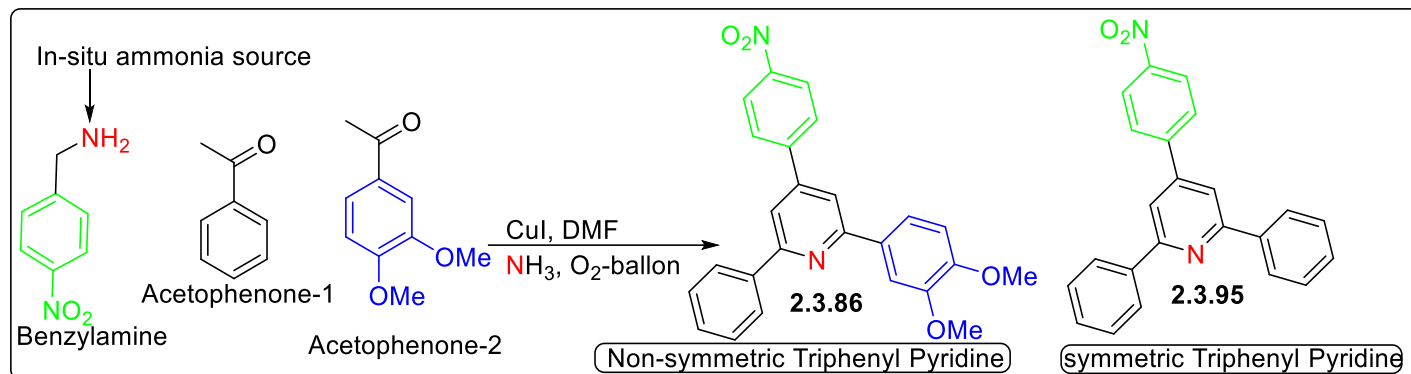


Figure 96 Huang et al disclosed Cu (II) catalysed reaction mechanism to form triphenyl pyridine from benzylamine (1 equiv.) and acetophenone (2 equiv.).

Development of synthetic method for formation of non-symmetric triphenyl pyridines

(a) Copper (II) triflate catalyzed triphenyl pyridine synthesis

As reaction mentioned in the **scheme 6** (Huang *et al* method [234]), synthetically yielded a symmetrical molecule (**2.3.76**), therefore a diverse set substituted phenyl containing reactants in their structures (4-nitro benzylamine, acetophenone and 3,4-dimethoxy acetophenones, as shown in **Scheme 7**) were tested in similar conditions. Multiple spots were seen on TLC where evidence for the desired compound (**2.3.86**, 16 % isolated) and side product of self-condensation product (**2.3.95**, 31% isolated) was found.



Scheme 7 Reaction used for investigation of synthesis of non-symmetrical triphenyl pyridine

(b) *Changes to the copper triflate catalyzed method*

Most of higher molecular weight substituted benzylamines and acetophenones are solids, To achieve proper mixing, it was necessary to investigate a range of solvents for the reagents reported by Huang *et al.* During this study, the formation of the self-condensed product was also found. However, most of aprotic polar solvents showed better efficacy for these reactions, with the use of DMF providing the improved yields as compared to the other solvents (**2.3.86**, 30% isolated; **2.3.95** 41% isolated). non-polar (toluene) and polar protic solvents (H₂O and MeOH) showed mild progress of reaction and the TLC plate showed evidence for mixtures with trailing spots as well as unreacted reagents were also found. Also, while carrying out the test reactions, it was observed that formation of self-condensation product is somewhat dependent on prolonged heating at high temperature (Scheme 7). Also, the yields of symmetric compounds were found higher as compared to their desired non-symmetric triphenyl pyridine analogues.

(c) *Optimisation of order of addition of reactants to improve the synthesis of non-symmetrical triphenyl pyridines*

In order to improve the non-symmetric triphenyl pyridine synthesis and reduce the formation of self-condensed products, the order for addition of these components was changed, as shown in **Scheme 7**. Thus, for example, 4-nitro-benzylamine was first added to a three necked 25 mL round bottom flask, which contained copper triflate (Cu(OTf)₂) in DMF and the mixture was heated at reflux for 10 mins under an oxygen atmosphere, as shown in **Scheme 7**. This was followed by slow addition of acetophenone (drop by drop), over about 5 mins, and this was followed by addition of 3,4-dimethoxy acetophenone and the mixture was stirred for a couple of hours. Interestingly, the severity of multiple spotting on the TLC plate was found reduced compared to before, while the desired compound (**2.3.86**) was attained in 32% yield along with self-condensed product (**2.3.95**, 11% isolated). While the yield was reduced, the selectivity for **2.3.86** was

improved for reaction. However, the overall conversion and yield decreased which could be reasonably possible as the heteroaromatic nitrogen atom in these triphenyl pyridines usually comes from *in-situ* generated ammonia (from benzylamine self-condensation and ammonolysis), which could be lost during the sequential addition of the solid reactants through progress of reaction and this was considered in the improvement of the reaction.

(d) Ammonification of reaction

In this case, similar addition of reactants to the reaction was done as outlined in the previous paragraph. However, after 20 mins of heating at reflux, various sources of ammonia were tested at 1.1 equiv. (NH_4Cl , NH_4OH , NH_3 in MeOH (also in 2.0 equiv), NH_4OAc) and the conversion and yields in most of these reactions were found significantly improved with higher yields of both desired product (**2.3.86**), along with self-condensed product. The use of NH_3 in MeOH (2 equiv.) showed the highest conversion rate (yielded 76% **2.3.86**), and therefore this was selected as the ammonia source for further reactions.

(e) Investigating of new catalyst for synthesis of non-symmetrical triphenyl pyridines

As in all these reactions reported above, the symmetrical self-condensed product was found in ample amounts (~ 5-30%), therefore efforts were made to evaluate other possible catalysts. As, previous work shows that copper-oxygen catalytic system could be useful to oxidize a system containing benzylamine (1 equiv.) and acetophenone (2 equiv.) to form triphenyl pyridine. Therefore, I preferred to investigate salts of copper with oxygen as oxidant and, also in parallel I tried various solvents with two acetophenone derivatives (1 equiv. each) along with various benzylamines (1 equiv.): copper catalysts (CuI (10, 20, 40 mol %), CuCl_2 (10-20 mol %), CuBr_2 (20 mol%), Cu_2O (10, 20 mol %), 20 mol % of $\text{Cu}(\text{OAc})_2$, $\text{Fe}(\text{OAc})_2$, $\text{Ag}(\text{OAc})_2$) in aprotic polar solvents (DMSO, DMF, THF, MeCN) as shown in **Table 9**. Most of the catalysts behaved similarly to copper (II) triflate except copper bromide and copper iodide, where in the latter case the self-condensed product formation was highly suppressed. Also, copper iodide has shown better results for non-symmetrical triphenyl pyridines synthesis (e.g. **2.3.86**, 76%) as well as for symmetrical triphenyl pyridines (**2.3.4**, 91%). A list of compounds formed by the investigated route, shown in **Figure 97**.

Table 9.A Repeating the previous methods for symmetrical triphenyl pyridine synthesis.

Catalyst	mol %	Reflux time (hours)	Oxidant	Ammonia source	Solvent	Yield (%)
I ₂ ^f	1.0 mol%	12	Air	<i>in-situ</i>	Neat	61 ^{a,j} (reported yield 93%)[232]
HOTf ^e	5 mol%	10	Air	<i>in-situ</i>	Neat	38 ^{a,j} (reported yield 87%)[233]
Cu(OTf) ₂ ^f	10 mol%	20 (100 °C)	Air	<i>in-situ</i>	Neat	68 ^{a,j} (reported yield 91%) [234]
FeBr ₂ ^f	10 mol%	10 (110 °C)	Air	<i>in-situ</i>	Neat	47 ^{a,j} (Reported yield 93%)[231]
Cu(OTf) ₂ ^m	10 mol%	14	O ₂ -ballon	<i>in-situ</i>	Neat	41 ^{a,l} [234]

Table 9.B Investigation of new reaction conditions for non-symmetric triphenyl pyridine synthesis as shown in scheme 7

Catalyst	mol %	Reflux time (hours)	Oxidant	Ammonia source	Solvent	Yield (%)
Cu(OTf) ₂ ^k	10 mol%	14	O ₂ -ballon	<i>in-situ</i>	Neat	16 ^a , 31 ^g
Cu(OTf) ₂ ^k	10 mol%	12	O ₂ -ballon	<i>in-situ</i>	CH ₃ CN	21 ^a , 38 ^g
Cu(OTf) ₂ ^k	10 mol%	8	O ₂ -ballon	<i>in-situ</i>	Toluene	11 ^a , 26 ^g
Cu(OTf) ₂ ^k	10 mol%	8	O ₂ -ballon	<i>in-situ</i>	DMF	30 ^a , 41 ^g
Cu(OTf) ₂ ^k	10 mol%	6	O ₂ -ballon	<i>in-situ</i>	H ₂ O	Unidentified mixtures
Cu(OTf) ₂ ^k	10 mol%	4	O ₂ -ballon	<i>in-situ</i>	MeOH	Trailing, Not separated
Cu(OTf) ₂ ^k	10 mol%	10	O ₂ -ballon	<i>in-situ</i>	DMF	32 ^a , 11 ^g
Cu(OTf) ₂ ^k	10 mol%	12	O ₂ -ballon	NH ₄ Cl	DMF	45 ^a , 29 ^g
Cu(OTf) ₂ ^k	10 mol%	10	O ₂ -ballon	NH ₄ OH	DMF	32 ^a , 26 ^g
Cu(OTf) ₂ ^k	10 mol%	6	O ₂ -ballon	NH ₃ (1.1 eq)	DMF	31 ^{a, b}
Cu(OTf) ₂ ^k	10 mol%	6	O ₂ -ballon	NH ₄ OAc	DMF	22 ^{a, b}
Cu(OTf) ₂ ^k	10 mol%	10	O ₂ -ballon	NH ₃ (2 eq)	DMF	49 ^a , 27 ^g
CuO ^k	10 mol %	12	O ₂ -ballon	NH ₃ (2 eq)	CH ₃ CN	17 ^{a, g}
CuO ^k	10 mol %	10	O ₂ -ballon	NH ₃ (2 eq)	DMF	29 ^{a, g}
CuO ^k	20 mol %	8	O ₂ -ballon	NH ₃ (2 eq)	DMF	35 ^{a, g}
CuO ^k	20 mol %	12	O ₂ -ballon	NH ₃ (2 eq)	THF	Mixture
CuCl ₂ ^k	10 mol %	6	O ₂ -ballon	NH ₃ (2 eq)	CH ₃ CN	traces
CuCl ₂ ^k	20 mol %	10	O ₂ -ballon	NH ₃ (2 eq)	DMF	41 ^a , 21 ^g
CuBr ₂ ^k	20 mol %	8	O ₂ -ballon	NH ₃ (2 eq)	DMF	32 ^a , 22 ^g
CuBr ₂ ^k	20 mol %	10	O ₂ -ballon	NH ₃ (2 eq)	CH ₃ CN	45 ^{a, b}
CuBr ₂ ^k	20 mol %	12	O ₂ -ballon	NH ₃ (2 eq)	THF	36 ^{a, b}
CuI ^k	10 mol %	12	O ₂ -ballon	NH ₃ (2 eq)	CH ₃ CN	41 ^{a, b}
CuI ^k	20 mol %	10	O ₂ -ballon	NH ₃ (2 eq)	CH ₃ CN	54 ^{a, b}
CuI ^k	20 mol %	5	O ₂ -ballon	NH ₃ (2 eq)	DMSO	Mixture ^b
CuI ^k	20 mol %	6	O ₂ -ballon	NH ₃ (2 eq)	DMF	76 ^a
CuI ^k	20 mol %	8	O ₂ -ballon	NH ₃ (2 eq)	DMF	13 ^{a, i}
CuI ^k	20 mol %	6	O ₂ -ballon	NH ₃ (1.1)	DMF	62 ^a
CuI ^k	10 mol %	8	O ₂ -ballon	NH ₃ (2 eq)	DMF	51 ^a
CuI ^k	20 mol %	12 ^d	O ₂ -ballon	NH ₃ (2 eq)	DMF	traces
CuI ^k	40 mol %	6	O ₂ -ballon	NH ₃ (2 eq)	DMF	67 ^a
CuI ^k	10 mol %	10	O ₂ -ballon	NH ₃ (2 eq)	THF	Traces
Cu(OAc) ₂ ^k	20 mol %	6	O ₂ -ballon	NH ₃ (2 eq)	DMF	40 ^a , 20 ^g
Fe(OAc) ₂ ^k	20 mol %	10	O ₂ -ballon	NH ₃ (2 eq)	DMF	27 ^a , 24 ^g

AgOAc ^k	20 mol %	8	O ₂ -ballon	NH ₃ (2 eq)	DMF	25 ^{a, b}
<i>For symmetrical molecule</i>						
CuI ^f	20 mol %	5 ^f	O ₂ -ballon	NH ₃ (2 eq)	DMF	91 ^{a, j}

For Table 9.A & B: ^a Isolated yields; ^b visible on either on TLC or MS, but was not isolated; ^c oxygen ballon; ^d Sonification (no refluxing was performed); ^e acetophenone: benzylamine: 1: 0.75 ratio; ^f acetophenone (2 equiv.) with benzylamine (1 equiv.); ^g self-condensation product (**2.3.95**); ^h Ar-environment; ⁱ uncharacterised multi spots; ^j synthesis of **2.3.4**; ^k acetophenone (1 equiv.), 4-Nitrobenzylamine (1.1 equiv.) & 3,4-Dimethoxy acetophenone (1 equiv.), yielded **2.3.86**; ^l **2.3.76** was the product; ^m reactants used as from Scheme 7.

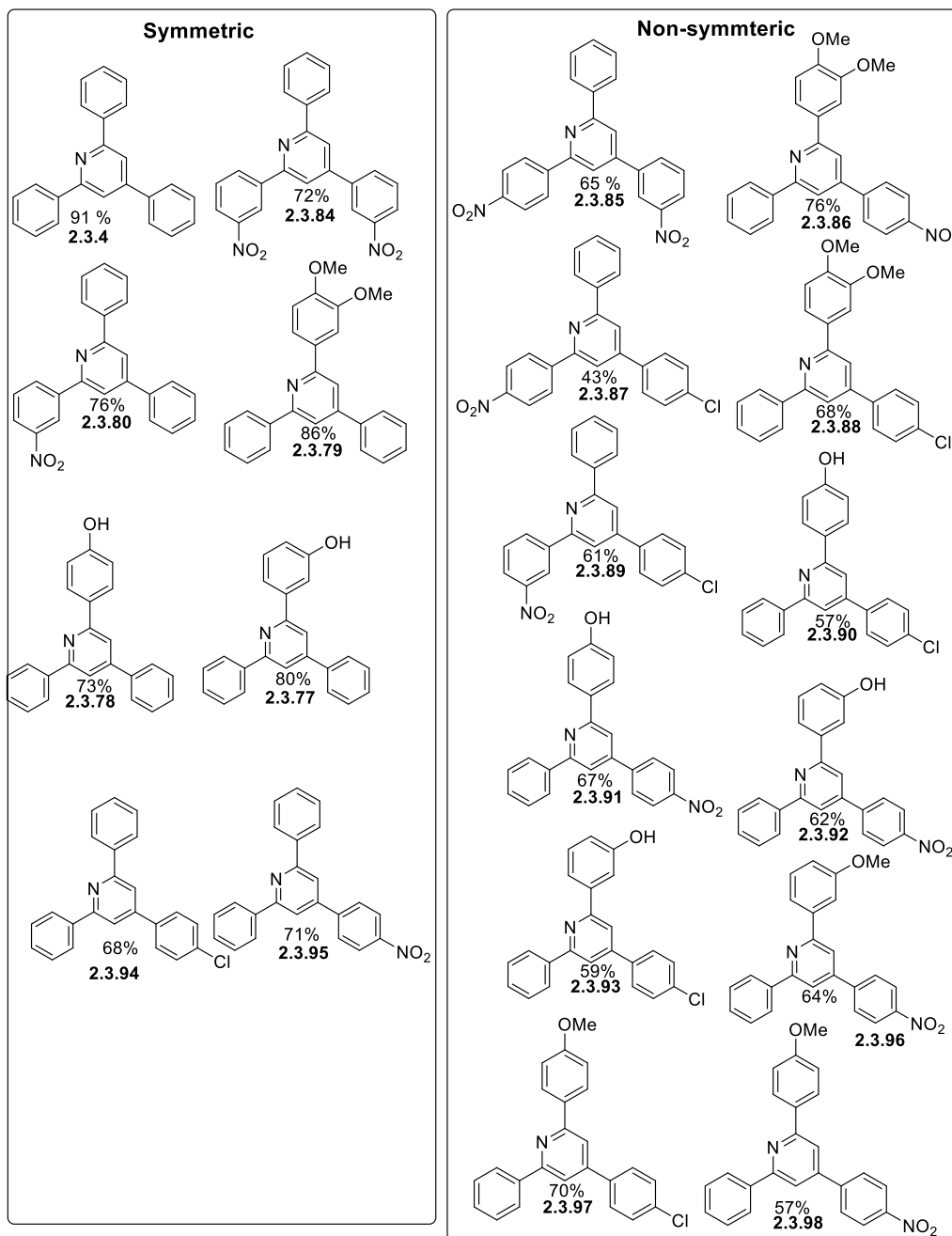


Figure 97 Scope of new investigated copper iodide assisted method in synthesis of symmetrical as well as non-symmetrical triphenyl pyridine.

The mechanism is likely to be similar to that proposed for FeBr₃ catalysed triphenyl pyridine synthesis [231]. The first step is copper catalysed oxidative self-condensation of primary amine (**Figure 98**) [238]. Later, copper Iodide promoted enol formation led to nucleophile addition at the imine carbon, which then undergo oxidative dehydrogenation. A second molecule of acetophenone alters the conformation of molecule into a tetrahedral intermediate, which condenses with ammonia to form a dihydropyridine derivative which later aromatises to the triphenyl pyridine.

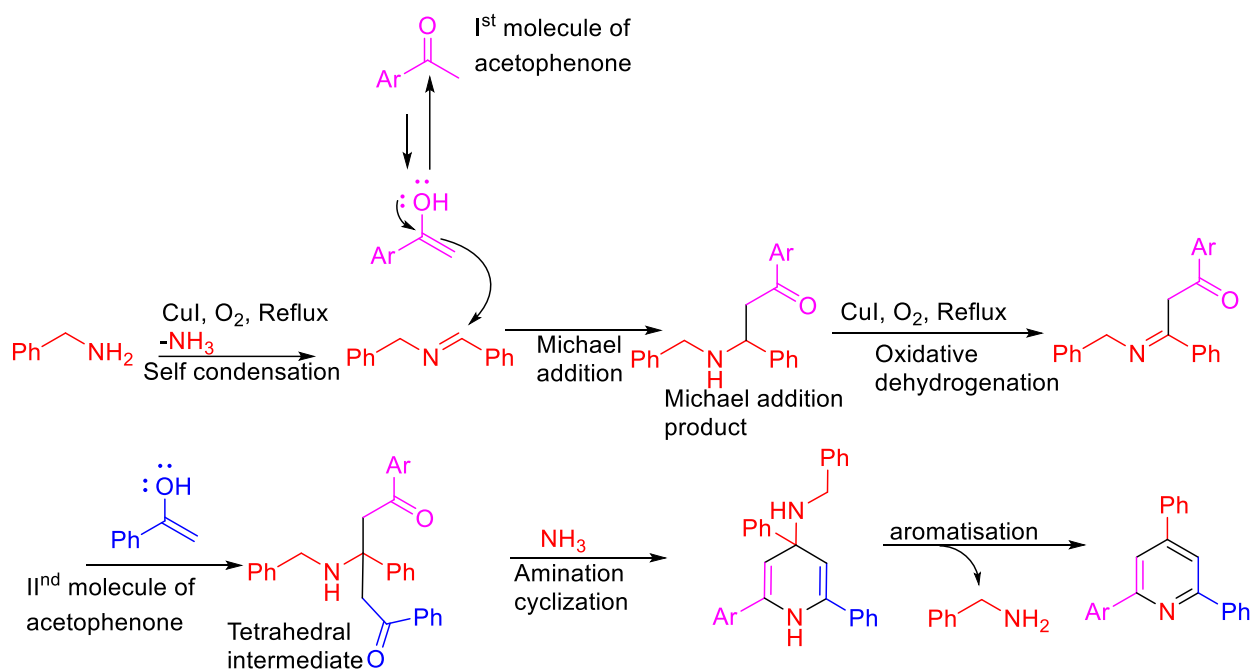


Figure 98 Proposed mechanism of formation of triphenyl pyridine.

Previous studies characterised triphenyl pyridines by ¹H/¹³C NMR but as in most cases, they failed to assign the signals to individual carbons or protons and in few cases, either I found missing protons or carbons signals, especially quaternary carbon signals not reported earlier. In cases, where I found proper signal assignment for a triphenyl pyridine, then I cited that paper after doing the assignment myself and these are reported in the experimental section of this thesis. However, for other compounds 1D-2D NMR spectroscopy was used where carbon signals were assigned after recording 13C/C-APT, ¹H and other NMR experiments. Special attention was given to the aromatic region carbon signals, as the proton NMR region was severely crowded with overlapping aromatic signals. The first representative compound selected for characterisation was **2.3.93**.

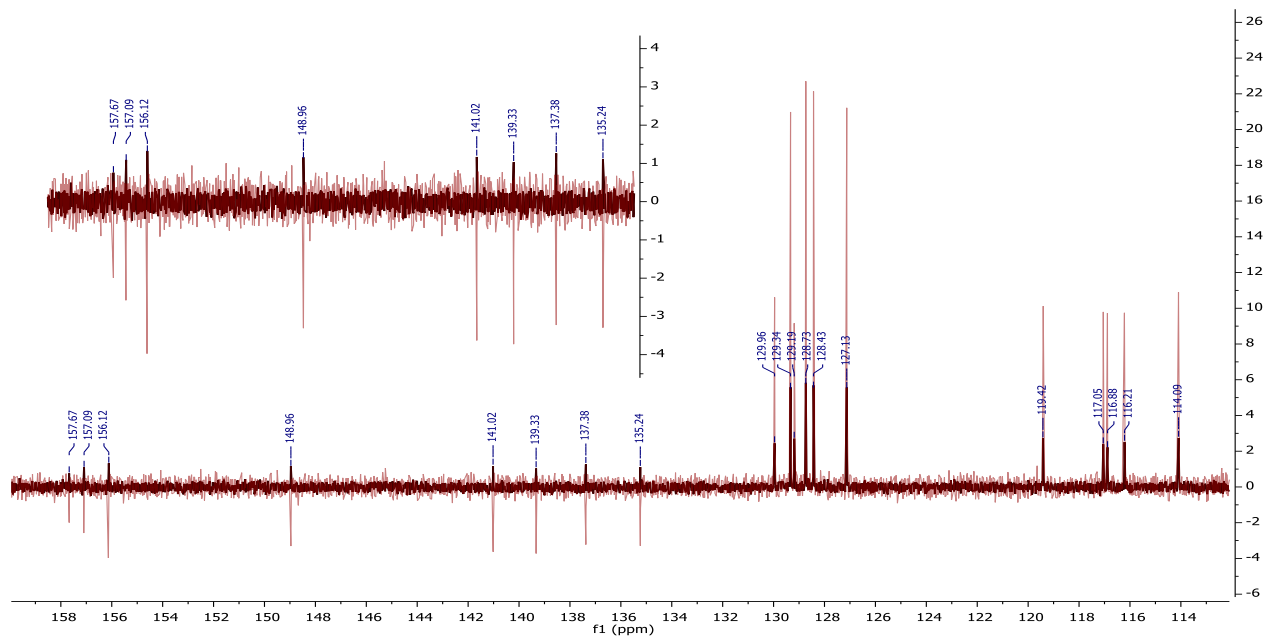


Figure 99 ^{13}C spectra where C-APT showing the quaternary carbons (for 8 carbons) of compound **2.3.93**

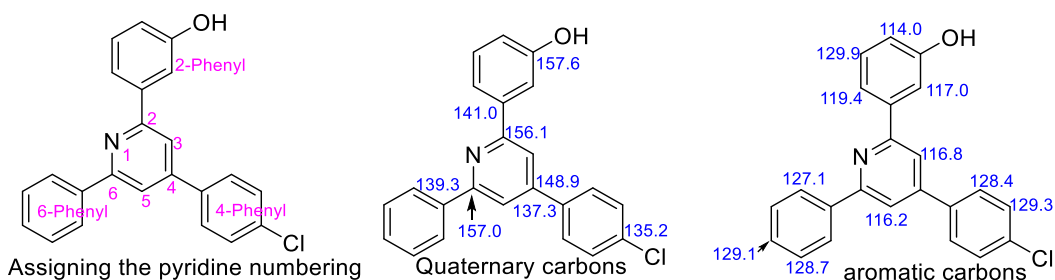
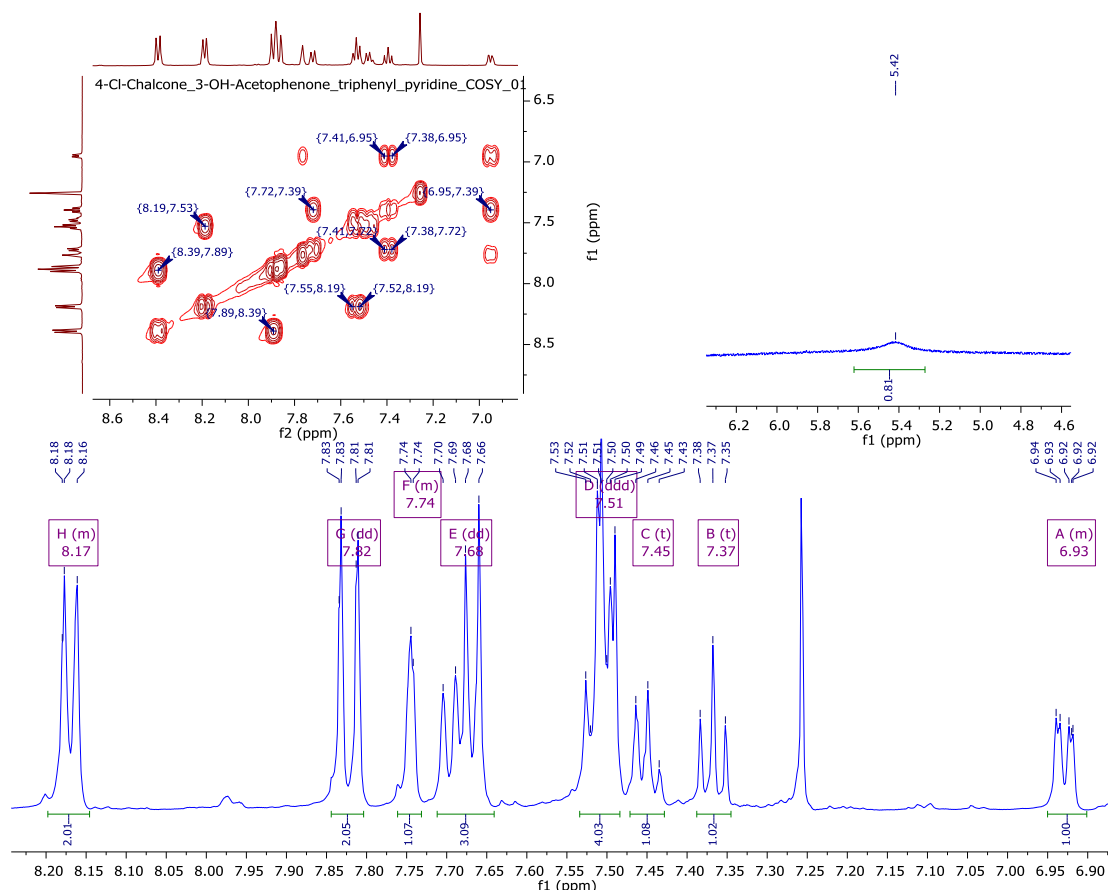


Figure 100 (a) assigning pyridine numbering; (b) assigning quaternary carbons (c) assigning aromatic (-CH-) signals of compound **2.3.93**.

Through ^{13}C and C-APT NMR it could be easy to observe eight quaternary carbons (marked down in C-APT) and 11 (-CH-, down) aromatic signals, where there were four signals of higher intensity in the aromatic region belonging to 2 aromatic CH carbons.



- Protons in region (δ 8.21 - 8.14 ppm) belonging to H-2 & H-6 of 6-phenyl ring. Both, H-3 and H-5 of pyridine aromatic protons are assigned to signals at δ 7.83 and 7.81 ppm.
- Region (δ 7.76 - 7.73 ppm) contains signals for protons: H-2 and H-6 of the 4-Phenyl substituent as well as one proton of the 2-phenyl substituent.
- gCOSY showed that 4 protons in region (δ 7.54 - 7.49 ppm) can be assigned to (H-3 & H-5) of the 6-phenyl substituent and H-3 & H-5 of the 4-phenyl substituent.
- While, signal at δ 7.46 ppm belongs to H-5 of 6-phenyl and δ 7.37 ppm belongs to H-5 of the 2-phenyl group.
- Also, the protons at δ 6.96 - 6.90 ppm are assigned to H-4 of the 2-phenyl substituent

Figure 101 ^1H and gCOSY spectra for of compound **2.3.93**: Interpretation of spectra was found in the agreement with earlier reported data for this compound [206].

The triphenyl pyridines synthesised contain various substituents which alter the electron density throughout the molecule. Therefore, various representative molecules were selected for detailed NMR analysis. The assignments for these are shown in **Figure 102** for compound **2.3.86**, **Figure 103** for compound **2.3.92** and **Figure 104** and **Figure 5** for compound **2.3.87**.

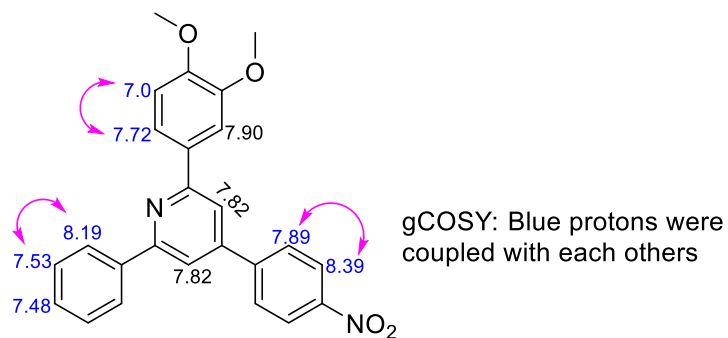


Figure 102 ¹H and gCOSY NMR based assignment of proton on 2.3.86

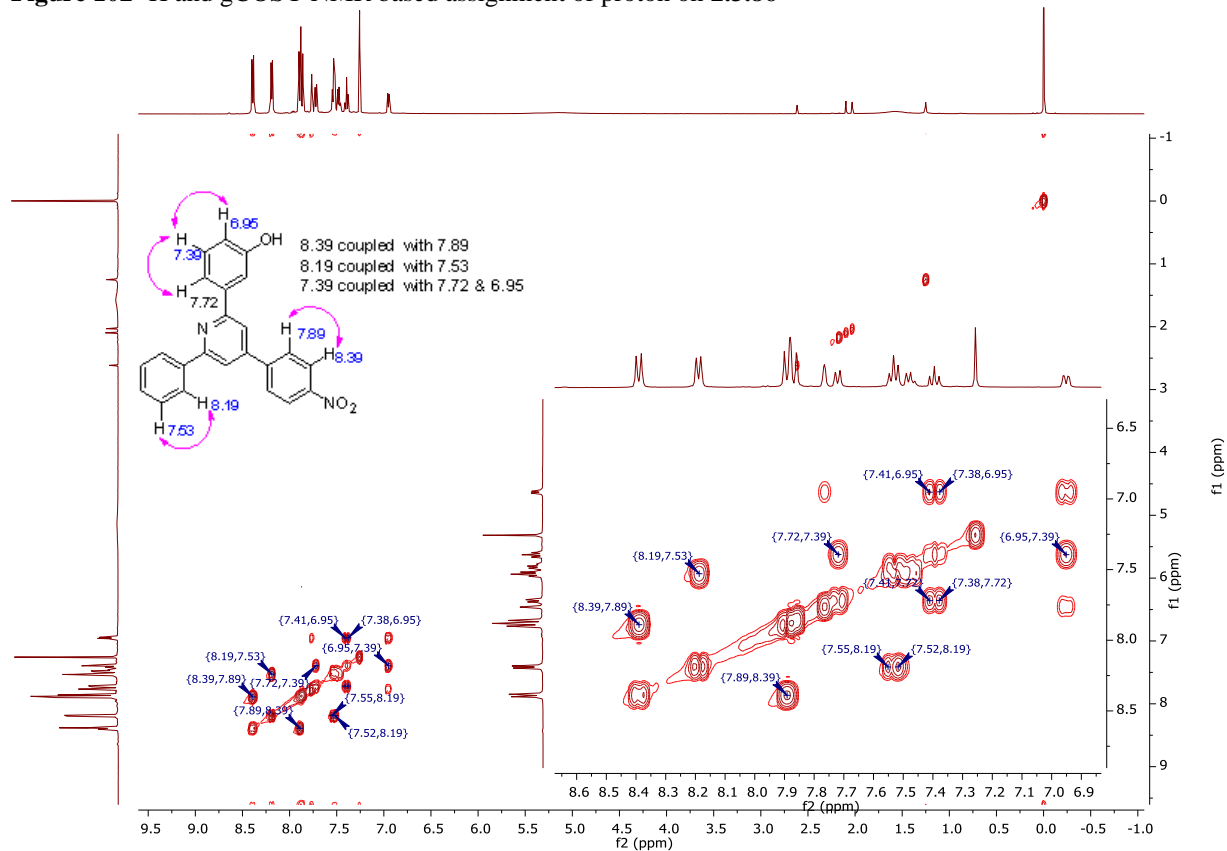


Figure 103 ¹H and gCOSY NMR based assignment of proton on 2.3.92

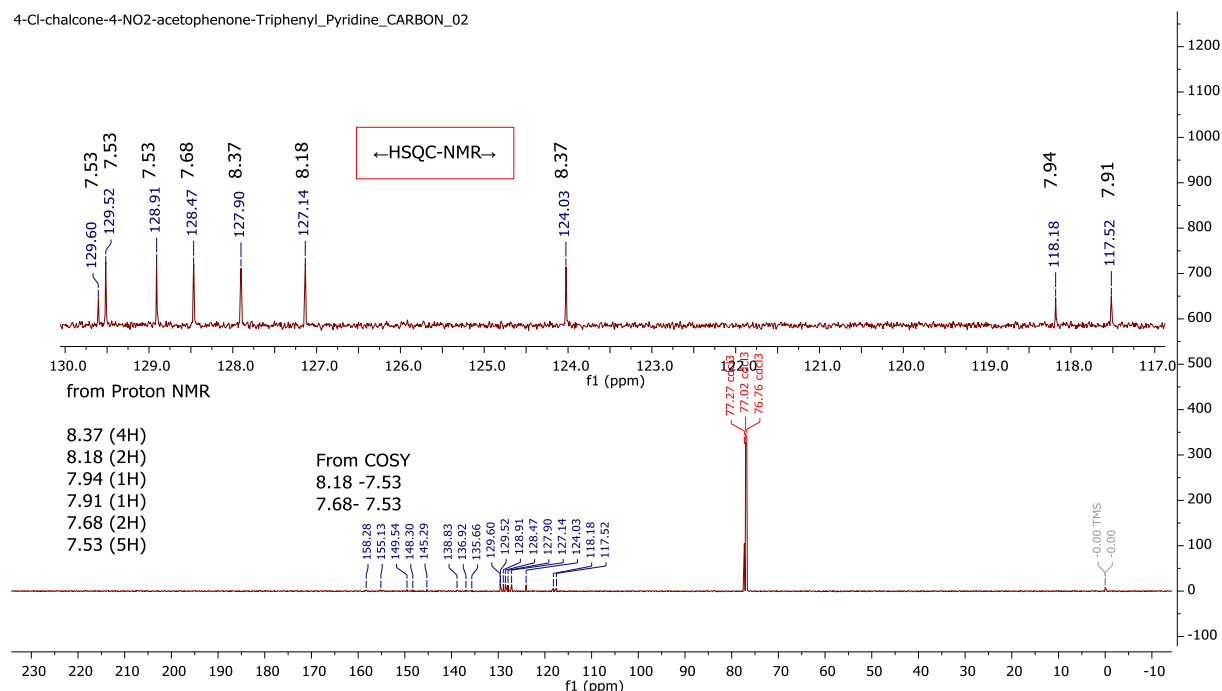


Figure 104 elucidating the information related to the chemical shift attained from ¹H, gCOSY, ¹³C & HSQC-NMR studies of **2.3.87**

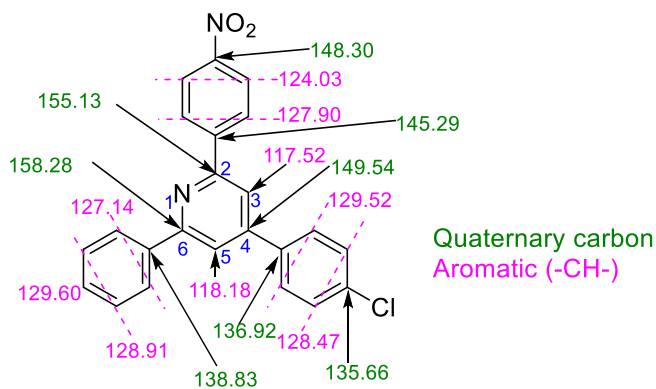
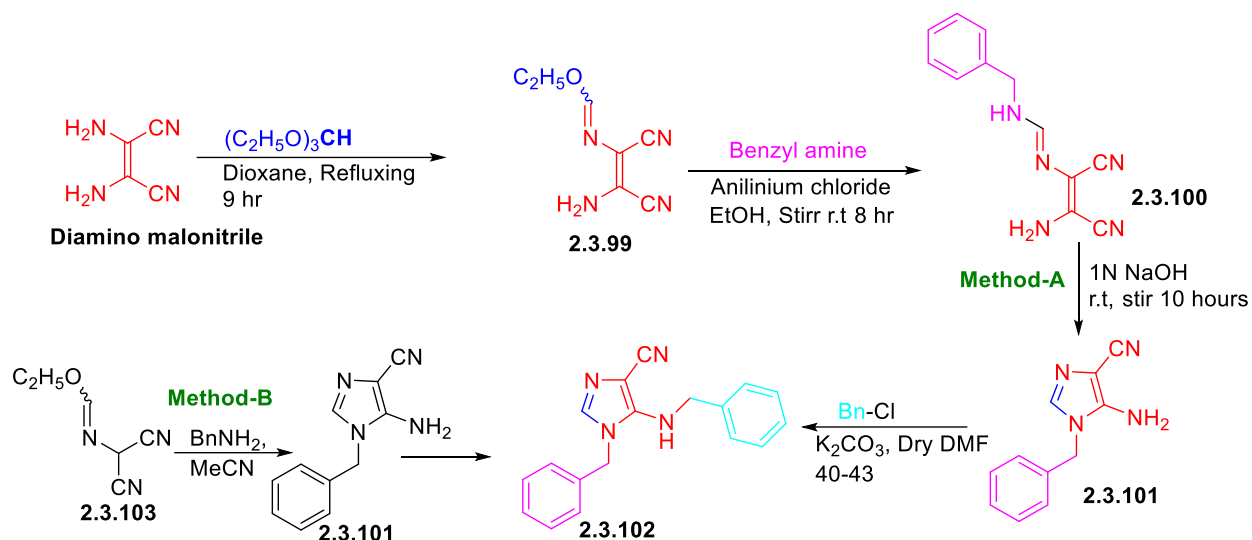


Figure 105 Assignment of ¹³C signals of **2.3.87** (quaternary as green, while aromatic as magenta)

Synthesis of Imidazoles

There are methods reported for synthesis of 5-amino-1-benzyl-1H-imidazole-4-carbonitrile (**2.3.101**), mainly by routes shown in Scheme 6: Method-A [239] or Method-B [240].



Scheme 6 Synthetic routes for formation of **2.3.102**

The molecular architecture of a target compound (**2.3.102**) was characterised using ^{13}C and C-APT, where quaternary and aromatic carbons are shown in red colour and benzylic proton were coloured in blue in **Figure 106**.

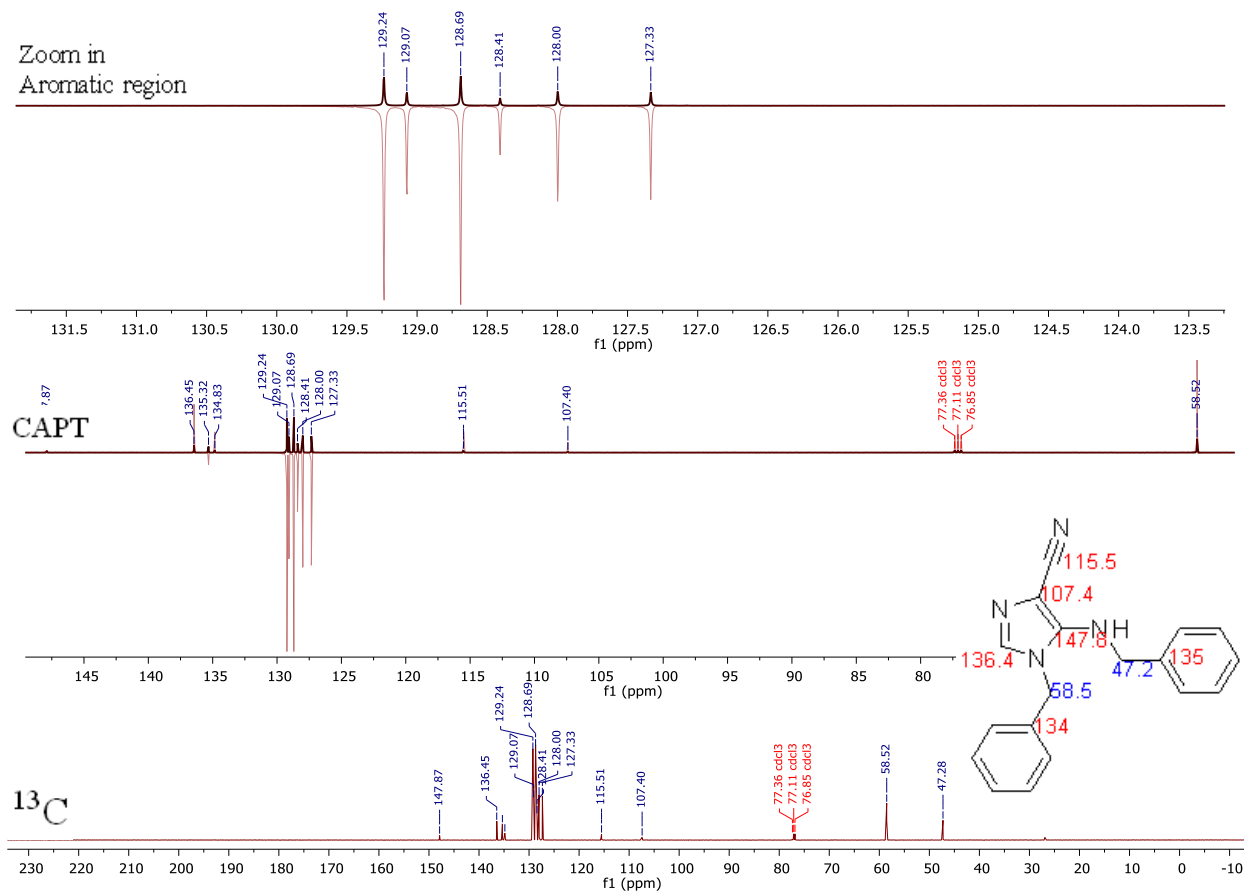
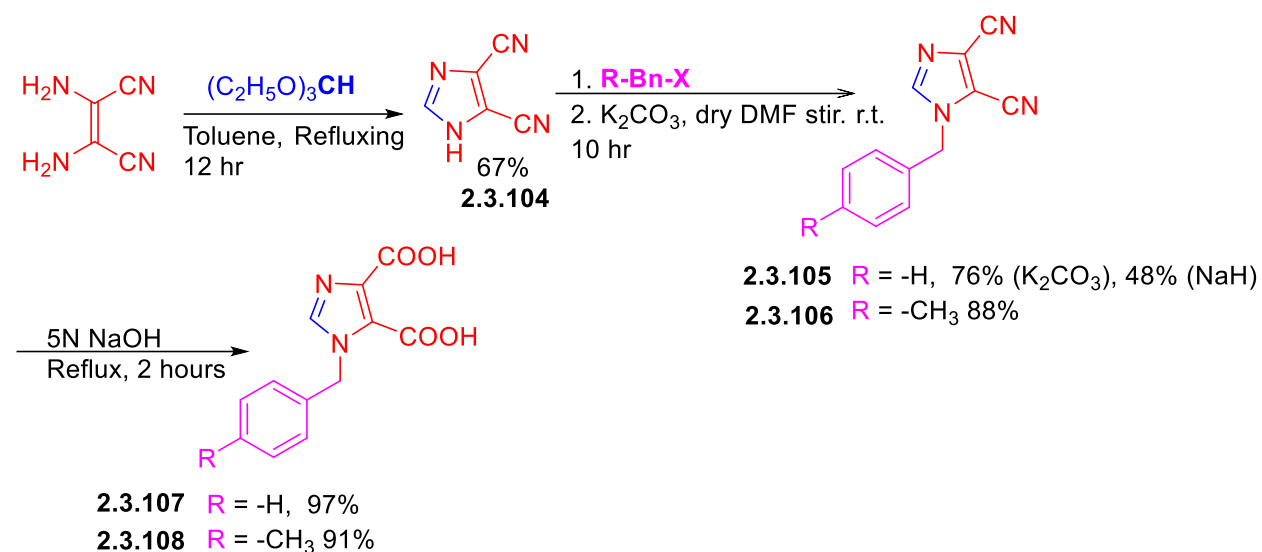


Figure 106 ^{13}C and C-APT NMR of **2.3.102**

In order to enhance the SAR of these chemotypes, similar imidazole structures were prepared without benzyl substitution (Scheme 7), where a dicarboxylic system was chosen in order to improve the interaction with a positively charged arginine amino acid side chain in the binding site of Bcl-2 proteins (in MCl-1, it is located as Arg263).

Although, sodium hydride was also reported for benzylation of imidazoles in literature but in my case, I was only able to achieve 48 % as isolated yield with this reagent. I found use of K_2CO_3 to be superior, which gave over 76% yield in the formation of both **2.3.105** & **2.3.106**. Later these compounds (**2.3.105** & **2.3.106**) were heated at reflux with 5N NaOH to yield (**2.3.1078** & **2.3.108**) [241]. During normal phase column the imidazole dicarboxylic acid could not be purified by column chromatography and crystallization was instead preferred using lukewarm EtOH. The purity of these compounds were evaluated using quantitative NMR [242] where it was found to be 93.4% was achieved for compound (**2.3.108**).



Scheme 7 Synthesis of *N*-benzylated imidazole dicarboxylic acids (**2.3.107** & **2.3.108**)

Quantitative NMR (qNMR) to determine the purity of imidazole dicarboxylic acid

To evaluate the purity of the imidazole dicarboxylic acid (*t*), a compound (the 4-methoxybenzyl derivative) was selected. Dimethyl sulfone (DMS) was used an internal standard (*ic*) as reference. The T_1 relaxation times of the nuclei in the sample were not known, although they can be quickly estimated with an inversion recovery experiment [242].

For calculation, I used the previous published method [242].

Here DMS 4.54 mg \pm 0.0228 was weighed out

My compound was weighed out 3.15 mg \pm 0.0405

The % purity was calculated using the following formula:

$$\% \text{ Purity} = \frac{N_{ic} \times INT_t \times MW_t \times M_{ic} \times P_{ic}}{N_t \times INT_{ic} \times MW_{ic} \times M_s}$$

where

N_{ic} = Number of protons that give rise to Internal calibrate

N_t = Number of protons of target analyte

INT_t = Area (integral) of the target analyte

INT_{ic} = Area (integral) of the internal calibrant

MW_t = Molecular weight of the target analyte

MW_{ic} = Molecular weight of the target analyte

M_{ic} = Weight of the internal calibrant

M_s = Weight of Sample

P_{ic} = Purity of internal standard (99.96 %)

$$\% \text{ Purity} = \frac{6 \times 17601.28 \times 276.244 \times 4.54}{2 \times 236569.43 \times 94.13 \times 3.15} \times 99.96$$

$$\% \text{ Purity} = 93.4\%$$

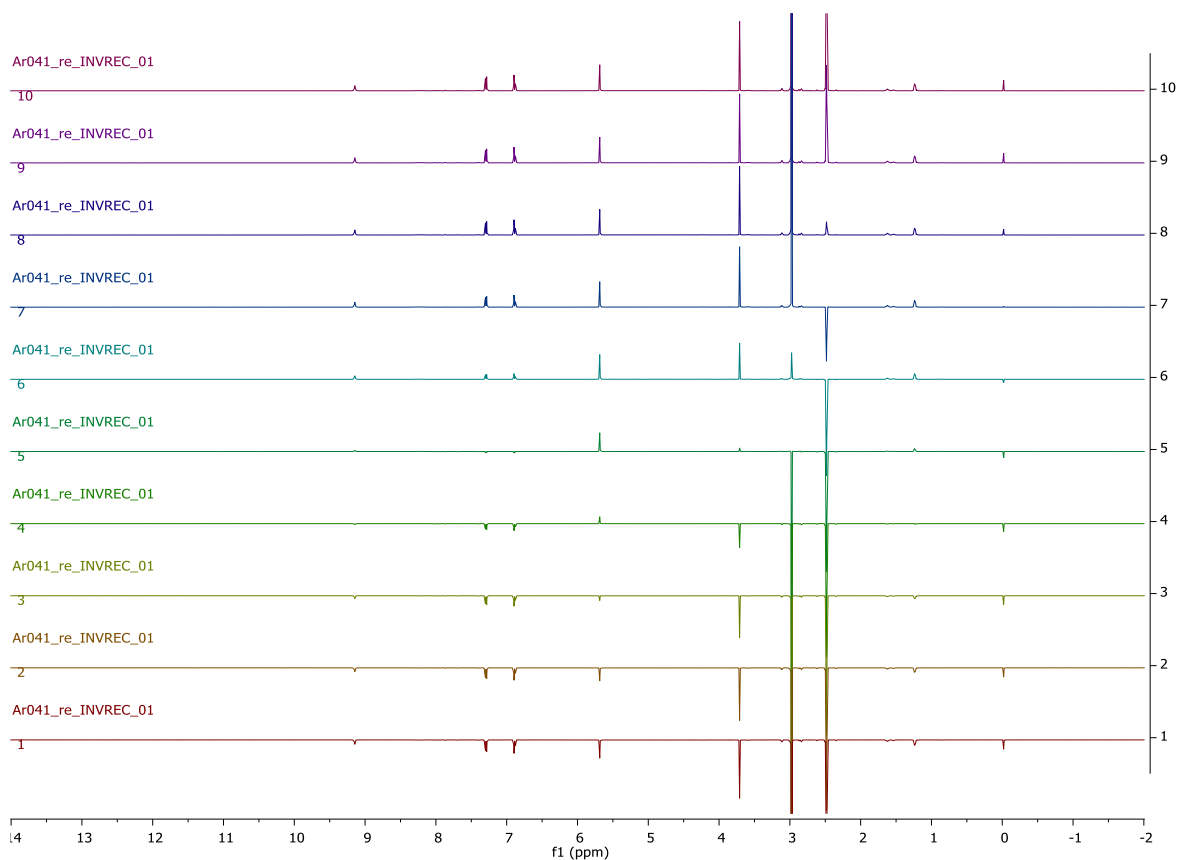
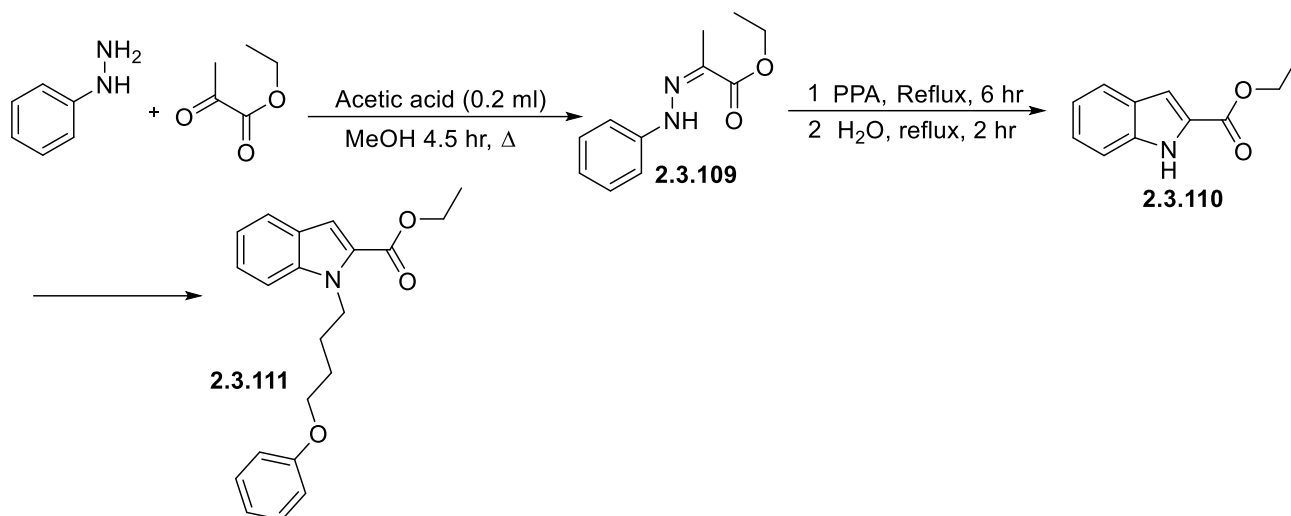


Figure 107 Inversion recovery NMR spectra for experiment to measure % purity of **2.3.108**

Synthesis of indole derivatives

From *objective 2.1*, it was clear that indole is a highly exploited heterocyclic framework for targeting the Bcl-2 family proteins, to induce apoptosis in cancer cells. Also, indole-2-carboxylic acids have already shown promising results in inhibition of Mcl-1 dependent cancer cells [87]. Therefore, I have utilised Fischer indole synthesis (as shown in **Figure 108**) to form an indole 2-carboxylate scaffold (**2.3.110**) which was later *N*-alkylated by using phenoxybutyl bromide to form **2.3.111**, as shown in **Scheme 8**.



Scheme 8 Synthesis of *N*-(1-phenoxybutyl)-indole 2-carboxylic acid, ethyl ester

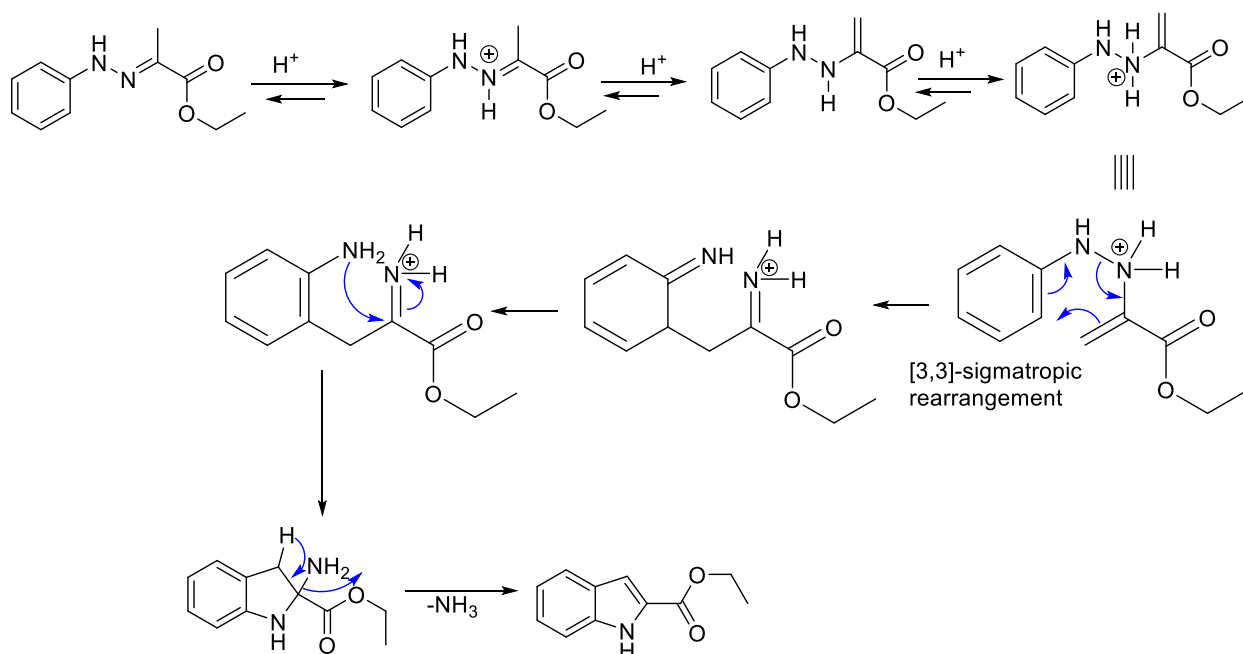
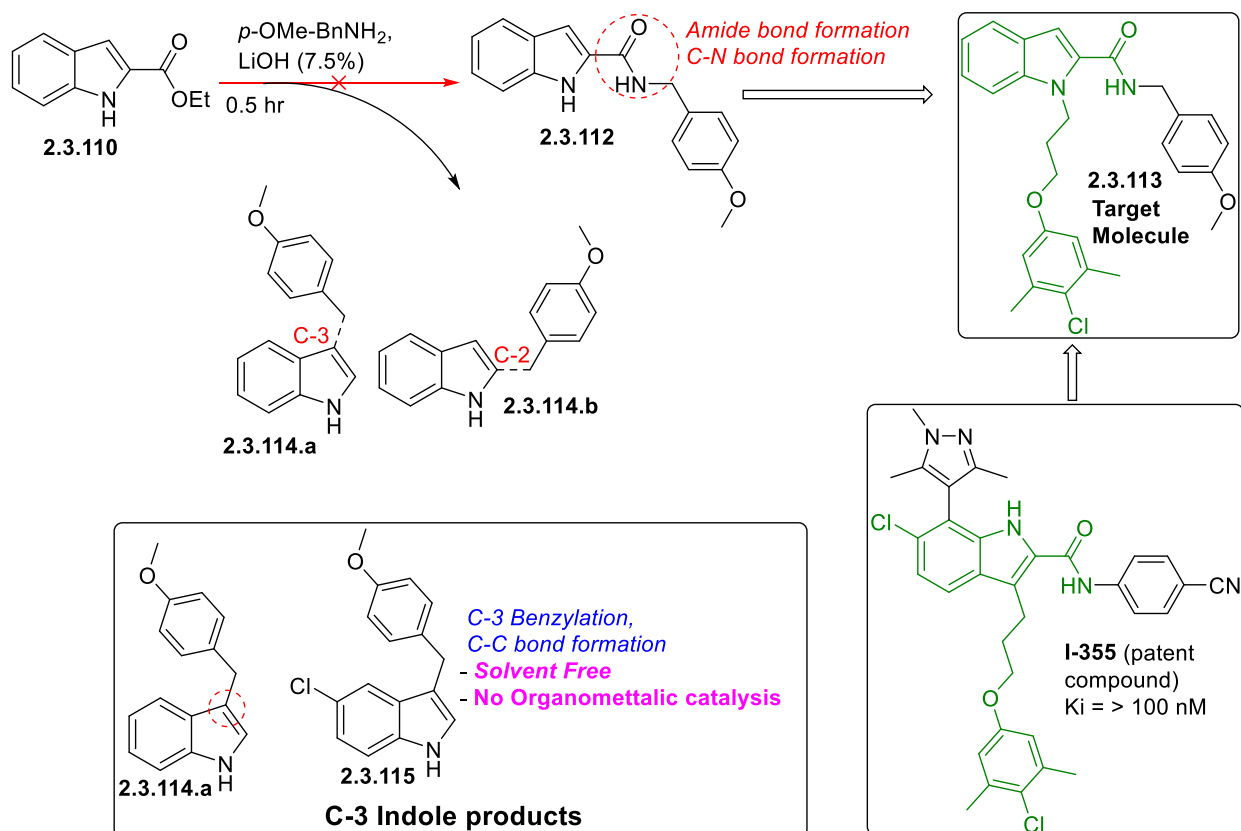


Figure 108 Mechanism of indole carboxylic acid, ethyl ester formation from phenyl hydrazone (Fischer indole synthesis).

Unexpected formation of benzylated indole

AbbVie pharmaceuticals reported that **I-355** was an inhibitor of Mcl-1, with a K_i value of 100 nM for inhibition of Mcl-1 protein. Whereas, I proposed a simpler analogue of **I-355**, i.e. **2.3.113** as a target molecule. Firstly, I tried amide bond formation by using ethyl 1H-indole-2-carboxylate ester (**2.3.110**) with benzylamine derivative, which was based on a green method reported by Miller *et al* [243] for converting an unactivated esters to amides using lithium hydroxide as a catalyst, as shown in **Scheme 9**.



Scheme 9 Unexpected C-3 benzylation

Surprisingly, I attained **2.3.114a**, as a result of formal C-3 benzylation of indole with concomitant loss of the carboxyethyl group, rather than expected amide bond formation (which would give **2.3.112**). NMR spectroscopic study and MS data suggested the presence of a benzyl substituent, at either C-2 or C-3 on indole ring, which was further supported by analysis of the differences observed in chemical shifts around the C-2 and C-3 position of indole ring, as follows:

(a) The proximity of benzylic protons ($-\text{CH}_2-$) in C-2 or C-3 to the NH- of the indole differs. The benzylic carbon may be expected to be more deshielded by the electronegative nitrogen atom if attached at C-2 rather than in C-3. Therefore, the benzylic carbon ($-\text{CH}_2-$) would be more downfield, as can be seen in **Table 10**.

(b) The chemical shift and coupling of the C-2 and C-3 signals in these benzylated products: In case of C-2 benzylation, C-2 signal will be quaternary and C-3 will be aromatic $-\text{CH}-$, while it will be opposite in case of C-3 benzylation, can be established from C-APT spectra as well as using HSQC and HMBC, as shown in **Figure 109**.

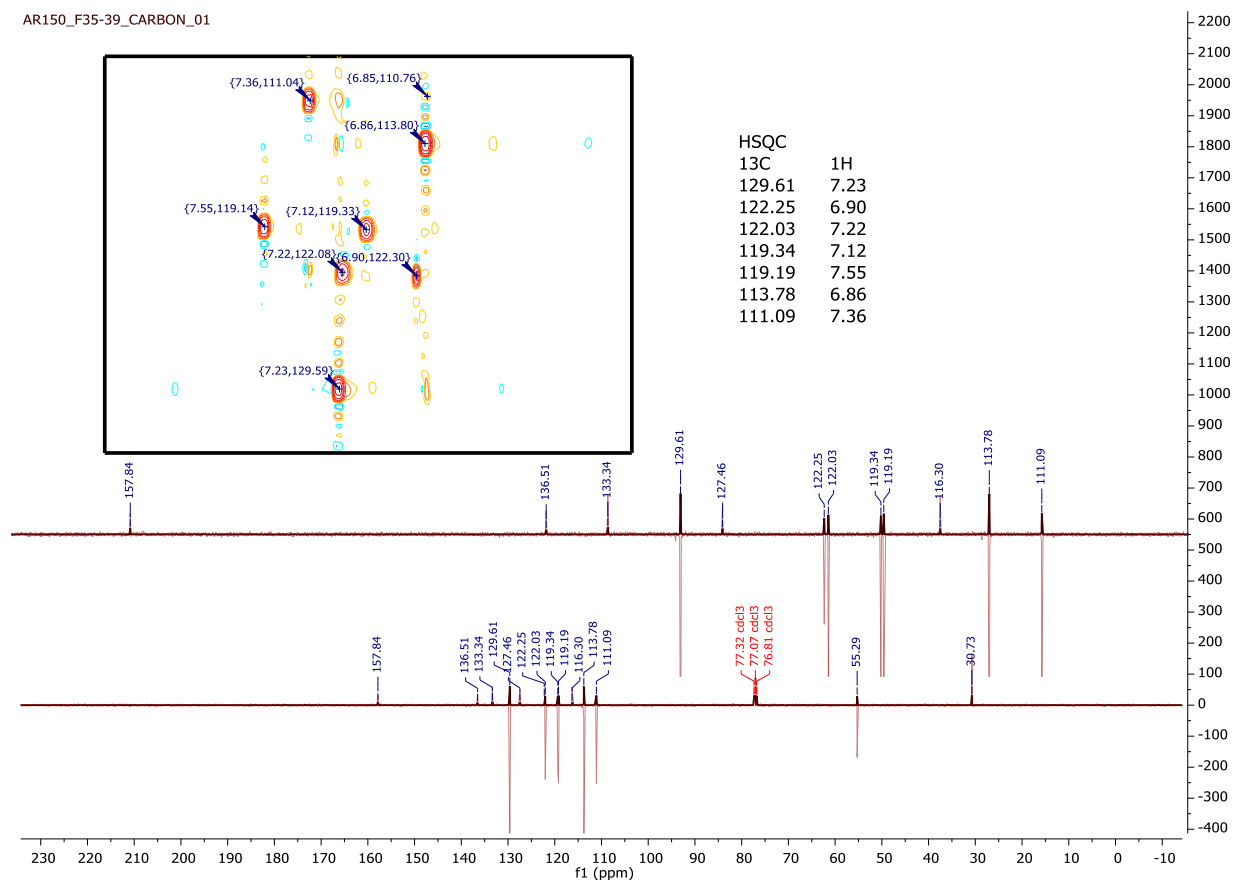
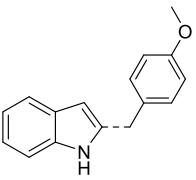
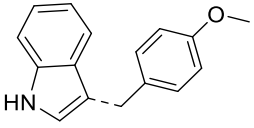


Figure 109 1D & 2D-NMR of **2.3.114**

From NMR data, the assigned ¹³C NMR spectra was compared with previously indoles (**2.3.114a** & **2.3.114b**) carbon NMR and tabulated in the **Table 10**. The data obtained indicated the product was **2.3.114a**

Table 10 C-2/C-3 benzylation of indole

Previous Reports of C-2/C-3 benzylation in Indole		Found	Inferences & outcomes	
C-2 Benzylation [244]	C-3 Benzylation [245, 246]	ppm		
				
158.6	158.2	157.8	157.84	Quaternary, Bn-C-4
138.5	136.8	136.5	136.51	Quaternary, Indole C-8
136.4	133.6	133.3	133.34	Quaternary, Bn-C-1
130.7	129.9 (2 x C)	129.6	129.61	Aromatic, Bn C-2 & C-6
130 (2 x C)	127.8	127.5	127.46	Quaternary, Indole C-9
128.9	122.5	122.2	122.25	Aromatic -CH-, Indole-C-2
121.4	122.4	122.0	122.03	Aromatic -CH-, Indole-C-6

120.1	119.7	119.3	119.34	Aromatic -CH-, Indole-C-5
119.9	119.5	119.2	119.19	Aromatic -CH-, Indole-C-4
114.3 (2 x C)	116.7	116.3	116.30	Quaternary, Indole C-3
110.6	114.1 (2 x C)	113.8 (2 x C)	113.78	Aromatic, Bn C-3 & C-5
101.0	111.4	111.1	111.09	Aromatic -CH-, Indole-C-7
55.5	55.6	55.3	55.29	-OCH ₃
34.0	31.0	30.7	30.72	-CH ₂ -Bn

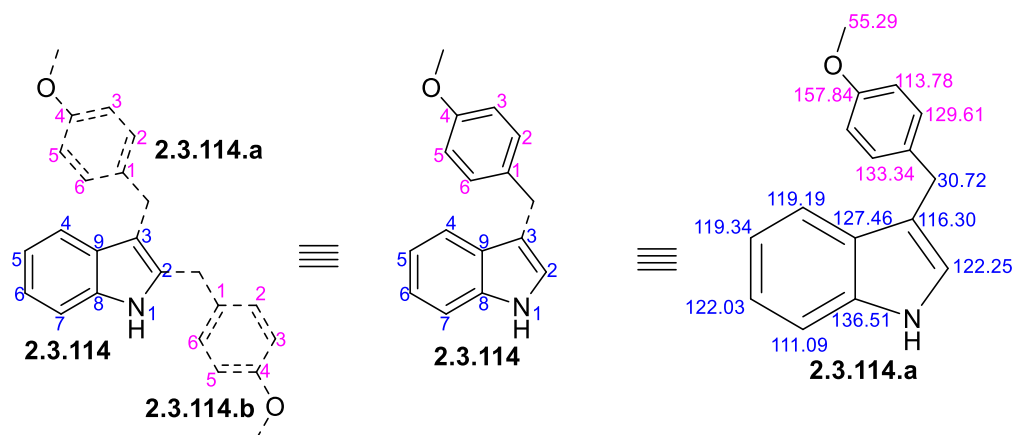
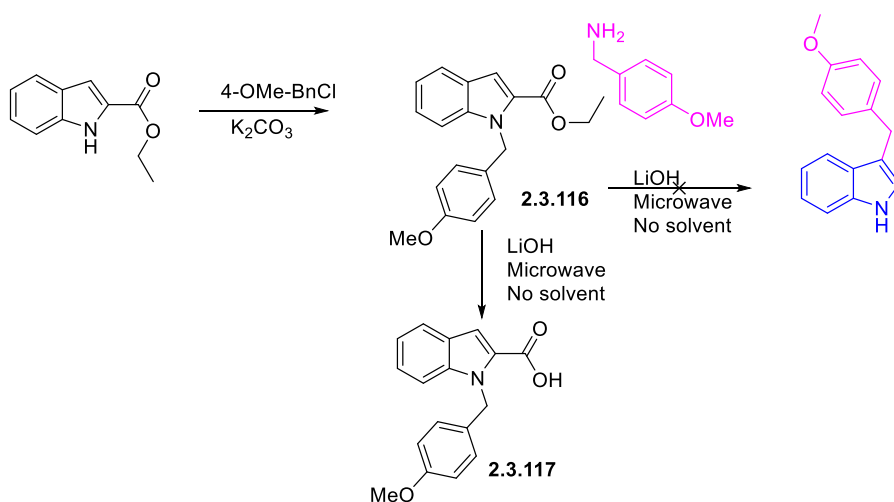


Figure 110 Conclusion from the assigned NMR and from previously available data.

To understand the unexpected benzylation, a few trials were attempted in order to rule out mechanistic possibilities. The first was to investigate whether N-benylation occurs first of all and whether migration of the benzyl group could occur from **2.3.116**, and decarboxylation from this potential precursor. However, **2.3.116** could not be converted to the observed compound (Scheme 10) but instead gave **2.3.117**, which did not undergo decarboxylation under the conditions



Scheme 10 Testing the Indole -NH- role in progression of unexpected C-3 benzylation.

2.3.3 Cytotoxicity of synthesized heterocycles

The chalcones showed moderate cytotoxicity towards the Mcl-1 dependent cell line investigated (H929 cell line). However, hydroxy chalcones were found comparatively more potent than their non-hydroxy equivalents. Similar observations were also seen with triphenyl pyridines where only hydroxy versions were more active (**2.3.77**, **2.3.78**, **2.3.90-2.3.93**, **2.3.97**) than non-hydroxylated versions. However, hydroxylated non-symmetric triphenyl pyridines were found slightly more potent than the non-hydroxylated symmetric ones (**2.3.90-2.3.93**, **2.3.97** versus **2.3.77**, **2.3.78**), which shows that significance of having hydroxyl substituents in the phenyl rings in order to attain greater potency towards the H929 cell line. Whereas, pyrazolines (**2.3.29**, **2.3.30**, **2.3.31**) were found more active when compared to their aromatic counterparts (**2.3.32**, **2.3.33**), which showed that rigidity in pyrazole structure reduces the cytotoxicity in H929 cells (pyrazoline **2.3.31** IC₅₀ = 70.43 μM versus pyrazole **2.3.32** IC₅₀ = not active). Surprisingly, N-substitution in pyrazoles improve their anticancer activity which improves as the length of carbon backbone increases, which could be translated as the length of carbon linker increases the accessibility of these phenyl rings to other adjacent hydrophobic pockets in the active site of the Bcl-2 family members (**2.3.44** (2-carbon length, 88.11 μM), **2.3.45** (3-carbon length, 75.39 μM), **2.3.46** (4-carbon length, 65.41 μM). However, both diphenyl pyridine derivatives were found more potent than pyrazolines, pyrazoles and their derivatives, which shows that free -NH₂ and -CN groups in **2.3.56** & **2.3.57** could have improved their molecular interaction through H-bond donor/acceptor interaction along with their physicochemical properties. A similar trend was also observed in imidazole, where free CN containing molecules shown similar moderate activities (**2.3.102**, **2.3.105**, **2.3.106**). Imidazole dicarboxylic acids **2.3.107** & **2.3.108** were found most potent among all the molecule chemotypes which could probably due to their carboxylic acids propensity to interact with arginine amino acid of active site of Bcl-2 family members. Similar differences in potencies were observed in **2.3.117** vs **2.3.116** which contain carboxylic acid and ester respectively in their structures as 26.07 μM vs 86.91 μM. While, benzylated-version (**2.3.114**: 57.40 μM & **2.3.115**: 46.32 μM) were found slightly more potent than similar benzylated compound (**2.3.116**: 86.91 μM) as indole-NH- seems to be contributing in H-bond donor interactions. All the IC₅₀ are provide in the **Table 11**.

Table 11 Cytotoxicity of synthesized heterocyclic compounds

BH3 α -helix based heterocycles	Chemotype/Scaffold	Cytotoxicity on Mcl-1 dependent cells (IC ₅₀ = μ M)
2.3.10	Non-hydroxy Chalcone	78.51
2.3.11		67.02
2.3.12		51.19
2.3.13		55.32
2.3.14		74.22
2.3.17		85.90
2.3.18		80.13
2.3.19		72.20
2.3.20		67.29
2.3.21		56.77
2.3.15	Hydroxy Chalcone	26.01
2.3.16		21.32
2.3.22		39.02
2.3.29	Pyrazoline	61.37
2.3.30		54.63
2.3.31		70.43
2.3.32	Pyrazole	NA ^{§, a}
2.3.33		94.39
2.3.42	N-substituted pyrazoline	63.86
2.3.43		71.12
2.3.44		88.11
2.3.45		75.39
2.3.46		65.41
2.3.56	Diphenyl pyridine	49.88
2.3.57		62.14
2.3.4	Symmetrical Triphenyl pyridine	NA ^{§, b}
2.3.75		NA ^{§, b}
2.3.76		NA ^{§, b}
2.3.77		37.74
2.3.78		23.20
2.3.79		NA ^{§, b}
2.3.80		NA ^{§, b}
2.3.84		NA ^{§, b}
2.3.94		NA ^{§, b}
2.3.95		NA ^{§, b}
2.3.85		NA ^{§, b}
2.3.86		NA ^{§, b}
2.3.87		NA ^{§, b}
2.3.88	NA ^{§, b}	
2.3.89	NA ^{§, b}	
2.3.90	12.44	

2.3.91	Non-symmetrical triphenyl pyridine	23.87
2.3.92		22.53
2.3.93		21.58
2.3.96		NA ^{s, b}
2.3.97		NT
2.3.98		NA ^{s, b}
2.3.101	N-substituted imidazole	NT
2.3.102		79.92
2.3.105	Imidazole dinitriles	87.11
2.3.106		94.25
2.3.107	Imidazole dicarboxylic acids	8.33
2.3.108		12.52
2.3.110	Indole	NT
2.3.111		69.32
2.3.114		57.40
2.3.115		46.32
2.3.116		86.91
2.3.117		26.07

^sN.A.: not active at 100 μ M; Cell death observed at 100 μ M: ^a23.06 %; ^b \geq 15 %; *NT* not tested

2.3.4 Conclusion & Future perspective

Various chemotypes were studied to target the hydrophobic pockets in the antiapoptotic Bcl-2 family members which includes Pyrazoles, pyrazolines, pyridines, imidazoles and indoles. Special attention was given new method development of non-symmetrical triphenyl pyridine where it was successfully investigated. The biology testing on these chemotypes showed the compounds with polar functionality (especially phenolic or carboxylic group containing molecules) were more active to H929 cancer cell line (Mcl-1 protein dependent cell line) than their chemically non-polar equivalents, which can be useful to investigate their biophysical studies or their mode of action as a futuristic apoptosis inducing agents.

Chapter 3

This chapter dedicated to *de novo* ligand design and mainly deals with non-peptidomimetic heterocyclic scaffolds which mimic the secondary structures of proteins, with a focus on the α -helix of BH3 apoptotic proteins. This chapter further divided into two sections, each linked to an objective.

Objective 1 Ligand-based design and synthesis of non-peptidomimetic BH3 α -helix based heterocyclic chemotypes

Objective 2 Rational design of multi-targeting macrocyclic ligands based on embedded carbohydrates (MECs) as protein (peptide)-protein interaction inhibitors

Objective 3.1 Ligand-based design and synthesis of non-peptidomimetic BH3 alpha helix based heterocyclic chemotypes

3.1.1 Introduction

The formation of stable or dynamic protein-protein complexes are pivotal in biological processes. As a result, any dysregulation of these protein-protein interactions (PPI), could lead to fatal disorders such as cancer, diabetes, as well as various other cellular deformities. Modifying these interactions with small molecules can be tricky, as these PPIs mainly occur over a large and flat surface area of a protein. Although, there are small pockets in between these interfaces (which, are also called as *hot spots*) which can accommodate high-affinity binding for small functional groups, which could be the side chain of an amino acid, for example [247]. Also, it has been seen that almost 60% of PPI sites involve an α -helix conformation of a peptide at the hot-spots [2]. Therefore, it is no surprise that considerable amount of efforts has been laid down in recent years to develop molecules that are α -helix mimetics, which can compete against the respective α -helices for specific PPIs. In this regard, various strategies have been used by researchers which have involved cyclic/stapled peptides, β -peptides, peptoids and terphenyl heterocyclic cores up until now. The development of stapled peptides recently attained much success, as this type of peptide inhibitor has been restrained conformationally into a helix and can lead to increase in potency/selectivity against a specific PPI and improves their resistance against metabolic hydrolysis as when compared to their unconstrained peptide parent molecules. One such example is **ATSP-7041** which is a specific dual inhibitor of MDM2 and MDMX, as shown in **Figure 1**. The co-crystal structure of **ATSP-7041** with MDMX showed that it utilizes three key residues: Phe19, Trp2 and Leu26, with additional interactions between Tyr22 and the ‘stapled’ moiety itself. Also, **ATSP-7041** had improved cell membrane penetrability, which enhanced its on-target bioavailability compared to its parent peptide.

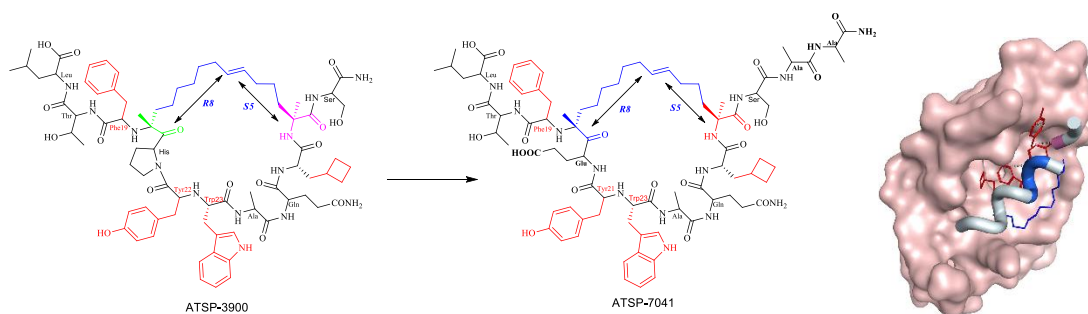


Figure 1 The chemical structure of **ATSP-3900** & **ATSP-7041**, highlighting R8 (Blue) and S5 (red) amino acids in the stapled peptide (R8 and S5 is α -methylated and that the all hydrocarbon linker consists of 11 carbon atoms). Useful in MDM2-MDMX interface inhibitor ($K_{iMDM2} = 0.9 \text{ nM}$ & $K_{iMDMX} = 6.8 \text{ nM}$).

3.1.2 Result and Discussion

3.1.2.1 Ligand design and synthesis

As reviewed in *objectives 2.1* and *2.2*, the BH3 helix of proapoptotic proteins interacts with anti-apoptotic proteins. The α -helix of mNoxaB BH3 domain binds to Mcl-1's four hydrophobic pockets, namely P₁, P₂, P₃ and P₄ through its E74, L78, I81, and V85 hydrophobic side chain, respectively [248]. Various strategies discussed in *objective 2.1* indicated that most of designed heterocyclic inhibitors were targeting only one pocket, or 2 adjacent pockets of Mcl-1. On the other hand, inhibitors such as those based on terphenyl and anthraquinoline scaffolds (**2.1.114-2.1.116**) were compounds mimicking the full α -helix of proapoptotic protein (BH3 helix) binding to Mcl-1 protein (see *objective 2.1*).

Here, I undertook a study to design new ligands (ligand-based design) where I used the terphenyl scaffold as the prototype, as shown in **Figure 2**.

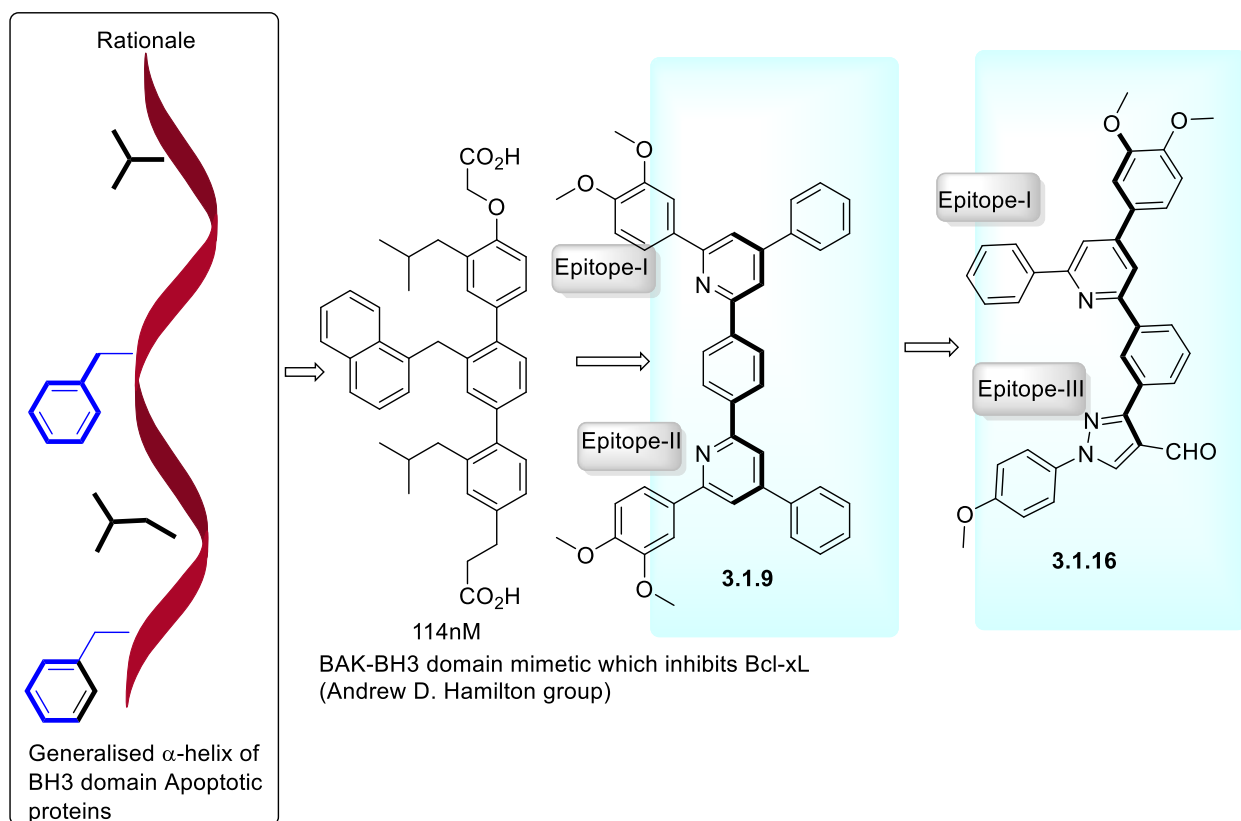
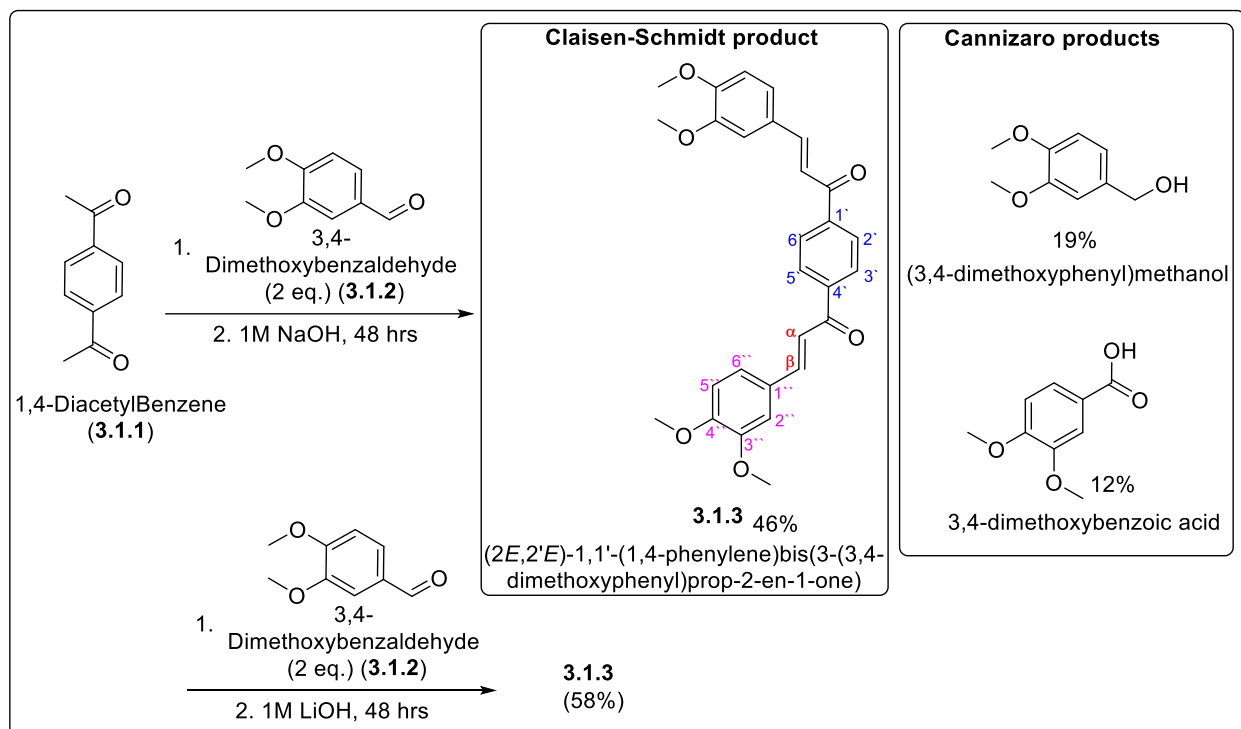


Figure 2 Rationale of α -helix mimic of BH3 design: Structures of **3.1.9** & **3.1.16** were designed in order to mimic the BH3 binding pocket, where BH3 helix mainly utilizes its hydrophobic amino acid side chains to interact with active site

The formation of bis-chalcones utilizes the Claisen Schmidt condensation as shown in **Scheme 3.1**. It is well known that Claisen Schmidt condensation reaction competes with the Cannizzaro reaction in solution (also discussed in *objective 2.3*) [187]. In this particular case, as Claisen Schmidt reaction is required twice, therefore, remnants of 1,4-diacetylbenzene were found in the product mixture in most cases. This led to reduced yields as when compared to mono-chalcone synthesis. However, use of the 1 M LiOH solution gave a better yield than 1M NaOH as summarized in **Scheme 3.1**.



Scheme 3.1 Synthesis of bis-chalcones

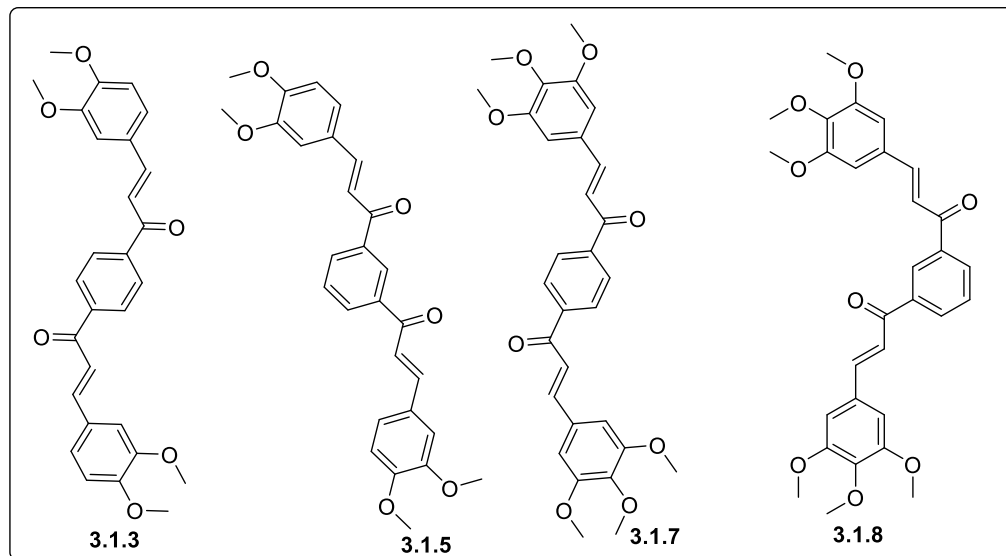


Figure 3 Various bis chalcones prepared as α -helix mimetics.

The formation of **3.1.3** was supported by NMR spectroscopy. It was concluded that signals for 1,4-diacetyl benzene ring protons are found downfield at δ 8.11 ppm (all 4 protons are chemically equivalent and are a singlet), while peaks at δ 7.79 and δ 7.38 ppm, which were coupled with each other, with a 3J -value of 15.6 Hz as shown in **Figure 4**; this supported the adoption of the E-configuration by the unsaturated propenone as shown in **Figure 5**. However, the use of C-APT and ^{13}C -NMR indicate the presence of 5 quaternary carbons (as 5 upward peaks in the C-APT spectrum, ppm values: 190.22, 151.76, 149.33, 141.47, 127.62) while the remaining downward pointing peaks either belong -CH- or -CH₃, as shown in **Figure 4**. Further, it was concluded that the presence of (-CH- peak) at 146.01 ppm is due to the β -carbon of propenone functional group, the latter which is linked to the α -carbon of propenone (123.45 ppm) while the 128.58 ppm peak is assigned to the 4 equivalent CH carbons of the 1,4-diacetyl benzene ring (**Figure 4 & 5**).

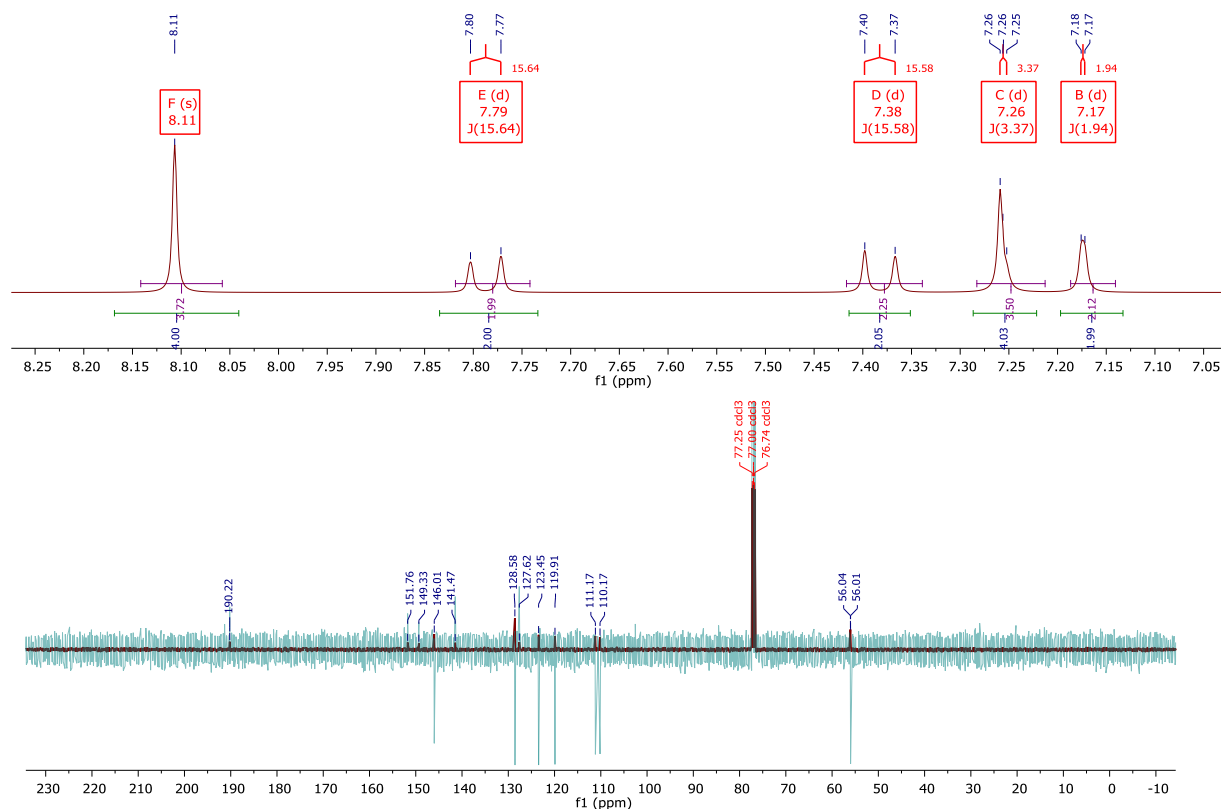


Figure 4 ^1H -NMR and ^{13}C /C-APT-NMR of **3.1.3**

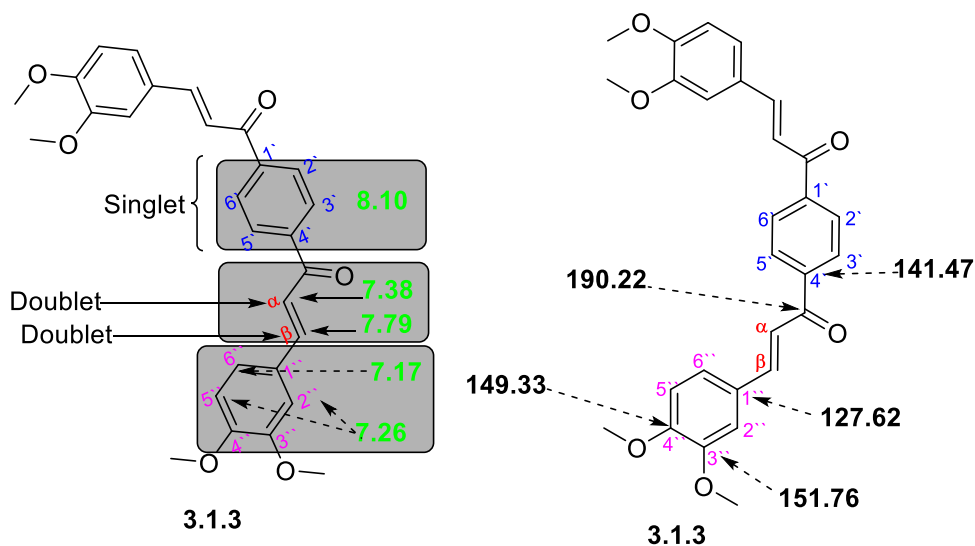


Figure 5 Assignment of selected protons and carbons NMR signals of **3.1.3**

In contrast to **3.1.3**, **3.1.5** has a 1,3-dimethoxybenzene residue, which does not have equivalent protons, therefore gCOSY was used to assign coupling between the relevant protons. Coupling was found between the aromatic protons at δ 8.22 ppm and δ 7.66 ppm alongside with previously mentioned couplings as in case of **3.1.3** as shown in **Figure 6 & 7**.

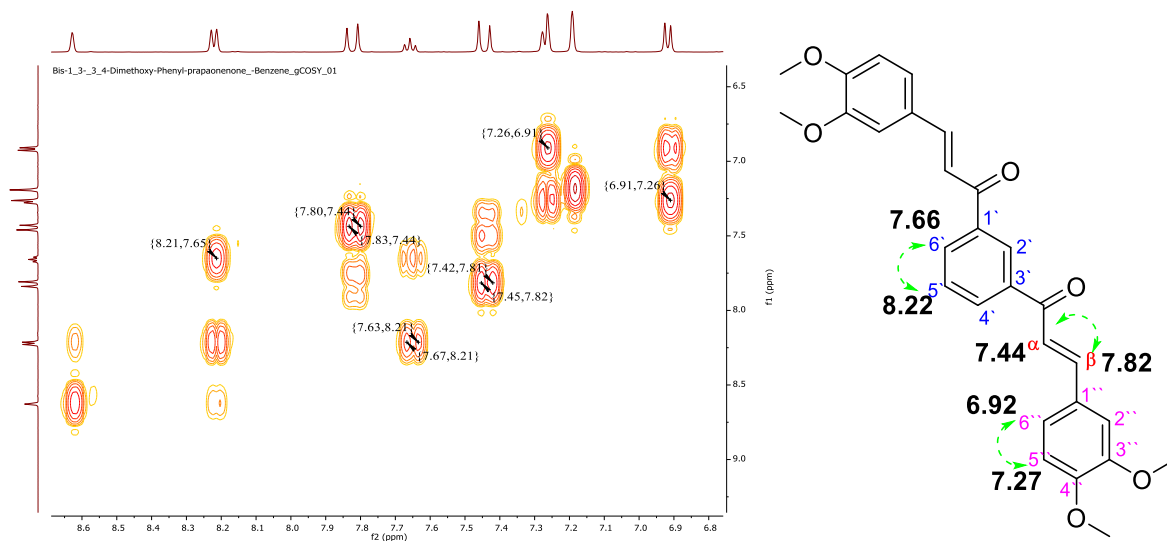


Figure 6 gCOSY of **3.1.5** with selected couplings and assignments depicted on the right.

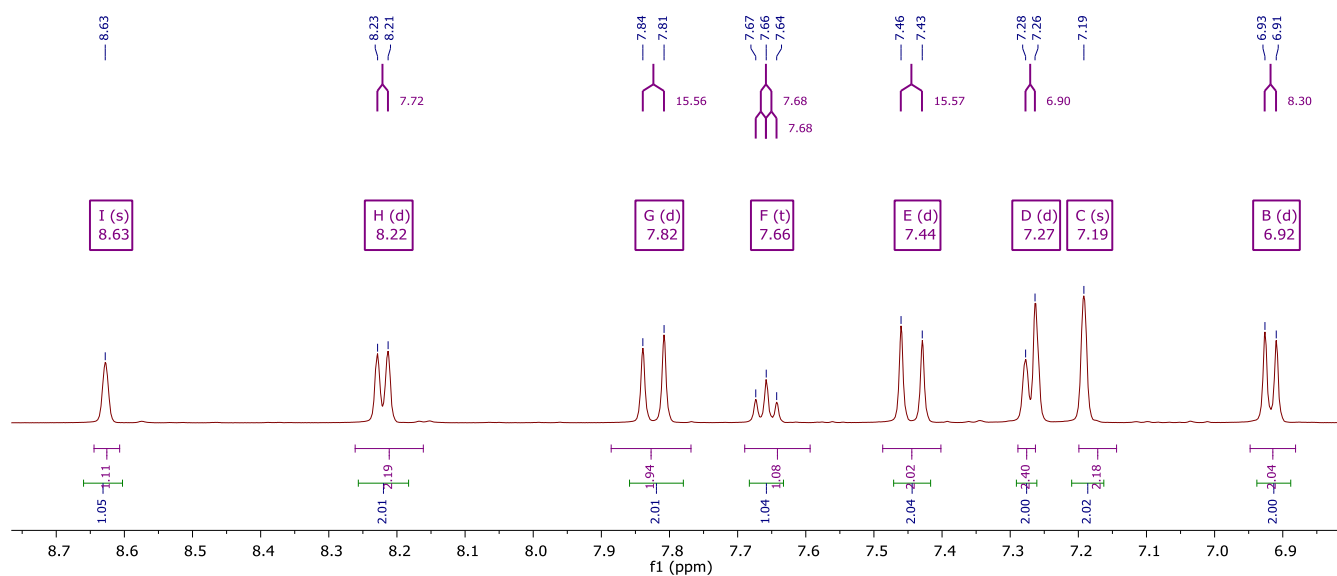
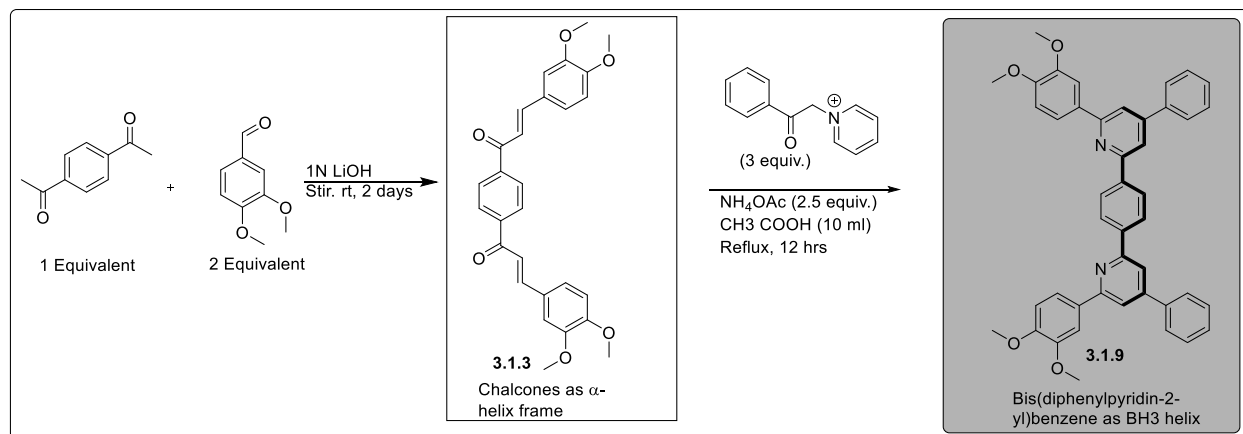


Figure 7 $^1\text{H-NMR}$ spectrum for **3.1.5**

In the case of bis(diphenylpyridin-2-yl)benzene as shown in **Scheme 3.2 (3.1.9)** as it is not reported earlier and therefore 1-D and 2-D NMR experiments were performed to characterize the molecule. From ^{13}C and C-APT spectrum, it was clear that 8 peaks were from quaternary carbons and 2 were from methyl carbons while remaining signals were aromatic -CH- carbons, as shown in **Figure 8**.



Scheme 3.2 Synthesis of bis(diphenylpyridin-2-yl)benzene (**3.1.9**) as BH3 α helix

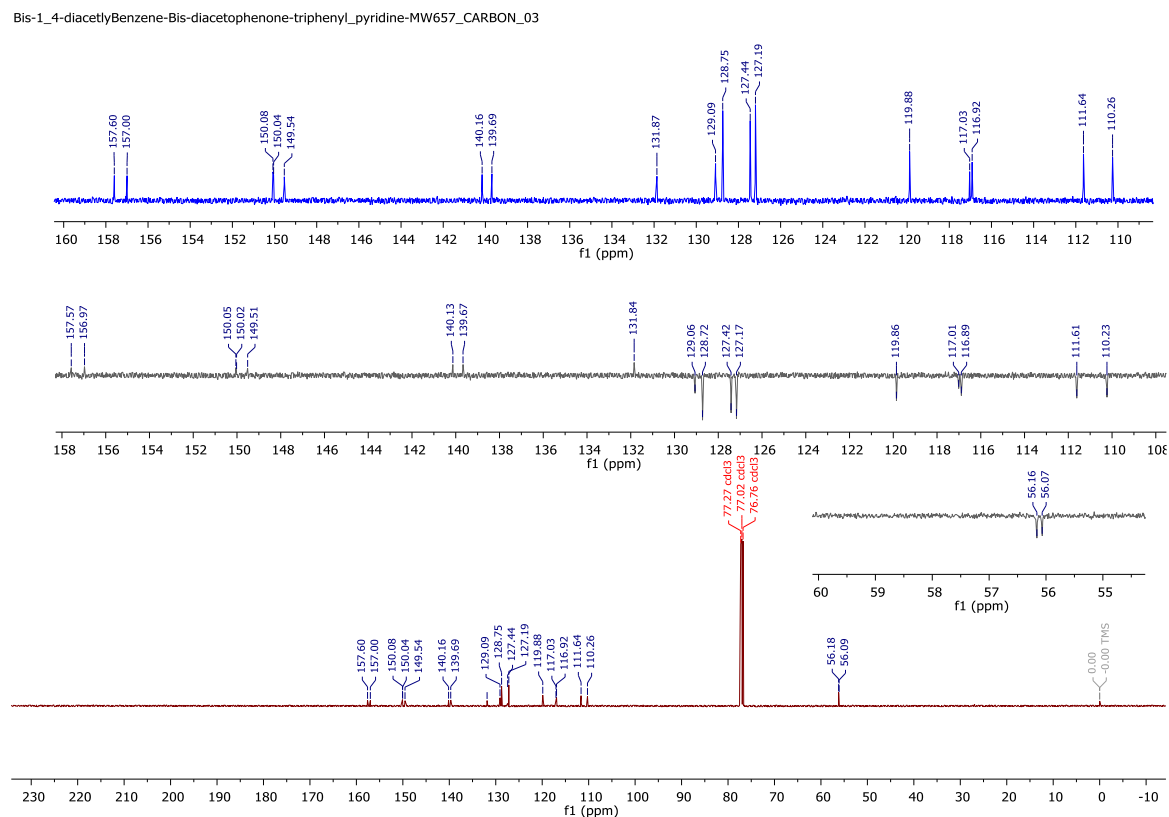


Figure 8 Recorded ^{13}C (full spectrum in brown & zoom aromatic region in blue) and C-APT (grey in colour) spectra for **3.1.9** (bis-triphenyl pyridine).

Furthermore, the 1H -NMR spectrum and the gCOSY shows the proton peaks and coupling as shown in **Figure 9** & **10**. The spectral data obtained are consistent with it being a symmetric molecule. From 1H -NMR spectrum and gCOSY, it was clearly concluded that protons at δ 8.23 ppm were coupled with those at δ 7.54 ppm & δ 7.48 ppm, while protons at δ 7.37 ppm were

coupled with those at δ 7.04 ppm. Based on symmetry (axis of symmetry) and signal integration, the assignments made are shown in **Figure 9**.

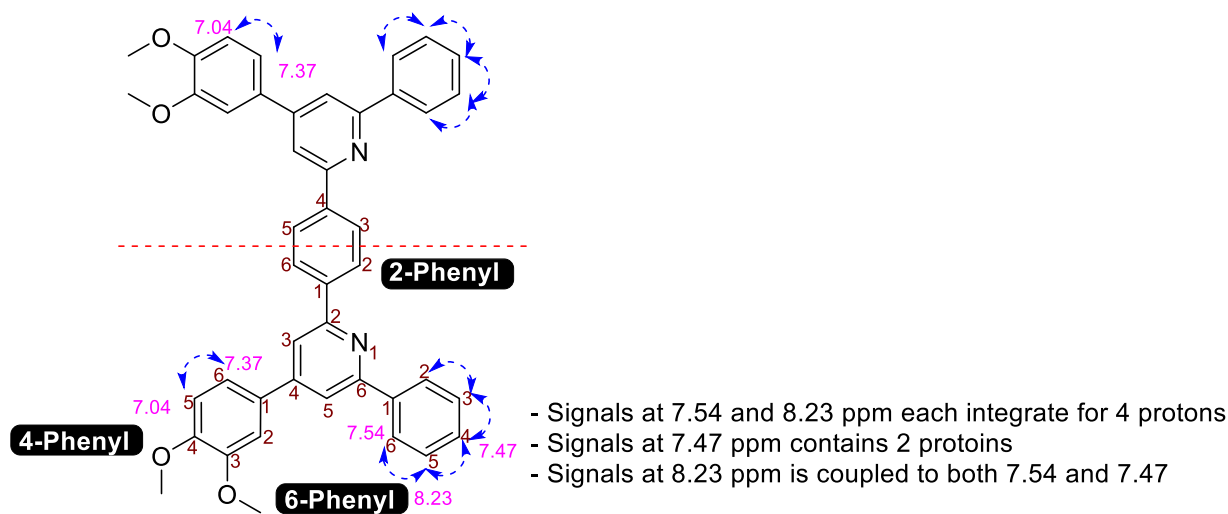


Figure 9 Observed coupling and selected assignment of $^1\text{H-NMR}$ signals (δ , ppm).

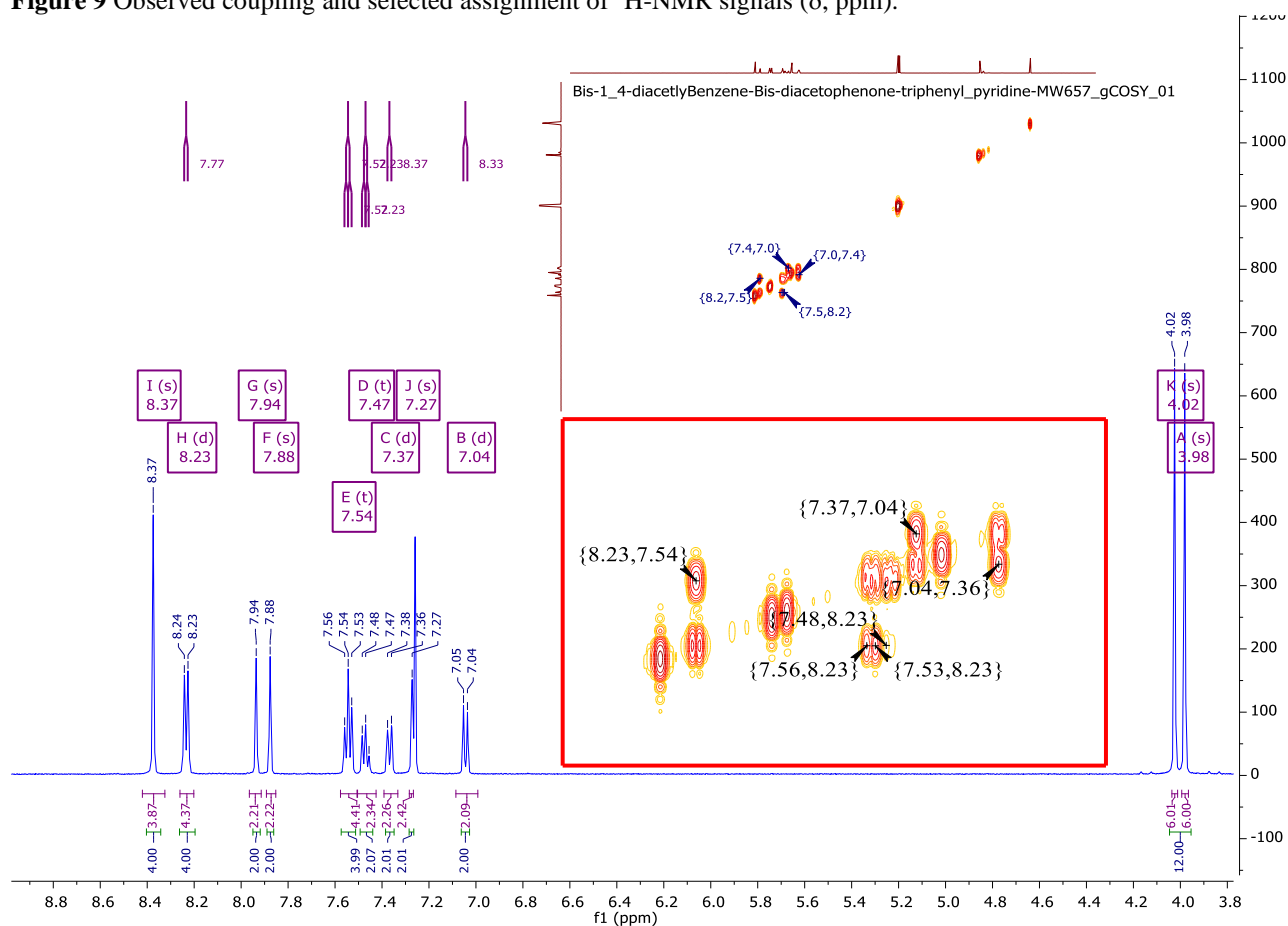


Figure 10 $^1\text{H-NMR}$ spectrum and gCOSY for **3.1.9**. Coupling is observed between protons at δ 8.23 ppm with those at δ 7.54 & 7.48 ppm. Protons at δ 7.37 couple to those at δ 7.04 ppm.

Heteronuclear correlation experiments (HSQC & HMBC) were also performed. Aromatic regions in this molecule have a range of carbons and protons and therefore more attention was given to these aromatic peaks. HSQC shows $^1J_{(C, H)}$ for corresponding protons and ^{13}C -carbons as shown in **Figure 11** and tabulated in a **Table 1**, while HMBC showed $^nJ_{(C, H)}$ $n = 2$ or 3 for corresponding protons ^{13}C -carbons as shown in **Figure 12** and tabulated in **Table 2**.

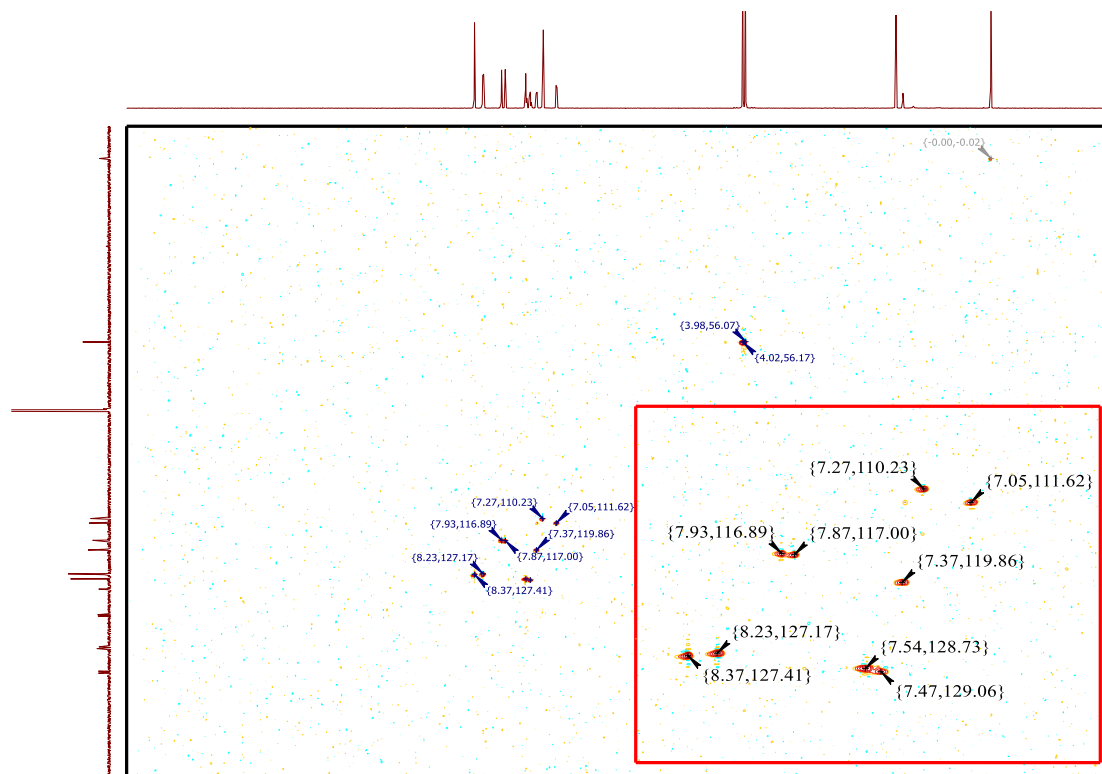


Figure 11 HSQC spectrum for **3.1.9**

Table 1 Correlations observed from HSQC of **3.1.9**. This showed $^1J_{(C, H)}$ for corresponding protons and ^{13}C -carbons in aromatic region listed below (see **Figure 9** for further information related to the aromatic carbon assignment).

HSQC		Assigned regions
Proton signal	Corresponding carbon signal	
7.05	111.62	4-Phenyl
7.27	110.23	
7.37	119.86	
7.47	129.06	6-Phenyl
7.54	128.73	Pyridine
7.87	117.00	
7.93	116.89	6-Phenyl
8.23	127.17	
8.37	127.41	2-Phenyl

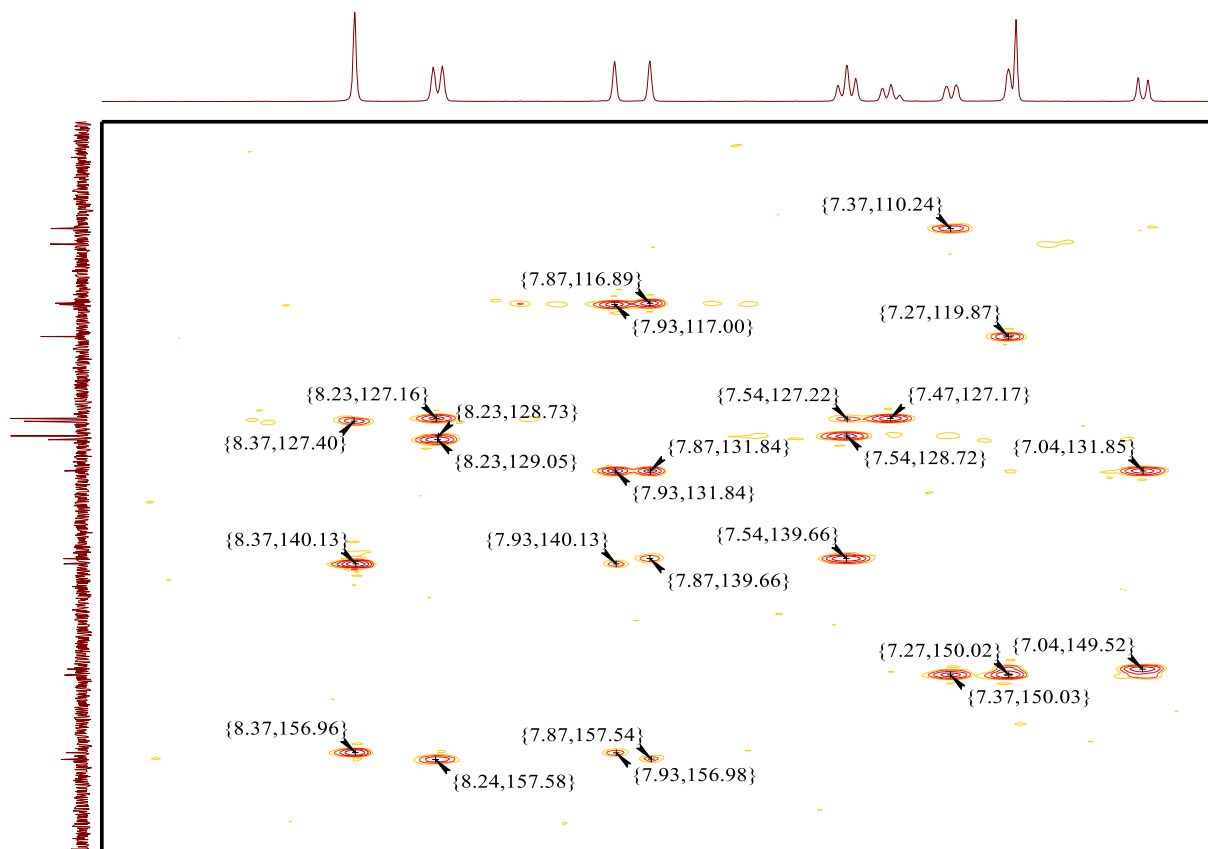


Figure 12 HSQC spectrum for **3.1.9**.

Table 2 HMBC shows $^3J_{(C,H)}$ $n \leq 3$ for corresponding protons and ^{13}C -carbons in aromatic region. Correlations observed are listed below.

HMBC	
Proton peaks	Corresponding carbon peaks
7.05	131.85, 149.52
7.27	119.87, 150.02
7.37	110.24, 150.03
7.47	127.17,
7.54	127.17, 128.72, 139.66
7.87	116.89, 131.84, 139.66, 157.60
7.93	117.00, 131.84, 140.13, 156.90
8.23	129.05, 127.16, 128.73
8.37	127.40, 140.13, 156.96

The HMBC correlation was used, in particular, for quaternary carbon assignment, as indicated by their correlations listed below:

(a) the C1 of the 6-Phenyl ring (see **Figure 9**) is at δ 139.66 ppm: there is a $^2J_{(C,H)}$ correlation between H-2 of 6-phenyl (at δ 7.54 ppm) and quaternary (C1) of the 6-Phenyl ring; $^3J_{(C,H)}$

correlation were observed between the H-5 of pyridine (at δ 7.87 ppm) and quaternary (C1) of 6-Phenyl.

(b) C1 of 4-Phenyl (see Figure 9) is at δ 131.84: $^3J_{(C,H)}$ correlation between H-5 of 4-phenyl (at 7.05 ppm) and quaternary (C1) of 4-Phenyl; $^3J_{(C,H)}$ correlation between H-5 of pyridine (at 7.87 ppm) and quaternary (C1) of 4-Phenyl; $^3J_{(C,H)}$ correlation between H-3 of pyridine (at 7.93 ppm) and quaternary (C1) of 2-Phenyl.

(c) C1 of 2-Phenyl is at δ 140.13: $^2J_{(C,H)}$ correlation between H-2/H-6 of 2-phenyl (at 8.37 ppm) and quaternary (C1) of 2-Phenyl; $^3J_{(C,H)}$ correlation between H-3 of pyridine (at 7.93 ppm) and quaternary (C1) of 6-Phenyl.

(d) C2 of Pyridine is at δ 157.00: $^3J_{(C,H)}$ correlation between H-2/H-6 of 2-phenyl (at 8.37 ppm) and quaternary (C2) of Pyridine; $^2J_{(C,H)}$ correlation between H-3 of pyridine (at 7.93 ppm) and quaternary (C2) of Pyridine.

(e) C6 of Pyridine is at δ 157.60: $^2J_{(C,H)}$ correlation between H-5 of pyridine (at 7.87 ppm) and quaternary (C6) of Pyridine.

(f) C-4 of Pyridine is at δ 150.04: $^3J_{(C,H)}$ correlation between H-6 of 4-phenyl (at 7.37 ppm) and quaternary (C4) of pyridine; $^3J_{(C,H)}$ correlation between H-2 of 4-phenyl (at 7.27 ppm) and quaternary (C4) of pyridine.

(g) C-4 of 4-phenyl is at δ 149.52: $^2J_{(C,H)}$ correlation between H-4 of pyridine (at 7.04 ppm) and quaternary (C4) of 4-Phenyl.

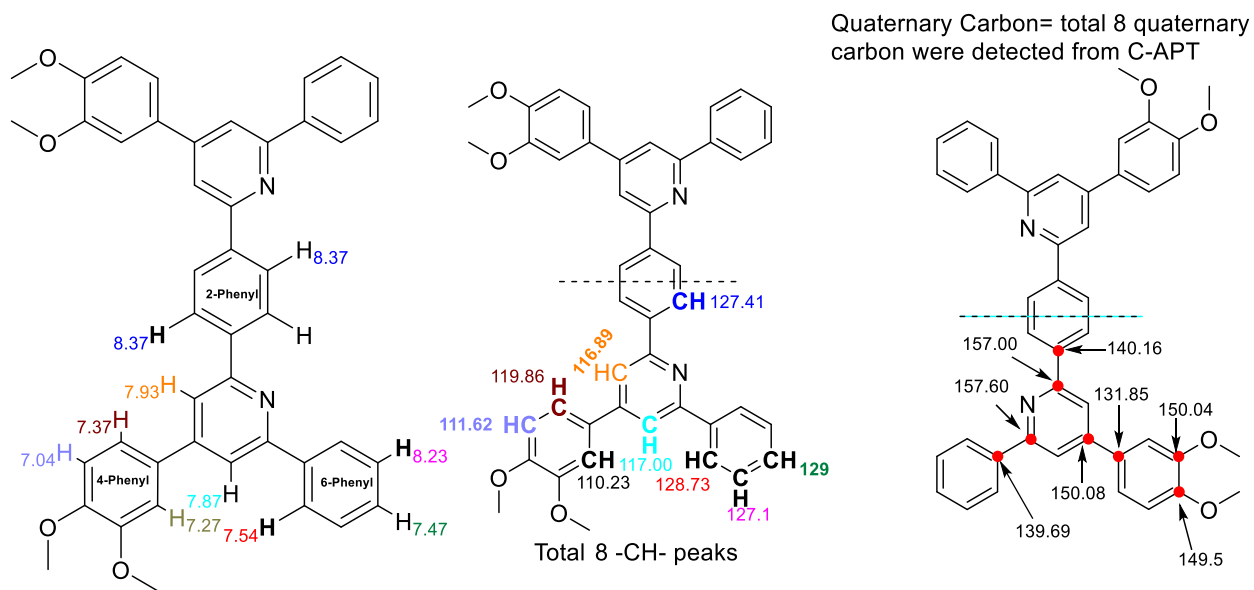
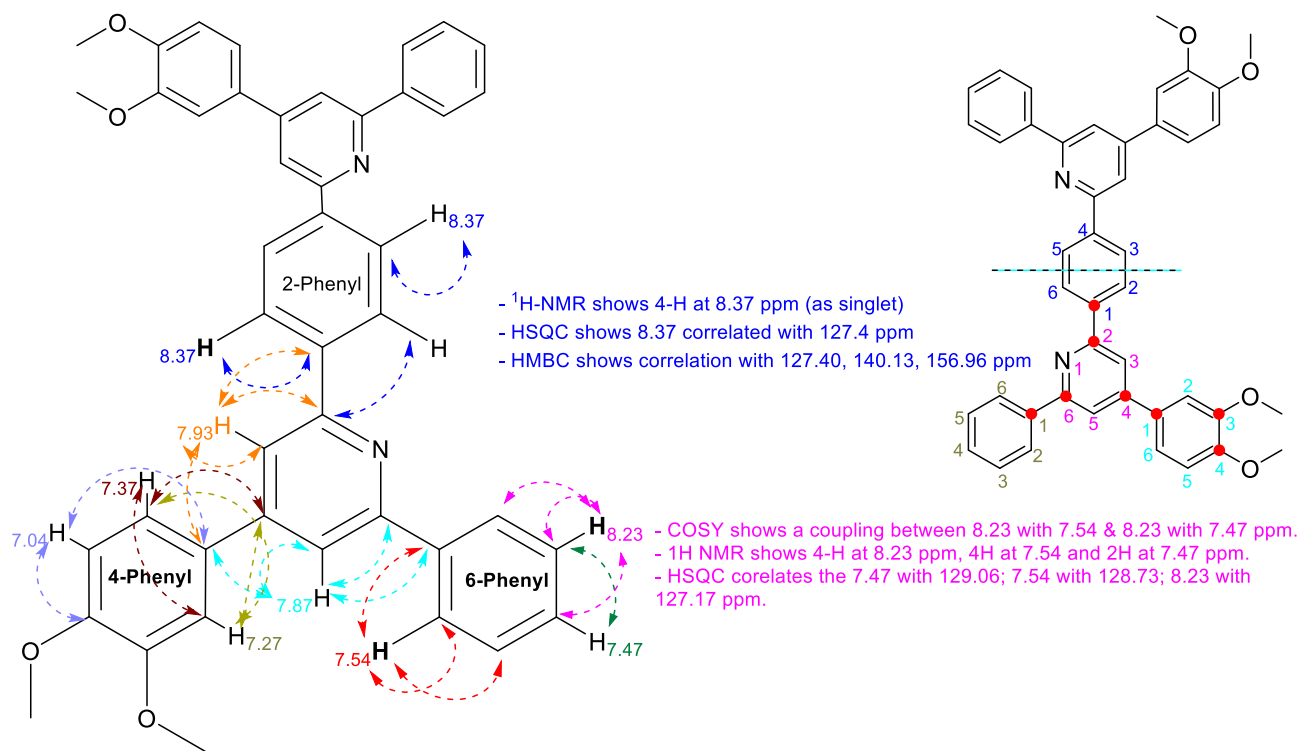
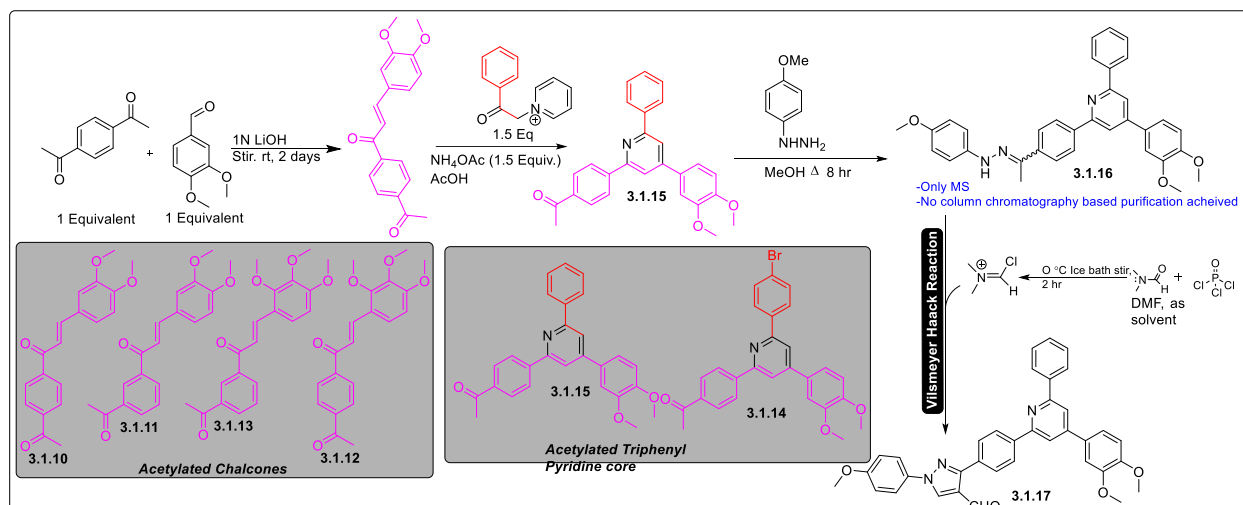
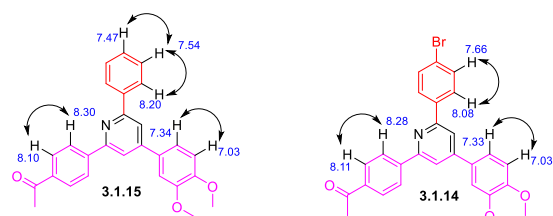


Figure 13 $^{1-3}\text{J}_{\text{C,H}}$ correlations observed by HSQC and HMBC (top) and ^1H & ^{13}C signal assignments for **3.1.9**



gCOSY coupling experiment concluded



Scheme 3.3 Synthesis of acetylated chalcones (**3.1.10-3.1.13**), acetylated triphenyl pyridine (**3.1.14** & **3.1.15**) and (pyrazolyl)phenylpyridine (**3.1.17**). Determination of 1H coupling in acetylated triphenyl pyridines (**3.1.14** & **3.1.15**) through gCOSY coupling experiment.

Later, the (pyrazol-3-yl)phenylpyridine derivative **3.1.16** was synthesized as shown in **Scheme 3.3**. As this is the first report of (pyrazolyl)phenylpyridine (**3.1.17**) therefore, 1-D and 2-D NMR spectral data was used to characterize the product and provide assignments as done for the **3.1.9**. The assignment of the spectrum of the latter was helpful here, as it also contains a triarylpyridine assigned above. Through gCOSY experiment it was observed that 8.35 ppm coupled with 7.9 ppm; 8.22 ppm coupled with 7.54 ppm; 7.72 ppm coupled with 7.03 ppm while 7.36 ppm coupled with 7.04 ppm. However, when proton spectrum was attained, it was found that the signals at 7.03 ppm (1H) and 7.04 ppm (2H) were merged together.

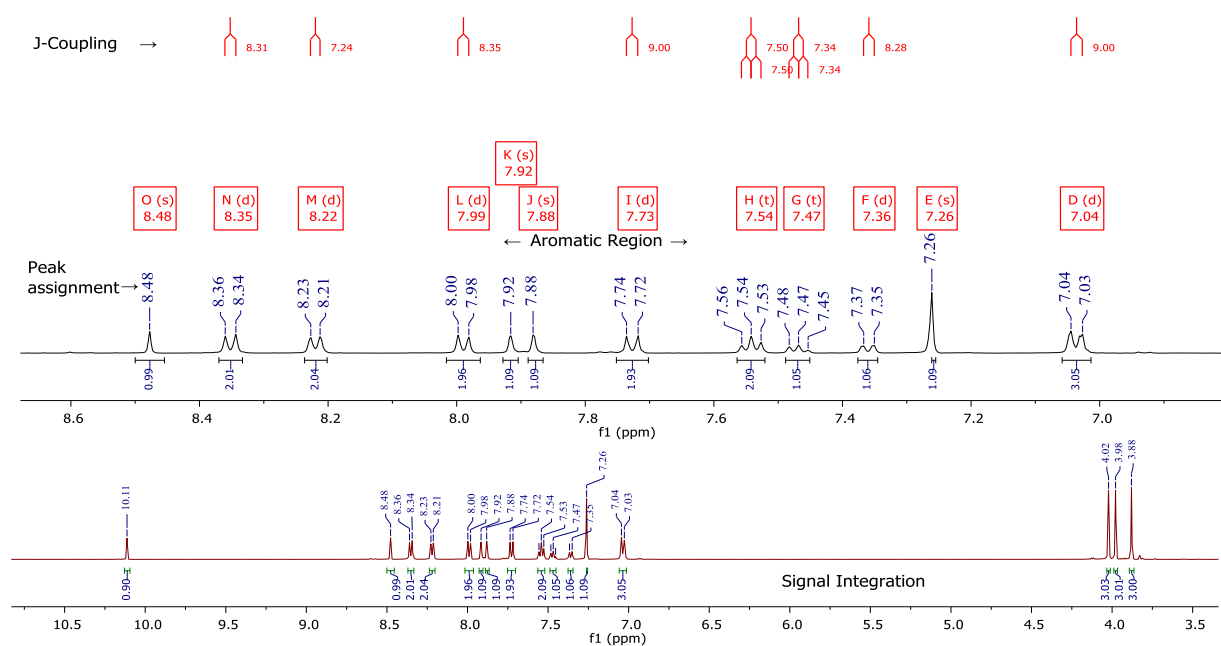


Figure 14 $^1\text{H-NMR}$ spectrum with J-coupling for **3.1.16**

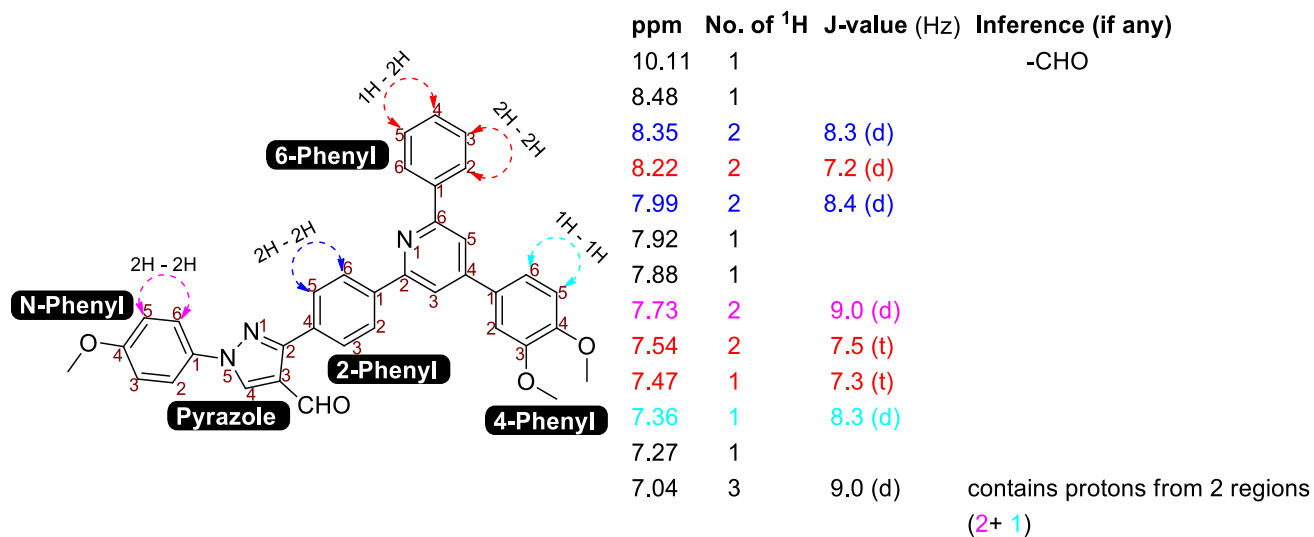


Figure 15 gCOSY based coupling observations (various color codes used) for **3.1.16** with ^3J values provided.

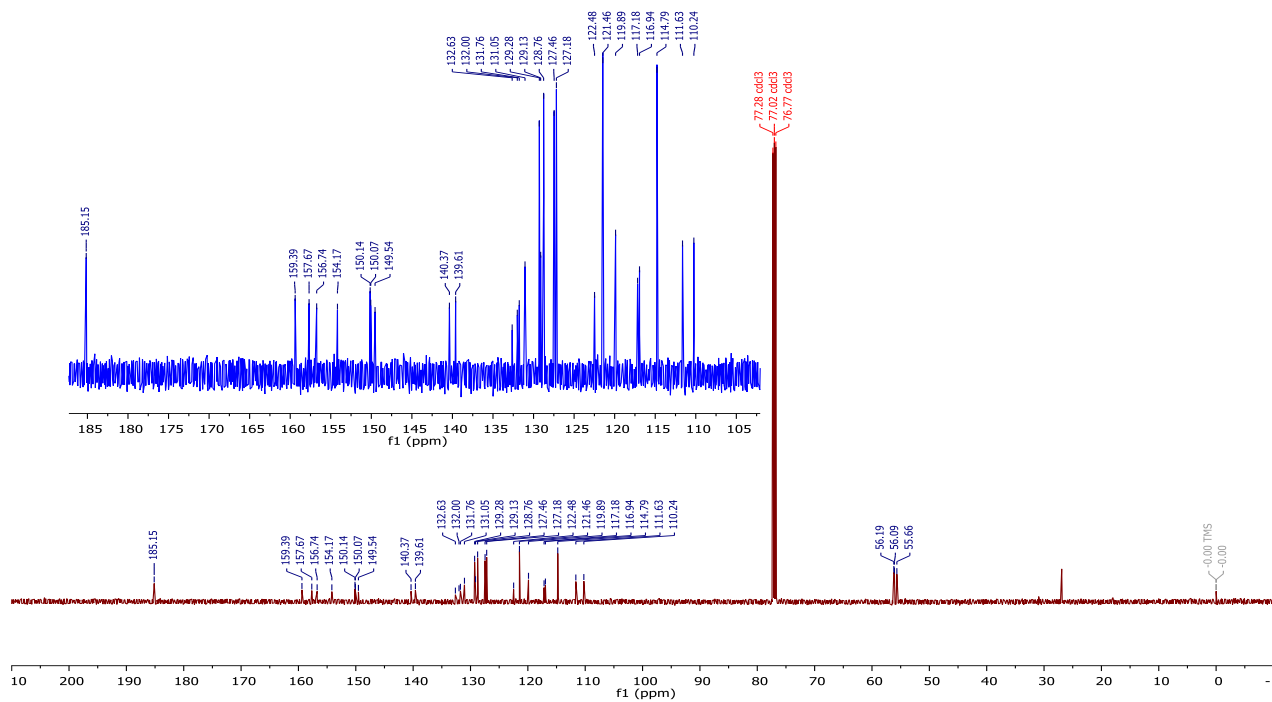


Figure 16 ^{13}C -spectrum (in brown peaks) of **3.1.16**, while peaks in blue showing aromatic region (except peak at 185.15 ppm which belongs to $-\text{CHO}$).

A proposal for the reaction mechanism utilized in the synthesis of **3.1.17** used double formylation on phenyl hydrazine derivative (**3.1.16**) as shown in **Figure 17**.

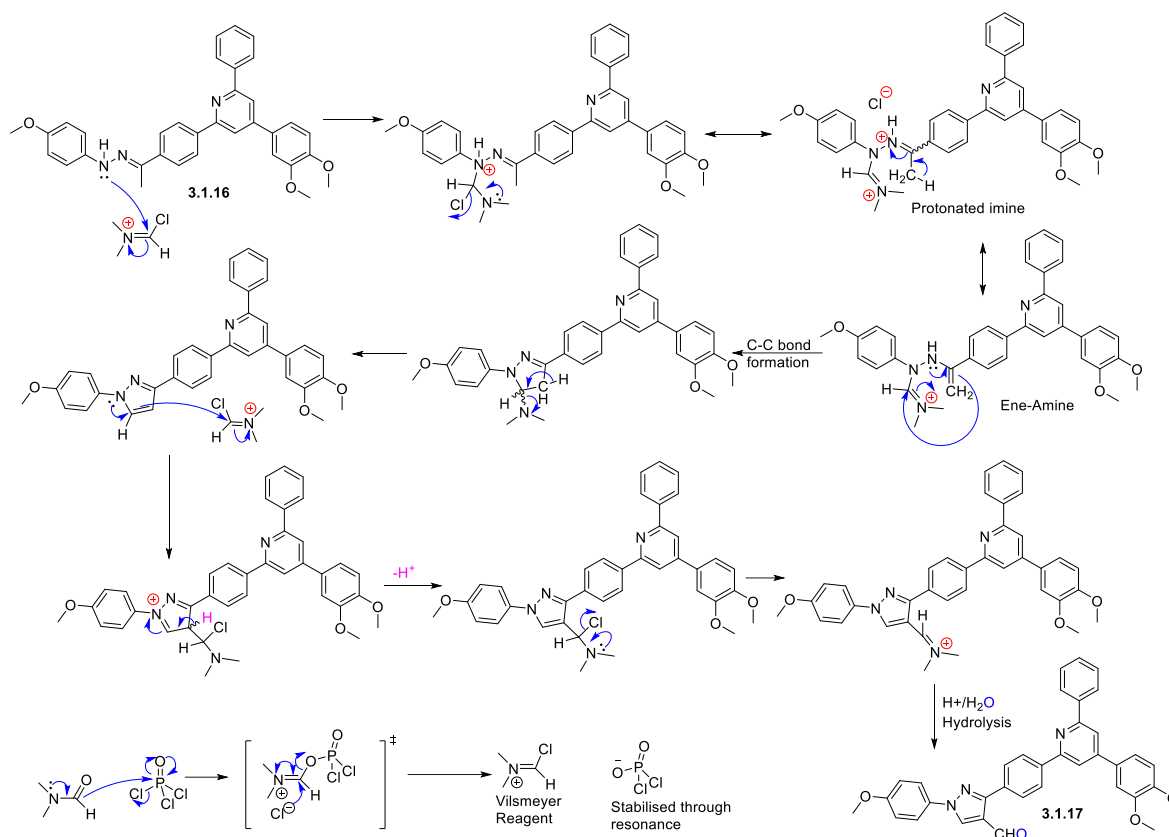


Figure 17 Mechanistic proposal for reaction promoted by the Vilsmeier Haack reagent.

3.1.2.2 Cytotoxicity evaluation of the BH3 α -helix mimetics

The MTT assay was performed to characterize the cytotoxicity of Bis-chalcones (**3.1.3**, **3.1.5**, **3.1.7** & **3.1.8**), bis(diphenylpyridin-2-yl)benzene (**3.1.9**), mono-acetylated chalcones (**3.1.10**, **3.1.11**, **3.1.12**, **3.1.13**), mono-acetylated triphenyl pyridines (**3.1.14** & **3.1.15**) and pyrazole-triphenyl conjugate (**3.1.17**). The cytotoxicity of the compounds of bis-chalcones (**3.1.3**, **3.1.4**, **3.1.7** & **3.1.8**) towards the H929 cancer cell line was evaluated (see in **Table 3**). They showed moderate inhibition towards this Mcl-1 dependent cell line. The pattern of cytotoxicity towards the Mcl-1 dependent cell line clearly showed that 1,4-disubstituted compounds were better compared to those with a 1,3-substitution pattern (**3.1.3** vs **3.1.5**; **3.1.7** vs **3.1.8**). This observation in relative tolerance can be correlated with their structural flatness similar to the α -helixes during protein-protein interaction, where 1,4-linkage represent a more firm backbone than 1,3-linkages ones which are slightly tilted to one end. The influence of additional methoxy groups on these structures (two versus three) gave rise to consistent toxicity. The 3,4,5 trimethoxy derivatives were more potent than 3,4 dimethoxy compounds (compare **3.1.3** vs **3.1.7** & **3.1.5** vs **3.1.8**), which can be correlated with the concept of binding of alpha helix in protein-protein interface where its small side chain

functional group interact fits in the individual pockets of protein as can be seen in Mcl-1/BH3 interactions (**Figure 47** under **objective 2.2** of *Chapter 2*, where four pockets (P₁ to P₄) were filled by small hydrophobic side chains of BH3 peptide). However, the proposed alpha-helix mimetic, bis(diphenylpyridin-2-yl)benzene (**3.1.9**) shows appreciable improvement in cytotoxicity compared to its predecessors (see **Table 3**) which demonstrated the utility of this kind of molecule/scaffold as in development of alpha-helix mimetics.

The mono-acetylated chalcones were inactive as none of them showed 50% cytotoxicity towards Mcl-1 dependent cancer cell line, even at higher concentration (100 μ M). I had expected some activity for these compounds, as they could fit in the binding pocket of Bcl-2 proteins (more specifically, Mcl-1) and might be expected to be more cell-permeable as they possess lower molecular sizes. Also, the acetylated triphenyl pyridines (**3.1.14** & **3.1.15**) derived from them did not show much activity when compared to their larger counterparts, specifically **3.1.9**. A brominated acetyl-triphenyl pyridine (**3.1.14**) showed 50 % cytotoxicity towards these Mcl-1 dependent cells at $82.19 \pm 5.2 \mu$ M as compared to inactive **3.1.15**. Further derivatization of **3.1.15** to final molecule **3.1.17** (pyrazole-triphenyl pyridine conjugate) led to the most potent compound against this Mcl-1 dependent cell line. However, when compared to **3.1.9**, **3.1.17** has a slightly twisted backbone which might be pushing the N-phenyl and phenyl group (6-phenyl of triphenyl pyridine substructure) of **3.1.17** into the hydrophobic pockets of Mcl-1 protein and therefore presented a more suitable candidate to be an alpha helix mimetic.

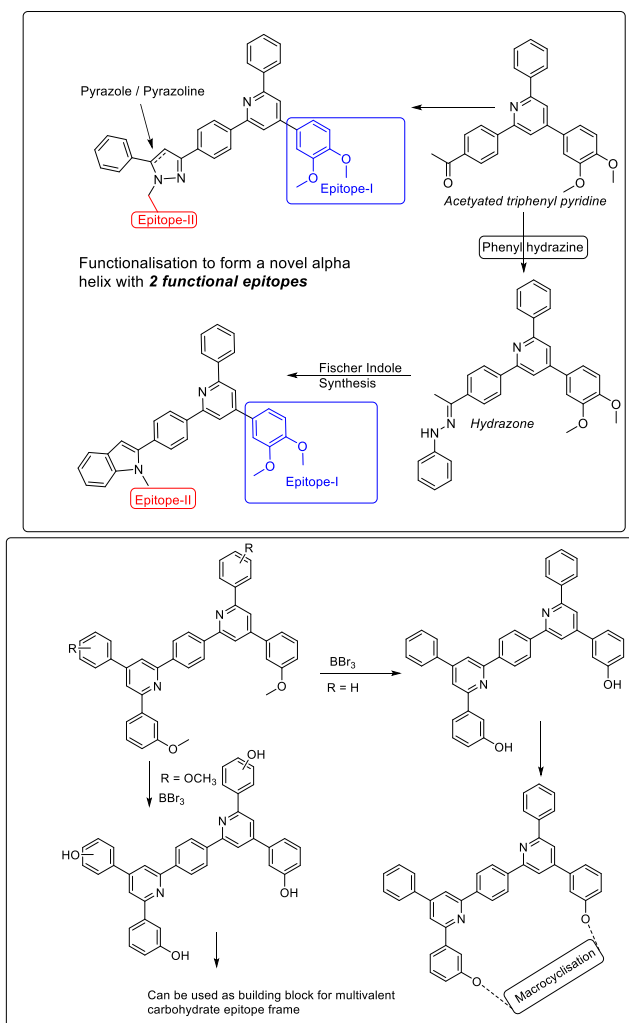
Table 3 MTT cytotoxicity profile of compounds towards the Mcl-1 dependent H929 cancer cell line (B-lymphocyte cell type).

BH3 α -helix based heterocycles	Chemotypes	Cytotoxicity (IC ₅₀ = μ M)
3.1.3	bis-chalcones as α -helix mimetics	65.71
3.1.5		70.09
3.1.7		49.88
3.1.8		62.14
3.1.9	bis(diphenylpyridin-2-yl)benzene as α -helix mimetic	39.08
3.1.10	Mono-acetylated chalcones as a building block for α -helix (as a substructure)	NA ^{s, a}
3.1.11		NA ^{s, b}
3.1.12		NA ^{s, c}
3.1.13		NA ^{s, d}
3.1.14	Mono-acetylated triphenyl pyridine (similar like molecules which target either only one or two adjacent pockets)	82.19
3.1.15		NA ^e
3.1.17	Pyrazole-triphenyl conjugate as non-peptidomimetic α -helix mimetic	33.14

^sNA: not active at 100 μ M; cell death observed at 100 μ M: ^a 19 %; ^b 8 %; ^c 41 % ^d 27 %; ^e 32 %.

3.1.3 Conclusions & future perspective

This section of the thesis provides the first report of bis(diphenylpyridin-2-yl)benzene (**3.1.9**), acetylated triphenyl pyridines (**3.1.14** & **3.1.15**) and pyrazole-triphenyl pyridine conjugate (**3.1.17**) as putative α -helix mimetics. Their synthesis can be concisely achieved from readily available precursors. The products were analyzed in detail by NMR spectroscopy and the heterocyclic compounds showed improved potency compared to bis chalcone precursors when their cytotoxicities were measured against the Mcl-1 dependent cancer cell line. It will be relevant to investigate their binding directly with Mcl-1 using appropriate biophysical assays as part of future work. The strategy described herein could be useful for generating new types of alpha-helix mimetics as summarized below in **Scheme 3.5**.



Scheme 3.5 Future design of secondary structures for PPI (left) based building blocks, multivalent carbohydrate for carbohydrate binding domains and macrocyclization (right) as a strategy of functionalization of these molecules for target.

Objective 3.2 Rational design of multi-targeting macrocyclic ligands based on embedded carbohydrates (MECs) as protein (peptide)-protein interaction inhibitors

3.2.1 Introduction

The protein-protein interactome of humans is estimated to involve 150,000-500,000 binary interactions, [249, 250] and most of these remain unmapped. The targeting of protein-protein (peptide) interactions or protein-protein (peptide) interfaces (PPIs) has developed as a research area due to the potential to identify inhibitors with the main goal to eventually give new pharmaceuticals. However, the objective of identifying good inhibitors is challenged by the large binding surfaces involved in PPIs (1200-4500 Å²) which can be fourfold larger than binding pockets (300-1000 Å²) typically targeted by many currently approved drugs. Developing inhibitors of PPIs is also considered difficult due to the relatively featureless and flat hydrophobic surfaces involved and highly dynamic processes at the interfaces [251]. These issues contribute to the challenge of identifying PPI inhibitors that would fit the Lipinski “rule-of-five”[252] criteria [253, 254].

Medium-sized cyclic peptides have been used to target PPIs [255, 256], but their peptide character means they are prone to metabolism and limits their bioavailability [257]. Nevertheless, studies with cyclic peptides can still be useful and give important information that can inform ligand-based design strategies. Structure-activity relationship studies with such inhibitors lead to the identification of critical interactions, mediated, perhaps by a few side chains of amino acids or their bioisosteres, at the interface cavity [258-261]. Subsequent ligand-based design, once critical information on the pharmacophore is available, can involve the replacement of some or all of the cyclic peptide backbone with a smaller molecular framework or scaffold, such as a monosaccharide or heterocycle. The ligand-based design also can involve the synthesis of an oligomer of some type, such as stapled peptides constrained in helical conformations or the application of a larger scaffold or framework such as a macrocycle (see **Figure 18**) [262, 263]. These approaches can lead to inhibitors that show improved selectivity, metabolic stability and/or enhance the systemic half-life of the molecules [264-266]. In my group, Dr. Ciaran O Reilly reported that macrocycles with an embedded carbohydrate (MEC) which enables at least three pharmacophoric groups to be grafted to the scaffold. Selectivity towards particular isoforms of target receptors can then be improved by the nature of the pharmacophoric groups. This has been

rationalized by molecular modeling using newly generated homology models of the target receptors.

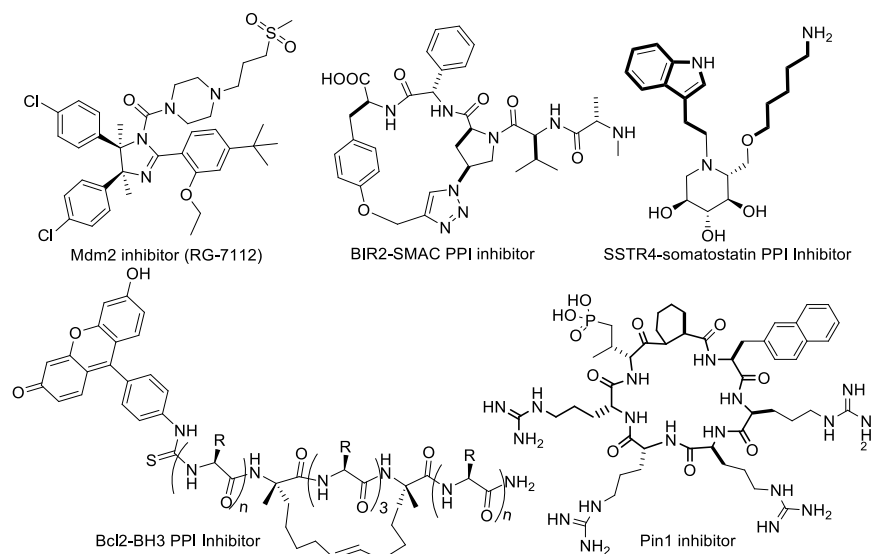


Figure 18 PPI inhibitors: (a) heterocycle based Mdm2-p53 PPI inhibitor RG7112 [267], (b) macrocyclic inhibitor of BIR2-SMAC PPI [268], (c) Iminosugar based inhibitor of SSTR4-somatostatin PPI [269] (d) Stapled peptide inhibitor of Bcl2-BH3 PPI [270]; (e) cell-permeable inhibitor of peptidyl-prolyl isomerase Pin1 PPI [271]

3.2.2 Results and Discussion

3.2.2.1 Ligand design strategy

Previous work from our group led to the identification of eannaphane-40 (**Figure 22**), 40 as a ligand for a number of serotonin receptor isoforms. This compound presents two amino acid side chains, or their bioisosteres, on a macrocyclic scaffold which has embedded carbohydrate (MEC) and triazole residues. Eannaphane-40 was found to induce apoptosis in leukemic cells, due to, at least, partial 5-HT₂ antagonist activity [272].

To further investigate, retro screening (or reverse screening) of eannaphane-40 against 55 proteins was first carried out showed that eannaphane-40 inhibited various labeled ligands to bind to GPCR proteins and ion channels (**Figure 19**) at 10 mM concentration. It showed >50% inhibition for eighteen of these proteins with highest inhibition observed for the sodium channel and NK-2 receptor and good affinities for a range of serotonin receptor isoforms/serotonin transporter. The K_i and IC_{50} values were therefore obtained for eannaphane-40 against these receptors. The dose-response curves are shown in **Figure 20** & **Figure 21**. Despite its promiscuity as a ligand in the screen, eannaphane-40 displayed low μ M or sub μ Molar K_d values against serotonin receptor isoforms, the serotonin transporter, the sodium channel, and the NK₂ receptor (see **Table 6**). After this screening, a goal was defined to improve the ligand design which would serve to increase

selectivity towards specific protein receptors identified from the screen. This forms the main aim of the research work presented herein.

Hence, the preliminary synthetic work was extended to prepare MECs incorporating glucopyranose residues as well as galactopyranose, thus introducing stereochemical diversity into the macrocycle scaffold as shown in **Chart 1**. Improved selectivity was investigated using a MEC which has two embedded carbohydrates, where an additional pharmacophoric group is incorporated (encoded in red color in **Figure 22**). The saccharides in the scaffold could be considered as some of the saccharides in glycans presented on glycoproteins or glycolipids at the cell membrane in that the latter also can be considered to have scaffolding roles [273-275].

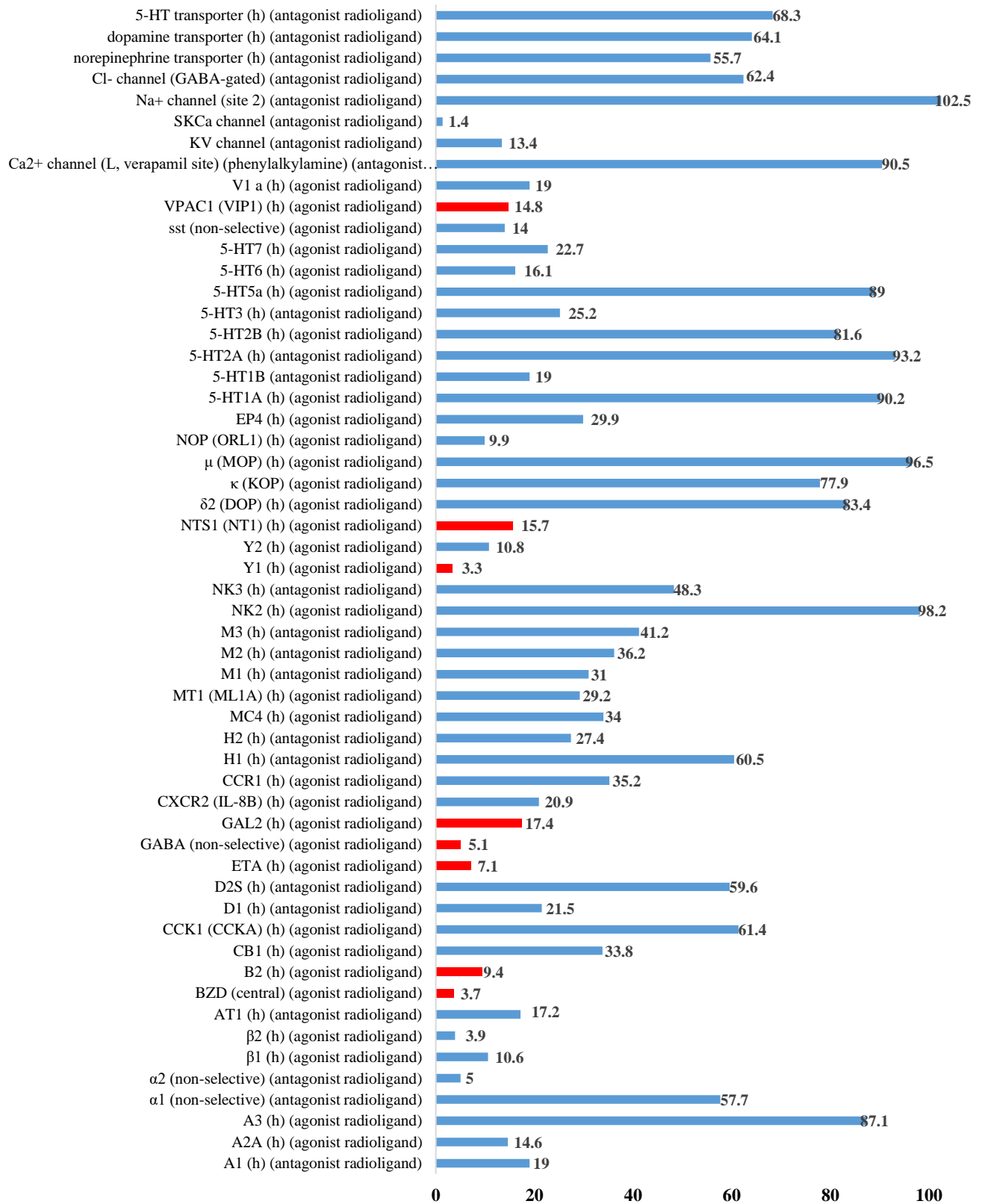


Figure 19 Inhibition (blue columns, % values provided) and stimulation of ligand binding (red bars, % values provided) by E40 (10 μM) in binding assays with 55 target proteins.

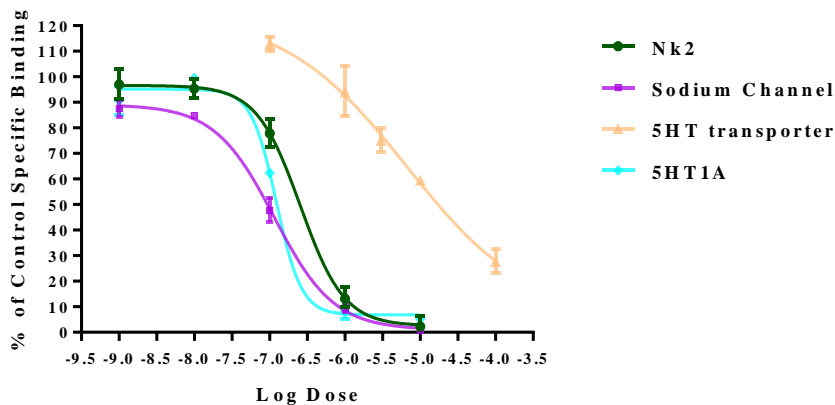


Figure 20 Dose-response curve (DRC) for eannaphane-40 against the NK₂ receptor, the sodium channel, 5HT-transporter and 5HT_{1A}

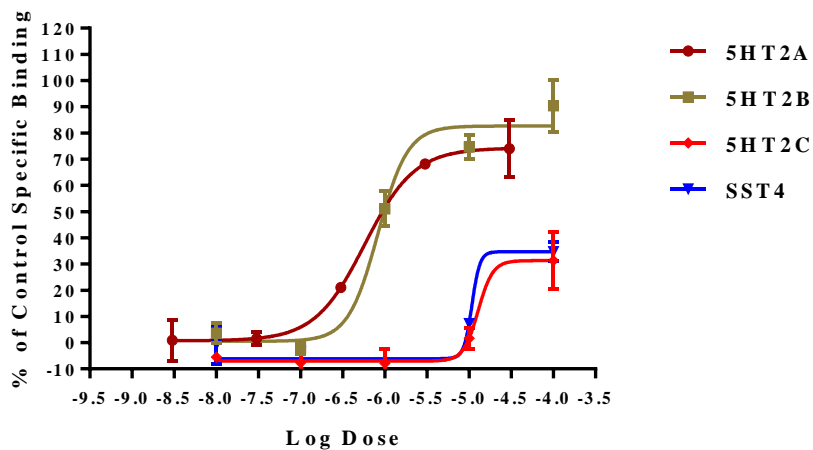


Figure 21 Dose-response curve for eannaphane-40 against 5HT_{2A}, 5HT_{2B}, 5HT_{2C} and the somatostatin receptor-4 (SST-4)

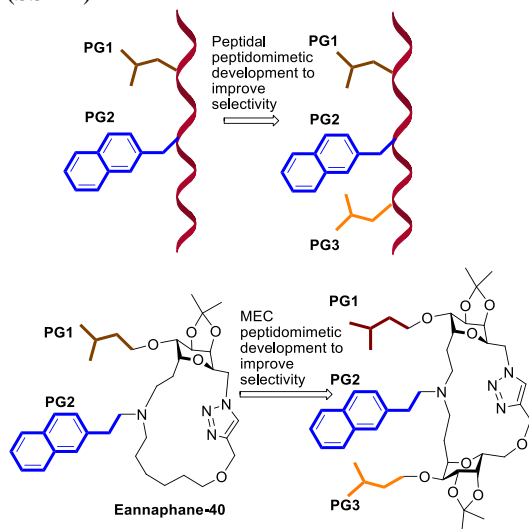


Figure 22 Ligand design strategy. One approach in peptidomimetic research is to incorporate an additional pharmacophoric group (PG), into a peptide to improve affinity/selectivity. Here an additional pharmacophoric group is incorporated onto a macrocyclic scaffold via an additional carbohydrate residue with a scaffolding role.

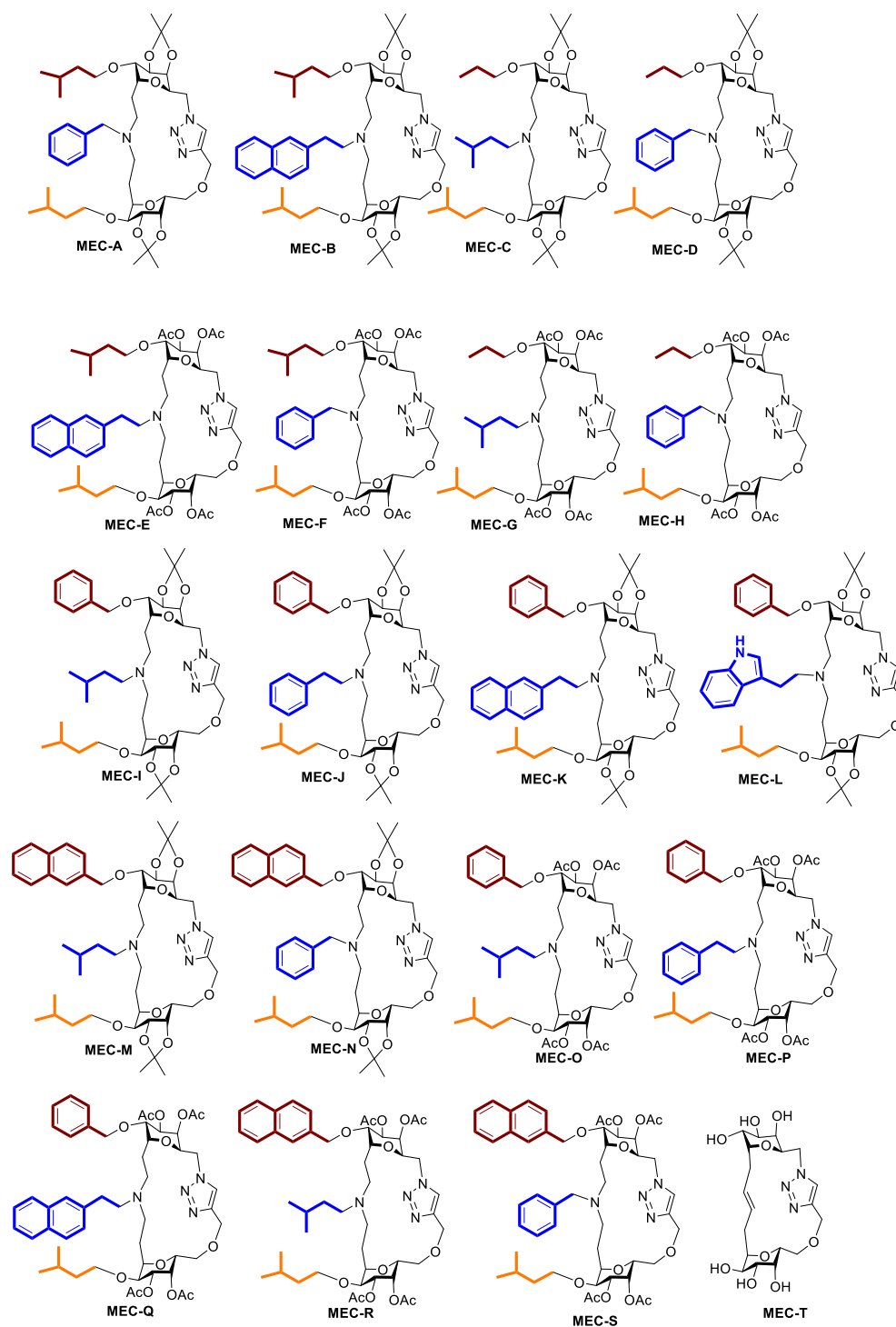


Chart 1. Structures of additional macrocycles synthesized

3.2.2.2 Molecular modelling, biological evaluation and validation of the ligand design strategy Homology modelling

The screening of eannaphane-40 against 55 receptor subtypes identified putative protein targets (**Figure 19-21**) for the synthesised MECs. Subsequently reverse docking [276-278] was performed

on the newly synthesized MECs against the selected targets of eannaphane-40 (serotonin receptors isoforms, serotonin transporter, Na Channel, NK₂ receptor) in order to identify if any of the compounds had an improved selectivity profile [279]. However, the 3D structure of only a few of the protein targets were available at the time of the writing of this thesis, and therefore homology modeling was needed to derive 3D structures for NK₂, 5HT_{1A} [280], 5HT_{2A} [281] and the sodium channel. For these four proteins, the sequences were retrieved from the national center for biotechnology information (NCBI) and a blast search was performed, in order to find a suitable template for the model building. This gave rise the following: for NK₂, an X-ray structure of *Drosophila* dopamine transporter bound to D-amphetamine was used [282]; for 5HT_{1A}, a crystal structure of the chimeric protein (*H. sapiens/E. coli*) of 5HT_{2B}-BRIL in complex with ergotamine was used [283]; for 5HT_{2A}, the crystal structure of the chimeric protein (*H. sapiens/E. coli*) of 5HT_{2B}-BRIL in complex with ergotamine was used [283]; finally for the Na⁺ Channel, the crystal structure of acid-sensing ion channel (*G. gallus / M. tener*) in complex with snake toxin and amiloride was used [284]. Later after the homology modeling, the structural consistency of the built homology models were assessed by examining a number of qualitative parameters, comparing the built model with their respective template structures as provided in **Table 4**.

The active site finder tool of MOE was implemented to identify the active sites in the homology models as shown in **Table 5**. In case of 5HT_{2A} and sodium channels, there are some reports disclosing the key information related to the active sites in these proteins. Kanagarajadurai *et al* reported the binding pocket of the ligand ketanserin [285] in their built homology model of 5HT_{2A}. Also, for the Na⁺ channel, the structural homology model was divided into 4 divisions (I, II, III, IV) with each division containing 6 segments. The veratridine binding site was located in segment 6 of division I (I-S6) and division IV (IV-S6) [286], shown in **Figure 23**. While, constructed Na⁺ channel model contains several outliers, most of them were distant from the veratridine binding segments, and these outliers were thus ignored. Attention was given instead to those amino acids which were in the proposed binding region of veratridine [286]. The binding region within 8 Å was truncated and further structural anomalies were analyzed by obtaining the Ramachandran plot and, the remaining outliers were minimized using the Amber 99 force-field.

Table 4. The parameters used for homology modelling and their qualitative analysis

		NK ₂	5HT _{1A}	5HT _{2A}	Na ⁺ Channel (Site 2) ^{δ*}
Template	<i>PDB_ChainNumber</i> ^f	2KS9_A ^ε	4IAR_A	4IB4_A	4NTX
	<i>Resolution (Å)</i>	<i>na</i>	2.70	2.70	2.27
	<i>Identity (%)</i>	54.44	41.00	55.05	55.35
	<i>Similarity (%)</i>	46.00	41.60	45.00	47.0
	<i>Coverage (%)</i>	85.00	91.00	69.00	83.00
RMSD ^g (Å)		0.503	0.954	1.065	0.468
Ramachandran plot	<i>Residues in most favoured regions (%)</i>	89.0	92.4	92.3	92
	<i>Residues in additional allowed regions (%)</i>	9.7	7.0	7.0	7.4
	<i>Residues in generously allowed regions (%)</i>	1	0.6	0.3	0.6
	<i>Residues in disallowed regions (%)</i>	0.3*	0	0.3*	0
ProSA	<i>Homology model</i> ^h	-4.33	-4.62	-4.05	-6.81
	<i>Template</i> ^h	-1.60	-4.52	-4.52	-7.43
Errat	<i>Homology model</i>	85.065	95.935	94.915	84.343
	<i>Template</i>	54.903 ^h	93.966	82.036	89.258

^f PDB codes used from RCSB-PDB ^εNMR Solution structure; ^g Calculated RMSD of superposing the homology model and their respective templates; ^h Z-Score; *0.3 indicate Asp278 (NK₂) and Asn233 (5HT_{2A}) in transmembrane loops (shown in supplementary information) and further minimization would be trivial; ^hNMR solution protein conformation; ^{δ*} only site 2 amino acid patch was evaluated against these parameters; Identity, tells how many amino acids are same in both the target sequence and template sequence; Similarity, tells how many similar type amino acids are in present both the target sequence and template sequence; Coverage, tells how much sequence of target is covered by template sequence.

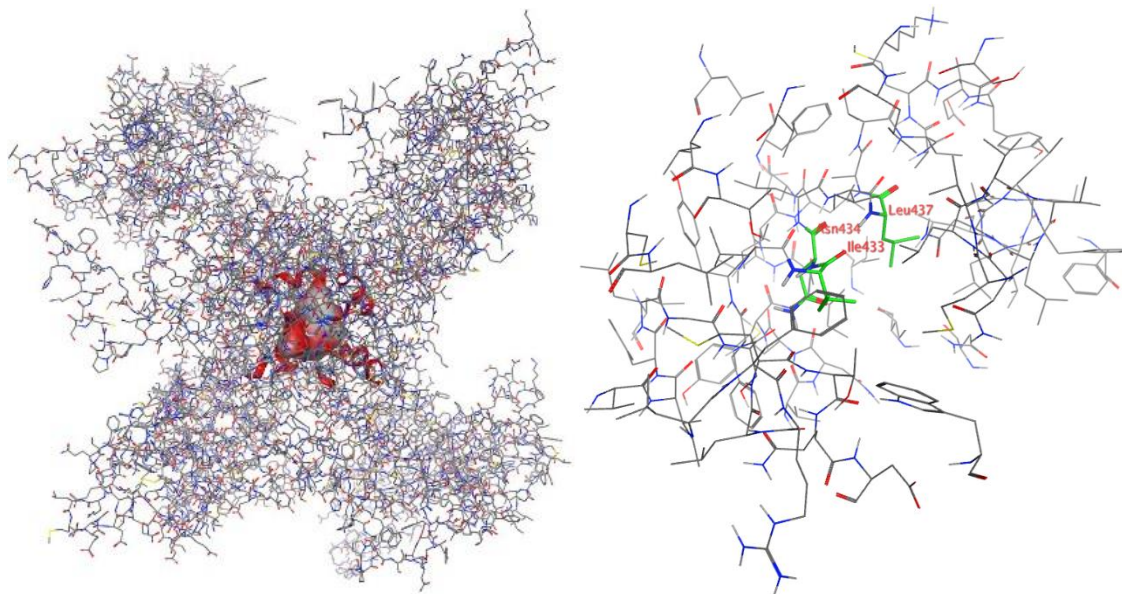


Figure 23 The surface defining the active site shown on the left is site 2 of the constructed homology model of the sodium channel with all atoms of protein shown. On the right, the extended active cavity of site 2 of sodium channel shows the key amino acid residues Ile433, Asn434 and Leu437 of the Division I segment 6 of the sodium channel. It also shows the binding of veratridine.

Table 5 The active patches allocated by active site finder on the proteins.

Protein	Site	Size	PLB	Hyd.	Side	Residues in the active patch
5HT _{1A}	1	251	4.04	89	131	Val31 Tyr35 Gln36 Thr39 Leu42 Leu43 Leu46 Ala93 Tyr96 Gln97 Val98 Asn100 Phe112 Ile113 Asp116 Val117 Cys120 Thr121 Ile124 Ile167 Cys187 Thr188 Ile189 Ser190 Lys191 Tyr195 Thr196 Ser199 Thr200 Ala203 Trp358 Phe361 Phe362 Val364 Ala365 Leu368 Pro369 Ser374 Cys375 His376 Met377 Pro378 Thr379 Leu380 Leu381 Gly382 Ala383 Ile384 Ile385 Asn386 Trp387 Leu388 Tyr390
5HT _{2A}	1	211	3.44	72	109	Val130 Ser131 Leu133 Thr134 Ile135 Tyr137 Gly138 Tyr139 Arg140 Trp141 Pro142 Trp151 Ile152 Asp155 Val156 Ser159 Thr160 Ile163 Ile206 Ser226 Cys227 Leu228 Leu229 Ala230 Asp231 Phe234 Val235 Gly238 Ser239 Ser242 Trp336 Phe339 Phe340 Asn343 Ala346 Glu355 Asp356 Ile358 Gly359 Leu362 Asn363 Val366 Trp367 Tyr370
5HT _{2B}	Ligand Binding Site					
5HT _{2C}						<i>Not active</i>
NK ₂	1	140	3.78	40	65	Glu9 Ala10 Asn11 Pro16 Glu17 Ser18 Asn19 Thr173 Met174 Asp175 Gln176 Gly177 Ala178 Trp185 Pro186 Glu187 Asp278 Ile279 Tyr280 Lys283 Phe284 Ile285 Gln286 Tyr289 Leu290
Na ⁺ channel	3	155	3.79	55	92	Thr378 Gln379 Asp380 Tyr381 Trp382 Glu383 Ser409 Phe410 Val413 Asn414 Leu417 Cys944 Gly945 Glu946 Met971 Asn975 Leu976 Leu979 Asn980 Leu983 Ala1420 Thr1421 Phe1422 Lys1423 Ser1462 Phe1463 Leu1466 Asn1467 Ile1470 Thr1713 Ser1714 Ala1715 Phe1764 Val1768 Asn1769 Tyr1771 Ile1772
Serotonin Transporter	Ligand Binding Site					

Inverse docking

All the MECs described herein were evaluated by inverse docking [279] against 6 proteins (4 homology models and 2 crystal structures from protein data bank). This methodology involves docking of the MECs against a set of the pre-evaluated targets, which in my case were already verified from the screening of eannaphane-40 (**Figure 19-21**). Initially, binding energies for every MEC synthesized for these proteins were calculated. Then these binding energies were compared among these proteins especially for 5HT_{1A}, NK₂, and Na-channel as these receptors showed submicromolar affinities for eannaphane-40 compared to other proteins (see **Table 6**). In order to evaluate their selectivity against 5HT_{1A}, NK₂ and the Na-Channel, a heuristic statistical approach was used, which involved generating a *preferential selectivity indicator*, defined as the ratio of an average mean of the binding energy of first 10 docking pose of individual MECs with a particular protein to the average mean of the binding energy of first 10 docking pose of same MECs with another protein. This methodology provided preferential selectivity indicators for particular MECs

among the targeted proteins of interest. Additionally, repetition of this methodology is repeated again by using another docking method (alpha triangle placement) [287]. Therefore for every protein vs protein comparison for a particular MEC, two different color codes were generated. Each corresponds to one of the docking methods, as shown in **Figure 24**. The line chart (**Figure 24**) provides an indication of the predicted selectivity of the synthetic compounds to these targets. It was thus predicted that MECs such as **MEC-B**, **MEC-J**, **MEC-M**, **MEC-Q** and **MEC-R** could potentially display improved selectivity among these proteins. Eannaphane-40 was chosen as a standard (control) during these docking experiments and the docking was found to predict the same pattern as, was found from the protein affinity screening (Na^+ channel/ 5HT_{1A} > Na^+ channel/ NK_2 > 5HT_{1A} / NK_2 , see **Table 6**). According to the Lipinski rule of five, the polar surface area should be less than 140 \AA^2 and compounds **MEC-Q** and **MEC-R** were not compatible with this. As observed, the line chart difference for compounds, **MEC-B** was found comparatively better than the remaining ones, therefore, used it for further biological evaluation, and the results are shown in **Table 6**, **Figure 31** & **Figure 32**.

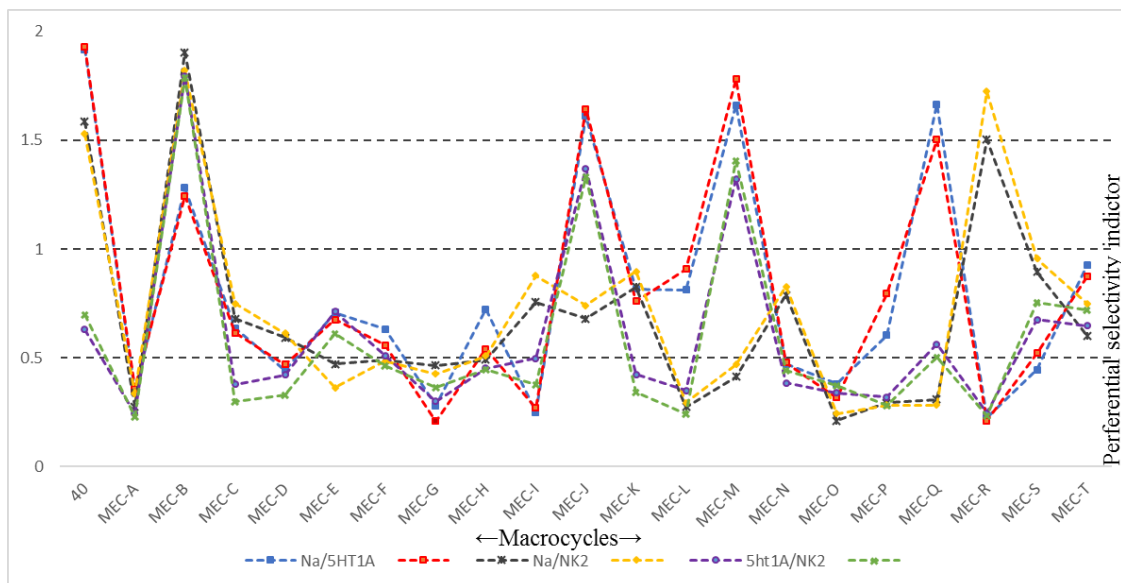


Figure 24 Line chart diagram representing MECs (on x-axis) and preferential selectivity indicator or index (on Y-axis). The preferential selectivity indicator (or index, PSI) is the ratio of calculated average binding energy for the 10 lowest energy docking poses of a MEC to a defined protein (e.g the Na channel) divided by the average of 10 docking poses energies of the same MEC for another defined protein (e.g 5HT_{1A}). This was done using two different docking methods for every MEC and protein combinations. The sodium channel: 5HT_{1A} PSI is shown with blue and orange dashed lines, that of Na-channel: NK_2 as grey and yellow dashed lines; that of 5HT_{1A} : NK_2 as violet and green dashed lines. A ratio of “1 or close to 1” indicates that the two proteins have similar docking binding energies and therefore that particular MEC would not have any preferential selectivity for either protein. However, a PSI value of >1 or <1 predicts selectivity. Also, any value less than 0.5 or greater than 1.5 shows higher preference for that particular protein. In order to validate the method, eannaphane-40 was used as a control for these experiments and it showed a similar

calculated binding energy trend as was attained from experimentally measured IC_{50} values trend for (i.e. Na-Channel:5HT_{1A} > Na-channel/NK₂ > 5HT_{1A}/NK₂).

The reverse docking experiment also generated the docking poses for these MECs with these proteins. Known potent inhibitors and drugs were also used in the docking with these proteins.

Docking of control inhibitors

The docking commenced with the serotonergic isoform 2A (5-HT_{2A}) and 2B (5-HT_{2B}). The coordinates for 5-HT_{2A} were used from its homology model [288] and for 5-HT_{2B}, a PDB was available on RSCB-PDB (4NC3, resolution 2.80Å) [289]. The consistency of the constructed 5HT_{2A} homology model was validated by comparing, the ketanserin docking interactions with the previously reported data [285] wherein case, found ketanserin utilizes similar binding conformation shape with respect to active site of 5HT_{2A} which contains Phe339, Phe340, Tyr370, and Val366 as hydrophobic residues and Asp155 as a hydrophilic residue. The ketanserin docking also showed parallel and T-shaped π - π interactions with Phe340 (3.88 Å) and Phe234 (4.20 Å) respectively. While the protonated nitrogen atom has a H-bond donor interaction with Asp155 (2.01 & 2.15 Å). Furthermore, docking of eannaphane-40 and **MEC-B** showed similar orientations of binding poses as shown in **Figure 25**.

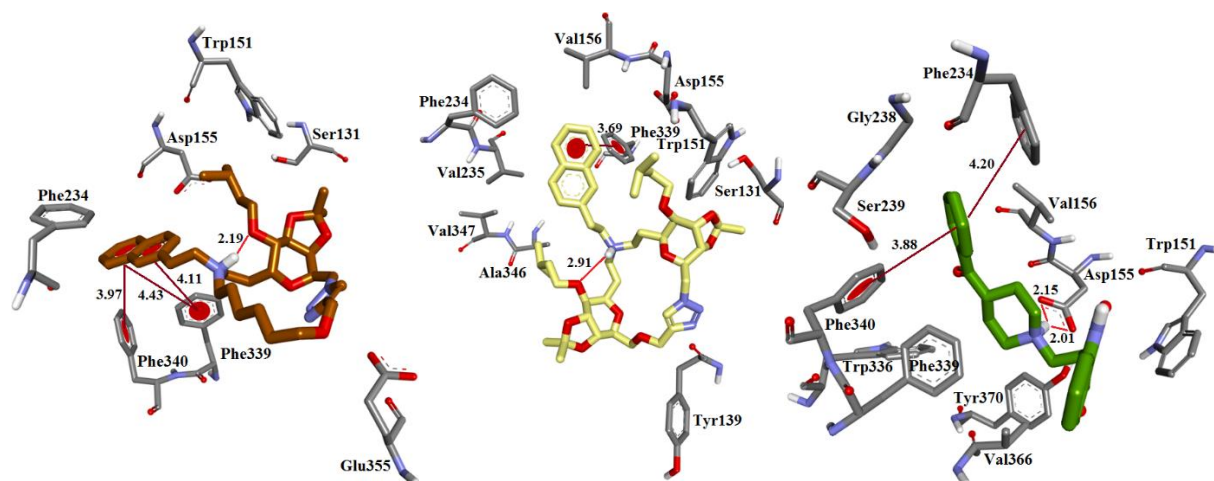


Figure 25 Interactive poses of eannaphane-40 (brown), **MEC-B** (yellow), ketanserin (green) with the active binding site of 5-HT_{2A}: eannaphane-40 showed π - π interaction with Phe340 (3.97 Å) and Phe339 (4.11 & 4.43 Å), while **MEC-B** showed π - π interaction with Phe339 (3.69 Å). Both showed intramolecular H-bonding between protonated nitrogen atom to the oxygen atom bonded to the isopentyl group.

Similarly, in 5HT_{2B}, key aromatic amino acids were identified in the cavity (Phe340 & Phe341) which assisted the ligands (mesulergine, eannaphane-40 and **MEC-B**) to adopt the binding conformations through π - π interactions. Additionally, mesulergine also showed a H-bond donor interaction with Asp135, as shown in **Figure 26**.

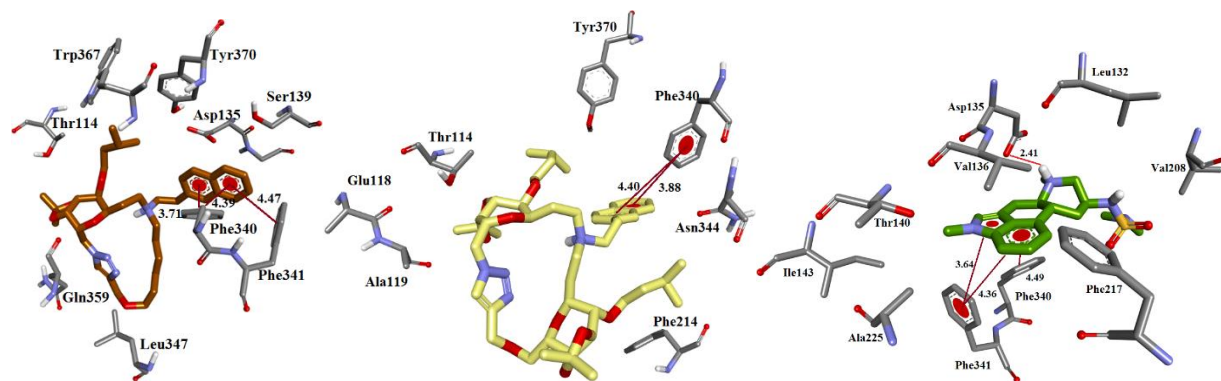


Figure 26 Binding interactions of eannaphane-40 (brown), **MEC-B** (yellow) and mesulergine (green) with active site of 5-HT_{2B}. Eannaphane-40 showed π - π interactions with Phe340 (3.71 & 4.39 Å) and Phe341 (4.47 Å), while **MEC-B** also shows π - π interactions with Phe340 (3.88 & 4.40). Also, mesulergine shows π - π interactions with Phe341 (3.64 & 4.36 Å), Phe340 (4.49 Å) and has H-bond donor interaction with Asp135 (2.41 Å).

In order, to see how 5-HT_{2A/2B/2C} are interrelated structurally a multi-sequence alignment (MSA) study was conducted (as shown in **Figure 27**), where conserved amino acid patches and point mutations among these isoforms were identified. From the MSA, the following conclusions were drawn: (i) 5HT_{2A} has a sequence identity of 43% with 5HT_{2B} and 54% with 5HT_{2C}; This showed a close evolutionary link between 5HT_{2A} with 5HT_{2C} in comparison to 5HT_{2B}; (ii) the amino acid sequence of 5HT_{2A}, which ranges from 211 to 228 and 291-293 show disordered regions, indicating higher degree of flexibility in these loops; (iii) The missing complementary amino acid (**X**) in ⁵⁹G⁵¹G**X** and ³⁵²S**X**³⁴⁰S of 5HT₂ subtypes C and B respectively, are proximal to the active site and probably altering the overall structure and could be further used for selective targeting of these isoforms in the future.

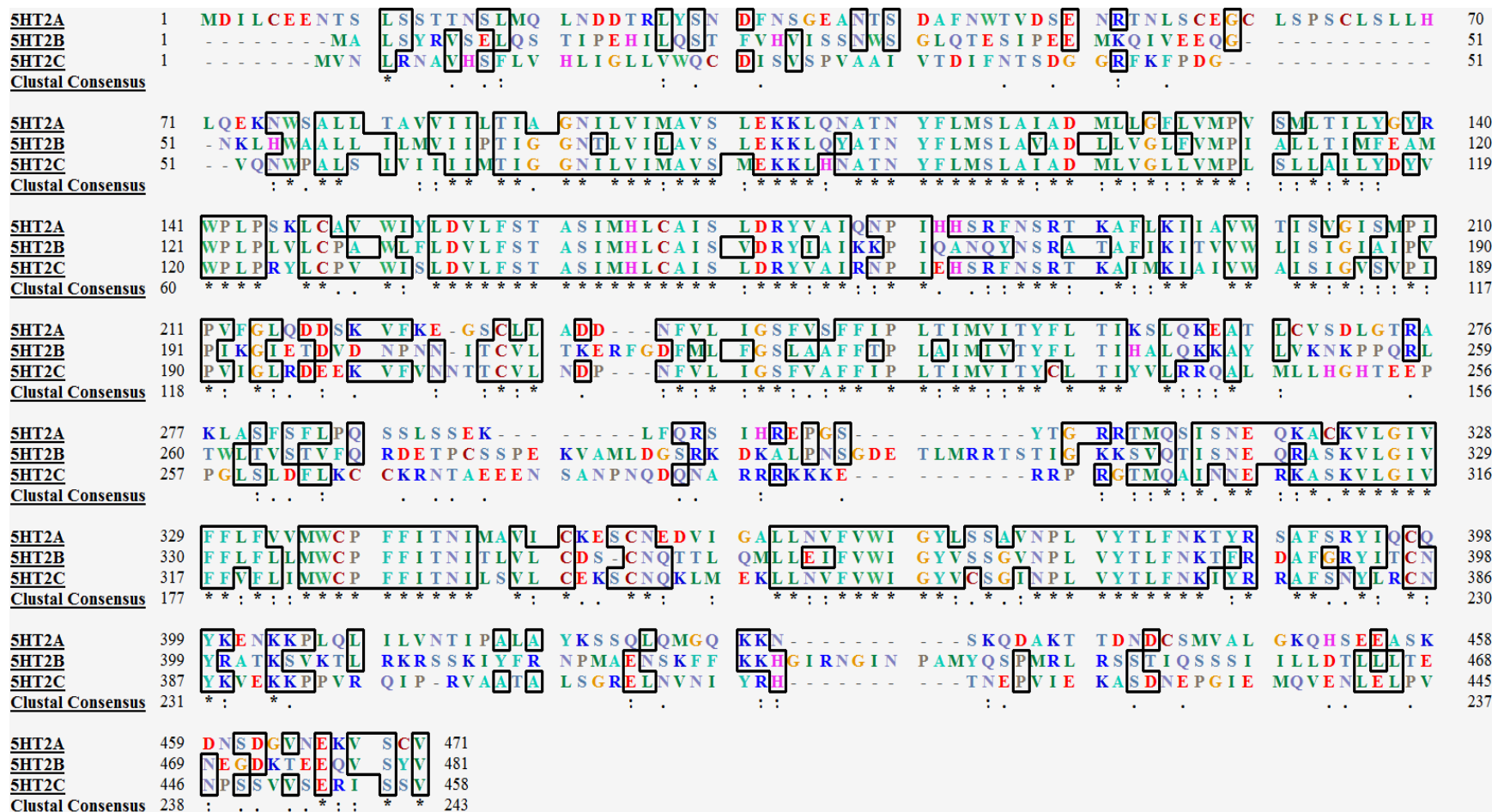


Figure 27 Multiple sequence alignment (MSA) of 5HT₂ isoforms, compared to the built homology models

In the case of 5HT_{1A}, the docking pose of **8-OH DPAT** ligand along with eannaphane-40 and **MEC-B** is shown in **Figure 28**. The docking of Eannaphane-40 showed comparatively similar binding to **8-OH DPAT**. Even, their interactive mode seems quite similar, as eannaphane-40 shows π - π interactions with Tyr66 (4.11 Å), H-bond acceptor interactions with the backbone of Ile159 (2.07 & 2.46 Å), while, **8-OH DPAT** ligand shows π - π interactions with Phe331 and H-bond donor interactions with side chain of Asp85 (1.98 & 3.0 Å). However, **MEC-B** showed a distinctive binding in comparison to Eannaphane-40 and **8-OH DPAT** and interacted via H-bond interactions with the guanidine of Lys161 (2.34 Å) and backbone (-NH-) of Ile159 (2.09 Å). Also, it showed an intramolecular interaction, which might possibly lead to its different binding orientation.

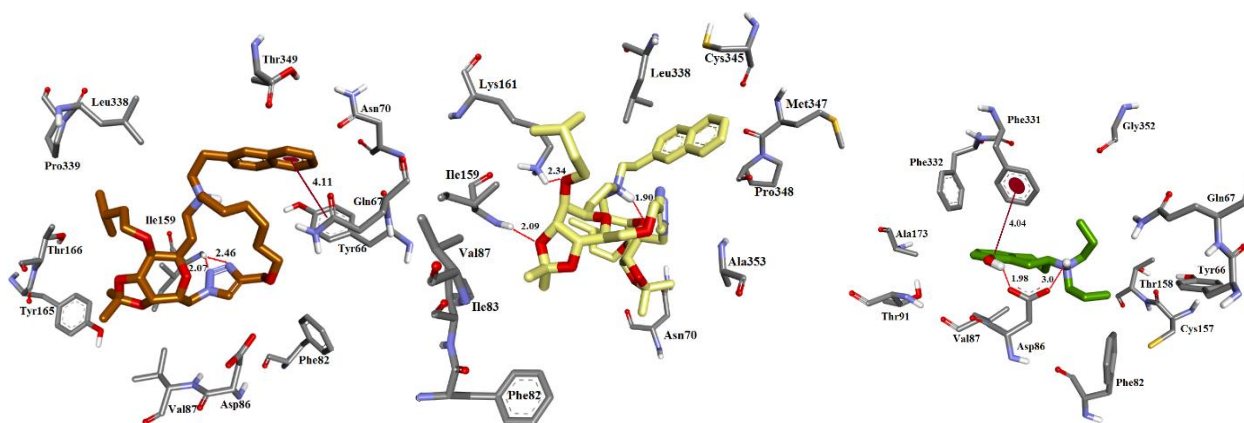


Figure 28 Binding interactions of eannaphane-40 (brown), **MEC-B** (yellow) and **8-OH DPAT** (green) with the active binding site of 5-HT_{1A}.

Similarly, in NK₂, an intramolecular interaction in **MEC-B** have seen when compared to the binding pose of eannaphane-40 and therefore possible reasoning of showing a difference in its binding conformation orientation, which can be further seen in **Figure 29** where both co-docked poses of eannaphane-40 and **MEC-B** are captured together.

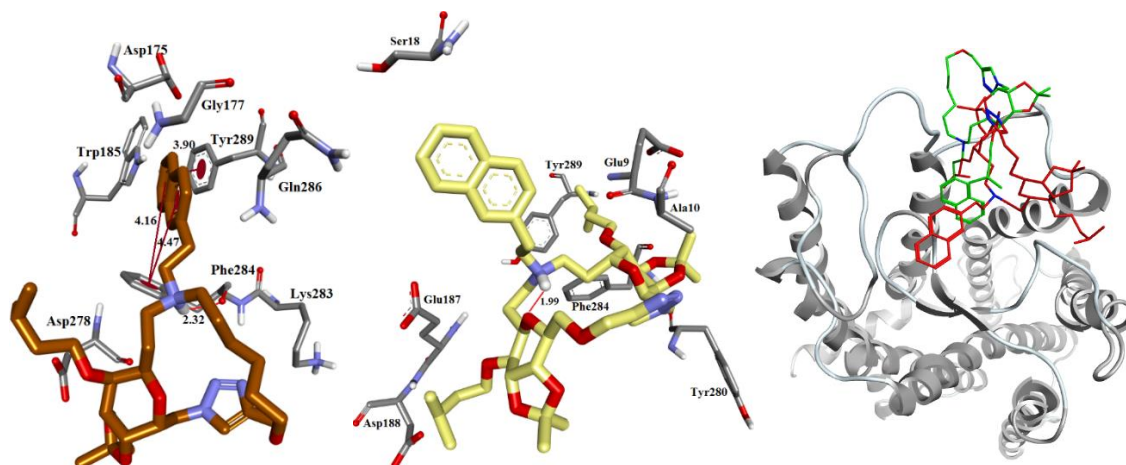


Figure 29 Interactive poses of eannaphane-40 (brown) **MEC-B** (yellow) and co-docked poses (eannaphane-40 as in green & **MEC-B** is in red) with active binding site of NK₂: Eannaphane-40 showed a π - π interaction with Phe284 (4.16 & 4.47 Å) and Tyr289 (3.90 Å), while MEC-B has intramolecular H-bond interaction (1.99 Å).

In sodium channel, binding interactions for **MEC-B** were different to those of eannaphane-40 which has two π - π interactions with Phe1775 and Phe1442 *via* its triazole backbone (3.99 Å & 4.47 Å). While, veratridine found multiple H-bond donor/acceptor interactions, as shown in **Figure 30**. However, presence of Ile433, Asn434 and Leu437 in all these ligand binding poses also indicate that these ligands share a common binding pocket which is located in segment 6 of division I (I-S6) and division IV (IV-S6) [286] of sodium channel, as shown in **Figure 30**.

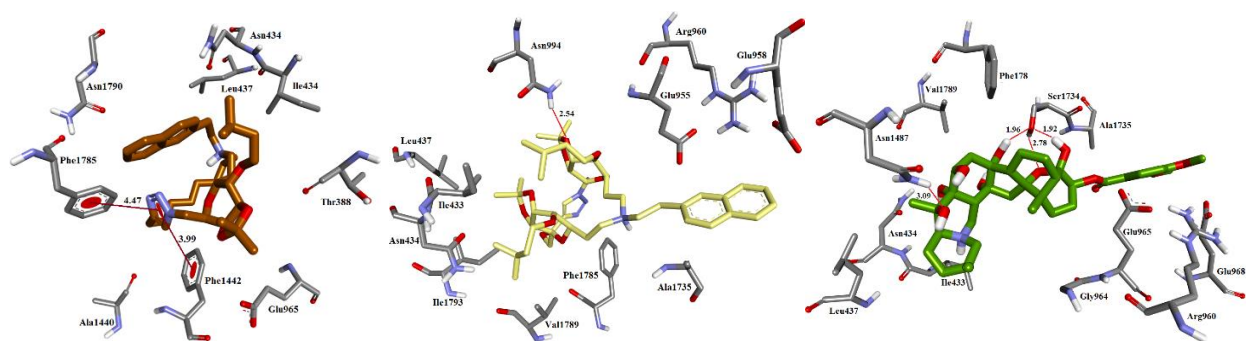


Figure 30 Interactive mode of eannaphane-40 (brown), **MEC-B** (yellow) and **veratridine** (green) with active binding site (site-2) of sodium channel.

The bioassays for **MEC-B** were performed, and these showed preferential selectivity to the 5HT_{1A} isoform as well as to the sodium channel over eannaphane-40 compared to the other receptors studied. The data in **Table 6** shows that **MEC-B** retained the activity towards the serotonergic isoform 5HT_{1A} (≤ 1.4 times that of eannaphane-40) while for the other receptors it was reduced in potency or affinity completely vanished as for the serotonin transporter.

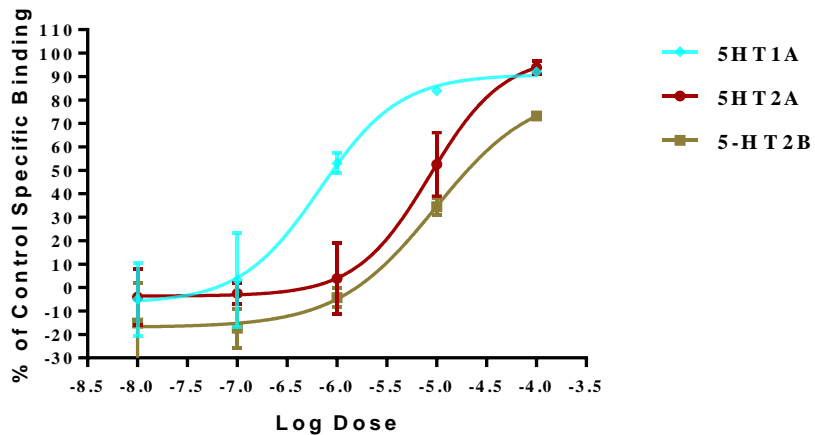


Figure 31 Dose Respons Curve for MEC-B against serotonin isoforms (5HT_{1A}, 5HT_{2A}, 5HT_{2B})

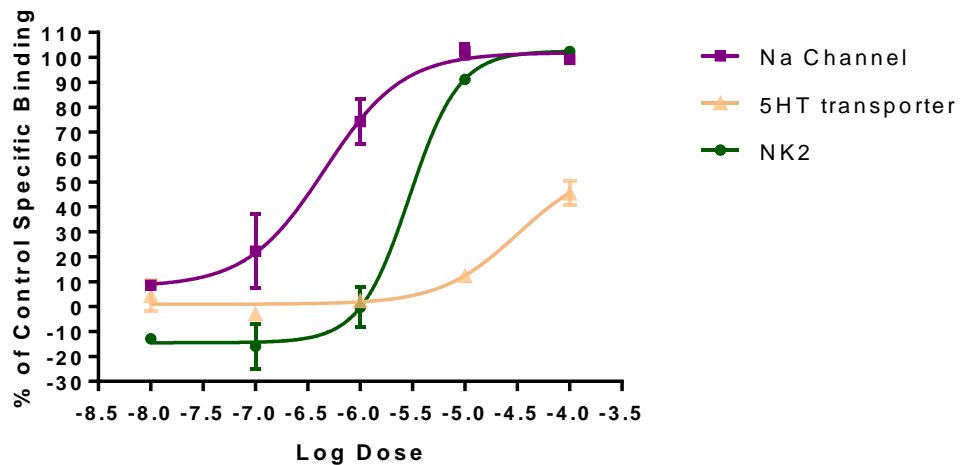


Figure 32 Dose Response Curve for MEC-B against the sodium channel, serotonin transporter and NK₂ receptor.

Table 6 Binding assay data

Proteins	Eannaphane-40 (Ki μ M)	MEC-B (Ki μ M)	Eannaphane-40 (IC ₅₀ μ M)	MEC-B (IC ₅₀ μ M)	Affinity ratio [§] (MEC-B:E40)	Affinity ratio [£] to 5HT _{1A}	Inhibitor used as reference control	Reference Compounds	
								Affinity	IC ₅₀
NK ₂ (<i>h</i>) (agonist radioligand)	0.14	1.6	0.26	3.0	11.43	3.81	[Nleu10]-NKA (4-10)	1.4nM	2.7nM
5-HT _{1A} (<i>h</i>) (agonist radioligand)	0.31	0.42	0.49	0.68	1.35	1.00	8-OH-DPAT	0.18nM	0.28nM
5-HT _{2A} (<i>h</i>) (antagonist radioligand)	0.97	4.7	1.8	8.7	4.85	11.19	Ketanserin	0.45nM	0.82nM
5-HT _{2B} (<i>h</i>) (antagonist)	0.87	8.2	1.6	15	9.43	11.52	Mesulergine	2.8nM	5.2nM
5-HT _{2C} (<i>h</i>) (antagonist radioligand)	>100	-	>100	-	<i>na</i>	<i>na</i>			
Na ⁺ channel (site 2) (antagonist radioligand)	0.1	0.41	0.12	0.46	4.1	0.98	Veratridine	8.1 μ M	8.9 μ M
5-HT transporter (<i>h</i>) (antagonist radioligand)	3.4	> 100	7.4	> 100	> 29.41	na	Imipramine	1.9nm	4.1nM

[§]ratio of Ki values. Comparative data shows improvement in affinity than the previous molecular scaffold

[£]5HT_{2A} affinity improvement over other receptor isotopes

3.2.3 Conclusion

This work presented a systematic design of MECs suitable for multi-targeting of receptors. The MECs contains 3 functional epitopes or pharmacophoric groups could be exploited further to modulate the target selectivity against a wide variety of GPCR and ion channels. Studies also found **MEC-B** as a new dual inhibitor of Na-channel and 5-HT_{1A} when compared to NK₂, 5-HT_{2A/2B} and serotonin transporter. Also, it has been observed in docking to serotonin isoforms that the naphthalene pharmacophore, found in eannaphane-40 and **MEC-B**, was involved in interacting with evolutionally conserved aromatic amino acids of these isoforms, as found for 5HT_{2A} (Phe239 and Phe240), 5HT_{2B} (Phe340 and Phe341) and 5HT_{1A} (Phe361 and Phe362). Also, performed homology modeling for four receptors (NK₂, 5-HT_{1A}, 5-HT_{2A}, site-2 of the sodium channel) which were complying with the previously reported models and evaluated them against qualitative structural tools, in order to warrant their correctness.

Chapter 4

This chapter mainly belongs to the biophysical studies of various proteins. The main studies that were performed in this chapter were:

- 1) Homology modeling and qualitative analysis of these models
- 2) The implication of various docking strategies
- 3) Studies of the various biophysical parameter in relation to their protein affinity (K_d values)

The main objective of this chapter was to characterize the unknown structures of the proteins which were highly underestimated and understudied in time. As my group mainly focuses on the characterization of the carbohydrate-based scaffold molecule design against a wide variety of proteins, therefore I limited my studies to the somatostatin proteins and fucosidase enzymes.

Thus, this chapter was divided into two parts, based on the objectives:

Objective 4.1 To increase understanding of ligand-based design for somatostatin receptors

Objective 4.2 To rationalize the targeting of D-fucose analogs with fucosidases of various origin

Objective 4.1 To develop a proper understanding of ligand design for somatostatin receptors

4.1.1 Introduction

The human somatostatin receptors (SSTRs) belong to the G-protein coupled receptors (GPCRs) and have 5 isoforms (SSTR-1 to 5), which closely resemble each other in structural homology and functional efficacy [290-293]. Their high structural resemblance is also linked to their synchronized roles in numerous cellular homeostasis and in several disorders, based on their tissue-specific isoform localization, as shown in **Figure 1**.

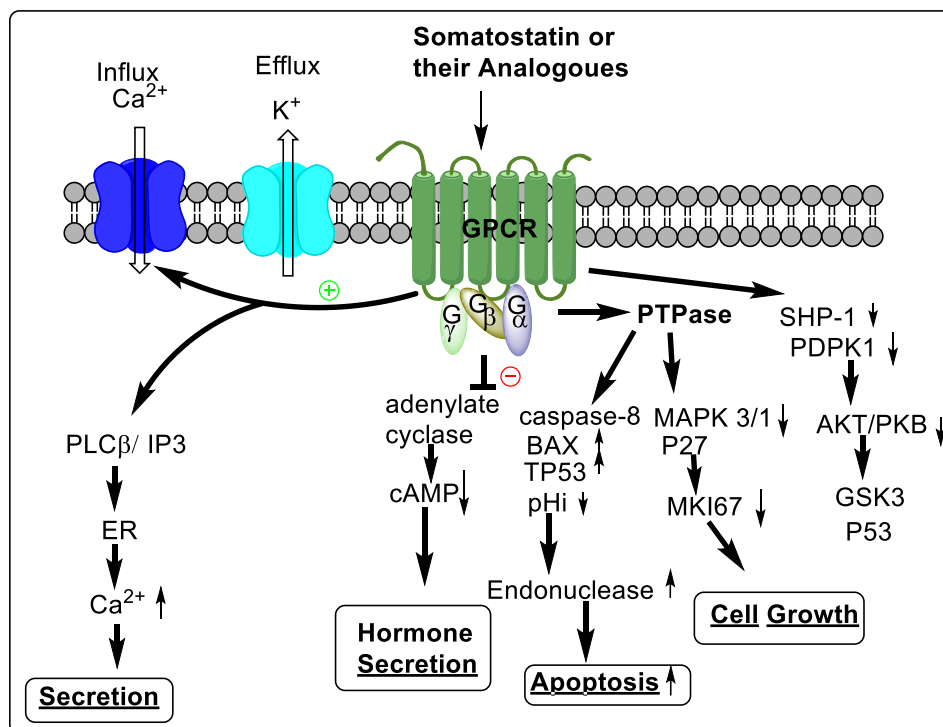


Figure 1 Signalling through SSRTs is multifaceted [294]: Somatostatin receptor (SSTR) binding to their receptors leads to (a) inhibition of adenylyl cyclase, (b) activation K channels and/or inhibits Ca-channels, (c) modulating the Phosphotyrosine phosphatases and mitogen-activated protein kinase, (d) increase in apoptosis via p53.

Additional interest has been placed in SSTR-4 and SSTR-5 in recent years. Agonism of SSTR-4 is believed to be relevant in Alzheimer disease [295], influencing memory strategies in the human brain [296]. Targeting SSTR-4 selectively also represents a promise for non-opioid pain control, the latter successfully shown by clinically studied agent J2156, which is a potent selective inhibitor of this target [297-299]. SSTR-4 is also believed to have a role in the migration of hepatic oval cells [300]. On the other hand, SSTR-5 has found roles in proliferation in pancreatic cancer [301], neuroendocrine tumors [302] and glucose homeostasis [303]. Therefore, the identification of compounds which have preferential selectivity or differential binding for these receptors is important and is tied in with the identification of agonists or antagonists and there are a number of

implications [304-306]. These receptors have not been crystallized to date and this hinders structure-based drug design for them. However, ligand-based design strategies, have established some key important features that a ligand should possess, to recognize these receptors. Accordingly, studies on the binding of somatostatins (SRIFs), especially its tetradecapeptide form (SRIF-14, see **Figure 2**) and its *N*-terminally extended peptide form (SRIF-28) with SSTRs, have indicated that tryptophan-8 (trp8) and lysine-9 (lys9) residues in these structures are recognized by all isomeric forms of SSTR, while phenylalanine-6 (phe6) is highlighted as being specifically important for SSTR-4 activation [307-312].

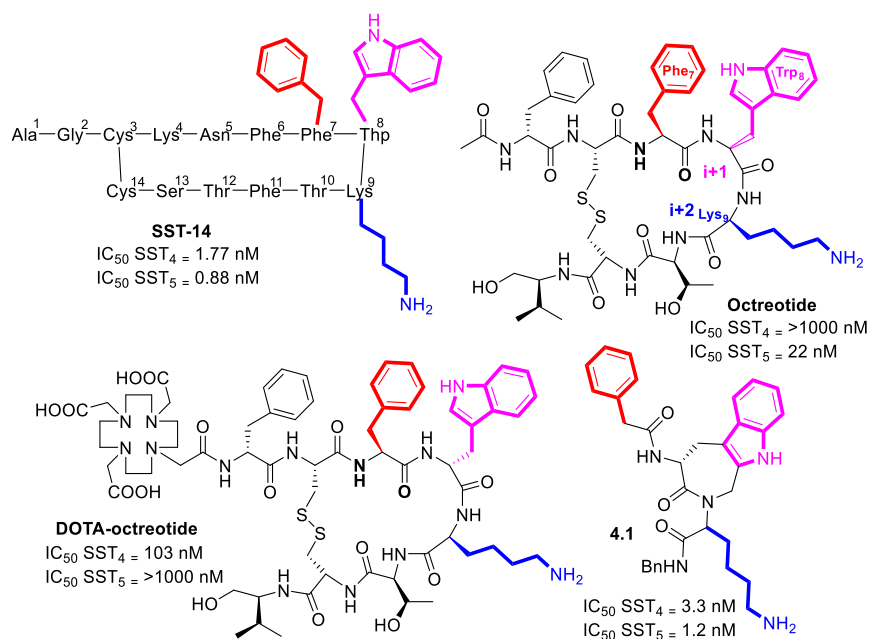


Figure 2 Structures of SST-14 and selected peptidomimetics with high binding affinities for SSTRs. Important pharmacophoric groups are shown in blue, purple and red.

To date, various non-peptide, and peptide analogs of somatostatin, with pharmacophoric groups have been synthesized and evaluated against SSTR-4 and SSTR-5, and their activity ranges from *nM* to *mM*; some of these molecules are shown in **Figure 2**. It is unclear why these molecules [313-319], have a varying degree of affinities. In this research, a set of peptidomimetics based on pyranose, iminosugar (multi-hydroxylated piperidine), macrocycle and peptidyl scaffolds were synthesized. To each scaffold was grafted pharmacophoric groups which are identical or bioisosteric to those found in amino acid sidechains (**Figure 3** and **Figure 4**). Two of these molecules have shown preferential selectivity for SSTR-4 over SSTR5. Docking to respective homology models of the proteins is included as part of this work.

4.1.2 Results and Discussion

Compounds designed to target SSTRs

Syntheses of some compounds used in this study has been reported earlier (see **Figure 2**) and these include the iminosugars [320-323], benzomacrolactones [324] and pyranoside **4.3** originally designed by *Hirschmann* and co-workers [325]. New compounds based on the pyranose ManNAc, the Eannaphane macrocycle, as well as acyclic/cyclic peptidyl scaffolds are shown in **Figure 3**. The basic design concept involved using the functional groups, inherent in the scaffolds, to graft pharmacophoric groups, and thus defining the points of attachment for amino acid side chains or their bioisosteres. For the pyranoses or iminosugars and benzomacrolactones, like **4.9** and **4.10**, these were inspired by natural product ring systems found in nature. Whereas **4.13** to **4.15** are not natural products, to the best of my knowledge, their core scaffolds can be considered to be ‘natural product-like’, in that they are chiral macrocycles and have functional groups found in natural products. The pharmacophoric groups were placed at distances from each other on the scaffolds approximating to those in SST-14. Thus, there are 3-5 bonds between atoms to where the pharmacophoric groups are attached. In addition, peptidyl mimetics **4.16** to **4.18** are included, which are similar in structure to octreotide.

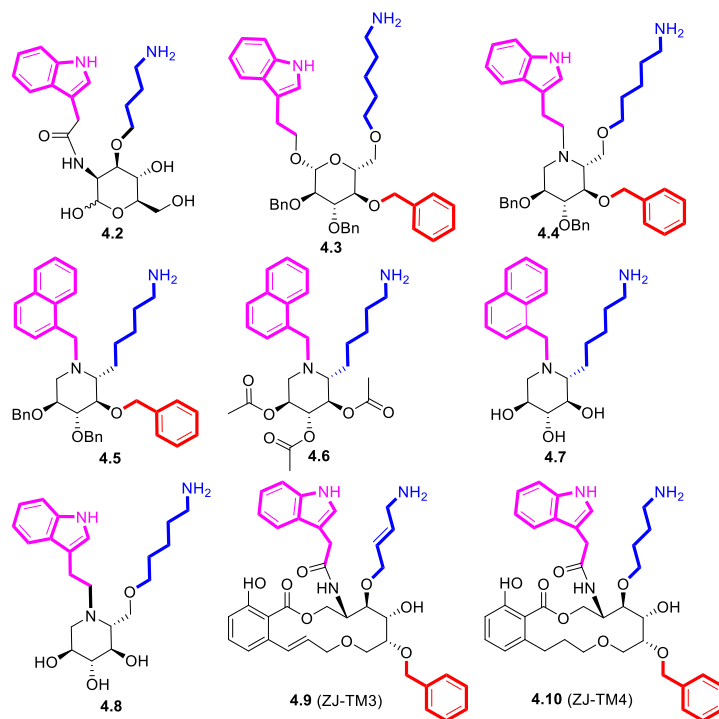


Figure 3 Structures of compounds previously synthesized *in-house* and Hirschman’s pyranoside **3**. The color codes are used to display the relevant amino acid side chain or their bioisosteres corresponding to those found to be important in somatostatin ligands.

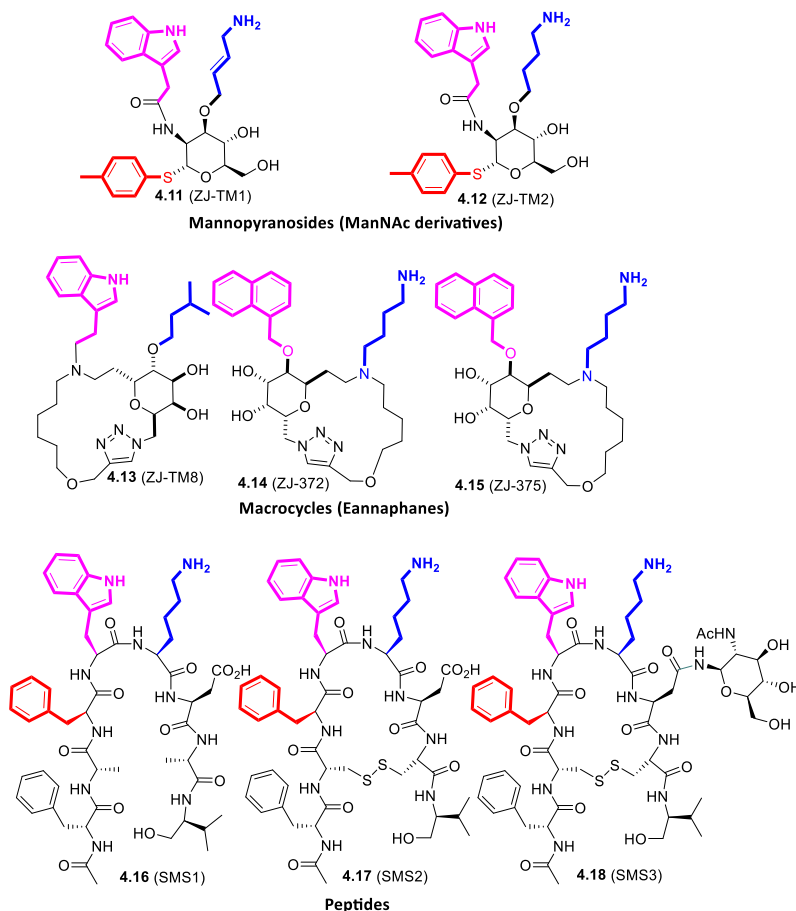


Figure 4 Structures of various new potential somatostatin mimetics included herein. The color codes are used to display the relevant amino acid side chains or their bioisosteres corresponding to those found important in somatostatin ligands.

Binding affinities, molecular modeling and structure-activity relationship

The binding affinity assays were performed against two somatostatin receptor isoforms (SSTR-4 and SSTR-5) and inhibitory constants (K_i) determined and these are shown in **Table 1**. Most of the molecules based on the different scaffolds displayed similar affinities, in most cases in the low micromolar range, for both isoforms with a limited number of exceptions where > fivefold selectivity differences were observed. The macrocycle **4.13** showed preferential selectivity for SSTR-5 over SSTR-4 while the iminosugar **4.8** had greater selective for SSTR-4 compared to SSTR-5. The iminosugar **4.7** and the glycosylated peptide **4.18** were the only agents which showed moderate preferential selectivity for SSTR-5 (**Table 1**). Iminosugar **2.7** differs from analogs **2.5** and **2.6**, which have similar affinities for both isoforms, in that **2.7** contains free hydroxyl groups. Peptide **2.18** differs only from **2.17** due to the presence of the GlcNAc residue linked via the asparagine and **2.17** displayed similar activity for both isoforms.

Table 1 Binding affinities (K_i) of peptidomimetics for SSTRs: SSTR-4 [326]: Binding studies were performed with cell membranes from transiently transfected COS-1 cells as described [327]. 10 μ g of membrane protein was incubated in 10 mM Hepes (pH 7.5), 5 mM. $MgCl_2$, bacitracin (20 μ g/ml), 0.5% bovine serum albumin, and 125I-labeled [Tyr11]-somatostatin-14 (30,000 cpm) with various concentrations of unlabeled somatostatin 14 (1 μ g) and compounds of interest for 2 hours at room temperature. Later, scintillation counting method was used for detection; SSTR-5 [328]: The SSTR-5 gene was cloned into pCMV6c expression vector [329] and transfected into COS1 cells. 20 μ g of membrane protein preparation was incubated in 500 μ L of Na^+ -free binding buffer (10 mM HEPES, 1% bovine serum albumin, 5mM $MgCl_2$, 1mg/ml bacitracin, pH 7.45) containing approximately 10 pM of [125I-Tyr11]-somatostatin-14 alone or with somatostatin-14 and compounds of interest at various concentrations for 2 hours at room temperature. Later, scintillation counting method was used for detection.

Somatostatin mimetic	Scaffold type	K_i , SSTR-4 (μ M)	K_i , SSTR-5 (μ M)	$logP$	LLE_{SSTR-4}	LLE_{SSTR-5}
4.2	Pyranose	>100	>100	-0.86	<i>n. a</i>	<i>n. a</i>
4.3 [325]	Pyranose	1.1	not available	7.79	-1.83	<i>n. a</i>
4.4	Iminosugar	4.4 \pm 0.89	5.0 \pm 0.66	7.58	-2.22	-2.27
4.5	Iminosugar	1.9 \pm 0.37	1.3 \pm 0.08	8.67	-2.94	-2.78
4.6	Iminosugar	5.4 \pm 0.60	5.1 \pm 0.91	2.89	2.38	2.40
4.7	Iminosugar	>100	23 \pm 1.39	1.57	<i>n. a</i>	3.06
4.8	Iminosugar	3.2 \pm 0.57	>100	0.48	5.01	<i>n. a</i>
4.9	Macrocycle	0.58 \pm 0.23	1.1 \pm 0.25	4.30	1.94	1.65
4.10	Macrocycle	1.9 \pm 0.41	3.2 \pm 0.71	4.48	1.24	1.01
4.11	Pyranose	2.1 \pm 0.26	3.9 \pm 0.23	2.33	3.34	3.08
4.12	Pyranose	6.8 \pm 1.02	12 \pm 1.35	2.38	2.79	2.54
4.13	Macrocycle	21 \pm 1.47	4.1 \pm 0.88	2.05	<i>n. a</i>	<i>n. a</i>
4.14	Macrocycle	>100	>100	2.50	<i>n. a</i>	<i>n. a</i>
4.15	Macrocycle	>100	>100	3.73	0.94	1.66
4.16	Peptide	>100	>100	5.65	<i>n. a</i>	<i>n. a</i>
4.17	Peptide	7.2 \pm 0.73	10 \pm 1.12	2.58	2.56	2.42
4.18	Peptide	20 \pm 1.77	3.4 \pm 0.52	5.87	-1.17	-0.40

Binding assays were carried out at CEREP (www.cerep.fr). LLE: Ligand Lipophilicity efficiency: linking potency and lipophilicity to estimate drug-likeness ($LLE = pK_i - logP$). [22, 330] *n. a* : not active/not applied.

In order, to hypothesize how the selectivities of these ligands might be influenced by scaffold and pharmacophoric groups, homology models of SSTR-4 and SSTR-5 were developed and utilized in docking. For the homology modeling, template-based modeling was implemented, which was based on accessed templates obtained from a BLASTp search as shown in **Table 2** and **Table 3**. A selection was made based on complementarity with respect to the sequences of SSTR-4 (from **Table 2**) and SSTR-5 (from **Table 3**). A protein sequence of the human delta opioid 7-transmembrane receptor (PDB: 4N6H [331], resolution = 1.80 Å, 48% sequence identity, 44.01% similarity, 72% coverage) was selected for SSTR-4 and a sequence of the nociceptin-orphanin FQ peptide receptor (PDB: 5DHH [332], resolution 3.0 Å, 41.76% sequence identity, 40.08% seq. similarity, 70% coverage) was selected for SSTR-5. These were retrieved from the Research Collaboratory for Structural Bioinformatics - Protein Data Bank (RCSB-PDB).

Table 2 Available templates for building the SSTR-4 homology model

Description	Query cover	E value	Ident.	PDB
1.8 A Structure of the human delta opioid 7TM receptor	77%	4e ⁻⁷⁶	45%	4N6H
Synchrotron structure of the human delta opioid receptor in complex with a bifunctional peptide	73%	2e ⁻⁷⁵	47%	4RWA
Crystal structure of active μ -opioid receptor bound to the agonist bu72	72%	5e ⁻⁷⁵	41%	5C1M
Crystal structure of nociceptin/orphanin fq peptide receptor (nop) in complex with c-35	72%	8e ⁻⁷⁰	44%	5DHG
Structure of N/OFQ opioid receptor in complex with a peptide mimetic	72%	1e ⁻⁶⁹	44%	4EA3
Structure of delta opioid receptor bound to naltrindole	74%	3e ⁻⁵⁷	47%	4EJ4
Structure of the human kappa opioid receptor in complex with jdtic	75%	3e ⁻⁵⁶	44%	4DJH
Crystal structure of μ -opioid receptor bound to a morphinan antagonist	70%	8e ⁻⁵³	43%	4DKL
XFEL structure of human angiotensin receptor	72%	2e ⁻⁴³	31%	4YAY
Crystal structure of human angiotensin receptor in complex with inverse agonist olmesartan	71%	4e ⁻⁴³	31%	4ZUD
Crystal structure of the human Cc chemokine receptor type 9 (CCR9) in complex with vercirnon	69%	9e ⁻³⁶	30%	5LWE

Table 3 Available templates for building the SSTR-5 homology model

Description	Query cover	E value	Ident.	PDB
Crystal structure of nociceptin/orphanin fq peptide receptor (nop) in complex with c-35	75%	2e ⁻⁶⁵	44%	5DHH
Structure of the N/OFQ opioid receptor in complex with a peptide mimetic	75%	3e ⁻⁶⁵	44%	4EA3
Structure of the human delta opioid 7-TM receptor	85%	3e ⁻⁵⁹	41%	4N6H
Synchrotron structure of human δ -opioid receptor in complex with a bifunctional peptide	82%	3e ⁻⁵⁹	41%	4RWA
Crystal structure of μ -opioid receptor bound to a morphinan antagonist	74%	6e ⁻⁴⁶	41%	4DKL
Structure of δ -opioid receptor bound to naltrindole	81%	1e ⁻⁴⁴	41%	4EJ4
Crystal structure of active μ -opioid receptor bound to the agonist Bu72	75%	8e ⁻⁶⁷	40%	5C1M
Structure of human κ -opioid receptor in complex with JDTC	82%	1e ⁻⁴²	37%	4DJH
XFEL structure of human Angiotensin Receptor	78%	3e ⁻³⁹	31%	4YAY
Crystal structure of human angiotensin receptor in complex with inverse agonist olmesartan	77%	1e ⁻³⁸	31%	4ZUD
Structure of apelin receptor in complex with agonist peptide	81%	8e ⁻³⁵	28%	5VBL

The built homology models were evaluated for structural consistency in a qualitative manner. Firstly, the RMSD value was compared between the homology model and the respective template. These were within acceptable limits (0.887 Å for SSTR-4 and 0.609 Å for SSTR-5, as shown in **Figure 5**). Next, Ramachandran plots were evaluated to investigate the geometry of amino acid residues in the homology models. For SSTR-4 93.4% of the amino acids were in the most favored geometries and for SSTR-5 this was 96% as shown in **Figure 6**. The ERRAT plots, which are for the determination of errors in model building indicate a high degree of confidence (83.45% for SSTR4, 91.20% for SSTR-5) as shown in **Figure 7** and **Figure 8**. The z-score plots were obtained by the protein structure analysis tool (ProSA), as it evaluated the overall model quality; a score of

-3.87 was obtained for SSTR-4 as compared with -4.51 for the template PDB file used (4N6H) as shown in **Figure 9**. A score of -3.08 was obtained for SSTR-5 as compared with a score of -3.23 for the template PDB used (5DHH) [10] as shown in **Figure 10**. These results provided assurance of a reasonable structural quality of the constructed homology models.

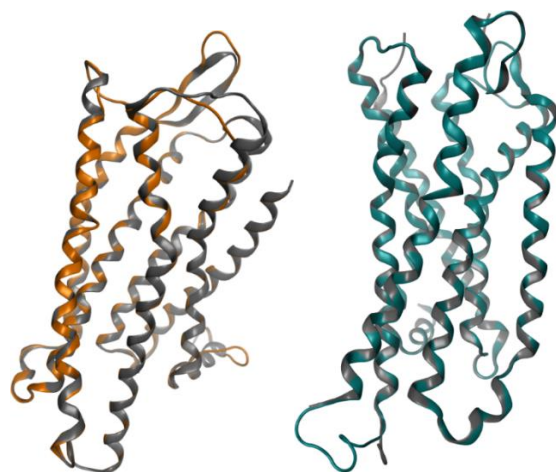


Figure 5 (a) Superpose of a homology model of SSTR-4 (Orange) with its template (Grey). (b) Superpose of homology model of SSTR-5 (Green) with its template (Grey).

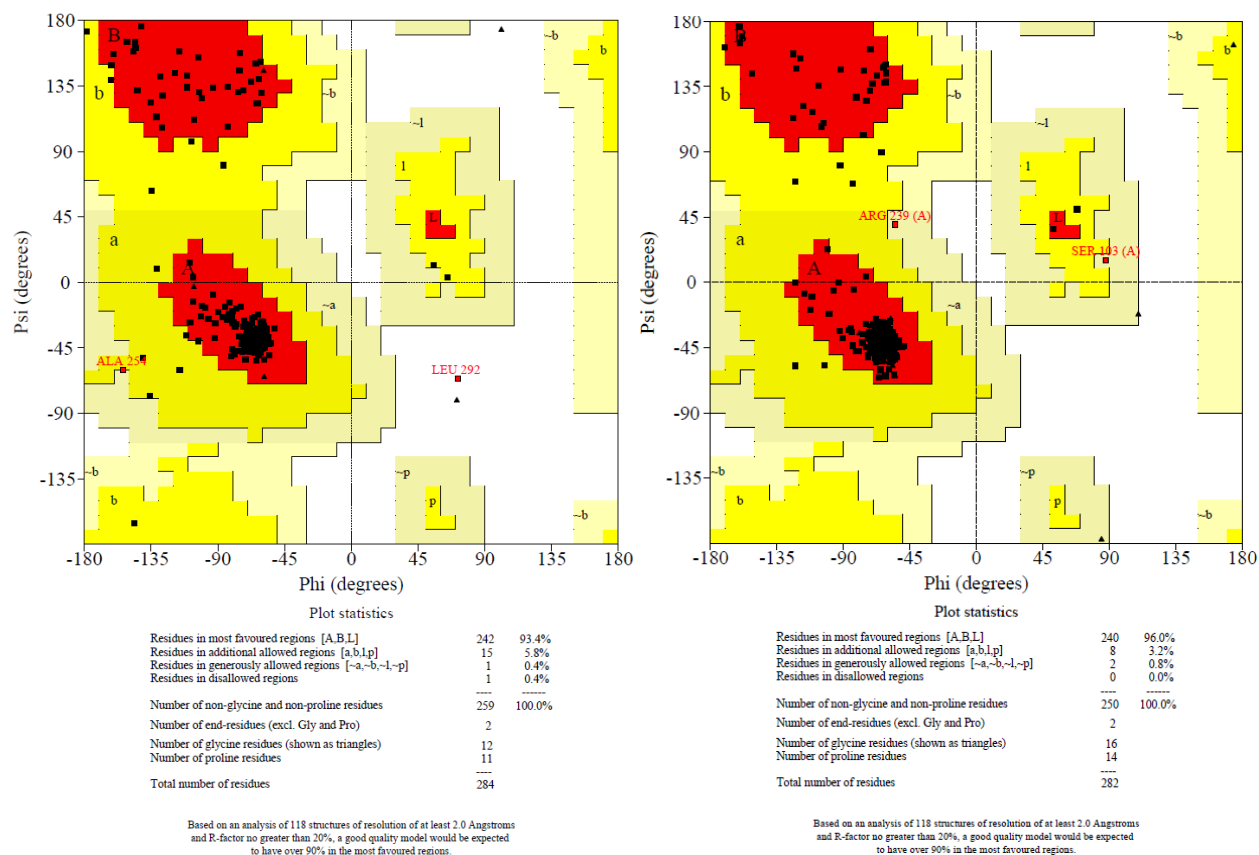
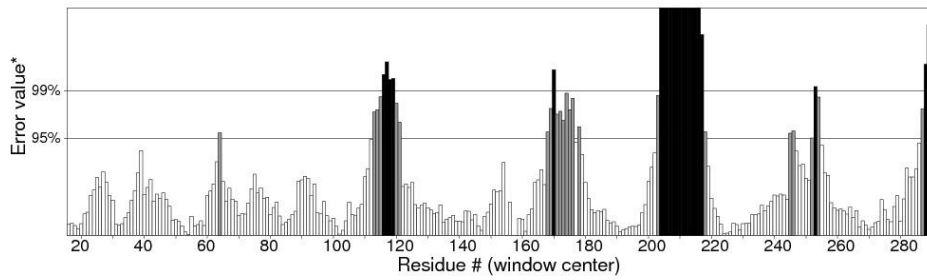


Figure 6 The Ramachandran on the SSTR-4 (left) and SSTR-5 (right)

Program: ERRAT2
 File: /var/www/SAVES/Jobs/8217896/erratt.pdb
 Chain#:1
 Overall quality factor**: 83.456



*On the error axis, two lines are drawn to indicate the confidence with which it is possible to reject regions that exceed that error value.

**Expressed as the percentage of the protein for which the calculated error value falls below the 95% rejection limit. Good high resolution structures generally produce values around 95% or higher. For lower resolutions (2.5 to 3Å) the average overall quality factor is around 91%.

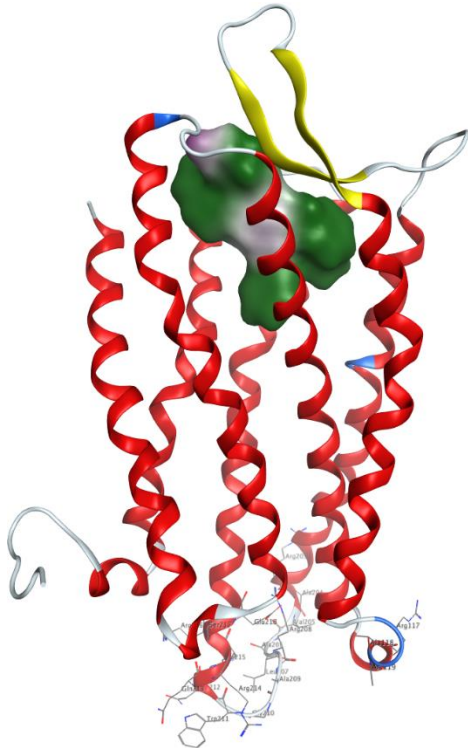
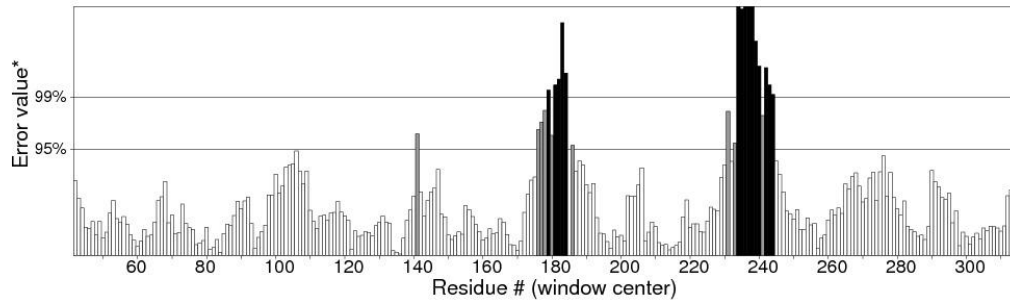


Figure 7 Errat plot for the SSTR-4 Homology model: Both the low confidence region 117-119 and 203-218 are localized in intracellular cytoplasmic domain and opposite to the orthosteric ligand site (surface plotted)

Program: ERRAT2
File: /var/www/SAVES/Jobs/8181326//errata.pdb
Chain#:1
Overall quality factor**: 91.209



*On the error axis, two lines are drawn to indicate the confidence with which it is possible to reject regions that exceed that error value.
**Expressed as the percentage of the protein for which the calculated error value falls below the 95% rejection limit. Good high resolution structures generally produce values around 95% or higher. For lower resolutions (2.5 to 3Å) the average overall quality factor is around 91%.

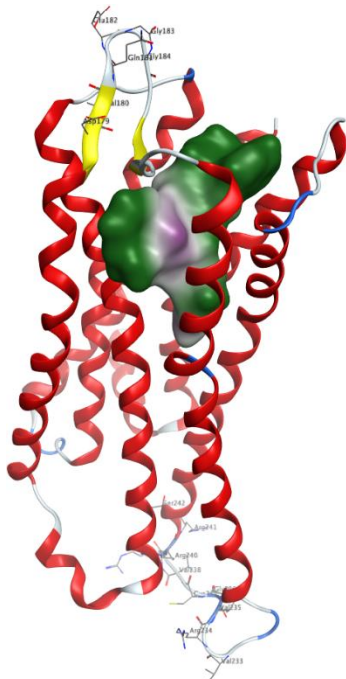


Figure 8 ERRAT plot for the SSTR-5 Homology model: The residues 179-184 is a part of loop and a tip of β -strand which is more than 4.5 Å away from the orthosteric binding cavity, while region 233-242 is a cytoplasmic domain positioning opposite to the orthosteric binding site and contains a loop region.

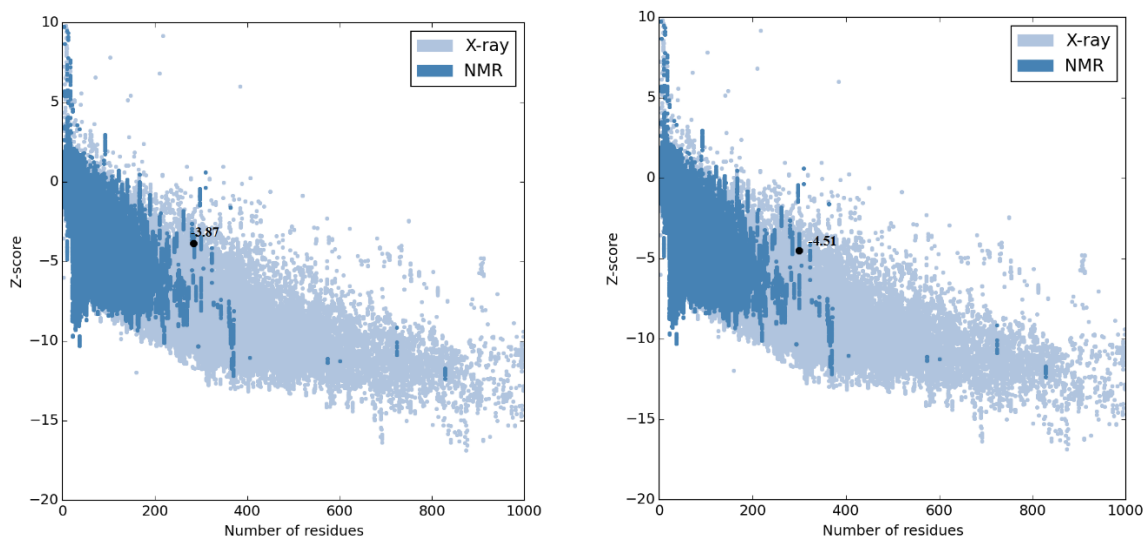


Figure 9 Comparative protein structure analysis (ProSA), calculates Z-score for (a) SSTR-4 homology model, (b) template (human delta opioid 7TM receptor, PDB- 4N6H).

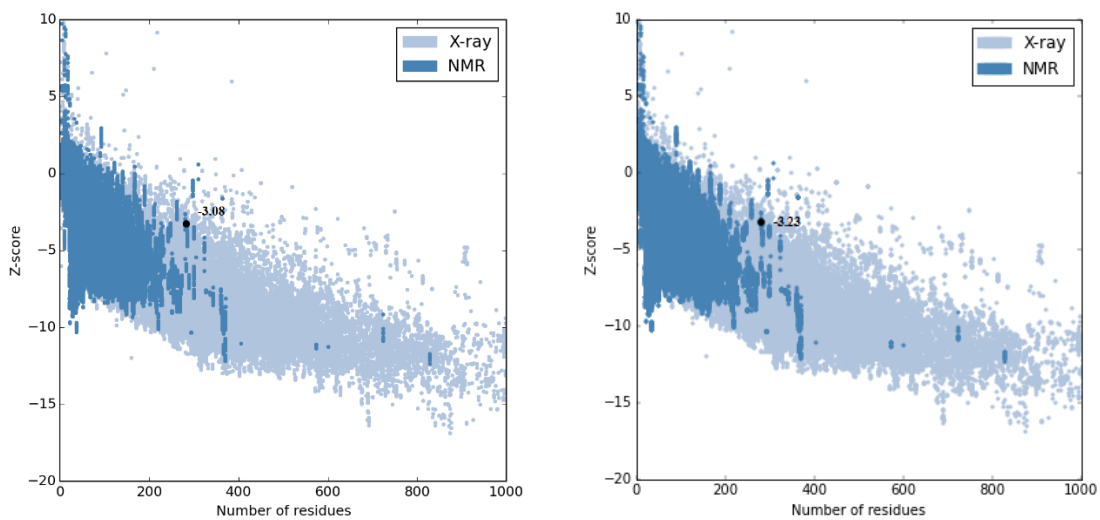


Figure 10 Comparative protein structure analysis (ProSA), calculates Z-score for (a) SSTR-5 homology model, (b) template (Nociceptin/orphanin Fq Peptide Receptor (nop), PDB- 5DHH).

Table 4 Comparative analysis of key residues within the active site domain of individual isoforms with the template amino acids.

Template	SSTR4	SSTR5	Template	SSTR4	SSTR5	Template	SSTR4	SSTR5
Gln107	Val67	Leu96	<i>Tyr131</i>	<i>Gly91</i>	<i>Gly120</i>	Val279	<i>Phe239</i>	<i>Phe264</i>
Asp110	Ser70	Gln99	<i>Met134</i>	<i>Met94</i>	<i>Gln123</i>	Gln280	<i>Tyr240</i>	<i>Phe265</i>
Ile111	Ala71	Asn100	<u><i>Phe135</i></u>	<u><i>Phe95</i></u>	<u><i>Phe124</i></u>	Val283	<i>Gln243</i>	<i>Asn268</i>
<u>Trp116</u>	<u>Trp76</u>	<u>Trp105</u>	<u><i>Cys200</i></u>	<u><i>Cys162</i></u>	<u><i>Cys186</i></u>	Leu301	Asn257	Tyr286
<u>Val126</u>	<u>Val86</u>	<u>Val115</u>	Ile219	Thr179	Thr205	Arg302	<i>His258</i>	<i>Phe287</i>
<i>Ile127</i>	<i>Leu87</i>	<i>Met116</i>	Ser223	Gly183	Gly209	Thr305	Leu261	Val290
<u><i>Asp130</i></u>	<u><i>Asp90</i></u>	<u><i>Asp119</i></u>	<u>Trp276</u>	<u>Trp236</u>	<u>Trp261</u>	<u>Tyr309</u>	<u><i>Tyr265</i></u>	<u><i>Tyr294</i></u>

Underlined amino acids are highly conserved through the GPCR family; Italics denote the key residues involved in antagonist/agonist binding interactions.

To identify the active cavity on the surface of both proteins, the Molecular Operating Environment active site detection tool (MOE 2015.1001) was employed [333, 334]. Nehrung *et al* had performed mutation-based studies on Asp90 (SSTR-4) and Asp119 (SSTR-5) in transmembrane domain 3 (TM3) of both SSTR-4/5 isoforms, and this showed that an ionic interaction with the positively charged lysine amino group in the side chain is important for the binding of endogenous somatostatin (SRIF-14) [335, 336]. However, Kontoyianni *et al.* suggested two possible ligand binding modes, indicating one which makes a *H*-bond with Gln243 while the other mode involves interaction with Asp90 with the latter also indicating that heteroaryl moieties could engage in π -stacking within the hydrophobic domain constituted by Phe175, Phe239, Trp171 and Tyr240 in the SSTR4 receptor [337]. Ozenberger and Hadcock reported a single site tyrosine substitution for Phe265 in the region of transmembrane domain 6 (TM6) of SSTR-5 and this resulted in altered ligand binding selectivity and loss of the binding preference of SSTR-5 for SRIF-28 over SRIF-14 [338]. To the best of my knowledge, at the time of writing of this thesis, no more structural data information was available for these proteins and their interactions with their ligands. This led us to compare the active sites in the homology models with that of the template protein (human delta-opioid receptor) used for generating the SSTR-4 homology model in the form where it was co-crystallised with its ligand. The template is also a GPCR protein, which would help to evaluate whether amino acids in the active site could be important for the binding of somatostatins and their mimetics (see **Table 4**). The binding cavity was found to be relatively large, which is

commensurate with its requirement to bind SST-14. Smaller non-peptidic ligands could thus occupy different parts of this cavity. To explore these possibilities, docking was investigated.

Firstly, a comparison of glucopyranoside **4.3** in SSTR-4 with peptidomimetics based on the iminosugar scaffold was made. The iminosugar derivative **4.4** retained potency to an extent, compared to **4.3**, but had low isoform selectivity ($K_i, \text{SSTR-4/ SSTR-5} = 1.13$, see Table 1). In the docking, the interaction of **4.4** with receptor site was found to be highly influenced by π -stacking interactions of its own aromatic rings (**Figure 11**) as well as with residues in the receptor. These were observed in both isoforms and may explain lack of selectivity observed.

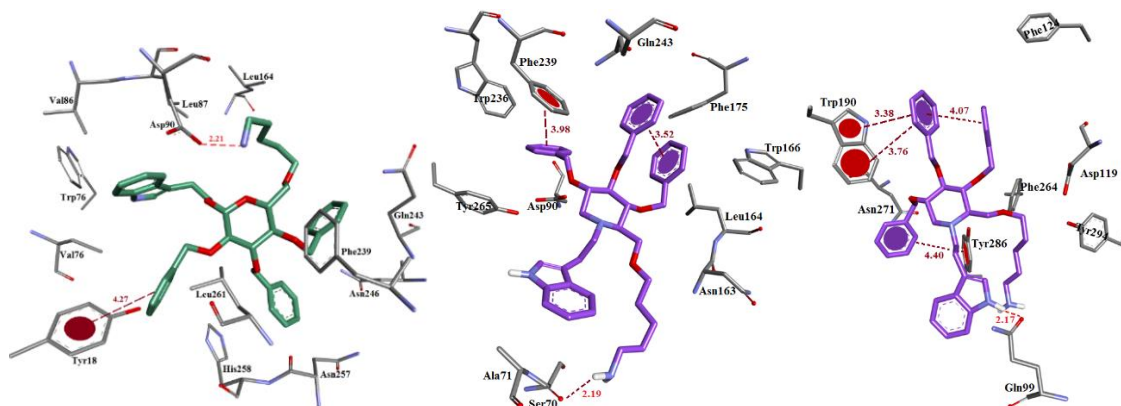


Figure 11 Compound **4.3** (green) exhibits a distinct binding mode, *via* interacting with Asp90 (2.21 Å) and aromatic π - π interaction with Tyr18. Iminosugar **4.4** (purple) lacks selectivity, displaying π - π interactions in SSTR-4 (3.52 Å) and in SSTR-5 (4.07 Å).

A similar loss of preferential isoform selectivity was also observed ($K_i, \text{SSTR-4: SSTR-5} = 1.46$, see Table 1) when comparing **4.4** with **4.5**. The similar π -stacking interactions of benzyl group aromatic rings for both isoforms are again believed to be the major influence in there being little selectivity (see, **Figure 12**), although there was a slight variation in the docked binding mode for **4.5**, when compared to **4.4**. The acetylated analog **4.6**, containing acetates rather than aromatic residues, showed low selectivity ($K_i, \text{SSTR-4: SSTR-5} = 1.05$) to **4.4** and **4.5**, which may be due to various interactions in the orthosteric binding sites of both these proteins [339-341].

In contrast, the trihydroxylated **4.7** displayed selectivity towards SSTR-5 albeit with low potency (shown in **Figure 12**). Molecular modeling of **4.7** showed that a *H*-bond donor interaction with one of the hydroxyl groups of the iminosugar core with the backbone of Asn268 of the receptor and there was an interaction of the naphthyl group with Phe201; these may explain the selectivity seen for **2.7** for SSTR-5. The modelled structure of **4.8** (more selective for SSTR-4) shows that its amino group has a shared interaction with the backbone of Asp90-Gly91 (2.82 Å) residues of

SSTR-4 while its indole ring engages in *H*-bond donor interactions with the amide group of the Gln243 (2.74 Å) side chain and π - π interactions with Phe239 (3.89 Å). These indicate that the presence of the indole group is helpful in stabilising/adopting the bound structure of **4.8** to SSTR-4; these interactions are not possible for SSTR5 and could account for the selectivity shown for **4.8**.

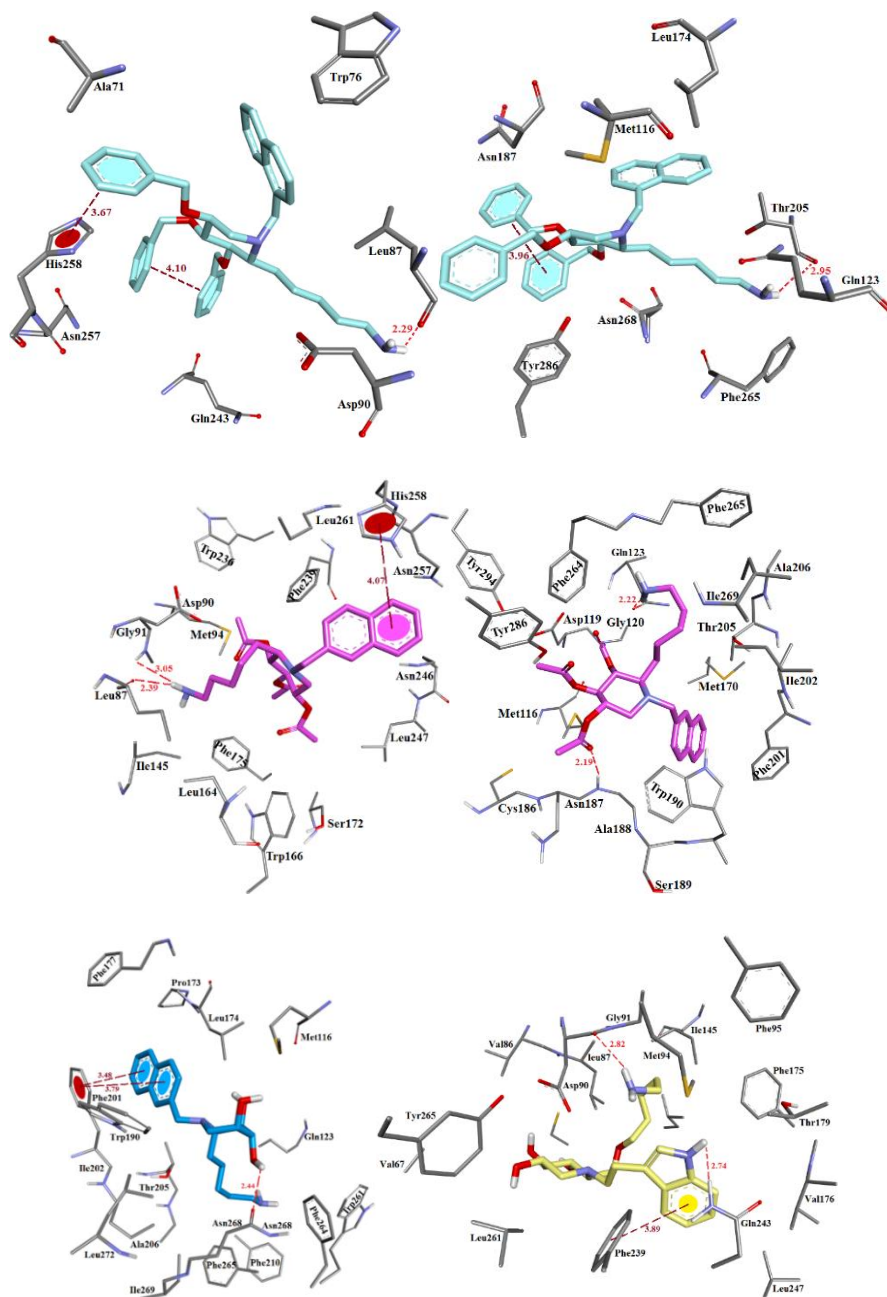


Figure 12 Iminosugars shown in a docked interactive mode. Tri-O-benzylated **4.5** (Cyan) with SSTR-4 (π - π interactions with His258 (3.67 Å) & *H*-bond donor interaction with Leu87 (2.29 Å)) and with SSTR-5 (*H*-bond donor interaction with Thr205 (2.95 Å)); Compound **4.6** (pink) with SSTR-4 (*H*-bond donor interactions with the backbone of Gly91(3.05 Å) and Leu87 (2.39 Å), π - π interaction with His258 (4.07 Å)) and with SSTR-5 (*H*-bonding donor-

acceptor interactions with Ala188 (2.19 Å) & Gln123 (2.32 Å)); Interaction of compound **4.7** (blue) with SSTR-5 (naphthyl functionality has π - π interaction with Phe201 (3.48 and 3.79 Å) and polar carbohydrate head has *H*-bond donor interaction with Asn268 (2.44 Å)); Compound **4.8** (yellow) with SSTR-4 (*H*-bond donor interactions with Asp90-Gly91 and Gln243).

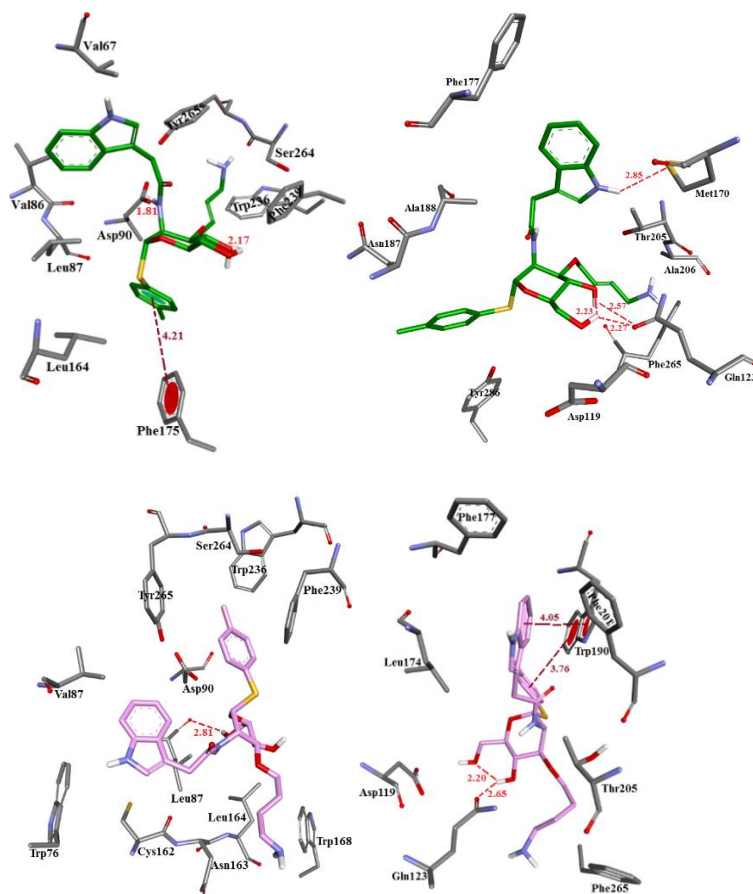


Figure 13 Docked mode of ManNAc derivatives: Compound **4.11** (green) with SSTR-4 (*H*-bond donor with Asp90 (1.81 Å) & π - π interaction with Phe175 (4.21 Å)) and with SSTR-5 (*H*-bond donor interaction with Met170 (2.85 Å), Gln123 (2.27 & 2.57 Å)); Compound **4.12** (pink) with SSTR4 (*H*-bond donor interaction with Leu87 (2.81 Å) and *para*-OMe-phenyl ring inserted into the hydrophobic cavity, constituted by the Tyr265, Trp236 and Phe239), and with SSTR-5 (π - π interaction with Trp190 (3.76 Å & 4.05 Å) and *H*-bond with Gln123 (2.65 Å) respectively).

The binding modes of ManNAc derivatives, **4.11** and **4.12** (**Figure 13**) showed interactions with both receptors consistent with relatively low selectivity (K_i , SSTR-4: SSTR-5 \approx 1.8, see Table 1). The SSTR isoform's active site cavities are large and this may contribute to poor selectivity observed for these pyranose derivatives [342].

The benzomacrolactone based mimetics **4.9** and **4.10** (**Figure 14**) which although having improved affinities compared to iminosugar and pyranose-based scaffolds showed low selectivities for the SSTR isoforms and this was also consistent with interactions observed in both binding sites. Changing the structure of the macrocyclic scaffold to that found in **4.14** and **4.15** showed a complete loss of affinity to both isoforms of these receptors, despite these scaffolds presenting

naphthyl and alkyl amine groups found in **4.5-4.7**. On the other hand, if the tryptophan side chain is incorporated onto this type of macrocycle, even without the apparently required lysine residue as in **4.13** then affinity is restored to a degree [343, 344]. Five-fold isoform selectivity was observed for **4.13** for SSTR-5 (see **Figure 14**) and this is proposed to arise due a π - π interaction with its Tyr-294.

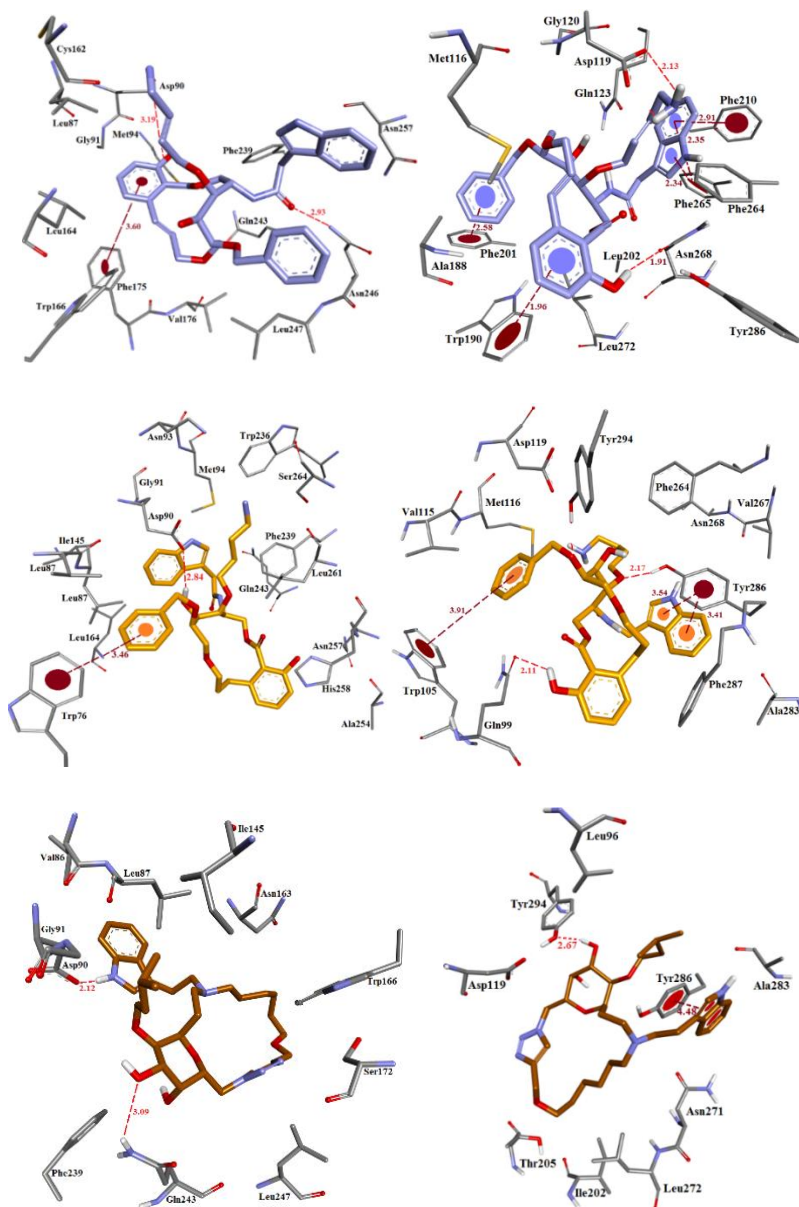


Figure 14 Interactive mode of macrocycles: (a) **4.9** (blue) with SSTR-4. The phenol moiety has π - π interaction with Phe175 (3.60 Å), the butenylamine shows *H*-bond donation to the COOH group of Asp90 (3.19 Å) and the amide carbonyl of the indole side chain has a *H*-bond acceptor interaction with Asn246 (2.93 Å)). For SSTR-5 the phenol moiety has a π - π interaction with Trp190 (1.96 Å), a *H*-bond acceptor interaction with the amide group of Asn268 (1.91 Å), a π - π interaction of the benzyl and indole groups with Phe201 (2.58 Å) and Phe265 (2.35 Å & 2.34 Å) respectively, and there are additional *H*-bond donor interactions of the butenylamine with the COOH group of Asp119 side chain (2.13 Å)). (b) **4.10** (orange) with SSTR4: a benzene residue was parallel to Trp76 in a π -sacking manner

(3.46 Å) and a *H*-bond donor interaction was observed for the free hydroxyl group with Asp90. This compound with SSTR-5 showed that the benzene residue has a T-shaped π - π interaction [345] with Trp105 (3.91 Å) whereas the indole displayed a sandwich-type π - π interaction [345] with Tyr286 (3.54 Å and 3.41 Å), whereas the phenolic (OH) and macrocycle *oxygen atom* shows *H*-bond donor and acceptor interactions with Gln99 (2.11 Å) and phenol of Tyr286 (2.17 Å) respectively); (c) **4.13** (brown) with SSTR-4 utilised *H*-bond donor/acceptor interactions with Asp90 (2.12 Å) and Gln123 (3.09 Å) respectively, while it shows a *H*-bond donor interaction with Tyr294 (2.67 Å) and π - π interaction with Tyr286 (4.48 Å) of SSTR-5.

Next, a comparison of the larger peptide ligands (**4.16-4.18**) by molecular modeling showed three features. Firstly **4.16** occupied a greater space in the receptor than the other ligands are shown so far [346]. Constraining the peptide into a cyclic structure giving **4.17** reduced the overall size of the cavity occupied by the peptide and also reduced conformational flexibility leading to improved binding [347]. The presence of the GlcNAc residue in **4.18** led to an increase in selectivity for SSTR-5 [348]. Interestingly, the GlcNAc unit of **4.18** showed intramolecular *H*-bond interactions in both the binding poses to both SSTR-4 and SSTR-5 isoforms, which led **4.18** to adopt a different conformation to **4.17**. For SSTR-5, the indole of **4.18** was proximal to Phe201 (shown in **Figure 15**) and this interaction was not observed for the various non-peptide-based structures described above. This indicates the potential utilization of an alternative site which could be explored in drug design (**Figure 15**).

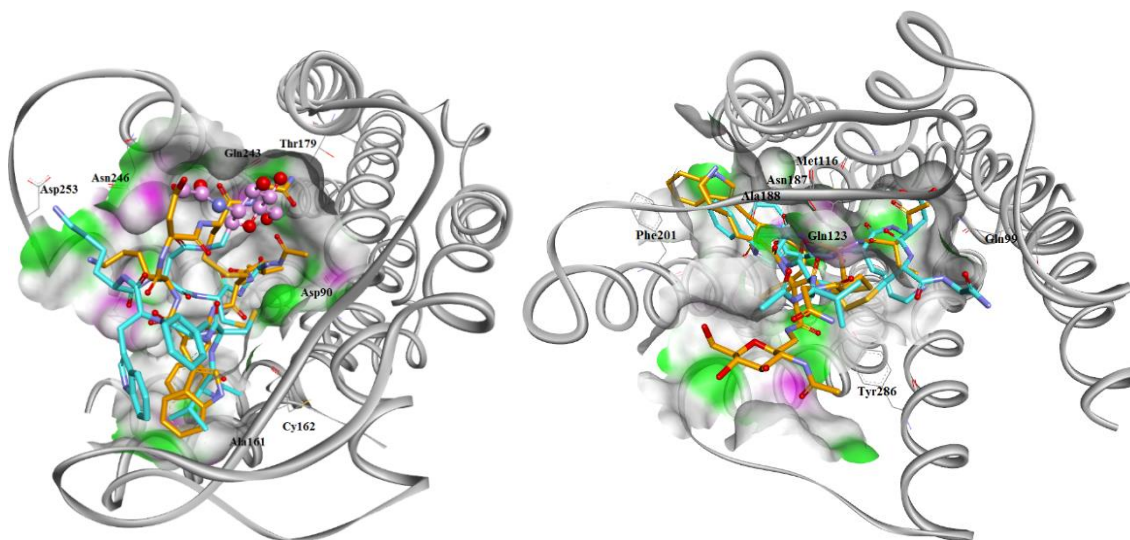


Figure 15 Peptides **4.17** (cyan) and **4.18** (orange) are docked to SSTR-4 (left) and SSTR-5 (right). In both cases, a number of peptide backbone intermolecular *H*-bond interactions were found. The amino acid functional epitopes (Lys, Trp, Phe) along with the glycosylated amino acid (ball and stick representation in the first structure on left, SSTR-4) behavior with proteins, was primarily considered. As observed for SSTR-4, **4.18** and **4.17** spanned the wide binding cavities and adopted unrelated binding modes. The **4.17** peptide backbone had *H*-bond acceptor/donor interactions with Asp90 (2.22 Å & 2.40 Å), Thr179 (2.75 Å), Gln243 (2.29 Å) and its Trp indole group displayed a *H*-bond donor interaction with the backbone of Cys162 (2.80 Å). In the case of **4.18**, the peptide backbone also showed *H*-bond acceptor/donor interactions with Asp90 (3.02 Å) as well as with Cys162 (2.65 Å), Asn246 (2.54 Å), His258 (2.18 Å). The Lys sidechain of SMS3 had *H*-bond acceptor interactions with the backbone of Asp253 (2.47 Å). However, in case of SSTR-5, there was a similar binding pattern for both **4.17/4.18**, as their peptide backbone interacted with the same amino acids of the cavity. The **4.17** peptide backbone interacts through *H*-bond acceptor/donor interactions with

Ala188 (2.16 Å), Asn187 (2.99 Å), Tyr286 (2.80 Å), Gln99 (2.34 Å) & Met116 (2.72 Å). On the other hand, the **4.18** peptide backbone interacts through *H*-bond acceptor/donor interactions with Gln123 (2.54 Å), Ala188(2.76 Å), Tyr286 (2.31 Å). The indole ring of **4.18** had π -stacking interactions with Phe201 (3.82 Å and 4.14 Å) while the GlcNAc residue had *H*-bond acceptor interactions with Asn187 (2.80 Å).

4.1.3 Conclusions and Future Perspective

Various scaffold or scaffold-based ligand design for somatostatin receptors, including iminosugars, ManNAc, (glyco)peptides and macrocycles inspired by natural products have been explored as ligands for somatostatin receptors. Their binding affinities for somatostatin receptors were determined and hypotheses for their modes of interaction with these receptors generated using molecular modeling. This has included construction of homology models for SSTR-4 and SSTR-5, which disclosed some key interactions with certain amino acid residues which from the docking was ligand-dependent. The study showed that various functional groups could interact with these key amino acid residues in a wide-ranging manner and this was due to the large active site cavity enabling it to interact with the ligands. Many of these key amino acids are evolutionarily conserved and only a few have been found to be mutated, and these are comprehensively listed in **Table 4**. Because of the size of this cavity, smaller sized ligands could adopt various different binding poses [349]. Some observations were also made in the case of the larger docked peptidyl somatostatin mimetics. The peptide backbone of **4.17** bonded to SSTR-4 more often through *H*-bond donor interactions which was very different to its proposed binding to SSTR-5. Study of the glycosylated **4.18** binding (shown in **Table 5**), indicated the possibility of two binding modes to SSTR-4 (indicated in **Table 5**) [337].

Moreover, it has been postulated that the interaction of ligands with His258 of SSTR-4 could lead to agonist activity. This interaction was seen in the docking of the iminosugars **4.5** and **4.6**, and glycosylated **4.18** [337]. In general, favorable interactions are predicted when the hydroxyl groups on various scaffolds were not protected allowing these hydrophilic groups interact with polar surface areas of the receptors. This was seen computationally in case of compounds **4.7**, **4.8**, **4.11-4.13** and **4.18** although have not received bioassay support as of yet for this for these compounds [350, 351]. This could be explored in future work or form the basis for the design of agonists.

This study has contributed to the identification of new inhibitors and provides a basis for the design and synthesis of ligands for SSTR-4 and SSTR-5 as well for generating hypotheses regarding their modes of binding. The homology models provided can be useful for performing any further structure-based ligand design for these receptors in lieu of crystal structures. More generally,

ligand-based design has potential to identify new pharmacophoric groups together with new scaffolds that can identify new chemical entities that target large active sites in proteins.

Table 5 Summary of predicted interactions of ligands with the SSTR-4 and SSTR-5 from docking

Compound	SSTR-4	SSTR-5
4.3	H→Asp90, <i>Bn</i> _i -π-π-Tyr18	<i>n. a</i>
4.4	H→Ser70, <i>Bn</i> _i -π-π-Phe239, <i>Bn</i> _i -π-π- <i>Bn</i> _i	H→Gln99, <i>Bn</i> _i -Trp190, <i>Bn</i> _i -π-π- <i>Bn</i> _i
4.5	H→Leu87, <i>Bn</i> _i -π-π-His258, <i>Bn</i> _i -π-π- <i>Bn</i> _i	H→Thr205, <i>Bn</i> _i -π-π- <i>Bn</i> _i
4.6	H→Leu87, H→Gly91, <i>Nap</i> _i -π-π-His258	H→Gln123, H←Ala188
4.7	<i>n. a</i>	H→Asn268, <i>Nap</i> _i -π-π-Phe201
4.8	H→Gly91, H→Gln123, <i>Ind</i> _i -π-π-Phe239	<i>n. a</i>
4.9	H→Asp90, H←Asn293, <i>PhO</i> _i -π-π-Phe175	H→Asp119, H→Asn268, <i>Bn</i> _i -π-π-Phe201, <i>Ind</i> _i -π-π-Phe210, <i>Ind</i> _i -π-π-Phe265, <i>Phe</i> _i -π-π-Trp190
4.10	<i>Bn</i> _i -π-π-Trp76, H→Asp90	H→Gln99, H→Tyr286, <i>Bn</i> _i -π-π-Trp105, <i>Ind</i> _i -π-π-Tyr286, <i>Ind</i> _i -π-π-Tyr286
4.11	H→Asp90, <i>S-Tol</i> _i -π-π-Phe175, <i>H</i> _i ↔[HO⋯HO]	H→Gln123, H-Met170, H→Phe265, <i>H</i> _i ↔[HO⋯HO]
4.12	H→Leu87	H→Gln123, <i>S-Tol</i> _i -π-π-Trp90, <i>Ind</i> _i -π-π-Trp90, Intra H↔[HO⋯HO]
4.13	H→Asp90, H→Gln243	H→Tyr294, <i>Ind</i> _i -π-π-Phe286
4.17	H→Asp90, H→Cys162, H→Thr179, H←Gln243,	H→Met116, H←Gln99, H←Tyr286, H←Asn187, H←Ala188
4.18	H→Asp90, H←Cys162, H←His258, H←Asn246, H→Asp253	H←Gln123, H←Tyr286, H←Asn187, H←Ala188, <i>Ind</i> _i -π-π-Phe201

H→: Hydrogen bond donor; H←: Hydrogen bond acceptor; *Bn*_i: Benzyl functionality of the molecule; *Ind*_i: indole functionality of the molecule, *S-Tol*_i: S-toluene functionality of the molecule; *Phe*_i: Phenyl functionality of the molecule; *PhO*_i: Phenoxy functionality of the molecule; *H*_i↔ intramolecular H-bonding of the molecule.

Objective 4.2 To rationalize the targeting of L-fucose analogs with fucosidases of various origin
4.2.1 Introduction

Iminosugars and their derivatives are inhibitors of enzymes of medicinal interest. These include glycosidases, glycosyltransferases [352, 353], glycogen phosphorylases [354], nucleoside-processing enzymes [355], a sugar nucleotide mutase [356, 357], metalloproteinases [358] and others [359]. Iminosugars inhibit glycosidases, due to their ability to bind at the active sites of these enzymes [360-362]. The range of enzymes inhibited by iminosugars indicates they have promise as new medicines for diseases such as diabetes, viral infections or lysosomal storage disorders [363]. α -Fucosidase is involved in the removal of non-reducing terminal L-fucose residues that are connected to oligosaccharides via α -1,2; α -1,3; α -1,4 or α -1,6-linkages. L-Fucose (**4.19**) is found on glycans that participate in cell-cell interactions and cell migration. These events are connected to physiological and pathological processes such as fertilization, embryogenesis, lymphocyte trafficking, immune responses, and cancer metastasis [364-366]. A variety of physiological and pathological events are associated with fucose containing glycoconjugates. For instance, aberrant distribution of α -fucosidase has been reported as being relevant to inflammation [367], cancer [368], and cystic fibrosis [369]. These enzymes have been recognized as diagnostic markers for the early detection of colorectal [370] and hepatocellular cancers, and this is due to the presence of α -fucosidase in patient serums. α -Fucosidase inhibitors may be used to study their functions and could form the basis of developing therapeutic agents [371]. Fuconojirimycins **4.21**, **4.22** and the 1-deoxy analog **4.20** (DFJ) are key inhibitors of α -L-fucosidases. Other compounds assessed for their fucosidase inhibitory properties are also shown in **Figure 16** with their reported K_i values.

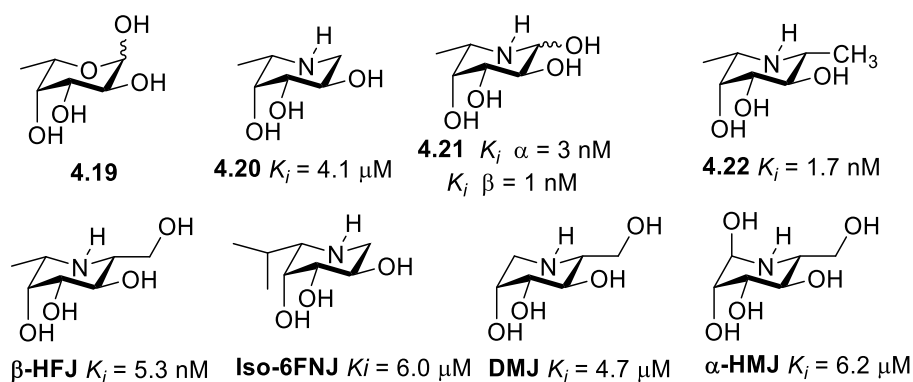


Figure 16 Various fucosidase inhibitors: L-fuconojirimycin **4.21** & **4.22** [372]; natural or semi-synthetic inhibitors contains 1-deoxyfuconojirimycin (**DFJ**), β -hydroxymethyl 1-deoxyfuconojirimycin (**β -HFJ**), 1-deoxymannojirimycin (**DMJ**), mannojirimycin (**α -HMJ**) [373, 374].

In recent years, *N*-alkylated iminosugars have shown improved *in vivo* and *in vitro* activities, mainly due to their improved lipophilicity, which may facilitate their crossing of the plasma membrane into cells [375-377]. In some cases, the appended alkyl groups are involved in hydrophobic interactions in the hydrophobic pocket of the target proteins. *N*-Butyl-1-deoxyfuconojirimycin (zavesca[®]) has been approved for Gaucher disease and *N*-hydroxyethyl-DNJ (glyset[®]) is used for type-II diabetes-associated complications [378]. Also, *N*-alkyl DNJs [379, 380] such as zavesca[®], *N*-nonyl-DNJ and **4.23a-c** [381] (shown in **Figure 17**) act as highly potent pharmacological chaperones for the potential treatment of Gaucher [382] and Pompe [383] diseases by ‘rescuing’ mutant enzymes. Kelly *et al* [384] and Overkleeft *et al* [385] have shown that additional attachment of a large lipophilic substituent (such as the adamantyl group) (see **4.23d-e** in **Figure 17**) increases the interaction with the glucocerebrosidase involved in lysosomal glycosphingolipid processing.

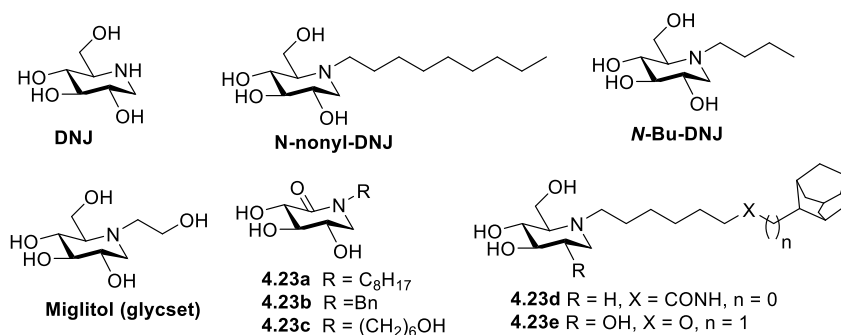


Figure 17 Bioactive *N*-alkylated iminosugars.

A number of *N*-alkyl DFJ derivatives have been synthesized previously. This includes an *N*-(aminopropyl) derivative prepared by Hung’s group which had an IC₅₀ of 70 nM as an inhibitor of the fucosidase from *T. maritima* [386]. Some *N*-alkyl DFJ derivatives have been evaluated against fucosyl transferases [387]. *N*-Methylated-DFJ showed weak anti-HIV activity and no cytotoxicity in a study where various glycosidase inhibitors were screened [388]. Conformationally constrained *N*-alkyl DFJ derivatives were inhibitors of bovine epididymis α -L-fucosidase [389]. An analog of castanospermine with the L-fuco configuration and its fucosidase activity was described by Paulsen and co-workers [390].

Herein, the synthesis of new *N*-alkylated-1-deoxyfuconojirimycins and their testing against α -fucosidases and cancer cell lines has been carried out. Molecular modeling has been used to generate hypotheses about their modes of binding. *N*-Decyl-1-deoxyfuconojirimycin (*N*-decyl-DFJ) was found to be toxic against various cancer cell lines.

4.2.2 Results and Discussion

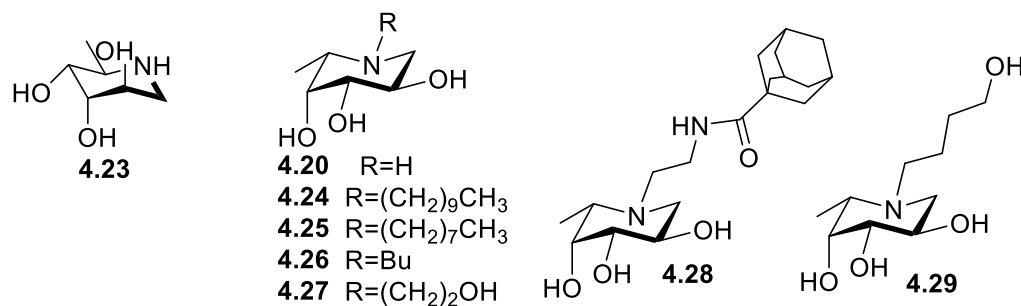


Figure 18 In-house synthesized compounds

4.2.2.1 Inhibition of fucosidases and structure-activity relationship

The N-alkyl DFJs were tested as inhibitors of the fucosidase from *T. maritima* (bacterial origin) and *B. taurus* (bovine origin), and the IC₅₀ values obtained are summarized in **Table 6**. The *T. maritima* enzyme shares 38% identity with its human counterpart and is speculated to have a role in the modification of hemicelluloses [48]. The bovine-derived fucosidase has been widely used in *N*-glycan, blood group oligosaccharide, and glycolipid analysis. Only DFJ (**4.20**) showed moderate inhibition (IC₅₀, 8 μM) of the fucosidase from *T. maritima*. The active site of the fucosidase from *T. maritima* did not tolerate the presence of a butyl or hydroxybutyl group on the piperidine. Examination of the binding pose of L-fucose with the α-fucosidase of *T. maritima* in a co-crystal structure [391] indicated that the L-fucose is tightly enveloped by residues in the enzyme. These residues (see in **Figure 19**) could prevent binding of N-substituted iminosugars assuming the fucopyranose mimetic **4.20** binds in a similar manner to L-fucopyranose.

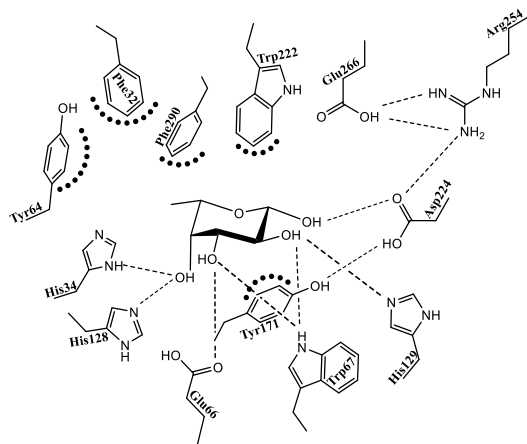


Figure 19 The interactions between α-fucosidase from *T. maritima* and α-L-fucopyranose. H-bonds are shown as dashed lines and van der Waals contacts are shown as bold dotted lines.

The *N*-butyl derivative **4.26** did not inhibit, at concentrations up to 100 μM, the fucosidase *B. taurus* from bovine kidney (Table 2), whereas the butanol derivative **4.29** had an IC₅₀ of 30 μM.

Also, determined an IC₅₀ of 0.3 μM for **4.20** which agreed with a reported IC₅₀ for **4.20** (0.4 μM) for the fucosidase from *B. taurus* [392]. However, lengthening the alkyl chain led to improved activity for as seen for N-decyl derivative **4.24** (IC₅₀ = 2.5 μM). By comparing the aliphatic side chains of **4.24-4.26**, it can be concluded that having a longer alkyl group gives rise to improved inhibitory activity. Compound **4.28** which had an adamantyl group on the *N*-side chain was less potent with an IC₅₀ of 90 μM. The *N*-ethanol derivative **4.27** showed IC₅₀ value of 27 μM, similar to that of the *N*-butanol derivative. The altronojirimycin derivative **4.23** (**Table 6**) did not show any inhibition towards the tested α-fucosidases. In addition to the IC₅₀ determination, some physicochemical parameters (LogP, LipE and logD) were calculated. In terms of oral administration, LogP values should be less than 5 according to Lipinski's rules of five, which most of the *N*-alkylated derivatives show [252]. LogP values between 2 and 3 are often considered optimal to achieve a compromise between permeability and first-pass clearance, which is quite comprehensively shown by compound **4.24**. LipE is another parameter which links the potency (IC₅₀) and lipophilicity (logD) in an attempt to estimate drug-likeness of a particular structure. A satisfactory LipE value would indicate selectivity for the target of interest versus a generic hydrophobic environment [393]. A LipE measurement of 6 represents one-million-fold selectivity for the target versus a generic hydrophobic environment while a LipE of zero indicates no selectivity. Compounds **2.20** and **2.27** had values higher than 6.

Table 6. IC₅₀ values (μM) and other parameters

Compound	IC ₅₀ (fucosidase from <i>B. taurus</i>)	IC ₅₀ (fucosidase from <i>T. maritima</i>)	LogP ^d	LogD	For fucosidase from <i>B. taurus</i>	
					pIC ₅₀	LipE ^e
4.20 (DFJ)	0.3 (0.4)[392]	8	-1.71	-2.23	6.52	8.75
4.25	25	<i>N. D.</i> ^b	1.723	1.02	4.60	3.57
4.24	2.5	<i>N. D.</i>	2.60	2.04	5.60	3.55
4.26	>100	>100	-0.04	-1.02	<4	<i>N. A.</i>
4.27	27	<i>N. D.</i>	-2.13	-1.83	4.56	6.40
4.29	30	>100	-0.07	1.05	4.52	3.47
4.28	90	<i>N. D.</i>	-1.25	-1.81	4.04	5.86
4.23	>100	>100	-1.71	-2.23	<4	<i>N. A.</i>

^b*N. D.* = not determined; ^dbased on Labute *et al* method calculated by CCG MOE2018.01; ^eLipE = pIC₅₀ - log D [393];

4.2.2.2 Molecular modeling

Molecular modeling was used in order to hypothesize how the fuconojirimycin derivatives may interact with the fucosidases and to provide a basis for the development of more potent inhibitors. The 3D-coordinates for the fucosidase from *T. maritima* (PDB code: 2ZXD) were retrieved from Royal Collaboratory for Structural Bioinformatics Protein Data Bank (RCSB-PDB) [394]. The

fucosidase of bovine origin was modeled using the α -L-fucosidase of *T. maritima* as a template. The sequence for the bovine fucosidase *B. taurus* was obtained from NCBI (National Center for Biotechnology Information). A BlastP search was then conducted which showed a number of possible templates for constructing the homology model (results from the BlastP search are provided in **Table 8**). Five templates were found with >35% of residues matching, and the length of each template was $\geq 85\%$ of that of the *B. taurus* input sequence and therefore homology models were built for each of these. These homology models were then evaluated based on their qualitative structural uniformity by (a) superimposition of the homology models over their templates (see in **Figure 21**), (b) Comparing ProSA Z-score of homology models with their templates (see in **Figures 22-26**), (c) Errat plots of models (see **Figure 27-31**) and Ramachandran plots (see in **Figure 32-34**). Model-4 (**Table 7**) developed based on the template of a fucosyl hydrolase from a strain of *T. maritima* was selected based on the data presented in Table 3 for further molecular modeling studies. Three residues were found to be outliers in this model, and they were later were energy minimized. The plots obtained before and after minimization are provided in **Figure 34**. Comparing the pairwise sequence alignment of fucosidase of *B. taurus* with that from *T. maritima* showed the similarity of their structures (**Figure 20**).

Table 7 Evaluation of the constructed homology models prepared from five available PDBs with identity $\geq 35\%$ in their amino acid sequence. Qualitative structural measurements are provided in the form of Ramachandran plot, ERRAT plot, Verify-3D, ProA, Z-Score and superpose of homology model with their templates.

Models	Ramachandran Plot ^a				ERRA T Plot	Verif y 3D	Superpose RMSD (Å)	ProSa Z-Score		
	% residue in favoured region	% residue in additional allowed region	% residue in generously allowed region	% residue in disallowed region				Template	Homolog y model	Templ ate
1	85.1	7.3	0.6	0.9	84.57	80.65	1HL9_B (0.739)	-7.26	-9.87	0.26
2	84.5	13	1.5	0.9	86.74	89.25	2ZWY_A (1.174)	-7.47	-10.29	0.27
3	88.2	9.3	1.5	0.9	82.20	80.11	1HL9_A (1.050)	-6.96	-9.33	0.25
4	85.1	12.1	1.9	0.9	86.04	87.37	2WSP_A (0.926)	-7.69	-10.27	0.25
5	69.7	25.7	3.1	1.5	79.73	86.24	1ODU_A (1.89)	-6.75	-9.81	0.31

(^a residues in Ramachandran plot are calculated as $\sim 0.3 = 1$)



Figure 20 The sequence alignment of model 4 with its template 2wsp_A showing evolutionary conserved residues.

Table 8 BlastP search generating possible template candidates for the *B. Taurus* fucosidase

Protein Names	Coverage	E-Value	Identity	PDB
Chain A, crystal structure of <i>Thermotoga maritima</i> alpha-fucosidase in complex with fucose	87%	4e-66	36%	1ODU_A
Chain A, alpha-l-fucosidase	87%	5e-66	35%	2ZWY_A
Chain A, crystal structure of thermotoga maritima alpha-fucosidase	87%	1e-65	35%	1HL9_A
Chain B, crystal structure of thermotoga maritima alpha-fucosidase	87%	1e-65	35%	1HL9_B
Chain A, <i>Thermotoga Maritima</i> alpha-l-fucosynthase, Tmd224g, in complex with Alpha-L-Fuc-(1-2)-Beta-L-Fuc-N3	87%	4e-65	35%	2WSP_A
Chain A, crystal structure of a bacterial fucosidase with Iminocyclitol (2s,3s, 4r,5s)-3,4-dihydroxy-2-ethynyl-5-methylpyrrolidine	84%	5e-37	26%	4PCT_A
Chain A, crystal structure of a bacterial fucosidase with inhibitor 1-phenyl-4- [(2s,3s,4r,5s)-3,4-dihydroxy-5-methylpyrrolidin-2-yl]triazole	84%	7e-37	26%	4PEE_A
Chain A, crystal structure of an alpha-l-fucosidase gh29 from <i>Bacteroides thetaiotaomicron</i>	84%	8e-37	26%	2WVW_A
Chain B, crystal structure of an alpha-l-fucosidase Gh29 From <i>Bacteroides thetaiotaomicron</i>	84%	8e-37	26%	2WVW_B
Chain A, crystal structure of a bacterial fucosidase with Iminocyclitol (2s,3s, 4r,5s)-3,4-dihydroxy-2-ethynyl-5-methylpyrrolidine	84%	8e-37	26%	5I5R_A
Chain A, crystal structure of an alpha-l-fucosidase Gh29 from <i>Bacteroides thetaiotaomicron</i> in complex with Deoxyfuconojirimycin	84%	8e-37	26%	2XIB_A

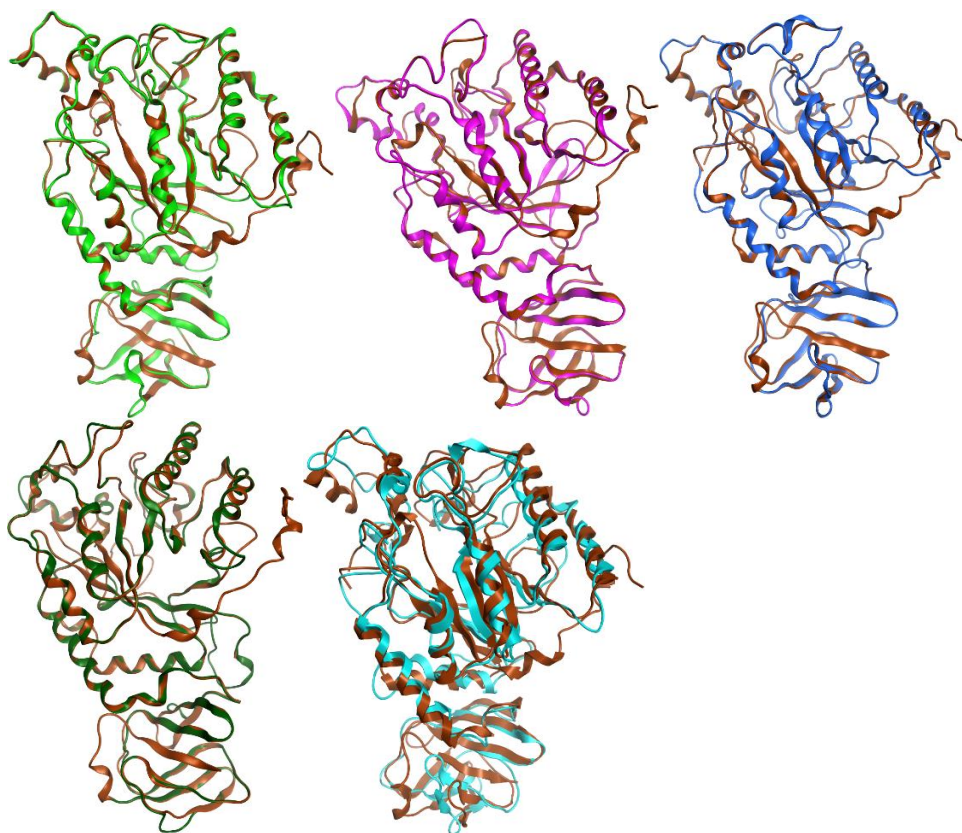


Figure 21 (A) Superpose of model 1 (green) with template (1HL9.B, Brown); (B) Superpose of model 2 (magenta) with template (2ZWY.A, Brown); (C) Superpose of model 3 (Blue) with template (1HL9.A, Brown); (D) Superpose of model 4 (Green) with template (2WSP.A, Brown); (E) Superpose of model 5 (cyan) with template (1ODU.A, Brown)

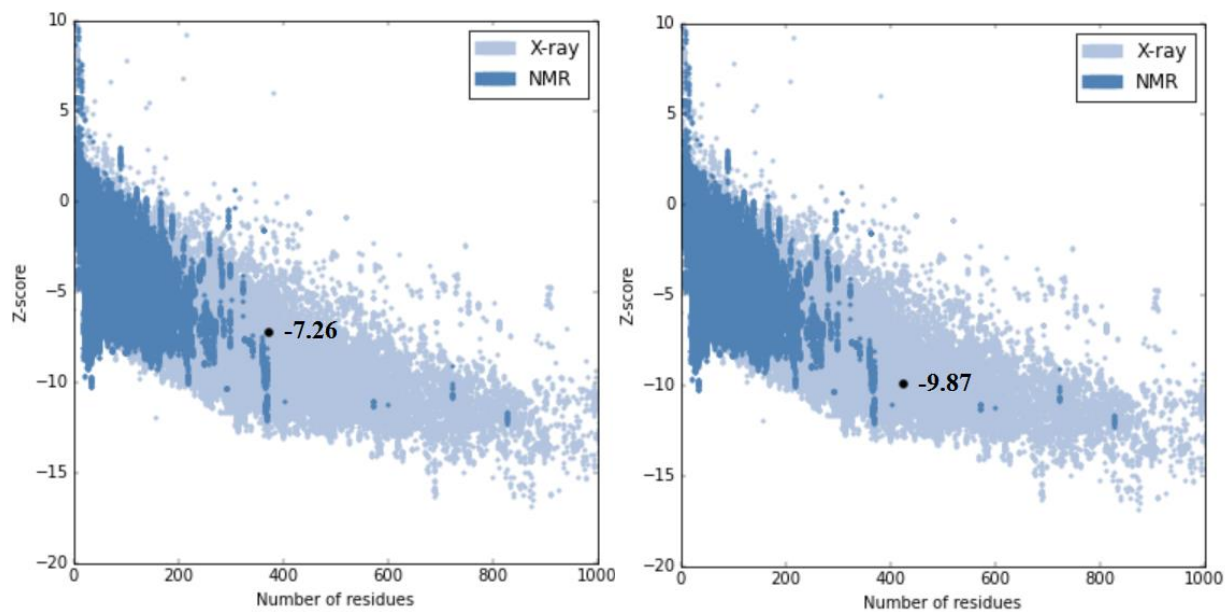


Figure 22 Comparative protein structure analysis (ProSA) calculates Z-score for (a) homology model 1 (left), (b) template (1HL9.B) (right).

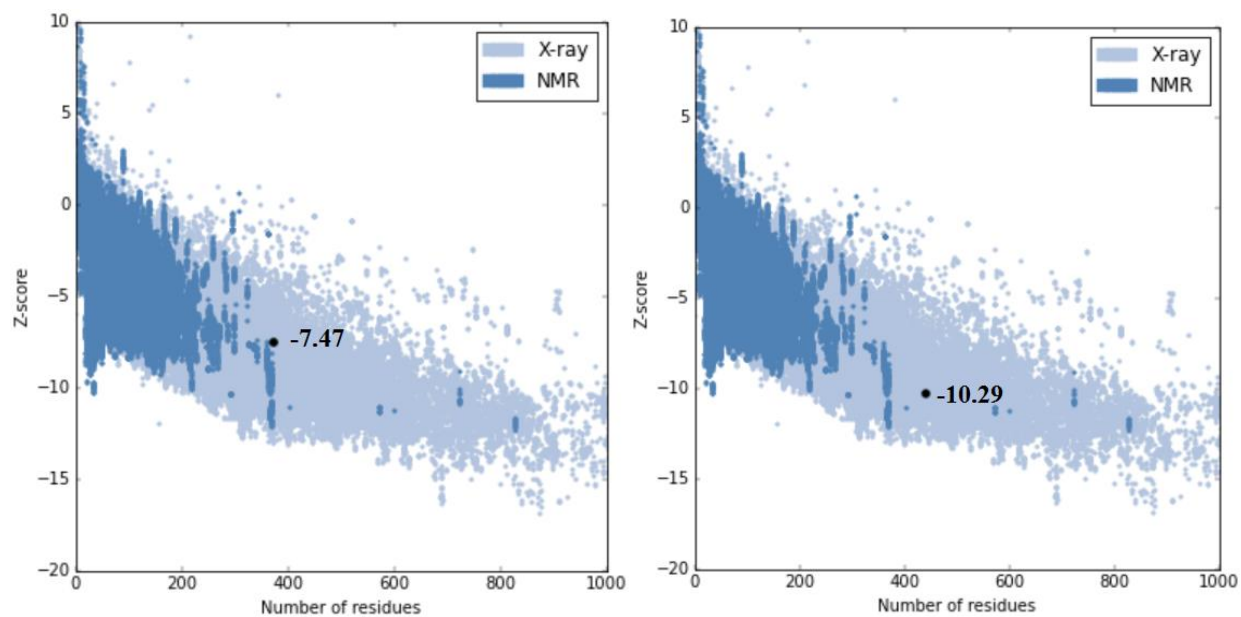


Figure 23 Comparative protein structure analysis (ProSA) calculates Z-score for (a) homology model 2 (left), (b) template (2ZWY.A) (right).

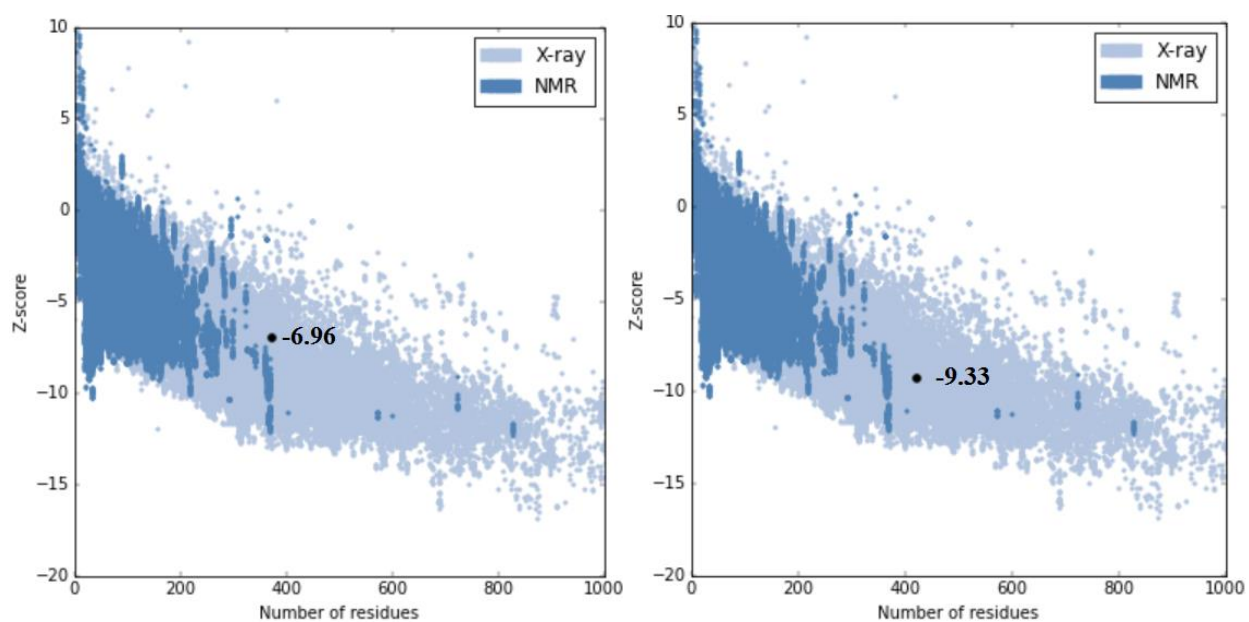


Figure 24 Comparative protein structure analysis (ProSA) calculates Z-score for (a) homology model 3 (left), (b) template (1HL9.A) (right).

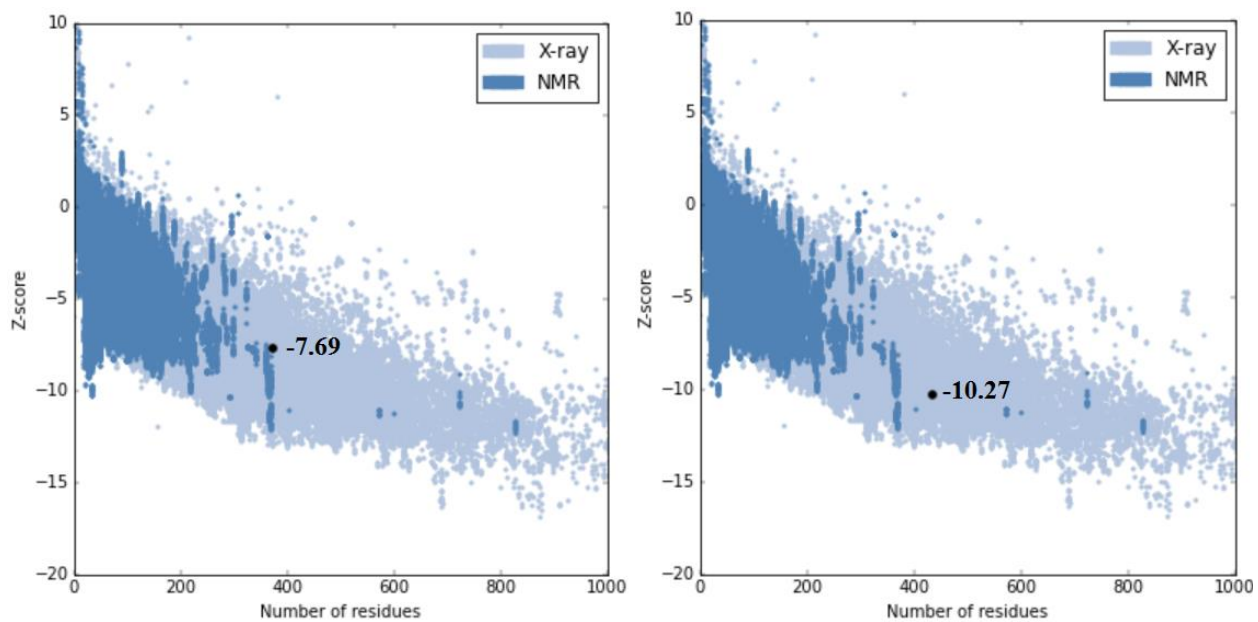


Figure 25 Comparative protein structure analysis (ProSA) calculates Z-score for (a) homology model 4 (left), (b) template (2WSP.A) (right).

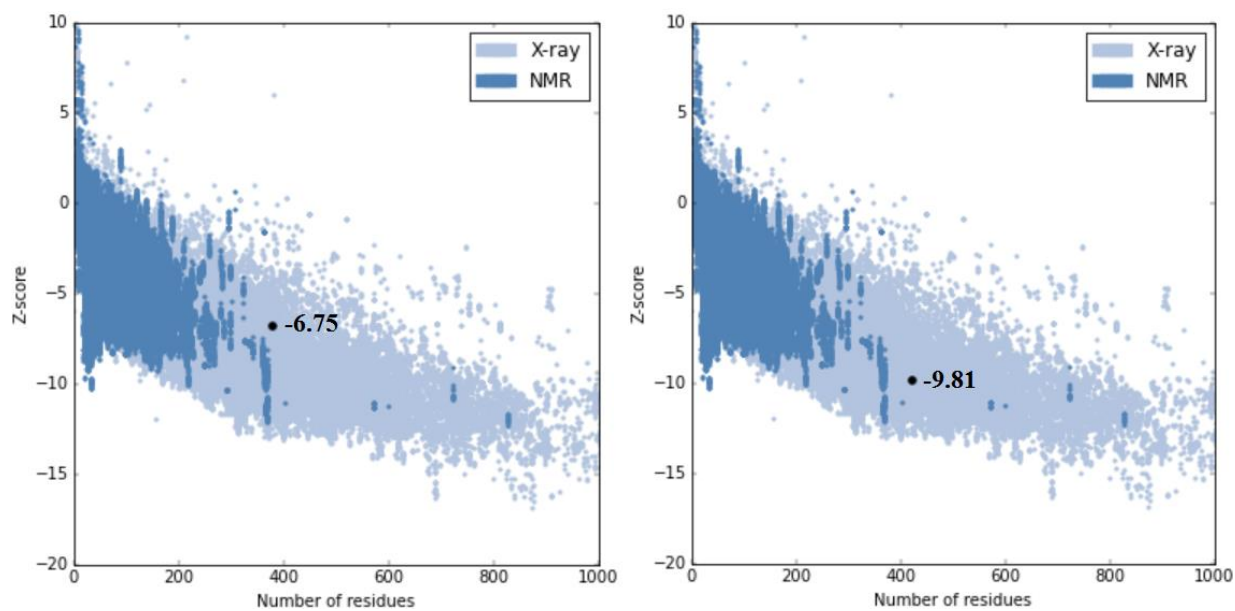
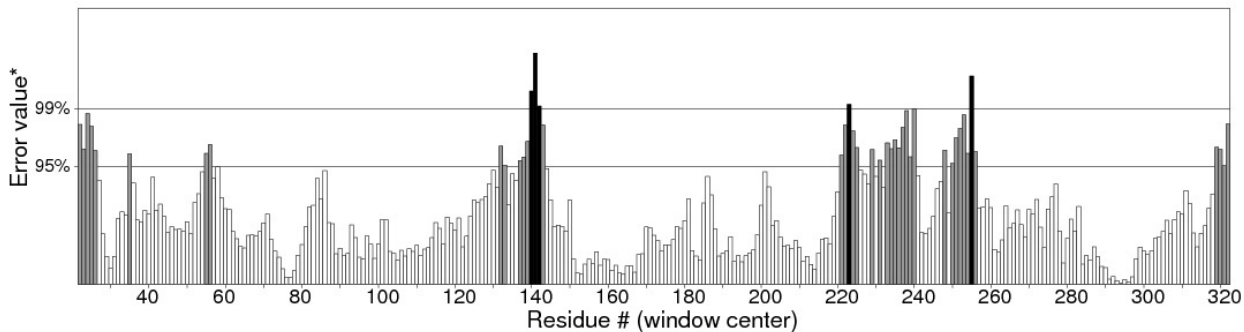


Figure 26 Comparative protein structure analysis (ProSA) calculates Z-score for (a) homology model 5 (left), (b) template (1ODU.A) (right).

Program: ERRAT2
File: /var/www/SAVES/Jobs/1946237//errata.pdb
Chain#:1
Overall quality factor**: 84.571

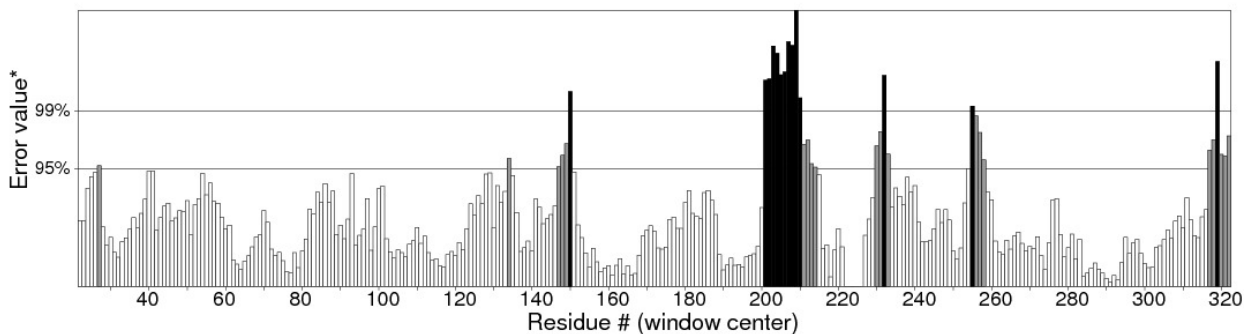


*On the error axis, two lines are drawn to indicate the confidence with which it is possible to reject regions that exceed that error value.

**Expressed as the percentage of the protein for which the calculated error value falls below the 95% rejection limit. Good high resolution structures generally produce values around 95% or higher. For lower resolutions (2.5 to 3Å) the average overall quality factor is around 91%.

Figure 27 ERRAT plot of Model 1.

Program: ERRAT2
File: /var/www/SAVES/Jobs/2477537//errata.pdb
Chain#:1
Overall quality factor**: 86.744

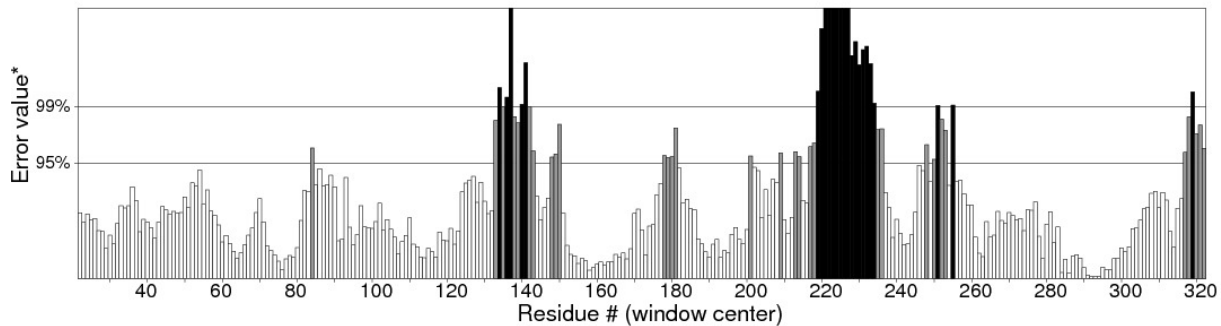


*On the error axis, two lines are drawn to indicate the confidence with which it is possible to reject regions that exceed that error value.

**Expressed as the percentage of the protein for which the calculated error value falls below the 95% rejection limit. Good high resolution structures generally produce values around 95% or higher. For lower resolutions (2.5 to 3Å) the average overall quality factor is around 91%.

Figure 28 The ERRAT plot of Model 2.

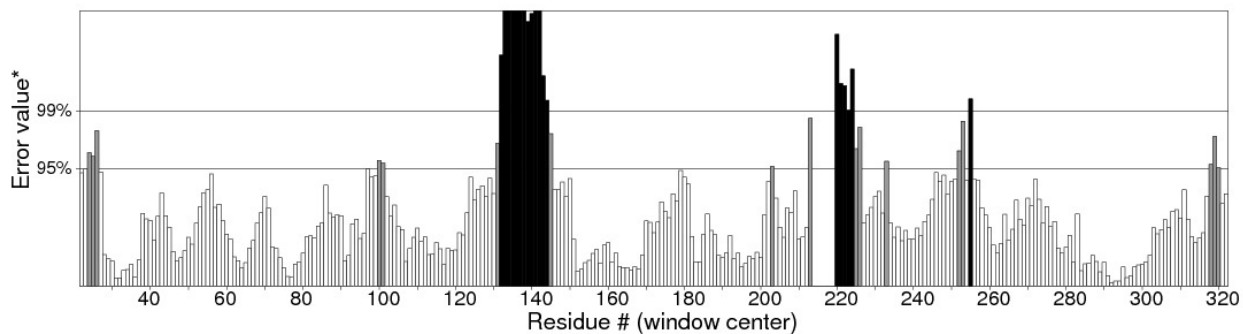
Program: ERRAT2
File: /var/www/SAVES/Jobs/5035651//errata.pdb
Chain#:1
Overall quality factor**: 82.203



*On the error axis, two lines are drawn to indicate the confidence with which it is possible to reject regions that exceed that error value.
**Expressed as the percentage of the protein for which the calculated error value falls below the 95% rejection limit. Good high resolution structures generally produce values around 95% or higher. For lower resolutions (2.5 to 3Å) the average overall quality factor is around 91%.

Figure 29 ERRAT plot of Model 3.

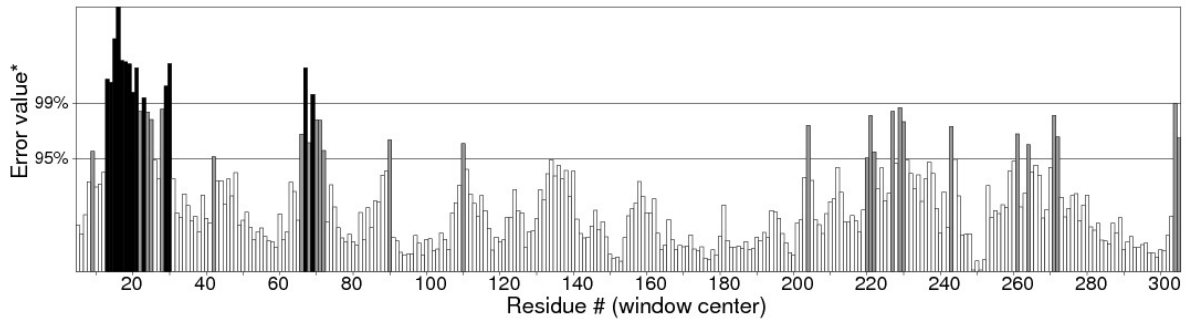
Program: ERRAT2
File: /var/www/SAVES/Jobs/5429263//errata.pdb
Chain#:1
Overall quality factor**: 86.040



*On the error axis, two lines are drawn to indicate the confidence with which it is possible to reject regions that exceed that error value.
**Expressed as the percentage of the protein for which the calculated error value falls below the 95% rejection limit. Good high resolution structures generally produce values around 95% or higher. For lower resolutions (2.5 to 3Å) the average overall quality factor is around 91%.

Figure 30 ERRAT plot of Model 4.

Program: ERRAT2
 File: /var/www/SAVES/Jobs/1278570//erratt.pdb
 Chain#:1
 Overall quality factor**: 79.730



*On the error axis, two lines are drawn to indicate the confidence with which it is possible to reject regions that exceed that error value.

**Expressed as the percentage of the protein for which the calculated error value falls below the 95% rejection limit. Good high resolution structures generally produce values around 95% or higher. For lower resolutions (2.5 to 3Å) the average overall quality factor is around 91%.

Figure 31 ERRAT plot of Model 5.

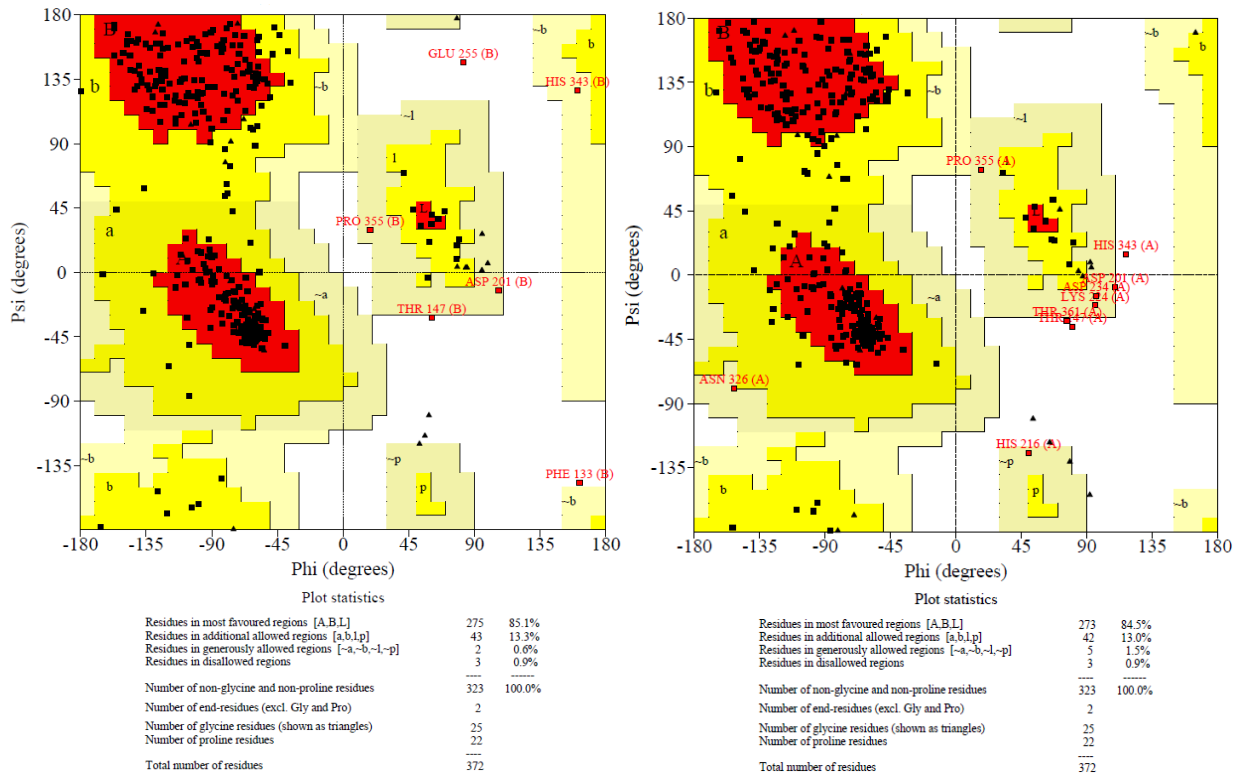


Figure 32 Ramachandran plot for Model 1 (left) and model 2 (right)

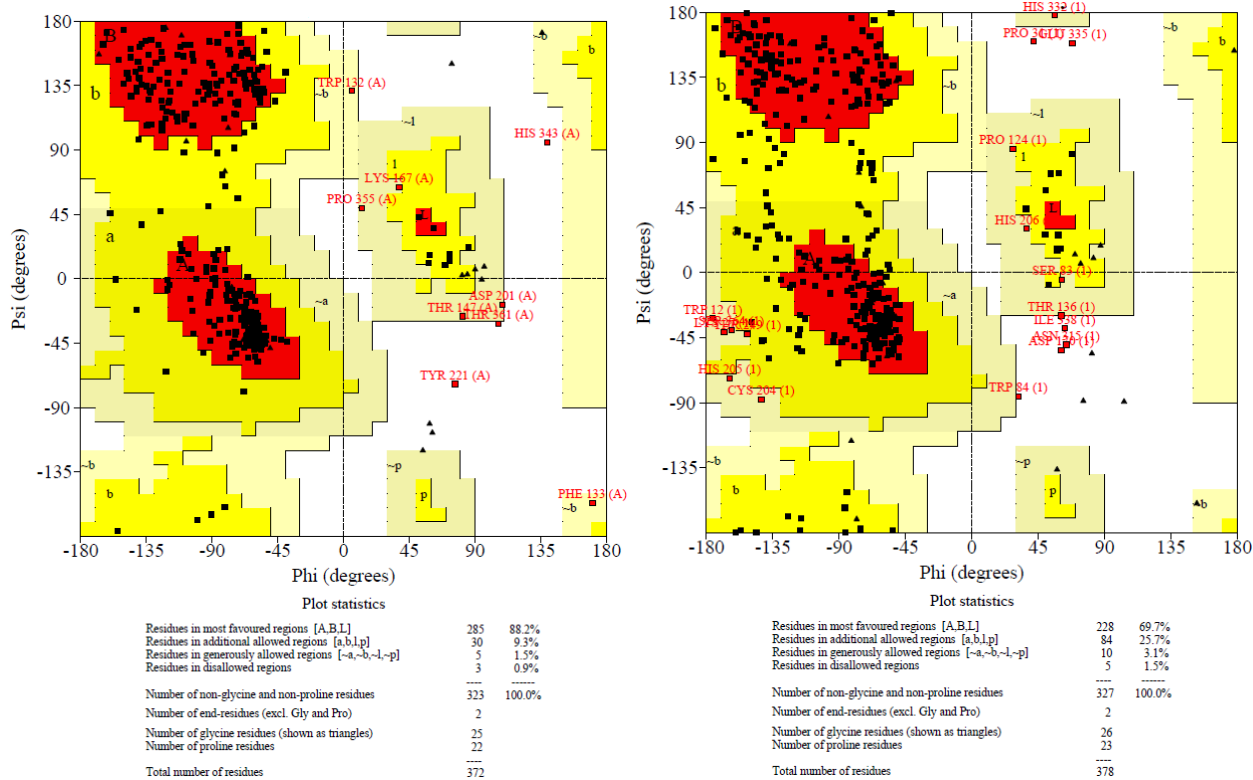


Figure 33 Ramachandran plot for Model 3 (left) and model 5 (right)

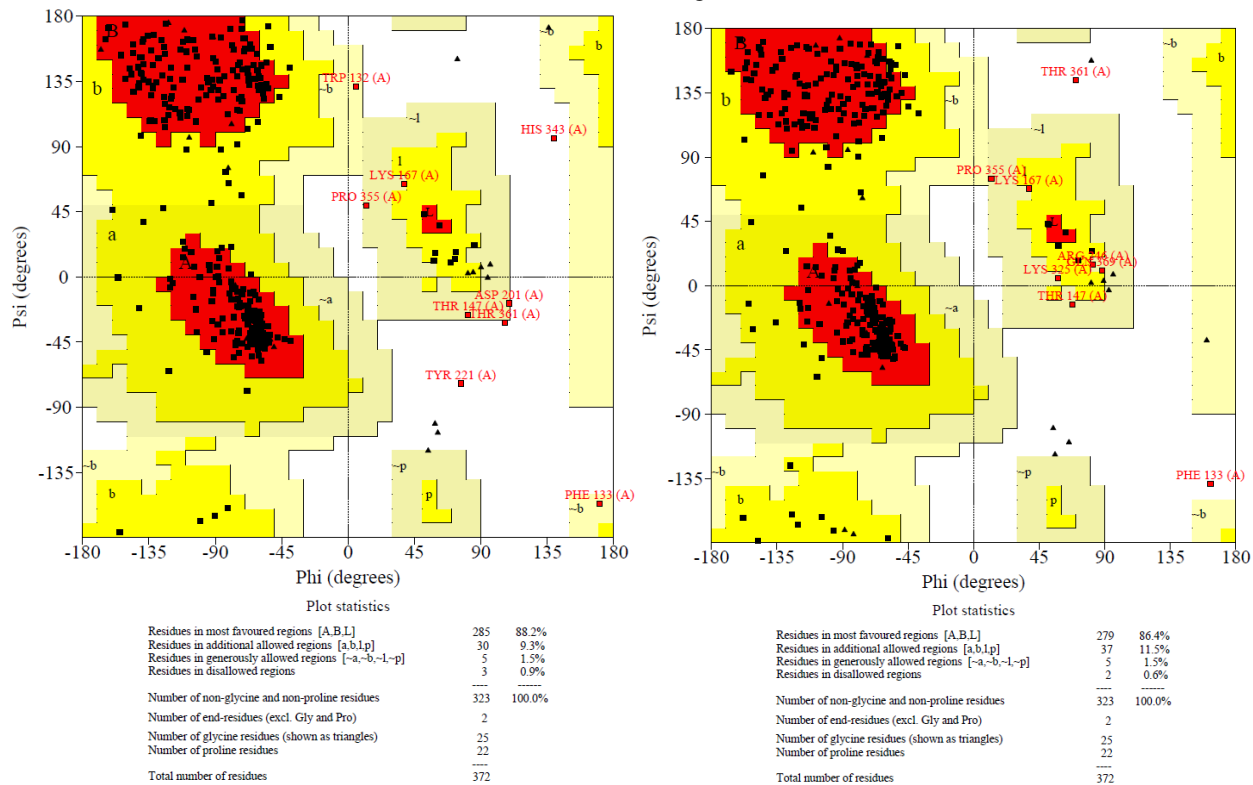


Figure 34 Ramachandran plot for Model 4 (left) and its energy minimized model (right)

The docking of **4.20** with the crystal structure for the fucosidase from *T. maritima* was carried out and it suggested a H-bond acceptor/donor network, where hydroxyl groups of the iminosugar interacted with the side chain of Glu66 (1.97 Å), Trp67 (2.33 Å) and Asp224 (2.04 Å), as shown in **Figure 35A**. The protonated nitrogen of the iminosugar had a H-bond donor interaction with the carboxyl group in the side chain of Asp224 (2.05 Å). The docking showed how closely the calculated binding mode of **4.20** resembles the already reported binding of iso-6FNJ in the crystal structure bound to the fucosidase from *T. maritima* (see **Figure 35B**). Furthermore, the docking of **4.20** with the homology model of the *B. taurus* fucosidase indicated similar binding interactions to those seen for *T. maritima*. The hydroxyl groups of **4.20** had H-bond acceptor/donor interactions with Val77 (2.25 Å) and Asn282 (2.31 Å), while the protonated nitrogen was predicted to have H-bond donor interactions with Cys240 (2.45 Å), see in **Figure 35C**. Also, a similar trend was noted after docking of **4.24** as its C-4 hydroxyl group was involved in a H-bond donor interaction with Cys240 (1.94 Å), while the protonated nitrogen had a H-bond donor interaction with Cys240 (1.92 Å). The nonane chain of **4.24** was placed by docking into a hydrophobic cavity constituted by aromatic residues (His82, Tyr126, Trp172) on one side while residues 281-283 and Trp248 were found on the other side of the domain. These are shown in **Fig. 35D**.

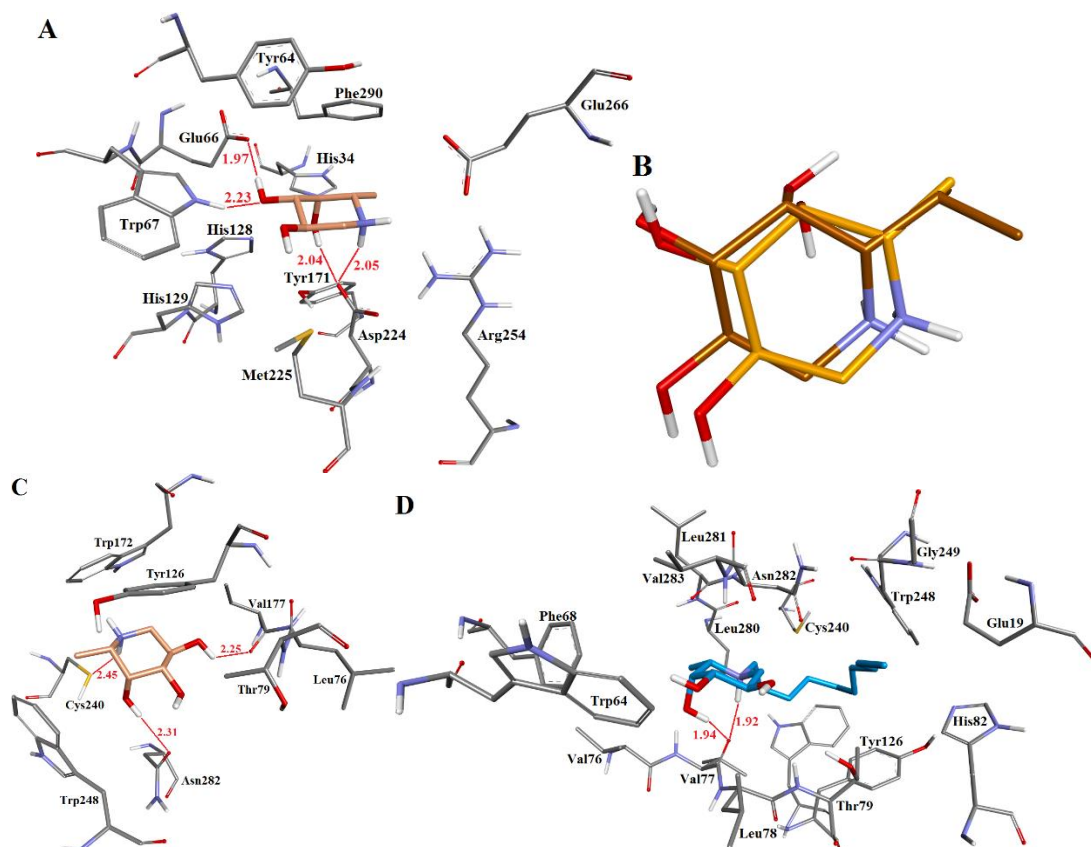


Figure 35 (A) The docking pose of **4.20** (orange) with the fucosidase of *T. maritima*; (B) superpose of binding pose of **2.20** (orange) with co-crystallised ligand (brown) of 2WSP_A (model 4, Table 3); (C) docking pose of **4.20** with fucosidase of *B. taurus*; (D) docking pose of **4.24** (blue) with fucosidase of *B. taurus*.

In order, to gain confidence regarding the reliability of the docked poses for **4.20** and **4.24**, they were selected for 100 ps molecular dynamics simulations (MD). The complex of **4.20** with the fucosidase of *T. maritima* showed stability after 10 picoseconds (ps) of the simulation (RMSD was consistently ~ 1.9 Å, **Figure 36A**). The same protocol was applied on the docked complex of **4.20** with the fucosidase of *B. taurus*; the ligand-protein complex showed fluctuation in first 10 ps and then the RMSD maintained a stable value ~ 2.8 Å (**Figure 36B**). The complex of **4.24** to fucosidase of *B. taurus* complex showed stability after 20 ps with an RMSD value of ~ 3.2 Å (**Figure 36C**). The MD simulation demonstrated the docked ligand-protein complexes were stable and generated confidence that they form the basis of a reasonable hypothesis as to the nature of inhibitor binding [395].

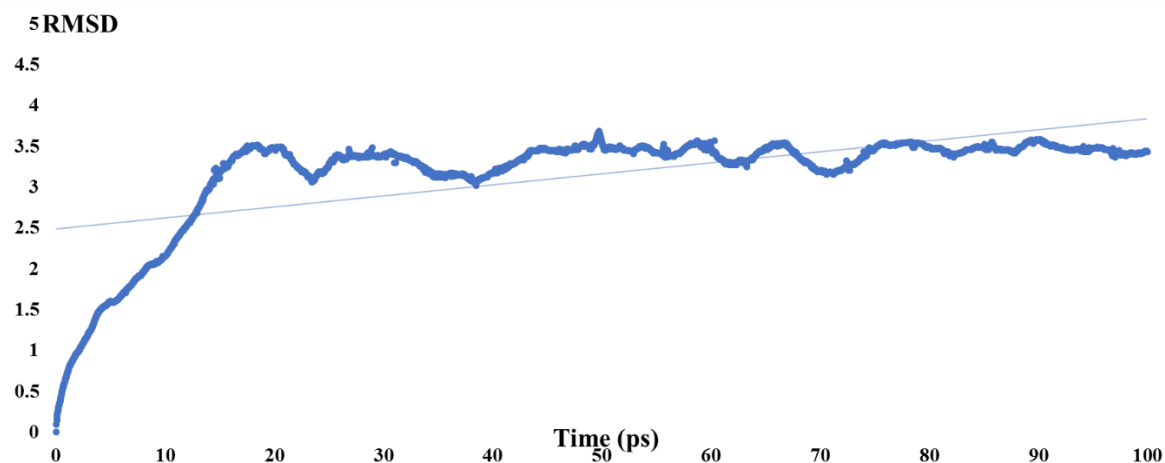
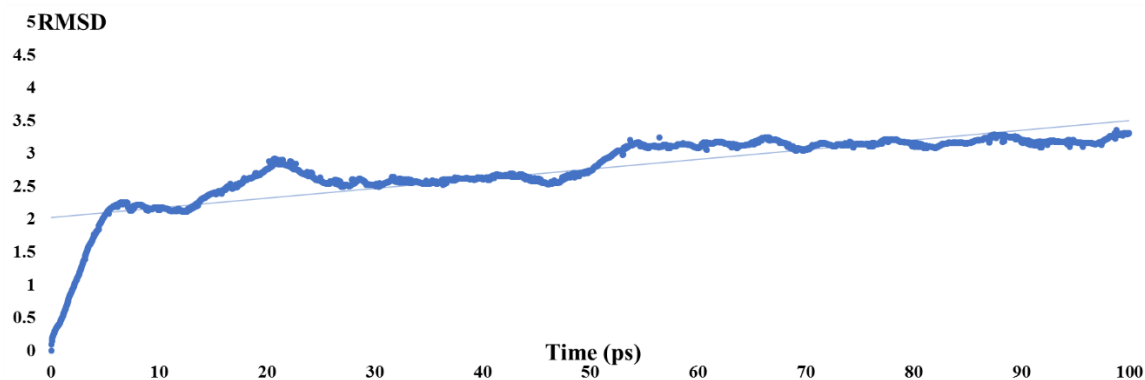
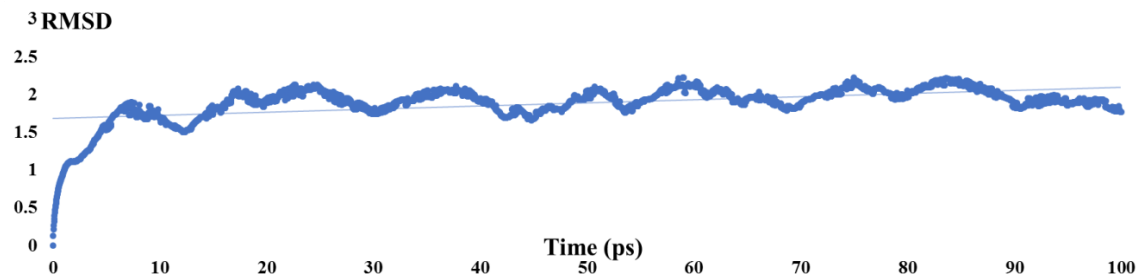


Figure 36 MD run over 100ps, (A) compound **4.20** (with fucosidase of *T. maritima*) with RMSD 1.88 Å; (A) Compound **4.20** with *B. taurus* fucosidase has RMSD 2.76 Å (C) Compound **4.24** with *B. taurus* fucosidase had an RMSD of 3.20 Å.

To further evaluate molecules against human fucosidase, a reverse docking strategy was performed [276]. The consistency and suitability of docking placement methods (in MOE 2018.01) with respect to the activities of compounds were evaluated. Hence the 3D structure of human alpha fucosidase was next modeled using the same template which was used for fucosidase of *B. taurus* origin (2WSP_A). The quality of the human homology model generated (**Figure 40A**) was evaluated using Ramachandran plot (residues in most favored regions (86.9%), residues in additional allowed regions (10.5%), residues in generously allowed regions (1.4%) residues in

disallowed regions (1.1%), see in **Figure 37**) and ProSA Z-score (see in **Figure 38**), Errat plot (88.86) in **Figure 39** and Verify 3D score (88.81%). The residues Lys52, Phe184, His396 and Asp432 were found as outliers and are not in the active site (**Figure 40B**)

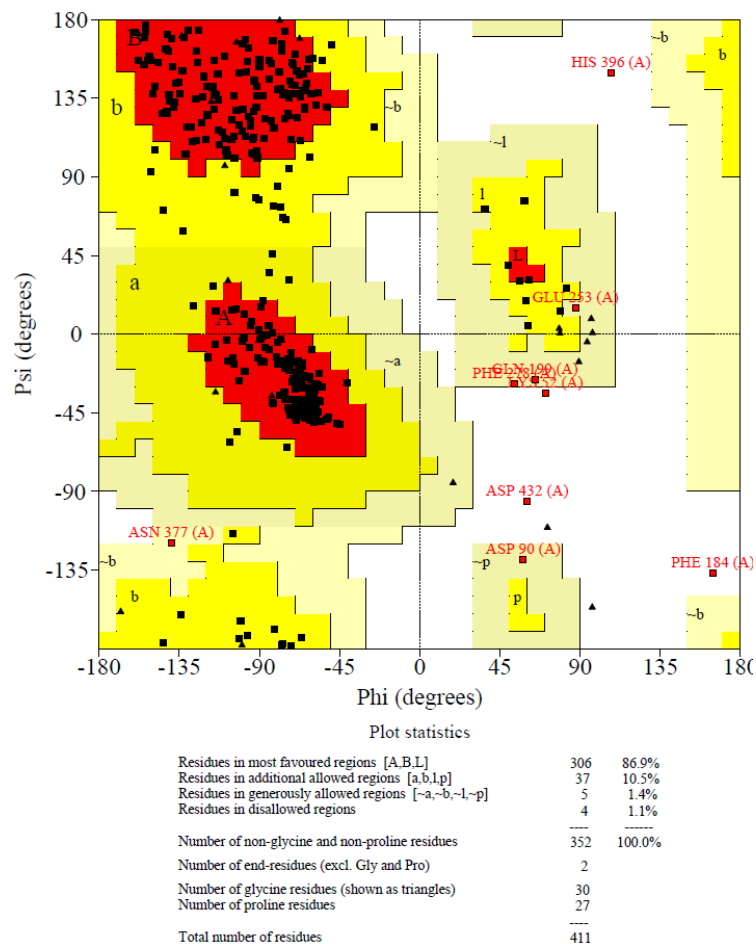


Figure 37 Ramachandran plot for human fucosidase homology model

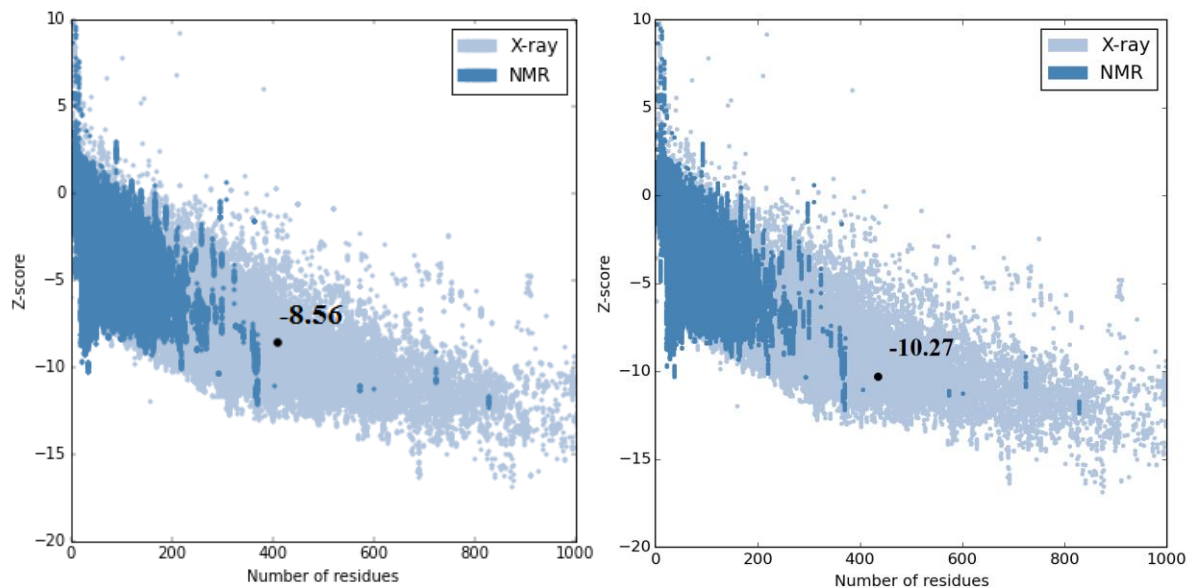
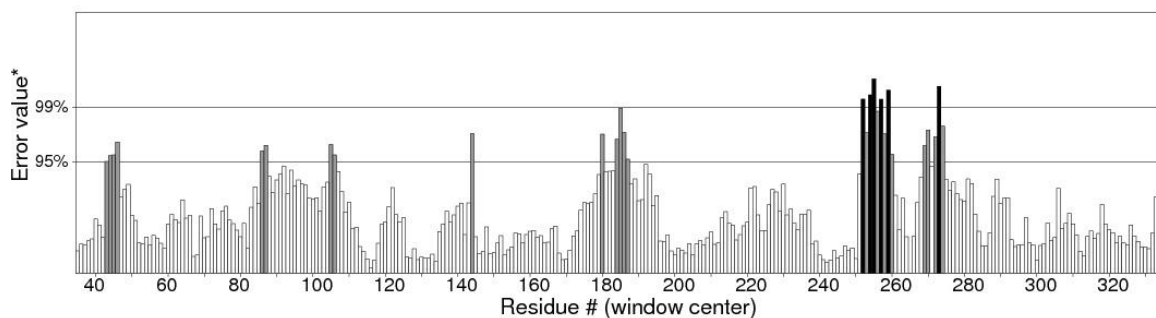


Figure 38 Comparative protein structure analysis (ProSA) calculates Z-score for (a) Human fucosidase homology model (left), (b) template (2WSP.A) (right).

Program: ERRAT2
 File: /var/www/SAVES/Jobs/49495657//erratt.pdb
 Chain#:1
 Overall quality factor**: 88.860



*On the error axis, two lines are drawn to indicate the confidence with which it is possible to reject regions that exceed that error value.
 **Expressed as the percentage of the protein for which the calculated error value falls below the 95% rejection limit. Good high resolution structures generally produce values around 95% or higher. For lower resolutions (2.5 to 3Å) the average overall quality factor is around 91%.

Figure 39 ERRAT plot of human fucosidase homology model

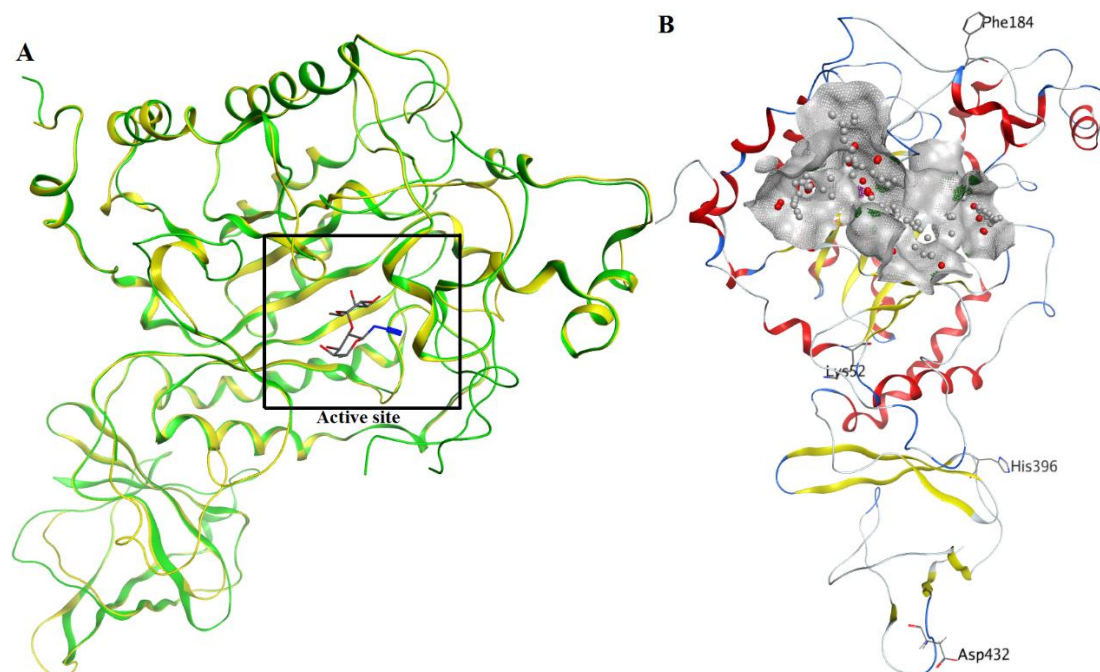


Figure 40 (A) The RMSD value between the template (2WSP, yellow) and the human fucosidase homology model (green), which are superposed, was 0.71. The black rectangle outlines the active site. (B) The binding site is shown in grey. The red spheres are atoms with potential to interact with hydrophobic groups, whereas the grey spheres correspond to atoms that have potential as H-bonding donors/acceptors.

The IC_{50}/K_D values (**Table 9**) for inhibitors (**Figure 41**) of the human fucosidase (HuF) from the work of Ho *et al* [396] were used to generate scatter plots (see **Figure 42**). Trend lines were generated and R^2 values were determined; these showed an association between the docking placement method with respect to the inhibitory properties. The docking scores are shown in **Table 9**.

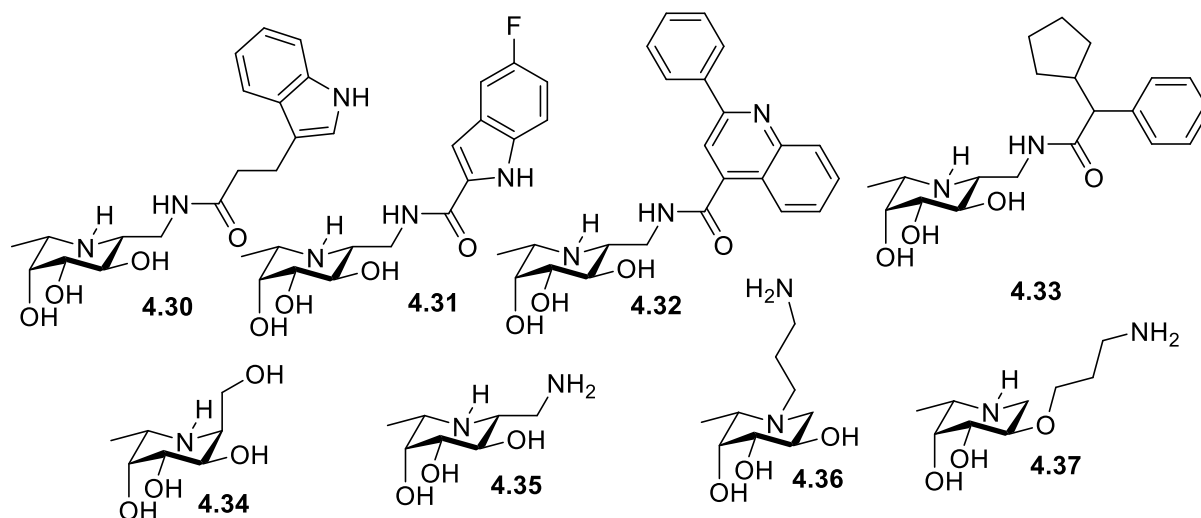


Figure 41 The compounds of Ho *et al* [386] used in the docking study.

Table 9 Comparison of scores attained from docking placement methods against the IC_{50}/K_D values for the compounds against human fucosidase (HuF) and *T. maritima* fucosidase.

Comps	K_i/IC_{50} for HuF (μM)	K_i/IC_{50} for TM (μM)	Alpha Triangle Method		Triangle Matcher Method		Alpha PMI Method	
			HuF ^a	TM ^b	HuF ^a	TM ^b	HuF ^a	TM ^b
4.30	0.0056 ^c	0.000105 ^c	-12.037	-12.114	-11.887	-12.199	-13.011	-12.357
4.31	0.0097 ^c	0.000259 ^c	-11.451	-11.78	-11.764	-12.002	-12.882	-12.41
4.32	0.0117 ^c	0.00119 ^c	-11.393	-11.491	-11.119	-11.833	-12.50	-12.042
4.33	0.018 ^c	0.00101 ^c	-11.108	-11.542	-10.810	-11.809	-12.619	-11.945
4.34	0.018 ^d	0.052 ^d	-10.920	-11.304	-10.991	-10.892	-12.451	-11.807
4.35	0.035 ^d	0.064 ^d	-10.543	-10.928	-10.605	-10.712	-11.521	-11.065
4.36	0.092 ^d	0.070 ^d	-10.008	-10.637	-9.332	-10.288	-11.402	-10.42
4.37	0.106 ^d	0.267 ^d	-10.219	-10.419	-9.290	-9.074	-11.477	-10.317

^a Human fucosidase homology model; ^b fucosidase of *T. maritima* ^c K_i values in μM ; ^d IC_{50} values in μM .

For this study, three different docking placement methods, available in MOE 2018.01, were investigated. Of the docking methods, the triangle matcher placement method performed better than the alpha triangle and alpha PMI placement methods. With this method, there were coefficients of determination of 0.908 and 0.8731, which were higher than those of the other two methods (see **Figure 42** and **Figure 43**).

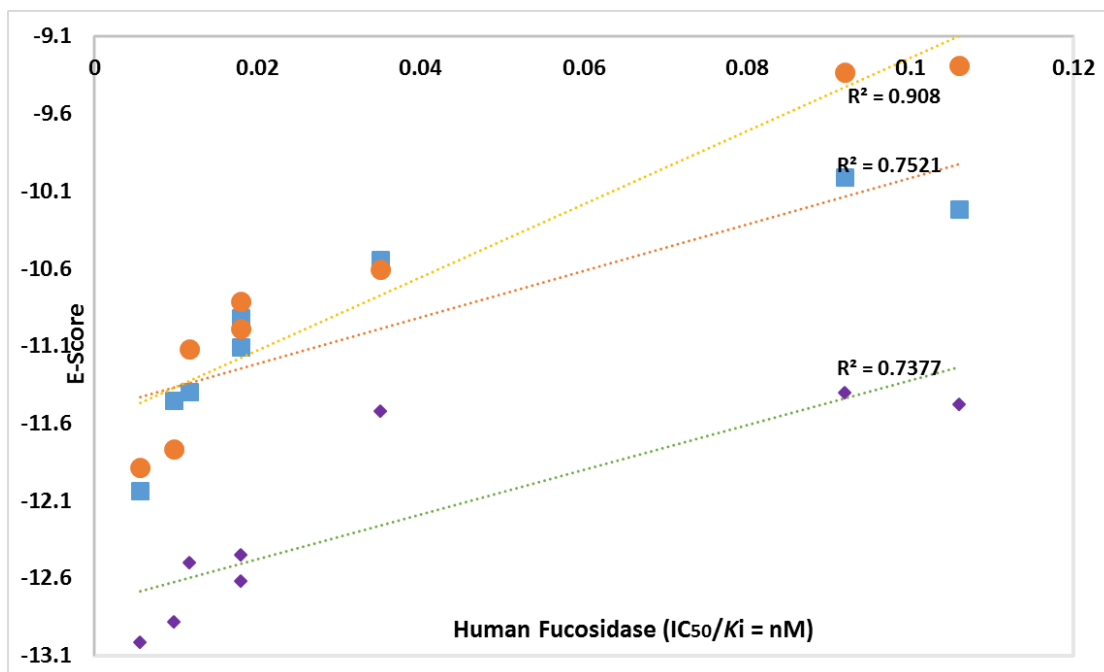


Figure 42 Plots of docking E-score (y-axis) and K_i/IC_{50} values (nM) for human fucosidase (x-axis) for three docking placement methods (See Table 4 for data used).

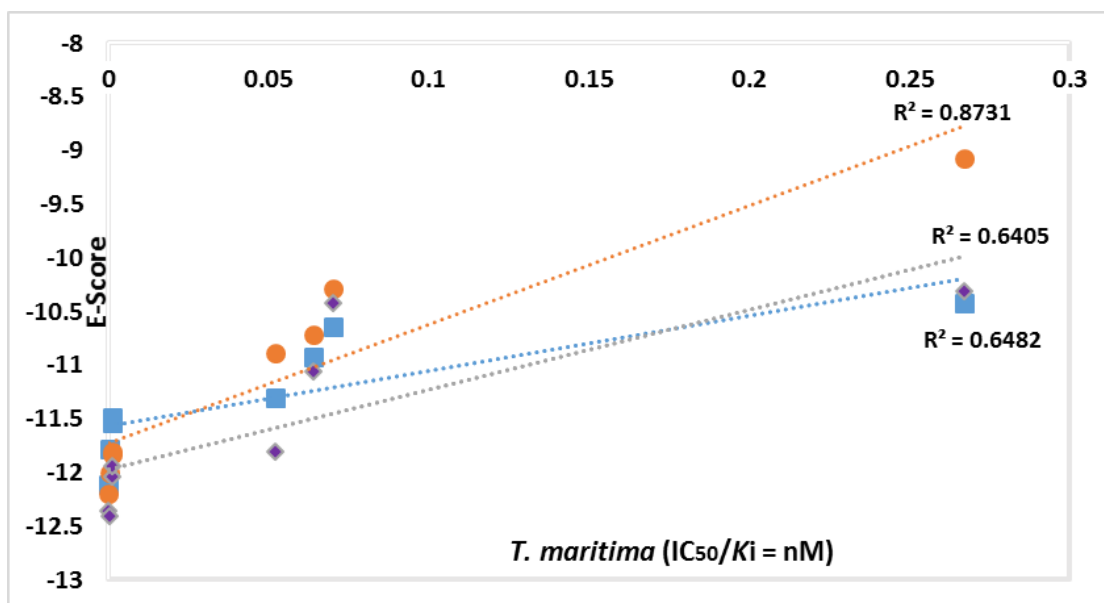


Figure 43 Plots of E-score (y-axis) and K_i/IC_{50} values (x-axis) for inhibitors of the *T. maritima* fucosidase for three docking placement methods (See Table 4 for data used).

The available enzyme inhibitory data from Ho *et al* [386] for the two different enzymes were used to generate the plot in **Figure 44**. These gave a trendline with an R^2 value of 0.7169. The R^2 values observed are sufficiently high to imply that the enzyme inhibitory properties for compounds are associated with binding to the specified active site cavity in the fucosidases [397].

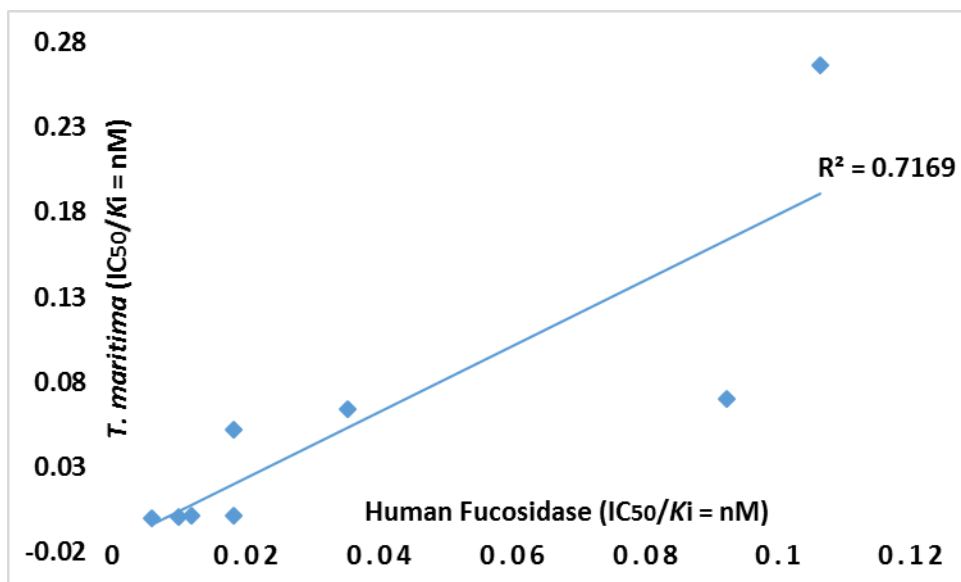


Figure 44 Plots of IC₅₀/K_D values for inhibitors of human fucosidase (x-axis) versus those of *T. maritima* fucosidase (y-axis, see Table 4 for the data used).

The three docking methods all predicted that the *N*-propyl amine derivative **4.36** could have a different binding location within the active site (E-Score = -10.288) compared to other DFJ derivatives (**Figure 45**).

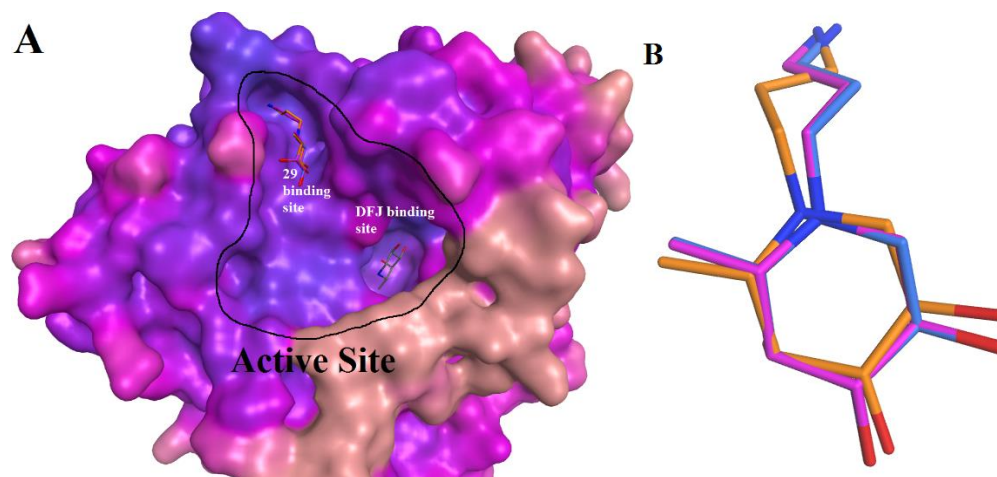


Figure 45 (A) The black contour line outlines the active binding site in fucosidase of *T. maritima*. Here **4.36 (29)** was predicted to differ in binding position with respect to DFJ **4.20**; **(B)** The docked conformations of **4.36**, corresponding to the three docking methods, are shown overlaid in blue (triangle matcher), magenta (alpha triangle), orange (alpha PMI).

In the docking of **4.26** (E-score = -5.613) and **4.29** (E-Score = -6.175) high E-scores were found, which are consistent with the lack of inhibition of the enzymes observed experimentally.

On the other hand, the *N*-butyl alcohol derivative **4.29** did show inhibitory activity ($IC_{50} = 30 \mu M$) towards the fucosidase of *B. taurus* and docking indicated this could be reasonably supported by the OH group of the butyl chain being involved in a hydrogen bonding interaction with the peptide backbone of Lys74 (2.97 Å) of this fucosidase.

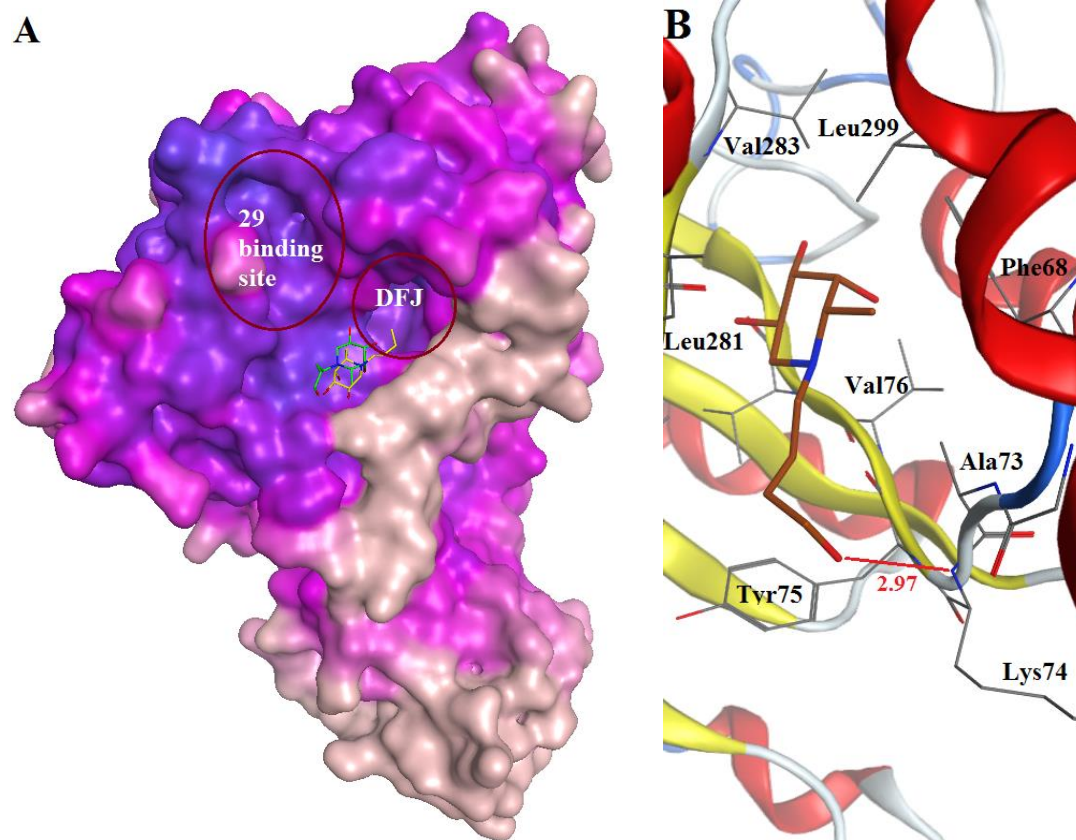


Figure 46 (A) The binding of **4.26** (yellow color) and **4.29** (cyan color) in fucosidase of *T. maritima*. This showed **4.26** and **4.29** outside the binding regions predicted to be occupied by **4.36** and **DFJ**. (B) The docking pose of **4.29** with respect to the fucosidase of *B. taurus* shown with predicted H-bonding interaction (green line) of Lys74.

The docking was also performed on human fucosidase (HuF) where binding of both the *N*-propylamine derivative **4.36** (E-score = -9.322) and *N*-decyl derivative **4.24** (E-score = -8.724) is predicted to occur (**Figure 46A**). The difference between the docking score of **4.24** (E-score = -8.724) to HuF and to the fucosidase of *T. maritima* (E-score = -6.901) indicates it may be of interest to evaluate **4.24** for its inhibition of human fucosidase in due course.

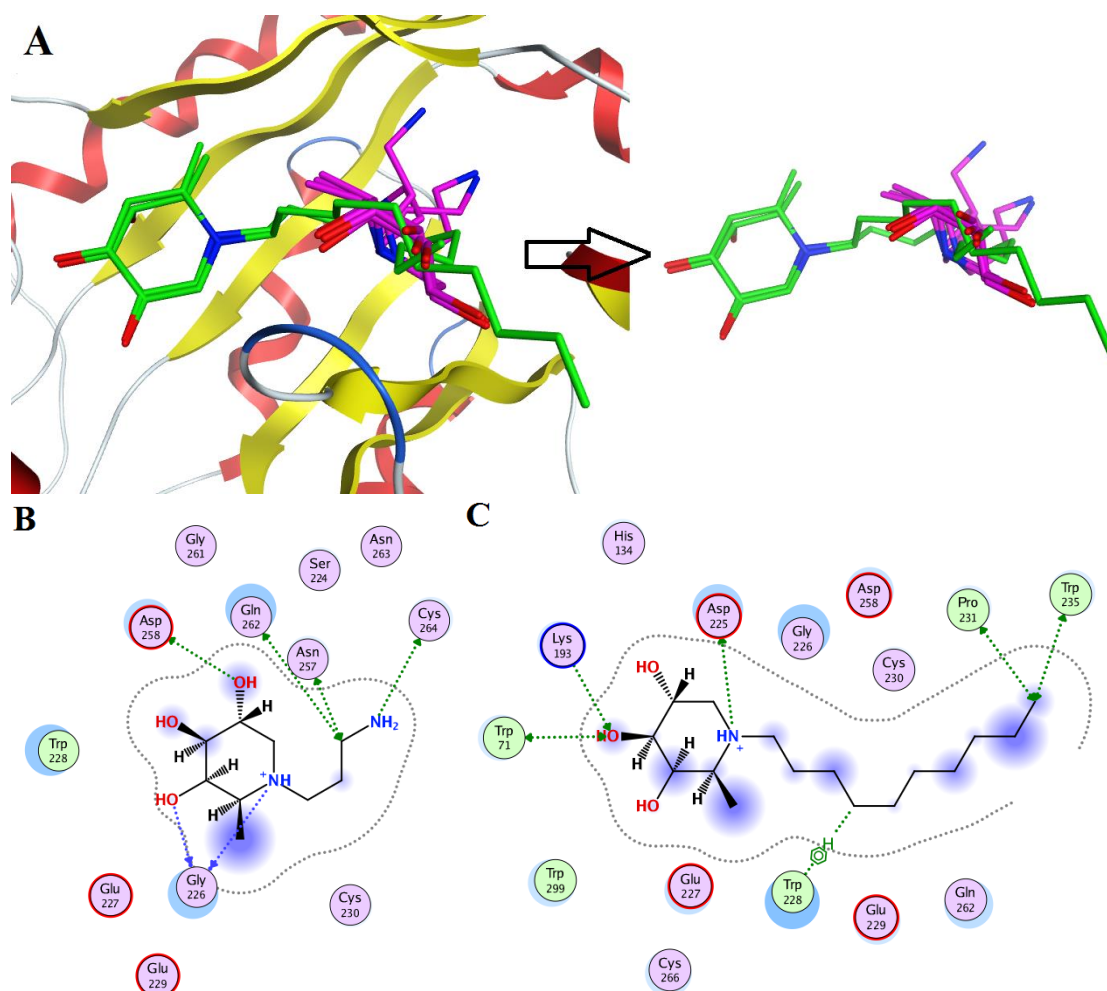


Figure 47 (A) The predicted binding of **4.36** (purple) and **4.24** (green) in the fucosidase of human origin, along with the clustered conformations. The predicted 2-D interaction of **4.36** (B) and **4.24** (C) with human fucosidase.

4.2.2.3 Cytotoxicity against BT-474, MCF-7 and DU-145 cell lines using the MTT assay

This study is completed assisted by Dr. Styliana Mirallai at NUI Galway, under the supervision of Michael Carty. The BT-474 (breast cancer), MCF-7 (breast cancer) and DU-145 (prostate cancer) cell lines, available at the National University of Ireland Galway (NUI Galway), were used to independently determine whether compounds **4.23**, **4.24**, **4.26**, **4.28** and **4.29** were cytotoxic using the MTT assay. Compound **4.24** was found to be the most toxic against all cell lines exhibiting a greater potency towards prostate cancer cell line (DU-145). Toxicity of pleurotin, a positive control, is also given in **Table 10** [64, 65]

Table 10 Cytotoxicity evaluation using the MTT colorimetric assay. IC₅₀ values were obtained after the incubation of cells with the test compounds in DMSO for 72 h.

Compounds	IC ₅₀ BT-474 (μM)	IC ₅₀ MCF-7 (μM)	IC ₅₀ DU-145 (μM)
Pleurotin (control)	1.94 ± 0.49*	0.28 ± 0.03*	0.43 ± 0.06*
4.23	>100	>100	>100
4.24	57.39 ± 3.38	30 ± 0.04	13.54 ± 0.75
4.26	>100	77 ± 1.53	60.99 ± 3.15
4.28	>100	>100	>100
4.29	>100	>100	>100

4.2.2.4 Inhibition of proliferation of human head and neck carcinoma cell lines

This testing was performed in laboratory of Christel Herold-Mende by Rolf Warta. The compound **4.24** was further tested for its inhibition of proliferation of human head and neck carcinoma cells (HNO41, HNO97, HNO210), as well that of patient-derived glioblastoma-initiating cells (NCH644 IDH1-wt GBM) using the CellTiter-Glo assay. Compound **4.24** inhibited the proliferation of all these cell lines with IC₅₀ values ranging from 12 μM to 17.6 μM (Table 6). The inhibition by pleurotin, a positive control, is also reported for these various cell types.

Table 11 Inhibition of proliferation of cancer cell lines by **4.24**

Cell line	IC ₅₀ of 2.24 [μM]	IC ₅₀ of puromycin [μM]
NCH644	17.6	0.27
HNO210	17.4	0.16
HNO97	12.0	0.24
HNO41	13.8	0.24

4.2.3 Conclusions

A series of *N*-alkylated fuconojirimycin analogues have been prepared and evaluated as inhibitors of fucosidases of bacterial and bovine origin. The best inhibitory activity for the new compounds, was observed for *N*-decyl-DFJ against the bovine fucosidase (IC₅₀ = 2.5 μM). The pairwise sequence alignment for the two enzymes showed their close resemblance, sharing evolutionary conserved domains. Homology models of the fucosidases from human and bovine origin were thus both constructed and used in docking and molecular dynamics. *N*-Decyl-DFJ was shown to inhibit growth of various cell lines, including IDH wild type glioblastoma cells [398] and could form the basis for development of more potent inhibitors of tumour cell growth.

Chapter 5 Experimental Section

Experimental section for Objective 2.2

Ligand structures and minimizations

The ligands were collected from various reports (see in **Figure 48** of *objective 2.2*). The molecules which have demonstrated preferential selectivity for Mcl-1 protein were carefully built with their assigned stereochemistry in MOE builder tool. These structures were later minimized by MMFF94x forcefield with steepest gradient (0.00001) and protonated at pH 7.4. Further these structures were individually saved pdb files and used in this format for docking.

Selection of Protein structure

A search for Mcl-1 protein structure on Protein Data Bank gave 34 Mcl-1 crystal structures with resolution ranging from 1.60 to 2.82 Å, which were further filtered based on species and the biophysical method adopted for these structures. The filtered structures were scrutinized against various crystallographic and protein stereochemistry parameters, see **Table 1** of *objective 2.2*. Only crystals with co-crystallized molecules were selected as that was required for assigning the binding site. Later these were superimposed on each other and the deviation in their backbone with respect to each other was evaluated by comparing their RMSD values. However, various approaches such as MRC, MLC and self-docking in relation to the RMSD evaluation were implemented to validate the adopted methodology for these studies. Based on these computational approaches, a pdb (3WIX) was selected for Mcl-1, which has a high resolution 1.8 Å crystal structure, along with very low crystallographic errors (as shown in **Table 1**) and also it fits all the reported co-crystallized inhibitors used in the study within a RMSD range of 0.69-1.09 Å (these results were only obtained from MOE docking).

Preparation of Protein Structure and Triangle matcher-based docking using MOE

In MOE 2018.01, the protein was prepared by, (a) removing of the water molecules from their crystal structures; (b) optimizing the missing atoms of amino acid residues, especially in the loops; and (c) protonation (required for the correction in the ionization and tautomeric state of amino acid residues) of the structure. Next, for docking the triangle matcher and GB/VI was selected as placement method and scoring algorithm respectively. Triangle matcher usually generates the ligand-protein poses by aligning the ligand atoms triplet on triplets of alpha spheres in a more systematic way (total number of returned poses was set 100,000, with time out 3000 s). The docking gradient (0.001) and 10,000 iteration cycles were selected as termination criterion.

However, pharmacophore restraint was left as such on default values. The cluster of conformations was chosen from the first 500 energy minimized poses within ≤ 2 Å.

Genetic algorithm-based grid docking using AutoDock

The Mcl-1 protein crystal and ligand structures were saved in pdbqt format to ensure the software compatibility in AutoDock 1.5.6. The AutoGrid was mapped around the co-crystallised ligand as $60 \times 60 \times 60$ Å³ (x, y, and z) with 0.400 Å spacing. The dock parameters were set up as follows: (a) maximum of 25 conformers were considered for each compound, (b) population size was set to 250 with the individual conformers were initialized randomly, (c) maximum numbers of generations were taken to be 27000, (d) maximum number of evaluations was set as 2500000.

GRIP docking by VlifeDock

This docking was performed on VlifeDock by using *inhouse* placement method and scoring was calculated by GRIP scoring function. This method generally generates a wide population of initial poses which ultimately evolve into the optimal binding mode.

Post docking analysis

Post docking analysis and interactions/ measurements with done in Accelrys discovery studio visualizer.

Experimental section for Objective 2.3

General Experimental conditions

Compounds prepared herein, that are already known in the literature already have been cited herein. Unless otherwise stated, their analytical data (¹H NMR and/or ¹³C NMR spectral data), obtained during this work was found to be in agreement with previously published data. NMR spectra were recorded with a 500 MHz Varian spectrometer. Chemical shifts are reported relative to CDCl₃ (δ 7.26) or CD₃OD (δ 3.31) or DMSO-*d*₆ (δ 2.50) for ¹H spectra and CDCl₃ (δ 77.16) or CD₃OD (δ 49.00) or DMSO-*d*₆ (δ 39.52) for ¹³C spectra. NMR spectra were processed and analysed using MestReNova software. ¹H NMR signals for representative compounds were assigned with the help of gCOSY, while ¹³C NMR signals were assigned with the help of C-APT, gHSQCAD and/or gHMBCAD. Coupling constants are reported in Hertz, with all *J* values reported uncorrected. High resolution mass spectra were measured on a Waters LCT Premier XE spectrometer, measuring in both positive and/or negative mode. Thin layer chromatography (TLC) was performed on aluminum sheets precoated with silica gel 60 (HF254, E. Merck) and spots visualized by UV and heating with cerium molybdate. The solvents (such as cyclohexane, EtOAc, CH₂Cl₂ and MeOH) used for normal phase column chromatography were obtained from suppliers (Fisher Scientific and Sigma-Aldrich). All the laboratory chemicals were purchased from Sigma

Aldrich or TCI or Acros. Anhydrous solvents were obtained from a Pure Solv™ Solvent Purification System.

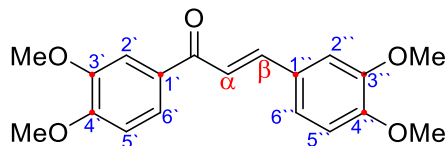
General procedure for synthesis of non-hydroxylated-chalcone

To the aryl ketone (1 equiv, reaction was performed on 100 mg-5 g scale), 1 M NaOH solution (5 - 50 mL) was added as well as a few drops of MeOH. After 30-45 mins, benzaldehyde derivative (1 equiv.) was added and left the reaction for 28-72 hours, while simultaneously reaction was monitored by TLC. After complete consumption of benzaldehyde, distilled water (5- 50 mL, depending on scale of reaction) was added and the mixture extracted with EtOAc (2 x 10-20 mL). The organic layer was dried over anhydrous sodium sulphate and EtOAc later was evaporated on rotarary evaporator. Then silica gel column chromatography was used to purify and obtain the desired compound (gradient elution, 4% to 8% EtOAc-cyclohexane).

General procedure for synthesis of hydroxylated-chalcone

To the aryl ketone (1 equiv., the reaction was performed on 500 mg-2 g scale), 1 M H₂SO₄ solution (10 - 20 mL) was added. After 15-45 mins, benzaldehyde derivative (1 equiv.) was added and the reaction left to stir for 48-72 hours, while at same time, the completion of the reaction was monitored by TLC. After reaction completion, crushed ice was added which led to precipitation of the organic components of the reactions, which were recovered by filtration using a vacuum. Later extraction with EtOAc was performed until no product remained in the aqueous layer. The organic layer was dried over anhydrous sodium sulphate and the solvent was removed under reduced pressure. Later, silica gel column chromatography was used to give chalcone (gradient elution, 15%-20% EtOAc-cyclohexane).

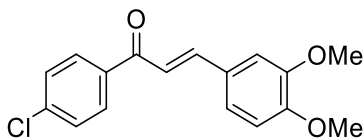
(E)-1,3-Bis(3,4-dimethoxyphenyl)prop-2-en-1-one (2.3.10)



Yield = 67%; yellow solid [399, 400]; m. p = 117-119 °C; ¹H NMR (500 MHz, CDCl₃) δ 7.77 (d, *J* = 15.5 Hz, 1H: β-H), 7.69 (d, *J* = 8.4, 1H: H-6'), 7.63 (d, *J* = 2.0 Hz, 1H: H-2'), 7.42 (d, *J* = 15.5 Hz, 1H: α-H), 7.24 (d, *J* = 1.9 Hz, 1H: H-6''), 7.17 (d, *J* = 1.9 Hz, 1H: H-2''), 6.94 (d, *J* = 8.4 Hz, 1H: H-2'), 6.91 (d, *J* = 8.3 Hz, 1H: H-2''), 3.98 (s, 6H: 2 x -OMe), 3.96 (s, 3H: -OMe), 3.94 (s, 3H: -OMe). ¹³C NMR (126 MHz, CDCl₃) δ 188.69 (-C=O), 153.13 (quaternary, C-4'), 151.28 (quaternary, C-4''), 149.25 (C-3''), 149.24 (C-3'), 144.15 (C-β), 131.57 (C-1'), 128.07 (C-1''),

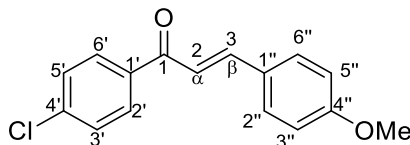
122.88 (C-6''), 122.85 (C-6'), 119.69 (C- α), 111.15 (C-2''), 110.86 (C-2'), 110.23 (C-5''), 109.92 (C-5'), 56.09 (-OCH₃), 56.08 (-OCH₃), 56.00 (-OCH₃), 55.99 (-OCH₃). HRMS-ESI: m/z calc for C₁₉H₂₁O₅: 329.1383, found: 329.1384 [M + H]⁺ (within 0.3 ppm difference).

(E)-1-(4-chlorophenyl)-3-(3, 4-dimethoxyphenyl)-prop-2-en-1-one (2.3.11)



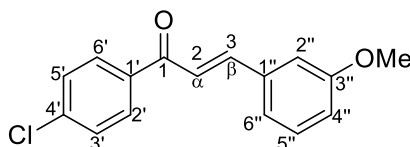
Yield = 52%; light brown solid [401]; m. p = 121-124 °C; ¹H NMR (500 MHz, CDCl₃) δ 7.98 – 7.95 (m, 2H: H₂' & H₆'), 7.77 (d, *J* = 15.6 Hz, H _{β}), 7.48 (d, *J* = 8.6 Hz, 2H, H₃' & H₅'), 7.34 (d, *J* = 15.6 Hz, H _{α}), 7.24 (dd, *J* = 8.3, 2.1 Hz, 1H, H₆''), 7.16 (d, *J* = 2.0 Hz, 1H, H₂''), 6.91 (d, *J* = 8.3 Hz, 1H, H₅''), 3.95 (6H, 2 x O-CH₃). ¹³C NMR (126 MHz, CDCl₃) δ 189.26 (C=O), 151.63 (C₃''), 149.29 (C₄''), 145.54 (C _{β}), 138.96 (C₄'), 136.78 (C₁'), 129.84 (C₂' & C₆'), 128.87 (C₃' & C₅'), 127.67 (C₁''), 123.31 (C₆''), 119.47 (C _{α}), 111.15 (C₅''), 110.13 (C₂''), 56.03 (-O-CH₃), 55.99 (O-CH₃). This compound's ¹³C spectra was in agreement with the previous published report by Raghavan et al [402]. HRMS-ESI: m/z calc for C₁₇H₁₆ClO₃: 303.0782, found: 303.0780 [M + H]⁺ (within 0.6 ppm difference)

(E)-1-(4-chlorophenyl)-3-(4-methoxyphenyl)-prop-2-en-1-one (2.3.12)



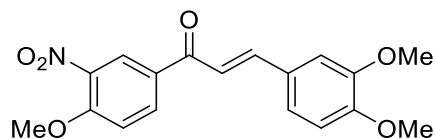
Yield = 58%; yellow solid [403]; m. p = 105-108 °C; ¹H NMR (500 MHz, CDCl₃) δ 7.98 – 7.94 (m, 2H: H-2' & H-6'), 7.79 (d, *J* = 15.6 Hz, 1H: β -H), 7.64 – 7.58 (m, 2H: H-2'' & H-6''), 7.50 – 7.45 (m, 2H: H-3' & H-5'), 7.38 (d, *J* = 15.7 Hz, 1H: α -H), 6.97 – 6.92 (m, 2H: H-3' & H-5'), 3.86 (s, OCH₃). ¹³C NMR (126 MHz, CDCl₃) δ 189.21 (-C=O), 161.86 (C-4''), 145.22 (C- β), 138.95 (C-4'), 136.83 (C-1'), 130.34 (C-2'' & C-6''), 129.84 (C-2' & C-6'), 128.88 (C-3' & C-5'), 127.45 (C-1''), 119.19 (C- α), 114.48 (C-3'' & C-5''), 55.44 (-OMe). HRMS-ESI: m/z calc for C₁₆H₁₄ClO₂: 273.0677, found: 273.0683 [M + H]⁺ (within 2.1 ppm difference)

(E)-1-(4-Chlorophenyl)-3-(3-methoxyphenyl)-2-propen-1-one (2.3.13)



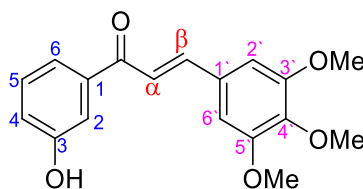
Yield = 51%; off-white color solid [403]; m. p = 98-102 °C; ¹H NMR (500 MHz, CDCl₃) δ 7.97 – 7.93 (m, 2H: H-2` & H-6`), 7.76 (d, J = 15.7 Hz, 1H: β-H), 7.48 – 7.43 (m, 3H: H-3` & H-5`; α-H), 7.33 (d, J = 7.9 Hz, 1H), 7.24 – 7.21 (m, 1H), 7.14 (t, J = 2.0 Hz, 1H), 6.97 (ddd, J = 8.2, 2.6, 1.0 Hz, 1H), 3.85 (3H, O-CH₃). ¹³C NMR (126 MHz, CDCl₃) δ 189.10 (C=O), 159.92 (C3`), 145.20 (C-β), 139.18 (C4'), 136.42(C1'), 136.02(C1`), 129.95, 129.87 (C2' & C6'), 128.90 (C3' & C5'), 121.75 (Cα), 121.10 (C6`), 116.42 (C4`), 113.50(C2`), 55.32 (O-CH₃). HRMS-ESI: m/z calc for C₁₆H₁₄ClO₂: 273.0677, found: 273.0669 [M + H]⁺ (within 2.9 ppm difference).

(E)-3-(3,4-dimethoxyphenyl)-1-(4-methoxy-3-nitrophenyl)-prop-2-en-1-one (**2.3.14**)



Yield = 63%; Light yellow solid [404]; m. p = 158-161 °C; ¹H NMR (500 MHz, CDCl₃) δ 8.54 (s, 1H: H-2`), 8.28 (d, J = 8.8 Hz, 1H: H-5`), 7.83 (d, J = 15.6 Hz, 1H: β-H), 7.35 (d, J = 15.6 Hz, 1H: α-H), 7.28 (d, J = 8.8 Hz, 1H: H-6`), 7.21 (d, J = 8.3 Hz, 1H: H-5`), 7.17 (s, 1H: H-2`), 6.92 (d, J = 8.3 Hz, 1H: H-6`), 4.06 (s, 3H: -OCH₃), 3.98 (s, 3H: -OCH₃), 3.95 (s, 3H: -OCH₃). ¹³C NMR (126 MHz, CDCl₃) δ 186.73 (Quaternary, -C=O), 155.97 (Quaternary, C-4'), 151.83 (Quaternary, C3`), 149.35 (Quaternary, C4`), 146.07 (trans-β-C), 139.27 (Quaternary, C3`), 134.39(Aromatic -CH-), 130.82 (Quaternary, C1'), 127.50 (Quaternary, C1`), 126.11(Aromatic -CH-), 123.59 (Aromatic -CH-), 118.22 (trans-α-C), 113.42 (Aromatic -CH-), 111.16 (Aromatic -CH-), 110.21(Aromatic -CH-), 56.90 (-OCH₃), 56.06, (-OCH₃) 56.04 (-OCH₃). HRMS-ESI: m/z calc for C₁₈H₁₈NO₆: 344.1129, found: 344.1141 [M + H]⁺ (within 3.5 ppm difference).

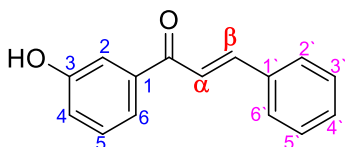
(E)-1-(3-Hydroxyphenyl)-3-(3,4,5-trimethoxyphenyl)prop-2-en-1-one (**2.3.15**)



Yield = 72%; yellow solid [405]; m. p = 168-170 °C; ¹³C NMR (126 MHz, CDCl₃) δ 190.35 (C=O, carbonyl), 156.17 (Quaternary, C-3), 153.51 (Quaternary, C-3` & C-5`), 145.38 (CH, C-β), 140.57 (Quaternary, C-1)139.78 (Quaternary, C-4'), 130.29 (Quaternary, C-1'), 129.92 (Aromatic CH, C-5), 121.32 (Aromatic CH, C-6), 121.03 (CH, C-α), 120.11 (Aromatic CH, C-4), 115.10 (Aromatic CH, C-2), 105.76 (Aromatic CH, C-2` & C-6`), 61.04 (C-4`-OCH₃), 56.27 (C-3` & C-5` -OCH₃). The melting point and ¹³C chemical shifts were with agreement Holt and co-worker study [406].

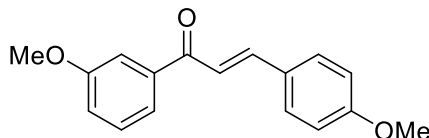
HRMS-ESI: m/z calc for C₁₈H₁₉O₅, 315.1227, found: 315.1230 [M + H]⁺ (within 1.0 ppm difference).

(E)-1-(3-hydroxyphenyl)-3-phenylprop-2-en-1-one (2.3.16)



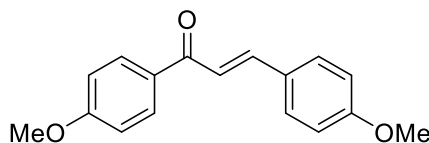
Yield = 63 %; light yellow solid [405]; m. p = 134–137 °C; ¹H NMR (500 MHz, CDCl₃) δ 7.82 (d, *J* = 15.7 Hz, 1H: β-H), 7.65 (dd, *J* = 6.4, 2.9 Hz, 2H: H-2'' & H-6''), 7.59 (d, *J* = 7.7 Hz, 1H: H-6'), 7.55 – 7.53 (m, 1H: H-2'), 7.51 (d, *J* = 15.7 Hz, 1H: α-H), 7.45 – 7.36 (overlapping signals, 4H: H-3'', H-4'', H-5'' & H-5'), 7.12 – 7.07 (overlapping signals, 1H, H-4'), 5.51 (s, 1H: -OH). ¹³C NMR (126 MHz, CDCl₃) δ 190.33 (Quaternary C, -C=O), 156.13 (Quaternary, C-3), 145.18 (-CH-, C-β), 139.72 (C-1'), 134.82 (C-1), 130.66 (C-5), 129.94 (C-6), 128.99 (C-3' & C-5'), 128.52 (C-2' & C-6'), 121.99 (C-4), 121.09 (-CH-, C-α), 120.16 (C-4'), 115.06 (C-2). HRMS-ESI: m/z calc for C₁₅H₁₃O₂: 225.0910, found: 225.0904 [M + H]⁺ (within 2.7 ppm difference)

(E)-1-(3-methoxyphenyl)-3-(4-methoxyphenyl)prop-2-en-1-one (2.3.17)



Yield = 42 %; white solid; m. p = 101-103 °C; ¹H NMR (500 MHz, CD₃OD) δ 7.72 (d, *J* = 15.6 Hz, 1H: β-H), 7.67 – 7.60 (m, 3H: H-5', H-2'' & H-6''), 7.55 – 7.49 (m, 2H: α-H, H-5'), 7.41 (d, *J* = 7.9 Hz, 1H: H-3'), 7.17 – 7.13 (m, 1H: H-4'), 6.97 – 6.91 (m, 2H: C-3'' & C-5''). The ¹H NMR was in good agreement with report published by Shadakshari *et al* [407]. ¹³C NMR (126 MHz, CD₃OD) δ 190.69 (-C=O), 162.06 (C-3'), 160.02 (C-4'), 144.98 (C-β), 139.54 (C-1'), 130.26 (C-2'' & C-6''), 129.41(C-3'), 127.40 (C-1''), 120.67 (C-2'), 119.08 (C-α), 118.66 (C-4'), 114.10 (C-3'' & C-5''), 112.66 (C-2'), 54.49 (2 x -OCH₃). HRMS-ESI: m/z calc for C₁₇H₁₇O₃: 269.1172, found: 269.1178 [M + H]⁺ (within 2.3 ppm difference).

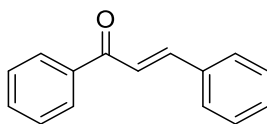
(E)-1,3-bis(4-methoxyphenyl)prop-2-en-1-one (2.3.18)



Yield = 55 %; white solid [408]; m. p = 105-106 °C; ¹H NMR (500 MHz, CDCl₃) δ 8.03 (d, *J* = 8.1 Hz, 2H: H-2' & H-6'), 7.78 (d, *J* = 15.6 Hz, 1H: H-β), 7.60 (d, *J* = 8.1 Hz, 2H: H-2'' & H-6''),

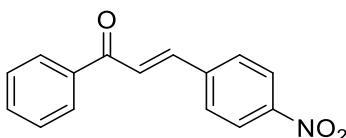
7.43 (d, $J = 15.6$ Hz, 1H: H- α), 6.98 (d, $J = 8.1$ Hz, 2H: H-3' & H-5'), 6.94 (d, $J = 8.1$ Hz, 2H: H-3'' & H-5''), 3.93 – 3.78 (s, 6H: 2 x -OMe). ^{13}C NMR (126 MHz, CDCl_3) δ 188.78 (-C=O), 163.27 (C-4'), 161.52 (C-4''), 143.81 (C- β), 131.38 (C-1'), 130.71 (C-2' & C-6'), 130.11 (C-2'' & C-6''), 127.84 (C-1''), 119.59 (C- α), 114.39 (C-3' & C-5'), 113.79 (C-3'' & C-5''), 55.49 (-OCH₃), 55.41 (-OCH₃). ^1H and ^{13}C NMR data was found in good agreement to that reported by Schmink *et al* [408]. HRMS-ESI: m/z calc for $\text{C}_{17}\text{H}_{17}\text{O}_3$: 269.1172, found: 269.1169 $[\text{M} + \text{H}]^+$ (within 1.1 ppm difference).

(E)-chalcone (2.3.1)



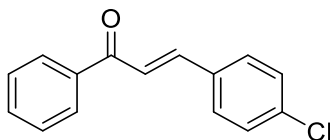
Yield = 78 %; yellow crystals [407, 408]; m. p = 58-60 °C; ^1H NMR (500 MHz, CDCl_3) δ 8.02 (d, $J = 8.6$ Hz, 2H: H-2' & H-6'), 7.77 (d, $J = 15.5$ Hz, 1H: H- β), 7.58-7.39 (m, 9H). ^{13}C NMR (126 MHz, CDCl_3) δ 189.01 (-C=O), 145.12 (C- β), 138.02 (C-1'), 135.106 (C-1''), 132.04 (Aromatic -CH-), 130.19 (Aromatic -CH-), 128.97 (Aromatic 2 x -CH-), 128.71 (Aromatic 2 x -CH-), 128.52 (Aromatic 2 x -CH-), 128.22 (Aromatic 2 x -CH-), 121.9 (C- α). ^1H and ^{13}C NMR data was found in good agreement to that reported by Schmink *et al.* [408]. HRMS-ESI: m/z calc for $\text{C}_{15}\text{H}_{13}\text{O}$: 209.0961, found: 209.0968 $[\text{M} + \text{H}]^+$ (within 3.3 ppm difference)

(E)-3-(4-nitrophenyl)-1-phenylprop-2-en-1-one (2.3.20)



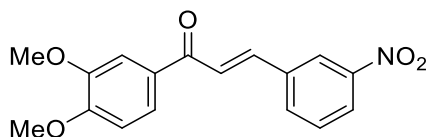
Yield = 36 %; light orange solid [409]; m. p = 119-120 °C; ^1H NMR (500 MHz, CDCl_3) 8.31 (d, $J = 8.7$ Hz, 2H), 8.02 (d, $J = 7.4$ Hz, 2H), 7.83 (m, 3H), 7.68 (m, 2H), 7.52 (t, $J = 7.6$ Hz, 2H). ^{13}C NMR (126 MHz, CDCl_3) δ 189.12 (-C=O), 148.03 (C-4''), 144.91 (β -H), 141.02 (C-1''), 137.21 (C-1'), 133.22 (C-1''), 128.83, 128.70, 128.43, 125.22, 122.11 (C- α). ^1H and ^{13}C NMR data was found in good agreement to that reported by Solin *et al* [409]. HRMS-ESI: m/z calc for: $\text{C}_{15}\text{H}_{12}\text{NO}_3$: 254.0812, found: 254.0818 $[\text{M} + \text{H}]^+$ (within 2.4 ppm difference).

(E)-3-(4-chlorophenyl)-1-phenylprop-2-en-1-one (2.3.19)



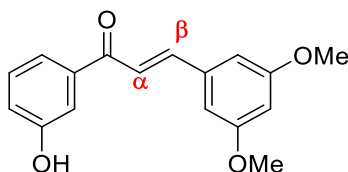
Yield = 63 %; white solid [408]; m. p = 101-103 °C; ¹H NMR (500 MHz, CDCl₃) δ 8.05 (d, *J* = 8.2 Hz, 2H: H-2' & H-6'), 7.79 (d, *J* = 15.5 Hz, 1H: H-β), 7.58-7.39 (m, 7H), 7.37 (m, 2H: H-α, aromatic-H). ¹³C NMR (126 MHz, CDCl₃) δ 190.0 (-C=O), 144.21 (C-β), 138.07 (C-1'), 136.02 (C-4''), 133.24 (C-1''), 132.51 (Aromatic -CH-, C-4'), 129.21 (Aromatic 2 x -CH-), 129.02 (Aromatic 2 x -CH-), 128.56 (Aromatic 2 x -CH-), 128.23 (Aromatic 2 x -CH-), 122.12 (C-α). ¹H and ¹³C NMR data was found in good agreement to that reported by Schminck *et al.* [408]. HRMS-ESI: m/z calc for C₁₅H₁₂ClO: 243.0571, found: 243.0575 [M + H]⁺ (within 1.6 ppm difference).

(E)-1-(3,4-dimethoxyphenyl)-3-(3-nitrophenyl)-prop-2-en-1-one (2.3.22)



Yield = 48 %; light yellow solid [410]; m. p = 165-169 °C; ¹H NMR (500 MHz, CDCl₃) δ 8.52 (s, 1H: H2''), 8.28 – 8.19 (m, 1H: H4''), 7.92 (d, *J* = 7.9 Hz, 1H: H2''), 7.83 (d, *J* = 15.6 Hz, 1H: β-H), 7.72 (dt, *J* = 8.4, 1.5 Hz, 1H: H6'), 7.67 (d, *J* = 15.6 Hz, 1H: α-H), 7.65 – 7.59 (m, 2H: H2' & H3''), 6.96 (d, *J* = 8.4 Hz, 1H: H3'), 3.99 (s, 6H: 2 x OMe). ¹³C NMR (126 MHz, CDCl₃) δ 187.71 (Quaternary, -C=O), 153.77 (Quaternary, C4'), 149.49 (Quaternary, C3'), 148.76 (Quaternary, C3''), 140.83 (trans-β-H), 136.90 (Quaternary, C1''), 134.38 (Aromatic -CH-), 130.78 (Quaternary, C1'), 130.02 (Aromatic -CH-), 124.49 (Aromatic -CH-), 124.32 (Aromatic -CH-), 123.36 (Aromatic -CH-), 122.19 (trans-α-H), 110.74 (Aromatic -CH-), 110.04 (Aromatic -CH-), 56.18 (-OMe), 56.13 (-OMe). HRMS-ESI: m/z calc for C₁₇H₁₆NO₅: 314.1023, found: 314.1024 [M + H]⁺ (within 0.3 ppm difference)

(E)-3-(3,5-dimethoxyphenyl)-1-(3-hydroxyphenyl)prop-2-en-1-one (2.3.21)



Yield = 56 %; light brown solid [411]; m. p = 177-180 °C; ¹H NMR (500 MHz, CDCl₃) δ 7.72 (d, *J* = 15.6 Hz, 1H: H-β), 7.58 (d, *J* = 7.8 Hz, 1H: H6'), 7.52 (s, 1H, H-2), 7.44 (d, *J* = 15.6 Hz, 1H: H-α), 7.39 (t, *J* = 7.8 Hz, 1H: H'4), 7.09 (dd, *J* = 7.8, 2.2 Hz, 1H: H5'), 6.78 (s, 2H: H2'' & H6''), 6.54 (s, 1H: H4''), 5.53 (Br s, 1H: -OH), 3.84 (s, 6H: 2 x OMe). ¹³C NMR (126 MHz, CDCl₃) δ 190.30 (Quaternary, -C=O), 161.09 (Quaternary, C-3'' & C-5''), 156.10 (Quaternary, C-3'), 145.17 (β-CH-), 139.67 (Quaternary, C-1''), 136.70 (Quaternary, C-1'), 129.94 (Aromatic -CH-), 122.50 (Aromatic -CH-), 121.11 (Aromatic -CH-), 120.17 (α-CH-), 115.07 (Aromatic -CH-),

106.40 (Aromatic -CH-C-2'' & C-6''), 102.92, 55.51 (2 x OCH₃). HRMS-ESI: m/z calc for C₁₇H₁₇O₄ 285.1121, found: 285.1123 [M + H]⁺ (within 0.7 ppm difference)

Synthesis of Pyrazolines and Pyrazoles

Pyrazolines from chalcones

Reaction of chalcones (1 equiv.) with hydrazine hydrate (1.5 equiv.) in methanol was performed in a sonicator for 2-2.5 hours. After completion of reaction, the mixture was cooled down and the pyrazoline products precipitated. These were later filtered off under vacuum. Silica gel column chromatography (gradient elution, EtOAc-cyclohexane, 8-15%) was used to improve the purity of the compounds.

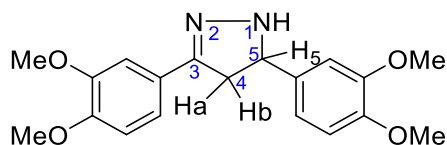
Pyrazoles from Pyrazolines

To a solution of the appropriate pyrazoline in DMSO, was added a catalytic amount of molecular iodine (10 mol %) and the reaction mixture was heated to reflux at 140–145 °C for 8 h. After the completion of the reaction (TLC), the crushed ice was poured on to the reaction mixture and it was stirred for 2 minutes. Later, aq. sodium thiosulfate and brine was added and the mixture extracted with EtOAc. The EtOAc layer was later dried over Na₂S₂O₃ and the solvent was then removed under reduced pressure and the product obtained after gradient column chromatography (EtOAc-cyclohexane, 6-12%).

Direct method for pyrazole formation from chalcones

To a stirred solution of the chalcone (1 equiv.) and TsNHNH₂ (1.2 equiv.) in EtOH was added molecular iodine (2 mol %) in an oven-dried flask, and then the reaction was heated at reflux for 10 min, and this was followed by the addition of K₂CO₃ immediately. The reaction proceeded for 1.5-2.0 hours until complete consumption of starting material had occurred as monitored by TLC. The reaction mixture was removed under reduced pressure and chromatography of the concentrate gradient elution, EtOAc-cyclohexane, 6-12% gave the pyrazole.

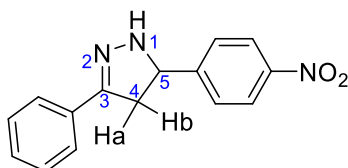
3,5-Bis(3,4-dimethoxyphenyl)-4,5-dihydro-1H-pyrazole (2.3.29)



Yield = 69 %; orange solid; m. p = 187-188 °C; ¹H NMR (500 MHz, CDCl₃) δ 7.42 (d, *J* = 1.9 Hz, 1H: Aromatic -H-), 7.04 (dd, *J* = 8.3, 1.9 Hz, 1H: Aromatic -H-), 6.96 (d, *J* = 1.9 Hz, 1H: Aromatic -H-), 6.90 (dd, *J* = 8.3, 1.9 Hz, 1H: Aromatic -H-), 6.84 (dd, *J* = 10.0, 8.3 Hz, 2H: Aromatic 2 x -H-), 4.87 (t, *J* = 10.0 Hz, 1H: Pyrazoline-H-5), 3.93 (s, 3H), 3.91 (s, 3H), 3.87 (s, 6H), 3.44 (dd, *J*

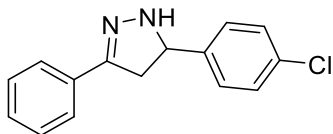
= 16.3, 10.5 Hz, 1H: Pyrazoline-Hb), 3.01 (dd, $J = 16.3, 9.4$ Hz, 1H: pyrazoline-Ha). ^{13}C NMR (126 MHz, CDCl_3) δ 151.63 (Pyrazoline C-3), 149.94 (3-Ph C-4), 149.24 (3-Ph C-3), 149.10 (5-Ph C-3), 148.59 (5-Ph C-4), 135.22 (5-Ph C-1), 125.86 (3-Ph C-1), 119.37 (2-Phenyl C-2), 118.62 (5-Phenyl C-2), 111.19 (2-Phenyl C-2), 110.54 (5-Phenyl C-2), 109.31 (5-Phenyl C-5), 108.17 (2-Phenyl C-5), 64.21 (pyrazoline C-5), 55.95 (-OMe), 55.91 (-OMe), 55.90 (-OMe), 55.87 (-OMe), 41.68 (Pyrazoline C-4). HRMS-ESI: m/z calc for $\text{C}_{19}\text{H}_{23}\text{N}_2\text{O}_4$: 343.1652, found: 343.1658 [$\text{M} + \text{H}$] $^+$ (within 1.7 ppm difference)

5-(4-Nitrophenyl)-3-phenyl-4,5-dihydro-1H-pyrazole (2.3.30)



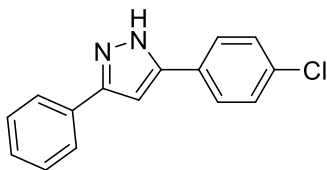
Yield = 62 %; light brown solid [412]; m. p = 177-180 °C; ^1H NMR (500 MHz, CDCl_3) δ 8.22 (d, $J = 8.7$ Hz, 1H: 3-Ph-H-4), 7.66 (dt, $J = 8.3, 2.0$ Hz, 3H: 4- NO_2 -Ph-H-3 &H-5; 1H-NH), 7.59 (d, $J = 8.7$ Hz, 2H: 3-Ph-H-3 &H-5), 7.42 – 7.32 (m, 4H: 4- NO_2 -Ph-H-2 &H-6; 3-Ph-H-2 &H-6), 5.05 (t, $J = 10.2$ Hz, 1H: pyrazoline-H-5), 3.58 (dd, $J = 16.3, 10.8$ Hz, 1H: Pyrazoline-Hb), 3.01 (dd, $J = 16.3, 9.7$ Hz, 1H: Pyrazoline-Ha). ^{13}C NMR (126 MHz, CDCl_3) δ 151.22 (Quaternary, Pyrazoline-C-3), 149.96 (Quaternary, 4- NO_2 -Ph-C-1), 147.51 (Quaternary, 4- NO_2 -Ph-C-4), 132.24 (Quaternary, 3-Ph-C-1), 129.18 (Aromatic -CH-, 3-Ph-C-4), 128.63 (Aromatic -CH-, 3-Ph-C-3 & C-5), 127.40 (Aromatic -CH-, 3-Ph-C-2 & C-6), 126.03 (Aromatic -CH-, 4- NO_2 -Ph-C-3 & C-5), 124.10 (Aromatic -CH-, 4- NO_2 -Ph-C-2 & C-6), 63.66 (Pyrazoline-C-5), 41.73 (Pyrazoline-C-4). HRMS-ESI: m/z calc for $\text{C}_{15}\text{H}_{14}\text{N}_3\text{O}_2$: 268.1081, found: 268.1084 [$\text{M} + \text{H}$] $^+$ (within 1.1 ppm difference).

5-(4-Chlorophenyl)-3-phenyl-4,5-dihydro-1H-pyrazole (2.3.31)



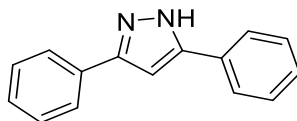
Yield = 76 %; orange solid; m. p = 148-151 °C; ^1H NMR (500 MHz, CDCl_3) δ 7.71 (d, $J = 8.4$ Hz, 2H), 7.66 (d, $J = 7.9$ Hz, 2H), 7.41 – 7.36 (m, 5H), 6.83 (Br, s, 1H: NH), 4.92 (t, $J = 9.8$ Hz, 1H: Pyrazoline-H-5), 3.49 (dd, $J = 16.3, 10.7$ Hz, 1H: Pyrazoline-Hb), 3.00 (dd, $J = 16.3, 9.0$ Hz, 1H: Pyrazoline-Ha) [413]. The melting point and ^1H NMR data was found in good agreement to that reported by Mishra *et al* [412]. HRMS-ESI: m/z calc for $\text{C}_{15}\text{H}_{14}\text{ClN}_2$: 257.0840, found: 257.0849 [$\text{M} + \text{H}$] $^+$ (within 3.5 ppm difference).

5-(4-Chlorophenyl)-3-phenyl-1H-pyrazole (2.3.32)



Yield = 42 %; white solid; m. p = 213-214 °C; ^1H NMR (600 MHz, CD_3OD) δ 7.79 (m, 4H: 3-Ph-H-2 & H-6; 4-Cl-Ph-H-3 & H-5), 7.44 (m, 4H: 3-Ph-H-3 & H-5; 4-Cl-Ph-H-2 & H-6), 7.36 (dd, $J = 7.4$ Hz, 1H), 7.01 (s, 1H). ^{13}C NMR (126 MHz, CDCl_3) δ 152.73 (Quaternary, Pyrazole-C-3), 145.08 (Quaternary, Pyrazole-C-5), 140.87 (4-Cl-Ph-C-1), 135.75 (3-Ph-C-1), 134.02 (4-Ph-C-1), 129.05 (Aromatic -CH-, 4-Cl-Ph-C-3 & C-5), 129.03 (Aromatic -CH-, 3-Ph-C-3 & C-5), 128.61 (Aromatic -CH-, 3-Ph-C-4), 126.87 (Aromatic -CH-, 3-Ph-C-2 & C-6), 125.53 (Aromatic -CH-, 4-Cl-Ph-C-2 & C-6), 100.27 (-CH-, Pyrazole-C-4). The melting point, ^1H and ^{13}C NMR data was found in good agreement to that reported by Zhang *et al* [414]. HRMS-ESI: m/z calc for $\text{C}_{15}\text{H}_{12}\text{ClN}_2$: 255.0684, found: 255.0684 $[\text{M} + \text{H}]^+$ (within 1.6 ppm difference).

3,5-Diphenyl-1H-pyrazole (2.3.2)



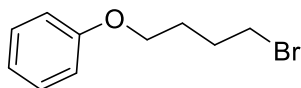
Yield = 53 %; Off white solid [415]; m. p = 203-205 °C; ^1H NMR (500 MHz, CDCl_3) δ 7.96 – 7.92 (m, 2H: 2-Ph-H-2 & H-6), 7.83 – 7.79 (m, 2H: 2-Ph-H-2 & H-6), 7.53 (d, $J = 7.7$ Hz, 2H: 2-Ph-H-3 & H-5), 7.48 (dd, $J = 8.3, 6.4$ Hz, 1H: 2-Ph-H-4), 7.39 (d, $J = 7.7$ Hz, 2H: 5-Ph-H-3 & H-5), 7.31 (d, $J = 7.7$ Hz, 1H: 5-Ph-H-4), 6.65 (d, $J = 2.2$ Hz, 1H), 6.26 (br, s, 1H: -NH-). ^{13}C NMR (126 MHz, CDCl_3) δ 151.65 (Quaternary, Pyrazole-C-3), 146.63 (Quaternary, Pyrazole-C-5), 133.13 (Quaternary, 5-Ph-C-1), 130.19 (Quaternary, 3-Ph-C-1), 129.76 (Aromatic -CH-, 3-Ph-C-2 & C-6), 128.89 (Aromatic -CH-, 5-Ph-C-3 & C-5), 128.70 (Aromatic -CH-, 5-Ph-C-2 & C-6), 128.55 (Aromatic -CH-, 5-Ph-C-3 & C-5), 127.90 (Aromatic -CH-, 5-Ph-C-4), 125.67 (Aromatic -CH-, 5-Ph-C-3 & C-5), 103.90 (-CH-, Pyrazole-C-4). HRMS-ESI: m/z calc for $\text{C}_{15}\text{H}_{13}\text{N}_2$: 221.1079, found: 221.1073 $[\text{M} + \text{H}]^+$ (within 2.7 ppm difference).

Synthesis of bromoalkoxybenzenes

To the appropriate phenol derivative (1 equiv.) in acetonitrile, K_2CO_3 (1.2 equiv.) was added and left for stirring for 5 mins. Later 1,4-dibromobutane (1 equiv.) was added. The reaction was heated 60-65 °C for 12 hours. The mixture was extracted with EtOAc and the organic layer was then dried over sodium sulphate and later, the solvent was removed under reduced pressure. Column

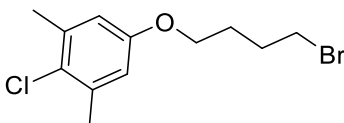
chromatography gave the desired bromoalkoxybenzenes (gradient elution, EtOAc-cyclohexane, 2.5-7 %)

(4-Bromobutoxy)-benzene (2.3.37)



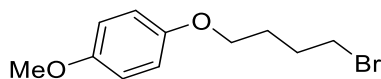
^1H NMR (500 MHz, CDCl_3) δ 7.28 (t, $J = 8.0$ Hz, 2H: Ph-H3 & H-5), 6.94 (t, $J = 8.0$ Hz, 1H: Ph-H4), 6.89 (d, $J = 8.0$ Hz, 2H: Ph-H-2 & H-6), 3.99 (t, $J = 6.0$ Hz, 2H: PhO-CH₂-CH₂), 3.48 (t, $J = 6.6$ Hz, 2H: CH₂-CH₂-Br), 2.06 (p, 2H: CH₂-CH₂-Br), 1.94 (p, 2H: PhO-CH₂-CH₂) [416]. ^{13}C NMR (126 MHz, CDCl_3) δ 158.82 (Ph-C-1), 129.45 (Ph C-2 & C-6), 120.71 (Ph C-4), 114.44 (Ph C-3 & C-5), 66.68 (PhO-CH₂-), 33.49 (Br-CH₂-CH₂-), 29.51 (Br-CH₂-CH₂-), 27.93 (PhO-CH₂-CH₂-). HRMS-ESI: m/z calc for $\text{C}_{10}\text{H}_{14}\text{BrO}$: 229.0223, found: 229.0231 [$\text{M} + \text{H}$]⁺ (within 3.5 ppm difference).

5-(4-Bromobutoxy)-2-chloro-1,3-dimethylbenzene (2.3.38)



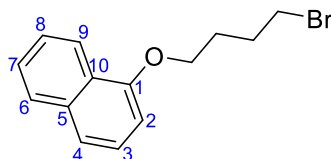
^1H NMR (500 MHz, CDCl_3) δ 6.62 (s, 2H: Ph C-2 & C-6), 3.94 (t, $J = 6.1$ Hz, 2H: PhO-CH₂-CH₂), 3.48 (t, $J = 6.7$ Hz, 2H: CH₂-CH₂-Br), 2.34 (s, 6H: 2 x OMe), 2.05 (p, $J = 14.3, 6.7$ Hz, 2H: CH₂-CH₂-Br), 1.92 (p, 2H: PhO-CH₂-CH₂). ^{13}C NMR (126 MHz, CDCl_3) δ 156.65 (Ph C-1), 137.09 (Quaternary, Ph C-3 & C-5), 126.25 (Quaternary, Ph C-4), 114.45 (Aromatic -CH-, Ph C-2 & C-6), 66.93 (PhO-CH₂-), 33.40 (Br-CH₂-CH₂-), 29.43 (Br-CH₂-CH₂-), 27.87 (PhO-CH₂-CH₂-), 20.93 (Ph-4-CH₃). HRMS-ESI: m/z calc for $\text{C}_{12}\text{H}_{17}\text{BrClO}$: 291.0146, found: 291.0148 [$\text{M} + \text{H}$]⁺ (within 0.7 ppm difference).

1-(4-Bromobutoxy)-4-methoxybenzene (2.3.39)



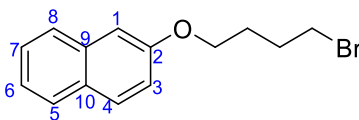
^1H NMR (500 MHz, CDCl_3) δ 6.83 (s, 4H: Phe H-2, H-3, H-5 & H-6), 3.95 (t, $J = 6.1$ Hz, 2H: PhO-CH₂-CH₂), 3.77 (s, 3H: -OMe), 3.49 (t, $J = 6.7$ Hz, 2H: CH₂-CH₂-Br), 2.06 (p, $J = 8.5, 6.5$ Hz, 2H: CH₂-CH₂-Br), 1.92 (p, $J = 6.1$ Hz, 2H: PhO-CH₂-CH₂). ^{13}C NMR (126 MHz, CDCl_3) δ 153.86 (Ph C-4), 153.02 (Ph C-1), 115.42 (Ph C-2 & C-6), 114.67 (Ph C-3 & C-5), 67.48 (PhO-CH₂-), 55.75 (-OMe), 33.52 (-CH₂-Br), 29.51 (CH₂-CH₂-Br), 28.02 (PhO-CH₂-CH₂-). HRMS-ESI: m/z calc for $\text{C}_{11}\text{H}_{16}\text{BrO}_2$: 259.0328, found: 259.0338 [$\text{M} + \text{H}$]⁺ (within 3.9 ppm difference).

1-(4-Bromobutoxy)naphthalene (2.3.40)



^1H NMR (500 MHz, CDCl_3) δ 8.28 – 8.24 (m, 1H), 7.81 – 7.77 (m, 1H), 7.47 (tt, $J = 6.8, 5.1$ Hz, 2H), 7.42 (dt, $J = 8.2, 1.0$ Hz, 1H), 7.36 (dd, $J = 8.3, 7.5$ Hz, 1H), 6.79 (dd, $J = 7.6, 1.0$ Hz, 1H), 4.18 (t, $J = 5.9$ Hz, 2H: PhO-CH₂-CH₂), 3.55 (t, $J = 6.5$ Hz, 2H: CH₂-CH₂-Br), 2.22 – 2.15 (m, 2H: CH₂-CH₂-Br), 2.13 – 2.06 (m, 2H: PhO-CH₂-CH₂). ^{13}C NMR (126 MHz, CDCl_3) δ 154.58 (Naphthyl C-1), 134.50 (Naphthyl C-10), 127.48 (Aromatic -CH-), 126.40 (Aromatic -CH-), 125.85 (Naphthyl C-9), 125.63 (Aromatic -CH-), 125.19 (Aromatic -CH-), 121.93 (Aromatic -CH-), 120.26 (Aromatic -CH-), 104.52 (Aromatic -CH- Naphthyl C-2), 66.99 (PhO-CH₂-), 33.55 (-CH₂-Br), 29.72 (CH₂-CH₂-Br), 27.92 (PhO-CH₂-CH₂-). HRMS-ESI: m/z calc for $\text{C}_{14}\text{H}_{16}\text{BrO}$: 279.0379, found: 279.0371 $[\text{M} + \text{H}]^+$ (within 2.9 ppm difference).

2-(4-Bromobutoxy)naphthalene (2.3.41)



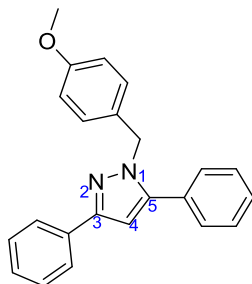
^1H NMR (500 MHz, CDCl_3) δ 7.77 – 7.70 (m, 3H), 7.43 (ddd, $J = 8.1, 6.9, 1.3$ Hz, 1H), 7.33 (ddd, $J = 8.1, 6.9, 1.2$ Hz, 1H), 7.14 – 7.11 (m, 2H), 4.10 (t, $J = 6.0$ Hz, 2H), 3.51 (t, $J = 6.6$ Hz, 2H), 2.14 – 2.07 (m, 2H), 2.04 – 1.97 (m, 2H). ^{13}C NMR (126 MHz, CDCl_3) δ 156.81 (Naphthyl C-2), 134.54 (quaternary), 129.40 (Aromatic -CH-), 128.97 (quaternary), 127.64 (Aromatic -CH-), 126.70 (Aromatic -CH-), 126.37 (Aromatic -CH-), 123.61 (Aromatic -CH-), 118.86 (Aromatic -CH-), 106.57 (Aromatic -CH-), 66.82 (PhO-CH₂-), 33.47 (-CH₂-Br), 29.53 (CH₂-CH₂-Br), 27.87 (PhO-CH₂-CH₂-), -0.00. HRMS-ESI: m/z calc for $\text{C}_{14}\text{H}_{16}\text{BrO}$: 279.0379, found: 279.0382 $[\text{M} + \text{H}]^+$ (within 0.3 ppm difference).

Synthesis of N-substituted pyrazoles

To the stirring solution of diphenyl pyrazole (1 equiv.), K_2CO_3 (1.1 equiv.) in DMF was added stirred for 10 mins at room temperature. Later, the required 4-bromoalkoxybenzene (phenoxyalkyl bromide) (1.0 equiv.) or benzyl halide (1.0 equiv.) was added and heated at reflux for 6-8 hours. The reaction was monitored by TLC and after completion an ice water was added. To clear the emulsion that formed during attempted separation of organic layer from aqueous layer, brine was added. The organic layer was collected, dried over sodium sulphate and the solvent was removed

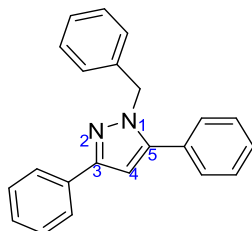
under reduced pressure. Later gradient column chromatography afforded final compounds (gradient elution, DCM-cyclohexane, 30-65 %).

1-(4-Methoxybenzyl)-3,5-diphenyl-1H-pyrazole (2.3.42)



Yield = 81 %; buff color solid; m. p = 228-232 °C; ¹H NMR (500 MHz, CDCl₃) δ 7.89 – 7.85 (m, 2H: 3-Ph-H-2 & H-6), 7.42 – 7.29 (m, 8H: 3-Ph-H-3, H-4 & H-5; 5-Ph-H-3, H-4 & H-5), 7.05 (d, *J* = 8.7 Hz, 2H: Benzylic H-2 & H-6), 6.82 – 6.79 (m, 2H: Benzylic H-3 & H-5), 6.64 (d, *J* = 2.3 Hz, 1H: Pyrazole-H-4), 5.32 (s, 2H: Benzylic protons -CH₂-), 3.77 (s, 3H: -OCH₃). ¹³C NMR (126 MHz, CDCl₃) δ 158.91 (Quaternary, N-Bn-C-4), 150.86 (Quaternary, Pyrazole-C-3), 145.26 (Quaternary, Pyrazole-C-5), 133.51 (Quaternary, 5-Phenyl-C-1), 130.74 (Quaternary, 3-Phenyl-C-1), 129.77 (Quaternary, N-Bn-C-1), 128.92 (Aromatic -CH₂-, 3-Ph-C-3 & C-5), 128.62 (Aromatic -CH₂-, 5-Ph-C-3 & C-5), 128.58 (Aromatic -CH₂-, 3-Ph-C-2 & C-6), 128.14 (Aromatic -CH₂-, 5-Ph-C-2 & C-6), 127.62 (Aromatic -CH₂-, 3-Ph-C-4; 5-Ph-C-4), 125.66 (Aromatic -CH₂-, N-Bn-C-3 & C-5), 113.94 (Aromatic -CH₂-, N-Bn-C-2 & C-6), 103.70 (Aromatic -CH₂-, Pyrazole-C-4), 55.23 (N-Bn-OCH₃), 52.80 (N-Bn-CH₂-). HRMS-ESI: m/z calc for C₂₃H₂₁N₂O: 341.1648, found: 341.1655 [M + H]⁺ (within 2.1 ppm difference).

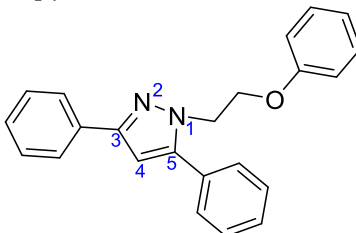
1-Benzyl-3,5-diphenyl-1H-pyrazole (2.3.43)



Yield = 68 %, Off-white color solid, M. p = 223-225 °C; ¹H NMR (500 MHz, CDCl₃) δ 7.91 – 7.83 (m, 2H: 3-Ph-H-2 & H-6), 7.45 – 7.20 (m, 11H: 3-Ph-H-3, H-4 & H-5; 5-Ph-H-3, H-4 & H-5; Benzylic-H-2, H-4 & H-6), 7.10 (d, *J* = 7.5 Hz, 2H: Benzylic H-3 & H-5), 6.65 (d, *J* = 2.2 Hz, 1H), 5.39 (s, 2H). ¹³C NMR (126 MHz, CDCl₃) δ 151.01 (Quaternary, Pyrazole-C-3), 145.50 (Quaternary, Pyrazole-C-5), 137.74 (Quaternary, N-Bn-C-1), 133.50 (Quaternary, 5-Phenyl-C-1), 130.66 (Quaternary, 3-Phenyl-C-1), 128.87 (Aromatic -CH₂-, 3-Ph-C-3 & C-5), 128.66 (Aromatic

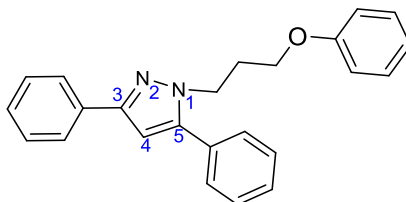
-CH₂-, 5-Ph-C-3 & C-5), 128.62 (Aromatic -CH₂-, 3-Ph-C-2 & C-6), 128.60 (Aromatic -CH₂-, 5-Ph-C-2 & C-6), 127.69 (Aromatic -CH₂-, 3-Ph-C-4), 127.41 (Aromatic -CH₂-, 5-Ph-C-4), 126.74 (Aromatic -CH₂-, N-Bn-C-3 & C-5), 125.70 (Aromatic -CH₂-, N-Bn-C-2 & C-6), 103.72 (Aromatic -CH₂-, Pyrazole-C-4), 53.30 (N-Bn-CH₂-). The ¹³C NMR spectroscopic data was in good agreement with data reported by Tang *et al* reported data [417]. HRMS-ESI: m/z calc for C₂₂H₁₉N₂⁺: 311.1543, found: 311.1547 [M + H]⁺ (within 1.3 ppm difference).

1-(2-Phenoxyethyl)-3,5-diphenyl-1H-pyrazole (2.3.44)



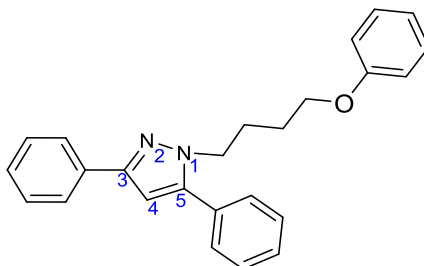
Yield = 74 %; white color solid; m. p = 239-242 °C; ¹H NMR (500 MHz, CDCl₃) δ 7.84 (d, *J* = 7.8 Hz, 2H: 3-Ph-H-2 & H-6), 7.59 – 7.54 (m, 2H: 5-Ph-H-2 & H-6), 7.50 – 7.47 (m, 2H: 5-Ph-H-3 & H-5), 7.46 – 7.44 (m, 1H: 5-Ph-H-4), 7.41 (t, *J* = 7.6 Hz, 2H: 3-Ph-H-3 & H-5), 7.32 (t, *J* = 7.2 Hz, 1H: 3-Ph-H-4), 7.23 (d, *J* = 8.3 Hz, 2H: -OPh-H-3 & H-5), 6.93 (t, *J* = 7.3 Hz, 1H: -OPh-H-4), 6.81 (d, *J* = 7.9 Hz, 2H: -OPh-H-2 & H-6), 6.60 (d, *J* = 1.5 Hz, 1H: Pyrazole-H-4), 4.53 (t, *J* = 5.6 Hz, 2H: -N-CH₂-CH₂-OPh), 4.45 (t, *J* = 5.6 Hz, 2H: (-N-CH₂-CH₂-OPh). ¹³C NMR (126 MHz, CDCl₃) δ 158.30 (-OPh-C-1), 151.24 (Pyrazole-C-3), 146.10 (Pyrazole-C-5), 133.44 (Quaternary, 5-Phenyl-C-1), 130.66 (Quaternary, 3-Phenyl-C-1), 129.45 (-OPh-C-3 & C-5), 129.29 (Aromatic -CH- 5-Ph-C-2 & C-6), 128.68 (Aromatic -CH- 5-Ph-C-3 & C-5), 128.67 (Aromatic -CH- 5-Ph-C-4), 128.62 (Aromatic -CH- 3-Ph-C-3 & C-5), 127.72 (Aromatic -CH- 3-Ph-C-4), 125.68 (Aromatic -CH- 3-Ph-C-2 & C-6), 121.05 (-OPh-C-4), 114.47 (-OPh-C-2 & C-6), 103.58 (Aromatic -CH-, Pyrazole-C-4), 66.64 (-N-CH₂-CH₂-OPh), 48.70 (-N-CH₂-CH₂-OPh). HRMS-ESI: m/z calc for C₂₃H₂₁N₂O⁺: 341.1648, found: 341.1643 [M + H]⁺ (within 1.5 ppm difference).

1-(3-Phenoxypropyl)-3,5-diphenyl-1H-pyrazole (2.3.45)



Yield = 82 %; white color solid; m. p = 251-254 °C; ¹H NMR (500 MHz, CDCl₃) δ 7.88 (dt, *J* = 7.9, 4.3 Hz, 2H: 3-Ph-H-2 & H-6), 7.49 – 7.21 (m, 10H: 3-Ph-H-3, H-4, H-5; 5-Ph-H-2, H-3, H-4, H-5, H-6; -OPh-H-3 & H-5), 6.97 – 6.91 (m, 1H: -OPh-H-4), 6.85 – 6.73 (m, 2H: -OPh-H-2 & H-6), 6.60 (dd, *J* = 5.7, 1.7 Hz, 1H: Pyrazole-H-4), 4.46 – 4.36 (m, 2H: -N-CH₂-CH₂-CH₂-OPh), 3.96 – 3.87 (m, 2H: -N-CH₂-CH₂-CH₂-OPh), 2.41 (q, *J* = 6.0 Hz, 2H: -N-CH₂-CH₂-CH₂-OPh). ¹³C NMR (126 MHz, CDCl₃) δ 158.58 (Quaternary, -OPh-C-1), 150.84 (Pyrazole-C-3), 145.53 (Pyrazole-C-5), 133.67 (Quaternary, 5-Phenyl-C-1), 130.67 (Quaternary, 3-Phenyl-C-1), 129.38 (-OPh-C-3 & C-5), 128.95 (Aromatic -CH- 5-Ph-C-2 & C-6), 128.67 (Aromatic -CH- 5-Ph-C-3 & C-5), 128.65 (Aromatic -CH- 5-Ph-C-4), 128.55 (Aromatic -CH- 3-Ph-C-3 & C-5), 127.65 (Aromatic -CH- 3-Ph-C-4), 125.62 (Aromatic -CH- 3-Ph-C-2 & C-6), 120.71 (-OPh-C-4), 114.41 (-OPh-C-2 & C-6), 103.32 (Aromatic -CH-, Pyrazole-C-4), 64.25(-N-CH₂-CH₂-CH₂-OPh), 46.19 (-N-CH₂-CH₂-CH₂-OPh), 30.07 (-N-CH₂-CH₂-CH₂-OPh). HRMS-ESI: m/z calc for C₂₄H₂₃N₂O: 355.1805, found: 355.1809 [M + H]⁺ (within 1.1 ppm difference).

1-(4-Phenoxybutyl)-3,5-diphenyl-1H-pyrazole (2.3.46)



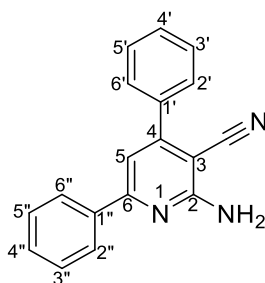
Yield = 87 %; white color solid; m. p = 256-259 °C; ¹H NMR (500 MHz, CDCl₃) δ 7.84 (d, *J* = 8.2 Hz, 2H: 3-Ph-H-2 & H-6), 7.46 – 7.36 (m, 7H: 3-Ph-H-3 & H-5; 5-Ph-H-2, H-3, H-4, H-5, H-6), 7.33 – 7.27 (m, 1H: 3-Ph-H-4), 7.27 – 7.20 (m, 2H: -OPh-H-3 & H-5), 6.91 (t, *J* = 7.3 Hz, 1H: -OPh-H-4), 6.80 (d, *J* = 7.9 Hz, 2H: -OPh-H-2 & H-6), 6.57 (d, *J* = 3.2 Hz, 1H: Pyrazole-H-4), 4.23 (t, *J* = 7.2 Hz, 2H: -N-CH₂-CH₂-CH₂-CH₂-OPh), 3.85 (t, *J* = 6.2 Hz, 2H: -N-CH₂-CH₂-CH₂-CH₂-OPh), 2.11 – 2.02 (m, 2H: -N-CH₂-CH₂-CH₂-CH₂-OPh), 1.72 (p, *J* = 6.4 Hz, 2H: -N-CH₂-CH₂-CH₂-CH₂-OPh). ¹³C NMR (126 MHz, CDCl₃) δ 158.83 (Quaternary, -OPh-C-1), 150.60 (Pyrazole-C-3), 144.96 (Pyrazole-C-5), 133.59 (Quaternary, 5-Phenyl-C-1), 130.90 (Quaternary, 3-Phenyl-C-1), 129.38 (-OPh-C-3 & C-5), 128.91 (Aromatic -CH- 5-Ph-C-2 & C-6), 128.75 (Aromatic -CH- 5-Ph-C-3 & C-5), 128.60 (Aromatic -CH- 5-Ph-C-4), 128.56 (Aromatic -CH- 3-Ph-C-3 & C-5), 127.57 (Aromatic -CH- 3-Ph-C-4), 125.60 (Aromatic -CH- 3-Ph-C-2 & C-6), 120.59 (-OPh-C-4), 114.44 (-OPh-C-2 & C-6), 103.38 (Aromatic -CH-, Pyrazole-C-4), 64.25(-N-

CH₂-CH₂-CH₂-CH₂-OPh), 46.19 (-N-CH₂-CH₂-CH₂-CH₂-OPh), 27.19 (-N-CH₂-CH₂-CH₂-CH₂-OPh), 26.27 (-N-CH₂-CH₂-CH₂-CH₂-OPh). HRMS-ESI: m/z calc for C₂₅H₂₅N₂O: 369.1961, found: 369.1960 [M + H]⁺ (within 0.3 ppm difference).

General procedure for synthesis of diphenyl pyridines

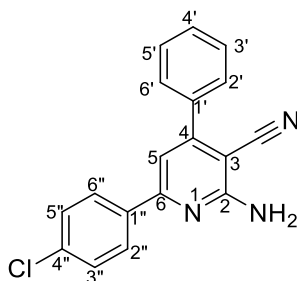
The relevant chalcone (1 equiv.) was stirred in the presence of malononitrile (1.1 equiv.), NH₄OAc (2.5 equiv.) in AcOH for 8 hours. After completion of the reaction, ice water was added, and the compound precipitated and was later recovered by filtration using a buchner funnel. The recovered solid was washed with distilled water (2 x 5 mL and dissolved in dichloromethane and the organic layer was washed with water. The DCM layer was dried over sodium sulphate, the solvent was removed under reduced pressure and gradient column chromatography gave the product (EtOAc-cyclohexane: 12-18 %).

2-Amino-4,6-diphenylnicotinonitrile (2.3.56)



Yield = 58 %; white buff color; m. p = 191-192 °C; (reported is 186-187°C [418]); ¹H NMR (500 MHz, CDCl₃) δ 8.03 – 7.97 (m, 2H), 7.64 (dd, *J* = 7.7, 1.7 Hz, 2H), 7.55 – 7.43 (m, 6H: H-3: 4-Phenyl-H-3, H-4, H-5 & 6-Phenyl- H-3, H-4, H-5), 7.22 (s, 1H: Pyridine H-5), 5.36 (br, s, 2H: NH₂). These protons signals are parallel to the earlier reported data [418]. ¹³C NMR (126 MHz, CDCl₃) δ 160.23 (Quaternary, Pyridine C-2), 159.85 (Quaternary, Pyridine C-6), 155.15 (Quaternary, Pyridine C-4), 137.96 (Quaternary, 4-Phenyl C-1), 136.95 (Quaternary, 6-Phenyl C-1), 130.21 (Aromatic -CH-, 4-Phenyl C-4), 129.84 (Aromatic -CH-, 6-Phenyl C-4), 128.95 (Aromatic -CH-, 4-Phenyl C-3 & C-5), 128.82 (Aromatic -CH-, 6-Phenyl C-3 & C-5), 128.18 (Aromatic -CH-, 6-Phenyl C-2 & C-6), 127.34 (Aromatic -CH-, 4-Phenyl C-2 & C-6), 117.14 (Aromatic -CH-, Pyridine C-5), 111.31 (Quaternary, CN), 88.32 (Aromatic -CH-, Pyridine C-). HRMS-ESI: m/z calc for C₁₈H₁₄N₃: 272.1188, found: 272.1192 [M + H]⁺ (1.5 ppm difference).

2-Amino-6-(4-chlorophenyl)-4-phenylnicotinonitrile (2.3.57)



Yield = 66 %; off-white color; m. p = 239-240 °C (reported was 233-235 °C [418]); ¹H NMR (500 MHz, CDCl₃) δ 7.99 (dd, *J* = 6.5, 2.9 Hz, 2H), 7.58 (d, *J* = 8.4 Hz, 2H), 7.51 – 7.47 (m, 5H), 7.17 (s, 1H: Pyridine H-5), 5.37 (Br, s, 2H: NH₂). ¹³C NMR (126 MHz, CDCl₃) δ 160.26 (Quaternary, pyridine- C-2), 160.07 (Quaternary, pyridine- C-6), 153.83 (Quaternary, pyridine C-4), 137.75 (Quaternary, 4-Phenyl C-1), 136.13 (Quaternary, 6-Phenyl C-1), 135.30 (Quaternary, 6-Phenyl C-4), 130.34 (Aromatic -CH-, 4-Phenyl C-4), 129.52 (Aromatic -CH-, 6-Phenyl C-3 & C-5), 129.24 (Aromatic -CH-, 6-Phenyl C-2 & C-6), 128.84 (Aromatic -CH-, 4-Phenyl C-3 & C-5), 127.34 (Aromatic -CH-, 4-Phenyl C-2 & C-6), 116.92 (Aromatic -CH-, Pyrdine C-5), 110.98 (Quaternary, CN), 88.00 (Aromatic -CH-, pyridine, C-3). HRMS-ESI: *m/z* calc for C₁₈H₁₃ClN₃: 306.0793, found: 306.0799 [M + H]⁺ (within 2.0 ppm difference).

Synthesis of triphenyl pyridines by conventional route

General procedure for synthesis of α-pyridinium methyl ketone salts

The α-pyridinium methyl ketone salts (**2.3.68** to **2.3.74**) were freshly prepared by treating the respective acetophenone (1 equiv.) with pyridine (5 mL) and I₂ (1 equiv.). After heating at reflux for over 4-5 hours, the excess pyridine was decanted into a solvent waste container and 2 x 2 mL of fresh pyridine was used for rinsing excess of iodine unreacted in the reaction. Later, most of the unreacted pyridine was removed under diminished pressure on a rotary evaporator which the residue removed using a high vacuum pump for 1 hour. The resulting residue, which could be obtained as a powder by trituration using a spatula, was used directly in the next step without purification.

General procedure for synthesis of triphenyl pyridine using methyl ketone pyridinium salt

Either of chalcone (**2.3.1** or **2.3.19** (100 mg)) in 10 mL of AcOH, NH₄OAc (2.5 equiv.), the α-pyridinium acetophenone salt (**2.3.68** to **2.3.74**, 1.5 equiv.) was subsequently added. The reaction was refluxed for 6-8 hours. The mixture was separated between EtOAc and water and the EtOAc layer was dried over sodium sulphate. Column chromatography gave the product (gradient elution, 5-10% EtOAc-cyclohexane).

Evaluation of previously reported methods for symmetrical triphenyl pyridines

(a) Iodine catalyzed triphenyl pyridine synthesis

A mixture of acetophenone (2.0 mmol), benzylamine (1.0 mmol), and molecular I₂ (2.5 mg, 0.01 mmol) was stirred at 140 °C for 10 h in a 25 mL sealed pressure tube, followed by further 1 h stirring in open air [232]. After completion, the reaction mixture was directly subjected to a normal phase column chromatography using (EtOAc: Cyclohexane, 4-10 %) as the eluent.

(b) Triflic acid assisted synthesis of triphenyl pyridine synthesis

Acetophenone (1.0 mmol, 1.0 equiv.), amine (0.75 mmol, 1.5 equiv.), and the HOTf (0.025 mmol) were added in 10 mL in pressure tube. The mixture was stirred at 120 °C for 12 hours, the mixture was quenched by sat. aq. NaHCO₃ and diluted with 20 mL of dichloromethane and washed with 10 mL of H₂O. The aqueous layer was extracted twice with dichloromethane (10 mL) and the combined organic phase was dried over Na₂SO₄ [233]. After evaporation of the solvents, the residue was purified by gradient normal phase chromatography (EtOAc-cyclohexane, 4-10 %).

(c) Copper triflate catalyzed Triphenyl pyridine synthesis

To a 10 mL pressure tube, a mixture of acetophenone (2 mmol), benzylamine (1.2 mmol), and Cu(OTf)₂ (36 mg, 0.1 mmol) was added, successively. Subsequently, the tube was flushed with argon and later filled with oxygen and sealed with stopper. The mixture was stirred at 100 °C for 20 h [234]. Upon completion, the crude product was cooled to room temperature and saturated NH₄Cl solution was added and left for 5 mins on stirring, later DCM was also added and separated. The DCM layer was washed with saturated NH₄Cl. Later washed DCM layer was dried over magnesium sulphate and subsequent gradient column chromatography (EtOAc: Cyclohexane, 4-10 %) was used to collect the pure compound.

(d) Ferrous bromide catalysed Triphenyl pyridine synthesis

To a mixture of benzylamines (1.2 mmol) and acetophenone (2.0 mmol), FeBr₂ (10 mol%) was added into a pressure tube (10 mL) with an oxygen balloon. The tube was stirred and heated at 110°C with constant magnetic stirring [231]. After completion of the reaction, the mixture was cooled to room temperature, diluted with DCM and dried over silica gel. The dried-up products were purified by gradient normal phase column chromatography using cyclohexane/EtOAc as eluents (EtOAc: Cyclohexane, 4-10 %).

Development of synthetic method for formation of Non-symmetrical Triphenyl pyridine

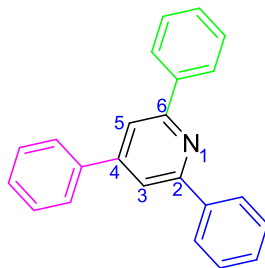
(1) Copper triflate catalyzed non-symmetrical Triphenyl pyridine synthesis

To a 10 mL pressure tube, a mixture of 4-methoxyacetophenone (1 equiv.), acetophenone (1 equiv.), benzylamine (1 equiv.), and Cu(OTf)₂ (36 mg, 0.1 mmol) were added. Subsequently, the tube was flushed with Argon and later filled with oxygen and sealed with stopper. The mixture was stirred at 100 °C for 20 h [234]. Upon completion, the crude product was cooled to room temperature and saturated ammonium chloride solution was added and left for 10 mins on stirring, later DCM was also added and separated. The DCM layer was washed with saturated ammonium chloride. Later washed DCM layer was dried over magnesium sulphate and subsequent gradient column chromatography was used to collect the pure compound (**2.3.76**, 41 %).

(2) Under similar reaction conditions [234], the reaction between 3, 4-dimethoxy-acetophenone (1 equiv.), acetophenone (1 equiv.) and 4-nitrobenzylamine (1 equiv.) was also performed and compound **2.3.76** was attained in 16 % yield.

(3) Improvement in method: Addition of acetophenone and benzylamine derivatives were performed in sequential order in a three necked 25 mL round bottom flask, where first 4-nitrobenzylamine was added with copper triflate/ other catalysts (10-40 mol %) and refluxed 10 mins under oxygen atmosphere, followed by slow addition of acetophenone (drop by drop) (~ nearly in a passage of 5 mins) was done, followed by addition of 3,4-dimethoxy acetophenone and addition of ammonia source after 20 mins of refluxing. The reaction was monitored by TLC. After completion of reactions, cold water was added, and DCM extraction was performed. The DCM layer was dried over sodium sulphate, evaporated on rotavap and purified by gradient column (EtOAc: Cyclohexane, 4-8%).

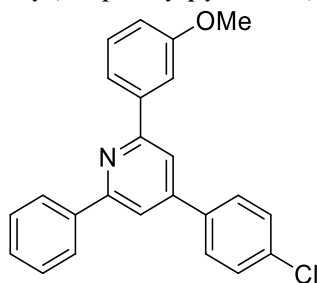
2,4,6-Triphenylpyridine (**2.3.4**)



Yield = 91%; white color solid; m. p = 143–145 °C (previously reported m. p = 134-135 [230], 136–137 °C [232], 130–132 °C [231]); ¹H NMR (500 MHz, CD₃OD) δ 8.34 (d, *J* = 7.5 Hz, 4H: 2-Phenyl H-2 & H-6; 6-Phenyl H-2 & H-6), 8.20 (s, 2H: pyridine H-3 & H-5), 8.05 (d, *J* = 7.3 Hz, 2H: 4-Phenyl H-2 & H-6), 7.61 – 7.46 (m, 9H: 2-Phenyl H-3, H-4 & H-5; 4-Phenyl H-3, H-4 &

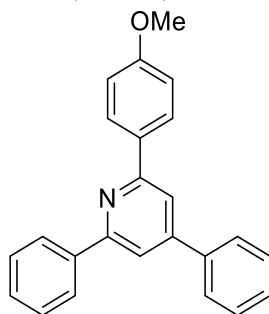
H-5; 6-Phenyl H-3, H-4 & H-5). ^{13}C NMR (126 MHz, CD_3OD) δ 156.42 (Quaternary, Pyridine, C-2 & C-6), 149.49 (Quaternary, Pyridine C-4), 138.71 (Quaternary, 2-Phenyl C-1; 6-Phenyl C-1), 137.63 (Quaternary, 4-Phenyl C-1), 129.20 (Aromatic -CH-, 4-Phenyl C-4), 129.13 (Aromatic -CH-, 4-Phenyl C-3 & C-5), 128.99 (Aromatic -CH-, 4-Phenyl C-2 & C-6), 128.64 (Aromatic -CH-, 2-Phenyl C-3 & C-5; 6-Phenyl C-3 & C-5), 127.27 (Aromatic -CH-, 2-Phenyl C-4; 6-Phenyl C-4), 126.86 (Aromatic -CH-, 2-Phenyl C-2 & C-6; 6-Phenyl C-2 & C-6), 116.49 (Aromatic -CH-, Pyridine C-3 & C-5). The ^1H and ^{13}C NMR data was found in good agreement to that reported by Huang *et al* [206, 234]. HRMS-ESI: m/z calc for $\text{C}_{23}\text{H}_{18}\text{N}$: 308.1439, found: 308.1451 [$\text{M} + \text{H}$] $^+$ (within 3.9 ppm difference).

4-(4-Chlorophenyl)-2-(3-methoxyphenyl)-6-phenylpyridine (2.3.75)



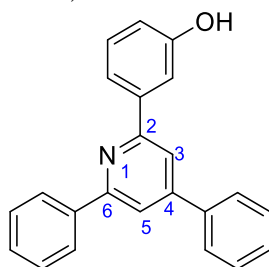
Yield = 37 %; off white solid; $m.p = 129\text{--}132\text{ }^\circ\text{C}$; ^1H NMR (500 MHz, CDCl_3) δ 8.19 (d, $J = 8.2$ Hz, 2H: 6-Phenyl H-2 & H-6), 7.84 (s, 1H: Pyridine H-3), 7.82 (s, 1H: Pyridine H-5), 7.79 (s, 1H: 2-Phenyl H-2), 7.73 (d, $J = 7.6$ Hz, 1H: 2-Phenyl H-6), 7.69 – 7.65 (m, 2H: 4-Phenyl H-2 & H-6), 7.54 – 7.40 (m, 6H: 6-Phenyl C-3, C-4 & C-5; 4-Phenyl H-3 & H-5; 2-Phenyl H-5), 7.02 – 6.99 (m, 1H : 2-Phenyl H-4), 3.93 – 3.92 (s, 3H: OMe). ^{13}C NMR (126 MHz, CDCl_3) δ 160.08 (2-Phenyl C-3), 157.62 (Pyridine C-6), 157.43 (Pyridine C-2), 148.94 (Pyridine C-4), 140.92 (2-Phenyl C-1), 139.35 (6-Phenyl C-1), 137.46 (4-Phenyl C-1), 135.22 (4-Phenyl C-4), 129.73 (6-Phenyl C-4), 129.34 (6-Phenyl C-3 & C-5), 129.18 (2-Phenyl C-3), 128.74 (4-Phenyl C-3 & C-5), 128.46 (4-Phenyl C-2 & C-6), 127.13 (6-Phenyl C-2 & C-6), 119.52 (2-Phenyl C-6), 116.96 (Pyridine C-3), 116.95 (Pyridine C-5), 114.73 (2-Phenyl C-2), 112.80 (2-Phenyl C-4), 55.44 (-OMe). HRMS-ESI: m/z calc for $\text{C}_{24}\text{H}_{19}\text{NOCl}$: 372.1155, found: 372.1151 [$\text{M} + \text{H}$] $^+$ (within 1.1 ppm difference).

2-(4-Methoxyphenyl)-4,6-diphenylpyridine (2.3.76)



Yield = 37%; white color solid; m. p = 117-119 °C (previously reported compound, yellow solid m. p = 87–89°C [419], white solid m. p = 107–108°C [420]); ¹H NMR (500 MHz, CDCl₃) δ 8.18 (dd, *J* = 12.8, 8.3 Hz, 4H: 6-Phenyl H-2 & H-6; 2-Phenyl H-2 & H-6), 7.83 (s, 1H: Pyridine H-5), 7.82 (s, 1H: Pyridine H-3), 7.73 (d, *J* = 8.0 Hz, 2H: 4-Phenyl H-2 & H-6), 7.54 – 7.41 (m, 6H: 4-Phenyl H-3, H-4 & H-5; 6-Phenyl H-3, H-4 & H-5), 7.03 (d, *J* = 8.3 Hz, 2H: 2-phenyl H-3, H-5), 3.87 (s, 3H, -OCH₃). ¹³C NMR (126 MHz, CDCl₃) δ 160.55 (2-Phenyl C-4), 157.33 (Pyridine C-6), 157.12 (Pyridine C-2), 150.08 (Pyridine C-4), 139.71(4-Phenyl C-1), 139.22(6-Phenyl C-1), 132.23 (2-Phenyl C-1), 129.08 (2-Phenyl C-2 & C-6), 128.96 (4-Phenyl C-4), 128.89 (6-Phenyl C-4), 128.67 (2-Phenyl C-3 & C-5), 128.39 (4-Phenyl C-3 & C-5), 127.17(2-Phenyl C-2 & C-6), 127.11 (4-Phenyl C-3 & C-5), 116.46 (pyridine C-3), 116.32 (pyridine C-5), 114.06 (2-Phenyl C-3 & C-5), 55.37 (-OMe). The ¹³C NMR data was found in good agreement to that reported by Huang *et al* [234] and Ren *et al* [421]. HRMS-ESI: *m/z* calc for C₂₄H₂₀NO: 338.1545, found: 338.1535 [M + H]⁺ (within 3 ppm difference).

3-(4,6-Diphenylpyridin-2-yl)phenol (2.3.77)

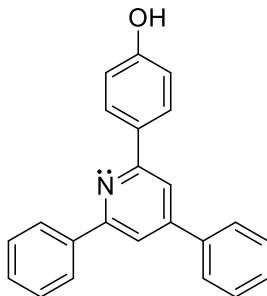


Yield = 80%; white color solid; m. p = 171–173 °C; (previous reported m. p = 180.0–180.7 °C [422]); ¹H NMR (500 MHz, CD₃OD) δ 8.16 (d, *J* = 7.4 Hz, 2H: 6-phenyl H-2 & H-6), 7.93 (s, 1H: Pyridine H-5), 7.89 (s, 1H: Pyridine C-3), 7.79 (d, *J* = 7.5 Hz, 2H: 4-Phenyl H-2 & H-6), 7.67 (s, 1H: 2-Phenyl H-2), 7.60 (d, *J* = 7.9 Hz, 1H: 2-Phenyl C-6), 7.54 – 7.39 (m, 6H: 6-Phenyl H-3, H-4 & H-5; 4-phenyl H-3, H-4 & H-5), 7.32 (d, *J* = 7.9 Hz, 1H: 2-Phenyl C-4), 6.88 (dd, *J* = 7.9, 2.3 Hz, 1H: 2-Phenyl C-5), 4.86 (Br, s, 1H) [422]. ¹³C NMR (126 MHz, CD₃OD) δ 157.56

(Quaternary, 2-Phenyl C-3), 157.53 (Quaternary, Pyridine C-6), 157.47 (Quaternary, Pyridine C-2), 150.41 (Quaternary, Pyridine C-4), 140.80 (Quaternary, 2-Phenyl C-1), 139.37 (Quaternary, 4-Phenyl C-1), 138.53 (Quaternary, 6-Phenyl C-1), 129.37 (Aromatic -CH-, 2-Phenyl C-5), 128.82 (Aromatic -CH-, 4-Phenyl C-3 & C-5), 128.76 (Aromatic -CH-, 2-Phenyl C-4), 128.72 (Aromatic -CH-, 4-Phenyl C-4), 128.31 (Aromatic -CH-, 2-Phenyl C-3 & C-5), 126.83 (Aromatic -CH-, 4-Phenyl C-2 & C-6; 6-Phenyl C-2 & C-6), 118.05 (Aromatic -CH-, 2-Phenyl C-6), 116.70 (Aromatic -CH-, 2-Phenyl C-2), 115.75 (Aromatic -CH-, Pyridine C-3 & C-5), 113.66 (Aromatic -CH-, 2-Phenyl C-4). HRMS-ESI: m/z calc for $C_{23}H_{18}NO$: 324.1388, found: 324.1386 $[M + H]^+$ (within 0.6 ppm difference).

1H NMR (500 MHz, $CDCl_3$) δ 8.17 (d, $J = 8.1$ Hz, 2H: 6-Phenyl H-2 & H-6), 7.88 (s, 1H: Pyridine H-5), 7.85 (s, 1H: Pyridine H-3), 7.73 (d, $J = 8.2$ Hz, 3H: 2-Phenyl H-2, 4-Phenyl H-2 & H-6), 7.69 (d, $J = 7.7$ Hz, 1H: 2-Phenyl H-6), 7.56 – 7.39 (m, 6H: 6-phenyl H-3, H-4, H-5, 4-phenyl H-3, H-4, H-5), 7.35 (t, $J = 7.9$ Hz, 1H: 2-phenyl H-5), 6.90 (dd, $J = 8.0, 2.3$ Hz, 1H: 2-Phenyl H-4), 4.56 (s, 1H: 3-OH). ^{13}C NMR (126 MHz, $CDCl_3$) δ 157.57 (2-Phenyl C-3), 157.04 (Pyridine C-6), 156.17 (Pyridine C-2), 150.24 (Pyridine C-4), 141.16 (2-Phenyl C-1), 139.51 (4-Phenyl C-1), 138.94 (6-Phenyl C-1), 129.92 (2-phenyl C-5), 129.13 (2 x Aromatic -CH-: Phenyl C-3 & C-5), 129.08 (Aromatic -CH-: Phenyl C-4), 129.03 (Aromatic -CH-: Phenyl C-4), 128.71 (2 x Aromatic -CH-: Phenyl C-3 & C-5), 127.18 (4-Phenyl C-2 & C-6; 6-Phenyl C-2 & C-6), 119.40 (2-Phenyl C-6), 117.43 (Pyridine C-5), 117.28 (Pyridine C-3), 116.18 (2-Phenyl C-4), 114.19 (2-Phenyl C-2). The 1H and ^{13}C NMR data was found in good agreement to that reported by Karki *et al* [422]. HRMS-ESI: m/z calc for $C_{23}H_{18}NO$: 324.1388, found: 324.1382 $[M + H]^+$ (within 3.5 ppm difference).

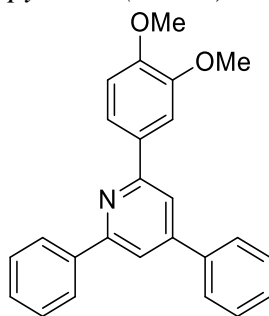
4-(4,6-Diphenylpyridin-2-yl)phenol (2.3.78)



Yield = 73%; white solid; m. p = 178-180 °C (previously reported m. p = 194.5–195.5 °C [422]), R.f = 0.33 (EtOAc-Cyclohexane 1:3); 1H NMR (500 MHz, $CDCl_3$) δ 8.19 (d, $J = 8.1$ Hz, 2H: 6-Phenyl H-2 & H-6), 8.13 (d, $J = 8.3$ Hz, 2H: 2-Phenyl H-2 & H-6), 7.84 (s, 1H: Pyridine H-5),

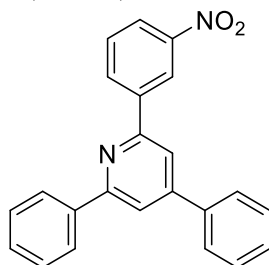
7.82 (s, 1H: Pyridine H-3), 7.74 (d, $J = 8.0$ Hz, 2H: 4-Phenyl H-2 & H-6), 7.56 – 7.46 (m, 6H: 4-Phenyl H-3, H-4 & H-5; 6-Phenyl H-3, H-4 & H-5), 6.97 (d, $J = 8.3$ Hz, 2H: 2-phenyl H-3, H-5), 4.90 (br, s, 1H: br, 1H, 2-phenyl 4-OH). ^{13}C NMR (126 MHz, CDCl_3) δ 157.38 (2-Phenyl C-4), 157.04 (Pyridine C-6), 156.54 (Pyridine C-2), 150.16 ((Pyridine C-4)), 139.68 ((4-Phenyl C-1)), 139.19(6-Phenyl C-1), 132.53 (2-Phenyl C-1), 129.10 (2-Phenyl C-2 & C-6), 129.00 (4-Phenyl C-4), 128.93 (6-Phenyl C-4), 128.69 (2-Phenyl C-3 & C-5), 128.68 (4-Phenyl C-3 & C-5), 127.18 (2-Phenyl C-2 & C-6), 127.12 (4-Phenyl C-3 & C-5), 116.58 (pyridine C-3), 116.36 (pyridine C-5), 115.57 (2-Phenyl C-3 & C-5). The ^1H and ^{13}C NMR data was found in good agreement to that reported by Karki *et al* [422]. HRMS-ESI: m/z calc for $\text{C}_{23}\text{H}_{16}\text{NO}$: 322.1232, found: 322.1223 [$\text{M} + \text{H}$] $^+$ (within 2.8 ppm difference).

2-(3,4-Dimethoxyphenyl)-4,6-diphenylpyridine (2.3.79)



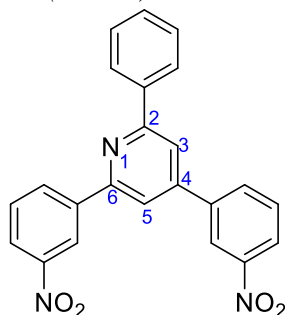
Yield = 86%; white color solid; m. p = 135–138 °C; ^1H NMR (500 MHz, CDCl_3) δ 8.20 (d, $J = 7.5$ Hz, 2H: 6-Phenyl H-2 & H-6), 7.86 – 7.83 (m, 3H: Pyrdine H-3 & H-5; 2-Phneyl H-2), 7.77 – 7.70 (m, 3H: 4-Phenyl H-2 & H-6; 2-Phenyl H-6), 7.43-7.54 (m, 6H: 4-Phenyl H-3, H-4 & H-5; 6-Phenyl H-3, H-4 & H-5), 7.00 (d, $J = 8.4$ Hz, 1H: 2-Phenyl H-5), 4.04 (s, 3H: -OMe), 3.96 (s, 3H: -OMe). ^{13}C NMR (126 MHz, CDCl_3) δ 157.34 (Pyridine C-6), 157.15(Pyridine C-2), 150.15 (Pyridine C-4), 150.11 (2-Phenyl C-4), 149.24 (2-Phenyl C-3), 139.67 (4-Phenyl C-1), 139.19 (6-Phenyl C-1), 132.61 (2-Phenyl C-1), 129.10 (4-Phenyl C-3 & C-5), 129.01(4-Phenyl C-4), 128.94 (6-Phenyl C-4), 128.71 (6-Phenyl C-3 & C-5), 127.19 (6-Phneyl C-2 & C-6), 127.11 (4-Phneyl C-2 & C-6), 119.69 (2-Phenyl C-6), 116.69 (Pyridne C-3), 116.56 (Pyrdine C-6), 111.10 (2-Phenyl C-5), 110.32 (2-Phneyl C-2), 56.05 (-OCH₃), 56.00 (-OCH₃). HRMS-ESI: m/z calc for $\text{C}_{25}\text{H}_{22}\text{NO}_2$: 368.1651, found: 368.1648 [$\text{M} + \text{H}$] $^+$ (within 0.8 ppm difference).

2-(3-Nitrophenyl)-4,6-diphenylpyridine (2.3.80)



Yield = 76%; light yellow color solid; m. p = 147–149 °C (previously reported m. p = 140–142°C [423]); ¹H NMR (500 MHz, CDCl₃) δ 9.04 (s, 1H: 4-Phenyl H-2), 8.58 (d, *J* = 7.8 Hz, 1H: 4-Phenyl H-4), 8.30 (d, *J* = 8.1 Hz, 1H: 4-Phenyl H-6), 8.20 (d, *J* = 7.9 Hz, 2H: 2-phenyl H2 & H-6), 7.97 (s, 1H: Pyridine H-3), 7.94 (s, 1H: Pyridine H-5), 7.76 (d, *J* = 7.7 Hz, 2H: 6-Phenyl H-2 & H-6), 7.69 (t, *J* = 8.0 Hz, 1H: 4-Phenyl H-5), 7.58 – 7.47 (m, 6H: 2-Phenyl H-3, H-4 & H-5; 6-Phenyl H-3, H-4 & H-5). ¹³C NMR (126 MHz, CDCl₃) δ 158.00 (pyridine C-6), 154.87 (Pyridine C-2), 150.84 (Pyridine C-4), 148.84 (2-Phenyl C-3), 141.28 (2-Pyridine C-1), 139.02 (4-Phenyl C-1), 138.53 (6-Phenyl C-1), 133.03 (2-phenyl C-6), 129.69 (4-Phenyl C-5), 129.44 (6-Phenyl C-4), 129.34 (2-Phenyl C-4), 129.26 (6-Phenyl C-3 & C-5), 128.87 (4-Phenyl C-3 & C-5), 127.22 (4-Phenyl C-2 & C-6), 127.15 (6-Phenyl C-2 & C-6), 123.68 (2-Phenyl C-4), 121.95 (2-Phenyl C-2), 118.24 (Pyridine C-5), 117.20 (Pyridine C-3). The ¹H and ¹³C NMR data was found in good agreement to that reported by Tan *et al* [423]. HRMS-ESI: m/z calc for C₂₃H₁₇N₂O₂: 353.1290, found: 353.1283 [M + H]⁺ (within 2.0 ppm difference).

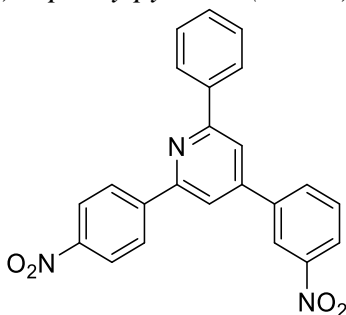
2,6-Bis(3-nitrophenyl)-4-phenylpyridine (2.3.84)



Yield = 72%; buff color solid; m. p = 148–150 °C; ¹H NMR (500 MHz, CDCl₃) δ 9.05 (s, 1H: 2-Phenyl H-2), 8.61 (m, 2H: 2-Phenyl C-4 & 4-Phenyl C-4), 8.35 (dd, *J* = 21.5, 6.2 Hz, 2H: 2-Phenyl C-6 & 4-Phenyl C-6), 8.25 – 8.16 (m, 3H: 4-Phenyl C-2; 6-Phenyl H-2 & H-6), 8.12 – 8.05 (m, 2H), 7.98 (s, 1H: Pyridine H-5), 7.96 (s, 1H: Pyridine H-3), 7.80 – 7.69 (m, 2H: 2-Phenyl C-5 & 4-Phenyl C-5), 7.52–7.56 (m, 3H: 6-Phenyl H-3, H-4, H-5). ¹³C NMR (126 MHz, CDCl₃) δ 158.51 (Quaternary, Pyridine C-6), 155.37 (Quaternary, Pyridine C-2), 148.92 (Quaternary, 4-Phenyl C-

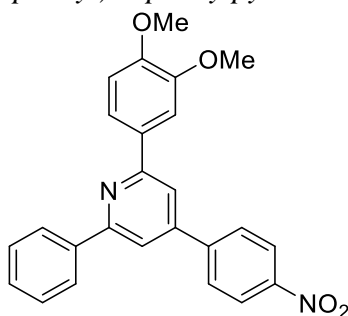
3), 148.66 (Quaternary, Pyridine C-4), 148.33 (Quaternary, 2-Phenyl C-3), 140.72 (Quaternary, 4-Phenyl C-1), 140.28 (Quaternary, 2-Phenyl C-1), 138.44 (Quaternary, 6-Phenyl C-1), 133.13 (Aromatic -CH-, 2-Phenyl C-6), 132.99 (Aromatic -CH-, 4-Phenyl C-6), 130.37 (Aromatic -CH-, 6-Phenyl C-4), 129.81 (Aromatic -CH-, 2-Phenyl C-5 & 4-Phenyl C-5), 128.96 (Aromatic -CH-, 6-Phenyl C-3 & C-5), 127.15 (Aromatic -CH-, 6-Phenyl C-2 & C-6), 123.98 (Aromatic -CH-, 2-Phenyl C-4 & 4-Phenyl C-4), 122.17 (Aromatic -CH-, 4-Phenyl C-2), 121.98 (Aromatic -CH-, 2-Phenyl C-2), 117.97 (Aromatic -CH-, Pyridine C-3), 116.90 (Aromatic -CH-, Pyridine C-5). HRMS-ESI: m/z calc for C₂₃H₁₆N₃O₄: 398.1141, found: 398.1151 [M + H]⁺ (within 2.5 ppm difference).

4-(3-Nitrophenyl)-2-(4-nitrophenyl)-6-phenylpyridine (2.3.85)



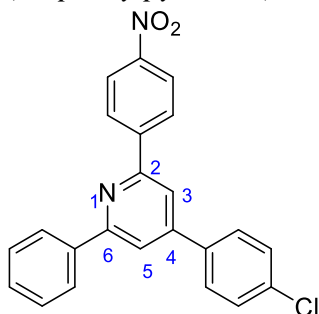
Yield = 65%; light yellow solid; m. p = 154–156 °C; ¹H NMR (500 MHz, CDCl₃) δ 8.62 (s, 1H: 4-Phenyl H-2), 8.39 (m, 5H: 2-Phenyl H-2, H-3 H-5 & H-6; 4-Phenyl H-4), 8.21 (d, *J* = 8.0 Hz, 2H: 6-Phenyl H-2 & H-6), 8.09 (d, *J* = 7.6 Hz, 1H: 4-Phenyl H-6), 7.99 (d, *J* = 14.3 Hz, 2H), 7.76 (t, *J* = 7.9 Hz, 1H: 4-Phenyl H-5), 7.54 (m, 3H: 6-Phenyl H-3, H-4 & H-5). ¹³C NMR (126 MHz, CDCl₃) δ 158.61 (Pyridine C-6), 155.47 (Pyridine C-2), 148.93 (Pyridine C-4), 148.42 (4-Phenyl C-3), 148.27 (2-Phenyl C-4), 144.87 (2-Phenyl C-1), 140.25 (4-Phenyl C-1), 138.45 (6-Phenyl C-1), 133.08 (4-Phenyl C-6), 130.38 (6-Phenyl C-4), 129.83 (4-Phenyl C-5), 128.97 (6-Phenyl C-3 & C-5), 127.95 (2-Phenyl C-2 & C-6), 127.15 (6-Phenyl c-2 & C-6), 124.06 (2-Phenyl C-3 & C-5), 123.99 (4-Phenyl C-4), 122.17 (4-Phenyl C-2), 118.20 (Pyridine C-3), 117.50 (Pyridine C-5). HRMS-ESI: m/z calc for C₂₃H₁₆N₃O₄: 398.1141, found: 398.1133 [M + H]⁺ (within 2.0 ppm difference).

2-(3,4-Dimethoxyphenyl)-4-(4-nitrophenyl)-6-phenylpyridine (2.3.86)



Yield = 76%; light yellow color solid; m. p = 167–170 °C; ^1H NMR (500 MHz, CDCl_3) δ 8.39 (d, J = 8.4 Hz, 2H: 4-Phenyl H-3 & H-5), 8.19 (d, J = 7.9 Hz, 2H: 6-Phenyl C-2 & C-6), 7.90 (d, J = 8.5 Hz, 2H: 4-Phenyl H-2 & H-6), 7.87 (s, 1H: 2-Phenyl H-2), 7.82 (d, J = 4.3 Hz, 2H: Pyridine H-3 & H-5), 7.72 (d, J = 8.3 Hz, 1H: 2-Phenyl H-6), 7.53 (d, J = 7.4 Hz, 2H: 6-Phenyl H-3 & H-5), 7.49 (d, J = 7.3 Hz, 1H: 6-Phenyl H-4), 7.01 (d, J = 8.4 Hz, 1H: 2-Phenyl H-5), 4.04 (s, 3H: -OMe), 3.97 (s, 3H: -OMe). ^{13}C NMR (126 MHz, CDCl_3) δ 157.84 (Pyridine C-2), 157.62 (Pyridine C-6), 150.45 (pyridine C-4), 149.36 (2-Phenyl C-4), 148.15 (2-Phenyl C-3), 147.82 (4-Phenyl C-1), 145.62 (4-Phenyl C-4), 139.13 (6-Phenyl C-1), 132.01 (2-Phenyl C-1), 129.41 (6-Phenyl C-4), 128.84 (6-phenyl C-3 & C-5), 128.20 (4-phenyl C-2 & C-6)), 127.11 (6-phenyl C-2 & C-6), 124.37 ((4-phenyl C-3 & C-5)), 119.78 (2-Phenyl C-2), 116.49 (Pyridine C-5), 116.38 (Pyridine C-3), 111.14 (2-Phenyl C-5). HRMS-ESI: m/z calc for $\text{C}_{25}\text{H}_{21}\text{N}_2\text{O}_4$: 413.1501, found: 413.1506 [$\text{M} + \text{H}$] $^+$ (within 1.2 ppm difference).

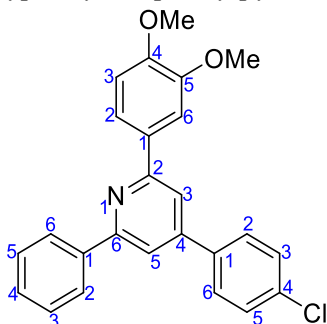
4-(4-Chlorophenyl)-2-(4-nitrophenyl)-6-phenylpyridine (2.3.87)



Yield = 43%; off white color solid; m. p = 127–129 °C; ^1H NMR (500 MHz, CDCl_3) δ 8.38 (s, 4H: 2-phenyl H-2, H-3, H-5, H-6), 8.20 – 8.14 (m, 2H: 6-Phenyl H-2 & H-6), 7.94 (s, 1H, Pyridine H-3), 7.91 (s, 1H: Pyridine H-5), 7.69 (d, J = 8.4 Hz, 2H: 4-Phenyl H-2 & H-6), 7.58 – 7.45 (m, 5H: 6-phenyl H-3, H-4, H-5; 4-Phenyl H-3 & H-5). ^{13}C NMR (126 MHz, CDCl_3) δ 158.28 (Pyridine C-6), 155.13 (Pyridine C-2), 149.54 (Pyridine C-4), 148.30 (2-Phenyl C-4), 145.29 (2-Phenyl C-1), 138.83 (6-Phenyl C-1), 136.92 ((4-Phenyl C-1)), 135.66 (4-Phenyl C-4), 129.60 (6-

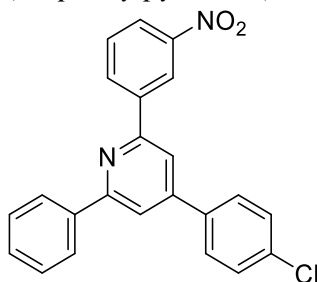
Phenyl C-4), 129.52 (4-Phenyl C-2 & C-6), 128.91 (6-Phenyl C-3 & C-5), 128.47 (4-Phenyl C-3 & C-5), 127.90 (2-Phenyl C-2 & C-6), 127.14 (6-Phenyl C-2 & C-5), 124.03 (2-Phenyl C-3 & C-5), 118.18 (Pyridine C-5), 117.52 (Pyridine C-3). HRMS-ESI: m/z calc for $C_{23}H_{16}N_2O_2Cl$: 387.0900, found: 387.0898 $[M + H]^+$ (within 0.5 ppm difference).

4-(4-Chlorophenyl)-2-(3,4-dimethoxyphenyl)-6-phenylpyridine (2.3.88)



Yield = 68%; buff color solid; m. p = 173–175 °C; 1H NMR (500 MHz, $CDCl_3$) δ 8.18 (d, $J = 7.6$ Hz, 2H: 6-Phenyl H-2 & H-6), 7.85 (s, 1H: 2-Phenyl H-2), 7.79 (d, $J = 5.7$ Hz, 2H: Pyridine H-3 & H-5), 7.71 (d, $J = 9.6$ Hz, 1H: 2-Phenyl H-6), 7.68 (d, $J = 8.3$ Hz, 2H: 4-Phenyl H-2 & H-6), 7.54 – 7.48 (m, 4H: 4-Phenyl H-3 & H-5; 6-Phenyl H-3 & H-5), 7.46 (d, $J = 7.2$ Hz, 1H: 6-Phenyl H-4), 6.99 (d, $J = 8.4$ Hz, 1H: 2-phenyl H-3), 4.03 (s, 3H: -OCH₃), 3.96 (s, 3H: -OCH₃). ^{13}C NMR (126 MHz, $CDCl_3$) δ 157.51 (Pyridine C-6), 157.30 (Pyridine C-2), 150.20 (2-Phenyl C-3), 149.26 (2-Phenyl C-4), 148.90 (Pyridine C-4), 139.48 (6-Phenyl C-1), 137.60 (4-Phenyl C-1), 135.14 (4-Phenyl C-4), 132.40 (2-Phenyl C-1), 129.31 (4-Phenyl C-3 & C-5), 129.12 (6-Phenyl C-4), 128.73 (6-phenyl C-3 & C-5), 128.45 (6-phenyl C-2 & C-6), 127.08 (4-phenyl C-2 & C-6), 119.69 (2-Phenyl C-6), 116.36 (Pyridine C-3), 116.24 (Pyridine C-5), 111.08 (2-phenyl C-5), 110.30 (2-Phenyl C-2), 56.06 (-OCH₃), 56.00 (-OCH₃). HRMS-ESI: m/z calc for $C_{25}H_{21}NO_2Cl$: 402.1261, found: 402.1245 $[M + H]^+$ (within 4.0 ppm difference).

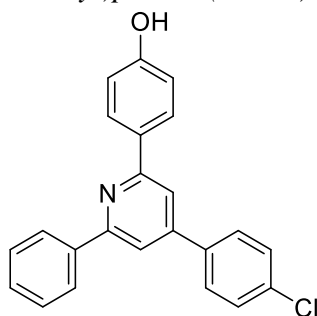
4-(4-Chlorophenyl)-2-(3-nitrophenyl)-6-phenylpyridine (2.3.89)



Yield = 61%; off-white color solid; m. p = 179-181 °C (previously reported m. p = 168-170 [424]); 1H NMR (500 MHz, $CDCl_3$) δ 9.02 (s, 1H: 4-Phenyl H-2), 8.58 (d, $J = 7.6$ Hz, 1H: 4-Phenyl H-

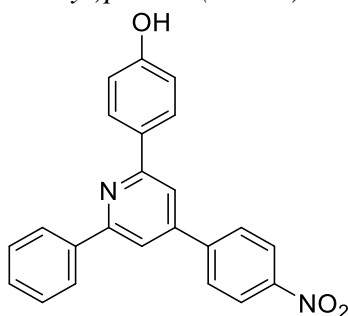
4), 8.31 (d, $J = 7.8$ Hz, 1H: 4-Phenyl H-6), 8.19 (d, $J = 7.4$ Hz, 2H: 2-Phenyl H-2 & H-6), 7.93 (s, 1H: Pyridine H-3), 7.90 (s, 1H: Pyridine H-5), 7.70 (m, 3H: 6-phenyl H-2 & H-6), 7.52 (m, 5H: 2-Phenyl H-3 & H-5; 6-Phenyl H-3, H-4 & H-5). ^{13}C NMR (126 MHz, CDCl_3) δ 158.15 (Pyridine C-6), 155.02 (Pyridine C-2), 149.55 (Pyridine C-4), 148.82 (4-Phenyl C-3), 141.07 (2-Phenyl C-1), 138.81 (6-Phenyl C-1), 136.91 (2-Phenyl C-1), 135.60 (Quaternary -C-, 2-Phenyl C-4), 133.00 (Aromatic -CH-, 4-Phenyl C-6), 129.71 (6-Phenyl C-4), 129.54 (Aromatic -CH-, 4-Phenyl C-5), 129.47 (6-Phenyl C-3 & C-5), 128.88 (2-Phenyl C-3 & C-5), 128.46 (6-Phenyl C-3 & C-5), 127.12 (2-Phenyl C-3 & C-5), 123.77 (Aromatic -CH-, 4-Phenyl C-4), 121.92 (Aromatic -CH-, 4-Phenyl C-2), 117.92 (pyridine C-5), 116.86 (pyridine C-3). The ^1H and ^{13}C NMR data was found in good agreement to that reported by Yan *et al* [206, 424]. HRMS-ESI: m/z calc for $\text{C}_{23}\text{H}_{16}\text{N}_2\text{O}_2\text{Cl}$: 387.0900, found: 387.0906 $[\text{M} + \text{H}]^+$ (within 2.0 ppm difference).

4-(4-(4-Chlorophenyl)-6-phenylpyridin-2-yl)phenol (2.3.90)



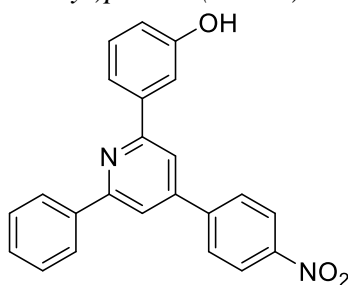
Yield = 57%: light yellow color solid; m. p = 163-166 °C (previously reported m. p = 159.0–159.6 °C); ^1H NMR (500 MHz, CD_3OD) δ 8.21 – 8.17 (m, 2H: 6-Phenyl H-2 & H-6), 8.08 (d, $J = 8.7$ Hz, 2H: 2-Phenyl C-2 & C-5), 7.92 (s, 2H: Pyridine H-3 & H-5), 7.86 (d, $J = 8.5$ Hz, 2H: 4-Phenyl C-2 & C-4), 7.57 – 7.49 (m, 4H: 4-Phenyl C-3 & C-5; 6-Phenyl C-3 & C-5), 7.45 (d, $J = 7.3$ Hz, 1H: 6-Phenyl C-3 & C-5), 6.94 (d, $J = 8.7$ Hz, 2H: 2-Phenyl C-3 & C-5). ^{13}C NMR (126 MHz, CD_3OD) δ 158.64 (2-Phenyl C-4), 157.80 (Pyridine C-6), 157.52 (Pyridine C-2), 148.99 (Pyridine C-4), 139.44 (6-Phenyl C-1), 137.38 (4-Phenyl C-1), 134.80 (4-Phenyl C-4), 130.61 (2-Phenyl C-1), 128.89 (2-Phenyl C-2 & C-6), 128.71 (6-Phenyl C-4), 128.42 (6-Phenyl C-3 & C-5), 128.31 (4-Phenyl C-2 & C-6), 128.26 (4-Phenyl C-3 & C-5), 126.81 (6-Phenyl C-2 & C-6), 115.56 (Pyridine C-3 & C-5), 115.08 (2-Phenyl C-3 & C-5). The ^1H and ^{13}C NMR data was found in good agreement to that reported by Thapa *et al* [206]. HRMS-ESI: m/z calc for $\text{C}_{23}\text{H}_{17}\text{NOCl}$: 358.0999, found: 358.0990 $[\text{M} + \text{H}]^+$ (within 2.5 ppm difference).

4-(4-(4-Nitrophenyl)-6-phenylpyridin-2-yl)phenol (**2.3.91**)



Yield = 67%; light brown color solid; m. p = 173–176 °C; ¹H NMR (500 MHz, CD₃OD) δ 8.40 (d, *J* = 8.6 Hz, 2H: 4-Phenyl C-3 & C-5), 8.22 (d, *J* = 7.8 Hz, 2H: 6-Phenyl H-2 & H-6), 8.15 – 8.06 (m, 4H: 2-Phenyl C-2 & C-5; 4-Phenyl C-2 & C-6), 8.00 (s, 2H: Pyridine H-3 & H-5), 7.53 (t, *J* = 7.6 Hz, 2H: 6-Phenyl H-3 & H-5), 7.46 (d, *J* = 7.1 Hz, 1H: 6-Phenyl H-4), 6.94 (d, *J* = 8.5 Hz, 2H: 2-Phenyl C-3 & C-5). ¹³C NMR (126 MHz, CD₃OD) δ 158.80 (2-Phenyl C-4), 157.94 (Pyridine C-6), 157.66 (Pyridine C-2), 148.19 (Pyridine C-4), 147.97 (4-Phenyl C-4), 145.11 (4-Phenyl C-1), 139.20 (6-Phenyl C-1), 130.35 (2-Phenyl C-1), 128.87 (6-Phenyl C-4), 128.35 (2-Phenyl C-2 & C-6), 128.29 (6-Phenyl C-3 & C-5), 128.15 (6-Phenyl C-2 & C-6), 126.81 (6-Phenyl C-2 & C-6), 123.80 (4-Phenyl C-3 & C-5), 115.81 (Pyridine C-3), 115.77 (Pyridine C-5), 115.13 (2-Phenyl C-3 & C-5). HRMS-ESI: *m/z* calc for C₂₃H₁₇NO₂: 369.1239, found: 369.1249 [M + H]⁺ (within 2.7 ppm difference).

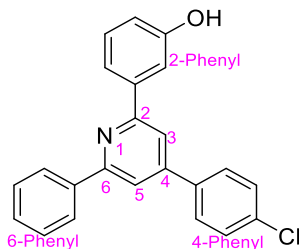
3-(4-(4-Nitrophenyl)-6-phenylpyridin-2-yl)phenol (**2.3.92**)



Yield = 62%; off white color solid; m. p = 162–165 °C; ¹H NMR (500 MHz, CDCl₃) δ 8.39 (d, *J* = 8.7 Hz, 2H: 4-Phenyl C-3 & C-5), 8.19 (d, *J* = 7.3 Hz, 2H: 6-Phenyl H-2 & H-6), 7.92 – 7.84 (m, 4H: 4-Phenyl C-2 & C-6; Pyridine H-3 & H-5), 7.77 (s, 1H: 2-Phenyl H-2), 7.72 (d, *J* = 7.8 Hz, 1H: 2-Phenyl H-6), 7.53 (t, *J* = 7.4 Hz, 2H: 6-Phenyl H-3 & H-5), 7.50 – 7.45 (m, 1H: 6-Phenyl H-4), 7.40 (t, *J* = 7.9 Hz, 1H: 2-Phenyl H-5), 6.98 – 6.92 (m, 1H: 2-Phenyl H-4), 5.15 (s, 1H: 3-OH). ¹³C NMR (126 MHz, CDCl₃) δ 158.00 (2-Phenyl C-3), 157.39 (Pyridine C-6), 156.14 (Pyridine C-3), 148.21 (Pyridine C-4), 147.90 (4-Phenyl C-4), 145.39 (4-Phenyl C-1), 140.70 (2-Phenyl C-1), 138.97 (6-Phenyl C-1), 130.09 (2-Phenyl C-5), 129.49 (6-Phenyl C-4), 128.85 (4-

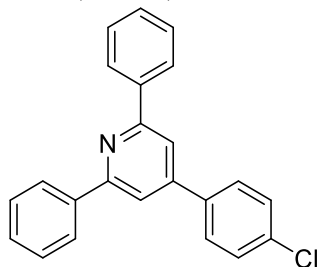
Phenyl C-2 & C-6), 128.19 (6-Phenyl C-3 & C-5), 127.15 (6-Phenyl C-2 & C-6), 124.40 (4-Phenyl C-3 & C-5), 119.50 (2-Phenyl C-6), 117.22 (Pyridine C-3), 117.04 (Pyridine C-5), 116.47 (2-Phenyl C-2), 114.11 (2-Phenyl C-4). HRMS-ESI: m/z calc for $C_{23}H_{17}N_2O_3$: 369.1239, found: 369.1248 $[M + H]^+$ (within 2.4 ppm difference).

3-(4-(4-Chlorophenyl)-6-phenylpyridin-2-yl)phenol (2.3.93)



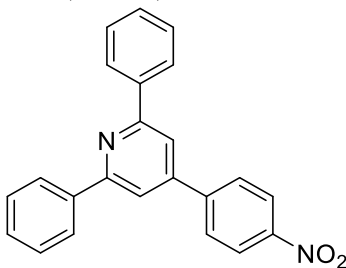
Yield = 59%; white color solid; m. p = 153–155 °C (previously reported m. p = 151.5-152.1 [206]); R_f = 0.61 (EtOAc-cyclohexane, 3:7); 1H NMR (500 MHz, $CDCl_3$) δ 8.21 – 8.14 (m, 2H: 6-Phenyl H-2 & H-6), 7.83 (s, 1H: Pyridine H-3), 7.81 (s, 1H: Pyridine H-5), 7.76 – 7.73 (m, 1H: 2-Phenyl H-2), 7.68 (m, 3H: 4-Phenyl H-2 & H-6; 2-Phenyl H-6), 7.54 – 7.43 (m, 5H: 6-Phenyl C-3, C-4 & C-5; 4-Phenyl H-3 & H-5), 7.37 (t, J = 7.9 Hz, 1H: 2-Phenyl H-5), 6.96 – 6.90 (m, 1H: 2-Phenyl H-4), 5.42 (broad, s, 1H: 3-OH). ^{13}C NMR (126 MHz, $CDCl_3$) δ 157.67 (Quaternary, 2-Phenyl C-3), 157.09 (Quaternary, Pyridine C-6), 156.12 (Quaternary, Pyridine C-2), 148.96 (Quaternary, Pyridine C-4), 141.02 (Quaternary, 2-Phenyl C-1), 139.33 (Quaternary, 6-Phenyl C-1), 137.38 (Quaternary, 4-Phenyl C-1), 135.24 (Quaternary, 4-Phenyl C-4), 129.96 (Aromatic -CH-, 6-Phenyl C-4), 129.34 (Aromatic -CH-, 4-Phenyl C-3 & C-5), 129.19 (Aromatic -CH-, 2-Phenyl C-3), 128.73 (Aromatic -CH-, 6-Phenyl C-3 & C-5), 128.43 (Aromatic -CH-, 4-Phenyl C-2 & C-6), 127.13 (Aromatic -CH-, 6-Phenyl C-2 & C-6), 119.42 (Aromatic -CH-, 2-Phenyl C-6), 117.05 (Aromatic -CH-, Pyridine C-3), 116.88 (Aromatic -CH-, Pyridine C-5), 116.21 (Aromatic -CH-, 2-Phenyl C-2), 114.09 (Aromatic -CH-, 2-Phenyl C-4). The 1H and ^{13}C NMR data was found in good agreement to that reported by Thapa *et al* [206]. HRMS-ESI: m/z calc for $C_{23}H_{17}NOCl$: 358.0994, found: 358.0995 $[M + H]^+$ (within 1.4 ppm difference).

4-(4-Chlorophenyl)-2,6-diphenylpyridine (2.3.94)



Yield = 68% ; white color solid; m. p = 128-129 °C (previously reported m. p = 127-130 [425], 121–122 °C [420], 111–112°C [231]); ¹H NMR (500 MHz, CDCl₃) δ 8.20 (d, *J* = 7.9 Hz, 4H: 6-Phenyl H-2 & H-6; 2-Phenyl H-2 & H-6), 7.84 (s, 2H: Pyridine H-3 & H-5), 7.68 (d, *J* = 8.3 Hz, 2H: 4-Phenyl H-2 & H-6), 7.55 – 7.43 (m, 8H: 2-Phenyl H-3, H-4 & H-5; 6-Phenyl H-3, H-4 & H-5; 4-Phenyl C-3 & C-5). ¹³C NMR (126 MHz, CDCl₃) δ 157.68 (Pyridine C-2 & C-6), 148.94 (Pyridine C-4), 139.40 (2-phenyl C-1 & 6-Phenyl C-1), 137.49 (4-Phenyl C-1), 135.19 (4-Phenyl C-4), 129.33 (4-Phenyl C-3 & C-5), 129.16 (4-Phenyl C-2 & C-6), 128.73 (2-Phenyl C-3 & C-5; 6-Phenyl C-3 & C-5), 128.45 (2-Phenyl C-4; 6-Phenyl C-4), 127.11 (2-Phenyl C-2 & C-6; 6-Phenyl C-2 & C-6), 116.80 (Pyridine C-3 & C-5). The ¹H and ¹³C NMR data was found in good agreement to that reported by previous studies [231] [420, 425]. HRMS-ESI: m/z calc for C₂₃H₁₇NCl: 342.1050, found: 342.1062 [M + H]⁺ (within 3.5 ppm difference).

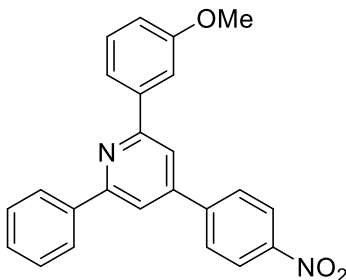
4-(4-Nitrophenyl)-2,6-diphenylpyridine (2.3.95)



Yield = 71 %; buff color solid; m. p = 187-189 °C (previously reported m. p = 195–197°C [226], 194–195 °C [426], 196–198 °C [427]); ¹H NMR (500 MHz, DMSO-*d*₆) δ 8.39 – 8.31 (m, 8H: 2-Phenyl H-2 & H-6; 6-Phenyl H-2 & H-6; 4-Phenyl H-3 & H-5), 8.28 (s, 2H: Pyridine H-3 & H-5), 7.55 (t, *J* = 7.5 Hz, 4H: 2-Phenyl H-3 & 5; 6-Phenyl H-3 & H-5), 7.49 (t, *J* = 7.2 Hz, 2H: 2-Phenyl H-4 & 6-Phenyl H-4). ¹³C NMR (126 MHz, DMSO-*d*₆) δ 156.68 (Pyridine C-2 & C-6) , 147.78 (Pyridine C-4), 147.23 (4-Phenyl C-1), 144.02 (4-Phenyl C-4), 138.40 (2-phenyl C-1 & 6-Phenyl C-1), 129.34 (2-phenyl C-1 & 6-Phenyl C-1), 128.78 (4-Phenyl C-2 & C-6), 128.68 (2-Phenyl C-3 & C-5; 6-Phenyl C-3 & C-5), 126.92 (2-Phenyl C-2 & C-6; 6-Phenyl C-2 & C-6), 123.91 (4-Phenyl C-3 & C-5), 116.88 (Pyridine C-3 & C-5). The ¹³C NMR data was found in good

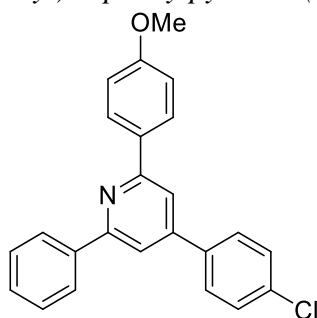
agreement to that reported by Ren *et al* [421]. HRMS-ESI: m/z calc for $C_{23}H_{17}N_2O_2$: 353.1290, found: 353.1289 $[M + H]^+$ (within 3.5 ppm difference)

2-(3-Methoxyphenyl)-4-(4-nitrophenyl)-6-phenylpyridine (2.3.96)



Yield = 64%; light yellow color solid; m. p = 142–144 °C; 1H NMR (500 MHz, $CDCl_3$) δ 8.39 (d, $J = 7.3$ Hz, 2H: 4-Phenyl H-3 & H-5), 8.20 (d, $J = 6.2$ Hz, 2H: 6-Phenyl H-2 & H-6), 7.95 – 7.69 (m, 6H: Pyridine H-3 & H-5; 2-Phenyl H-4 & H-6; 4-Phenyl H-2 & H-6), 7.59 – 7.41 (m, 4H: 6-Phenyl H-3, H-4 & H-5; 2-Phenyl H-5), 7.03 (d, $J = 6.6$ Hz, 1H: 2-Phenyl H-4), 3.94 (s, 3H). ^{13}C NMR (126 MHz, $CDCl_3$) δ 160.15 (2-Phenyl C-3), 157.92 (Pyridine C-6), 157.73 (Pyridine C-2), 148.18 (pyridine C-4), 147.84 (4-Phenyl C-4), 145.43 (4-Phenyl C-1), 140.53 (2-Phenyl C-1), 138.98 (6-Phenyl C-1), 129.83 (6-Phenyl C-4), 129.46 (2-Phenyl C-5), 128.84 (4-Phenyl C-2 & C-6), 128.18 (6-Phenyl C-3 & C-5), 127.14 (6-Phenyl C-2 & C-6), 124.38 (4-Phenyl C-3 & C-5), 119.50 (2-Phenyl C-6), 117.10 (Pyridine C-3), 117.09 (Pyridine C-5), 114.89 (2-Phenyl C-1), 112.91 (2-Phenyl C-2), 55.46 (3-OMe). HRMS-ESI: m/z calc for $C_{24}H_{19}N_2O_3$: 383.1396, found: 383.1389 $[M + H]^+$ (within 1.8 ppm difference).

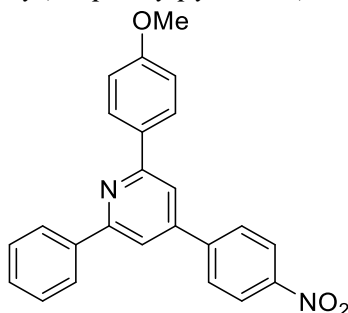
4-(4-Chlorophenyl)-2-(4-methoxyphenyl)-6-phenylpyridine (2.3.97)



Yield = 70 %; off white color solid; m. p = 136–140 °C; 1H NMR (500 MHz, $CDCl_3$) δ 8.17 (m, 4H: 2-Phenyl H-2 & H-6; 6-Phenyl H-2 & H-6), 7.78 (s, 1H: Pyridine H-3), 7.77 (s, 1H: Pyridine H-5), 7.67 (d, $J = 8.4$ Hz, 1H: 4-Phenyl H-2 & H-6), 7.54 – 7.42 (m, 5H: 4-Phenyl H-3 & H-5; 2-Phenyl H-3, H-4 & H-5), 7.04 (d, $J = 8.7$ Hz, 2H: 2-Phenyl H-3 & H-5), 3.89 (s, 3H: OMe). ^{13}C NMR (126 MHz, $CDCl_3$) δ 160.66 (2-Phenyl C-4), 157.53 (Pyridine C-6), 157.30 (Pyridine C-2), 148.85 (Pyridine C-4), 139.53 (6-Phenyl C-1), 137.66 (4-Phenyl C-1), 135.11 (4-Phenyl C-4),

132.04 (2-Phenyl C-1), 129.30 (4-Phenyl C-3 & C-5), 129.09 (6-Phenyl C-4), 128.71 (4-Phenyl C-2 & C-6), 128.45 (6-Phenyl C-3 & C-5), 128.41 (2-Phenyl C-2 & C-6), 127.11 (6-Phenyl C-2 & C-6), 116.16 (Pyridine C-5), 116.03 (Pyridine C-3), 114.11 (2-Phenyl C-3 & C-5), 55.01 (4-OMe). HRMS-ESI: m/z calc for C₂₄H₁₉NOCl: 372.1155, found: 372.1151 [M + H]⁺ (within 1.1 ppm difference).

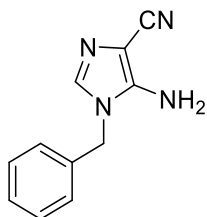
2-(4-Methoxyphenyl)-4-(4-nitrophenyl)-6-phenylpyridine (2.3.98)



Yield = 57%; off white color solid; m. p = 154–157 °C; ¹H NMR (500 MHz, CDCl₃) δ 8.37 (d, *J* = 8.5 Hz, 2H: 4-Phenyl H-3 & H-5), 8.18 (dd, *J* = 10.7, 8.3 Hz, 4H: 2-Phenyl H-2 & H-6), 7.87 (d, *J* = 8.5 Hz, 2H: 4-Phenyl H-2 & H-6), 7.80 (s, 2H: Pyridine H-3 & H-5), 7.53 (t, *J* = 7.5 Hz, 2H), 7.47 (t, *J* = 7.2 Hz, 1H), 7.04 (dd, *J* = 8.9, 2.7 Hz, 2H), 3.89 (s, 3H: -OCH₃). ¹³C NMR (126 MHz, CDCl₃) δ 160.86 (2-Phenyl C-4), 157.79 (Pyridine C-6), 157.56 (Pyridine C-2), 148.11 (Pyridine C-4), 147.72 (4-Phenyl C-1), 145.61 (4-Phenyl C-4), 139.14 (6-Phenyl C-1), 131.61 (2-Phenyl C-1), 129.36 (6-Phenyl C-4), 128.80 (6-Phenyl C-3 & C-5), 128.44 (4-Phenyl C-2 & C-6), 128.14 (2-Phenyl C-2 & C-6), 127.10 (4-Phenyl C-3 & C-5), 124.33 (6-Phenyl C-2 & C-6), 116.23 (Pyridine C-3), 116.12 (Pyridine C-5), 114.18 (2-Phenyl C-3 & C-5), 55.41 (-OCH₃). HRMS-ESI: m/z calc for C₂₄H₁₉N₂O₃: 383.1396, found: 383.1397 [M + H]⁺ (within 0.3 ppm difference).

Synthesis of imidazole

5-Amino-1-benzyl-1H-imidazole-4-carbonitrile (2.3.101)

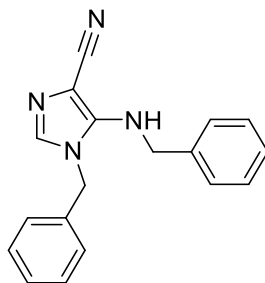


The diaminonitrile (1gm) treated with Triethyl orthoformate in dioxane solvent and refluxed for 9 hours. After monitoring by TLC shows complete consumption of diaminonitrile during reaction, dioxane was evaporated on rotavap, which left a brown colour residue. The residue was dissolved into diethyl ether (2 x 10 mL) and filtered under vacuum and mother liquor was collected and left

overnight. Later the subsequent seeds of crystals (long needle-shaped brown crystals) were collected and treated with benzylamine and freshly prepared anilinium chloride (10 mol %) in EtOH under dark at room stirring for 8 hours. Later EtOH was removed by rotavap and dried residue was treated with 1 M NaOH solution to afford **2.3.101**. The compound stick arounds the magnet bead and NaOH solution was easily decanted. After decanting, triturated with the help of spatulate was done in slight hexane and EtOAc (~1:1) and compound get precipitated which was later filtered off.

Yield = 88%; light green color solid; m. p = 192-194 °C (previously reported m. p = 196-198 °C [428]); ¹H NMR (500 MHz, CDCl₃) δ 7.43 – 7.33 (m, 4H: Bn-H-2, H-3, H-5 & H-6), 7.25 (s, 1H: Imidazole H-2), 7.20 (s, 1H: Bn-H-4), 5.04 (s, 2H: Bn-CH₂-), 4.24 (br, s, 2H: NH₂) [428]. ¹³C NMR (126 MHz, CDCl₃) δ 156.33 (Quaternary, Imidazole-C-5), 137.29 (Aromatic -CH-, Imidazole C-2), 134.18 (Quaternary, Bn-C-1), 129.21 (Aromatic -CH-, Bn-C3 & C5), 128.89 (Aromatic -CH-, Bn-C4), 127.83 (Aromatic -CH-, Bn-C2 & C6), 112.55 (Quaternary, -CN), 96.92 (Quaternary, Imidazole-C-4), 50.60 (Bn-CH₂-). HRMS-ESI: m/z calc for C₁₉H₂₁O₅: 199.0978, found: 199.0979 [M + H]⁺ (within 0.5 ppm difference).

1-Benzyl-5-(benzylamino)-1H-imidazole-4-carbonitrile (2.3.102)



The **2.3.101** (1 equiv.) was treated with K₂CO₃ (1.2 equiv.) and benzyl chloride (1 equiv.) in DMF for 12 hours (heated at 40-43 °C) to afford compound. Later, aqueous work up was performed and EtOAc layer was collected, dried over sodium sulphate and, removed under reduced pressure, which was purified through column chromatography (EtOAc: Cyclohexane, 35-50 %).

¹H NMR (500 MHz, CDCl₃) δ 7.37 – 7.24 (m, 6H), 7.23 – 7.15 (m, 3H), 7.02 (d, *J* = 1.4 Hz, 1H), 6.81 – 6.59 (m, 2H), 4.62 (s, 2H), 4.24 (s, 2H). ¹³C NMR (126 MHz, CDCl₃) δ 147.87 (Quaternary, Imidazole-C-5), 136.45 (Quaternary, N1-Bn-C-1), 135.32 (Aromatic -CH-, Imidazole-C-2), 134.83 (Quaternary, NH-Bn-C1), 129.24 (Aromatic -CH-, N1-Bn-C3 & C-5), 129.07 (Aromatic -CH-, NH-Bn-C3 & C-5), 128.69 (Aromatic -CH-, N1-Bn-C2 & C-6), 128.41 (Aromatic -CH-, NH-Bn-C2 & C-6), 128.00 (Aromatic -CH-, NH-Bn-C-4), 127.33 (Aromatic -CH-, N1-Bn-C4),

115.51 (-CN), 107.40(Imidazole 4-CN) , 58.52 (-OCH₃) (Imidazole-N-Bn -CH₂-), 47.28 (Imidazole-NH-Bn -CH₂-). HRMS-ESI: m/z calc for C₁₈H₁₇N₄: 289.1448, found: 289.1450 [M + H]⁺ (within 0.7 ppm difference).

General procedure for synthesis of N-benzyl-1H-imidazole-4,5-dicarbonitrile

The 4,5-dicyanoimidazole was dissolved in DMF along with K₂CO₃ (1.2 equiv.), benzyl chloride derivatives (1 equiv.) and left for stirring 10 hours at room temperature. The aqueous work up was performed where the EtOAc layer was dried over sodium sulphate and removed under reduced pressure and later gradient column chromatography was (EtOAc: Cyclohexane, 40-50 %) performed.

General procedure for N-benzyl-imidazole-4,5-dicarboxylic acid

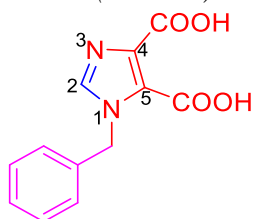
Either of the compounds (**2.3.105** or **2.3.106**) in 25 mL RBF were refluxed with 5N NaOH to yield (dicarboxylic acids: **2.3.107** & **2.3.108**) [241]. Later after monitoring the reaction completion on TLC, the acid base extraction was performed, and purity of these compounds were estimated with qNMR.

Quantification of NMR (qNMR)

The sensitive of weighing balance is essential to get accurate results therefore a microbalance was used for weighing. Initially the balance was calibrated, which includes centering of bubble and weighing of pre-calibrated weights (in this case I used 10 mg) and I found an error of +0.031 mg. The weighing was done on plastic caps in order to avoid butter paper. After completing the weighing of internal standard and my compound of interest, I also weight again the empty cap, looking for any residual left there, so that I can consider it further during calculations. I added all Internal std + compound directly to the NMR tube followed by addition of 600 μ L of DMSO-*d*₆, taken from fresh vial by using micropipette. This whole procedure is followed from J med chem author guidelines of purity [242]. To obtain quantitative data, the ¹H NMR spectra, with a relaxation delay set from 15 s up to 30 s, 30° and 45°C pulse angle, 2.0447 s acquisition time, and spectral widths of 16 ppm (-2 ppm- 14 ppm). In all the spectra the baseline was automatically corrected with Whittaker Smoother method.

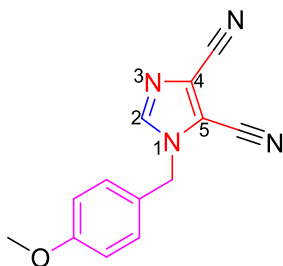
With the aim to have precise quantitative analysis the longest T1 value of molecule was used to set up the proper relaxation delay. The integration was performed manually. In my calculation I used benzyl protons. Here, the internal standard (DMS) used 4.54 mg +-0.0228 and my compound weight is 3.15 mg \pm 0.0405.

1-Benzyl-1H-imidazole-4,5-dicarboxylic acid (2.3.107)



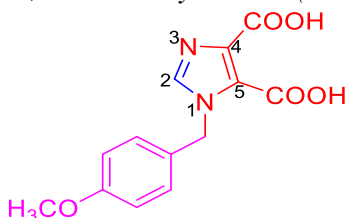
Yield = 97%; off-white color solid; m. p = 207-210 °C; ^{13}C NMR (126 MHz, DMSO- d_6) δ 159.44 (Quaternary, 5-COOH), 158.72 (Quaternary, 4-COOH), 138.42 (Aromatic -CH-, Imidazole C-2), 135.79 (Quaternary Bn-C-1), 131.04 (Quaternary, Imidazole C-5), 128.51 (Aromatic -CH-, Bn-C-3 & Bn-C-5), 127.89 (Aromatic -CH-, Bn-C-4), 127.40, 126.51 (Quaternary, Imidazole C-5), 50.70 (Ph-CH $_2$ -). The ^{13}C NMR data was found in good agreement to that reported by Delest *et al* [241]. HRMS-ESI: m/z calc for C $_{12}$ H $_{11}$ N $_2$ O $_4$ +: 247.0713, found: 247.0718 [M + H] $^+$ (within 2.0 ppm difference).

1-(4-Methoxybenzyl)-1H-imidazole-4,5-dicarbonitrile (2.3.106)



Yield = 88%; white color solid; ^1H NMR (500 MHz, CDCl $_3$) δ 7.66 – 7.61 (m, 1H, imidazole H-2), 7.24 (dd, J = 8.3, 1.2 Hz, 2H, Bn-H2 & H6), 6.97 – 6.92 (m, 2H, Bn-H3 & H5), 5.20 (s, 2H, Bn -CH-), 3.83 (s, 3H; -OCH $_3$). These values are parallel to reported [429]. ^{13}C NMR (126 MHz, CDCl $_3$) δ 160.65 (Quaternary, Bn-C-4), 140.74 (Aromatic -CH-, Imidazole-C-2), 129.88 (Aromatic -CH-, Bn C-2 & C-6), 124.07 (Quaternary, Imidazole C-5), 123.39 (Quaternary, Imidazole C-4), 115.01 (Aromatic -CH-, Bn C-3 & C-5), 111.45 (Imidazole 5-CN), 107.92 (Imidazole 4-CN), 55.42 (-OCH $_3$), 51.44 (Bn -CH $_2$ -). The ^1H and ^{13}C NMR data was found in good agreement to that reported by Xie *et al* [430]. HRMS-ESI: m/z calc for C $_{13}$ H $_{11}$ N $_4$ O: 239.0927, found: 239.0932 [M + H] $^+$ (within 2.1 ppm difference)

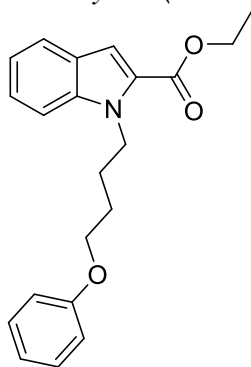
1-(4-Methoxybenzyl)-1H-imidazole-4,5-dicarboxylic acid (2.3.108)



^1H NMR (500 MHz, DMSO- d_6) δ 9.27 (s, 1H: Imidazole-H-2), 7.46 – 7.18 (m, 2H: Bn-H-2 & H-6), 7.10 – 6.75 (m, 2H: Bn-H-3 & H-5), 5.72 (s, 2H: Bn-CH $_2$ -), 3.73 (s, 3H: -OCH $_3$). ^{13}C NMR (126 MHz, DMSO- d_6) δ 159.84 (Quaternary, 5-COOH), 159.61 (Quaternary, Bn-C-4), 159.29 (Quaternary, 4-COOH), 138.54 (Aromatic -CH-, Imidazole C-2), 131.42 (Quaternary, Bn-C-4), 130.02 (Aromatic -CH-, Bn C-2 & C-6), 128.06 (Quaternary, Imidazole C-5), 126.95 (Quaternary, Imidazole C-4), 114.48 (Aromatic -CH-, Bn C-3 & C-5), 55.58 (-OCH $_3$), 50.88 (Bn -CH $_2$ -). HRMS-ESI: m/z calc for C $_{13}$ H $_{13}$ N $_2$ O $_5$: 277.0819, found: 277.0811 [M + H] $^+$ (within 2.9 ppm difference)

Synthesis of indole derivatives

Ethyl 1-(4-phenoxybutyl)-1H-indole-2-carboxylate (**2.3.111**)



To 1 equiv. of phenyl hydrazine, 1 equiv. of pyruvate ester was added in presence of 0.2 mL of AcOH and MeOH as solvent and the mixture was heated at reflux for 4.5 hours. The yellowish-orange precipitate was collected by filtration and also further washed with cold water to give *ethyl (Z)-2-(2-phenylhydrazono)propanoate*, **2.3.109**, HRMS-ESI: m/z calc for C $_{11}$ H $_{15}$ N $_2$ O $_2$: 207.1128, found: 207.1131 [M + H] $^+$ (within 1.5 ppm difference)). This precipitate was placed on a Schlenk line to remove traces of water and polyphosphoric acid was added then (5 mL) and reflux for 6 hours. Later, water was directly added drop by drop (note: highly exothermic reaction) and heated at reflux for a further 2 hours. Later, DCM was added and the organic layer was separated from the aqueous layer, collected, dried over sodium sulphate, evaporated on a rotary evaporator to give *ethyl 1H-indole-2-carboxylate*, **2.3.110**; HRMS-ESI: m/z calc for C $_{11}$ H $_{12}$ NO $_2$: 190.0863, found: 190.0867 [M + H] $^+$ (within 2.1 ppm difference)). Later, similar reaction conditions were used to give **2.3.111**.

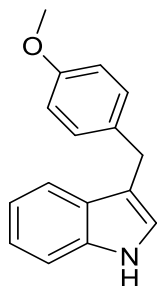
^1H NMR (500 MHz, CDCl $_3$) δ 7.67 (d, J = 8.0 Hz, 1H: Indole H-4), 7.41 (d, J = 8.5 Hz, 1H: indole H-7), 7.36 – 7.29 (m, 2H: Indole H-6 & H-3), 7.28 – 7.19 (m, 2H: OPh H-3 & H-5), 7.14 (t, J = 7.4 Hz, 1H: H-5), 6.92 (t, J = 7.3 Hz, 1H: OPh H-4), 6.87 (d, J = 8.2 Hz, 2H: OPh H-2 & H-6),

4.65 (t, $J = 7.4$ Hz, 2H: PhO-CH₂-CH₂-CH₂-CH₂-indole), 4.37 (q, $J = 7.1$ Hz, 2H: Ester -CH₂-), 3.96 (t, $J = 6.3$ Hz, 2H: PhO-CH₂-CH₂-CH₂-CH₂-indole), 2.06 – 1.94 (m, 2H: PhO-CH₂-CH₂-CH₂-CH₂-indole), 1.88 – 1.80 (m, 2H: PhO-CH₂-CH₂-CH₂-CH₂-indole), 1.40 (t, $J = 7.1$ Hz, 3H: ester -CH₃). ¹³C NMR (126 MHz, CDCl₃) δ 162.03 (-C=O), 158.93 (OPh C-1), 139.03 (Indole C-8), 129.40 (OPh C-3 & C-5), 127.44 (Indole C-2), 125.98 (Indole C-9), 124.92 (indole CH), 122.65 (indole CH), 120.61 (indole CH), 120.51 (indole CH), 114.50 (OPh C-2 & C-6), 110.58 (indole C-3), 110.45 (indole C-7), 67.43 (PhO-CH₂-CH₂-CH₂-CH₂-indole), 60.52 (Ester -CH₂-), 44.36 (PhO-CH₂-CH₂-CH₂-CH₂-indole), 27.38 (PhO-CH₂-CH₂-CH₂-CH₂-indole), 26.68 (PhO-CH₂-CH₂-CH₂-CH₂-indole), 14.37 (Ester-CH₃). HRMS-ESI: m/z calc for C₂₁H₂₄NO₃: 338.1751, found: 338.1754 [M + H]⁺ (within 0.9 ppm difference).

General procedure for 3-Methoxybenzyl-1H-indoles

To a 10 mL glass microwave tube, respective ethyl indole-2-carboxylate derivatives (1 equiv.) with 4-methoxybenzylamine (1 equiv.), and lithium hydroxide (7.5 mol %) were added along with stirring bead. The tube was sealed with a septum and placed inside the microwave. The reaction mixture was heated to 200 °C using an initial microwave power of 200 Watts for 30 min. Later gradient column chromatography was (EtOAc: Cyclohexane, 30-40 %) performed.

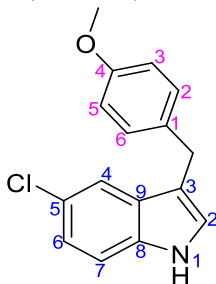
3-(4-methoxybenzyl)-1H-indole (2.3.114a)



Yield = 66%; light yellow color [431]; m. p = 97-99°C; ¹H NMR (500 MHz, CDCl₃) δ 7.92 (br, s, 1H, -NH-), 7.56 (d, $J = 7.9$ Hz, 1H: Indole H-4), 7.37 (d, $J = 8.1$ Hz, 1H, indole H-7), 7.27 – 7.18 (m, 3H: Bn H-2 & H-6; indole H-6), 7.12 (t, $J = 7.5$ Hz, 1H: Indole H-5), 6.90 (s, 1H: indole H-2), 6.86 (d, $J = 8.6$ Hz, 2H: Bn H-3 & H-5), 4.10 (s, 2H: Bn-CH₂-), 3.81 (s, 3H, OMe). ¹³C NMR (126 MHz, CDCl₃) δ 157.84 (Quaternary, Bn C-4), 136.51 (Quaternary, Indole C-8), 133.34 (Quaternary, Bn C-1), 129.61 (Aromatic -CH- Bn C-2 & C-6), 127.46 (Quaternary indole C-9), 122.25 (Aromatic -CH- indole H-2), 122.03 (Aromatic -CH- indole H-6), 119.34 (Aromatic -CH- indole H-5), 119.19 (Aromatic -CH- indole H-4), 116.30 (Quaternary indole C-3), 113.78, 111.09 (Aromatic -CH- indole H-7), 55.29 (-OMe), 30.73 (benzylic -CH₂-). The ¹H and ¹³C NMR data

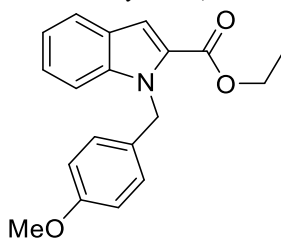
was found in good agreement to that reported by Jiang *et al* [245] and Seck *et al* [246]. HRMS-ESI: m/z calc for C₁₆H₁₆NO: 238.1226, found: 238.1229 [M + H]⁺ (within 1.3 ppm difference).

5-Chloro-3-(4-methoxybenzyl)-1H-indole (2.3.115)



¹H NMR (500 MHz, CDCl₃) δ 7.96 (br, s, 1H, -NH-), 7.46 (s, 1H: Indole H-4), 7.24 (d, *J* = 8.4 Hz, 1H: indole H-7), 7.17 (d, *J* = 8.1 Hz, 2H: Bn H-2 & H-6), 7.12 (d, *J* = 8.6 Hz, 1H: indole H-6), 6.91 (s, 1H: indole H-2), 6.83 (d, *J* = 8.3 Hz, 2H: Bn H-3 & H-5), 4.00 (s, 2H: benzylic protons), 3.78 (s, 3H: -OMe). ¹³C NMR (126 MHz, CDCl₃) δ 157.92 (Bn C-4), 134.81 (indole C-8), 132.77 (Bn C-1), 129.49 (Bn C-2 & C-6), 128.53 (indole C-9), 125.07 (indole C-5), 123.59 (indole C-2), 122.33 (indole C-6), 118.65 (Indole C-4), 116.13 (indole C-3), 113.84 (Bn C-3 & C-5), 112.04 (indole C-7), 55.27 (-OMe), 30.51 (Bn -CH₂-). HRMS-ESI: m/z calc for C₁₆H₁₅ClNO: 272.0837, found: 272.0831 [M + H]⁺ (within 2.2 ppm difference)

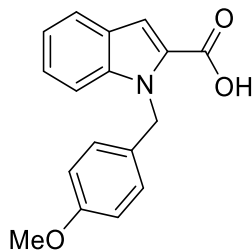
Ethyl 1-(4-methoxybenzyl)-1H-indole-2-carboxylate (2.3.116)



To ethyl indole-2-carboxylate (**2.1.110**) (100 mg, 0.52 mM, 1 equiv.), K₂CO₃ (88 mg, 0.63 mM, 1.2 equiv.) was stirred in DMF. After 10 mins, 4-methoxybenzyl chloride (81 mg, 0.52 mM, 1 equiv.) was added. After, stirring at room temperature for overnight, aqueous work up was performed where the DCM layer was dried over sodium sulphate and removed under reduced pressure and later gradient column chromatography was (EtOAc: Cyclohexane, 10-20 %) performed, obtained pale yellow colored oil; ¹H NMR (500 MHz, CDCl₃) δ 7.69 (d, *J* = 7.9 Hz, 1H: Indole H-4), 7.37 (m, 2H: indole H-3 & H-7), 7.30 (s, 1H: Indole H-6), 7.14 (t, *J* = 7.4 Hz, 1H: Indole H-5), 7.01 (d, *J* = 8.6 Hz, 2H: Bn H-2 & H-6), 6.77 (d, *J* = 8.7 Hz, 2H: Bn H-3 & H-5), 5.77 (s, 2H: Benzylic protons), 4.33 (d, *J* = 7.1 Hz, 2H: Ester -CH₂-), 3.73 (s, 3H: OMe), 1.36 (t, *J* = 7.1 Hz, 3H: ester CH₃). ¹³C NMR (126 MHz, CDCl₃) δ 161.99 (Carbonyl -C=O), 158.67

(Bn C-4), 139.45 (Indole C-8), 130.41 (Bn C-1), 127.66 (Indole C-2), 127.64 (Bn C-2 & C-6), 126.12 (Indole C-9), 125.16 (Indole C-6), 122.62 (Indole C-4), 120.74 (Indole C-5), 113.92 (Bn C-3 & C-5), 110.93 (indole C-7), 110.86 (indole C-3), 60.57 (ester -CH₂-), 55.20 (-OMe), 47.30 (Benzylic -CH₂-), 14.32 (ester -CH₃-). The ¹H and ¹³C NMR data was found in good agreement to that reported by Higuchi *et al* [432] and Ching *et al* [433]. HRMS-ESI: m/z calc for C₁₉H₂₀NO₃⁺: 310.1438, found: 310.1432 [M + H]⁺ (within 1.9 ppm difference).

1-(4-Methoxybenzyl)-1H-indole-2-carboxylic acid (2.3.117)



To **2.3.116** (61 mg, 0.19 mM, 1 equiv.), different concentrations of LiOH (0.1, 0.5, 3.5 equiv.) were tried in microwave sealed tube and heated to 200 °C for 30 mins to form same compound (**2.3.117**) as white color solid; ¹H NMR (500 MHz, D₂O) δ 7.75 (d, *J* = 8.0 Hz, 1H: Indole H-4), 7.45 (d, *J* = 8.4 Hz, 1H: indole H-7), 7.28 (t, *J* = 7.2 Hz, 1H: indole H-6), 7.17 (t, *J* = 7.4 Hz, 1H: Indole H-5), 7.14 – 7.11 (s, 1H: indole H-3), 7.02 (d, *J* = 8.7 Hz, 2H: Bn H-2 & H-6), 6.83 (d, *J* = 8.6 Hz, 2H: Bn H-3 & H-5), 5.76 (s, 2H: benzylic protons), 3.73 (s, 3H: OMe). ¹³C NMR (126 MHz, D₂O) δ 169.74 (Carbonyl -C=O), 157.65 (Bn C-4), 137.94 (Indole C-8), 135.69 (Indole C-2), 131.55 (Bn C-1), 127.73 (Bn C-2 & C-6), 126.31 (Indole C-9), 123.68 (Indole C-6), 121.84 (Indole C-4), 120.30 (Indole C-5), 113.91 (Bn C-3 & C-5), 111.13 (indole C-7), 106.99 (indole C-3), 55.21 (-OMe), 46.43 (Benzylic -CH₂-). The ¹H and ¹³C NMR data was found in good agreement to that reported by Ching *et al* [433] HRMS-ESI: m/z calc for C₁₇H₁₆NO₃: 282.1125, found: 282.1129 [M + H]⁺ (within 1.4 ppm difference).

Cytotoxicity evaluation of synthesized compounds

This work has been done with the help of collaborator (Dr. Eva Szegdi, Apoptosis Research Centre, NUI Galway). Based on my protein of interest, H929 cell line was selected as it one of the Mcl-1 dependent cell line [93].

Cell culture

There is growing interest of evaluating the cytotoxicity of anticancer molecules as a preliminary screening in anticancer drug discovery projects. Here, I selected the H929 cancer cell line as it is found a Mcl-1 dependent cell lines. H929 (ATCC® CRL-9068™) is B-lymphocyte type cells,

lymphoblast in morphology, retrieve from bone marrow. These cells are different than the conventional adherent cell lines, also called as suspension cell line. This is categorised in biosafety 1 (according to U.S. Public Health Service Guidelines). They cultured in a modified RPMI-1640 Medium which contains 2 mM L-glutamine, 10 mM HEPES, 1 mM sodium pyruvate, 4500 mg/L glucose, and 1500 mg/L sodium bicarbonate, for use in incubators using 5% CO₂ in air. Additional sodium bicarbonate may be required for use in incubators containing higher percentages of CO₂. This reduced level of sodium bicarbonate (NaHCO₃, 1.5 g/L) is intended for use in 5% CO₂ in air. Additional sodium bicarbonate may be required for use in incubators containing higher percentages of CO₂ [434]

Cell counting and cell number determination

For the cytotoxicity studies, cells were grown in petri dish and doubled their population in 48 hours which is further diluted with media to maintain to population to 500,00 cells /mL. The cell counting was preferred over with a dye staining technique (trypan blue dye) using hemocytometer was determine the number of cells in a petridish. Viable cells do not feed trypan blue dye while dead ones do, which allows the differentiation of viable from the dead cells using an optical microscope and, later counting was performed. The hemocytometer is a device used to count cells which consist nine squares with an area of 1 mm² each and all of them constituting a volume chamber with a depth of 0.1 mm, in which cells are mounted for counting after sealing it with a glass cover slip. The viable cells were visually counted in each one of the nine squares. Each square of the grid contains a volume of: $Volume = Area * depth = 1 \text{ mm}^2 * 0.1 \text{ mm} = 0.1 \text{ mm}^3 = 0.0001 \text{ m}$. The more squares counted the better would be the precision in cell number approximation, as cells do not tend to perfectly spread in the chamber.

MTT cell proliferation assay

MTT is a pale yellow tetrazolium dye that gets reduced only by metabolically active cells, turning it into an insoluble, purple formazan dye. MTT reduction is specifically carried out by oxidoreductase enzymes in the mitochondria. As intensity of reduction of yellow tetrazolium dye is dependent on the number of viable cells, therefore it helps to estimate metabolic live cells which is proportional to the optical density (OD) of the purple formazan product produced by the cells. Therefore, if cell viability is affected by the any drug molecule or substance, it will affect dye reduction and hence an alteration would be seen in optical density, which can be measured through multiplate reader.

MTT assay protocol

The testing was performed in 96 well plate where 100 μ L of cells suspension was added (500,000 cells/ mL). Later, seeding was performed where cells were left in this 96 well plate for 24 hours in incubation. Next day, treatment was performed with various concentration of the synthetics in triplicate. After 48 hours, the MTT solution was added and 3 hours later MTT stop solution was added. The reading was then note after 24 hours.

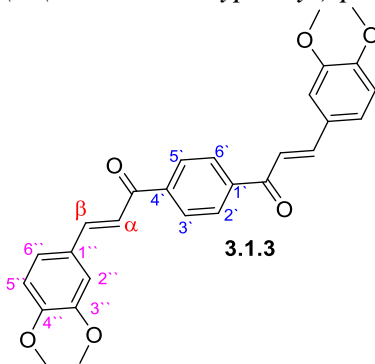
Experimental Section of Objective 3.1

Preparation of bis-chalcones

Impurity and TLC profiles from reactions described herein

This study involved mainly the formation of mono/bis α , β -unsaturated carbonyl compounds (bis-chalcones) where impurities were not reported in detail previously. What I observed that most of times that there is another reaction (Cannizzaro reaction) which is competing with the Claisen Schmidt condensation. In all cases, the TLC analysis of the product mixture shows multiple spots after the reaction is completed. The fastest moving (first) and second spot belong to the respective acetophenone and benzaldehyde reactants, while the third and fourth component were products from the Claisen-Schmidt condensation (either the mono-acetylated α , β -unsaturated carbonyl compound or the bis- α , β -unsaturated carbonyl compound). The slowest moving components were from the Cannizzaro reaction. This TLC analysis is helpful to differentiate the products and therefore, assist in the successful separation of products formed during these reactions.

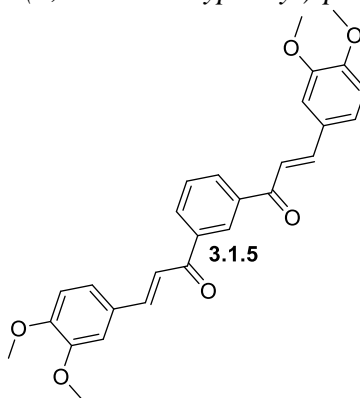
(2E, 2'E)-1,1'-(1,4-Phenylene)-bis(3-(3,4-dimethoxyphenyl)-prop-2-en-1-one) (3.1.3)



1,4-Diacetyl benzene (**3.1.1**) (200 mg, 1.23 mM, 1 equivalent) was stirred 10-15 mins in a 25 mL round bottom flask (RBF) in 1M LiOH (10 ml), along with ~2 ml of MeOH in order to dissolve the ketone. 3,4-Dimethoxy benzaldehyde (**3.1.2**, 410 mg, 2.46 mM, 2.0 equivalent) was then added to the reaction mixture. After 48 hours, TLC analysis indicated the complete consumption of **3.1.2** and the presence of multiple components using EtOAc-cyclohexane (1:3) as eluant. The MeOH

was removed under reduced pressure and the product extracted into dichloromethane (DCM). The organic layer was washed twice with distilled water and then dried over sodium sulphate (Na₂SO₄) and the solvent was removed under reduced pressure. Gradient column chromatography (EtOAc-cyclohexane 14% to 22%) gave the title compound (Yield = 329 mg, 58%; Yellow solid; m. p. = 213-214 °C, R_f = 0.52 (EtOAc-cyclohexane, 1:3)) as well as 3,4-dimethoxy benzoic acid, which is a more polar by-product; ¹H NMR (500 MHz, CDCl₃) δ (ppm): 8.11 (s, 4H: H-2', H-3', H-4', H-5'), 7.79 (d, *J* = 15.6 Hz, 2H: 2 x β-C of propenone), 7.38 (d, *J* = 15.6 Hz, 2H: 2 x α-CH of propenone), 7.26 (d, *J* = 3.4 Hz, 4H: 2 x C-2'' & 2 x C-5''), 7.17 (d, *J* = 1.9 Hz, 2H: 2 x C-6''), 3.96 (d, *J* = 9.3 Hz, 12H: 2 x 3-OCH₃ & 2 x 4-OCH₃); ¹³C NMR (126 MHz, CDCl₃) δ (ppm): 190.22 (C=O), 151.76 (quaternary, C-3''), 149.33 (quaternary, C-4''), 146.01 (C-β), 141.47 (C-1' & C-4'), 128.58 (C-2', C-3', C-5', C-6'), 127.62 (C-1''), 123.45 (C-α), 119.91 (C-6''), 111.17 (C-2''), 110.17 (C''-5), 56.04 (3-OCH₃), 56.01 (4-OCH₃). HRMS-ESI: *m/z* calc for C₂₈H₂₆O₆: 459.1808, found: 459.1791 [M + H]⁺ (3.7 ppm difference)

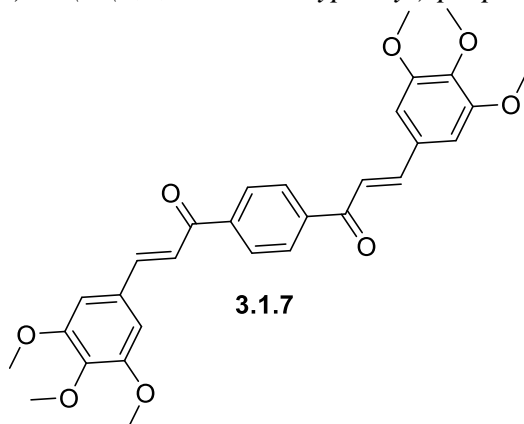
(2*E*,2'*E*)-1,1'-(1,3-phenylene)-bis(3-(3,4-dimethoxyphenyl)-prop-2-en-1-one) (**3.1.5**)



To 1,3-diacetyl benzene (**3.1.4**) (400 mg, 2.47 mM, 1 equiv.) and 1M LiOH solution (15ml), along with ~2 mL MeOH was stirred in 25 mL round bottom flask (RBF) for 10-15 mins at room temperature. Later, 3,4-dimethoxy benzaldehyde (**3.1.2**) (820 mg, 4.95 mM, 2.0 equiv.) was added to the reaction mixture. Like the reaction of **3.1.3**, TLC analysis after the complete consumption of **3.1.2** (36 hours) showed formation of 5 spots (EtOAc-Cyclohexane, 1:3), while **3.1.2** was still present. Therefore, to push the reaction to completion 40 mg (~ 5 % of the original weight of **3.1.2**) was added. After leaving overnight, the TLC profile did not change much so the reaction was worked up as for **3.1.3**. The MeOH was removed under reduced pressure and the product extracted into DCM. The organic layer was washed twice with distilled H₂O and then dried over Na₂SO₄) and the solvent removed under reduced pressure. Gradient column chromatography (EtOAc-

Cyclohexane, 19:81) gave the title compound (yield = 586 mg, 52%; dark-yellow solid; m. p. = 224-226 °C; R_f = 0.54 (EtOAc-Cyclohexane, 1:3); ^1H NMR (500 MHz, CDCl_3) δ (ppm): 8.63 (s, 1H: H-2`), 8.22 (d, J = 7.7 Hz, 2H: H-4` & H-6`), 7.82 (d, J = 15.6 Hz, 2H: 2 x β -H of propenone), 7.66 (t, J = 7.7 Hz, 1H: H-5`), 7.44 (d, J = 15.6 Hz, 2H: 2 x α -H of propenone), 7.27 (d, J = 6.9 Hz, 2H: H-5`), 7.19 (s, 2H: H-2`), 6.92 (d, J = 8.3 Hz, 2H: H-6`), 3.96 (d, J = 11.0 Hz, 12H: 2 x 3-OCH₃ & 2 x 4-OCH₃). ^{13}C NMR (126 MHz, CDCl_3) δ (ppm): 189.95 (C = O), 151.75 (quaternary, C-3`), 149.35 (quaternary, C-4`), 145.93 (C- β), 138.92 (C-1` & C-3`), 132.23 (C-4` & C-6`), 128.98 (C-2`), 128.19 (C-5`), 127.67 (C-1`), 123.57 (C- α), 119.57 (C-6`), 111.16 (C-2`), 110.18 (C-5`), 56.05 (3-OCH₃ & 4-OCH₃). HRMS-ESI: m/z calc for $\text{C}_{28}\text{H}_{27}\text{O}_6$: 459.1801, found: 459.1799 [M + H]⁺; $\text{C}_{56}\text{H}_{52}\text{O}_{12}$: 939.3356, found: 939.3341 [2M + Na]⁺ (1.6 ppm difference).

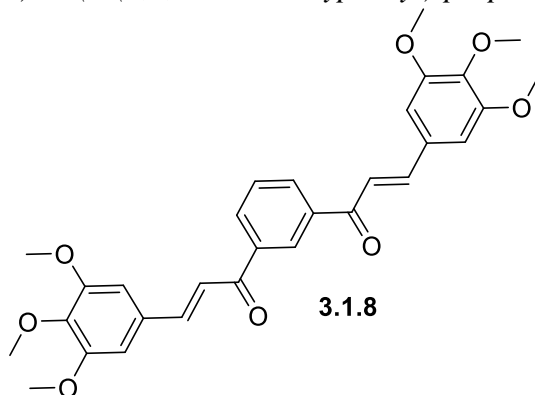
(2*E*,2'*E*)-1,1'-(1,4-Phenylene)-bis(3-(3,4,5-trimethoxyphenyl)-prop-2-en-1-one) (**3.1.7**)



To 1,4 diacetyl benzene (**3.1.1**) (400 mg, 2.47 mM, 1 equiv.) and LiOH (1M, 15 ml), along with ~2 mL MeOH was stirred in 50 mL round bottom flask (RBF) for 15 mins at room temperature. Later, 3,4,5-trimethoxy benzaldehyde (**3.1.6**) (969 mg, 4.94 mM, 2 equiv.) was added to the reaction mixture where the reaction turns yellowish orange initially, which on prolong stirring further turns to a dark orange color. After TLC confirmation of reaction completion, MeOH was removed under reduced pressure and the product extracted into DCM. The organic layer was washed twice with distilled H₂O and then dried over Na₂SO₄ and the solvent removed under reduced pressure. column chromatography (EtOAc-Cyclohexane, 17:83) gave the title compound (yield = 818 mg, 64%; Yellowish-orange solid; m. p. 235-236 °C; R_f = 0.55 (EtOAc-Cyclohexane, 1:3). ^1H NMR (500 MHz, CDCl_3 -*d*) δ 8.12 (s, 4H: H-2`, H-3`, H-4`, H-5`), 7.75 (d, J = 15.7 Hz, 2H: 2 x β -C of propenone), 7.40 (d, J = 15.6 Hz, 2H: 2 x α -CH of propenone), 6.88 (s, 4H: 2 x H-2` & H-6`), 3.94 (s, 12H), 3.92 (s, 6H); ^{13}C NMR (126 MHz, CDCl_3) δ 190.20 (C=O), 153.57

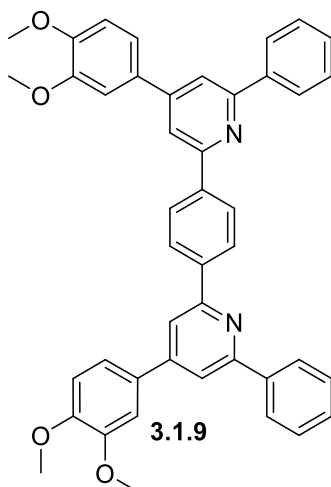
(C-3'' & C-5''), 146.11 (C-β), 141.39 (C-1' & C-4'), 140.84 (C-4''), 130.06 (C-1''), 128.69 (C-2', C-3', C-5' & C-6'), 121.28 (C-α), 105.88 (C-2'' & C-6''), 61.06 (4-OCH₃), 56.29 (3-OCH₃ & 5-OCH₃); (HRMS-ESI: m/z calc for C₃₀H₃₁O₈: 519.2019, found: 519.2021 [M + H]⁺, 0.2 ppm difference)

(2*E*,2'*E*)-1,1'-(1,3-Phenylene)-bis(3-(3,4,5-trimethoxyphenyl)-prop-2-en-1-one) (**3.1.8**)



To 1,3-diacetyl benzene (**3.1.4**) (2 g, 12.33 mM, 1 equiv.) and LiOH (1M, 50 ml) along with ~ 5 ml of MeOH was stirred in 100 mL round bottom flask (RBF) for 35-40 mins. Later, 3,4,5-trimethoxy benzaldehyde (**3.1.6**) (5.080 g, 25.89 mM, 2.1 equiv.) was added to the reaction mixture. After completion of the reaction, the MeOH was removed under reduced pressure and the product extracted into DCM. The organic layer was washed twice with distilled H₂O and brine was added for better separation of interface, then dried over Na₂SO₄ and the organic solvent was removed under reduced pressure. Successive column chromatography (EtOAc-Cyclohexane, 16:84) gave the title compound (Yield = 2.171 gms + 692 mg + 109 mg = 2.972 gms, 47 %; Yellow solid; m. p 241-244 °C); ¹H NMR (500 MHz, CDCl₃) δ (ppm) 8.63 (s, 1H: H-2'), 8.23 (d, *J* = 7.7 Hz, 2H: H-4' & H-6'), 7.78 (d, *J* = 15.6 Hz, 2H: 2 x β-H of propenone), 7.67 (t, *J* = 7.7 Hz, 1H: H-5'), 7.45 (d, *J* = 15.6 Hz, 2H: 2 x α-H of propenone), 6.89 (s, 4H: 2 x H-2'', H-6''), 3.93 (s, 12H: 2 x 3-OCH₃ & 5-OCH₃), 3.91 (s, 6H: 2 x 4-OCH₃); ¹³C NMR (126 MHz, CDCl₃) δ 189.88 (C=O), 153.56 (C-3'' & C-5''), 146.01 (C-β), 140.81 (quaternary, C-4''), 138.78 (C-1' & C-3'), 132.40 (C-4' & C-6'), 130.09 (C-2'), 129.07 (C-5'), 128.27 (C-1''), 120.90 (C-α), 105.94 (C-2'' & C-6''), 61.05 (4-OCH₃), 56.32 (3-OCH₃ & 5-OCH₃); HRMS-ESI: m/z calc for C₃₀H₃₁O₈: 519.2019, found: 519.2011 [M + H]⁺ (1.5 ppm difference); m/z calc for C₃₀H₃₀O₈Na⁺: 541.1838, found: 541.1838 [M + Na]⁺ (0.0 ppm difference)

Preparation of bis triphenyl pyridine 3.1.9



Bis-Triphenyl Pyridine [1,4-bis(4-(3,4-dimethoxyphenyl)-6-phenylpyridin-2-yl)-benzene] (3.1.9)

Initially, fresh α -pyridinium methyl ketone salt, was prepared from treatment of acetophenone (1.00 g ~ 1 mL, 8.57 mM, 1.03 g/cm³) with pyridine (10 mL) and I₂ (1.26g, 8.32 mM), after refluxing over 12 hours, the excess of pyridine was decanted into a solvent waste container and 2 x 2 mL of fresh pyridine for rinsing the any excess of Iodine. Later, most of pyridine was removed under reduced pressure and high vacc was also used for 3 hours to remove any remaining residues of pyridine. The salt was scratched from the RBF surface, which was collected as lumps was pestle with help of mortar and pestle which then turned into a free-flowing powder.

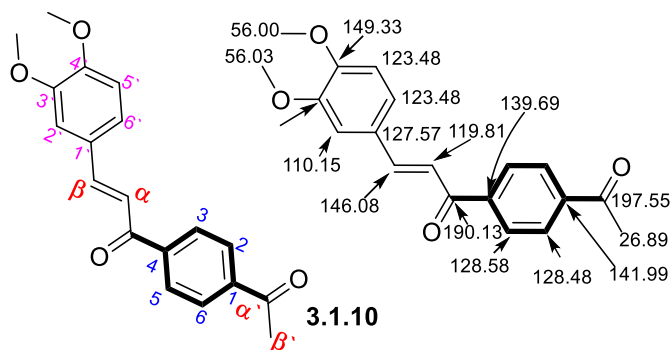
To compound **3.1.3** (100 mg, 0.218 mM) in 10 mL of acetic acid, NH₄OAc (42 mg, 0.545 mM, 2.5 equiv.), α -pyridinium acetophenone salt (free flow powder, 129 mg, 0.654, 3 equiv.) were subsequently added. The reaction was heated at reflux for 12 hours until reactant was completely consumed. The reaction was later worked up with water (2 x 15 mL) in 50 mL separating funnel and ethyl acetate layer (10 mL + 5 mL) was taken, dried over sodium sulphate. Later chromatography (EtOAc-cyclohexane, 1:9), yielded the title compound (Yield = 91 mg, 64%) as a buff coloured solid; m.p 267-269 °C; ¹H NMR (500 MHz, CDCl₃) δ (ppm) 8.37 (s, 4H: 2 x (2-Phenyl H-2, H-3, H-5 & H-6)), 8.23 (d, *J* = 7.8 Hz, 4H: 2 x (6-Phenyl H-2 & H-6)), 7.94 (s, 2H: 2 x 6-Phenyl-H-4), 7.88 (s, 2H), 7.54 (t, *J* = 7.5 Hz, 4H: 2 x (6-Phenyl H-3 & H-5)), 7.47 (t, *J* = 7.2 Hz, 2H: 2 x 6-Phenyl H-4), 7.37 (d, *J* = 8.4 Hz, 2H: 2 x 4-Phenyl H-6), 7.27 (s, 2H: : 2 x 4-Phenyl H-2), 7.04 (d, *J* = 8.3 Hz, 2H: : 2 x 4-Phenyl H-5: overlapping signals), 4.02 (s, 6H: 2 x 4-OMe), 3.98 (s, 6H: 2 x 3-OMe); ¹³C NMR (126 MHz, CDCl₃) δ (ppm) 157.60 (Pyridine C-6), 157.00 (Pyridine C-2), 150.08 (4-Phenyl C-3), 150.04 (Pyridine C-4), 149.54 (4-Phenyl C-4), 140.16(2-

Phenyl C-1), 139.69(6-Phenyl C-1), 131.87(4-Phenyl C-1), 129.09 (6-Phenyl C-4), 128.75(6-Phenyl C-2 & C-6), 127.44 (2-Phenyl C-2 & C-6), 127.19 (6-Phenyl C-3 & C-5), 119.88 (4-Phenyl C-6), 117.03 (Pyridine C-4), 116.92 (Pyridine C-3), 111.64 (4-Phenyl C-5), 110.26 (4-Phenyl C-2), 56.18 (-OCH₃), 56.09 (-OCH₃); HRMS-ESI: m/z calc for C₄₄H₃₆N₂O₄: 657.2753, found: 657.2758 [M + H]⁺ (within 0.8 ppm difference)

General method for preparation of acetylated chalcones

Experience from bis-chalcones synthesis, indicated it was clear that the spot next to the respective acetophenone and benzaldehyde spots observed, was the mono-acetylated chalcones, therefore the focus was put on isolation of that component during chromatographic separation. In order to prepare these mono-acetylated chalcones, the required acetophenone (**3.1.1**: 1,4-diacetylated or **3.1.4**: 1,3 -deacetylated benzene version) (200 mg, 1.23 mM, 1 equiv.) with LiOH (1M) in a mixture of solvents (MeOH-H₂O, 1:9) was stirred for 20-25 mins at room temperature. Later, either 3,4-dimethoxy benzaldehyde (205 mg, 1.23 mM) or 3,4,5 trimethoxy benzaldehyde (243 mg, 1.23 mM) was added to the reaction. After 48 hours, the MeOH was evaporated and left solid residue was dissolved in DCM (~ 20 mL) and washed with water (2 washing of ~ 10 mL). The DCM layer was later, dried over sodium sulphate. The column chromatography was used to separate the compounds (EtOAc-Cyclohexane, 12:88).

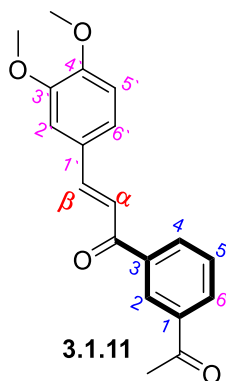
(E)-1-(4-Acetylphenyl)-3-(3,4-dimethoxyphenyl)prop-2-en-1-one (3.1.10)



Yield = 271 mg, 71%; Yellow solid; m. p. = 164-167 °C; R_f = 0.58 (EtOAc-cyclohexane, 1:3); ¹H NMR (500 MHz, CDCl₃) δ (ppm) 8.07 (s, 4H: H-2, H-3, H-5 & H-6), 7.77 (d, *J* = 15.6 Hz, 1H: β-H), 7.36 (d, *J* = 15.6 Hz, 1H: α-H), 7.24 (s, 1H: C-5'), 7.17 (s, 1H: C-2'), 6.92 (d, *J* = 8.3 Hz, 1H:C-6'), 3.95 (d, *J* = 8.2 Hz, 6H: 3-OCH₃ & 4-OCH₃), 2.67 (s, 3H: CH₃ of acetyl); ¹³C NMR (126 MHz, CDCl₃) δ (ppm) 197.55 (C=O of acetyl), 190.13(C=O of propenone), 151.78 (C-3'), 149.33 (C-3'), 146.08 (β-C), 141.99 (C-1), 139.69 (C-4), 128.58 (C-3 & C-5), 128.48 (C-2 & C-6), 127.57 (C-1'), 123.48 (C-α), 119.81 (C-6'), 111.16 (C-2'), 110.15 (C-5'), 56.03 (3-OCH₃),

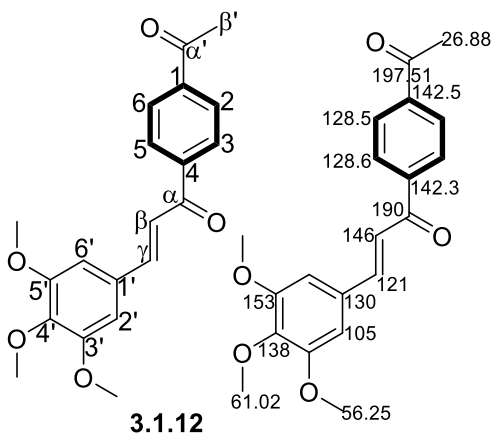
56.00 (4-OCH₃), 26.89 (-CH₃); HRMS-ESI: m/z calc for C₁₉H₁₈O₄: 311.1283, found: 311.1279 [M + H]⁺ (0.4 ppm difference).

(E)-1-(3-acetylphenyl)-3-(3,4-dimethoxyphenyl)-prop-2-en-1-one (**3.1.11**)



Yield = 244 mg, 64%; Yellow solid; m. p. = 171-174 °C; R_f = 0.56 (EtOAc-Cyclohexane, 1:3); ¹H NMR (500 MHz, CDCl₃) δ (ppm) 8.58 (s, 1H: H-2), 8.19 (dd, *J* = 24.1, 7.7 Hz, 2H: H-4 & H-6), 7.81 (d, *J* = 15.6 Hz, 1H: β-H), 7.62 (t, *J* = 7.8 Hz, 1H: : H-5), 7.41 (d, *J* = 15.6 Hz, 1H: α-H), 7.27 (d, *J* = 7.4 Hz, 1H: H-5'), 7.18 (s, 1H: H-2'), 6.92 (d, *J* = 8.3 Hz, 1H: : H-6'), 3.96 (s, 6H: 3-OCH₃ & 4-OCH₃), 2.69 (3H: methyl protons of acetyl); ¹³C NMR (126 MHz, CDCl₃) δ (ppm) 197.54 (-C=O of acetyl), 189.69 (-C=O of unsaturated carbonyl), 151.73 (quaternary, C-3'), 149.32 (quaternary, C-4'), 145.94 (C-β), 138.90 (C-3), 137.39 (C-1), 132.74 (C-6), 132.04 (C-4), 129.00(C-2), 128.06(C-5), 127.61(C-1'), 123.50(C-α), 119.37(C-6'), 111.14(C-2'), 110.22(C-5'), 56.04 (4-OCH₃), 56.02 (3-OCH₃), 26.79 (-CH₃); HRMS-ESI: m/z calc for C₁₉H₁₈O₄: 311.1283, found: 311.1268 [M + H]⁺ (4.8 ppm difference).

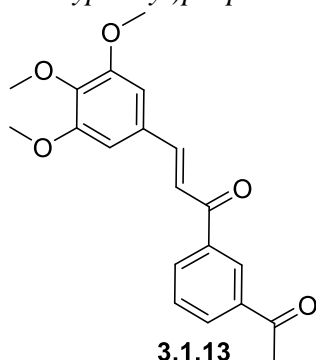
(E)-1-(4-acetylphenyl)-3-(3,4,5-trimethoxyphenyl)-prop-2-en-1-one (**3.1.12**)



Yield = 327 mg, 78%; Yellowish-orange solid; m. p 183-184 °C; R_f = 0.58 (EtOAc-Cyclohexane, 1:3); ¹H NMR (500 MHz, CDCl₃) δ (ppm) 8.16 – 8.01 (m, 4H: H-2, H-3, H-5 & H-6: overlapping

signal), 7.73 (d, $J = 15.6$ Hz, 1H: β -H), 7.37 (d, $J = 15.6$ Hz, 1H: α -H), 6.87 (s, 2H: H-2' & H-6'), 3.93 (s, 6H: 3-OCH₃ & 4-OCH₃), 2.67 (s, 3H: 5-OCH₃); ¹³C NMR (126 MHz, CDCl₃) δ (ppm) 197.51(-C=O of acetyl), 190.08 (-C=O of unsaturated carbonyl), 153.53 (C-3' (-OCH₃) & C-5 (-OCH₃)), 146.06 (C- β), 141.74 (C-1), 140.80 (C-4), 139.80 (C'-4 (-OCH₃)), 130.01 (C-1'), 128.63 (C-3 & C-5), 128.50 (C-2 & C-6), 121.19 (C- α), 105.85 (C-2' & C-6'), 61.02 (4-OCH₃), 56.25 (3-OCH₃ & 5-OCH₃), 26.88 (-CH₃); HRMS-ESI: m/z calc for C₂₀H₂₀O₅: 341.1389, found: 341.1386 [M + H]⁺ (0.9 ppm difference).

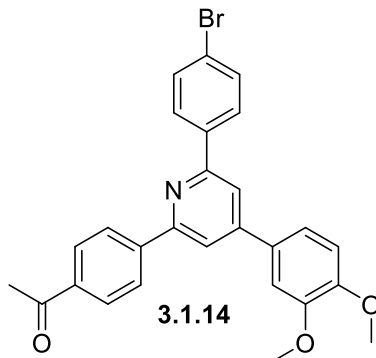
(E)-1-(3-acetylphenyl)-3-(3,4,5-trimethoxyphenyl)prop-2-en-1-one (**3.1.13**)



Yield = 268 mg, 64%; Yellow solid; m. p = 188-189 °C; ¹H NMR (500 MHz, CDCl₃) δ (ppm) 8.58 (s, 1H: H-2), 8.20 (dd, $J = 20.9, 7.8$ Hz, 2H: H-4 & H-6), 7.77 (d, $J = 15.6$ Hz, 1H: α -H), 7.63 (t, $J = 7.7$ Hz, 1H: H-5), 7.43 (d, $J = 15.6$ Hz, 1H: α -H), 6.89 (s, 2H: H-2' & H-6'), 3.94 (s, 6H: 3-OCH₃ & 4-OCH₃), 2.69 (s, 3H: methyl protons of acetyl); ¹³C NMR (126 MHz, CDCl₃) δ (ppm) 197.51 ((-C=O of acetyl), 189.66(-C=O of unsaturated carbonyl), 153.53(quaternary, C-3' & C-5'), 145.95(C- β), 138.72(C-3), 137.43 (C-1), 132.77(C-6), 132.21(C-4), 130.07 (C-2), 129.05(C-5), 128.07 (C-1'), 120.76 (C- α), 105.91 (C-2' & C-6'), 61.02 (4-OCH₃), 56.29 (3-OCH₃ & 5-OCH₃), 26.80 (-CH₃); HRMS-ESI: m/z calc for C₂₀H₂₀O₅: 341.1389, found: 341.1375 [M + H]⁺ (within 1.4 ppm difference).

Preparation of acetylated triphenyl pyridines

1-(4-(6-(4-bromophenyl)-4-(3,4-dimethoxyphenyl)-pyridin-2-yl)-phenyl)-ethan-1-one (3.1.14)

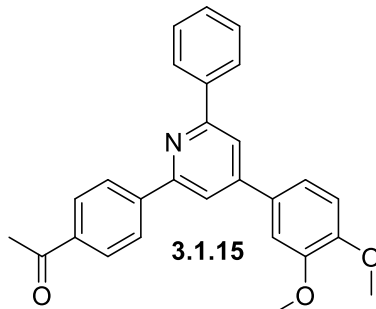


The fresh α -pyridinium 4-bromo acetophenone salt, was prepared by treatment of 4-bromoacetophenone (100 mg, 0.505 mM) with pyridine (5 mL, was used as a solvent) and I_2 (63 mg, 0.505 mM), after refluxing over 4 hours, the remaining pyridine was decanted off and 2 x 1 mL of fresh pyridine was used for rinsing off any excess Iodine. Later, most of the pyridine was removed under reduced pressure followed by high vacuum for 1 hour. Scratching of the residue gave a solid which was used without purification in the next reaction.

To compound **3.1.10** (100 mg, 0.32 mM) in 10 mL of acetic acid NH_4OAc (25 mg, 0.327 mM, 1.5 equiv.), α -pyridinium 4-bromo acetophenone salt (free flow powder, 90 mg, 0.327, 1.5 equiv.) were subsequently added. The reaction was heated at reflux for 6-7 hours until the reactant was completely consumed as judged by TLC analysis. The reaction mixture was later worked up with EtOAc and H_2O (2 X 10 mL) in 50 mL separating funnel. The ethyl acetate layer was dried over sodium sulphate. Later flash column chromatography was done at (EtOAc-Cyclohexane, 8:92), yielded as light brown color solid. Yield = 105 mg, 67%; m.p 227-230 °C; 1H NMR (500 MHz, $CDCl_3$) δ (ppm) 8.28 (d, $J = 8.4$ Hz, 2H: 2-Phenyl H-2 & H-6), 8.11 (d, $J = 8.3$ Hz, 2H: 2-Phenyl H-3 & H-5), 8.08 (d, $J = 8.5$ Hz, 2H: 6-Phenyl H-2 & H-6), 7.90 (d, $J = 1.2$ Hz, 1H: Pyridine H-3), 7.86 (d, $J = 1.2$ Hz, 1H: Pyridine H-5), 7.66 (d, $J = 8.5$ Hz, 2H: 6-Phenyl H-3 & H-5), 7.33 (dd, $J = 8.3, 2.1$ Hz, 1H: 4-Phenyl C-6), 7.22 (d, $J = 2.0$ Hz, 1H: 4-Phenyl C-2), 7.03 (d, $J = 8.3$ Hz, 1H: 4-Phenyl C-5), 4.01 (s, 3H: 4-OMe), 3.97 (s, 3H: 3-OMe), 2.68 (s, 3H: methyl of acetyl); ^{13}C NMR (126 MHz, $CDCl_3$) δ (ppm) 197.84 (C=O of acetyl f), 156.59 (Pyridine C-2), 156.27 (Pyridine C-2), 150.48 (4-Phenyl-C3), 150.25 (pyridine C-4), 149.59 (4-Phenyl-C-4), 143.68 (2-Phenyl C-1), 138.23 (6-Phenyl C-1), 137.30 (2-Phenyl C-4), 131.91 (6-Phenyl C-3 & C-5), 131.29 (4-Phenyl C-1), 128.80 (2-Phenyl C-3 & C-5), 128.69 (6-Phenyl C-2 & C-6), 127.24 (2-Phenyl C-2 & C-6), 123.71 (6-Phenyl C-4), 119.92 (4-Phenyl C-6), 117.60 (Pyridine C-5), 117.30 (Pyridine

C-3), 111.64 (4-Phenyl C-5), 110.17 (4-Phenyl C-2), 56.20 (4-OMe), 56.08 (3-OMe), 26.78 (methyl of acetyl); HRMS-ESI: m/z calc for C₂₇H₂₃NO₃Br: 590.0841, found: 590.0834 [M + H]⁺, 1.4 ppm difference.

1-(4-(4-(3,4-dimethoxyphenyl)-6-phenylpyridin-2-yl)phenyl)ethan-1-one (3.1.15)



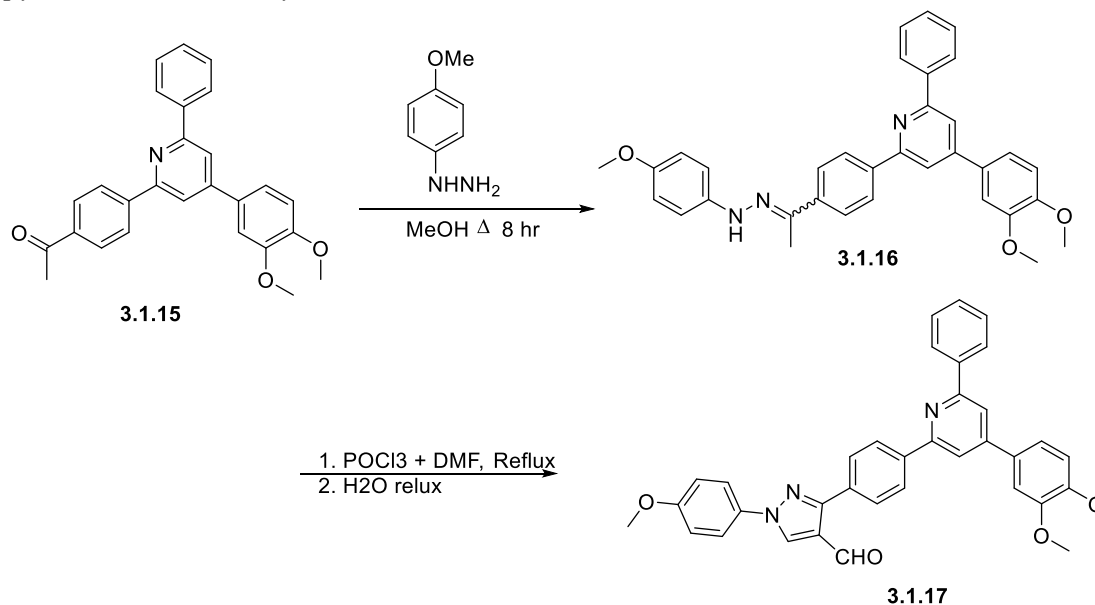
The fresh α -pyridinium 4-bromo acetophenone salt, was prepared by treatment of acetophenone (100 mg, 0.832) with pyridine (5 mL) and I₂ (126 mg, 0.833), after refluxing over 3.5-4 hours, the remaining pyridine was decanted off and 2 x 1 mL of fresh pyridine was used for rinsing off any excess Iodine. . Later, most of the pyridine was removed under reduced pressure followed by high vacuum for 1 hour. Scratching of the residue gave a solid which was used without purification in the next reaction.

To compound **3.1.10** (100 mg, 0.32 mM) in 10 mL of acetic acid, NH₄OAc (42 mg, 0.545 mM, 2.5 equiv.), α -pyridinium acetophenone salt (64 mg, 0.327, 1.5 equiv.) were subsequently added. The reaction was refluxed for 5 hours until reactant gets completely consumed. The reaction was later worked up with EtOAc/water in 25 mL separating funnel, while ethyl acetate layer later dried over sodium sulphate. Column chromatography was 8% (EtOAc: Cyclohexane), yielded as off-white color solid. Yield = 96 mg, 73%; m.p 219-221 °C; ¹H NMR (500 MHz, CDCl₃) δ (ppm) 8.30 (d, *J* = 7.5 Hz, 2H: 2-Phenyl C-2 and C-6), 8.20 (d, *J* = 7.9 Hz, 2H: 6-Phenyl C-2 and C-6), 8.10 (d, *J* = 7.5 Hz, 2H: 2-Phenyl C-3 and C-5), 7.89 (s, 2H: Pyridine C-3 & C-5), 7.54 (t, *J* = 7.5 Hz, 2H: 6-Phenyl C-3 and C-5), 7.47 (t, *J* = 7.3 Hz, 1H: 6-Phenyl C-4), 7.34 (d, *J* = 8.3 Hz, 1H: 4-Phenyl C-6), 7.24 (s, 1H: 4-Phenyl C-2), 7.03 (d, *J* = 8.3 Hz, 1H: 4-Phenyl C-5), 4.01 (s, 3H: 4-OMe), 3.97 (s, 3H: 3-OMe), 2.67 (s, 3H: methyl of acetyl); ¹³C NMR (126 MHz, CDCl₃) δ (ppm) 197.87 (C=O of acetyl), 157.79 (Pyridine C-6), 156.11 (Pyridine C-2), 150.25 (4-Phenyl-C3), 150.15 (pyridine C-4), 149.55 (4-Phenyl-C4), 143.91 (2-Phenyl C-1), 139.38 (6-Phenyl C-1), 137.20 (2-Phenyl C-4), 131.49 (4-Phenyl C-1), 129.22 (6-Phenyl C-4), 128.77 (2-Phenyl C-3 & C-4 : 6-Phenyl C-2 & C-6), 127.25 (6-Phenyl C-3 and C-5), 127.14 (2-Phenyl C-2 & C-6), 119.88 (4-Phenyl C-6), 117.60 (Pyridine C-5), 117.29 (Pyridine C-3), 111.62 (4-Phenyl C-5), 110.19 (4-

Phenyl C-2), 56.17 (4-OMe), 56.07 (3-OMe), 26.77 (methyl of acetyl); HRMS-ESI: m/z calc for $C_{27}H_{23}NO_3$: 410.1756, found: 410.1750 $[M + H]^+$ (within 1.5 ppm difference).

Preparation of Pyrazole-pyridine conjugate

[3-(4-(4-(3,4-dimethoxyphenyl)-6-phenylpyridin-2-yl)phenyl)-1-(4-methoxyphenyl)-1H-pyrazole-4-carbaldehyde] (**3.1.17**)



Scheme 3.4 Synthesis of phenyl hydrazone (**3.1.16**) & Pyrazole-Triphenyl Pyridine conjugate (**3.1.17**)

To compound (64.0 mg, 0.157 mM, 1 equiv.) in 50 mL RBF, (4-Methoxyphenyl)hydrazine hydrochloride (28 mg, 0.159, 1.01 equiv.) was added and refluxed for 8 hours where the reaction turned from yellow to brown red in color. The brown red was compound was characterized by mass and TLC (HRMS-ESI: m/z calc for $C_{34}H_{32}N_3O_3$: 530.2444, found: 530.2452 $[M + H]^+$, 1.5 ppm difference). Further, the MeOH was evaporated under reduced pressure and left on high vacc for 2 hours in order to dry the intermediate for the Vilsmeier Meyer Hack (VMH) reaction, which usually requires anhydrous conditions, as shown in **Scheme 3.4**.

Phosphorous oxychloride (POCl₃) (0.036 mL, 0.398 mM, 2.5 equiv.) was added to 20 mL of dry DMF over an ice-bath and left stirred for 2 hours where the ice was replenished regularly to maintain the temperature close to 0 °C throughout. Note: this reaction can be performed with 5 mL of DMF if the reaction is carried out at less than 100 mg scale, but the ratio of 1:500 between the Vilsmeier reagent: DMF solvent (formed *insitu*, as shown in **Scheme 3.3**) was maintained as a precaution in order to avoid the intermolecular cross reactive intermediate formation.

After 2 hours, this solution was transferred to the RBF containing the phenyl hydrazone derivative (**3.1.16**) by using dry glass syringe. The reaction was left to heat at reflux overnight. After, consumption of phenyl hydrazone derivative (**3.1.16**), the distilled water was added gradually as to avoid any exothermic reaction between unreacted POCl₃/ Vilsmeier reagent. The reaction was again left for refluxing for 30 mins. After 30 mins, DCM (10mL x 2 times) was added and brine solution was added. The DCM layer was dried over sodium sulphate and chromatography was performed (EtOAc-cyclohexane, 1:5).

Yield = 38 mg, 42%; Yellow solid; m. p 247-249 °C; ¹H NMR (500 MHz, CDCl₃) δ (ppm) 10.11 (s, 1H, CHO), 8.48 (s, 1H: Pyrazole H-5), 8.35 (d, *J* = 8.4 Hz, 2H: 2-Phenyl H-2 & H-6), 8.22 (d, *J* = 7.2 Hz, 2H: 6-Phenyl H-2 & H-6), 7.99 (d, *J* = 8.4 Hz, 2H: 2-Phenyl H-3 & H-5), 7.92 (s, 1H), 7.88 (s, 1H), 7.73 (d, *J* = 9.0 Hz, 2H: N-Phenyl H-2 & H-6), 7.54 (t, *J* = 7.5 Hz, 2H: 6-Phenyl H-3 & H-5), 7.47 (t, *J* = 7.3 Hz, 1H: 6-Phenyl H-4), 7.36 (d, *J* = 8.3 Hz, 1H: 4-Phenyl H-6), 7.26 (s, 1H: 4-Phenyl H-2), 7.04 (d, *J* = 9.0 Hz, 3H: 4-Phenyl H-5, N-Phenyl H3 & H5), 4.02 (s, 3H: 4-OMe), 3.98 (s, 3H: 3-OMe), 3.88 (s, 3H: N-Phenyl OCH₃); ¹³C NMR (126 MHz, CDCl₃) δ (ppm) 185.15 (-CHO), 159.39 (N-Phenyl C-4, quaternary carbon), 157.67 (Pyridine C-6, quaternary carbon), 156.74 (Pyridine C-2, quaternary carbon), 154.17 (Pyrazole C-1 quaternary carbon), 150.14 (pyridine C-4 quaternary carbon), 150.07 (4-Phenyl C-3 quaternary carbon), 149.54 (4-Phenyl C-4 quaternary carbon), 140.37 (2-Phenyl C-1), 139.61 (6-Phenyl C-1), 132.63 (N-Phenyl C-1, quaternary), 132.00 (2-Phenyl C-4, quaternary carbon), 131.76 (4-Phenyl C-1, quaternary carbon), 131.05 (N-Phenyl C-3, -CH-), 129.28 (2-Phenyl C-2 & C-6, -CH-), 129.13 (6-Phenyl C-4, -CH-), 128.76 (6-Phenyl C-3 & C-5, -CH-), 127.46 (2-Phenyl C-3 & C-5, -CH-), 127.18 (6-Phenyl C-2 & C-6, -CH-), 122.48 (Pyrazole C-2, quaternary carbon), 121.46 (N-Phenyl C-2 & C-6, -CH-), 119.89(4-Phenyl C-6), 117.18 (Pyridine C-5), 116.94 (Pyridine C-6), 114.79 (N-Phenyl C-3 & C-5, -CH-), 111.63 (4-Phenyl C-5), 110.24 (4-Phenyl C-2), 56.19(4-Phenyl 3-O-CH₃), 56.09 (4-Phenyl 3-O-CH₃), 55.66 (N-Phenyl 4-OCH₃); (HRMS-ESI: m/z calc for C₃₆H₃₀N₃O₄: 568.2236, found: 568.2230 [M + H]⁺, within 1.1 ppm difference)

Cytotoxicity evaluation of synthesized heterocyclic compounds as BH3 mimetics

The Mcl-1 dependent H929 cell line was used. The testing was performed in 96 well plate RPMI medium 1640 supplemented with 10% fetal bovine serum, HEPES (10 mM), sodium bicarbonate (24 mM), sodium pyruvate (1 mM), 2-mercaptoethanol (0.05 mM), penicillin (60 mg/mL) and streptomycin (100 mg/mL). Cell culture was kept in a humidified incubator with 5% CO₂ at 37

°C. Cell seeding: Every well was pipette in with 100 μ l of solution (cell concentration 500,000 / mL). After 48 hours, for first preliminary testing, three concentrations were selected 1 μ M, 10 μ M and 100 μ M for every compound. Those compounds which showed more than 50 % cell death were further tested with their serial concentration (0, 20, 40, 60, 100 μ M). The cell viability vs dose plot calculations were performed in excel.

Experimental section of Objective 4.1

Homology Modelling & refinement

The 3D structures for SSTR-4 and SSTR-5 were unavailable at Protein Data Bank. Therefore, 3D homology models for these isoforms were developed. The protein sequences were retrieved from NCBI (National Center for Biotechnology Information) with sequence accession code NP_001043 and NP_001044 for SSRT4 and SSRT5 respectively. Further, BLAST-P search with Blosum62 substitution matrix, found the available templates for building the SSTR-4 and SSTR-5 homology models. Based on alignment score, sequence identity and query cover with these somatostatin isoform proteins, the closest templates were imported to MOE 2015.1001 and subsequently homology modelling was performed. Later, 500 Homology models were generated by using GB/VI energy function, with a gradient of 0.001 KJ-mol⁻¹Å⁻¹. The final models for both the isoforms were evaluated for their structural quality through various available *in-silico* tools: Ramachandran plot (accessed by the PROCHECK, see Ramachandran graph plot for SSTR-4 and SSTR-5), ERRAT plot, ProSA (Comparative Z-score values between the homology models versus their corresponding templates, for SSTR-4 and for SSTR-5).

Molecular Docking

The chemical structures of somatostatinergics with defined stereochemistry were drawn in MOE2015.1001 builder. Further addition of partial charges and energy minimization was carried out using the lowest gradient (0.001) to get a steepest energy minimized structure of the ligands. Later, MOE site finder tool helped to identify active amino acids patch for docking. The purpose of Site Finder is to calculate possible active cavity in a receptor from the 3D atomic coordinates of the receptor. These calculations helped in determining potential sites involved in ligand binding. In this way, it accommodated the interaction energies between the receptor and different probes in an attempt to locate energetically favorable sites. These coordinates were characterized as alpha sphere which were represented as dummy atoms for further docking. The docking was initiated thereafter using triangular matcher placement algorithm and London *dG* scoring methodology which was set to produce 1,000,000 conformations and later retained only the first 1000 minimum

free energy docking poses for every ligand. The final energy of binding pose was calculated using the Generalized Born solvation model (GB/VI). Further, clustering of the docking pose assisted to filtered out the most favoured conformation with the isoform receptors. The hydrogen bond acceptor-donor measurements were accounted based on the information provided by Jeffrey.

Experimental section of Objective 4.2

Molecular modelling

The PDB for fucosidase of *T. maritima* was available from the RCSB-PDB, while for the fucosidase of *B. taurus*, a homology model was constructed. The sequence for the *B. taurus* fucosidase (Accession: AAI12589.1 GI: 86827599) was obtained from NCBI (National Center for Biotechnology Information). Next a BlastP search along with the BLOSSUM62 substitution matrix, generated putative template PDBs with the minimum identity of 35% and 87% sequence coverage. Later, homology modelling on templates having more than 35 % identity and at least 85% of coverage of the query sequence was conducted. The software programme MOE 2018.01 implementing the Amber 99 forcefield was used [435]. After generated homology models were assessed. Initially, the generated homology model and the template were superimposed giving an RMSD difference, which was less than 1 Å . The Z-score for the templates and homology models, was assessed using ProSA, a protein structure analysis tool, respectively ([436]. Next, the Ramachandran plot was generated. In the Ramachandran plot, the core or the allowed regions are those satisfying the ψ/ϕ angle pairs for residues in a protein [8, 437]. For those amino acids which did not comply with the requirements of the Ramachandran plot, further energy minimization was done. ERRAT plots, which are for the determination of errors in model building were performed [438]. Verify 3D was used to determine the compatibility of the constructed homology model (3D) with its own amino acid sequence (1D) by assigning a structural class based on its location and environment (alpha, beta, loop, polar, nonpolar etc); a score of >80% was considered acceptable [439]. The active site for docking was identified with the active site finder tool of MOE and later, the docked pose of the largest ensembled cluster within a RMSD of 2 Å, was selected [272]. The triangle matcher placement method and GBVI/WSA dG scoring was used for the docking. Molecular dynamics (MD) was performed on the selected docked poses of compounds, **2** and **16** [395]. This analysis was carried out also using MOE 2018. 01 software [435]. Partial charges were calculated, and energy minimizations were done. MD was carried for a duration of 100 ps. The adopted docking procedure was validated using the co-crystallized structure of iso-6FNJ binding

to fucosidase was obtained from the PDB (2ZZD). After docking iso-6FNJ to the fucosidase, an RMSD value of 0.391 Å between the co-crystallized structure and the docked structure indicated that the adopted docking procedure was reliable.

References

- [1] J.P. Hughes, S. Rees, S.B. Kalindjian, K.L. Philpott, Principles of early drug discovery, *British journal of pharmacology*, 162 (6), 2011 1239-1249.
- [2] E.A. Ponomarenko, E.V. Poverennaya, E.V. Ilgisonis, M.A. Pyatnitskiy, A.T. Kopylov, V.G. Zgoda, A.V. Lisitsa, A.I. Archakov, The size of the human proteome: the width and depth, *International journal of analytical chemistry*, 2016 2016.
- [3] J.C. Mobarec, R. Sanchez, M. Filizola, Modern homology modeling of G-protein coupled receptors: which structural template to use?, *Journal of medicinal chemistry*, 52 (16), 2009 5207-5216.
- [4] A. Negi, S. Bhushan, P. Gupta, P. Garg, R. Kumar, Cystathionine β -lyase-like protein with pyridoxal binding domain characterized in leishmania major by comparative sequence analysis and homology modelling, *ISRN Computational Biology*, 2013 2013.
- [5] C. ULC, Molecular Operating Environment (MOE), 1010 Sherbooke St, West, Suite, 910 2017.
- [6] P. Labute, The generalized Born/volume integral implicit solvent model: estimation of the free energy of hydration using London dispersion instead of atomic surface area, *Journal of computational chemistry*, 29 (10), 2008 1693-1698.
- [7] G.J. Kleywegt, T.A. Jones, Phi/psi-chology: Ramachandran revisited, *Structure*, 4 (12), 1996 1395-1400.
- [8] R.A. Laskowski, M.W. MacArthur, D.S. Moss, J.M. Thornton, PROCHECK: a program to check the stereochemical quality of protein structures, *Journal of applied crystallography*, 26 (2), 1993 283-291.
- [9] M.W. MacArthur, R.A. Laskowski, J.M. Thornton, Knowledge-based validation of protein structure coordinates derived by X-ray crystallography and NMR spectroscopy, *Current Opinion in Structural Biology*, 4 (5), 1994 731-737.
- [10] M. Wiederstein, M.J. Sippl, ProSA-web: interactive web service for the recognition of errors in three-dimensional structures of proteins, *Nucleic acids research*, 35 (suppl 2), 2007 W407-W410.
- [11] D. Eisenberg, R. Lüthy, J.U. Bowie, [20] VERIFY3D: Assessment of protein models with three-dimensional profiles, *Methods in enzymology*, 277 1997 396-404.
- [12] P.C. Hawkins, A.G. Skillman, A. Nicholls, Comparison of shape-matching and docking as virtual screening tools, *Journal of medicinal chemistry*, 50 (1), 2007 74-82.
- [13] C.W. Cotman, A.J. Anderson, A potential role for apoptosis in neurodegeneration and Alzheimer's disease, *Molecular neurobiology*, 10 (1), 1995 19-45.
- [14] C.A. Lipinski, F. Lombardo, B.W. Dominy, P.J. Feeney, Experimental and computational approaches to estimate solubility and permeability in drug discovery and development settings, *Advanced drug delivery reviews*, 23 (1-3), 1997 3-25.
- [15] C.A. Lipinski, Lead-and drug-like compounds: the rule-of-five revolution, *Drug Discovery Today: Technologies*, 1 (4), 2004 337-341.
- [16] A. Leo, C. Hansch, D. Elkins, Partition coefficients and their uses, *Chemical reviews*, 71 (6), 1971 525-616.
- [17] X. Liu, B. Testa, A. Fahr, Lipophilicity and its relationship with passive drug permeation, *Pharmaceutical research*, 28 (5), 2011 962-977.
- [18] J.A. Arnott, S.L. Planey, The influence of lipophilicity in drug discovery and design, *Expert opinion on drug discovery*, 7 (10), 2012 863-875.
- [19] M.J. Waring, Defining optimum lipophilicity and molecular weight ranges for drug candidates—molecular weight dependent lower log D limits based on permeability, *Bioorganic & medicinal chemistry letters*, 19 (10), 2009 2844-2851.
- [20] M.P. Gleeson, Generation of a set of simple, interpretable ADMET rules of thumb, *Journal of medicinal chemistry*, 51 (4), 2008 817-834.
- [21] M.P. Gleeson, A. Hersey, D. Montanari, J. Overington, Probing the links between in vitro potency, ADMET and physicochemical parameters, *Nature reviews Drug discovery*, 10 (3), 2011 197.
- [22] P.D. Leeson, B. Springthorpe, The influence of drug-like concepts on decision-making in medicinal chemistry, *Nature Reviews Drug Discovery*, 6 (11), 2007 881.
- [23] J.D. Hughes, J. Blagg, D.A. Price, S. Bailey, G.A. DeCrescenzo, R.V. Devraj, E. Ellsworth, Y.M. Fobian, M.E. Gibbs, R.W. Gilles, Physicochemical drug properties associated with in vivo toxicological outcomes, *Bioorganic & medicinal chemistry letters*, 18 (17), 2008 4872-4875.

- [24] H. Van De Waterbeemd, D.A. Smith, K. Beaumont, D.K. Walker, Property-based design: optimization of drug absorption and pharmacokinetics, *Journal of medicinal chemistry*, 44 (9), 2001 1313-1333.
- [25] B. Testa, P. Crivori, M. Reist, P.-A. Carrupt, The influence of lipophilicity on the pharmacokinetic behavior of drugs: concepts and examples, *Perspectives in Drug Discovery and Design*, 19 (1), 2000 179-211.
- [26] K. Azzaoui, J. Hamon, B. Faller, S. Whitebread, E. Jacoby, A. Bender, J.L. Jenkins, L. Urban, Modeling promiscuity based on in vitro safety pharmacology profiling data, *ChemMedChem: Chemistry Enabling Drug Discovery*, 2 (6), 2007 874-880.
- [27] A. Bender, J. Scheiber, M. Glick, J.W. Davies, K. Azzaoui, J. Hamon, L. Urban, S. Whitebread, J.L. Jenkins, Analysis of pharmacology data and the prediction of adverse drug reactions and off-target effects from chemical structure, *ChemMedChem: Chemistry Enabling Drug Discovery*, 2 (6), 2007 861-873.
- [28] J.U. Peters, P. Schnider, P. Mattei, M. Kansy, Pharmacological promiscuity: dependence on compound properties and target specificity in a set of recent Roche compounds, *ChemMedChem: Chemistry Enabling Drug Discovery*, 4 (4), 2009 680-686.
- [29] N. Greene, M.D. Aleo, S. Louise-May, D.A. Price, Y. Will, Using an in vitro cytotoxicity assay to aid in compound selection for in vivo safety studies, *Bioorganic & medicinal chemistry letters*, 20 (17), 2010 5308-5312.
- [30] D.A. Price, J. Blagg, L. Jones, N. Greene, T. Wager, Physicochemical drug properties associated with in vivo toxicological outcomes: a review, *Expert opinion on drug metabolism & toxicology*, 5 (8), 2009 921-931.
- [31] C.H. Reynolds, S.D. Bembenek, B.A. Tounge, The role of molecular size in ligand efficiency, *Bioorganic & medicinal chemistry letters*, 17 (15), 2007 4258-4261.
- [32] S.D. Bembenek, B.A. Tounge, C.H. Reynolds, Ligand efficiency and fragment-based drug discovery, *Drug discovery today*, 14 (5-6), 2009 278-283.
- [33] M.S. Ayouf, Y. Wahby, H. Abdel-Hamid, M. Teleb, M.M. Abu-Serie, A. Noby, Design, synthesis and biological evaluation of novel α -acyloxy carboxamides via Passerini reaction as caspase 3/7 activators, *European journal of medicinal chemistry*, 168 2019 340-356.
- [34] A. Affini, S. Hagenow, A. Zivkovic, J. Marco-Contelles, H. Stark, Novel indanone derivatives as MAO B/H3R dual-targeting ligands for treatment of Parkinson's disease, *European journal of medicinal chemistry*, 148 2018 487-497.
- [35] M. Vass, É. Schmidt, F. Horti, G.M. Keserű, Virtual fragment screening on GPCRs: a case study on dopamine D3 and histamine H4 receptors, *European journal of medicinal chemistry*, 77 2014 38-46.
- [36] Z. Zhang, C. Liu, X. Li, T. Song, Z. Wu, X. Liang, Y. Zhao, X. Shen, H. Chen, Fragment-based design, synthesis, and biological evaluation of N-substituted-5-(4-isopropylthiophenol)-2-hydroxynicotinamide derivatives as novel Mcl-1 inhibitors, *European journal of medicinal chemistry*, 60 2013 410-420.
- [37] R. van der Vlag, H. Guo, U. Hapko, N. Eleftheriadis, L. Monjas, F.J. Dekker, A.K. Hirsch, A combinatorial approach for the discovery of drug-like inhibitors of 15-lipoxygenase-1, *European journal of medicinal chemistry*, 174 2019 45-55.
- [38] I. Adlere, S. Sun, A. Zarca, L. Roumen, M. Gozelle, C.P. Viciano, B. Caspar, M. Arimont, J. Bebelman, S. Bridson, Structure-based exploration and pharmacological evaluation of N-substituted piperidin-4-yl-methanamine CXCR4 chemokine receptor antagonists, *European journal of medicinal chemistry*, 162 2019 631-649.
- [39] B. Sadek, J.S. Schwed, D. Subramanian, L. Weizel, M. Walter, A. Adem, H. Stark, Non-imidazole histamine H3 receptor ligands incorporating antiepileptic moieties, *European journal of medicinal chemistry*, 77 2014 269-279.
- [40] D. Hanahan, R.A. Weinberg, Hallmarks of cancer: the next generation, *cell*, 144 (5), 2011 646-674.
- [41] D. Brenner, H. Blaser, T.W. Mak, Regulation of tumour necrosis factor signalling: live or let die, *Nature Reviews Immunology*, 15 (6), 2015 362.
- [42] J.L. Yap, L. Chen, M.E. Lanning, S. Fletcher, Expanding the Cancer Arsenal with Targeted Therapies: Disarmament of the Antiapoptotic Bcl-2 Proteins by Small Molecules: Miniperspective, *Journal of medicinal chemistry*, 60 (3), 2016 821-838.
- [43] M. Roy, A. Vom, P. Czabotar, G. Lessene, Cell death and the mitochondria: therapeutic targeting of the BCL-2 family-driven pathway, *British journal of pharmacology*, 171 (8), 2014 1973-1987.
- [44] A. Delbridge, A. Strasser, The BCL-2 protein family, BH3-mimetics and cancer therapy, *Cell death and differentiation*, 22 (7), 2015 1071.
- [45] M.N. Stein, M. Hussain, W.M. Stadler, G. Liu, I.V. Tereshchenko, S. Goodin, C. Jeyamohan, H.L. Kaufman, J. Mehnert, R.S. DiPaola, A Phase II Study of AT-101 to Overcome Bcl-2-Mediated Resistance to Androgen Deprivation Therapy in Patients With Newly Diagnosed Castration-Sensitive Metastatic Prostate Cancer, *Clinical genitourinary cancer*, 14 (1), 2016 22-27.

- [46] A.W. Tolcher, P. LoRusso, J. Arzt, T.A. Busman, G. Lian, N.S. Rudersdorf, C.A. Vanderwal, W. Kirschbrown, K.D. Holen, L.S. Rosen, Safety, efficacy, and pharmacokinetics of navitoclax (ABT-263) in combination with erlotinib in patients with advanced solid tumors, *Cancer chemotherapy and pharmacology*, 76 (5), 2015 1025-1032.
- [47] T.J. Kipps, H. Eradat, S. Grosicki, J. Catalano, W. Cosolo, I.S. Dyagil, S. Yalamanchili, A. Chai, S. Sahasranaman, E. Punnoose, A phase 2 study of the BH3 mimetic BCL2 inhibitor navitoclax (ABT-263) with or without rituximab, in previously untreated B-cell chronic lymphocytic leukemia, *Leukemia & lymphoma*, 56 (10), 2015 2826-2833.
- [48] Q. Ding, X. He, W. Xia, J.-M. Hsu, C.-T. Chen, L.-Y. Li, D.-F. Lee, J.-Y. Yang, X. Xie, J.-C. Liu, Myeloid cell leukemia-1 inversely correlates with glycogen synthase kinase-3 β activity and associates with poor prognosis in human breast cancer, *Cancer research*, 67 (10), 2007 4564-4571.
- [49] L. Song, D. Coppola, S. Livingston, W.D. Cress, E.B. Haura, Mcl-1 regulates survival and sensitivity to diverse apoptotic stimuli in human non-small cell lung cancer cells, *Cancer biology & therapy*, 4 (3), 2005 267-276.
- [50] K. Boisvert-Adamo, W. Longmate, E.V. Abel, A.E. Aplin, Mcl-1 is required for melanoma cell resistance to anoikis, *Molecular Cancer Research*, 7 (4), 2009 549-556.
- [51] J.-Z. Qin, H. Xin, L.A. Sitailo, M.F. Denning, B.J. Nickoloff, Enhanced killing of melanoma cells by simultaneously targeting Mcl-1 and NOXA, *Cancer Research*, 66 (19), 2006 9636-9645.
- [52] M.H. Kang, Z. Wan, Y.H. Kang, R. Sposto, C.P. Reynolds, Mechanism of synergy of N-(4-hydroxyphenyl) retinamide and ABT-737 in acute lymphoblastic leukemia cell lines: Mcl-1 inactivation, *Journal of the National Cancer Institute*, 100 (8), 2008 580-595.
- [53] E. Brotin, M. Meryet-Figuière, K. Simonin, R.E. Duval, M. Villedieu, J. Leroy-Dudal, E. Saison-Behmoaras, P. Gauduchon, C. Denoyelle, L. Poulain, Bcl-XL and MCL-1 constitute pertinent targets in ovarian carcinoma and their concomitant inhibition is sufficient to induce apoptosis, *International journal of cancer*, 126 (4), 2010 885-895.
- [54] W. Sieghart, D. Losert, S. Strommer, D. Cejka, K. Schmid, S. Rasoul-Rockenschaub, M. Bodingbauer, R. Crevenna, B.P. Monia, M. Peck-Radosavljevic, Mcl-1 overexpression in hepatocellular carcinoma: a potential target for antisense therapy, *Journal of hepatology*, 44 (1), 2006 151-157.
- [55] C. Akgul, Mcl-1 is a potential therapeutic target in multiple types of cancer, *Cellular and molecular life sciences*, 66 (8), 2009 1326-1336.
- [56] K. Simonin, E. Brotin, S. Dufort, S. Dutoit, D. Goux, M. N'Diaye, C. Denoyelle, P. Gauduchon, L. Poulain, Mcl-1 is an important determinant of the apoptotic response to the BH3-mimetic molecule HA14-1 in cisplatin-resistant ovarian carcinoma cells, *Molecular cancer therapeutics*, 2009 1535-7163. MCT-1509-0493.
- [57] A.P. Martin, A. Miller, L. Emdad, M. Rahmani, T. Walker, C. Mitchell, M.P. Hagan, M.A. Park, A. Yacoub, P.B. Fisher, Lapatinib resistance in HCT116 cells is mediated by elevated MCL-1 expression, decreased BAK activation, and not by ERBB receptor mutation, *Molecular pharmacology*, 2008.
- [58] R.W. Stam, M.L. Den Boer, P. Schneider, J. de Boer, J. Hagelstein, M.G. Valsecchi, P. de Lorenzo, S.E. Sallan, H.J. Brady, S.A. Armstrong, Association of high-level MCL-1 expression with in vitro and in vivo prednisone resistance in MLL-rearranged infant acute lymphoblastic leukemia, *Blood*, 115 (5), 2010 1018-1025.
- [59] M. Konopleva, R. Contractor, T. Tsao, I. Samudio, P.P. Ruvolo, S. Kitada, X. Deng, D. Zhai, Y.-X. Shi, T. Sneed, Mechanisms of apoptosis sensitivity and resistance to the BH3 mimetic ABT-737 in acute myeloid leukemia, *Cancer cell*, 10 (5), 2006 375-388.
- [60] A.M. Keuling, K.E. Felton, A.A. Parker, M. Akbari, S.E. Andrew, V.A. Tron, RNA silencing of Mcl-1 enhances ABT-737-mediated apoptosis in melanoma: role for a caspase-8-dependent pathway, *PloS one*, 4 (8), 2009 e6651.
- [61] S.-H. Wei, K. Dong, F. Lin, X. Wang, B. Li, J.-j. Shen, Q. Zhang, R. Wang, H.-Z. Zhang, Inducing apoptosis and enhancing chemosensitivity to gemcitabine via RNA interference targeting Mcl-1 gene in pancreatic carcinoma cell, *Cancer chemotherapy and pharmacology*, 62 (6), 2008 1055-1064.
- [62] I.E. Wertz, S. Kusam, C. Lam, T. Okamoto, W. Sandoval, D.J. Anderson, E. Helgason, J.A. Ernst, M. Eby, J. Liu, Sensitivity to antitubulin chemotherapeutics is regulated by MCL1 and FBW7, *Nature*, 471 (7336), 2011 110.
- [63] L.W. Thomas, C. Lam, S.W. Edwards, Mcl-1; the molecular regulation of protein function, *FEBS letters*, 584 (14), 2010 2981-2989.
- [64] M. Germain, V. Duronio, The amino terminus of the anti-apoptotic Bcl-2 homologue Mcl-1 regulates its localization and function, *Journal of Biological Chemistry*, 2007.
- [65] H.-F. Yang-Yen, Mcl-1: a highly regulated cell death and survival controller, *Journal of biomedical science*, 13 (2), 2006 201-204.
- [66] K.M. Kozopas, T. Yang, H.L. Buchan, P. Zhou, R.W. Craig, MCL1, a gene expressed in programmed myeloid cell differentiation, has sequence similarity to BCL2, *Proceedings of the National Academy of Sciences*, 90 (8), 1993 3516-3520.

- [67] M. Rechsteiner, S.W. Rogers, PEST sequences and regulation by proteolysis, *Trends in biochemical sciences*, 21 (7), 1996 267-271.
- [68] B. Mojsa, I. Lassot, S. Desagher, Mcl-1 ubiquitination: unique regulation of an essential survival protein, *Cells*, 3 (2), 2014 418-437.
- [69] D. Zhai, C. Jin, A. Satterthwait, J. Reed, Comparison of chemical inhibitors of antiapoptotic Bcl-2-family proteins, *Cell death and differentiation*, 13 (8), 2006 1419.
- [70] G. Wang, Z. Nikolovska-Coleska, C.-Y. Yang, R. Wang, G. Tang, J. Guo, S. Shangary, S. Qiu, W. Gao, D. Yang, Structure-based design of potent small-molecule inhibitors of anti-apoptotic Bcl-2 proteins, *Journal of medicinal chemistry*, 49 (21), 2006 6139-6142.
- [71] R.M. Mohammad, D. Young, B. Chen, A. Aboukameel, J. Chen, Z. Nikolovska-Coleska, A. Al-Katib, S. Wang, ApoG2, a potent, non-toxic small-molecule inhibitor of Bcl-2 family: A preclinical trial in lymphoma, *AACR*, 2006.
- [72] J. Wei, S. Kitada, M.F. Rega, J.L. Stebbins, D. Zhai, J. Cellitti, H. Yuan, A. Emdadi, R. Dahl, Z. Zhang, Apogossypol derivatives as pan-active inhibitors of antiapoptotic B-cell lymphoma/leukemia-2 (Bcl-2) family proteins, *Journal of medicinal chemistry*, 52 (14), 2009 4511-4523.
- [73] J. Wei, J.L. Stebbins, S. Kitada, R. Dash, W. Placzek, M.F. Rega, B. Wu, J. Cellitti, D. Zhai, L. Yang, BI-97C1, an optically pure Apogossypol derivative as pan-active inhibitor of antiapoptotic B-cell lymphoma/leukemia-2 (Bcl-2) family proteins, *Journal of medicinal chemistry*, 53 (10), 2010 4166-4176.
- [74] J. Wei, S. Kitada, J.L. Stebbins, W. Placzek, D. Zhai, B. Wu, M.F. Rega, Z. Zhang, J. Cellitti, L. Yang, Synthesis and biological evaluation of Apogossypolone derivatives as pan-active inhibitors of antiapoptotic B-cell lymphoma/leukemia-2 (Bcl-2) family proteins, *Journal of medicinal chemistry*, 53 (22), 2010 8000-8011.
- [75] J. Wei, J.L. Stebbins, S. Kitada, R. Dash, D. Zhai, W.J. Placzek, B. Wu, M.F. Rega, Z. Zhang, E. Barile, An optically pure apogossypolone derivative as potent pan-active inhibitor of anti-apoptotic bcl-2 family proteins, *Frontiers in oncology*, 1 2011 28.
- [76] M. Leone, D. Zhai, S. Sareth, S. Kitada, J.C. Reed, M. Pellecchia, Cancer prevention by tea polyphenols is linked to their direct inhibition of antiapoptotic Bcl-2-family proteins, *Cancer Research*, 63 (23), 2003 8118-8121.
- [77] N.A. Cohen, M.L. Stewart, E. Gavathiotis, J.L. Tepper, S.R. Bruekner, B. Koss, J.T. Opferman, L.D. Walensky, A competitive stapled peptide screen identifies a selective small molecule that overcomes MCL-1-dependent leukemia cell survival, *Chemistry & biology*, 19 (9), 2012 1175-1186.
- [78] P.J. Real, Y. Cao, R. Wang, Z. Nikolovska-Coleska, J. Sanz-Ortiz, S. Wang, J.L. Fernandez-Luna, Breast cancer cells can evade apoptosis-mediated selective killing by a novel small molecule inhibitor of Bcl-2, *Cancer research*, 64 (21), 2004 7947-7953.
- [79] Y.-H. Zhang, A. Bhunia, K.F. Wan, M.C. Lee, S.-L. Chan, V.C.-K. Yu, Y.-K. Mok, Chelerythrine and sanguinarine dock at distinct sites on BclXL that are not the classic BH3 binding cleft, *Journal of molecular biology*, 364 (3), 2006 536-549.
- [80] P.H. Bernardo, T. Sivaraman, K.-F. Wan, J. Xu, J. Krishnamoorthy, C.M. Song, L. Tian, J.S. Chin, D.S. Lim, H.Y. Mok, Synthesis of a rhodanine-based compound library targeting Bcl-XL and Mcl-1, *Pure and Applied Chemistry*, 83 (3), 2011 723-731.
- [81] Y. Wan, S. Wu, G. Xiao, T. Liu, X. Hou, C. Chen, P. Guan, X. Yang, H. Fang, Design, synthesis and preliminary bioactivity studies of 2-thioxo-4-thiazolidinone derivatives as Bcl-2 inhibitors, *Bioorganic & medicinal chemistry*, 23 (9), 2015 1994-2003.
- [82] E. Whiting, M.R. Raje, J. Chauhan, P.T. Wilder, D. Van Eker, S.J. Hughes, N.G. Bowen, G.E. Vickers, I.C. Fenimore, S. Fletcher, Discovery of Mcl-1 inhibitors based on a thiazolidine-2, 4-dione scaffold, *Bioorganic & medicinal chemistry letters*, 28 (3), 2018 523-528.
- [83] Y. Feng, X. Ding, T. Chen, L. Chen, F. Liu, X. Jia, X. Luo, X. Shen, K. Chen, H. Jiang, Design, synthesis, and interaction study of quinazoline-2 (1 H)-thione derivatives as novel potential Bcl-xL inhibitors, *Journal of medicinal chemistry*, 53 (9), 2010 3465-3479.
- [84] S. Kolb, O. Mondésert, M.L. Goddard, D. Jullien, B.O. Villoutreix, B. Ducommun, C. Garbay, E. Braud, Development of novel thiazolopyrimidines as CDC25B phosphatase inhibitors, *ChemMedChem: Chemistry Enabling Drug Discovery*, 4 (4), 2009 633-648.
- [85] B. Zhou, X. Li, Y. Li, Y. Xu, Z. Zhang, M. Zhou, X. Zhang, Z. Liu, J. Zhou, C. Cao, Discovery and Development of Thiazolo [3, 2-a] pyrimidinone Derivatives as General Inhibitors of Bcl-2 Family Proteins, *ChemMedChem*, 6 (5), 2011 904-921.
- [86] Y. Xu, M. Zhou, Y. Li, C. Li, Z. Zhang, B. Yu, R. Wang, Characterization of the Stereochemical Structures of 2H-Thiazolo [3, 2-a] pyrimidine Compounds and Their Binding Affinities for Anti-apoptotic Bcl-2 Family Proteins, *ChemMedChem*, 8 (8), 2013 1345-1352.

- [87] A. Friberg, D. Vigil, B. Zhao, R.N. Daniels, J.P. Burke, P.M. Garcia-Barrantes, D. Camper, B.A. Chauder, T. Lee, E.T. Olejniczak, Discovery of potent myeloid cell leukemia 1 (Mcl-1) inhibitors using fragment-based methods and structure-based design, *Journal of medicinal chemistry*, 56 (1), 2012 15-30.
- [88] J.P. Burke, Z. Bian, S. Shaw, B. Zhao, C.M. Goodwin, J. Belmar, C.F. Browning, D. Vigil, A. Friberg, D.V. Camper, Discovery of tricyclic indoles that potently inhibit Mcl-1 using fragment-based methods and structure-based design, *Journal of medicinal chemistry*, 58 (9), 2015 3794-3805.
- [89] N.F. Pelz, Z. Bian, B. Zhao, S. Shaw, J.C. Tarr, J. Belmar, C. Gregg, D.V. Camper, C.M. Goodwin, A.L. Arnold, Discovery of 2-indole-acylsulfonamide myeloid cell leukemia 1 (Mcl-1) inhibitors using fragment-based methods, *Journal of medicinal chemistry*, 59 (5), 2016 2054-2066.
- [90] S. Shaw, Z. Bian, B. Zhao, J.C. Tarr, N. Veerasamy, K.O. Jeon, J. Belmar, A.L. Arnold, S.A. Fogarty, E. Perry, Optimization of Potent and Selective Tricyclic Indole Diazepinone Myeloid Cell Leukemia-1 Inhibitors Using Structure-Based Design, *Journal of medicinal chemistry*, 61 (6), 2018 2410-2421.
- [91] B. Zhao, J. Sensintaffar, Z. Bian, J. Belmar, T. Lee, E.T. Olejniczak, S.W. Fesik, Structure of a Myeloid cell leukemia-1 (Mcl-1) inhibitor bound to drug site 3 of Human Serum Albumin, *Bioorganic & medicinal chemistry*, 25 (12), 2017 3087-3092.
- [92] M. Bruncko, L. Wang, G.S. Sheppard, D.C. Phillips, S.K. Tahir, J. Xue, S. Erickson, S. Fidanze, E. Fry, L. Hasvold, Structure-guided design of a series of MCL-1 inhibitors with high affinity and selectivity, *Journal of medicinal chemistry*, 58 (5), 2015 2180-2194.
- [93] J. Levenson, H. Zhang, J. Chen, S. Tahir, D. Phillips, J. Xue, P. Nimmer, S. Jin, M. Smith, Y. Xiao, Potent and selective small-molecule MCL-1 inhibitors demonstrate on-target cancer cell killing activity as single agents and in combination with ABT-263 (navitoclax), *Cell death & disease*, 6 (1), 2015 e1590.
- [94] S. Luan, Q. Ge, Y. Chen, M. Dai, J. Yang, K. Li, D. Liu, L. Zhao, Discovery and structure-activity relationship studies of N-substituted indole derivatives as novel Mcl-1 inhibitors, *Bioorganic & medicinal chemistry letters*, 27 (9), 2017 1943-1948.
- [95] T. Liu, Y. Wan, R. Liu, L. Ma, M. Li, H. Fang, Design, synthesis and preliminary biological evaluation of indole-3-carboxylic acid-based skeleton of Bcl-2/Mcl-1 dual inhibitors, *Bioorganic & medicinal chemistry*, 25 (6), 2017 1939-1948.
- [96] G. Xu, T. Liu, Y. Zhou, X. Yang, H. Fang, 1-Phenyl-1H-indole derivatives as a new class of Bcl-2/Mcl-1 dual inhibitors: Design, synthesis, and preliminary biological evaluation, *Bioorganic & medicinal chemistry*, 25 (20), 2017 5548-5556.
- [97] Z. Wang, W. Xu, T. Song, Z. Guo, L. Liu, Y. Fan, A. Wang, Z. Zhang, Fragment-Based Design, Synthesis, and Biological Evaluation of 1-Substituted-indole-2-carboxylic Acids as Selective Mcl-1 Inhibitors, *Archiv der Pharmazie*, 350 (1), 2017 e1600251.
- [98] G. Akçay, M.A. Belmonte, B. Aquila, C. Chuaqui, A.W. Hird, M.L. Lamb, P.B. Rawlins, N. Su, S. Tentarelli, N.P. Grimster, Inhibition of Mcl-1 through covalent modification of a noncatalytic lysine side chain, *Nature chemical biology*, 12 (11), 2016 931.
- [99] Z. Zhang, T. Song, T. Zhang, J. Gao, G. Wu, L. An, G. Du, A novel BH3 mimetic S1 potently induces Bax/Bak-dependent apoptosis by targeting both Bcl-2 and Mcl-1, *International journal of cancer*, 128 (7), 2011 1724-1735.
- [100] Z. Zhang, G. Wu, F. Xie, T. Song, X. Chang, 3-Thiomorpholin-8-oxo-8 H-acenaphtho [1, 2-b] pyrrole-9-carbonitrile (S1) based molecules as potent, dual inhibitors of B-cell lymphoma 2 (Bcl-2) and myeloid cell leukemia sequence 1 (Mcl-1): structure-based design and structure- activity relationship studies, *Journal of medicinal chemistry*, 54 (4), 2011 1101-1105.
- [101] Z. Zhang, H. Yang, G. Wu, Z. Li, T. Song, X. qian Li, Probing the difference between BH3 groove of Mcl-1 and Bcl-2 protein: Implications for dual inhibitors design, *European journal of medicinal chemistry*, 46 (9), 2011 3909-3916.
- [102] Z. Zhang, T. Song, X. Li, Z. Wu, Y. Feng, F. Xie, C. Liu, J. Qin, H. Chen, Novel soluble myeloid cell leukemia sequence 1 (Mcl-1) inhibitor (E, E)-2-(benzylaminocarbonyl)-3-styrylacrylonitrile (4g) developed using a fragment-based approach, *European journal of medicinal chemistry*, 59 2013 141-149.
- [103] T. Song, X. Li, X. Chang, X. Liang, Y. Zhao, G. Wu, S. Xie, P. Su, Z. Wu, Y. Feng, 3-Thiomorpholin-8-oxo-8H-acenaphtho [1, 2-b] pyrrole-9-carbonitrile (S1) derivatives as pan-Bcl-2-inhibitors of Bcl-2, Bcl-x L and Mcl-1, *Bioorganic & medicinal chemistry*, 21 (1), 2013 11-20.
- [104] T. Song, Z. Wang, F. Ji, Y. Feng, Y. Fan, G. Chai, X. Li, Z. Li, Z. Zhang, Deactivation of Mcl-1 by Dual-Function Small-Molecule Inhibitors Targeting the Bcl-2 Homology 3 Domain and Facilitating Mcl-1 Ubiquitination, *Angewandte Chemie International Edition*, 55 (46), 2016 14250-14256.

- [105] N.M. Haste, C.C. Hughes, D.N. Tran, W. Fenical, P.R. Jensen, V. Nizet, M.E. Hensler, Pharmacological properties of the marine natural product marinopyrrole A against methicillin-resistant *Staphylococcus aureus*, *Antimicrobial agents and chemotherapy*, 2011 AAC. 01211-01210.
- [106] K. Doi, R. Li, S.-S. Sung, H. Wu, Y. Liu, W. Manieri, G. Krishnegowda, A. Awwad, A. Dewey, X. Liu, Discovery of marinopyrrole A (maritoclax) as a selective Mcl-1 antagonist that overcomes ABT-737 resistance by binding to and targeting Mcl-1 for proteasomal degradation, *Journal of Biological Chemistry*, 287 (13), 2012 10224-10235.
- [107] Z. Fang, Y.n. Song, P. Zhan, Q. Zhang, X. Liu, Conformational restriction: an effective tactic in 'follow-on'-based drug discovery, *Future medicinal chemistry*, 6 (8), 2014 885-901.
- [108] C. Cheng, Y. Liu, M.E. Balasis, N.L. Simmons, J. Li, H. Song, L. Pan, Y. Qin, K. Nicolaou, S.M. Sebti, Cyclic marinopyrrole derivatives as disruptors of Mcl-1 and Bcl-xL binding to Bim, *Marine drugs*, 12 (3), 2014 1335-1348.
- [109] Y. Wan, J. Wang, F.e. Sun, M. Chen, X. Hou, H. Fang, Design, synthesis and preliminary biological studies of pyrrolidine derivatives as Mcl-1 inhibitors, *Bioorganic & medicinal chemistry*, 23 (24), 2015 7685-7693.
- [110] Y. Wan, T. Liu, X. Li, C. Chen, H. Fang, Improved binding affinities of pyrrolidine derivatives as Mcl-1 inhibitors by modifying amino acid side chains, *Bioorganic & medicinal chemistry*, 25 (1), 2017 138-152.
- [111] M. Prakesch, A.Y. Denisov, M. Naim, K. Gehring, P. Arya, The discovery of small molecule chemical probes of BCL-XL and MCL-1, *Bioorganic & medicinal chemistry*, 16 (15), 2008 7443-7449.
- [112] S. Broch, B. Aboab, F. Anizon, P. Moreau, Synthesis and in vitro antiproliferative activities of quinoline derivatives, *European journal of medicinal chemistry*, 45 (4), 2010 1657-1662.
- [113] S. Broch, H. Hénon, A.-L. Debaud, M.-L. Fogeron, N. Bonnefoy-Bérard, F. Anizon, P. Moreau, Synthesis and biological activities of new di- and trimeric quinoline derivatives, *Bioorganic & medicinal chemistry*, 18 (19), 2010 7132-7143.
- [114] E. Saugues, A.-L. Debaud, F. Anizon, N. Bonnefoy, P. Moreau, Synthesis and biological activities of polyquinoline derivatives: new Bcl-2 family protein modulators, *European journal of medicinal chemistry*, 57 2012 112-125.
- [115] D.J. Richard, R. Lena, T. Bannister, N. Blake, W.E. Pierceall, N.E. Carlson, C.E. Keller, M. Koenig, Y. He, D. Minond, Hydroxyquinoline-derived compounds and analoguing of selective Mcl-1 inhibitors using a functional biomarker, *Bioorganic & medicinal chemistry*, 21 (21), 2013 6642-6649.
- [116] N.A. Meanwell, Fluorine and fluorinated motifs in the design and application of bioisosteres for drug design, *Journal of medicinal chemistry*, 61 (14), 2018 5822-5880.
- [117] B. Jeffries, Z. Wang, J. Graton, S.D. Holland, T. Brind, R.D. Greenwood, J.-Y. Le Questel, J.S. Scott, E. Chiarparin, B. Linclau, Reducing the Lipophilicity of Perfluoroalkyl Groups by CF₂-F/CF₂-Me or CF₃/CH₃ Exchange, *Journal of medicinal chemistry*, 61 (23), 2018 10602-10618.
- [118] L. Chen, P. Wilder, B. Drennen, J. Tran, B. Roth, K. Chesko, P. Shapiro, S. Fletcher, Structure-based design of 3-carboxy-substituted 1, 2, 3, 4-tetrahydroquinolines as inhibitors of myeloid cell leukemia-1 (Mcl-1), *Organic & biomolecular chemistry*, 14 (24), 2016 5505-5510.
- [119] E. Lee, P. Czabotar, B. Smith, K. Deshayes, K. Zobel, P. Colman, W. Fairlie, Crystal structure of ABT-737 complexed with Bcl-xL: implications for selectivity of antagonists of the Bcl-2 family, *Cell death and differentiation*, 14 (9), 2007 1711.
- [120] J.M. Rodriguez, L. Nevola, N.T. Ross, G.i. Lee, A.D. Hamilton, Synthetic Inhibitors of Extended Helix-Protein Interactions Based on a Biphenyl 4, 4'-Dicarboxamide Scaffold, *ChemBioChem*, 10 (5), 2009 829-833.
- [121] Z. Zhang, X. Li, T. Song, Y. Zhao, Y. Feng, An anthraquinone scaffold for putative, two-face Bim BH3 α -helix mimic, *Journal of medicinal chemistry*, 55 (23), 2012 10735-10741.
- [122] Z. Zhang, X. Liang, X. Li, T. Song, Q. Chen, H. Sheng, Design and application of a rigid quinazolone scaffold based on two-face Bim α -helix mimicking, *European journal of medicinal chemistry*, 69 2013 711-718.
- [123] F. Abulwerdi, C. Liao, M. Liu, A.S. Azmi, A. Aboukameel, A.S. Mady, T. Gulappa, T. Cierpicki, S. Owens, T. Zhang, A novel small-molecule inhibitor of mcl-1 blocks pancreatic cancer growth in vitro and in vivo, *Molecular cancer therapeutics*, 13 (3), 2014 565-575.
- [124] M.E. Lanning, W. Yu, J.L. Yap, J. Chauhan, L. Chen, E. Whiting, L.S. Pidugu, T. Atkinson, H. Bailey, W. Li, Structure-based design of N-substituted 1-hydroxy-4-sulfamoyl-2-naphthoates as selective inhibitors of the Mcl-1 oncoprotein, *European journal of medicinal chemistry*, 113 2016 273-292.
- [125] E. Fire, S.V. Gullá, R.A. Grant, A.E. Keating, Mcl-1-Bim complexes accommodate surprising point mutations via minor structural changes, *Protein Science*, 19 (3), 2010 507-519.
- [126] A.M. Petros, S.L. Swann, D. Song, K. Swinger, C. Park, H. Zhang, M.D. Wendt, A.R. Kunzer, A.J. Souers, C. Sun, Fragment-based discovery of potent inhibitors of the anti-apoptotic MCL-1 protein, *Bioorganic & medicinal chemistry letters*, 24 (6), 2014 1484-1488.

- [127] X. Cao, J.L. Yap, M.K. Newell-Rogers, C. Peddaboina, W. Jiang, H.T. Papaconstantinou, D. Jupiter, A. Rai, K.-Y. Jung, R.P. Tubin, The novel BH3 α -helix mimetic JY-1-106 induces apoptosis in a subset of cancer cells (lung cancer, colon cancer and mesothelioma) by disrupting Bcl-xL and Mcl-1 protein-protein interactions with Bak, *Molecular cancer*, 12 (1), 2013 1.
- [128] B. Drennen, J.A. Scheenstra, J.L. Yap, L. Chen, M.E. Lanning, B.M. Roth, P.T. Wilder, S. Fletcher, Structural Re-engineering of the α -Helix Mimetic JY-1-106 into Small Molecules: Disruption of the Mcl-1-Bak-BH3 Protein-Protein Interaction with 2, 6-Di-Substituted Nicotinates, *ChemMedChem*, 11 (8), 2016 827-833.
- [129] X. Ding, Y. Li, L. Lv, M. Zhou, L. Han, Z. Zhang, Q. Ba, J. Li, H. Wang, H. Liu, De Novo Design, Synthesis and Evaluation of Benzylpiperazine Derivatives as Highly Selective Binders of Mcl-1, *ChemMedChem*, 8 (12), 2013 1986-2014.
- [130] Y. Tanaka, K. Aikawa, G. Nishida, M. Homma, S. Sogabe, S. Igaki, Y. Hayano, T. Sameshima, I. Miyahisa, T. Kawamoto, Discovery of potent Mcl-1/Bcl-xL dual inhibitors by using a hybridization strategy based on structural analysis of target proteins, *Journal of medicinal chemistry*, 56 (23), 2013 9635-9645.
- [131] X. Li, X. Liang, T. Song, P. Su, Z. Zhang, Design, synthesis and structure-activity relationship studies of morpholino-1H-phenalene derivatives that antagonize Mcl-1/Bcl-2, *Bioorganic & medicinal chemistry*, 22 (21), 2014 5738-5746.
- [132] G. Wang, Y. Wang, L. Wang, L. Han, X. Hou, H. Fu, H. Fang, Design, synthesis and preliminary bioactivity studies of imidazolidine-2, 4-dione derivatives as Bcl-2 inhibitors, *Bioorganic & medicinal chemistry*, 23 (23), 2015 7359-7365.
- [133] O. Kutzki, H.S. Park, J.T. Ernst, B.P. Orner, H. Yin, A.D. Hamilton, Development of a potent Bcl-xL antagonist based on α -helix mimicry, *Journal of the American Chemical Society*, 124 (40), 2002 11838-11839.
- [134] A. Kazi, J. Sun, K. Doi, S.-S. Sung, Y. Takahashi, H. Yin, J.M. Rodriguez, J. Becerril, N. Berndt, A.D. Hamilton, The BH3 α -helical mimic BH3-M6 disrupts Bcl-XL, Bcl-2, and MCL-1 protein-protein interactions with Bax, Bak, Bad, or Bim and induces apoptosis in a Bax-and Bim-dependent manner, *Journal of Biological Chemistry*, 286 (11), 2011 9382-9392.
- [135] C.I. Gloaguen, A.S. Voisin-Chiret, J. Sopkova-de Oliveira Santos, J. Fogha, F. Gautier, M. De Giorgi, G.g. Burzicki, S. Perato, C.c. Pétigny-Lechartier, K. Simonin-Le Jeune, First evidence that oligopyridines, α -helix foldamers, inhibit Mcl-1 and sensitize ovarian carcinoma cells to Bcl-xL-targeting strategies, *Journal of medicinal chemistry*, 58 (4), 2015 1644-1668.
- [136] S. Hedir, M. De Giorgi, J. Fogha, M. De Pascale, L.-B. Weiswald, E. Brotin, B. Marekha, C. Denoyelle, C. Denis, P. Suzanne, Structure-guided design of pyridoclox derivatives based on Noxa/Mcl-1 interaction mode, *European journal of medicinal chemistry*, 159 2018 357-380.
- [137] P.W. Glunz, Recent encounters with atropisomerism in drug discovery, *Bioorganic & medicinal chemistry letters*, 28 (2), 2018 53-60.
- [138] L. Mendez, G. Henriquez, S. Sirimulla, M. Narayan, Looking back, looking forward at halogen bonding in drug discovery, *Molecules*, 22 (9), 2017 1397.
- [139] A.E. Tron, M.A. Belmonte, A. Adam, B.M. Aquila, L.H. Boise, E. Chiarparin, J. Cidado, K.J. Embrey, E. Gangl, F.D. Gibbons, Discovery of Mcl-1-specific inhibitor AZD5991 and preclinical activity in multiple myeloma and acute myeloid leukemia, *Nature communications*, 9 2018.
- [140] C. Fang, B. D'Souza, C.F. Thompson, M.C. Clifton, J.W. Fairman, B. Fulroth, A. Leed, P. McCarren, L. Wang, Y. Wang, Single diastereomer of a macrolactam core binds specifically to myeloid cell leukemia 1 (MCL1), *ACS medicinal chemistry letters*, 5 (12), 2014 1308-1312.
- [141] S. Lee, T.E. Wales, S. Escudero, D.T. Cohen, J. Luccarelli, C.G. Gallagher, N.A. Cohen, A.J. Huhn, G.H. Bird, J.R. Engen, Allosteric inhibition of antiapoptotic MCL-1, *Nature structural & molecular biology*, 23 (6), 2016 600.
- [142] C. Yang, S. Chen, M. Zhou, Y. Li, Y. Li, Z. Zhang, Z. Liu, Q. Ba, J. Li, H. Wang, Development of 3-Phenyl-N-(2-(3-phenylureido) ethyl)-thiophene-2-sulfonamide Compounds as Inhibitors of Antiapoptotic Bcl-2 Family Proteins, *ChemMedChem*, 9 (7), 2014 1436-1452.
- [143] I.L. Conlon, D. Van Eker, S. Abdelmalak, W.A. Murphy, H. Bashir, M. Sun, J. Chauhan, K.M. Varney, R. Godoy-Ruiz, P.T. Wilder, Kröhnke pyridines: Rapid and facile access to Mcl-1 inhibitors, *Bioorganic & medicinal chemistry letters*, 28 (10), 2018 1949-1953.
- [144] R. Liu, L. Liu, T. Liu, X. Yang, Y. Wan, H. Fang, Discovery and development of substituted tyrosine derivatives as Bcl-2/Mcl-1 inhibitors, *Bioorganic & medicinal chemistry*, 26 (17), 2018 4907-4915.
- [145] A.S. Mady, C. Liao, N. Bajwa, K.J. Kump, F.A. Abulwerdi, K.L. Lev, L. Miao, S.M. Grigsby, A. Perdih, J.A. Stuckey, Discovery of Mcl-1 inhibitors from integrated high throughput and virtual screening, *Scientific reports*, 8 (1), 2018 10210.

- [146] C.-H. Zheng, H. Yang, M. Zhang, S.-H. Lu, D. Shi, J. Wang, X.-H. Chen, X.-H. Ren, J. Liu, J.-G. Lv, Design, synthesis, and activity evaluation of broad-spectrum small-molecule inhibitors of anti-apoptotic Bcl-2 family proteins: characteristics of broad-spectrum protein binding and its effects on anti-tumor activity, *Bioorganic & medicinal chemistry letters*, 22 (1), 2012 39-44.
- [147] M. Wang, W. Tian, C. Wang, S. Lu, C. Yang, J. Wang, Y. Song, Y. Zhou, J. Zhu, Z. Li, Design, synthesis, and activity evaluation of selective inhibitors of anti-apoptotic Bcl-2 proteins: The effects on the selectivity of the P1 pockets in the active sites, *Bioorganic & medicinal chemistry letters*, 26 (21), 2016 5207-5211.
- [148] S. Desrat, A. Pujals, C. Colas, J. Dardenne, C. Gény, L. Favre, V. Dumontet, B.I. Iorga, M. Litaudon, M. Raphaël, Pro-apoptotic meiogynin A derivatives that target Bcl-xL and Mcl-1, *Bioorganic & medicinal chemistry letters*, 24 (21), 2014 5086-5088.
- [149] S. Desrat, C. Remeur, F. Roussi, Development of an efficient route toward meiogynin A-inspired dual inhibitors of Bcl-xL and Mcl-1 anti-apoptotic proteins, *Organic & biomolecular chemistry*, 13 (19), 2015 5520-5531.
- [150] S. Desrat, C. Remeur, C. Geny, G. Riviere, C. Colas, V. Dumontet, N. Birlirakis, B. Iorga, F. Roussi, From meiogynin A to the synthesis of dual inhibitors of Bcl-xL and Mcl-1 anti-apoptotic proteins, *Chemical Communications*, 50 (62), 2014 8593-8596.
- [151] A.A. Samra, A. Robert, C. Gov, L. Favre, L. Eloy, E. Jacquet, J. Bignon, J. Wiels, S. Desrat, F. Roussi, Dual inhibitors of the pro-survival proteins Bcl-2 and Mcl-1 derived from natural compound meiogynin A, *European journal of medicinal chemistry*, 148 2018 26-38.
- [152] M.F. van Delft, A.H. Wei, K.D. Mason, C.J. Vandenberg, L. Chen, P.E. Czabotar, S.N. Willis, C.L. Scott, C.L. Day, S. Cory, The BH3 mimetic ABT-737 targets selective Bcl-2 proteins and efficiently induces apoptosis via Bak/Bax if Mcl-1 is neutralized, *Cancer cell*, 10 (5), 2006 389-399.
- [153] J. Michels, F. Obrist, I. Vitale, D. Lissa, P. Garcia, P. Behnam-Motlagh, K. Kohno, G.S. Wu, C. Brenner, M. Castedo, MCL-1 dependency of cisplatin-resistant cancer cells, *Biochemical pharmacology*, 92 (1), 2014 55-61.
- [154] G. Choudhary, S. Al-Harbi, S. Mazumder, B. Hill, M. Smith, J. Bodo, E. Hsi, A. Almasan, MCL-1 and BCL-xL-dependent resistance to the BCL-2 inhibitor ABT-199 can be overcome by preventing PI3K/AKT/mTOR activation in lymphoid malignancies, *Cell death & disease*, 6 (1), 2015 e1593.
- [155] M.M. Williams, R.S. Cook, Bcl-2 family proteins in breast development and cancer: could Mcl-1 targeting overcome therapeutic resistance?, *Oncotarget*, 6 (6), 2015 3519.
- [156] H.V. Kemami Wangun, A. Wood, C. Fiorilla, J.K. Reed, P.J. McCarthy, A.E. Wright, Gymnochromes E and F, cytotoxic phenanthroperylenequinones from a deep-water crinoid, *Holopus rangii*, *Journal of natural products*, 73 (4), 2010 712-715.
- [157] L. Calcul, R. Chow, A.G. Oliver, K. Tenney, K.N. White, A.W. Wood, C. Fiorilla, P. Crews, NMR strategy for unraveling structures of bioactive sponge-derived oxy-polyhalogenated diphenyl ethers, *Journal of natural products*, 72 (3), 2009 443-449.
- [158] C. Gény, G. Rivière, J.r. Bignon, N. Birlirakis, E. Guittet, K. Awang, M. Litaudon, F. Roussi, V. Dumontet, Anacardic acids from *Knema hookeriana* as modulators of Bcl-xL/Bak and Mcl-1/Bid interactions, *Journal of natural products*, 79 (4), 2016 838-844.
- [159] C.c. Apel, C. Gény, V. Dumontet, N. Birlirakis, F. Roussi, V.C. Pham, H. Doan Thi Mai, V.H. Nguyen, V.M. Chau, M. Litaudon, Endiandric acid analogues from *Beilschmiedia ferruginea* as dual inhibitors of Bcl-xL/Bak and Mcl-1/Bid interactions, *Journal of natural products*, 77 (6), 2014 1430-1437.
- [160] H. Oh, P.R. Jensen, B.T. Murphy, C. Fiorilla, J.F. Sullivan, T. Ramsey, W. Fenical, Cryptosphaerolide, a cytotoxic Mcl-1 inhibitor from a marine-derived ascomycete related to the genus *Cryptosphaeria*, *Journal of natural products*, 73 (5), 2010 998-1001.
- [161] M.C. Clifton, D.M. Dranow, A. Leed, B. Fulroth, J.W. Fairman, J. Abendroth, K.A. Atkins, E. Wallace, D. Fan, G. Xu, A maltose-binding protein fusion construct yields a robust crystallography platform for MCL1, 2015.
- [162] S. Guettler, J. LaRose, E. Petsalaki, G. Gish, A. Scotter, T. Pawson, R. Rottapel, F. Sicheri, Structural basis and sequence rules for substrate recognition by Tankyrase explain the basis for cherubism disease, *Cell*, 147 (6), 2011 1340-1354.
- [163] P.E. Czabotar, E.F. Lee, G.V. Thompson, A.Z. Wardak, W.D. Fairlie, P.M. Colman, Mutation to Bax beyond the BH3 domain disrupts interactions with pro-survival proteins and promotes apoptosis, *Journal of Biological Chemistry*, 286 (9), 2011 7123-7131.
- [164] M.L. Stewart, E. Fire, A.E. Keating, L.D. Walensky, The MCL-1 BH3 helix is an exclusive MCL-1 inhibitor and apoptosis sensitizer, *Nature chemical biology*, 6 (8), 2010 595-601.
- [165] S. Dutta, S. Gullá, T.S. Chen, E. Fire, R.A. Grant, A.E. Keating, Determinants of BH3 binding specificity for Mcl-1 versus Bcl-xL, *Journal of molecular biology*, 398 (5), 2010 747-762.

- [166] E. Fire, S.V. Gulla, R.A. Grant, A.E. Keating, Mcl-1–Bim complexes accommodate surprising point mutations via minor structural changes, *Protein Science*, 19 (3), 2010 507-519.
- [167] E.F. Lee, P.E. Czabotar, H. Yang, B.E. Sleebbs, G. Lessene, P.M. Colman, B.J. Smith, W.D. Fairlie, Conformational changes in Bcl-2 pro-survival proteins determine their capacity to bind ligands, *Journal of Biological Chemistry*, 284 (44), 2009 30508-30517.
- [168] G.J. Kleywegt, M.R. Harris, J.y. Zou, T.C. Taylor, A. Wählby, T.A. Jones, The Uppsala electron-density server, *Acta Crystallographica Section D: Biological Crystallography*, 60 (12), 2004 2240-2249.
- [169] M. Rueda, G. Bottegoni, R. Abagyan, Consistent improvement of cross-docking results using binding site ensembles generated with elastic network normal modes, *Journal of chemical information and modeling*, 49 (3), 2009 716-725.
- [170] C.R. Corbeil, C.I. Williams, P. Labute, Variability in docking success rates due to dataset preparation, *Journal of computer-aided molecular design*, 26 (6), 2012 775-786.
- [171] MOlecular Opertaing Environment.
- [172] S. Forli, R. Huey, M.E. Pique, M.F. Sanner, D.S. Goodsell, A.J. Olson, Computational protein–ligand docking and virtual drug screening with the AutoDock suite, *Nature protocols*, 11 (5), 2016 905.
- [173] M. VLife, 3.5 (2008) Molecular design suite. VLife Sciences Technologies Pvt. Ltd., Pune, India, 2012.
- [174] T. Lee, Z. Bian, B. Zhao, L.J. Hogdal, J.L. Sensintaffar, C.M. Goodwin, J. Belmar, S. Shaw, J.C. Tarr, N. Veerasamy, Discovery and biological characterization of potent myeloid cell leukemia-1 inhibitors, *FEBS letters*, 591 (1), 2017 240-251.
- [175] F. Svensson, U. Norinder, A. Bender, Improving screening efficiency through iterative screening using docking and conformal prediction, *Journal of chemical information and modeling*, 57 (3), 2017 439-444.
- [176] L. Ferreira, R. dos Santos, G. Oliva, A. Andricopulo, Molecular docking and structure-based drug design strategies, *Molecules*, 20 (7), 2015 13384-13421.
- [177] R.A. Copeland, Conformational adaptation in drug-target interactions and residence time, *Future medicinal chemistry*, 3 (12), 2011 1491-1501.
- [178] H.M. Ashtawy, N.R. Mahapatra, Task-specific scoring functions for predicting ligand binding poses and affinity and for screening enrichment, *Journal of chemical information and modeling*, 58 (1), 2017 119-133.
- [179] M. Schneider, J.-L. Pons, W. Bourguet, G. Labesse, Towards accurate high-throughput ligand affinity prediction by exploiting structural ensembles, docking metrics and ligand similarity, *bioRxiv*, 2019 574517.
- [180] Y. Fukunishi, Y. Yamashita, T. Mashimo, H. Nakamura, Prediction of Protein– compound Binding Energies from Known Activity Data: Docking-score-based Method and its Applications, *Molecular informatics*, 37 (6-7), 2018 1700120.
- [181] P. Greenidge, C. Kramer, J.-C. Mozziconacci, W. Sherman, Improving docking results via reranking of ensembles of ligand poses in multiple X-ray protein conformations with MM-GBSA, *Journal of chemical information and modeling*, 54 (10), 2014 2697-2717.
- [182] S. Makeneni, D.F. Thieker, R.J. Woods, Applying pose clustering and MD simulations to eliminate false positives in molecular docking, *Journal of chemical information and modeling*, 58 (3), 2018 605-614.
- [183] K. Doi, R. Li, S.-S. Sung, H. Wu, Y. Liu, W. Manieri, G. Krishnegowda, A. Awwad, A. Dewey, X. Liu, Discovery of marinopyrrole A (maritoclax) as a selective Mcl-1 antagonist that overcomes ABT-737 resistance by binding to and targeting Mcl-1 for proteasomal degradation, *Journal of Biological Chemistry*, 2012 jbc. M111. 334532.
- [184] C. Colas, F. Roussi, B. Iorga, Focused ligand libraries as tools for in silico design of anti-apoptotic proteins inhibitors, *Chemistry for Life Sciences*, 2011 41-46.
- [185] T. Zhang, L.D. Walensky, A. Saghatelian, A non-apoptotic role for BAX and BAK in eicosanoid metabolism, *ACS chemical biology*, 2015.
- [186] H. Zhang, Q. Wei, G. Zhu, J. Qu, B. Wang, A facile and expeditious approach to substituted 1H-pyrazoles catalyzed by iodine, *Tetrahedron Letters*, 57 (24), 2016 2633-2637.
- [187] D.C. Pinto, A.M. Silva, J.A. Cavaleiro, J. Elguero, New bis (chalcones) and their transformation into bis (pyrazoline) and bis (pyrazole) derivatives, *European Journal of Organic Chemistry*, 2003 (4), 2003 747-755.
- [188] S. Fustero, M. Sánchez-Roselló, P. Barrio, A. Simón-Fuentes, From 2000 to mid-2010: a fruitful decade for the synthesis of pyrazoles, *Chemical Reviews*, 111 (11), 2011 6984-7034.
- [189] E. Palaska, M. Aytemir, I.T. Uzbay, D. Erol, Synthesis and antidepressant activities of some 3, 5-diphenyl-2-pyrazolines, *European journal of medicinal chemistry*, 36 (6), 2001 539-543.
- [190] K. Alex, A. Tillack, N. Schwarz, M. Beller, Zinc-catalyzed synthesis of pyrazolines and pyrazoles via hydrohydrazination, *Organic letters*, 10 (12), 2008 2377-2379.

- [191] O. Mahé, D. Frath, I. Dez, F. Marsais, V. Levacher, J.-F. Brière, TBD-organocatalysed synthesis of pyrazolines, *Organic & biomolecular chemistry*, 7 (18), 2009 3648-3651.
- [192] M.A. Sanchez-Carmona, D.A. Contreras-Cruz, L.D. Miranda, Base-free two-step synthesis of 1, 3-diketones and β -ketoesters from α -diazocarbonyl compounds, trialkylboranes, and aromatic aldehydes, *Organic & biomolecular chemistry*, 9 (19), 2011 6506-6508.
- [193] K. Kumari, D.S. Raghuvanshi, V. Jouikov, K.N. Singh, Sc (OTf) 3-catalyzed, solvent-free domino synthesis of functionalized pyrazoles under controlled microwave irradiation, *Tetrahedron Letters*, 53 (9), 2012 1130-1133.
- [194] M.J. Hayter, D.J. Bray, J.K. Clegg, L.F. Lindoy, New bis-Pyrazole Derivatives Synthesized From Aryl- and Xylyl-Linked bis (β -Diketone) Precursors, *Synthetic communications*, 36 (6), 2006 707-714.
- [195] B. Willy, T.J. Mueller, Regioselective Three-Component Synthesis of Highly Fluorescent 1, 3, 5-Trisubstituted Pyrazoles, *European Journal of Organic Chemistry*, 2008 (24), 2008 4157-4168.
- [196] X. Zhang, J. Kang, P. Niu, J. Wu, W. Yu, J. Chang, I₂-Mediated Oxidative C–N Bond Formation for Metal-Free One-Pot Synthesis of Di-, Tri-, and Tetrasubstituted Pyrazoles from α , β -Unsaturated Aldehydes/Ketones and Hydrazines, *The Journal of organic chemistry*, 79 (21), 2014 10170-10178.
- [197] N. Shao, T. Chen, T. Zhang, H. Zhu, Q. Zheng, H. Zou, Cascade regioselective synthesis of pyrazoles from nitroallylic acetates and N-tosyl hydrazine, *Tetrahedron*, 70 (4), 2014 795-799.
- [198] S.I. Sviridov, A.A. Vasil'ev, S.V. Shorshnev, Straightforward transformation of isoxazoles into pyrazoles: renewed and improved, *Tetrahedron*, 63 (49), 2007 12195-12201.
- [199] D.C. Pinto, A.M. Silva, L.M. Almeida, J.A. Cavaleiro, J. Elguero, 3-Aroyl-5-hydroxyflavones: Synthesis and Transformation into Aroylpyrazoles, *European Journal of Organic Chemistry*, 2002 (22), 2002 3807-3815.
- [200] B. Aegurla, R.K. Peddinti, Metal-Free Sulfonylation of α , β -Conjugated Systems by Using Sulfonyl Hydrazides, *Asian Journal of Organic Chemistry*, 7 (5), 2018 946-954.
- [201] H.H. Sayed, E.M. Morsy, E.M. Fiefel, Synthesis and reactions of some novel nicotinonitrile, thiazolotriazole, and imidazolotriazole derivatives for antioxidant evaluation, *Synthetic Communications®*, 40 (9), 2010 1360-1370.
- [202] T. Murata, M. Shimada, S. Sakakibara, T. Yoshino, T. Masuda, T. Shintani, H. Sato, Y. Koriyama, K. Fukushima, N. Nunami, Synthesis and structure–activity relationships of novel IKK- β inhibitors. Part 3: Orally active anti-inflammatory agents, *Bioorganic & Medicinal Chemistry Letters*, 14 (15), 2004 4019-4022.
- [203] N.S. El-Sayed, A.N. Shirazi, M.G. El-Meligy, A.K. El-Ziaty, D. Rowley, J. Sun, Z.A. Nagib, K. Parang, Synthesis of 4-aryl-6-indolylpyridine-3-carbonitriles and evaluation of their antiproliferative activity, *Tetrahedron letters*, 55 (6), 2014 1154-1158.
- [204] F. Tamaddon, D. Azadi, Nicotinium methane sulfonate (NMS): A bio-renewable protic ionic liquid and bi-functional catalyst for synthesis of 2-amino-3-cyano pyridines, *Journal of Molecular Liquids*, 249 2018 789-794.
- [205] R. Karki, C. Song, T.M. Kadayat, T.B.T. Magar, G. Bist, A. Shrestha, Y. Na, Y. Kwon, E.-S. Lee, Topoisomerase I and II inhibitory activity, cytotoxicity, and structure–activity relationship study of dihydroxylated 2, 6-diphenyl-4-aryl pyridines, *Bioorganic & medicinal chemistry*, 23 (13), 2015 3638-3654.
- [206] P. Thapa, T.M. Kadayat, S. Park, S. Shin, T.B.T. Magar, G. Bist, A. Shrestha, Y. Na, Y. Kwon, E.-S. Lee, Synthesis and biological evaluation of 2-phenol-4-chlorophenyl-6-aryl pyridines as topoisomerase II inhibitors and cytotoxic agents, *Bioorganic chemistry*, 66 2016 145-159.
- [207] T.B.T. Magar, S.H. Seo, T.M. Kadayat, H. Jo, A. Shrestha, G. Bist, P. Katila, Y. Kwon, E.-S. Lee, Synthesis and SAR study of new hydroxy and chloro-substituted 2, 4-diphenyl 5H-chromeno [4, 3-b] pyridines as selective topoisomerase II α -targeting anticancer agents, *Bioorganic & medicinal chemistry*, 26 (8), 2018 1909-1919.
- [208] S. Park, T.M. Kadayat, K.-Y. Jun, T.B.T. Magar, G. Bist, A. Shrestha, E.-S. Lee, Y. Kwon, Novel 2-aryl-4-(4'-hydroxyphenyl)-5H-indeno [1, 2-b] pyridines as potent DNA non-intercalative topoisomerase catalytic inhibitors, *European journal of medicinal chemistry*, 125 2017 14-28.
- [209] B. Corry, N.M. Smith, The role of thermodynamics and kinetics in ligand binding to G-quadruplex DNA, *Chemical communications*, 48 (71), 2012 8958-8960.
- [210] N. Smith, G. Labrunie, B. Corry, P.L.T. Tran, M. Norret, M. Djavaheri-Mergny, C.L. Raston, J.-L. Mergny, Unraveling the relationship between structure and stabilization of triarylpyridines as G-quadruplex binding ligands, *Organic & biomolecular chemistry*, 9 (17), 2011 6154-6162.
- [211] Z.A. Waller, P.S. Shirude, R. Rodriguez, S. Balasubramanian, Triarylpyridines: a versatile small molecule scaffold for G-quadruplex recognition, *Chemical Communications*, (12), 2008 1467-1469.
- [212] N. Montazeri, S. Mahjoob, Highly efficient and easy synthesis of 2, 4, 6-triarylpyridines catalyzed by pentafluorophenylammonium triflate (PFPA⁺Tf⁻) as a new recyclable solid acid catalyst in solvent-free conditions, *Chinese Chemical Letters*, 23 (4), 2012 419-422.
- [213] J. Safari, Z. Zarnegar, M.B. Borujeni, Mesoporous nanocrystalline MgAl₂O₄: A new heterogeneous catalyst for the synthesis of 2, 4, 6-triarylpyridines under solvent-free conditions, *Chemical Papers*, 67 (7), 2013 688-695.

- [214] H. Alinezhad, M. Tajbakhsh, N. Ghobadi, Nano-Fe₃O₄-supported, hydrogensulfate ionic liquid-catalyzed, one-pot synthesis of polysubstituted pyridines, *Synthetic Communications*, 45 (17), 2015 1964-1976.
- [215] Y. Zhao, J. Li, C. Li, K. Yin, D. Ye, X. Jia, PTSA-catalyzed green synthesis of 1, 3, 5-triarylbenzene under solvent-free conditions, *Green Chemistry*, 12 (8), 2010 1370-1372.
- [216] Y. Chen, T. Zhang, D. Wang, J. Zhou, Y. Zhang, Y. Li, Cerium (IV) carboxymethylcellulose (CMC-Ce IV) as an efficient and reusable catalyst for the one-pot pseudo-four component synthesis of 2, 4, 6-triphenylpyridines, *Journal of Chemical Sciences*, 129 (4), 2017 421-430.
- [217] A. Maleki, R. Firouzi-Haji, L-Proline functionalized magnetic nanoparticles: A novel magnetically reusable nanocatalyst for one-pot synthesis of 2, 4, 6-triarylpyridines, *Scientific reports*, 8 (1), 2018 17303.
- [218] D.S. Rekunge, I.A. Kale, G.U. Chaturbhuj, An efficient, green solvent-free protocol for the synthesis of 2, 4, 6-triarylpyridines using reusable heterogeneous activated Fuller's earth catalyst, *Journal of the Iranian Chemical Society*, 2018 1-8.
- [219] M. Safaiee, B. Ebrahimghasri, M.A. Zolfigol, S. Baghery, A. Khoshnood, D.A. Alonso, Synthesis and application of chitosan supported vanadium oxo in the synthesis of 1, 4-dihydropyridines and 2, 4, 6-triarylpyridines via anomeric based oxidation, *New Journal of Chemistry*, 2018.
- [220] Y.-M. Ren, Z. Zhang, S. Jin, Convenient and efficient method for synthesis of 2, 4, 6-triarylpyridines using catalytic amount of PEG1000-based dicationic acidic ionic liquid under solvent-free conditions, *Synthetic Communications*, 46 (6), 2016 528-535.
- [221] M. Wang, Z. Yang, Z. Song, Q. Wang, Three-Component One-Pot Synthesis of 2, 4, 6-Triarylpyridines without Catalyst and Solvent, *Journal of Heterocyclic Chemistry*, 52 (3), 2015 907-910.
- [222] J. Safari, S. Gandomi-Ravandi, M.B. Borujeni, Green and solvent-free procedure for microwave-assisted synthesis of 2, 4, 6-triarylpyridines catalysed using MgAl₂O₄ nanocrystals, *Journal of chemical sciences*, 125 (5), 2013 1063-1070.
- [223] W. Zecher, F. Kröhnke, Eine neue synthese substituierter pyridine, I. Grundzüge der synthese, *Chemische Berichte*, 94 (3), 1961 690-697.
- [224] F. Kröhnke, W. Zecher, J. Curtze, D. Drechsler, K. Pfléghar, K. Schnalke, W. Weis, Syntheses using the Michael addition of phridinium salts, *Angewandte Chemie International Edition in English*, 1 (12), 1962 626-632.
- [225] X. Qing, T. Wang, F. Zhang, C. Wang, One-pot synthesis of 2, 4, 6-triarylpyridines from β -nitrostyrenes, substituted salicylic aldehydes and ammonium acetate, *RSC Advances*, 6 (98), 2016 95957-95964.
- [226] P.V. Shinde, V.B. Labade, J.B. Gujar, B.B. Shingate, M.S. Shingare, Bismuth triflate catalyzed solvent-free synthesis of 2, 4, 6-triaryl pyridines and an unexpected selective acetalization of tetrazolo [1, 5-a]-quinoline-4-carbaldehydes, *Tetrahedron Letters*, 53 (12), 2012 1523-1527.
- [227] M. Safaiee, B. Ebrahimghasri, M.A. Zolfigol, S. Baghery, A. Khoshnood, D.A. Alonso, Synthesis and application of chitosan supported vanadium oxo in the synthesis of 1, 4-dihydropyridines and 2, 4, 6-triarylpyridines via anomeric based oxidation, *New Journal of Chemistry*, 42 (15), 2018 12539-12548.
- [228] M. Kiafar, M.A. Zolfigol, M. Yarie, A.A. Taherpour, The first computational study for the oxidative aromatization of pyrazolines and 1, 4-dihydropyridines using 1, 2, 4-triazolinediones: an anomeric-based oxidation, *RSC Advances*, 6 (104), 2016 102280-102291.
- [229] M.A. Zolfigol, M. Yarie, Fe₃O₄@ TiO₂@ O₂PO₂ (CH₂) NHSO₃H as a novel nanomagnetic catalyst: Application to the preparation of 2-amino-4, 6-diphenylnicotinonitriles via anomeric-based oxidation, *Applied Organometallic Chemistry*, 31 (5), 2017 e3598.
- [230] M. Adib, H. Tahermansouri, S.A. Koloogani, B. Mohammadi, H.R. Bijanzadeh, Kröhnke pyridines: an efficient solvent-free synthesis of 2, 4, 6-triarylpyridines, *Tetrahedron Letters*, 47 (33), 2006 5957-5960.
- [231] K. Gopalaiah, D.C. Rao, K. Mahiya, A. Tiwari, Iron-Catalyzed Aerobic Oxidative Cleavage and Construction of C-N Bonds: A Facile Method for Synthesis of 2, 4, 6-Trisubstituted Pyridines, *Asian Journal of Organic Chemistry*, 7 (9), 2018 1872-1881.
- [232] H. Xu, J.-C. Zeng, F.-J. Wang, Z. Zhang, Metal-Free Synthesis of 2, 4, 6-Trisubstituted Pyridines via Iodine-Initiated Reaction of Methyl Aryl Ketones with Amines under Neat Heating, *Synthesis*, 49 (08), 2017 1879-1883.
- [233] X. Zhang, Z. Wang, K. Xu, Y. Feng, W. Zhao, X. Xu, Y. Yan, W. Yi, HOTf-catalyzed sustainable one-pot synthesis of benzene and pyridine derivatives under solvent-free conditions, *Green Chemistry*, 18 (8), 2016 2313-2316.
- [234] H. Huang, X. Ji, W. Wu, L. Huang, H. Jiang, Copper-Catalyzed Formal C-N Bond Cleavage of Aromatic Methylamines: Assembly of Pyridine Derivatives, *The Journal of organic chemistry*, 78 (8), 2013 3774-3782.
- [235] C. Zhang, C. Tang, N. Jiao, Recent advances in copper-catalyzed dehydrogenative functionalization via a single electron transfer (SET) process, *Chemical Society Reviews*, 41 (9), 2012 3464-3484.

- [236] H. Tian, X. Yu, Q. Li, J. Wang, Q. Xu, General, Green, and Scalable Synthesis of Imines from Alcohols and Amines by a Mild and Efficient Copper-Catalyzed Aerobic Oxidative Reaction in Open Air at Room Temperature, *Advanced Synthesis & Catalysis*, 354 (14-15), 2012 2671-2677.
- [237] M.C. Bagley, C. Glover, E.A. Merritt, The Bohlmann-Rahtz pyridine synthesis: From discovery to applications, *Synlett*, 2007 (16), 2007 2459-2482.
- [238] K. Gopalaiah, A. Saini, A Solvent-Free Process for Synthesis of Imines by Iron-Catalyzed Oxidative Self-or Cross-Condensation of Primary Amines Using Molecular Oxygen as Sole Oxidant, *Catalysis Letters*, 146 (9), 2016 1648-1654.
- [239] R.S. Hosmane, B.B. Lim, F.N. Burnett, Rearrangements in heterocyclic synthesis: a novel translocation of an (N-amino-N-methylamino) methylene group from a heterocyclic N-amino-N-methylformamidine side chain to the vinylogous nitrile function, *The Journal of Organic Chemistry*, 53 (2), 1988 382-386.
- [240] S. Costanzi, S.P. Rouse, L. Vanbaelinghem, T.J. Prior, D.F. Ewing, A.N. Boa, G. Mackenzie, Dimroth-type rearrangement of 1-benzyl- and 1-glycosyl-5-aminoimidazoles to 4-(N-substituted amino) imidazoles, *Tetrahedron Letters*, 53 (4), 2012 412-415.
- [241] B. Delest, J.-Y. Tisserand, J.-M. Robert, M.-R. Nourrisson, P. Pinson, M. Duflos, G. Le Baut, P. Renard, B. Pfeiffer, Synthesis of 1-benzyl-8, 9-dihydroimidazo [4, 5-c] pyrrolo [3, 2-g] quinolin-4 (5H)-one via palladium-catalyzed intramolecular arylation, *Tetrahedron*, 60 (29), 2004 6079-6083.
- [242] G.F. Pauli, S.-N. Chen, C. Simmler, D.C. Lankin, T. Gödecke, B.U. Jaki, J.B. Friesen, J.B. McAlpine, J.G. Napolitano, Importance of purity evaluation and the potential of quantitative ¹H NMR as a purity assay: miniperspective, *Journal of medicinal chemistry*, 57 (22), 2014 9220-9231.
- [243] S.A. Miller, N.E. Leadbeater, Direct, rapid, solvent-free conversion of unactivated esters to amides using lithium hydroxide as a catalyst, *RSC Advances*, 5 (113), 2015 93248-93251.
- [244] V. Soni, S.M. Khake, B. Punji, Nickel-Catalyzed C (sp²)-H/C (sp³)-H Oxidative Coupling of Indoles with Toluene Derivatives, *ACS Catalysis*, 7 (6), 2017 4202-4208.
- [245] X. Jiang, W. Tang, D. Xue, J. Xiao, C. Wang, Divergent dehydrogenative coupling of indolines with alcohols, *ACS Catalysis*, 7 (3), 2017 1831-1835.
- [246] C. Seck, M.D. Mbaye, S. Gaillard, J.L. Renaud, Bifunctional Iron Complexes Catalyzed Alkylation of Indoles, *Advanced Synthesis & Catalysis*, 360 (23), 2018 4640-4645.
- [247] M. Jesus Perez de Vega, M. Martin-Martinez, R. Gonzalez-Muniz, Modulation of protein-protein interactions by stabilizing/mimicking protein secondary structure elements, *Current topics in medicinal chemistry*, 7 (1), 2007 33-62.
- [248] C.L. Day, C. Smits, F.C. Fan, E.F. Lee, W.D. Fairlie, M.G. Hinds, Structure of the BH3 domains from the p53-inducible BH3-only proteins Noxa and Puma in complex with Mcl-1, *Journal of molecular biology*, 380 (5), 2008 958-971.
- [249] M.P. Stumpf, T. Thorne, E. de Silva, R. Stewart, H.J. An, M. Lappe, C. Wiuf, Estimating the size of the human interactome, *Proceedings of the National Academy of Sciences*, 105 (19), 2008 6959-6964.
- [250] K. Venkatesan, J.-F. Rual, A. Vazquez, U. Stelzl, I. Lemmens, T. Hirozane-Kishikawa, T. Hao, M. Zenkner, X. Xin, K.-I. Goh, An empirical framework for binary interactome mapping, *Nature methods*, 6 (1), 2009 83-90.
- [251] D.G. Rattray, L.J. Foster, Dynamics of protein complex components, *Current Opinion in Chemical Biology*, 48 2019 81-85.
- [252] C.A. Lipinski, F. Lombardo, B.W. Dominy, P.J. Feeney, Experimental and computational approaches to estimate solubility and permeability in drug discovery and development settings¹, *Advanced drug delivery reviews*, 46 (1-3), 2001 3-26.
- [253] B.C. Doak, J. Zheng, D. Dobritzsch, J. Kihlberg, How beyond rule of 5 drugs and clinical candidates bind to their targets, *Journal of medicinal chemistry*, 59 (6), 2015 2312-2327.
- [254] D.E. Scott, A.R. Bayly, C. Abell, J. Skidmore, Small molecules, big targets: drug discovery faces the protein-protein interaction challenge, *Nature Reviews Drug Discovery*, 15 (8), 2016 533-550.
- [255] E.M. Driggers, S.P. Hale, J. Lee, N.K. Terrett, The exploration of macrocycles for drug discovery—an underexploited structural class, *Nature Reviews Drug Discovery*, 7 (7), 2008 608-624.
- [256] P. Matsson, B.C. Doak, B. Over, J. Kihlberg, Cell permeability beyond the rule of 5, *Advanced drug delivery reviews*, 101 2016 42-61.
- [257] J. Wang, V. Yadav, A.L. Smart, S. Tajiri, A.W. Basit, Toward oral delivery of biopharmaceuticals: an assessment of the gastrointestinal stability of 17 peptide drugs, *Molecular pharmaceutics*, 12 (3), 2015 966-973.
- [258] J. Wilbs, S.J. Middendorp, C. Heinis, Improving the Binding Affinity of in-Vitro-Evolved Cyclic Peptides by Inserting Atoms into the Macrocyclic Backbone, *ChemBioChem*, 17 (24), 2016 2299-2303.

- [259] T.A. Cardote, A. Ciulli, Cyclic and Macrocyclic Peptides as Chemical Tools To Recognise Protein Surfaces and Probe Protein–Protein Interactions, *ChemMedChem*, 11 (8), 2016 787-794.
- [260] I.S. Moreira, P.A. Fernandes, M.J. Ramos, Hot spots—A review of the protein–protein interface determinant amino-acid residues, *Proteins: Structure, Function, and Bioinformatics*, 68 (4), 2007 803-812.
- [261] B. Ma, T. Elkayam, H. Wolfson, R. Nussinov, Protein–protein interactions: structurally conserved residues distinguish between binding sites and exposed protein surfaces, *Proceedings of the National Academy of Sciences*, 100 (10), 2003 5772-5777.
- [262] R.R. Araghi, A.E. Keating, Designing helical peptide inhibitors of protein–protein interactions, *Current opinion in structural biology*, 39 2016 27-38.
- [263] V. Azzarito, K. Long, N.S. Murphy, A.J. Wilson, Inhibition of α -helix-mediated protein–protein interactions using designed molecules, *Nature chemistry*, 5 (3), 2013 161.
- [264] J.E. Bock, J. Gavenonis, J.A. Kritzer, Getting in shape: controlling peptide bioactivity and bioavailability using conformational constraints, *ACS chemical biology*, 8 (3), 2012 488-499.
- [265] A.B. Mahon, P.S. Arora, End-capped α -helices as modulators of protein function, *Drug Discovery Today: Technologies*, 9 (1), 2012 e57-e62.
- [266] P.M. Cromm, S. Schaubach, J. Spiegel, A. Fürstner, T.N. Grossmann, H. Waldmann, Orthogonal ring-closing alkyne and olefin metathesis for the synthesis of small GTPase-targeting bicyclic peptides, *Nature communications*, 7 2016.
- [267] M.R. Arkin, Y. Tang, J.A. Wells, Small-molecule inhibitors of protein-protein interactions: progressing toward the reality, *Chemistry & biology*, 21 (9), 2014 1102-1114.
- [268] P.G. Dougherty, Z. Qian, D. Pei, Macrocycles as protein–protein interaction inhibitors, *Biochemical Journal*, 474 (7), 2017 1109-1125.
- [269] A. Negi, J. Zhou, S. Sweeney, P.V. Murphy, Ligand design for somatostatin receptor isoforms 4 and 5, *European Journal of Medicinal Chemistry*, 2018.
- [270] N.T. Ross, W.P. Katt, A.D. Hamilton, Synthetic mimetics of protein secondary structure domains, *Philosophical Transactions of the Royal Society of London A: Mathematical, Physical and Engineering Sciences*, 368 (1914), 2010 989-1008.
- [271] W. Bedewy, H. Liao, N.A. Abou-Taleb, S.F. Hammad, T. Nasr, D. Pei, Generation of a cell-permeable cycloheptapeptidyl inhibitor against the peptidyl–prolyl isomerase Pin1, *Organic & biomolecular chemistry*, 15 (21), 2017 4540-4543.
- [272] J. Zhou, M. Reidy, C. O'Reilly, D.V. Jarikote, A. Negi, A. Samali, E. Szegezdi, P.V. Murphy, Decorated Macrocycles via Ring-Closing Double-Reductive Amination. Identification of an Apoptosis Inducer of Leukemic Cells That at Least Partially Antagonizes a 5-HT₂ Receptor, *Organic letters*, 17 (7), 2015 1672-1675.
- [273] D. Madariaga, N. Martínez-Sáez, V.J. Somovilla, H. Coelho, J. Valero-González, J. Castro-López, J.L. Asensio, J.s. Jiménez-Barbero, J.s.H. Busto, A. Avenoza, Detection of tumor-associated glycopeptides by lectins: the peptide context modulates carbohydrate recognition, *ACS chemical biology*, 10 (3), 2014 747-756.
- [274] I. Sutkeviciute, M. Thépaut, S. Sattin, A. Berzi, J. McGeagh, S. Grudinin, J.r. Weiser, A. Le Roy, J.J. Reina, J. Rojo, Unique DC-SIGN clustering activity of a small glycomimetic: a lesson for ligand design, *ACS chemical biology*, 9 (6), 2014 1377-1385.
- [275] S.M. Muthana, C.T. Campbell, J.C. Gildersleeve, Modifications of glycans: biological significance and therapeutic opportunities, *ACS chemical biology*, 7 (1), 2012 31-43.
- [276] P.S. Kharkar, S. Warriar, R.S. Gaud, Reverse docking: a powerful tool for drug repositioning and drug rescue, *Future medicinal chemistry*, 6 (3), 2014 333-342.
- [277] R. Zheng, T.-s. Chen, T. Lu, A comparative reverse docking strategy to identify potential antineoplastic targets of tea functional components and binding mode, *International journal of molecular sciences*, 12 (8), 2011 5200-5212.
- [278] A. Lee, K. Lee, D. Kim, Using reverse docking for target identification and its applications for drug discovery, *Expert opinion on drug discovery*, 11 (7), 2016 707-715.
- [279] Y. Chen, D. Zhi, Ligand–protein inverse docking and its potential use in the computer search of protein targets of a small molecule, *Proteins: Structure, Function, and Bioinformatics*, 43 (2), 2001 217-226.
- [280] D. Warszycki, M. Rueda, S. Mordalski, K. Kristiansen, G. Satała, K. Rataj, Z. Chilmonczyk, I. Sylte, R. Abagyan, A.J. Bojarski, From homology models to a set of predictive binding pockets—a 5-HT_{1A} receptor case study, *Journal of chemical information and modeling*, 57 (2), 2017 311-321.
- [281] S. Podlewska, R. Kafel, E. Lacivita, G. Satała, A.J. Kooistra, M. Vass, C. de Graaf, M. Leopoldo, A.J. Bojarski, S. Mordalski, Structural insights into serotonin receptor ligands polypharmacology, *European journal of medicinal chemistry*, 151 2018 797-814.

- [282] K.H. Wang, A. Penmatsa, E. Gouaux, Neurotransmitter and psychostimulant recognition by the dopamine transporter, *Nature*, 521 (7552), 2015 322-327.
- [283] D. Wacker, C. Wang, V. Katritch, G.W. Han, X.-P. Huang, E. Vardy, J.D. McCorvy, Y. Jiang, M. Chu, F.Y. Siu, Structural features for functional selectivity at serotonin receptors, *Science*, 340 (6132), 2013 615-619.
- [284] I. Bacconguis, C.J. Bohlen, A. Goehring, D. Julius, E. Gouaux, X-Ray structure of acid-sensing ion channel 1–snake toxin complex reveals open state of a Na⁺-selective channel, *Cell*, 156 (4), 2014 717-729.
- [285] K. Kanagarajadurai, M. Malini, A. Bhattacharya, M.M. Panicker, R. Sowdhamini, Molecular modeling and docking studies of human 5-hydroxytryptamine 2A (5-HT_{2A}) receptor for the identification of hotspots for ligand binding, *Molecular BioSystems*, 5 (12), 2009 1877-1888.
- [286] S. Cestèle, W.A. Catterall, Molecular mechanisms of neurotoxin action on voltage-gated sodium channels, *Biochimie*, 82 (9-10), 2000 883-892.
- [287] J. Zhou, A. Negi, S.I. Mirallai, R. Warta, C. Herold-Mende, M.P. Carty, X.-S. Ye, P.V. Murphy, N-Alkyl-1, 5-Dideoxy-1, 5-Imino-L-Fucitols as Fucosidase Inhibitors: Synthesis, Molecular Modelling and Activity Against Cancer Cell Lines, *Bioorganic Chemistry*, 2018.
- [288] W. Lewgowd, A.J. Bojarski, M. Szczesio, A. Olczak, M.L. Glowka, S. Mordalski, A. Stanczak, Synthesis and structural investigation of some pyrimido [5, 4-c] quinolin-4 (3H)-one derivatives with a long-chain arylpiperazine moiety as potent 5-HT 1A/2A and 5-HT 7 receptor ligands, *European journal of medicinal chemistry*, 46 (8), 2011 3348-3361.
- [289] W. Liu, D. Wacker, C. Gati, G.W. Han, D. James, D. Wang, G. Nelson, U. Weierstall, V. Katritch, A. Barty, Serial Femtosecond Crystallography of G Protein–Coupled Receptors, *Science*, 342 (6165), 2013 1521-1524.
- [290] D. Hoyer, H. Lübbert, C. Bruns, Molecular pharmacology of somatostatin receptors, *Naunyn-Schmiedeberg's archives of pharmacology*, 350 (5), 1994 441-453.
- [291] W. Meyerhof, The elucidation of somatostatin receptor functions: a current view, *Reviews of Physiology Biochemistry and Pharmacology*, Volume 133, Springer 1998, pp. 55-108.
- [292] T.K. Bjarnadóttir, D.E. Gloriam, S.H. Hellstrand, H. Kristiansson, R. Fredriksson, H.B. Schiöth, Comprehensive repertoire and phylogenetic analysis of the G protein-coupled receptors in human and mouse, *Genomics*, 88 (3), 2006 263-273.
- [293] T. Reisine, G.I. Bell, Molecular biology of somatostatin receptors, *Endocrine reviews*, 16 (4), 1995 427-442.
- [294] D. Ferone, F. Gatto, M. Arvigo, E. Resmini, M. Boschetti, C. Teti, D. Esposito, F. Minuto, The clinical–molecular interface of somatostatin, dopamine and their receptors in pituitary pathophysiology, *Journal of Molecular Endocrinology*, 42 (5), 2009 361-370.
- [295] K.E. Sandoval, K.A. Witt, A.M. Crider, M. Kontoyianni, Somatostatin Receptor-4 Agonists as Candidates for Treatment of Alzheimer’s Disease, in: Atta-ur-Rahman (Ed.) *Drug Design and Discovery in Alzheimer's Disease*, Elsevier, 1000 AE Amsterdam, Netherlands, 2014, pp. 566-597.
- [296] F. Gastambide, C. Viollet, G. Lepousez, J. Epelbaum, J.-L. Guillou, Hippocampal SSTR4 somatostatin receptors control the selection of memory strategies, *Psychopharmacology*, 202 (1-3), 2009 153.
- [297] N. Schuelert, S. Just, R. Kuelzer, L. Corradini, L.C. Gorham, H. Doods, The somatostatin receptor 4 agonist J-2156 reduces mechanosensitivity of peripheral nerve afferents and spinal neurons in an inflammatory pain model, *European journal of pharmacology*, 746 2015 274-281.
- [298] K. Sándor, K. Elekes, Á. Szabó, E. Pintér, M. Engström, S. Wurster, J. Szolcsányi, Z. Helyes, Analgesic effects of the somatostatin sst4 receptor selective agonist J-2156 in acute and chronic pain models, *European journal of pharmacology*, 539 (1-2), 2006 71-75.
- [299] [Patent] R. Giovannini, Y. Cui, H. Doods, M. Ferrara, S. Just, R. Kuelzer, I. Lingard, R. Mazzaferro, K. Rudolf, New somatostatin receptor subtype 4 (sstr4) agonists, WO/2014/184275 (20.11.2014).
- [300] Y. Jung, S.-H. Oh, D. Zheng, T.D. Shupe, R.P. Witek, B.E. Petersen, A potential role of somatostatin and its receptor SSTR4 in the migration of hepatic oval cells, *Laboratory investigation*, 86 (5), 2006 477-489.
- [301] S.V. de Sá, M.L. Corrêa-Giannella, M.C. Machado, J.J.S. de Souza, M.A.A. Pereira, R.A. Patzina, S.A.C. Siqueira, M.C.C. Machado, D. Giannella-Neto, Somatostatin receptor subtype 5 (SSTR5) mRNA expression is related to histopathological features of cell proliferation in insulinomas, *Endocrine-Related Cancer*, 13 (1), 2006 69-78.
- [302] L. Chinezu, A. Vasiljevic, E. Jouanneau, P. François, A. Borda, J. Trouillas, G. Raverot, Expression of somatostatin receptors, SSTR 2A and SSTR 5, in 108 endocrine pituitary tumors using immunohistochemical detection with new specific monoclonal antibodies, *Human pathology*, 45 (1), 2014 71-77.
- [303] X. Wang, J. Yang, M. Norman, J. Magnusson, F. DeMayo, F. Brunicardi, SSTR5 ablation in islet results in alterations in glucose homeostasis in mice, *FEBS letters*, 579 (14), 2005 3107-3114.

- [304] E.J. Spary, A. Maqbool, T.F. Batten, Expression and localisation of somatostatin receptor subtypes sst1–sst5 in areas of the rat medulla oblongata involved in autonomic regulation, *Journal of Chemical Neuroanatomy*, 35 (1), 2008 49-66.
- [305] Y.C. Patel, Somatostatin and its receptor family, *Front. Neuroendocrinol.*, 20 (3), 1999 157-198.
- [306] G. Abbenante, B. Becker, S. Blanc, C. Clark, G. Condie, G. Fraser, M. Grathwohl, J. Halliday, S. Henderson, A. Lam, Biological diversity from a structurally diverse library: systematically scanning conformational space using a pyranose scaffold, *Journal of Medicinal Chemistry*, 53 (15), 2010 5576-5586.
- [307] L.N. Møller, C.E. Stidsen, B. Hartmann, J.J. Holst, Somatostatin receptors, *Biochim. Biophys. Acta-Biomembranes*, 1616 (1), 2003 1-84.
- [308] R. Baldelli, Somatostatin analogs therapy in gastroenteropancreatic neuroendocrine tumors: current aspects and new perspectives, *Frontiers in endocrinology*, 5 2014 7.
- [309] J.C. Reubi, J.-C. Schär, B. Waser, S. Wenger, A. Heppeler, J.S. Schmitt, H.R. Mäcke, Affinity profiles for human somatostatin receptor subtypes SST1–SST5 of somatostatin radiotracers selected for scintigraphic and radiotherapeutic use, *European journal of nuclear medicine*, 27 (3), 2000 273-282.
- [310] T.W. Speer, Targeted radionuclide therapy, Lippincott Williams & Wilkins, Philadelphia, USA, 2012.
- [311] I. Lewis, W. Bauer, R. Albert, N. Chandramouli, J. Pless, G. Weckbecker, C. Bruns, A novel somatostatin mimic with broad somatotropin release inhibitory factor receptor binding and superior therapeutic potential, *Journal of Medicinal Chemistry*, 46 (12), 2003 2334-2344.
- [312] A. Michael Crider, K.A. Witt, Somatostatin sst4 ligands: chemistry and pharmacology, *Mini reviews in medicinal chemistry*, 7 (3), 2007 213-220.
- [313] D.J. Suich, S.A. Mousa, G. Singh, G. Liapakis, T. Reisine, W.F. DeGrado, Template-constrained cyclic peptide analogues of somatostatin: subtype-selective binding to somatostatin receptors and antiangiogenic activity, *Bioorganic & medicinal chemistry*, 8 (9), 2000 2229-2241.
- [314] A. Tatsi, T. Maina, R. Cescato, B. Waser, E.P. Krenning, M. de Jong, P. Cordopatis, J.-C. Reubi, B.A. Nock, [DOTA] Somatostatin-14 analogs and their 111 In-radioligands: Effects of decreasing ring-size on sst 1–5 profile, stability and tumor targeting, *European journal of medicinal chemistry*, 73 2014 30-37.
- [315] W. Rajeswaran, W.A. Murphy, J.E. Taylor, D.H. Coy, Exploration of the DTrp-NMeLys motif in the search for potent somatostatin antagonists, *Bioorganic & medicinal chemistry*, 10 (6), 2002 2023-2029.
- [316] W. Meutermans, G.T. Le, B. Becker, Carbohydrates as scaffolds in drug discovery, *ChemMedChem*, 1 (11), 2006 1164-1194.
- [317] O. Van der Poorten, A. Knuhtsen, D.S. Pedersen, S. Ballet, D. Tourwé, Side chain cyclized aromatic amino acids: great tools as local constraints in peptide and peptidomimetic design, *J. Med. Chem.*, 59 (24), 2016 10865-10890.
- [318] C. Caumes, T. Hjelmgaard, O. Roy, M. Reynaud, D. Servent, C. Taillefumier, S. Faure, Synthesis and binding affinities for sst receptors of cyclic peptoid SRIF-mimetics, *MedChemComm*, 3 (12), 2012 1531-1535.
- [319] S.P. Rohrer, J.M. Schaeffer, Identification and characterization of subtype selective somatostatin receptor agonists, *Journal of Physiology-Paris*, 94 (3), 2000 211-215.
- [320] S. Barron, P.V. Murphy, Synthesis of iminosugar derivatives presenting naphthyl and alkyl amine interacting groups and binding to somatostatin receptors, *MedChemComm*, 5 (8), 2014 1150-1158.
- [321] Y. Zhao, M. Liu, V. Chagnault, J. Wang, X. Zhang, P.V. Murphy, Biological study of a somatostatin mimetic based on the 1-deoxynojirimycin scaffold, *Bioorganic & medicinal chemistry letters*, 21 (2), 2011 824-828.
- [322] S.G. Gouin, P.V. Murphy, Synthesis of somatostatin mimetics based on the 1-deoxymannojirimycin scaffold, *The Journal of organic chemistry*, 70 (21), 2005 8527-8532.
- [323] V. Chagnault, J. Lalot, P.V. Murphy, Synthesis of Somatostatin Mimetics Based on 1-Deoxynojirimycin, *ChemMedChem*, 3 (7), 2008 1071-1076.
- [324] J. Zhou, M.-C. Matos, P.V. Murphy, Synthesis of a Benzomacrolactone-Based Somatostatin Mimetic, *Organic Letters*, 13 (21), 2011 5716-5719.
- [325] R. Hirschmann, K. Nicolaou, S. Pietranico, J. Salvino, E.M. Leahy, P.A. Sprengeler, G. Furst, C.D. Strader, A.B. Smith III, Nonpeptidal peptidomimetics with beta.-D-glucose scaffolding. A partial somatostatin agonist bearing a close structural relationship to a potent, selective substance P antagonist, *Journal of the American Chemical Society*, 114 (23), 1992 9217-9218.
- [326] L. Rohrer, F. Raulf, C. Bruns, R. Buettner, F. Hofstaedter, R. Schüle, Cloning and characterization of a fourth human somatostatin receptor, *Proceedings of the National Academy of Sciences*, 90 (9), 1993 4196-4200.
- [327] F.-W. Kluxen, C. Bruns, H. Lübbert, Expression cloning of a rat brain somatostatin receptor cDNA, *Proceedings of the National Academy of Sciences*, 89 (10), 1992 4618-4622.

- [328] Y. Yamada, S. Kagimoto, A. Kubota, K. Yasuda, K. Masuda, Y. Someya, Y. Ihara, Q. Li, H. Imura, S. Seino, Cloning, functional expression and pharmacological characterization of a fourth (hSSTR4) and a fifth (hSSTR5) human somatostatin receptor subtype, *Biochemical and biophysical research communications*, 195 (2), 1993 844-852.
- [329] Y. Yamada, S.R. Post, K. Wang, H.S. Tager, G.I. Bell, S. Seino, Cloning and functional characterization of a family of human and mouse somatostatin receptors expressed in brain, gastrointestinal tract, and kidney, *Proceedings of the National Academy of Sciences*, 89 (1), 1992 251-255.
- [330] T. Ryckmans, M.P. Edwards, V.A. Horne, A.M. Correia, D.R. Owen, L.R. Thompson, I. Tran, M.F. Tutt, T. Young, Rapid assessment of a novel series of selective CB 2 agonists using parallel synthesis protocols: a lipophilic efficiency (LipE) analysis, *Bioorganic & medicinal chemistry letters*, 19 (15), 2009 4406-4409.
- [331] G. Fenalti, P.M. Giguere, V. Katritch, X.-P. Huang, A.A. Thompson, V. Cherezov, B.L. Roth, R.C. Stevens, Molecular control of [dgr]-opioid receptor signalling, *Nature*, 506 (7487), 2014 191-196.
- [332] R.L. Miller, A.A. Thompson, C. Trapella, R. Guerrini, D. Malfacini, N. Patel, G.W. Han, V. Cherezov, G. Caló, V. Katritch, The Importance of Ligand-Receptor Conformational Pairs in Stabilization: Spotlight on the N/OFQ G Protein-Coupled Receptor, *Structure*, 23 (12), 2015 2291-2299.
- [333] P.J. Goodford, A computational procedure for determining energetically favorable binding sites on biologically important macromolecules, *Journal of medicinal chemistry*, 28 (7), 1985 849-857.
- [334] J. Liang, C. Woodward, H. Edelsbrunner, Anatomy of protein pockets and cavities: measurement of binding site geometry and implications for ligand design, *Protein Science*, 7 (9), 1998 1884-1897.
- [335] R.B. Nehring, W. Meyerhof, D. Richter, Aspartic acid residue 124 in the third transmembrane domain of the somatostatin receptor subtype 3 is essential for somatostatin-14 binding, *DNA and cell biology*, 14 (11), 1995 939-944.
- [336] K. Kaupmann, C. Bruns, F. Raulf, H.P. Weber, H. Mattes, H. Lübbert, Two amino acids, located in transmembrane domains VI and VII, determine the selectivity of the peptide agonist SMS 201-995 for the SSTR2 somatostatin receptor, *The EMBO journal*, 14 (4), 1995 727.
- [337] Z. Liu, A.M. Crider, D. Ansbrosio, C. Hayes, M. Kontoyianni, A structure-based approach to understanding somatostatin receptor-4 agonism (sst4), *Journal of chemical information and modeling*, 52 (1), 2011 171-186.
- [338] B.A. Ozenberger, J.R. Hadcock, A single amino acid substitution in somatostatin receptor subtype 5 increases affinity for somatostatin-14, *Molecular Pharmacology*, 47 (1), 1995 82-87.
- [339] A. Christopoulos, T. Kenakin, G protein-coupled receptor allostery and complexing, *Pharmacological reviews*, 54 (2), 2002 323-374.
- [340] B.K. Kobilka, X. Deupi, Conformational complexity of G-protein-coupled receptors, *Trends in pharmacological sciences*, 28 (8), 2007 397-406.
- [341] J.G. Baker, S.J. Hill, Multiple GPCR conformations and signalling pathways: implications for antagonist affinity estimates, *Trends in pharmacological sciences*, 28 (8), 2007 374-381.
- [342] Y. Ge, A.P. Turner, Too large to fit? Recent developments in macromolecular imprinting, *Trends in biotechnology*, 26 (4), 2008 218-224.
- [343] E.A. Villar, D. Beglov, S. Chennamadhavuni, J.A. Porco Jr, D. Kozakov, S. Vajda, A. Whitty, How proteins bind macrocycles, *Nature chemical biology*, 10 (9), 2014 723-731.
- [344] L.A. Marcaurelle, E. Comer, S. Dandapani, J.R. Duvall, B. Gerard, S. Kesavan, M.D. Lee IV, H. Liu, J.T. Lowe, J.-C. Marie, An aldol-based build/couple/pair strategy for the synthesis of medium-and large-sized rings: discovery of macrocyclic histone deacetylase inhibitors, *Journal of the American Chemical Society*, 132 (47), 2010 16962-16976.
- [345] M.O. Sinnokrot, C.D. Sherrill, Substituent effects in π - π interactions: Sandwich and T-shaped configurations, *Journal of the American Chemical Society*, 126 (24), 2004 7690-7697.
- [346] O. Sperandio, C.H. Reynès, A.-C. Camproux, B.O. Villoutreix, Rationalizing the chemical space of protein-protein interaction inhibitors, *Drug discovery today*, 15 (5), 2010 220-229.
- [347] C. Gilon, D. Halle, M. Chorev, Z. Selinger, G. Byk, Backbone cyclization: a new method for conferring conformational constraint on peptides, *Biopolymers*, 31 (6), 1991 745-750.
- [348] C.R. Bertozzi, L.L. Kiessling, Chemical glycobiology, *Science*, 291 (5512), 2001 2357-2364.
- [349] B. Ma, M. Shatsky, H.J. Wolfson, R. Nussinov, Multiple diverse ligands binding at a single protein site: A matter of pre-existing populations, *Protein science*, 11 (2), 2002 184-197.
- [350] J.L. Dashnau, K.A. Sharp, J.M. Vanderkooi, Carbohydrate intramolecular hydrogen bonding cooperativity and its effect on water structure, *The Journal of Physical Chemistry B*, 109 (50), 2005 24152-24159.
- [351] F.A. Quiocho, Carbohydrate-binding proteins: tertiary structures and protein-sugar interactions, *Annual review of biochemistry*, 55 (1), 1986 287-315.

- [352] C.H. Wong, D.P. Dumas, Y. Ichikawa, K. Koseki, S.J. Danishefsky, B.W. Weston, J.B. Lowe, Specificity, Inhibition, and Synthetic Utility of a Recombinant Human Alpha-1,3-Fucosyl-Transferase, *Journal of the American Chemical Society*, 114 (18), 1992 7321-7322.
- [353] P. Compain, O.R. Martin, Design, synthesis and biological evaluation of iminosugar-based glycosyltransferase inhibitors, *Current Topics in Medicinal Chemistry*, 3 (5), 2003 541-560.
- [354] L. Somsak, V. Nagy, Z. Hadady, T. Docsa, P. Gergely, Glucose analog inhibitors of glycogen phosphorylases as potential antidiabetic agents: Recent developments, *Current Pharmaceutical Design*, 9 (15), 2003 1177-1189.
- [355] V.L. Schramm, P.C. Tyler, Imino-sugar-based nucleosides, *Current Topics in Medicinal Chemistry*, 3 (5), 2003 525-540.
- [356] R.E. Lee, M.D. Smith, L. Pickering, G.W.J. Fleet, An approach to combinatorial library generation of galactofuranose mimics as potential inhibitors of mycobacterial cell wall biosynthesis: Synthesis of a peptidomimetic of uridine 5'-diphosphogalactofuranose (UDP-Galf), *Tetrahedron Letters*, 40 (49), 1999 8689-8692.
- [357] R.E. Lee, M.D. Smith, R.J. Nash, R.C. Griffiths, M. McNeil, R.K. Grewal, W.X. Yan, G.S. Besra, P.J. Brennan, G.W.J. Fleet, Inhibition of UDP-Gal mutase and mycobacterial galactan biosynthesis by pyrrolidine analogues of galactofuranose, *Tetrahedron Letters*, 38 (38), 1997 6733-6736.
- [358] H. Moriyama, T. Tsukida, Y. Inoue, K. Yokota, K. Yoshino, H. Kondo, N. Miura, S. Nishimura, Azasugar-based MMP/ADAM inhibitors as antipsoriatic agents, *Journal of Medicinal Chemistry*, 47 (8), 2004 1930-1938.
- [359] A.E. Stütz, Iminosugars as Glycosidase Inhibitors: Nojirimycin and Beyond, 1999 Wiley-VCH: Weinheim.
- [360] P. Sears, C.H. Wong, Carbohydrate mimetics: A new strategy for tackling the problem of carbohydrate-mediated biological recognition, *Angewandte Chemie-International Edition*, 38 (16), 1999 2301-2324.
- [361] T.M. Gloster, G.J. Davies, Glycosidase inhibition: assessing mimicry of the transition state, *Organic & Biomolecular Chemistry*, 8 (2), 2010 305-320.
- [362] V.H. Lillelund, H.H. Jensen, X.F. Liang, M. Bols, Recent developments of transition-state analogue glycosidase inhibitors of non-natural product origin, *Chemical Reviews*, 102 (2), 2002 515-553.
- [363] O.R. Martin, P. Compain, Iminosugars: Recent insights into their bioactivity and potential as therapeutic agents - Preface, *Current Topics in Medicinal Chemistry*, 3 (5), 2003 -.
- [364] D.J. Becker, J.B. Lowe, Fucose: biosynthesis and biological function in mammals, *Glycobiology*, 13 (7), 2003 41r-53r.
- [365] E. Staudacher, alpha 1,3-fucosyltransferases, *Trends in Glycoscience and Glycotechnology*, 8 (44), 1996 391-408.
- [366] D.H. Dube, C.R. Bertozzi, Glycans in cancer and inflammation. Potential for therapeutics and diagnostics, *Nature Reviews: Drug Discovery*, 4 (6), 2005 477-488.
- [367] D. Ayude, J. Fernandez-Rodriguez, F.J. Rodriguez-Berrocal, V.S. Martinez-Zorzano, A. de Carlos, E. Gil, M.P. de la Cadena, Value of the serum alpha-L-fucosidase activity in the diagnosis of colorectal cancer, *Oncology*, 59 (4), 2000 310-316.
- [368] K. Yuan, C.M. Listinsky, R.K. Singh, J.J. Listinsky, G.P. Siegal, Cell surface associated alpha-L-fucose moieties modulate human breast cancer neoplastic progression, *Pathology Oncology Research*, 14 (2), 2008 145-156.
- [369] M.C. Glick, V.A. Kothari, A.H. Liu, L.I. Stoykova, T.F. Scanlin, Activity of fucosyltransferases and altered glycosylation in cystic fibrosis airway epithelial cells, *Biochimie*, 83 (8), 2001 743-747.
- [370] S.D. Szajda, A. Jankowska, K. Zwierz, Carbohydrate markers in colon carcinoma, *Disease Markers*, 25 (4-5), 2008 233-242.
- [371] Z.J. Tu, Y.N. Lin, C.H. Lin, Development of fucosyltransferase and fucosidase inhibitors, *Chemical Society Reviews*, 42 (10), 2013 4459-4475.
- [372] M. Dubernet, A. Defoin, C. Tarnus, Asymmetric synthesis of the 1-fuco-nojirimycin, a nanomolar α -L-fucosidase inhibitor, *Bioorganic & medicinal chemistry letters*, 16 (5), 2006 1172-1174.
- [373] N. Asano, K. Yasuda, H. Kizu, A. Kato, J.Q. Fan, R.J. Nash, G.W. Fleet, R.J. Molyneux, Novel α -L-fucosidase inhibitors from the bark of *Angylocalyx pynaertii* (Leguminosae), *The FEBS Journal*, 268 (1), 2001 35-41.
- [374] Z. Tu, Y.-N. Lin, C.-H. Lin, Development of fucosyltransferase and fucosidase inhibitors, *Chemical Society reviews*, 42 (10), 2013 4459-4475.
- [375] Y. Zhao, W. Liu, Y. Zhou, X. Zhang, P.V. Murphy, N-(8-(3-ethynylphenoxy) octyl-1-deoxynojirimycin suppresses growth and migration of human lung cancer cells, *Bioorganic & medicinal chemistry letters*, 20 (24), 2010 7540-7543.
- [376] Y. Zhao, Y. Zhou, K.M. O'Boyle, P.V. Murphy, Biological study of the Angiogenesis Inhibitor N-(8-(3-ethynylphenoxy) octyl-1-deoxynojirimycin, *Chemical biology & drug design*, 75 (6), 2010 570-577.
- [377] Y. Zhao, Y. Zhou, K.M. O'Boyle, P.V. Murphy, Hybrids of 1-deoxynojirimycin and aryl-1, 2, 3-triazoles and biological studies related to angiogenesis, *Bioorganic & medicinal chemistry*, 16 (12), 2008 6333-6337.

- [378] A. Mitrakou, N. Tountas, A. Raptis, R. Bauer, H. Schulz, S. Raptis, Long-term effectiveness of a new α -glucosidase inhibitor (BAY m1099-miglitol) in insulin-treated Type 2 diabetes mellitus, *Diabetic medicine*, 15 (8), 1998 657-660.
- [379] L. Yu, K. Ikeda, A. Kato, I. Adachi, G. Godin, P. Compain, O. Martin, N. Asano, α -1-C-Octyl-1-deoxynojirimycin as a pharmacological chaperone for Gaucher disease, *Bioorganic & medicinal chemistry*, 14 (23), 2006 7736-7744.
- [380] G. Godin, P. Compain, O.R. Martin, K. Ikeda, L. Yu, N. Asano, α -1-C-Alkyl-1-deoxynojirimycin derivatives as potent and selective inhibitors of intestinal isomaltase: remarkable effect of the alkyl chain length on glycosidase inhibitory profile, *Bioorganic & medicinal chemistry letters*, 14 (24), 2004 5991-5995.
- [381] G.-N. Wang, G. Reinkensmeier, S.-W. Zhang, J. Zhou, L.-R. Zhang, L.-H. Zhang, T.D. Butters, X.-S. Ye, Rational design and synthesis of highly potent pharmacological chaperones for treatment of N370S mutant Gaucher disease, *Journal of medicinal chemistry*, 52 (10), 2009 3146-3149.
- [382] T.D. Butters, Gaucher disease, *Current opinion in chemical biology*, 11 (4), 2007 412-418.
- [383] C. Porto, M. Cardone, F. Fontana, B. Rossi, M.R. Tuzzi, A. Tarallo, M.V. Barone, G. Andria, G. Parenti, The pharmacological chaperone N-butyldeoxynojirimycin enhances enzyme replacement therapy in Pompe disease fibroblasts, *Molecular Therapy*, 17 (6), 2009 964-971.
- [384] Z. Yu, A.R. Sawkar, L.J. Whalen, C.-H. Wong, J.W. Kelly, Isofagomine-and 2, 5-anhydro-2, 5-imino-D-glucitol-based glucocerebrosidase pharmacological chaperones for Gaucher disease intervention, *Journal of medicinal chemistry*, 50 (1), 2007 94-100.
- [385] T. Wennekes, R.J. van den Berg, W. Donker, G.A. van der Marel, A. Strijland, J.M. Aerts, H.S. Overkleeft, Development of adamantan-1-yl-methoxy-functionalized 1-deoxynojirimycin derivatives as selective inhibitors of glucosylceramide metabolism in man, *The Journal of organic chemistry*, 72 (4), 2007 1088-1097.
- [386] C.-W. Ho, Y.-N. Lin, C.-F. Chang, S.-T. Li, Y.-T. Wu, C.-Y. Wu, C.-F. Chang, S.-W. Liu, Y.-K. Li, C.-H. Lin, Discovery of different types of inhibition between the human and *Thermotoga maritima* α -Fucosidases by fuconojirimycin-based derivatives, *Biochemistry*, 45 (18), 2006 5695-5702.
- [387] I. Jefferies, B.R. Bowen, Synthesis of inhibitors of α -1, 3-fucosyltransferase, *Bioorganic & Medicinal Chemistry Letters*, 7 (9), 1997 1171-1174.
- [388] G.W. Fleet, A. Karpas, R.A. Dwek, L.E. Fellows, A. Tyms, S. Petrusson, S.K. Namgoong, N.G. Ramsden, P.W. Smith, J.C. Son, Inhibition of HIV replication by amino-sugar derivatives, *FEBS letters*, 237 (1-2), 1988 128-132.
- [389] A. Peer, A. Vasella, Synthesis of an L-Fucose-Derived Cyclic Nitrone and its Conversion to α -L-Fucosidase Inhibitors, *Helvetica chimica acta*, 82 (7), 1999 1044-1065.
- [390] H. Paulsen, M. Matzke, B. Orthen, R. Nuck, W. Reutter, Monosaccharide mit Stickstoff im Ring, XXXIX. Synthese von modifizierten α -L-Fucosidase-Inhibitoren, die 1, 5-Didesoxy-1, 5-imino-L-fucit als Basisstruktur enthalten, *European Journal of Organic Chemistry*, 1990 (10), 1990 953-963.
- [391] G. Sulzenbacher, C. Bignon, T. Nishimura, C.A. Tarling, S.G. Withers, B. Henrissat, Y. Bourne, Crystal structure of *Thermotoga maritima* α -L-fucosidase - Insights into the catalytic mechanism and the molecular basis for fucosidosis, *Journal of Biological Chemistry*, 279 (13), 2004 13119-13128.
- [392] S. Ogawa, M. Mori, G. Takeuchi, F. Doi, M. Watanabe, Y. Sakata, Convenient synthesis and evaluation of enzyme inhibitory activity of several N-alkyl-, N-phenylalkyl, and cyclic isourea derivatives of 5a-Carba- α -DL-fucopyranosylamine, *Bioorganic & Medicinal Chemistry Letters*, 12 (20), 2002 2811-2814.
- [393] M.D. Shultz, Setting expectations in molecular optimizations: strengths and limitations of commonly used composite parameters, *Bioorganic & medicinal chemistry letters*, 23 (21), 2013 5980-5991.
- [394] H.J. Wu, C.W. Ho, T.P. Ko, S.D. Papat, C.H. Lin, A.H.J. Wang, Structural Basis of α -Fucosidase Inhibition by Iminocyclitols with K_i Values in the Micro-to Picomolar Range, *Angewandte Chemie International Edition*, 49 (2), 2010 337-340.
- [395] R.Z. Batran, D.H. Dawood, S.A. El-Seginy, T.J. Maher, K.S. Gugnani, A.N. Rondon-Ortiz, Coumarinyl pyranopyrimidines as new neuropeptide S receptor antagonists; design, synthesis, homology and molecular docking, *Bioorganic chemistry*, 75 2017 274-290.
- [396] B. Campos, Z. Gal, A. Baader, T. Schneider, C. Sliwinski, K. Gassel, J. Bageritz, N. Grabe, A. von Deimling, P. Beckhove, Aberrant self-renewal and quiescence contribute to the aggressiveness of glioblastoma, *The Journal of pathology*, 234 (1), 2014 23-33.
- [397] S.-Y. Huang, S.Z. Grinter, X. Zou, Scoring functions and their evaluation methods for protein-ligand docking: recent advances and future directions, *Physical Chemistry Chemical Physics*, 12 (40), 2010 12899-12908.
- [398] R.J. Molenaar, J.P. Maciejewski, J.W. Wilmink, C.J. Noorden, Wild-type and mutated IDH1/2 enzymes and therapy responses, *Oncogene*, 2018 1.

- [399] M. Tiecco, R. Germani, F. Cardellini, Carbon–carbon bond formation in acid deep eutectic solvent: chalcones synthesis via Claisen–Schmidt reaction, *RSC Advances*, 6 (49), 2016 43740-43747.
- [400] C.-Y. Cai, L. Rao, Y. Rao, J.-X. Guo, Z.-Z. Xiao, J.-Y. Cao, Z.-S. Huang, B. Wang, Analogues of xanthenes—Chalcones and bis-chalcones as α -glucosidase inhibitors and anti-diabetes candidates, *European journal of medicinal chemistry*, 130 2017 51-59.
- [401] P. Regenass, D. Abboud, F. Daubeuf, C. Lehalle, P. Gizzi, S. Riché, M. Hachet-Haas, F. Röhmer, V. Gasparik, D. Boeglin, Discovery of a Locally and Orally Active CXCL12 Neutraligand (LIT-927) with Anti-inflammatory Effect in a Murine Model of Allergic Airway Hypereosinophilia, *Journal of medicinal chemistry*, 61 (17), 2018 7671-7686.
- [402] S. Raghavan, P. Manogaran, B.K. Kuppaswami, G. Venkatraman, K.K.G. Narasimha, Synthesis and anticancer activity of chalcones derived from vanillin and isovanillin, *Medicinal Chemistry Research*, 24 (12), 2015 4157-4165.
- [403] K. Lahtchev, D. Batovska, P. St P, V. Ubiyvovk, A. Sibirny, Antifungal activity of chalcones: A mechanistic study using various yeast strains, *European journal of medicinal chemistry*, 43 (10), 2008 2220-2228.
- [404] H.N. Pati, H.L. Holt, R. LeBlanc, J. Dickson, M. Stewart, T. Brown, M. Lee, Synthesis and cytotoxic properties of nitro- and aminochalcones, *Medicinal Chemistry Research*, 14 (1), 2005 19-25.
- [405] C.P. Shah, P.S. Kharkar, Discovery of novel human inosine 5'-monophosphate dehydrogenase 2 (hIMPDH2) inhibitors as potential anticancer agents, *European journal of medicinal chemistry*, 158 2018 286-301.
- [406] T. Keenan, D.R. Yaeger, N.L. Courage, C.T. Rollins, M.E. Pavone, V.M. Rivera, W. Yang, T. Guo, J.F. Amara, T. Clackson, Synthesis and activity of bivalent FKBP12 ligands for the regulated dimerization of proteins, *Bioorganic & medicinal chemistry*, 6 (8), 1998 1309-1335.
- [407] U. Shadakshari, S.K. Nayak, Enantioselective conjugate addition of diethylzinc to chalcones catalysed by N-trityl aziridine-2-(S)-(diphenyl) methanol and Ni (acac) 2, *Tetrahedron*, 57 (38), 2001 8185-8188.
- [408] J.R. Schmink, J.L. Holcomb, N.E. Leadbeater, Testing the validity of microwave-interfaced, in situ Raman spectroscopy as a tool for kinetic studies, *Organic letters*, 11 (2), 2008 365-368.
- [409] N. Solin, L. Han, S. Che, O. Terasaki, An amphoteric mesoporous silica catalyzed aldol reaction, *Catalysis communications*, 10 (10), 2009 1386-1389.
- [410] Y.S. Kim, V. Kumar, S. Lee, A. Iwai, L. Neckers, S.V. Malhotra, J.B. Trepel, Methoxychalcone inhibitors of androgen receptor translocation and function, *Bioorganic & medicinal chemistry letters*, 22 (5), 2012 2105-2109.
- [411] S.A. Lahsasni, F.H. Al Korbi, N.A.-A. Aljaber, Synthesis, characterization and evaluation of antioxidant activities of some novel chalcones analogues, *Chemistry Central Journal*, 8 (1), 2014 32.
- [412] A. Mishra, P. Rai, Y.K. Pandey, J. Singh, J. Singh, An Eco-Sustainable Synthetic Approach for 4, 5-Dihydro-1H-pyrazoles via DBU Catalysis in Micellar Medium, *ChemistrySelect*, 2 (34), 2017 10979-10983.
- [413] N. Raghav, M. Singh, SAR studies of differently functionalized chalcones based hydrazones and their cyclized derivatives as inhibitors of mammalian cathepsin B and cathepsin H, *Bioorganic & medicinal chemistry*, 22 (15), 2014 4233-4245.
- [414] Z. Zhang, Y.-J. Tan, C.-S. Wang, One-pot synthesis of 3, 5-diphenyl-1H-pyrazoles from chalcones and hydrazine under mechanochemical ball milling, *Heterocycles: an international journal for reviews and communications in heterocyclic chemistry*, 89 (1), 2014 103-112.
- [415] B. Bhat, S. Puri, M. Qurishi, K. Dhar, G. Qazi, Synthesis of 3, 5-diphenyl-1 H-pyrazoles, *Synthetic communications*, 35 (8), 2005 1135-1142.
- [416] C. Ding, L. Tong, J. Fu, Quadruple Stimuli-Responsive Mechanized Silica Nanoparticles: A Promising Multifunctional Nanomaterial for Diverse Applications, *Chemistry—A European Journal*, 23 (60), 2017 15041-15045.
- [417] M. Tang, Y. Wang, H. Wang, Y. Kong, Aluminum Chloride Mediated Reactions of N-Alkylated Tosylhydrazones and Terminal Alkynes: A Regioselective Approach to 1, 3, 5-Trisubstituted Pyrazoles, *Synthesis*, 48 (18), 2016 3065-3076.
- [418] J. Tang, L. Wang, Y. Yao, L. Zhang, W. Wang, One-pot synthesis of 2-amino-3-cyanopyridine derivatives catalyzed by ytterbium perfluorooctanoate [Yb (PFO) 3], *Tetrahedron letters*, 52 (4), 2011 509-511.
- [419] W.W. Tan, Y.J. Ong, N. Yoshikai, Synthesis of Highly Substituted Pyridines through Copper-Catalyzed Condensation of Oximes and α , β -Unsaturated Imines, *Angewandte Chemie International Edition*, 56 (28), 2017 8240-8244.
- [420] H. Zhang, J. Shen, G. Cheng, B. Wu, X. Cui, Base-Promoted Synthesis of 2, 4, 6-Triarylpyridines from Enaminones and Chalcones, *Asian Journal of Organic Chemistry*, 7 (6), 2018 1089-1092.
- [421] Z.-H. Ren, Z.-Y. Zhang, B.-Q. Yang, Y.-Y. Wang, Z.-H. Guan, Copper-catalyzed coupling of oxime acetates with aldehydes: A new strategy for synthesis of pyridines, *Organic letters*, 13 (19), 2011 5394-5397.

- [422] R. Karki, P. Thapa, M.J. Kang, T.C. Jeong, J.M. Nam, H.-L. Kim, Y. Na, W.-J. Cho, Y. Kwon, E.-S. Lee, Synthesis, topoisomerase I and II inhibitory activity, cytotoxicity, and structure–activity relationship study of hydroxylated 2, 4-diphenyl-6-aryl pyridines, *Bioorganic & medicinal chemistry*, 18 (9), 2010 3066-3077.
- [423] W.W. Tan, Y.J. Ong, N. Yoshikai, Synthesis of Highly Substituted Pyridines through Copper-Catalyzed Condensation of Oximes and α , β -Unsaturated Imines, *Angewandte Chemie*, 129 (28), 2017 8352-8356.
- [424] C.-G. Yan, X.-M. Cai, Q.-F. Wang, T.-Y. Wang, M. Zheng, Microwave-assisted four-component, one-pot condensation reaction: an efficient synthesis of annulated pyridines, *Organic & biomolecular chemistry*, 5 (6), 2007 945-951.
- [425] J. Han, X. Guo, Y. Liu, Y. Fu, R. Yan, B. Chen, One-pot synthesis of benzene and pyridine derivatives via copper-catalyzed coupling reactions, *Advanced Synthesis & Catalysis*, 359 (15), 2017 2676-2681.
- [426] E. Tabrizian, A. Amoozadeh, S. Rahmani, E. Imanifar, S. Azhari, M. Malmir, One-pot, solvent-free and efficient synthesis of 2, 4, 6-triarylpyridines catalyzed by nano-titania-supported sulfonic acid as a novel heterogeneous nanocatalyst, *Chinese Chemical Letters*, 26 (10), 2015 1278-1282.
- [427] M. Kamali, One-pot, solvent-free, and efficient synthesis of 2, 4, 6-triarylpyridines using $\text{CoCl}_2 \cdot 6\text{H}_2\text{O}$ as a recyclable catalyst, *Cogent Chemistry*, 2 (1), 2016 1171123.
- [428] Z. Sun, R.S. Hosmane, An improved synthesis of 9-benzyladenine: A model for adenosine and its analogues, *Synthetic Communications*, 31 (4), 2001 549-554.
- [429] M. Xie, R.K. Ujjinamatada, M. Sadowska, R.G. Lapidus, M.J. Edelman, R.S. Hosmane, A novel, broad-spectrum anticancer compound containing the imidazo [4, 5-e][1, 3] diazepine ring system, *Bioorganic & medicinal chemistry letters*, 20 (15), 2010 4386-4389.
- [430] M. Xie, R.G. Lapidus, M. Sadowska, M.J. Edelman, R.S. Hosmane, Synthesis, anticancer activity, and SAR analyses of compounds containing the 5: 7-fused 4, 6, 8-triaminoimidazo [4, 5-e][1, 3] diazepine ring system, *Bioorganic & medicinal chemistry*, 24 (12), 2016 2595-2602.
- [431] S. Baehn, S. Imm, K. Mevius, L. Neubert, A. Tillack, J.M. Williams, M. Beller, Selective Ruthenium-Catalyzed N-Alkylation of Indoles by Using Alcohols, *Chemistry—A European Journal*, 16 (12), 2010 3590-3593.
- [432] K. Higuchi, Y. Sato, S. Kojima, M. Tsuchimochi, K. Sugiura, M. Hatori, T. Kawasaki, Preparation of 2, 2-disubstituted 1, 2-dihydro-3H-indol-3-ones via oxidation of 2-substituted indoles and Mannich-type reaction, *Tetrahedron*, 66 (6), 2010 1236-1243.
- [433] K.-C. Ching, T.N.Q. Tran, S.N. Amrun, Y.-W. Kam, L.F. Ng, C.L. Chai, Structural Optimizations of Thieno [3, 2-b] pyrrole Derivatives for the Development of Metabolically Stable Inhibitors of Chikungunya Virus, *Journal of medicinal chemistry*, 60 (7), 2017 3165-3186.
- [434] S. S. Kamble, G. S. Shankarling, Amalgamation of CSR and DES: An Energy Efficient Protocol for the One-Pot Synthesis of 2, 4, 6-Triaryl Pyridine Derivatives, *ChemistrySelect*, 3 (37), 2018 10464-10467.
- [435] Chemical Computing Group ULC, Molecular Operating Environment (MOE), 2018.01, 2018.
- [436] M. Wiederstein, M.J. Sippl, ProSA-web: interactive web service for the recognition of errors in three-dimensional structures of proteins, *Nucleic acids research*, 35 (suppl_2), 2007 W407-W410.
- [437] G.N. Ramachandran, C. Ramakrishnan, V. Sasisekharan, Stereochemistry of polypeptide chain configurations, *Journal of molecular biology*, 7 (1), 1963 95-99.
- [438] C. Colovos, T.O. Yeates, Verification of protein structures: patterns of nonbonded atomic interactions, *Protein Science*, 2 (9), 1993 1511-1519.
- [439] R. Lüthy, J.U. Bowie, D. Eisenberg, Assessment of protein models with three-dimensional profiles, *Nature*, 356 (6364), 1992 83.